Pramana – journal of physics

Editor

R Nityananda
Raman Research Institute, Bangalore

Associate Editor

H R Krishnamurthy
Indian Institute of Science, Bangalore

Editorial Board

G S Agarwal, *University of Hyderabad, Hyderabad*
V Balakrishnan, *Indian Institute of Technology, Madras*
M Barma, *Tata Institute of Fundamental Research, Bombay*
P Chaddah, *Centre for Advanced Technology, Indore*
B M Deb, *Panjab University, Chandigarh*
P K Kaw, *Institute for Plasma Research, Gandhinagar*
H S Mani, *Indian Institute of Technology, Kanpur*
N Mukunda, *Indian Institute of Science, Bangalore*
T Padmanabhan, *Inter-University Centre for Astronomy and Astrophysics, Pune*
J C Parikh, *Physical Research Laboratory, Ahmedabad*
G Rajasekaran, *Institute of Mathematical Sciences, Madras*
V S Ramamurthy, *Institute of Physics, Bhubaneswar*
R Ramaswamy, *Jawaharlal Nehru University, New Delhi*
K R Rao, *Bhabha Atomic Research Centre, Bombay*
Probir Roy, *Tata Institute of Fundamental Research, Bombay*
A K Sood, *Indian Institute of Science, Bangalore*

Editor of Publications of the Academy

G Srinivasan
Raman Research Institute, Bangalore

Subscription Rates

(Effective from 1989)

All countries except India	1 year	3 years	5 years
(Price includes AIR MAIL charges)	US$ 175	$ 470	$ 700
India	1 year Rs. 100	10 years Rs. 500	

All correspondence regarding subscription should be addressed to the **Circulation Department** of the Academy

---

Editorial Office

Indian Academy of Sciences, C V Raman Avenue,
P.B. No. 8005, Bangalore 560080, India

Telephone: 342546
Telex: 845-2178 ACAD IN
Telefax: 91-80-346094

© 1993 by the Indian Academy of Sciences. All rights reserved.

"Information for contributors" is printed in the last issue of every volume.

Regd. No. KRN-A 64

Pramana journal of physics Vol. 41 (No. 1), July 1993

Contents

Underwater optical generation of sound: Oblique incidence .... *M S Sodha, V Rai, M P Verma, S Konar and K P Maheshwari* 1

Dielectric studies of some binary liquid mixtures using microwave cavity techniques .... *V Subramanian, B S Bellubbi and J Sobhanadri* 9

Effect of strain on vibrational modes in strained layer superlattices .... *Sujata Rath and Sankar P Sanyal* 21

Second order elastic anomalies in barium titanate from cubic to tetragonal phase transition .... *B Subramanyam and K S Viswanathan* 31

The effect of second neighbour repulsion on fcc binary alloy phase diagrams: A Monte Carlo study .... *Rita Khanna and T R Welberry* 41

Field-cooled measurements of harmonic generation in magnetization of high-T_c superconductors .... *S B Roy, Shailendra Kumar, A K Pradhan, P Chaddah, Ram Prasad, N C Soni and Kalyan Adhikary* 51

Critical current density of a sample of melt grown $Y_{1\cdot2}Ba_{1\cdot8}Cu_{2\cdot4}O_x$ .... *V Ganesan, R Srinivasan, R Gopalan and T Rajasekaran* 61

Electronic structure of a superconducting Bi2212 crystal by angle resolved ultra violet photoemission .... *N L Saini, J Kanski, P Srivastava, L Ilver, K B Garg and S Durcok* 67

Rapid Communication

Symmetry breaking in quantum chaotic systems .... *Akhilesh Pandey, Ramakrishna Ramaswamy and Pragya Shukla* L75

Indexed in CURRENT CONTENTS ISSN 0304–4289

Edited and published by G Srinivasan for the Indian Academy of Sciences, Bangalore 560080. Typeset at Thomson Press (I) Ltd., New Delhi 110001 and printed at Macmillan India Press, Madras 600041.

Regd No KRN A 64

Pramana journal of physics Vol. 41 (No. 2), August 1993

Contents

Review

Resolved photon processes .... *Manuel Drees and Rohini M Godbole* 83

Research Articles

q-Deformation of algebraic structures of quantum and classical mechanics .... *Debendranath Sahoo and M C Valsakumar* 125

Inflation driven by energy and curvature dependent bulk viscosity .... *C Wolf* 139

$^{6}_{\Lambda\Lambda}$He hypernucleus in $\alpha + 2\Lambda$ cluster model .... *Mahmood Mian* 145

Deuteron-induced reaction studies of the nuclear structure of ^{178}Hf .... *Raymond K Sheline, Michael M Minor, Prakash C Sood and Dennis G Burke* 151

Neutron flow or collective degrees of freedom for near barrier heavy-ion fusion .... *S Kailas and A Navin* 163

Momentum space distribution of electrons in an atom using hydrogenic wave functions .... *Nazakat Ullah* 171

L-shell subshell ionization of Au, Pb and Bi by low energy proton impact .... *K N Pandey, D N Tripathi, R N Chakraborty and D K Rai* 175

Kinetic properties of an acoustic-like mode in a two-ion quasi-neutral plasma .... *C B Dwivedi* 185

Rapid Communication

Conservation laws in stochastic deposition evaporation models in one dimension .... *Deepak Dhar and Mustansir Barma* R193

Comments

Comment on: Modified perturbation series for the anharmonic oscillator using linearization technique .... *Biswanath Rath and K Pattnayak* C199

Reply to the comment on 'Modified perturbation series for the anharmonic oscillator using linearization technique .... *Nazakat Ullah* C201

Indexed in CURRENT CONTENTS ISSN 0304-4289

Edited and published by G Srinivasan for the Indian Academy of Sciences, Bangalore 560080. Typeset at Thomson Press (I) Ltd, New Delhi 110001 and printed at Macmillan India Press, Madras 600041

Regd. No. KRN-A 64

Pramana journal of physics Vol. 41 (No. 3), September 1993

Contents

Research Articles

Anomalies in second order elastic constants and gyrotropic constants of triglycine sulphate near phase transition .... *B Subramanyam and K S Viswanathan* 203

Surface acoustic wave distribution and acousto-optic interaction in proton exchanged $LiNbO_3$ waveguides .... *P Annachelvi, A Selvarajan and G V Anand* 209

Switching of partially switched $KNbO_3$ single crystals containing cooperatively ordered impurity dipoles .... *S G Ingle and R N Kakde* 219

Investigations on thermoelectric power of lanthanum oxide doped ferroelectric sodium vanadate .... *D V Pawar, T S Magdum, S P Rasal and S H Chavan* 233

Electronic structure of hydrogen and muonium in Al, Mg and Cu .... *Pawan Singh and S Prakash* 239

Laser produced plasma: A pumping source for cadmium photo-ionization laser .... *Rekha Tambay and Raj K Thareja* 257

A translational energy spectrometer to probe interatomic potentials: Dissociation dynamics of CO_2^+ ions .... *M Krishnamurthy, U T Raheja and D Mathur* 271

Brief Report

Further studies on Ag/BPSCCO tapes using low purity materials .... *S R Shukla, Y S Reddy, N Kumar, S K Sharma and R G Sharma* 285

Rapid Communication

Influence of various gases on single bubble sonoluminescence .... *Vijay H Arakeri* L291

Indexed in CURRENT CONTENTS ISSN 0304–4289

Edited and published by G Srinivasan for the Indian Academy of Sciences, Bangalore 560080. Typeset at Thomson Press (I) Ltd., New Delhi 110001 and printed at Macmillan India Press, Madras 600041.

Regd. No. KRN-A 64

Pramana journal of physics Vol. 41 (No. 4), October 1993

Contents

Controlling of chaos by weak periodic perturbations in Duffing–van der Pol oscillator .... *S Rajasekar* 295

Mathematical analysis of isobaric decay chain in alpha particle induced reactions .... *S Mukherjee, N L Singh and J Rama Rao* 311

Measurement and analysis of the excitation functions for alpha particle induced reactions on niobium .... *S Mukherjee, M H Rashid and S N Chintalapudi* 329

Sub-barrier fission fragment angular distributions for the system ^{19}F + ^{232}Th .... *S Kailas, A Navin, A Chatterjee, P Singh, A Saxena, D M Nadkarni, D C Biswas, R K Choudhury and S S Kapoor* 339

Ab-initio Hartree–Fock self-consistent-field calculations – An indigenous development of computer programs .... *Sambhu N Datta* 345

Ab-initio nonrelativistic and relativistic Hartree–Fock calculations for both closed- and open-shell molecules using GTO basis .... *Sambhu N Datta* 363

Electron impact excitation of Ni XIX using the *R*-matrix method .... *Man Mohan, M Le Dourneuf, A Hibbert and V M Burke* 371

Dynamics of immiscible radial viscous fingering: A numerical study .... *Subir K Sarkar and David Jasnow* 389

Indexed in CURRENT CONTENTS ISSN 0304–4289

Edited and published by G Srinivasan for the Indian Academy of Sciences, Bangalore 560 080. Typeset at Thomson Press (I) Ltd., New Delhi 110 001 and printed at Macmillan India Press, Madras 600 041.

Regd. No. KRN-A 64

Pramana journal of physics Vol. 41 (No. 5), November 1993

Contents

Research Articles

A model for the analysis of the heat release from a supercooled liquid at the glass transition ....*M Rajeswari and A K Raychaudhuri* 401

Thermal expansion of orthorhombic and tetragonal phases of the high T_C superconductors $RE_1Ba_2Cu_3O_y$ (RE = Y, Gd, Dy) ....*Om Prakash, Ashok Rao, O Prakash and P N Dheer* 421

Magnetic properties of ultra-fine particles of $Mn_{0\cdot5}Fe_{0\cdot5}Fe_2O_4$ spinel system .... *R V Upadhyay and R V Mehta* 429

Electric field gradient in transition metal – scandium ....*B B Panigrahi and N C Mohapatra* 443

Heating mechanism in relation to the laser machining process ....*Bekir S Yilbas and Ahmet Z Sahin* 453

SERS studies on 1-4 dihydroxyanthraquinone at Ag electrode ....*V G Srikanth, S Edwin Jayaraj and V Ramakrishnan* 467

A design of an inexpensive demountable X-ray tube .... *V S Pai, N V Moghe and V B Sapre* 473

Rapid Communication

Geometric phase as a simple closed-form integral .... *Apoorva G Wagh and Veer Chand Rakhecha* L479

Indexed in CURRENT CONTENTS ISSN 0304–4289

Edited and published by G Srinivasan for the Indian Academy of Sciences, Bangalore 560080. Typeset at Thomson Press (I) Ltd., New Delhi 110001 and printed at Macmillan India Press, Madras 600041.

Regd. No. KRN-A 64

Pramana journal of physics Vol. 41 (No. 6), December 1993

Contents

Uniqueness of the solutions of multichannel scattering equation in three particle system .... *Suprokash Mukherjee* 483

Energy levels of a two-dimensional anharmonic oscillator: Hill determinant approach .... *M R M Witwit* 493

Integration method for the Dirac equation .... *V G Bagrov and V V Obukhov* 503

Quantum instability for a wave packet kicked periodically by a quadratic potential .... *A K Sikri and M L Narchal* 509

A semi-empirical formula for the energy spacings in Λ-hypernuclear excitation spectra .... *M Z Rahman Khan and Nasra Neelofer* 515

L-dependent heavy ion fusion potentials .... *S V S Sastry, A K Mohanty and S K Kataria* 525

Collective bounce-off phenomenon in ^{139}La + Ag(Br) reaction at 1·1 A GeV energy .... *B Singh, H S Palsania, V Kumar, K B Bhalla and S Lokanathan* 535

Subject Index 551

Author Index 557

Information for contributors

Indexed in CURRENT CONTENTS ISSN 0304–4289

Edited and published by G Srinivasan for the Indian Academy of Sciences, Bangalore 560 080. Typeset at Thomson Press (I) Ltd., New Delhi 110 001 and printed at Macmillan India Press, Madras 600 041.

PRAMANA
— journal of
physics

© Printed in India

Vol. 41, No. 1,
July 1993
pp. 1–7

Underwater optical generation of sound: Oblique incidence

M S SODHA*, V RAI[†], M P VERMA, S KONAR and K P MAHESHWARI
School of Physics, Devi Ahilya University, Khandwa Road, Indore 452001, India
*Vice-Chancellor, Lucknow University, Lucknow 226007, India
[†] For correspondence

MS received 26 March 1993

Abstract. This paper addresses itself to the problem of thermoacoustic generation by an obliquely incident laser beam in a body of water. Far-field directivity pattern of thermoacoustic source (TS) has been studied analytically and numerically. Our study suggests the possibility of getting highly directional sound beams in a simple configuration.

Keywords. Laser generation of sound; thermoacoustic source (TS); far-field directivity pattern; directional sound beams.

PACS Nos 42·60; 43·35

1. Introduction

Laser excited thermoacoustic sources (TS) may offer a promising way of communicating with submarines from an air-borne system. These optical sources have two major advantages over those generated by conventional means: i) They do away with the need of placing a transducer in water and ii) the sound field generated is generally directional [1–2].

When an intensity modulated laser beam is incident on a body of water it produces a periodic sequence of compressions and rarefactions of the medium due to heating of the water body. These acoustic perturbations have the same frequency as the modulation frequency of the laser intensity and propagate with velocity corresponding to this frequency. Westervelt and Larson [3] were the first to investigate the strength and directivity of TS generated by an intensity modulated laser beam incident normally on a water body. However, the effect of the pressure-release characteristic of the air-water interface was not considered in their theory. Later Lyamshev [4] presented a refined theory incorporating this characteristic of the air-water boundary. Since then many authors [2, 5–7] have investigated different configurations of the thermal generation of sound so as to improve the strength and directivity of these sources. In particular, Berthelot and Busch-Vishniac [5] (BB) have studied a configuration of laser generation of sound exploiting the thermal mechanism in which the intensity modulated laser beam is incident obliquely on a water surface. It should be noted that the BB theory of oblique incidence assumes uniform distribution of the laser intensity over the cross-section of the beam. The beam is assumed to be narrow so that it can be effectively replaced by a ray. They restrict the field (observation) point to lie in the plane of incidence.

The symmetry of the problem, however, suggests that the sound field will depend on the angular displacement of the field point from the plane of incidence. We have, therefore, revised BB analysis obtaining an expression for the sound field at any distant point in the water not restricted to lie in the plane of incidence. It should be added that the first assumption, which is valid when the transverse dimensions of the laser beam is very small compared to the acoustic wavelength of the sound produced, is retained in our theory. The reason for this is that most of the real situations honour the validity of this assumption.

2. The present theory

If the distance up to which the heat generated by the incident laser beam diffuses during an acoustic period can be considered to be smaller than the transverse linear dimension of the laser beam, the acoustic pressure [8] p in the linear approximation satisfies

$$\nabla^2 p - \frac{1}{c^2}\frac{\partial^2 p}{\partial t^2} = -\frac{\beta}{c_p}\frac{\partial Q}{\partial t}. \tag{1}$$

In this equation c is the velocity of the acoustic perturbations in the medium, β the logarithmic coefficient of thermal expansion, c_p the specific heat per unit mass, and Q the optical energy absorbed per unit time per unit volume of the medium. It should be noted that the viscosity effects of the medium have been neglected in deriving the above equation for the acoustic pressure.

Equation (1) is a fundamental equation known as inhomogeneous wave equation in the literature. Our aim is to find out the amplitude of the acoustic pressure at a given field point in the body of water.

If the heat is produced by the energy loss from a laser beam modulated at a frequency ω, the quantity Q in (1) can be written as

$$Q = \alpha I \exp(-\alpha\hat{z} - i\omega t), \tag{2}$$

where I represents the incident intensity of the laser beam, α its absorption coefficient in water, and $\hat{z}$ the distance travelled by the beam from the point of entry into water.

Since we are considering the thermal mechanism, the TS will radiate sound at the modulation frequency of the laser source only. Thus, we have

$$p(\mathbf{R},t) = \tilde{p}(\mathbf{R})\exp(-i\omega t) \tag{3}$$

where the acoustic pressure amplitude $\tilde{p}(\mathbf{R})$ is a function of space only.

It can be shown that the amplitude of the acoustic pressure $\tilde{p}(\mathbf{R})$ can be written as

$$\tilde{p}(\mathbf{R}) = (i\alpha\beta\omega/4\pi c_p)\int_{V'} I\exp(-\alpha z)\frac{\exp(ik|\mathbf{R}-\mathbf{R}_s|)}{|\mathbf{R}-\mathbf{R}_s|}\mathrm{d}V' \tag{4}$$

where V' is the total volume of the TS and the function

$$\frac{\exp(ik|\mathbf{R}-\mathbf{R}_s|)}{|\mathbf{R}-\mathbf{R}_s|}$$

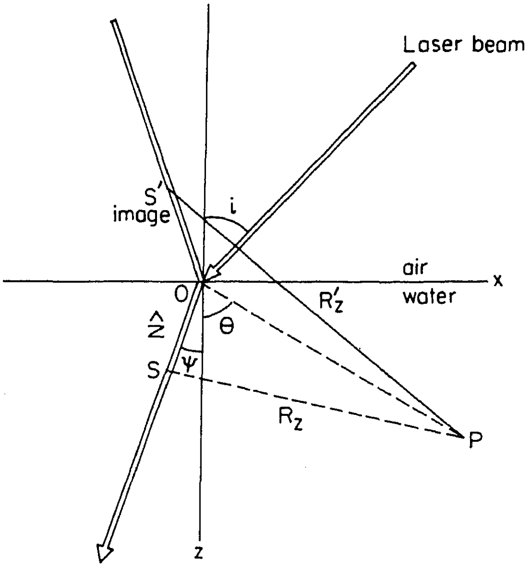

Figure 1. Schematics of optoacoustic generation of sound.

represents the effect of a source of unit strength situated at $\mathbf{R}_s$ and measured at a field point $\mathbf{R}$.

The geometry of the problem is shown in figure 1. For a CW laser in visible or infrared region, the refractive index of air with respect to water is $\approx 0{\cdot}75$. Therefore the angle of refraction ψ is given by

$$\sin\psi \simeq 0{\cdot}75 \sin i. \tag{5}$$

Let us take a source point S in water which is a distance $\hat{Z}$ ($=$ OS) away from the origin. The three coordinates of the point S will be $(-\hat{Z}\sin\psi, 0, \hat{Z}\cos\psi)$. We choose a field point P which is a distance R away from the origin of the coordinate system and makes an angle Θ with the z-axis. If ϕ is the angle between the $x-z$ plane and the plane containing the field point P and the z-axis, then the coordinates of P are $(R\sin\Theta\cos\phi, R\sin\Theta\sin\phi, R\cos\Theta)$. Now, the distance R_z between the field point P and the source point can be expressed in the far-field approximation (i.e., $\mathrm{OS} = \hat{Z} \ll R$) as

$$R_z \simeq R - \hat{Z}(\cos\Theta\cos\psi - \sin\Theta\sin\psi\cos\phi). \tag{6}$$

In the case of the image source, we can write

$$R_z' \simeq R + \hat{Z}(\cos\Theta\cos\psi + \sin\Theta\sin\psi\cos\phi). \tag{7}$$

Assuming uniform distribution of the intensity over the wavefront of the laser beam equation (4) in the present case reduces to

$$\tilde{p}(R,\Theta,\phi) = (i\alpha\beta\omega \mathrm{IS}/4\pi c_p)\int_0^\infty \exp(-\alpha\hat{z})(\exp(ik|\mathbf{R}_z|)/|\mathbf{R}_z|)\mathrm{d}\hat{Z} \tag{8}$$

where S is the cross-sectional area of the laser beam and R_z is given by (6). It should be noted that (8) is valid only when the transverse dimensions of the laser beam is much smaller than an acoustic wavelength. A similar expression can be written for the contribution to $\tilde{p}(R,\Theta,\phi)$ from the image source with an opposite phase:

$$\tilde{p}(R,\Theta,\phi) = -(i\alpha\beta\omega \mathrm{IS}/4\pi c_p)\int_0^{\infty} \exp(-\alpha\hat{z})(\exp(ik|\mathbf{R}'_z|)/|\mathbf{R}'_z|)\mathrm{d}\hat{Z} \tag{9}$$

where R'_z is given by (7).

The following expression is obtained for the amplitude of the resultant acoustic pressure:

$$\begin{aligned}|\tilde{p}_{\mathrm{res}}(\mathbf{R})| &= |\tilde{p}(\mathbf{R})| + |\tilde{p}_{\mathrm{image}}(\mathbf{R})|\\ &= \tilde{p}_{\mathrm{res}}(\mathbf{R}) = \frac{K}{\alpha R}\,\frac{2\sigma|\cos\Theta\cos\psi|}{\begin{bmatrix}\{1+\sigma^2(\cos^2\Theta\cos^2\psi-\sin^2\Theta\sin^2\psi\cos^2\phi\}^2\\ +4\sigma^2\sin^2\Theta\sin^2\psi\cos^2\phi\end{bmatrix}^{1/2}}.\end{aligned} \tag{10}$$

where K is a constant ($K=\alpha\beta\omega\mathrm{IS}/4\pi c_p$), and σ is the ratio of the acoustic wave number (k) to the optical absorption coefficient α. The directivity function can be written as

$$D(\Theta,\phi) = \frac{2\sigma|\cos\Theta\cos\psi|}{\begin{bmatrix}\{1+\sigma^2(\cos^2\Theta\cos^2\psi-\sin^2\Theta\sin^2\psi\cos^2\phi\}^2\\ +4\sigma^2\sin^2\Theta\sin^2\psi\cos^2\phi\end{bmatrix}^{1/2}}. \tag{11}$$

It should be noted that our directivity function for TS depends on both the angles Θ and ϕ, and reduces to the BB expression for $\phi = 0$.

3. Results and discussion

The directivity pattern shown in (11) clearly indicates interdependence of Θ and ϕ. A significant observation that can be made immediately is that $D(-\Theta,\phi) = D(\Theta,\phi)$. This may appear rather unexpected in view of the geometry of the TS (figure 1), but, is not at all strange as our results and also those of reference 5 to which our results go in the limit $\phi = 0$ are the resultant effect of the source generated in water and the image source arising due to the boundary condition $p = 0$ at $z = 0$.

In addition to dependence on the coordinates Θ and ϕ, the directivity function $D(\Theta,\phi)$ depends on parameters namely $\sigma = k/\alpha$ and ψ. These parameters are fixed by the geometry, the laser source, and sound frequencies (chosen keeping in mind the relevant properties of sea water). Once σ and ψ are selected only Θ and ϕ determine the directivity. We have therefore organized the graphs showing the dependence of $D(\Theta,\phi)$ on Θ, ϕ and ψ in six polar diagrams (figures 2a to 4b). These graphs are to be considered in pairs. Thus, figures 2a and 2b show the dependence of $D(\Theta,\phi)$ on $\phi(0<\phi<\pi)$ for five chosen Θ values, a fixed ψ, and $\sigma = 10$ and $\sigma = 3$, respectively. Figures 3a and 3b show the dependence on ϕ for three chosen ψ values, a fixed $\sigma(=10)$ and two Θ values while figures 4a and 4b depict the dependence of $D(\Theta,\phi)$ on $\Theta(0<\Theta<\pi/2)$ for four chosen ϕ values and a fixed ψ for two distinct σ values ($\sigma = 10$ and $\sigma = 3$), respectively. The six graphs taken collectively present interesting features of the directivity pattern. The patterns clearly suggest the interdependence

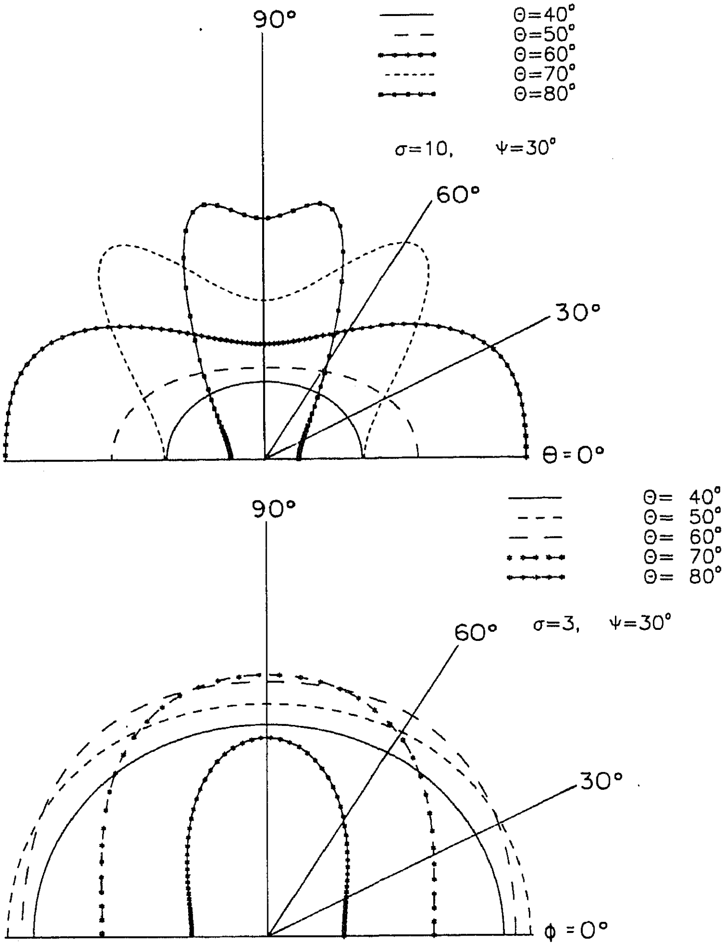

Figure 2. Directivity $D(\Theta, \phi)$ as a function of ϕ. **a)** $\sigma = 10$, $\psi = 30°$; **b)** $\sigma = 3$, $\psi = 30°$.

of Θ and ϕ demonstrating that the maximum intensity is obtained in the neighbourhood of a particular ϕ at a given Θ even though this maximum may not be substantially different from the one obtained from another set of (Θ, ϕ). However, the sharpness of the acoustic field is distinctly pronounced in the case $\sigma = 10$ as compared to $\sigma = 3$ (cf. figures 2a, 2b and 4a, 4b).

Figures 4a and 4b further show that $D(\Theta, \phi)$ goes to the same limiting values at $\Theta = 0$ for all different ϕ as they should. The limits in the two figures differ mainly because of the different σ values chosen and can be easily understood as the different σ values essentially determine the array length via the absorption coefficient α. One can see that as k/α acquires a smaller value the intensity in $\Theta = 0$ direction increases substantially. This is because either or both of two factors namely (i) the conversion efficiency increases as $k \rightarrow \alpha$ and (ii) as the array length reduces the intensity along the length of the array increases. These observations are in general in accordance with the properties of linear arrays [1].

This configuration of the laser generation of sound seems to be useful in applications which demand highly directional sound beams; e.g., in situations when one

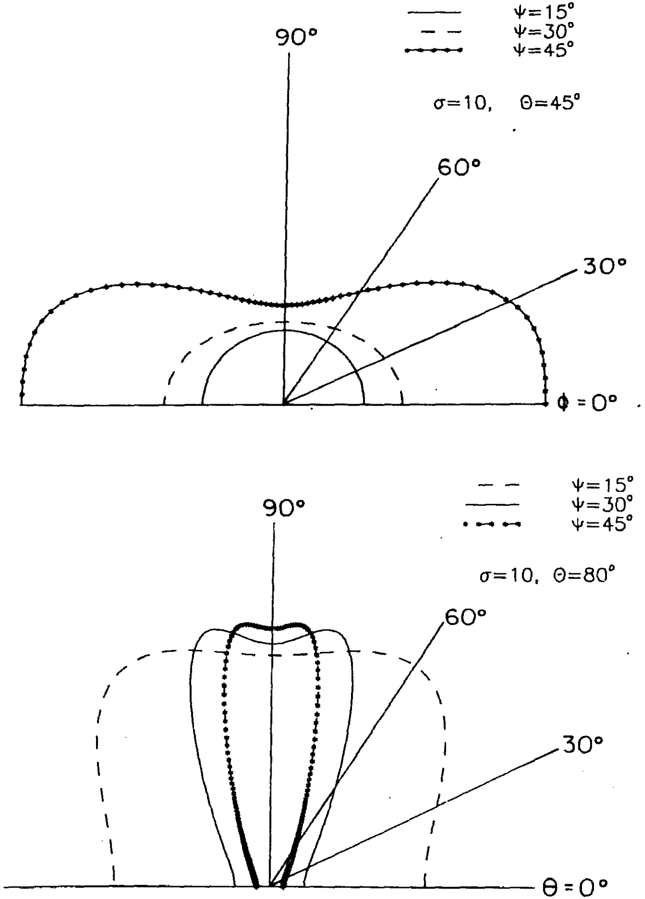

Figure 3. **a)** $\sigma = 10$, $\Theta = 45°$; **b)** $\sigma = 10$, $\Theta = 80°$.

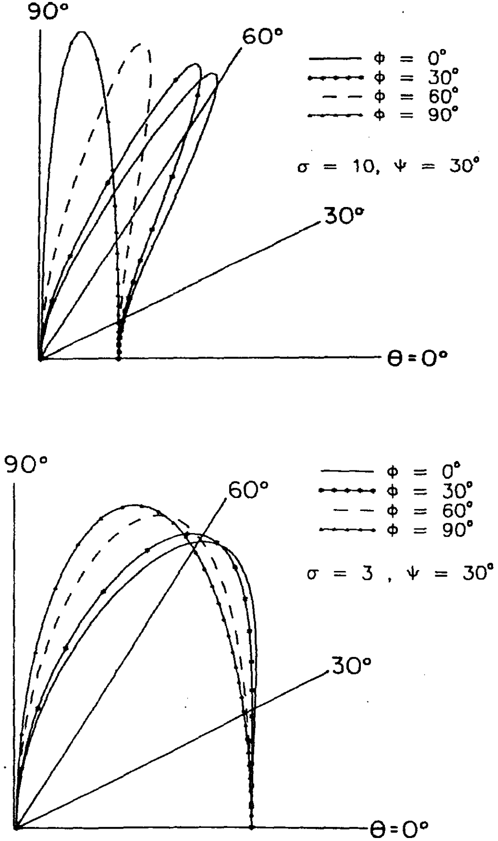

Figure 4. Directivity $D(\Theta, \phi)$ as a function of Θ. **a)** $\sigma = 10$, $\psi = 30°$; **b)** $\sigma = 3$, $\psi = 30°$.

approximately knows the position of the submarine to be communicated with. The main advantage of the present configuration of TS lies in the fact that the generated acoustic field can be controlled very easily by varying the parameters k and α of the laser beam and the angle of incidence. The configuration suggested in this paper turns out to be the simplest possible when one compares it with those existing in the literature. Moreover, in most practical applications the laser beam strikes the water surface obliquely. Therefore, the results of the present study might be helpful in applications where lasers are used to generate highly directional sound beams; e.g., air-sea communication.

Acknowledgements

This work is financially supported by the Department of Electronics, Government of India. We are thankful to the referee for some very useful suggestions.

References

[1] L M Lyamshev and L V Sedov, *Sov. Phys. Acoust.* **27**, 4 (1981)
[2] Y H Berthelot and I J Busch-Vishniac, *J. Acoust. Soc. Am.* **81**, 317 (1987)
[3] P J Westervelt and R S Larson, *J. Acoust. Soc. Am.* **54**, 121 (1973)
[4] L M Lyamshev, *Sov. Phys. Acoust.* **23**, 96 (1977)
[5] Y H Berthelot and I J Busch-Vishniac, in *Progress in underwater acoustics*, edited by H M Merklinger (Plenum, New York, 1987) p. 603
[6] Y H Berthelot, *J. Acoust. Soc. Am.* **83**, 1399 (1988)
[7] A D Pierce and H A Hsieh, in *Progress in underwater acoustics*, edited by H M Merklinger (Plenum, New York, 1987), p. 595
[8] P M Morse and K U Ingand, *Theoretical acoustics* (McGraw Hill, New York: 1968) Ch. 6, p. 241

PRAMANA
— journal of
physics

© Printed in India

Vol. 41, No. 1,
July 1993
pp. 9–20

Dielectric studies of some binary liquid mixtures using microwave cavity techniques

V SUBRAMANIAN, B S BELLUBBI and J SOBHANADRI
Department of Physics, Indian Institute of Technology, Madras 600036, India

MS received 15 February 1993; revised 22 April 1993

Abstract. The excess parameter studies in the microwave frequency region (X-band) on complex dielectric permittivity for the binary mixtures are reported. The methods employed are fixed cavity perturbation technique and adjustable plunger cavity technique. Also Gopalakrishna method is used to calculate the relaxation time of the polar solute in a non-polar solvent. The samples under study are acetonitrile, chlorobenzene, dimethyl formamide, carbon tetrachloride and benzene.

Keywords. Cavity techniques; excess dielectric parameter; acetonitrile; dimethyl formamide and chlorobenzene binary mixtures; relaxation time.

PACS Nos 77·20; 77·40

1. Introduction

When a binary mixture is formed, the expected properties such as thermodynamic parameters, volume measurement, dielectric parameters and refractive index do not vary linearly [1]. The deviation of these parameters from the linear behaviour (termed as *excess parameters*) is considered to be very important and helps to find the nature of bonding between the two liquids. The polar–non-polar binary mixtures are studied with acetonitrile(AN), chlorobenzene(CBZ) and dimethyl formamide(DMF) in carbon tetrachloride(CTC) and benzene(BZ). The binary mixture of polar–polar combination is also studied with AN in CBZ. Gopalakrishna's method [2] is used to study the variation of relaxation time of polar liquid, AN, highly diluted mixture in non-polar solvents, CTC and BZ. Adjustable plunger cavity method described elsewhere [3] is used for most of the dilute solution studies.

2. Experimental techniques

2.1 *Fixed cavity perturbation technique*

The expression to find the complex dielectric permittivity of a solid sample (cylindrical or rectangular shaped) inserted in an electric field maximum position in a rectangular cavity (TE_{10p} mode; p can be any integer denoting the number of half wavelengths inside the cavity in the propagation direction) given by Murthy and Raman [4] is modified for liquid samples to get

$$\varepsilon' = 1 + \frac{V_c*(1/f_2^2 - 1/f_1^2)*f_0^2}{4V_s} \tag{1}$$

and

$$\varepsilon'' = \frac{V_c * f_0^2 * (1/(f_2^2 Q_2) - 1/(f_1^2 Q_1))}{4 * V_s} - \frac{(\varepsilon' - 1)}{Q_0} \tag{2}$$

where

f_0, f_1 and f_2 = Resonant frequencies of the empty, with holder and with sample loaded cavity respectively.

and

Q_0, Q_1 and Q_2 = Quality factors of the empty, with holder and with sample loaded cavity respectively

V_c and V_s = Volume of the cavity and sample respectively.

The derivations are based on the lumped resonance circuit approximation. The resonance frequency of the cavity changes because of the change in the lumped capacitance due to the insertion of the sample. The sample is kept at the electric field maximum in the cavity.

2.2 *Adjustable plunger cavity technique*

A plunger waveguide is converted into a cavity by introducing a coupling hole in the entrance and shorting the other end with the calibrated plunger. The sample occupies the entire volume of the cavity. The frequency is kept constant and the length of the plunger cavity is changed. Hence several nodes appear as one increases the length of the cavity plunger. Whenever the length of the cavity equals the half integral multiples of the guide wavelength inside the medium, the plunger waveguide resonates. The distance through which the plunger is moved between two successive cavity nodes gives half of the wavelength (λ_d) of the microwave inside the medium. The measurement of reflected power at resonance gives the attenuation coefficient of the sample [3].

$$P_1 = 1 - \frac{1}{2\lambda_d}\left[\frac{\beta^2(1 - \exp(-2\alpha\lambda_d))}{2\alpha(\alpha^2 + \beta^2)} + \lambda_d \exp(-\alpha\lambda_d)\right] \tag{3}$$

where α is the attenuation constant to be calculated, λ_d the wavelength inside the medium measured, β the propagation constant, $2 * \pi/\lambda_d$ and ρ_1 the normalized reflected power at TE_{101} mode.

2.3 *Relaxation time measurement*

Sobhanadri [5] and Gopalakrishna [2] have suggested two different techniques of measuring the relaxation time of binary mixture. Both the methods use single frequency concept. Sobhanadri's method requires the measurement of refractive index of the mixture as well as the complex dielectric permittivity. This method gives the dipole moment of the particular mixture directly and from that, the relaxation time can be calculated.

Gopalakrishna's method uses the concentration variation at single frequency. The derivations are based on the Debye's equation [6] for the complex dielectric permittivity as a function of frequency for a dilute solution of a polar compound in a non-polar solvent and is given by

$$\frac{\varepsilon^*-1}{\varepsilon^*+2}=\frac{\varepsilon_\infty-1}{\varepsilon_\infty+2}+\frac{4\pi n\mu^2}{9KT}\frac{1}{1+i\omega\tau} \tag{4}$$

where n is the concentration of dipole molecules and ε^* is the complex dielectric permittivity, ω is the angular frequency of the microwave, τ is the relaxation time of the mixture, K is the Boltzman's constant and T is the temperature. Splitting ε^* into real and imaginary parts

$$\frac{\varepsilon'^2+\varepsilon'+\varepsilon''^2-2}{(\varepsilon'+2)^2+\varepsilon''^2}=\frac{\varepsilon_\infty-1}{\varepsilon_\infty+2}+\frac{4\pi n\mu^2}{9KT}\frac{1}{1+\omega^2\tau^2},$$

$$=x(\text{say}), \tag{5}$$

$$\frac{3\varepsilon''}{(\varepsilon'+2)^2+\varepsilon''^2}=\frac{4\pi n\mu^2}{9KT}\frac{\omega\tau}{1+\omega^2\tau^2},$$

$$=y(\text{say}). \tag{6}$$

Writing $(\varepsilon_\infty-1)/(\varepsilon_\infty+2)$ as P,

$$x=P+y/\omega\tau. \tag{7}$$

For various low dilution mixtures, the values of x and y are calculated by measuring ε' and ε''. The slope of the graph, x against y, gives the relaxation time. The slope observed is not a constant as expected, but varies with concentration. Hence, a graph between the relaxation time and concentration can be plotted.

3. Experimental procedure

The samples used here are all analytical grade samples and twice distilled before use. All the measurements are carried out at room temperature (27°C) and at 9·1 GHz frequency.

3.1 *Fixed cavity perturbation*

The experiments are carried out using a microwave bench consisting of an X-band Klystron (Varian X-13). The cavity used here is a reflection type TE_{105} mode rectangular cavity with resonance frequency 9·15674 GHz. A specially designed sample holder is used to keep the sample at the electric field maximum in the cavity. To avoid the error in measuring the volume of the sample, a standardization procedure is adopted. The shift in resonance frequency with holder and with sample of known dielectric permittivity is measured. By this the constant $(V_c * f_0^2/(4 * V_s))$ is calculated. The cavity resonance is plotted and the resonance frequency and the quality factor are noted for cavity with holder and with sample. Using these, the complex dielectric permittivity can be calculated.

3.2 *Adjustable plunger cavity*

A standard non-lossy sample, benzene or carbontetrachloride fills the entire cavity volume. The reflected power at a cavity resonance is noted. This serves as the reference (zero) level for all the future power measurements. The maximum power flow into the cavity (P_0) is also noted. Now the sample liquid fills the cavity and the reflected power is monitored for various thicknesses of the sample. All the power measurements are normalized with respect to P_0. The cavity resonances for the first two nodes are obtained. The distance moved between two successive nodes gives half the wavelength of the microwave (λ_d) inside the sample. The reflected power at resonance for the first node is noted as P_1. Using (3), the attenuation coefficient can be calculated. The complex dielectric permittivity can be calculated from α and β.

4. Results and discussion

The binary mixtures of AN in BZ, CTC and CBZ are studied. The excess dielectric parameters in each case is plotted in figures 1, 2 and 5 respectively. Figures 3 and 4 describe the variation of dielectric parameters for the binary mixtures of DMF in BZ and CTC. The variation of dielectric parameters for the binary mixtures of CBZ in CTC is described in figure 6.

All the samples chosen are aprotic in nature. The excess parameters are calculated by the formula defined by Payne and Theodorou [7].

$$\Delta\varepsilon_m^* = \varepsilon_m^* - (X_1\varepsilon_1^* + X_2\varepsilon_2^*) \tag{8}$$

where ε_m^* is the dielectric parameter for the mixture, ε_1^* and ε_2^* are the values for pure components, and X_1 and X_2 are their respective mole fractions. For the ideal mixture, the excess parameter is zero, but real mixtures have finite values. The excess may be positive or negative depending on the complex formation.

For the aprotic binary systems, primary interactions will be dipole–dipole and dipole–induced dipole interactions. This is controlled by the molecular structure of the added component in the case of AN.

It is well-known from the conventional thermodynamic studies [1, 8] that AN–BZ and AN–CTC binary mixtures show positive excess heats, free energy and small negative excess volume. The excess functions are observed to be small for BZ mixtures than CTC mixtures. The excess heat is a measure of the number of hydrogen bonds or other electrostatic interactions broken as a result of formation of the binary mixture. The excess entropy is negative if some orientational ordering exists as a result of hydrogen bond formation or due to self assosciation as in the case of AN. At higher concentration of AN, the excess entropy is negative. But on dilution, it becomes less negative. At around 0·3 to 0·4 mole fraction, the excess heat is positive and its value is maximum.

Kolling [9] had fit the non-linear variation of dielectric parameter with mole fraction at radio frequency (5 MHz) to get the correlation functions and dipolarities. Work on excess dielectric parameter at radio frequency is reported by Kolling [10] on AN. The excess functions clearly show a maximum in the mole fraction range 0·5–0·55.

The excess dielectric permittivity is associated with the polarization and loss is related to the molecular motions which are governed by complex forces of intermolecular interactions. Thus the excess loss can be regarded as a parameter which reflects the entropy change in a binary system. Hence the observed excess dielectric parameters for AN–BZ and AN–CTC binary mixtures in the microwave region coincide well with the excess entropy data and RF data. A similar trend is also observed for DMF–BZ and DMF–CTC mixtures.

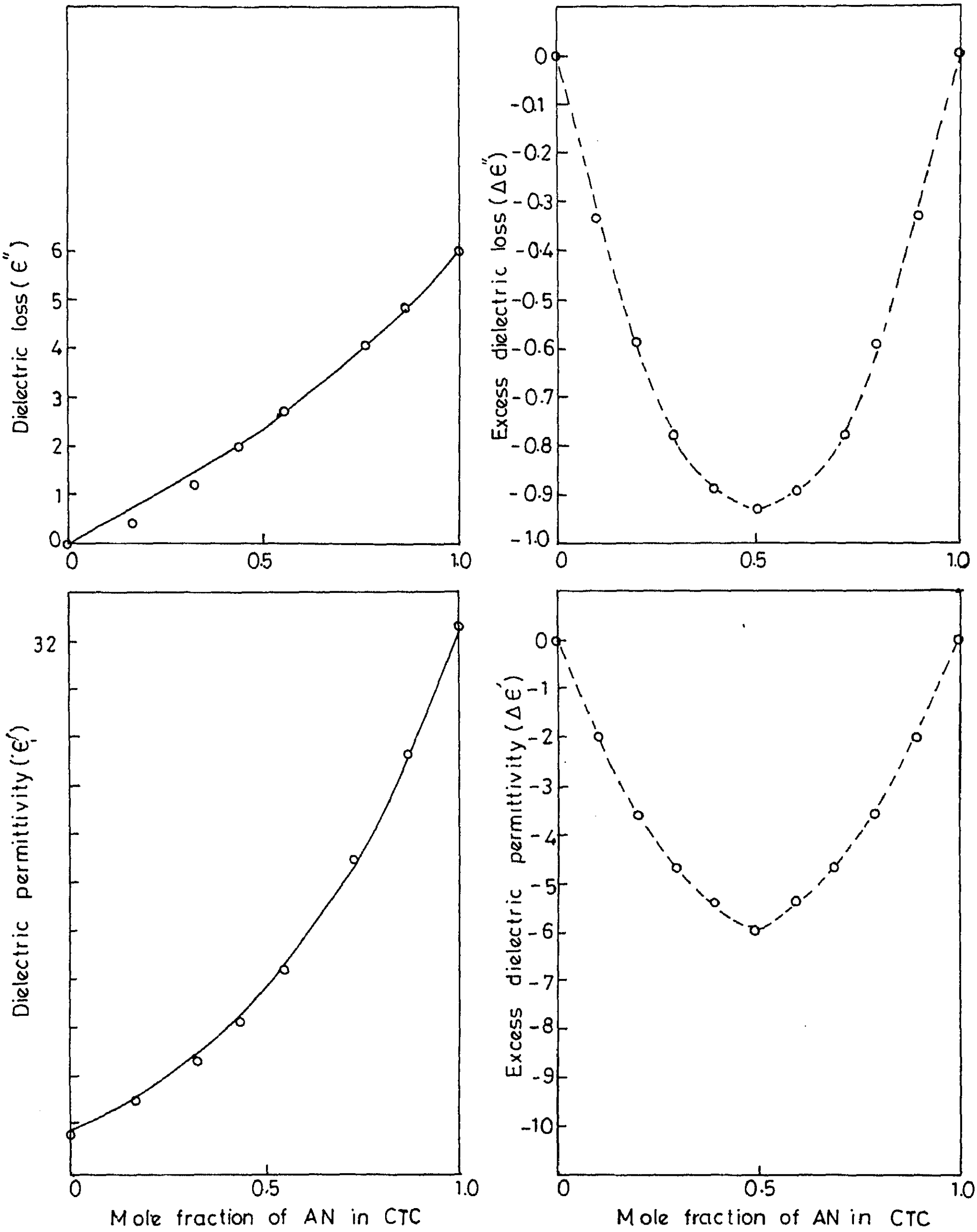

Figure 1. Dielectric permittivity, loss, excess dielectric permittivity and excess dielectric loss for AN–CTC system.

The excess permittivity for AN–CBZ system is negative whereas the excess loss is positive. But around 33 GHz, the excess loss is observed as negative [11]. It appears to be that the excess dielectric loss is zero for a microwave frequency between *X* band and *Q* band for all the binary mixture combination. It may be explained from the fact that the dielectric loss is observed as maximum around 21 GHz for pure CBZ whereas AN has the maximum loss around 33 GHz. For CBZ–CTC system, the

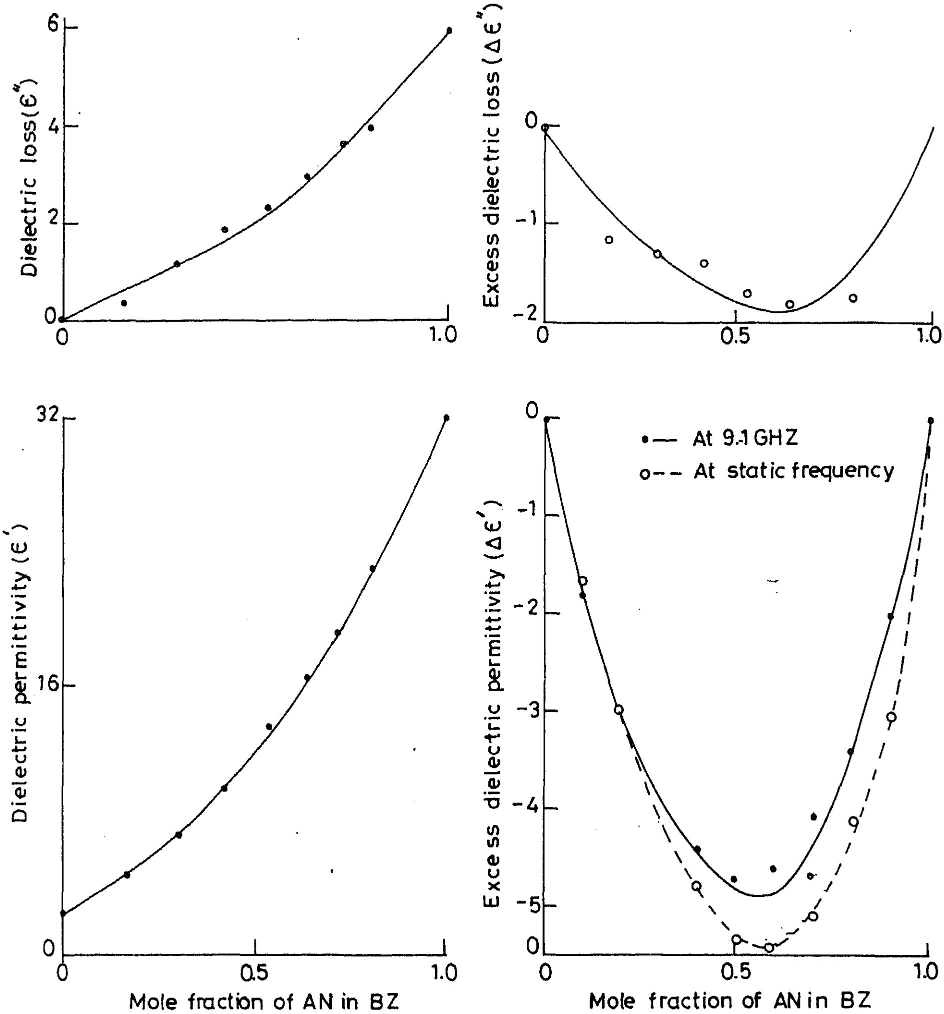

Figure 2. Dielectric permittivity, loss, excess dielectric permittivity and excess dielectric loss for AN–BZ system.

excess dielectric parameter is positive at 9·1 GHz reflecting the trend of AN–CBZ system.

One of the aprotic samples, AN is highly diluted in CTC and BZ and the relaxation time is measured using Gopalakrishna's method. This is shown graphically in figure 7. It is observed that the relaxation time tends to increase around 0·15 mole fraction in both cases. To verify this trend, the relaxation time is measured using conventional plunger technique by plotting Cole–Cole plots.

Though the cosolvents CTC and BZ are non-polar, these affect the relaxation time of the aprotic polar molecules. Even in the very dilute condition, the influence of CTC and BZ is not negligible. The hindrance of these non-polar solvents is at the maximum around 0·15–0·2 mole fraction and the magnitude is higher for CTC than BZ. The peak of the relaxation time may be attributed to the formation of stable complex mixture.

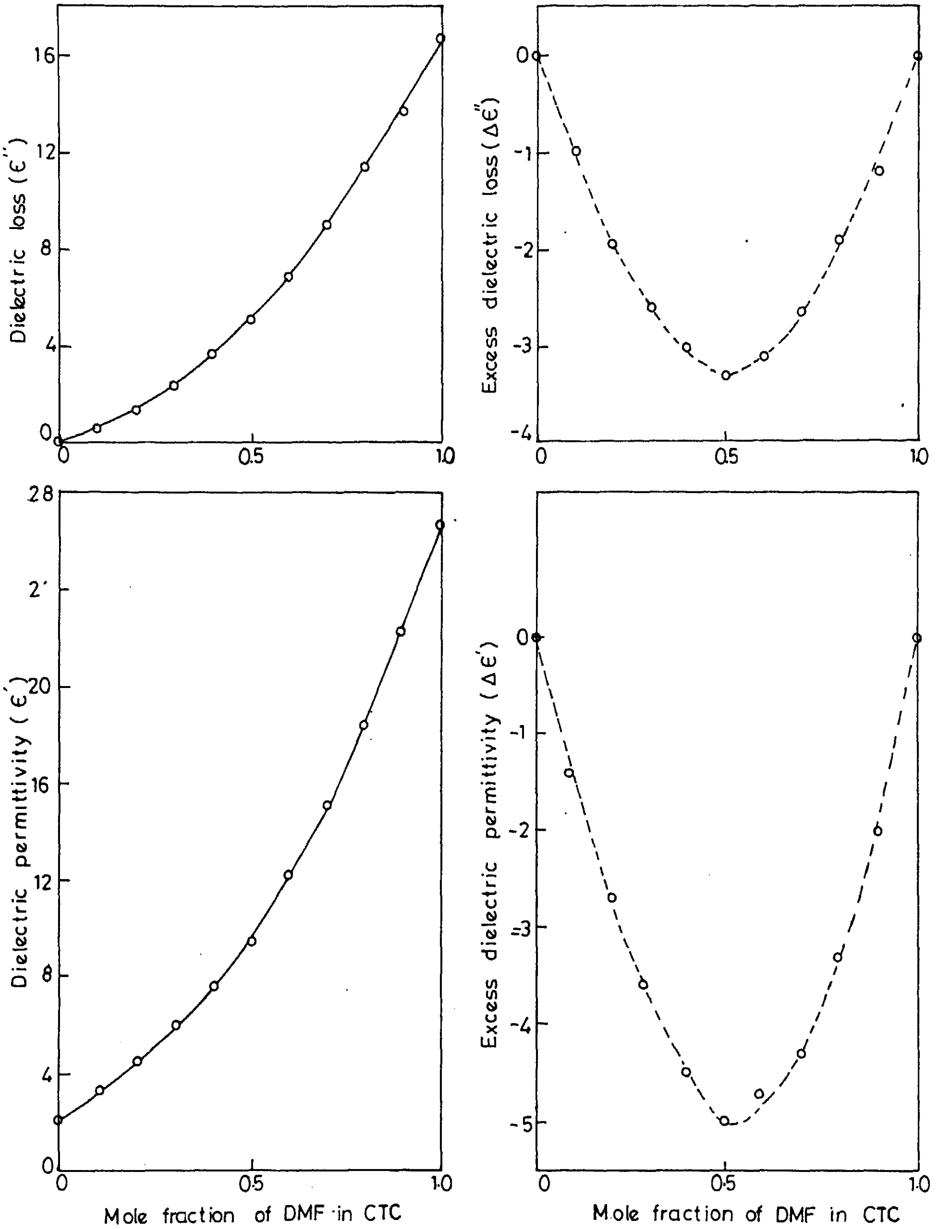

Figure 3. Dielectric permittivity, loss, excess dielectric permittivity and excess dielectric loss for DMF–CTC system.

It is generally accepted that correlation times from infrared, Raman and NMR relaxations are single particle in origin corresponding to auto-correlation functions. On the other hand, dielectric relaxation is a many molecule property and involves complex cross-correlation functions also. Tiffon *et al* [12] have shown from NMR studies of AN in CTC that the self association between AN molecules continue down to 0·2 mole fraction and below that the single particle (auto-correlation) times decrease

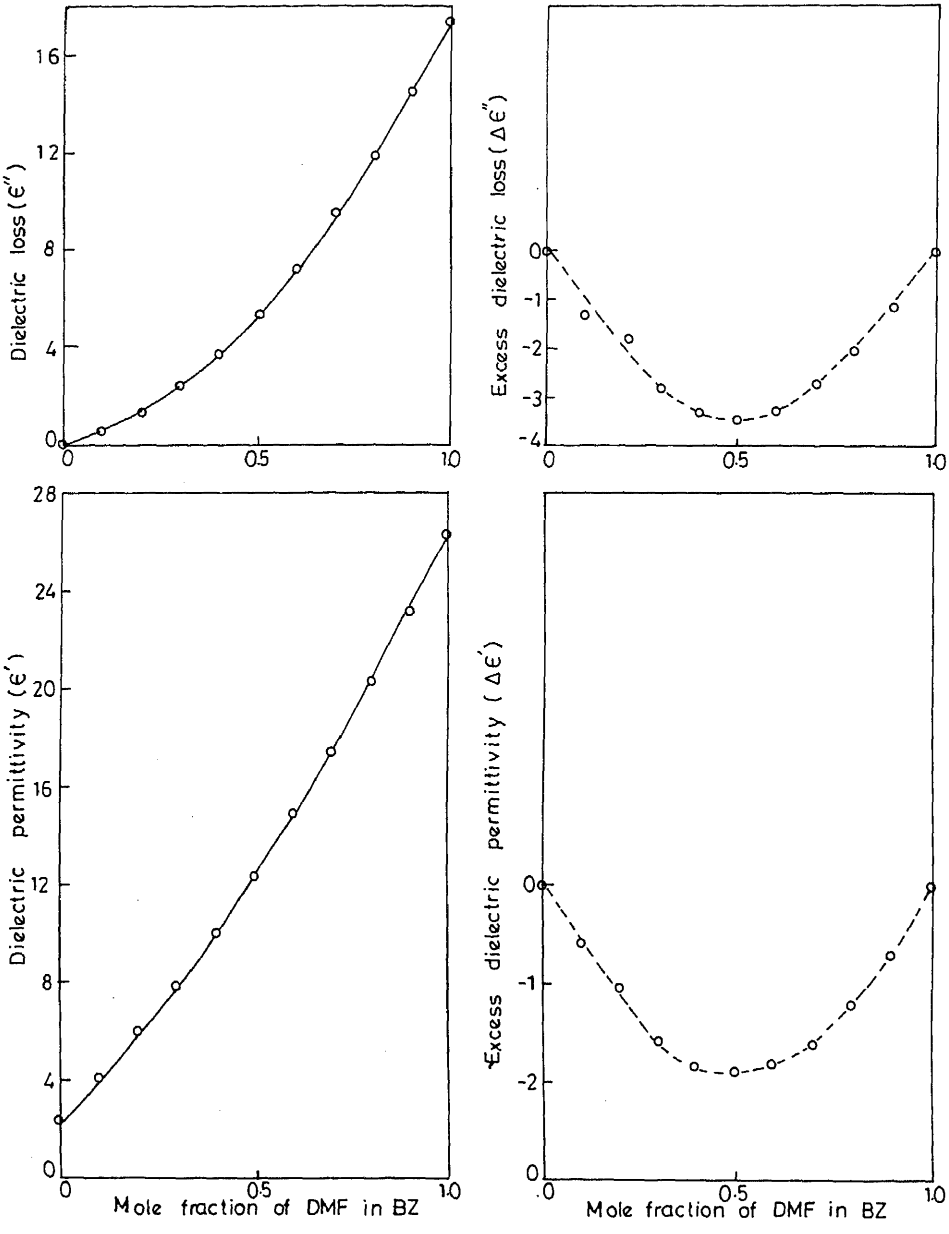

Figure 4. Dielectric permittivity, loss, excess dielectric permittivity and excess dielectric loss for DMF–BZ system.

drastically. This is consistent with the far infrared results of Knoesinger *et al* [13] who found that AN clusters remain in CTC down to 0·2 mole fraction. Evans [14] summarized these results and compared the molecular dynamics of AN from different techniques with the computer simulation calculations.

The higher sensitivity of the cavity perturbation technique enabled evaluation of the relaxation time even in the very dilute region as evident from figure 7 where the relaxation time is maximum around 0·15–0·2 mole fraction. From this it can be

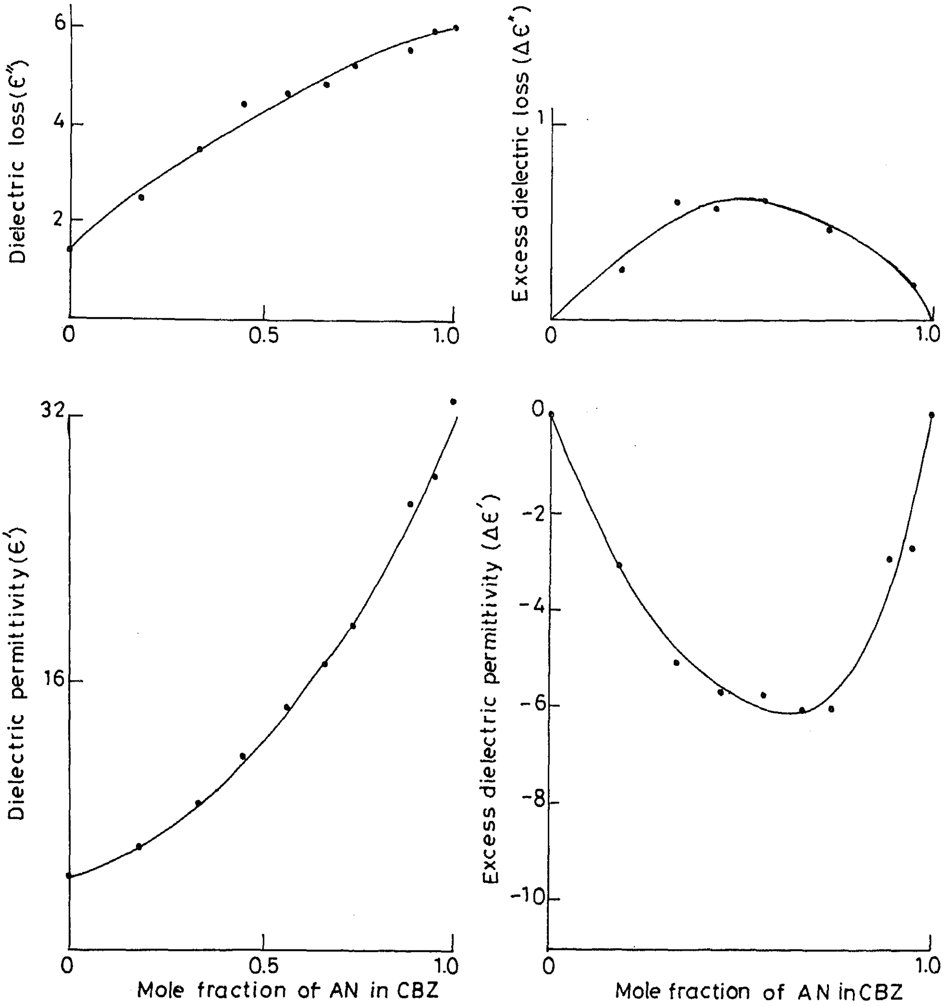

Figure 5. Dielectric permittivity, loss, excess dielectric permittivity and excess dielectric loss for AN–CBZ system.

inferred that self association and AN clusters remain in non-polar solvent down to 0·2 mole fraction.

5. Conclusion

The excess dielectric parameters at 9·1 GHz for the binary mixtures AN–CTC, AN–BZ, AN–CBZ, DMF–CTC, DMF–BZ and CBZ–CTC are studied using cavity perturbation and adjustable plunger cavity techniques. The excess dielectric loss reflects the excess entropy of the system. The observed excess parameters coincide well with the RF data for AN binary systems. The relaxation time measured for the highly diluted AN in CTC and BZ systems are studied using Gopalakrishna's method. The relaxation time is maximum around 0·15–0·2 mole fraction. The trend is verified using conventional plunger and Cole–Cole plot technique. The maximum in the

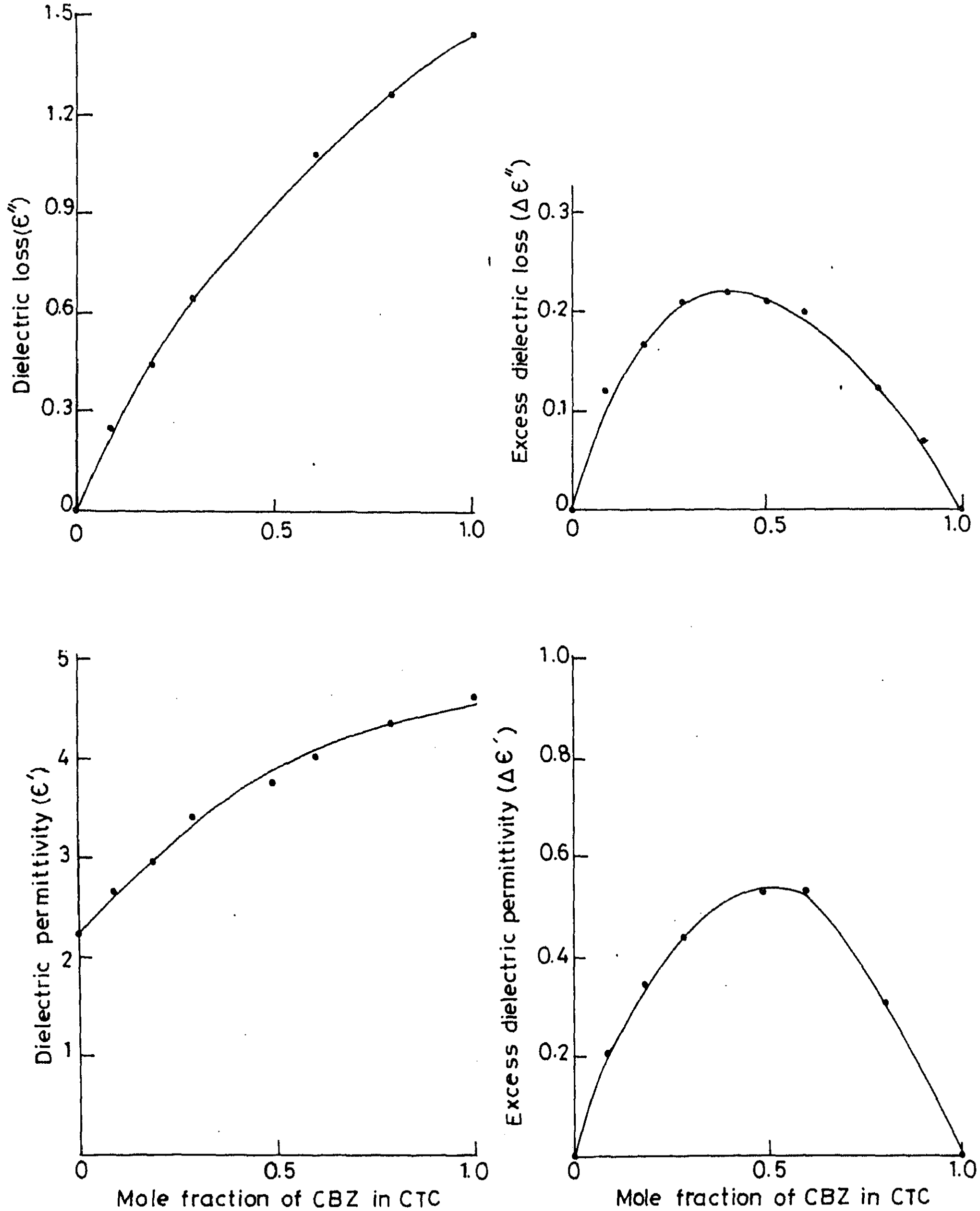

Figure 6. Dielectric permittivity, loss, excess dielectric permittivity and excess dielectric loss for CBZ–CTC system.

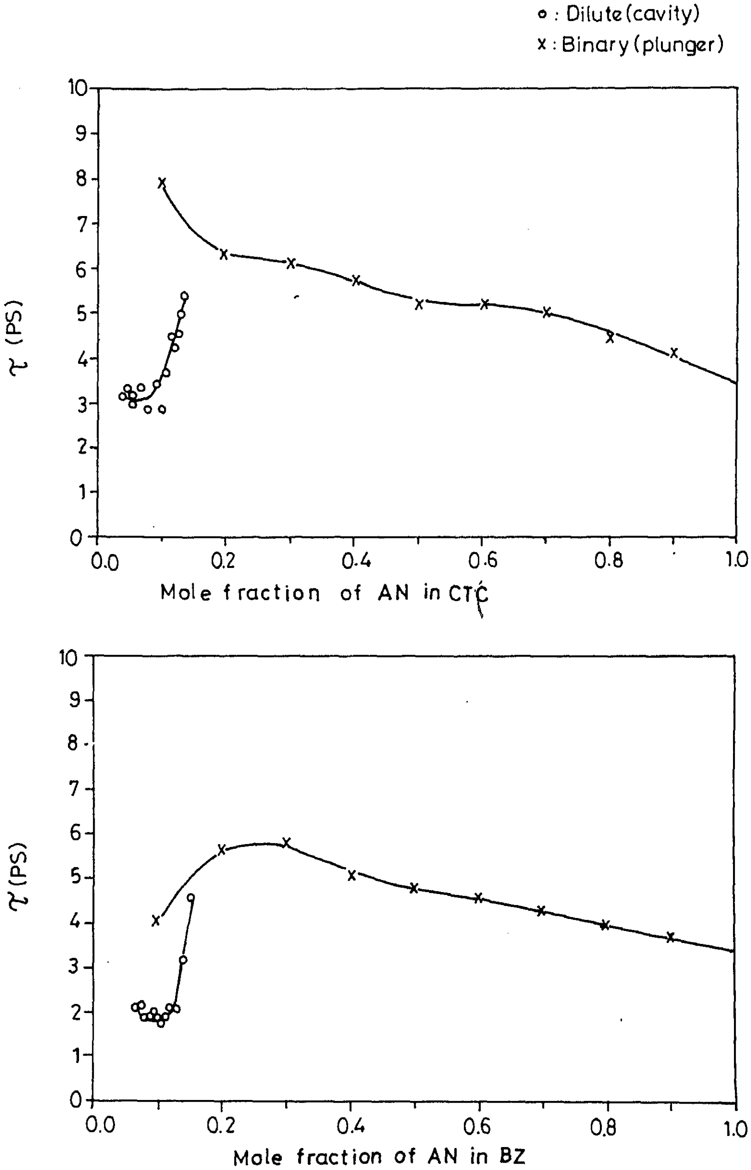

Figure 7. The relaxation time behaviur of diluted AN–CTC and AN–BZ systems.

relaxation time behaviour may be attributed to the formation of stable complex mixture even though the solvent is a non-polar sample. This variation of relaxation time also ensures the self assosciation of AN down to 0·2 mole fraction in non-polar solvent.

Acknowledgments

One of the authors, VS, wishes to acknowledge CSIR, India for financial support in the form of a Senior Research Fellowship (NET). BS wishes to acknowledge UGC, India for its support under the Quality Improvement Programme. The authors are thankful for the financial support in the form of an INDO-US project for procuring some of the experimental facilities.

References

[1] J S Rowlinson, *Liquids and liquid mixtures*, Edn2, (Butterworth Science Publication, London, 1956)
[2] K V Gopala Krishna, *Trans. Faraday Soc.* **53**, 767 (1957)
[3] V Subramanian, B S Bellubbi and J Sobhanadri, *Rev. Sci. Instrum.* **64**, 231 (1993)
[4] V R K Murthy and R Raman, *Phys. Status Solidi* **70**, 847 (1989)
[5] J Sobhanadri, *Trans. Faraday Soc.* **56**, 340 (1960)
[6] P J W Debye, *Polar molecules*, (Chemical Catalog Company, 1929) p. 90
[7] Richard Payne and Theodorou E Ignatius, *J. Phys. Chem.* **76**, 2892 (1972)
[8] A D Buckingham, E Lippert and S Bratos, *Organic liquids* (John Wiley (1978)) p. 293
[9] Kolling W Orland, *Anal. Chem.*, **58**, 674 (1985)
[10] Kolling W Orland, *Anal. Chem.*, **59**, 870 (1987)
[11] B S Bellubbi, *Dielectric dispersion studies in some binary liquid mixtures*, PhD thesis, Indian Institute of Technology, Madras, (1992)
[12] Bernard Tiffon, Bernard Ancian and Jacques-Emile Dubois, *J. Chem. Phys.* **74**, 6981 (1981)
[13] E Knozinger, D Leutloff and R Wittenbeck, *J. Mol. Struc.*, **60**, 115 (1980)
[14] M Evans, *J. Mol. Liq.*, **25**, 149 (1983)

PRAMANA
— journal of
physics

© Printed in India

Vol. 41, No. 1,
July 1993
pp. 21–29

Effect of strain on vibrational modes in strained layer superlattices

SUJATA RATH and SANKAR P SANYAL
Department of Physics, C V Raman Building, Barkatullah University, Bhopal 462026, India

MS received 6 February 1993; revised 4 May 1993

Abstract. We have investigated the lattice vibrational properties of a two-component strained layer semiconductor superlattice $(GaAs)_{n_1}(GaSb)_{n_2}$ using a one-dimensional linear chain model and transfer matrix method [1]. Effect of strain, arising due to the lattice mismatch ($\approx 7\%$) has been considered explicitly in the equation of motion. We show for the first time that the optical vibrational frequency increases (in the case of $(GaAs)_4\,(GaSb)_n$) or decreases (in the case of $(GaAs)_n(GaSb)_4$) with increase of layer thickness n, in either type of superlattices. Raman scattering measurements on some other similar systems support our findings.

Keywords. Vibrational modes; strained layer; superlattices; linear chain model; transfer matrix.

PACS Nos 63·20; 63·90; 68·35

1. Introduction

The electronic and lattice vibrational properties of the semiconductor superlattices (SSL) have been investigated with great interest in the past few years. This is mainly because of the possible applications of these materials in electronic devices. However, these SSL are quite interesting from the fundamental physics point of view and can be realized from the fact that they show diverse physical properties, particularly some of which cannot be observed in the bulk materials (e.g. confinement of optical phonons). A sizable amount of work on the phonon and optical properties of SSL, using both experimental and theoretical techniques is now available in literature [2–10].

Fabrication of a perfect SSL, however depends on the matching of the lattice constants of the components. The most celebrated and extensively studied compound SSL is GaAs–AlAs in which lattice mismatch is the smallest ($\approx 0{\cdot}13\%$) [11]. However, Raman measurements on InGaAs/GaAs strained layer superlattices (SLSL) where the lattice mismatch is nearly $\approx 7\%$ have also been reported [12]. It is now well established that during the growth, each of the atomic layers of the constituents of the lattice mismatched (or strained layer) SSL accomodates strain in order that such systems are structurally and thermodynamically stable [13]. In most of the systems, the strain generated due to lattice mismatch is isotropic and gives rise to change in the volume without affecting the crystal symmetry. In view of this fact, the SLSL allow the use of lattice mismatched materials without the generation of misfit dislocations, thereby providing freedom from the need for precise lattice matching and widens the choice of compatible materials for device fabrication.

Some of the consequences of the generation of strain at the interfaces of the heterostructures are that they change the energy gap, effective mass and shift of the phonon frequencies. The changes in vibrational modes are extremely useful for characterization of the distribution of strain in the components of the superlattices. The effect of such strain on electronic structure in SLSL has been reviewed in ref. [14]. Despite the fact that the SLSL are the 'would be' materials for the future electronic devices, very little is understood as far as their vibrational properties are concerned. So far, only limited efforts have been made to study the changes in the vibrational energy levels using Raman scattering [12, 15].

In the present paper, we investigate the effect of strain on the vibrational properties of SLSL using a simple theoretical approach which essentially contains the features that one can expect in such systems. Such a theoretical model has already been successfully applied to study the phonon dispersion in multicomponent SSL [1, 8]. For this purpose, we choose GaAs–GaSb SLSL in which the amount of lattice mismatch is quite large ($\approx 7\%$), and also the vibrational modes for bulk constituents are already analysed by using neutron scattering technique. However, our theoretical approach is general and can be applied to any SLSL system. In § 2, we present the theory and in § 3, we discuss our calculated results.

2. Model and method of calculation

In order to understand the role of strain arising from the lattice mismatch on the phonon dispersion curves in a two component compound SLSL, we have made use of a linear chain model which depicts qualitative features such as folding of acoustic and confinement of optic phonons in SSL [1].

The equation of motion of any atom in either of the components can be written as

$$m_j \omega^2 u_n = -(C_i + \Delta C_i)(u_{n-1} + u_{n+1} - 2u_n), \tag{1}$$

where $m_j (j = 1, 2)$ are the masses of the respective atoms, u_n the displacements of various atoms at site n, $C_i (i = 1, 2\text{-components})$ the nearest neighbour force constants. ΔC_i is the change in force constants due to the strain generated by the lattice mismatch and can be expressed as

$$\Delta C_i = [p_i(\varepsilon^i_{zz}) + q_i(\varepsilon^i_{xx} + \varepsilon^i_{yy})] m_j, \tag{2}$$

with

$$p_i = k^i_{11} \omega^2; \quad q_i = k^i_{12} \omega^2.$$

Here k_{ij} are dimensionless fourth rank tensors and $\varepsilon_{\alpha\beta} (\alpha, \beta = x, y, z)$ is the strain tensor whose non-zero components are given by

$$\varepsilon^i_{xx} = \varepsilon^i_{yy} = \frac{a_\parallel - a_i}{a_i}; \quad \varepsilon^i_{zz} = \left[\frac{2C^i_{12}}{C^i_{11}}\right] \varepsilon^i_{xx}, \tag{3}$$

with $a_\parallel$ as the inplane lattice parameter, a_i are the lattice constants of various constitutents, C^i_{11} and C^i_{12} are the elastic constants of the corresponding components.

With the assumption that the lattice mismatch is accompanied by uniform deformation and minimization of the elastic energy, the inplane lattice parameter $a_\parallel$ is given by [16]

$$a_\parallel = a_i \left[1 \pm \frac{\delta S_i d_i}{S_1 d_1 + S_2 d_2}\right], \tag{4}$$

with $d_i = 2n_i a_i$ as the layer thickness, S_i is the bulk shear modulus given by

$$S_i = 2\left[C^i_{11} + C^i_{12} - \frac{2(C^i_{12})^2}{C^i_{11}} \right], \tag{5}$$

and the mismatch

$$\delta = \frac{a_1 - a_2}{\langle a \rangle},$$

with $\langle a \rangle = 1/2\ (a_1 + a_2)$.

The solutions of the equations of motion [eq. (1)] for atoms A and B in component 1 for lth cell can be written as

$$\begin{aligned} u^A_l(z) &= a_l \exp[ik_1(z - lD)] + b_l \exp[-ik_1(z - lD)]. \\ u^B_l(z) &= \alpha_1 u^A_l(z), \end{aligned} \tag{6}$$

where z is the position of the atom in the unit cell l along the growth direction, k_1 is the wave vector and D is the periodicity of the SLSL. Similarly, the solutions for the second component are

$$\begin{aligned} u^{A'}_l(z) &= c_l \exp[ik_2(z - lD)] + d_l \exp[-ik_2(z - lD)], \\ u^{B'}_l(z) &= \alpha_2 u^{A'}_l(z). \end{aligned} \tag{7}$$

Substitution of (6) and (7) in (1) leads to

$$\alpha_i = \frac{2(C_i + \Delta C_i) - m_j \omega^2}{2(C_i + \Delta C_i)\cos k_i a_i} = \frac{2(C_i + \Delta C_i)\cos k_i a_i}{2(C_i + \Delta C_i) - m_j \omega^2}. \tag{8}$$

The bulk dispersion relation of any component can be obtained from (8).

Use of equation of motion of the atoms on either side of the interface within cell l and between cells l and $(l + 1)$ results in

$$\begin{aligned} & f_1 a_l + \bar{f}_1 b_l - c_l - d_l = 0. \\ & -\alpha_1 \bar{s}_1 f_1 a_l - \alpha_1 s_1 \bar{f}_1 b_l + \alpha_2 \bar{s}_2 c_l + \alpha_2 s_2 d_l = 0. \end{aligned} \tag{9}$$

$$\begin{aligned} & -a_{l+1} - b_{l+1} + f_2 c_l + \bar{f}_2 d_l = 0. \\ & \alpha_1 \bar{s}_1 a_{l+1} + \alpha_1 s_1 b_{l+1} - \alpha_2 \bar{s}_2 f_2 c_l - \alpha_2 s_2 \bar{f}_2 d_l = 0, \end{aligned} \tag{10}$$

with

$$f_i = \exp(ik_i d_i); \quad \bar{f}_i = \exp(-ik_i d_i).$$

$$s_i = \exp(ik_i a_i); \quad \bar{s}_i = \exp(-ik_i a_i).$$

We introduce two column vectors one for each component [17]

$$|u_l\rangle = \begin{pmatrix} a_l \\ b_l \end{pmatrix}; \quad |v_l\rangle = \begin{pmatrix} c_l \\ d_l \end{pmatrix}, \tag{11}$$

and four (2×2) unimodular matrices H_1, H_2, K_1 and K_2, given by

$$H_i = \Delta_i^{-1/2} \begin{bmatrix} 1 & 1 \\ \alpha_i \bar{s}_i & \alpha_i s_i \end{bmatrix},$$

$$K_i = \Delta_i^{-1/2} \begin{bmatrix} f_i & \bar{f}_i \\ \alpha_i \bar{s}_i f_i & \alpha_i s_i \bar{f}_i \end{bmatrix}, \tag{12}$$

with

$$\Delta_i = \alpha_i (s_i - \bar{s}_i)$$

such that (9) and (10) replace the boundary conditon for a continuum theory. Use of (11) and (12) in (9) and (10) leads to

$$H_1 u_l = K_2 v_l. \tag{13}$$

$$H_2 v_l = K_1 u_{l+1}. \tag{14}$$

Elimination of v_l from (13) and (14) results in

$$|u_{l+1}\rangle = T|u_l\rangle, \tag{15}$$

where T is a 2×2 unimodular transfer matrix which has the property of relating the coefficients of the displacement vectors in one cell to that in the previous one and is expressed as

$$T = K_1^{-1} H_2 K_2^{-1} H_1. \tag{16}$$

The dispersion relation for two component diatomic SLSL can now be obtained from (16) and is given by

$$\begin{aligned} \cos QD &= 1/2 \,\mathrm{Tr}\, T, \\ &= \cos(k_1 d_1)\cos(k_2 d_2) - 1/2 \left[\frac{(C_2 + \Delta C_2)}{(C_1 + \Delta C_1)} \frac{\tan(k_1 a)}{\tan(k_2 a)} A \right. \\ &\quad + \frac{(C_1 + \Delta C_1)}{(C_2 + \Delta C_2)} \frac{\tan(k_2 a)}{\tan(k_1 a)} A^{-1} \\ &\quad \left. - \left(\frac{(C_2 + \Delta C_2)^2 A + (C_1 + \Delta C_1)^2 A^{-1} - 2(C_1 + \Delta C_1)(C_2 + \Delta C_2)}{(C_1 + \Delta C_1)(C_2 + \Delta C_2)\tan(k_2 a)\tan(k_2 a)} \right) \right] \\ &\quad \sin(k_1 d_1) \sin(k_2 d_2) \end{aligned} \tag{17}$$

where

$$A = \frac{2(C_1 + \Delta C_1) - m_j \omega^2}{2(C_2 + \Delta C_2) - m_j \omega^2}.$$

3. Results and discussion

In the present model, we have considered only the nearest neighbour interaction. The force constants C_i can be calculated from the zone centre LO phonon mode for both GaAs and GaSb. The strain energy introduces a small change in the force constant (see (1)), which has been evaluated from the measured data on elastic constants and parameters of deformation potentials [14]. The calculated values of force constants (C_1 and C_2) are 2·310 and 2·200 N/m for GaAs and GaSb, respectively. The parameters used to calculate the change in force constants due to change in layer thickness are given in table 1. The calculated phonon dispersion curves (PDC)

Table 1. Inplane lattice constant ($a_{\parallel}$), strain components and change in force constants for $(GaAs)_{n_1}(GaSb)_{n_2}$ SLSL.

No. of layers n_1	n_2	$a_{\parallel}$ (Å)	ε_{xx} (dimensionless)	ε_{zz}	ΔC_1 (N/m)
4	4	5·800	0·0265	−0·0240	−0·270
4	8	5·870	0·0392	−0·0354	−0·398
4	12	5·910	0·0466	−0·0422	−0·474
4	16	5·940	0·0574	−0·0466	−0·523
4	20	5·960	0·0549	−0·0496	−0·558

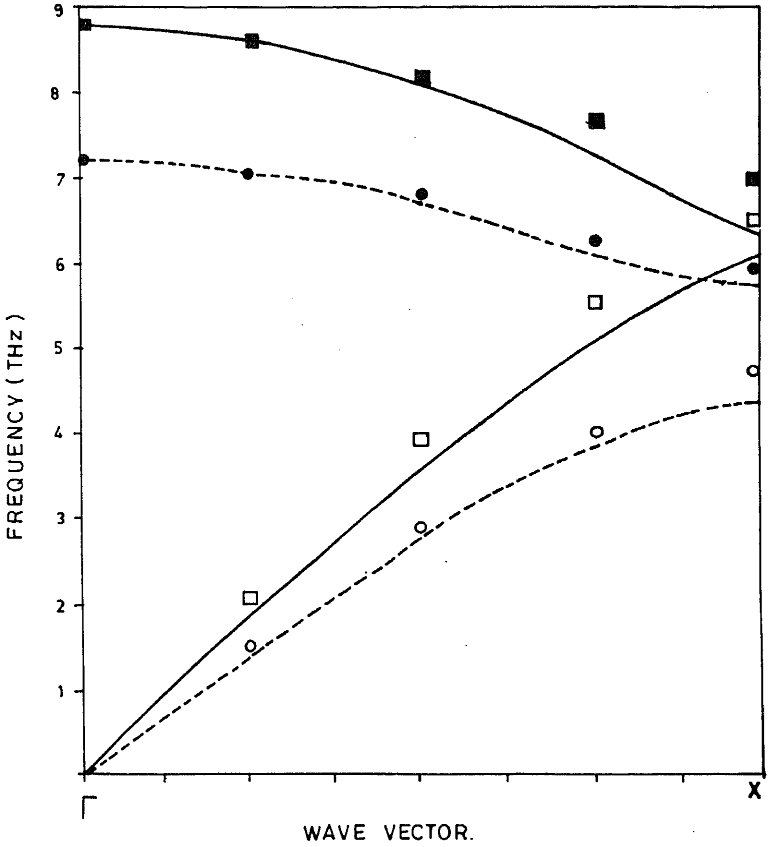

Figure 1. Calculated phonon dispersion curves of GaAs (———) and GaSb (--) compared with experimental data taken from [18] and [19] respectively.

for GaAs and GaSb are presented in figure 1 and compared with neutron scattering results [18, 19]. For simplicity, in the present calculations, we have considered the longitudinal modes only. It is worth pointing out that the present simple one-dimensional model can reproduce adequately the gross features of the measured PDC of these compounds along the Δ direction. In figure 2 we have plotted the variation of lattice constant of $(GaAs)_4(GaSb)_n$ and $(GaAs)_n(GaSb)_4$ as a function of layer thickness for each component. The variation of lattice constants with layer thickness

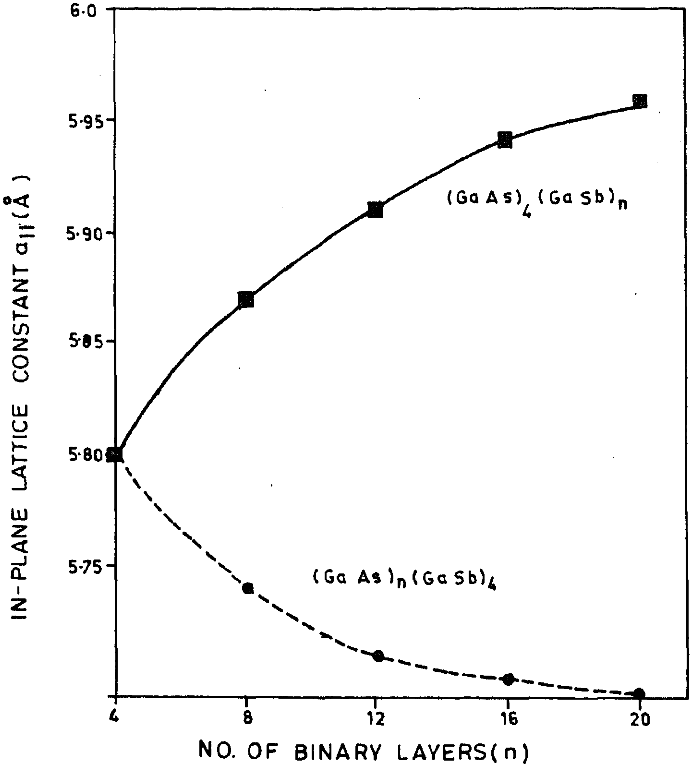

Figure 2. Inplane lattice constant as a function of number of binary layers for $(GaAs)_n$ $(GaSb)_4$ and $(GaAs)_4$ $(GaSb)_n$ SLSL.

can easily be explained from the fact that with the increase of layer thickness of GaSb, the volume of the unit cell increases. This results in the increase in inplane lattice constant. Similar argument holds for the decrease in lattice constant for $(GaAs)_n(GaSb)_4$.

Figure 3 depicts the PDC of $(GaAs)_{12}$ $(GaSb)_{12}$ strained and unstrained SLSL. The phonon dispersion curves for $(GaAs)_{12}(GaSb)_{12}$ have been calculated from (17) which show the dispersion relation (frequency (ω) as a function of reduced wave vector (QD)). These curves are plotted in figures 3(a) and (b) for unstrained and strained SSL respectively. For unstrained SSL, ΔC_i has been taken to be zero. The interesting feature, as can be noted from figure 3(b), is that the inplane strain substantially suppresses the confined optical GaAs-like LO mode, but does not affect much the propagating acoustic modes. In general, the nature of the PDC of the SLSL remains unchanged due to strain, except lowering of the highest LO frequency.

In order to understand the above aspect quantitatively, in figure 4 we have plotted the variation of the highest GaAs LO frequency, as a function of layer thickness. In doing such analysis, we have started with $(GaAs)_4(GaSb)_4$ and increased the number of binary layers in one component, keeping the other constant. The figure 4 shows nearly similar trend in variation as in figure 2. A comparison of these two figures reveals that the change in volume, associated with the change in lattice constants increases (or decreases) the highest LO mode of GaAs. It is also expected that after a certain critical value of the number of binary layers, (or thickness) the constituents

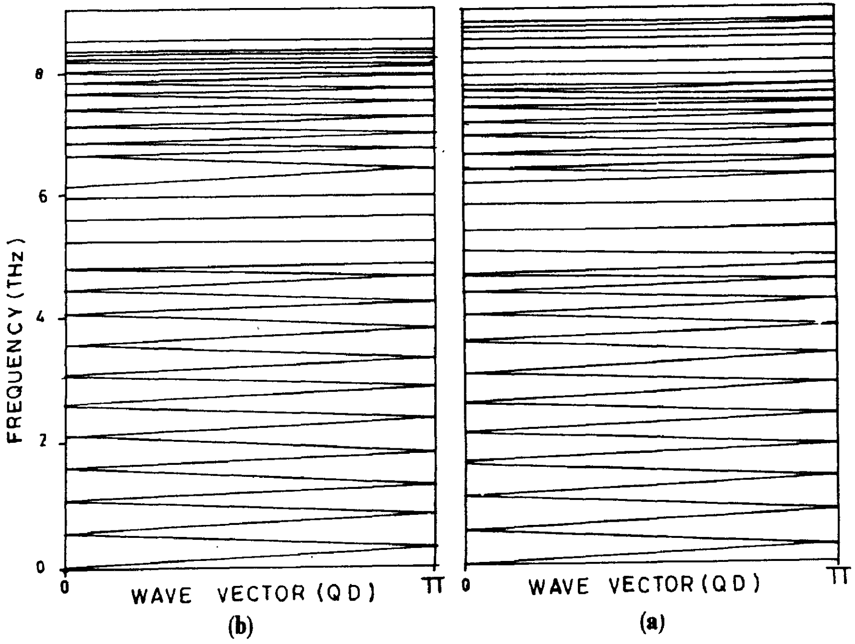

Figure 3. Phonon dispersion curves of $(GaAs)_{12}$ $(GaSb)_{12}$ unstrained (a) and $(GaAs)_{12}$ $(GaSb)_{12}$ strained (b) SLSL.

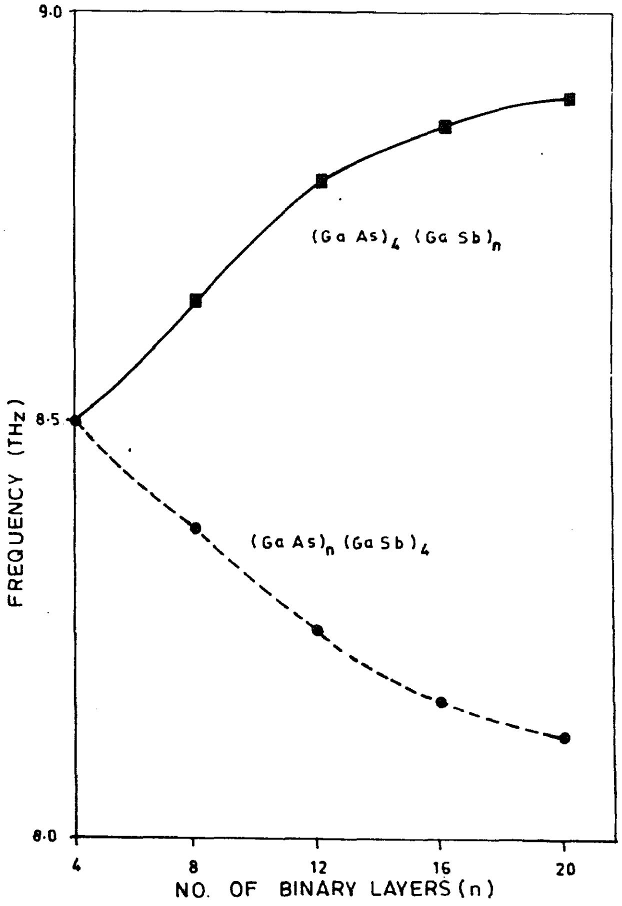

Figure 4. Highest GaAs LO frequency as a function of number of binary layers for $(GaAs)_n(GaSb)_4$ and $(GaAs)_4(GaSb)_n$ SLSL.

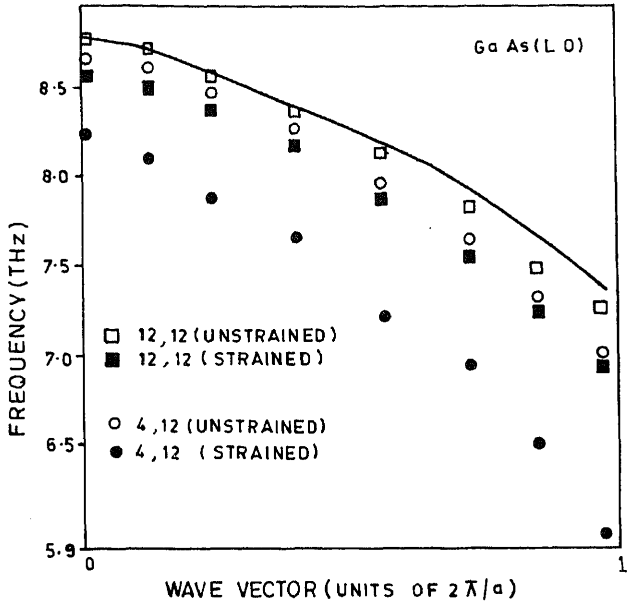

Figure 5. Dispersion curve for GaAs LO mode for different layer thicknesses. Solid line: bulk GaAs.

will behave like bulk materials, thereby no further depression (or increase) in this mode will be observed.

In figure 5, we have plotted the highest LO mode frequency of GaAs as a function of reduced wave vector. The LO dispersion curve for GaAs in unstrained $(GaAs)_{12}(GaSb)_{12}$ is quite similar to the bulk material. However, inclusion of strain substantially reduces the frequency. In addition, to understand the effect of strain generated due to unequal binary layers, we have also plotted the GaAs-LO mode for $(GaAs)_4(GaSb)_{12}$ superlattices. It is clearly seen that the strain due to unequal binary layers is also significant and affect the PDC of SLSL. The lowering of the GaAs-LO mode, obtained from the present investigation can be justified from the arguments already given for InGaAs/GaAs superlattice [12]. However, for the GaAs–GaSb SLSL no measurement of zone-centre phonon has been reported so far. We emphasise the need of measurement of the phonon properties of such systems for a quantitative verification of our results.

In conclusion, we have reported, for the first time, the results of our investigations on the phonon properties in SLSL, using a simple theoretical model. The strain energy, in general increases (or reduces) the volume, thereby affecting the highest GaAs like LO mode.

Acknowledgements

The authors are thankful to DST, DAE and MPCST for partial financial support. One of us (SR) is grateful to DAE for the award of a senior fellowship.

References

[1] S Rath and S P Sanyal, *Phys. Stat. Solidi* **B176**, 63 (1993)

[2] A K Ramdas and S Rodriguez, in *Semiconductors and semimetals*, edited by J K Furdyna and J Kossut (Academic, New York, 1988) Vol. 25
[3] M V Klein, *IEEE J. Quantum Electron.* **22**, 1780 (1986)
[4] J Sapriel and B D Rouhani, *Surface Sci. Rep.* **10**, 189 (1989)
[5] M Cardona, *Superlattices and microstructures* **5**, 27 (1989)
[6] B Jusserand and M Cardona, in *Light scattering in solids* (Springer Verlag, Heidelberg, 1989) Vol. 5, p. 49
[7] M Cardona, in *Spectroscopy of semiconductor microstructures* (Plenum, New York, 1990)
[8] S Rath, P K Jha and S P Sanyal, *Solid State Physcis Symp. (India)* **C33**, 43 (1991)
[9] M Cardona, *Superlattices and microstructures* **7**, 183 (1990)
[10] P Molinas-Mata and M Cardona, *Superlattices and Microstructures* **10**, 39 (1991), and references therein
[11] P Voisin, in *Semiconductor physics*, edited by C E T Gonsalves da Silva, L E Oliveiza and J R Leile (World Scientific, Singapore, 1987) p. 46
[12] F Iikawa, F Cerdeira C Vazquez-Lopez, P Motisuke, M A Sacilotti, A P Roth and R A Masut, *Solid State Commun.* **68**, 211 (1988) and references therein
[13] T P Pearsell, in *Semiconductors and semimetals* (Academic, New York, 1990) Vol. 32, p. 1
[14] F H Pollak, in *Semiconductors and semimetals* (Academic, New York, 1990) Vol. 32, p. 1
[15] E Anastassakis, Y S Rapits, M Hunerman, W Richter and M Cardona, *Phys. Rev.* **B38**, 7702 (1988) and references therein
[16] G C Osbourn, *J. Appl. Phys.* **53**, 1586 (1982)
[17] A Yariv and P Yeh, in *Optical waves in crystals* (Wiley, New York, 1984)
[18] D Strauch and B Dorner, *J. Phys.* **C2**, 1497 (1990)
[19] M K Farr, J G Trayler and S K Sinha, *Phys. Rev.* **B11**, 1587 (1975)

PRAMANA
— journal of
physics

© Printed in India

Vol. 41, No. 1,
July 1993
pp. 31–39

Second order elastic anomalies in barium titanate from cubic to tetragonal phase transition

B SUBRAMANYAM and K S VISWANATHAN
Department of Physics, Indian Institute of Technology, Madras 600 036, India

MS received 30 January 1993; revised 26 April 1993

Abstract. The anomalies of the second order elastic constants have been derived for barium titanate for the phase transition from cubic to tetragonal. The equilibrium values of the components of the order parameter and the strain variables have been obtained from the stability conditions. The fluctuations in the order parameter have been derived from the Landau–Khalatnikov equations. Expression for the shift in the zero point energy in the tetragonal phase is obtained and is shown to be proportional to $(T-T_c)^2$. The anomalies for all the second order elastic constants have been derived and relations among them reported. It is shown that the second order elastic anomalies suffer a discontinuity at the transition temperature.

Keywords. Elastic anomalies; phase transition; barium titanate.

PACS Nos **64·70; 62·20; 64·60**

1. Introduction

Barium titanate is a classical example of a substance undergoing a first order phase transition. The optical, dielectric, piezoelectric, elastic and other properties of $BaTiO_3$ and similar ferroelectric compounds have been reviewed in several articles and monographs [1–14]. $BaTiO_3$ is paraelectric and has a cubic $pm\bar{3}m(0_h^1)$ perovskite structure above the Curie temperature of 120°C. At the Curie point, the crystal becomes polar and its structure changes from cubic to a tetragonal phase. The resulting space group is $p4mm(C_{4v}^1)$, a subgroup of $pm\bar{3}m$. Below the Curie point, the vector of spontaneous polarization is directed along the [001] direction. On lowering the temperature, the dipole moment increases and the crystal becomes correspondingly more tetragonal, with an increase in the lattice constant along the polar direction (tetragonal *c*-axis) and a decrease in a direction (*a*-axis) perpendicular to it.

$BaTiO_3$ undergoes two other displacive phase transitions on cooling. Below 5°C the spontaneous polarization points in the [011] direction. The point group symmetry is $mm2(C_v)$, and the crystal system is orthorhombic. This group is not a subgroup of the tetragonal phase above (*p*4.*mm*), but is a subgroup of the parent phase above ($pm\bar{3}m$). Finally on cooling further, below − 70°C, $BaTiO_3$ undergoes a further phase transition from orthorhombic to the rhombohedral R_{3m} (C_{3v}^5) phase, in which the polarization vector is directed along the [111] direction. This too is not a subgroup of the orthorhombic phase but a subgroup of the parent group $pm\bar{3}m$. All the three phase transitions cannot be described by a continuous second order phase transition, but are first order phase transitions. There is no piezoelectric effect above the Curie 120°C point in $BaTiO_3$.

The temperature variation of the elastic contants and the consequent anomalies have been investigated by several authors [1, 6, 8–10]. Variation of C_{11} and C_{44} were measured by Luthi and Rehwald [13] in the vicinity of the upper transition at $T_c = 401\,\mathrm{K}$. C_{11} was found to vary as $C_{11}(T) = C_{11}^0 - A_1(T - T_0)^{-\mu}$ with a critical exponent $\mu = 0{\cdot}41$ and T_0 is paraelectric Curie temperature (lower stability limit).

There are other ferroelectrics [4] like $KNbO_3(T_c = 435°C)$, $KTaO_3(T_c = -260°C)$ and $PbTiO_3(T_c = 490°C)$, which are chemically similar to $BaTiO_3$ and whose dielectric and structural properties are almost identical. The theory given in this paper will apply equally well to these ferroelectrics also.

In this paper, we study systematically the anomalies of the second order elastic (SOE) constants arising from the phase transition from the cubic to the tetragonal phase. The equilibrium values of the components of the order parameter and the strain variables in the two phases are obtained from the stability conditions [15] while the fluctuations in the order parameter in the two phases are derived from the Landau–Khalatnikov equations. The strains developed during a phase transition are infinitesimal and the third order deformation energy is one order smaller than the second order deformation energy. Hence the corrections brought about by third and fourth order deformation energies to the equilibrium values are negligible in comparison with second order deformation energy. We shall therfore neglect them in future calculations. In § 4, we give an expression for all the SOE anomalies in a single formula for the tetragonal phase. Relations among the anomalies of the SOE constants have been derived. It is shown that the SOE constants are temperature dependent, showing a discontinuity at the transition temperature.

2. The equilibrium values of the order parameters and the strain variables

The free energy F of the system is a sum of the elastic energy, the Landau energy and the coupling energy between the components of the order parameters and the strain variables. The latter two have been given by Fatuzzo and Merz [4] for the phase transition of barium titanate and similar compounds. We have

$$\begin{aligned} F = {} & (1/2)\sum_{ij} C_{ij}\eta_i\eta_j + (a/2)(P_x^2 + P_y^2 + P_z^2) + (b/4)(P_x^4 + P_y^4 + P_z^4) \\ & + C(P_x^2P_y^2 + P_y^2P_z^2 + P_z^2P_x^2) + g_{11}(\eta_1P_x^2 + \eta_2P_y^2 + \eta_3P_z^2) \\ & + g_{12}\{\eta_1(P_z^2 + P_y^2) + \eta_2(P_z^2 + P_x^2) + \eta_3(P_x^2 + P_y^2)\} \\ & + g_{44}(\eta_4P_yP_z + \eta_5P_zP_x + \eta_6P_xP_y) \end{aligned} \tag{1}$$

where $a = a'(T - T_c)$, a' being a constant.

The coefficients b and C are constants, more or less independent of temperature. Further, g_{11}, g_{12} and g_{44} are coupling constants and $\eta_i (i = 1$ to $6)$ are the six components of the strain tensor. P_x, P_y and P_z are the three components of order parameter. The equilibrium values of the order parameter components as well as the strain variables can be obtained from the stability conditions: These are

$$\begin{aligned} &(\partial F/\partial P_i)_0 = 0 \quad (\text{for } i = x, y, z). \\ &(\partial F/\partial \eta_i)_0 = 0 \quad (\text{for } i = 1 \text{ to } 6). \end{aligned} \tag{2}$$

In the cubic phase above 120°C, barium titanate is paraelectric: The simplest solution of equations (2) are given by

$$P_x = P_y = P_z = 0. \tag{3}$$

The solutions of the set of nine equations in (2) lead to the following equilibrium values for the order parameter and strain variables:

$$P_{xo} = P_{yo} = P_{z0} = 0 \tag{4}$$

and

$$\eta_{10} = \eta_{20} = \eta_{30} = \eta_{40} = \eta_{50} = \eta_{60} = 0. \tag{5}$$

Barium titanate undergoes a phase transition from cubic to tetragonal structure as it is cooled through 120°C. In the tetragonal phase, it is ferroelectric with an electrical polarization along the *c*-axis. It can be seen that the set of equations (2) admit another solution, in which

$$P_x = P_y = 0; \quad P_z \neq 0. \tag{6}$$

This solution corresponds to the ferroelectric tetragonal phase. When (6) holds, the equilibrium values of the strain variables and electrical polarization for the tetragonal phase are given by

$$\eta_{10} = \eta_{20} = \frac{x+y}{3} P_{z0}^2, \tag{7}$$

$$\eta_{30} = \frac{x-2y}{3} P_{z0}^2, \tag{8}$$

where

$$x = -\frac{g_{11} + 2g_{12}}{C_{11} + 2C_{12}} \tag{9a}$$

and

$$y = \frac{g_{11} - g_{12}}{C_{11} - C_{12}} \tag{9b}$$

$$\eta_{40} = \eta_{50} = \eta_{60} = 0. \tag{10}$$

Further the equilibrium value of the electrical polarization is described by

$$P_{z0}^2 = -aP, \tag{11a}$$

where

$$P = \frac{1}{b - (2/3)\dfrac{(g_{11} + 2g_{12})^2}{C_{11} + 2C_{12}} - \dfrac{(4/3)(g_{11} - g_{12})^2}{C_{11} - C_{12}}}. \tag{11b}$$

It is seen from (7) and (8) that the lattice deformations are propotional to the square of the spontaneous electrical polarization, in agreement with the experimental results.

3. The Landau – Khalatnikov (LK) equations

The LK equation relates the regression in the fluctuations of the order parameter towards equilibrium to the thermodynamic restoring force. While the stability conditions give the equilibrium values of the components of the order parameter, the LK equation gives expressions for the fluctuations of the order parameter from its equilibrium value.

The LK equations for the three components of the order parameter can be written as

$$\dot{P}_x = -\Gamma_1(\partial F/P_x), \tag{12a}$$

$$\dot{P}_y = -\Gamma_2(\partial F/P_y), \tag{12b}$$

$$\dot{P}_z = -\Gamma_3(\partial F/P_z), \tag{12c}$$

where Γ_1 Γ_2 and Γ_3 are the kinetic coefficients.

We shall consider the solution of the LK equation for the ferroelectric phase between 120° and 5°C. To solve these equations, we shall write

$$P_x = P_{x0} + P_x^*; \quad P_y = P_{y0} + P_y^*; \quad P_z = P_{z0} + P_z^* \text{ and } \eta_i = \eta_{i0} + \eta_i^*. \tag{13}$$

Symmetry of the tetragonal structure ensures that

$$\Gamma_1 = \Gamma_2. \tag{14}$$

By expanding $\partial F/\partial P_i$ $(i = x, y, z)$ about the equilibrium values of the components of the order parameter and the strain variables, and ignoring product terms of higher orders, one obtains

$$\partial F/\partial P_i = (\partial F/\partial P_i)_0 + \sum_j (\partial^2 F/\partial P_i \partial P_j)_0 P_j^* + \sum_j (\partial^2 F/\partial P_i \partial \eta_j)_0 \eta_j^*. \tag{15}$$

Further by writing P_i^* proportional to $e^{i\Omega t}$ (Ω is the angular frequency of the acoustic wave) we see that the LK equations reduce to

$$\{i\Omega + \Gamma_1(\partial^2 F/\partial P_x^2)_0\}P_x^* + \Gamma_1(\partial^2 F/\partial P_x \partial P_y)_0 P_y^* + \Gamma_1(\partial^2 F/\partial P_x \partial P_z)_0 P_z^*$$
$$= -\Gamma_1 \sum_i (\partial^2 F/\partial P_x \partial \eta_i)_0 \eta_i^*, \tag{16a}$$

$$\{i\Omega + \Gamma_1(\partial^2 F/\partial P_y^2)_0\}P_y^* + \Gamma_1(\partial^2 F/\partial P_y \partial P_x)_0 P_x^* + \Gamma_1(\partial^2 F/\partial P_y \partial P_z)_0 P_z^*$$
$$= -\Gamma_1 \sum_i (\partial^2 F/\partial P_y \partial \eta_i)_0 \eta_i^* \tag{16b}$$

$$\{i\Omega + \Gamma_3(\partial^2 F/\partial P_z^2)_0\}P_z^* + \Gamma_3(\partial^2 F/\partial P_z \partial P_y)_0 P_y^* + \Gamma_3(\partial^2 F/\partial P_z \partial P_x)_0 P_x^*$$
$$= -\Gamma_3(\partial^2 F/\partial P_z \partial \eta_i)_0 \eta_i^*. \tag{16c}$$

By differentiating the free energy twice with respect to P_x, P_y and P_z, and making use of the expressions for the equilibrium values of the parameters given by equations (7) to (11) we find that

$$(\partial^2 F/\partial P_x^2)_0 = (\partial^2 F/\partial P_y^2)_0 = a\{1 - 2CP + (2/3)P(g_{11} + 2g_{11})^2(C_{11} + 2C_{12})^{-1}$$
$$- (2/3)P(g_{11} - g_{12})^2(C_{11} - C_{12})^{-1}\}, \tag{17a}$$

$$(\partial^2 F/\partial P_z^2)_0 = a\{1 - 3b + (2/3)P(g_{11} + 2g_{12})^2(C_{11} + 2C_{12})^{-1}$$
$$+ 4/3P(g_{11} - g_{12})^2(C_{11} - C_{12})^{-1}\}. \tag{17b}$$

In the same way, the equilibrium values of $(\partial^2 F/\partial P_i \partial P_j)_0$ and $(\partial^2 F/\partial_i \partial \eta_j)_0$ can be evaluated. The following relations only exist with others equal to zero.

$$(\partial^2 F/\partial P_x \partial \eta_5)_0 = (\partial^2 F/\partial P_y \partial \eta_4)_0 = g_{44} P_{z0}, \tag{18a}$$

$$(\partial^2 F/\partial P_z \partial \eta_1)_0 = (\partial^2 F/\partial P_z \partial \eta_2)_0 = 2g_{12} P_{z0}, \tag{18b}$$

$$(\partial^2 F/\partial P_z \partial \eta_3)_0 = 2g_{11} P_{z0}. \tag{18c}$$

Substituting (18) and (17) in (16) the fluctuations of the order parameter about the equilibrium values reduce to the form

$$P_x^* = A\eta_5^* \tag{19}$$

$$P_y^* = A\eta_4^*, \tag{20}$$

$$P_z^* = \sum_{i=1}^{6} \alpha_i \eta_i^*, \tag{21}$$

where

$$A = -(\Gamma_1 g_{44} P_{z0})/P_1, \tag{22a}$$

$$\alpha_1 = \alpha_2 = -2(\Gamma_3 g_{12} P_{z0})/P_3, \tag{22b}$$

$$\alpha_3 = -2(\Gamma_3 g_{11} P_{z0})/P_3, \tag{22c}$$

$$\alpha_4 = \alpha_5 = \alpha_6 = 0. \tag{22d}$$

Further

$$P_1 = i\Omega + \Gamma_1(\partial^2 F/\partial P_x^2)_0, \tag{23a}$$

$$P_3 = i\Omega + \Gamma_3(\partial^2 F/\partial P_z^2)_0. \tag{23b}$$

4. The elastic anomalies in the tetragonal phase

Substituting equation (13) in (1) for the free energy, we find that

$$\begin{aligned} F = (1/2)&\Big\{\sum_{ij} C_{ij}(\eta_{i0} + \eta_i^*)(\eta_{j0} + \eta_j^*)\Big\} \\ &+ (a/2)\{P_x^{*^2} + P_y^{*^2} + (P_{z0} + P_z^*)^2\} + (b/4)\{P_x^{*^4} + P_y^{*^4} + (P_{z0} + P_z^*)^4\} \\ &+ C\{P_x^{*^2} P_y^{*^2} + (P_x^{*^2} + P_y^{*^2})(P_{z0} + P_z^*)^2\} \\ &+ g_{11}\{\eta_{10} + \eta_1^*)P_x^{*^2} + (\eta_{20} + \eta_2^*)P_y^{*^2} + (\eta_{30} + \eta_3^*)(P_{z0} + P_z^*)^2\} \\ &+ g_{12}\{(\eta_{10} + \eta_1^*)[P_y^{*^2} + (P_{z0} + P_z^*)^2] \\ &\quad + (\eta_{20} + \eta_2^*)[P_x^{*^2} + (P_{z0} + P_z^*)^2] + (\eta_{30} + \eta_3^*)(P_x^{*^2} + P_y^{*^2})\} \\ &+ g_{44}\{(\eta_{40} + \eta_4^*)P_y^*(P_{z0} + P_z^*) + (\eta_{50} + \eta_5^*)P_x^*(P_{z0} + P_z^*) \\ &\quad + (\eta_{60} + \eta_6^*)P_y^* P_x^*\} \end{aligned} \tag{24}$$

In the above expression for free energy, the linear terms in η_i^* vanish in view of the stability conditions. We denote by F_0, F_2, F_3 and F_4 respectively the terms of orders zero, two, three and four in the strain variables. The zero order term F_0 gives the shift in the zero point energy at the transition temperature. Its derivative with respect to temperature will give the specific heat anomaly at the transition temperature. In fact,

$$F_0 = (1/2)\sum_{ij} C_{ij}\eta_{i0}\eta_{j0} + (a/2)\, P_{z0}^2 + (b/4)P_{z0}^4 + g_{11}\eta_{30}P_{z0}^2$$
$$+ g_{12}P_{z0}^2(\eta_{10} + \eta_{20}). \tag{25}$$

By substituting the values of P_{z0}^2, η_{i0} etc. in the above expression and simplifying we find that

$$F_0 = -a^2 P/4 = -(a'^2/4)P(T - T_c)^2 \tag{26}$$

The change in the zero point energy is proportional to $(T - T_c)^2$ near the phase transition; consequently the change in specific heat proportional to $(T_c - T)$ is given by the formula

$$C_v = (\partial F_0/\partial T)_V = (a'^2 P/2)(T_c - T). \tag{27}$$

4.1 *Anomalies in the second order elastic (SOE) constants*

By collecting all the terms which are quadratic in strain variables, we can write the expression for the second order deformation energy as

$$F_2 = (1/2)\sum_{ij} C_{ij}^* \eta_i^* \eta_j^* \tag{28}$$

where C_{ij}^* represent the modified SOE constants. Let us write

$$C_{ij}^* = C_{ij} + \Delta C_{ij}^* \tag{29}$$

ΔC_{ij}^* then gives the anomalies in SOE constants arising from the phase transition. Now

$$\begin{aligned} F_2 &= (1/2)\sum_{ij} C_{ij}\eta_i^*\eta_j^* + \Delta F_2 \\ &= (1/2)\sum_{ij} C_{ij}\eta_i^*\eta_j^* + (a/2)\{P_x^{*^2} + P_y^{*^2} + P_z^{*^2}\} + (3b/2)\{P_{z0}^2 P_z^{*^2}\} \\ &\quad + CP_{z0}^2(P_x^{*^2} + P_y^{*^2}) + g_{11}(\eta_{10}P_x^{*^2} + \eta_{20}P_y^{*^2} + \eta_{30}P_z^{*^2} + 2P_{z0}\eta_3^* P_z^*) \\ &\quad + g_{12}\{\eta_{10}(P_y^{*^2} + P_z^{*^2}) + \eta_{20}(P_z^{*^2} + P_x^{*^2}) + \eta_{30}(P_x^{*^2} + P_y^{*^2}) \\ &\qquad + 2P_{z0}(\eta_1^* P_z^* + \eta_2^* P_z^*)\} + g_{44}P_{z0}(\eta_4^* P_y^* + \eta_5^* P_x^*\}. \end{aligned} \tag{30}$$

Substituting the expressions for P_x^*, P_y^*, P_z^* from (19) to (21) and collecting all terms containing $\eta_i^*\eta_j^*$ in this expression, we find that

$$\begin{aligned} \Delta C_{ij}^*/2 = A^2(\delta_{i5}\delta_{j5} + \delta_{i4}\delta_{j4})\{a/2 + CP_{z0}^2 + g_{12}(\eta_{10} + \eta_{30}) + g_{11}\eta_{10}\} \\ + \alpha_i\alpha_j(a/2 + (3b/2)P_{z0}^2 + g_{11}\eta_{30} + 2g_{12}\eta_{10}) \\ + 2P_{z0}(g_{12}\alpha_i\delta_{j1} + g_{12}\alpha_i\delta_{j2} + g_{11}\alpha_i\delta_{j3}) \\ + g_{44}P_{z0}A(\delta_{i4}\delta_{j4} + \delta_{i5}\delta_{j5}). \end{aligned} \tag{31}$$

The above equation gives the anomalies for all the SOE constants in a single formula. By giving integral values for the indices i and j ranging from one to six, we can obtain anomalies for the individual SOE constants. The existence of elastic anomalies shows that the velocities of sound waves undergo a change during the phase transition. In view of the complex nature of ΔC_{ij}^*, the waves are attenuated in this region.

The following relations among the elastic anomalies can easily be verified.

$$\Delta C_{11}^* = \Delta C_{12}^* = \Delta C_{22}^* \tag{32a}$$

$$\Delta C_{13}^* = \Delta C_{23}^* \tag{32b}$$

$$\Delta C_{44}^* = \Delta C_{55}^* \tag{32c}$$

The anomalies in the individual SOE constants are given by

$$\begin{aligned}\Delta C_{11}^* = {} & -8\Gamma_3^2 g_{12}^2 a^2/P_3^2\{-3bP^2/2 + (P^2/3)(g_{11}+2g_{12})^2(C_{11}+2C_{12})^{-1} \\ & \quad + P/2 + (2P^2/3)(g_{11}-g_{12})^2(C_{11}-C_{12})^{-1}\} \\ & + 8\Gamma_3 g_{12}^2 Pa/P_3\end{aligned} \tag{33a}$$

$$\begin{aligned}\Delta C_{33}^* = {} & -8\Gamma_3^2 g_{11}^2 a^2/P_3^2\{-3bP^2/2 + (P^2/3)(g_{11}+2g_{12})^2(C_{11}+2C_{12})^{-1} \\ & \quad + P/2 + (2P^2/3)(g_{11}-g_{12})^2(C_{11}-C_{12})^{-1}\} \\ & + 8\Gamma_3 g_{11}^2 Pa/P_3\end{aligned} \tag{33b}$$

$$\begin{aligned}\Delta C_{13}^* = {} & -8\Gamma_3^2 g_{11} g_{12}/P_3^2\{-3bP^2/2 + (P^2/3)(g_{11}+2g_{12})^2(C_{11}+2C_{12})^{-1} \\ & \quad + P/2 + (2P^2/3)(g_{11}-g_{12})^2(C_{11}-C_{12})^{-1}\} \\ & + 8\Gamma_3 g_{12} g_{11} Pa/P_3\end{aligned} \tag{33c}$$

$$\begin{aligned}\Delta C_{44}^* = {} & -2\Gamma_1^2 g_{44}^2 a^2/P_1^2\{-CP^2/2 + (P^2/3)(g_{11}+2g_{12})^2(C_{11}+2C_{12})^{-1} \\ & \quad + P/2 - (P^2/3)(g_{11}-g_{12})^2(C_{11}-C_{12})^{-1}\} \\ & + 2\Gamma_1 g_{44}^2 Pa/P_1\end{aligned} \tag{33d}$$

We shall now define the relaxation time τ for the system by the relation

$$\tau = \{\Gamma_3(\partial^2 F/\partial P_z^2)_0\}^{-1} = \{\Gamma_1(\partial^2 F/\partial P_x^2)_0\}^{-1}. \tag{34}$$

For simplicity, we assume that the relaxation time is isotropic. Then equations (23a) and (23b) become

$$P_1 = \Gamma_1 q_1 a(1 + i\Omega\tau) \tag{35a}$$

$$P_3 = \Gamma_3 q_3 a(1 + i\Omega\tau) \tag{35b}$$

where $q_1 a$ and $q_3 a$ are given by (23a) and (23b) respectively.

Now the relaxation time has a temperature dependence given by Lemanov [12] as

$$\tau = \tau_0/|T_c - T| \tag{36}$$

where τ_0 has a value of order $(10^{-11}$–$10^{-10})$ sK. Under most experimental conditions, the acoustic frequency is chosen in the range 10^8–10^9 Hz. Hence $\Omega\tau_0$ has a value of the order of 10^{-2}–10^{-3}.

Substituting (35a) and (35b) in (33a) to (33d), we find that all the elastic anomalies have the form

$$\Delta C^*_{ij} = \frac{F_{ij}(A_{ij} - B_{ij} i\Omega\tau)}{(1 + i\Omega\tau)^2} \tag{37}$$

where F_{ij}, A_{ij} and B_{ij} are constants that can easily be determined from (33a)–(33d). Further, the real parts of these constants are given by

$$R(\Delta C^*_{ij}) = F_{ij}\{A_{ij} - \Omega^2\tau^2(A_{ij} + 2B_{ij})\}(1 + \Omega^2\tau^2)^{-2} \tag{38a}$$

When $T = T_c$, $\Omega\tau \rightarrow \infty$ and it follows that

$$R(\Delta C^*_{ij}) \rightarrow 0.$$

When $|T - T_c| = \Omega\tau_0 = 10^{-2}$, we have $\Omega\tau = 1$ and

$$R(\Delta C^*_{ij}) = \frac{-F_{ij}B_{ij}}{2}. \tag{38b}$$

We further see that the stationary point for the expression on the RHS of (38a) is reached for the value of $\Omega^2\tau^2 = 1 + 2A_{ij}/(A_{ij} + 2B_{ij})$ and for this value,

$$R(\Delta C^*_{ij}) = -F_{ij}(A_{ij} + 2B_{ij})^2/\{8(A_{ij} + B_{ij})\} \tag{38c}$$

When $\Omega\tau \rightarrow 0$, $R(\Delta C^*_{ij}) = F_{ij}A_{ij}$.

This is the asymptotic value of the elastic anomalies in the low symmetry phase. The temperature dependence of the elastic anomalies can now be easily understood. It follows that the elastic constants $C^*_{ij} = C_{ij} + R(\Delta C^*_{ij})$ have a dip at the transition temperature of order $-F_{ij}(A_{ij} + 2B_{ij})^2/\{8(A_{ij} + B_{ij})\}$. Within a temperature range of 10^{-1} K the elastic constants reach their low symmetry value of

$$C_{ij} + F_{ij}A_{ij}. \tag{38d}$$

We conclude that the SOE anomalies are temperature dependent, showing a discontinuity at the transition temperature.

References

[1] D Berlin Court and H Jaffe, *Phys. Rev.* **111**, 143 (1958)
[2] R Blinc and B Zeks, *Soft modes in ferroelectrics and antiferroelectrics*, (North-Holland Publishing Company, Amsterdam) (1974)
[3] A D Bruce and R A Cowley, *Structural phase transitions* (*Taylor & Francis Ltd*, London) 2–110 (1981)
[4] E Fatuzzo and W J Merz, *Ferroelectricity*, (North-Holland Publishing Company, Amsterdam) Ch. 2 and 3 (1967)
[5] P A Fleury and K Lyons, *Structural phase transitions-1*, edited by K A Muller and H Thomas (Spinger Verlag, Berlin, Heidelberg, New York) (1981)
[6] S Fushimi and T Ikeda, *Rev. Elec. Commun. Lab* (Tokyo) **14**, 161 (1966)
[7] C W Garland, *Physical acoustics*, W P Mason and R N Thruston (New York, Academic Press) Vol. VII (1970)
[8] T F Heuter and D P Neuhaus, *J. Acoust. Soc. Am.* **27**, 292 (1955)
[9] E J Huibregtesem, W H Bressey and M E Drougard, *J. Appl. Phys.* **30**, 899 (1959)

[10] T Ikeda, *J. Phys. Soc. Jpn.* **13**, 809 (1958)
[11] Sh Kashida, I Hatta, A Ikushima and Y Yamada, *J. Phys. Soc. Jpn.* **34**, 997 (1973)
[12] V V Lemanov, *Optical and acoustic waves in solids—Modern Topics, Proc. of the Second Int. Conf. on Condensed Matter Phys.* (1982)
[13] B Luthi and W Rehwald, *Structural phase transitions 1* edited by K A Muller and H Thomas, (Springer Verlag, Berlin, Heidelberg, New York) (1981)
[14] W Rehwald, *Adv. Phys.* **22**, 721 (1973)
[15] A F Devonshire, *Philos. Mag.* **40**, 1040 (1949)

[redacted]

PRAMANA
— journal of
physics

© Printed in India

Vol. 41, No. 1,
July 1993
pp. 41–49

The effect of second neighbour repulsion on fcc binary alloy phase diagrams: A Monte Carlo study

RITA KHANNA and T R WELBERRY
Research School of Chemistry, The Australian National University, P.O. Box 4, Canberra, ACT 0200, Australia

MS received 19 November 1992; revised 21 April 1993

Abstract. We report the results of the Monte Carlo simulation of the phase diagram of fcc binary alloys using a 3-D Ising model with nearest and next-nearest neighbour repulsive interactions. Calculations are carried out for a ratio of second- to first-neighbour interaction energies of 0·4. The resulting phase diagram contains three superstructures A_2B_2, A_2B and A_5B, each separated by a disordered fcc phase. There was no evidence for the formation of an A_3B phase. These results are in qualitative agreement with CVM results.

Keywords. Monte Carlo simulation; phase diagram; binary alloys.

PACS No. 81·30

1. Introduction

A problem of great importance in the thermodynamic properties of alloys is the information regarding the range and the stability of various possible phases. Nearest neighbour Ising models have long been used to approximate binary alloys and the calculated phase diagrams have found qualitative agreement with the experimentally observed ones. Despite such unquestionable success, it is, however, clear that such models cannot hope to explain the tremendous variety of phase diagrams observed in nature. The model can be made more realistic and general by adding second and even further neighbour and/or multibody interaction [1, 2]. The ground state problem in the case of fcc binary alloy with nearest and next-nearest neighbour (nn and nnn) pair interactions has been completely solved. Kanamori and Kakehashi [3] have derived a list of ground state structures up to fourth neighbour interactions. However the results of this simple energy model show that a large number of observed fcc superstructures can be accounted for by nn and nnn interactions. Many of the structures predicted by the fourth neighbour interaction have not been experimentally observed. In this paper we focus our attention on ordering in a fcc binary alloy using nn and nnn repulsive interactions.

The model adopted here consists of a binary system with atomic species A and B occupying a rigid fcc lattice. In the Ising spin language, a site i occupied by an A atom is represented by an up spin $S_i = 1$, and a site occupied by a B atom by a down spin $S_i = -1$. The configurational energy is determined, within the framework of 3D Ising model, by the sum of effective pair interactions between the first and second nearest neighbours, denoted, respectively, by J_1 and J_2 [4, 5]. The Hamiltonian is equivalent to an Ising magnet in a magnetic field H

$$H = J_1 \sum_{\mathrm{nn}} S_i S_j + J_2 \sum_{\mathrm{nnn}} S_i S_j - H \sum S_i. \tag{1}$$

where the sum nn extends over all nearest neighbour pairs and nnn over all next-nearest neighbour pairs. For antiferromagnetic ordering ($J_1 > 0$), three distinct types of families of ordered structures are observed depending on the magnitude of the ratio $\alpha = J_2/J_1$ and are labelled as: (1) $\langle 1\,0\,0 \rangle$ family for $\alpha < 0$, (2) $\langle 1\,1/2\,0 \rangle$ family for $0 < \alpha < 0{\cdot}5$, and (3) $\langle 1/2\,1/2\,1/2 \rangle$ family for $\alpha > 0{\cdot}5$ [6, 7]. In a recent study of cation ordering in oxide systems [8], we have looked at the ordering in the regime ($\alpha > 0{\cdot}5$) and found that α has a strong influence on the range and stability of various observed phases. In this paper, we will solely concentrate on the ordered structures in the region defined by ($0 < \alpha < 0{\cdot}5$). The ground state structures expected in this parameter range are to be found at the stoichiometries: A_2B_2, A_2B, A_3B and A_5B (see figure 1).

Using the cluster variation method (CVM), Sanchez and deFontaine [4, 6] have obtained a prototype phase diagram for ($0 < \alpha < 0{\cdot}5$). The phase diagram reported for $\alpha = 0{\cdot}25$ was only partially complete as the low symmetry structure A_5B was not

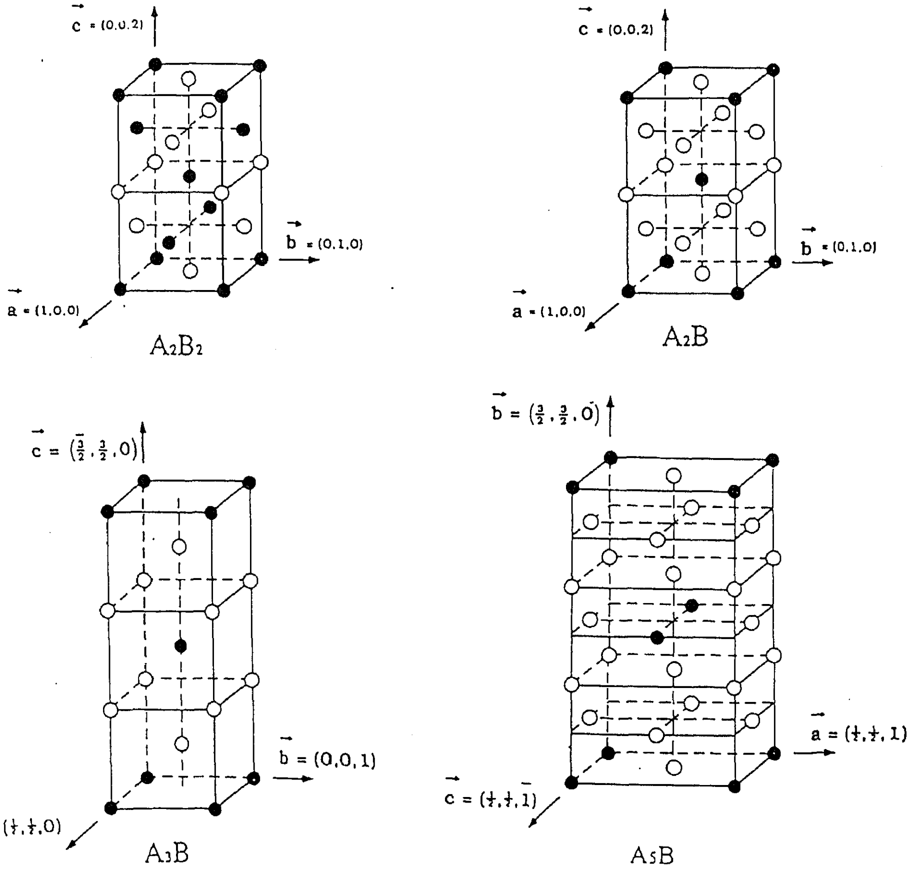
$\vec{c} = (0,0,2)$
$\vec{b} = (0,1,0)$
$\vec{a} = (1,0,0)$
A_2B_2
$\vec{c} = (0,0,2)$
$\vec{b} = (0,1,0)$
$\vec{a} = (1,0,0)$
A_2B
$\vec{c} = (\bar{\tfrac{3}{2}}, \tfrac{3}{2}, 0)$
$\vec{b} = (0,0,1)$
$\vec{a} = (\tfrac{1}{2}, \tfrac{1}{2}, 0)$
A_3B
$\vec{b} = (\tfrac{3}{2}, \tfrac{3}{2}, 0)$
$\vec{a} = (\tfrac{1}{2}, \tfrac{1}{2}, 1)$
$\vec{c} = (\tfrac{1}{2}, \tfrac{1}{2}, \bar{1})$
A_5B

Figure 1. Schematic unit cells for the structures of the $\langle 1\,1/2\,0 \rangle$ family: **(a)** A_2B_2, **(b)** A_2B, **(c)** A_3B, **(d)** A_5B.

included in the calculations. CVM results, in general, agree well with Monte Carlo results near stiochiometric compositions, but they have been found to deviate considerably in regions away from the stiochiometric compositions. Even though CVM calculations have been known to produce many of the topological features of the phase diagrams, it has been argued that a CVM phase diagram is a product more of the approximation used to produce it than the true phase diagram of the model Hamiltonian [9]. At the present time, one of the most reliable phase diagrams for binary alloys (Cu–Au, $\alpha < 0$) has been obtained by Binder [10] using Monte Carlo simulation. A complete Monte Carlo phase diagram for $0 < \alpha < 0{\cdot}5$ is not available, though Binder *et al* [11] have obtained transition temperatures at a few isolated points for $\alpha = 0{\cdot}25$. In this paper, we carry out a complete phase diagram calculation using Monte Carlo methods for $\alpha = 0{\cdot}4$.

2. The Monte Carlo method

We consider a system of $N = 4L^3$ spins on an fcc lattice with periodic boundary conditions. L was measured in units of the lattice constant, a, and has to be chosen such that the periodic boundary conditions are consistent with the expected ordered structures without the need of introducing antiphase boundaries in the structure. From some of the expected orderings shown in figure 1, A_2B ordering will require L to be a multiple of 3, while A_3B ordering will require L to be an even number. We chose L to be a multiple of 6(12, 18, 24 etc), so that it is consistent with all the expected structures. The structures A_2B_2 and A_5B are also consistent with this choice. The simulations were performed using single spin-flip Glauber dynamics in the grand canonical ensemble, with the concentration, c_B, varying as a function of temperature and magnetic field. Starting from an initial configuration, the system was allowed to evolve according to the Metropolis algorithm [12]. The data were collected for typically five to ten thousand Monte Carlo steps per site (MCSS).

Labelling the four sublattices of the unit cell of the fcc lattice from 1 to 4, we introduce the sublattice magnetizations m_ν,

$$m_\nu = (1/N) \sum_{i \in \nu} \langle S_i \rangle, \qquad \nu = 1 \text{ to } 4 \tag{2}$$

where $\langle\ \rangle$ is computed by taking time averages over different Monte Carlo runs. The total magnetization M is given by

$$M = m_1 + m_2 + m_3 + m_4 \tag{3}$$

and is related to the average concentration c_B of B atoms by

$$c_B = (1 - M)/2. \tag{4}$$

Order parameter distribution functions were used to locate the phase boundary and to determine the order of the transition [13]. $P(\phi)\mathrm{d}\phi$ is defined as the probability the order parameter will take on a value in the range $[\phi, \phi + \delta\phi]$. Instead of using specific order parameters for each superstructure, we have carried out the distribution function analysis using only the magnetization order parameter M. From the peak positions of $P(M)$, one can unambiguously identify the composition of various stable phases present in the system. There is no need for *a priori* assumptions regarding the presence of different phases and no phases can be left out of the phase diagram as in the case of CVM calculations for $\alpha = 0{\cdot}25$. In this work, a peak position in $P(M)$ could be located with an accuracy of 0·002. The lattice size dependence of the order parameter was used to identify the order of the transition.

3. Simulation results

The phase diagram obtained from the analysis of distribution function data is shown in figure 2. As only pair interactions have been used in this simulation and the interaction parameters have been assumed to be independent of the concentration, this phase diagram is symmetric about $c_B = 0{\cdot}5$. The phase diagram is dominated by three superstructure phases separated by a disorded fcc phase (labelled here as F). The three superstructures observed are: A_2B_2, A_2B and A_5B and are labelled as such in the phase diagram. There is no evidence whatsoever for the A_3B phase observed in some of the CVM simulations.

The A_2B_2 phase extends from $c_B = 0{\cdot}5$ to 0·425 at low temperatures. The region of stability of this phase narrows with the increasing temperature and transforms into a disordered phase at $k_B T/J_1 \sim 1{\cdot}05$ ($c_B = 0{\cdot}5$). The transition from the A_2B_2 phase to the disordered F phase is clearly of first order and is also marked by a well defined co-existence region between the phase boundaries. Distribution function plots of magnetization as a function of magnetic field and lattice size are shown in figure 3. The closest gap between the two peaks in the transition region identifies the limits of the co-existence region and can be computed with a fair degree of accuracy.

The next stable superstructure A_2B, observed in the concentration range $c_B = 0{\cdot}28$ to 0·38, is surrounded on both sides by the disordered F phase and is stable below $k_B T/J_1 \sim 1{\cdot}0$. The distribution function plots for F to A_2B transition and A_2B to F transition are shown in figures 4 and 5 respectively. Both these transitions are of first order and have well defined co-existence regions. According to CVM simulations, we should observe the next superstructure around $c_B = 0{\cdot}25$ with a formula of A_3B. We however could not see any evidence of a superstructure in this composition range.

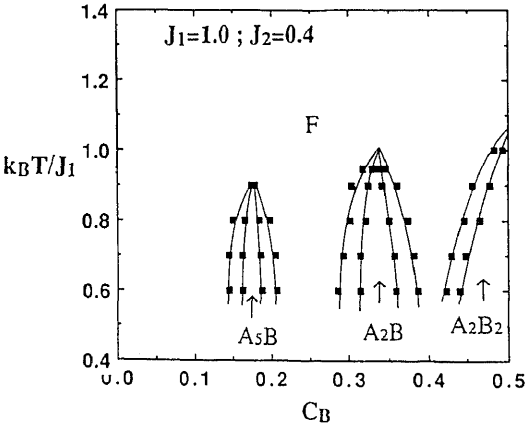

Figure 2. Temperature–composition phase diagram for the parameter set: $J_1 = 1{\cdot}0$; $J_2 = 0{\cdot}4$. Various observed ordered structures are indicated as such in the phase diagram.

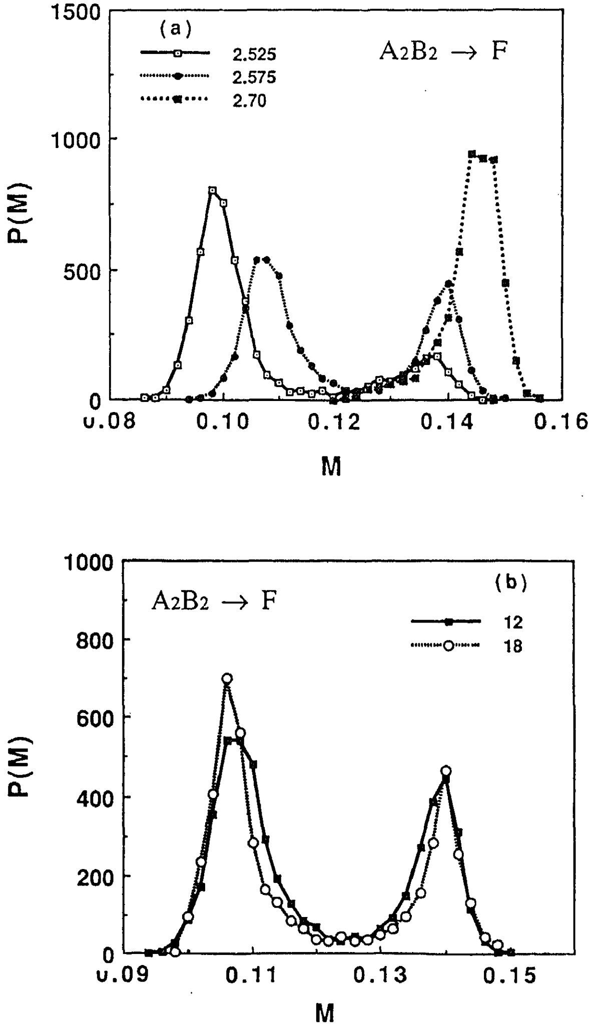

Figure 3. Plots of the distribution function $P(M)$ vs M for $J_2 = 0{\cdot}4$ and $k_B T/J_1 = 0{\cdot}7$ for the A_2B_2 to F transition. (**a**) Plots of $P(M)$ for three different values of the field H/J_1. The magnitudes of H/J_1 are indicated against the plot symbol. The lattice size for these simulations was $L = 12$. (**b**) Plots of $P(M)$ for two different lattice sizes across the transition. The lattice size L is indicated against the plot symbol.

The peaks in the distribution function data were very similar to those observed for a disordered phase (figure 6).

The third superstructure observed was A_5B in the concentration range $c_B = 0{\cdot}14$ to 0·21. The overall shape of the phase boundaries for this phase is very similar to those for the A_2B phase. The distribution function plots for F to A_5B transition and A_5B to F transition are shown in figures 7 and 8 respectively. Both of these transitions are also of the first order. No new superstructure was observed in the concentration range $c_B = 0{\cdot}0$ to 0·14.

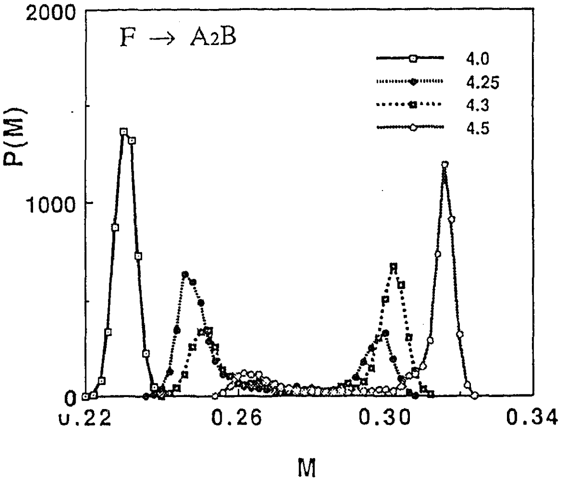

Figure 4. Plots of the distribution function $P(M)$ vs M for $J_2 = 0{\cdot}4$ and $k_B T/J_1 = 0{\cdot}7$ for the F to A_2B transition for four different values of the field H/J_1. The magnitudes of H/J_1 are indicated against the plot symbol. The lattice size for these simulations was $L = 12$.

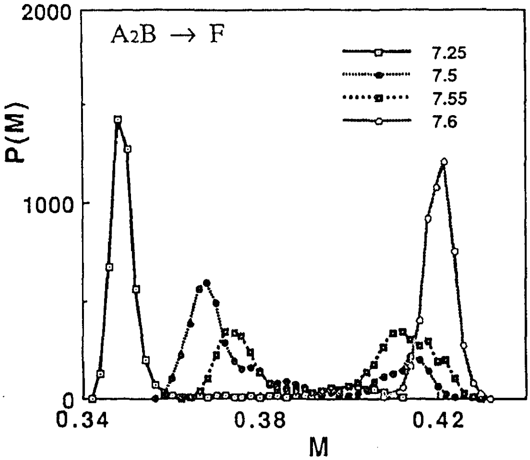

Figure 5. Plots of the distribution function $P(M)$ vs M for $J_2 = 0{\cdot}4$ and $k_B T/J_1 = 0{\cdot}7$ for the A_2B to F transition for four different values of the field H/J_1. The magtitudes of H/J_1 are indicated against the plot symbol. The lattice size for these simulations was $L = 12$.

4. Discussion

Sanchez and de Fontaine [4,6] have computed temperature-composition phase diagrams for fcc binary alloys for $\alpha = 0{\cdot}25$, $0{\cdot}35$ and $0{\cdot}45$ using the cluster variation method. Apart from the A_5B phase which was left out in the $\alpha = 0{\cdot}25$ simulation, the three other observed superstructures in all three simulations were at A_2B_2, A_2B and A_3B compositions. Our Monte Carlo results for $\alpha = 0{\cdot}4$ are consistent with CVM results in this regard. The Monte Carlo phase boundaries appear to be quite similar

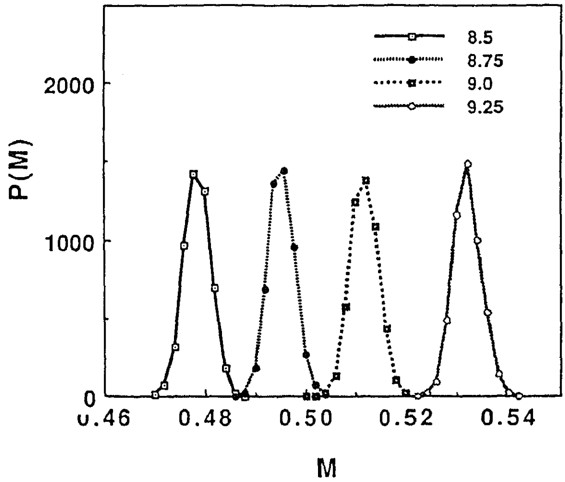

Figure 6. Plots of the distribution function $P(M)$ vs M for $J_2 = 0{\cdot}4$ and $k_B T/J_1 = 0{\cdot}7$ in the composition region where A_3B phase should have been observed. The magnitudes of H/J_1 are indicated against the plot symbol. The lattice size for these simulations was $L = 12$.

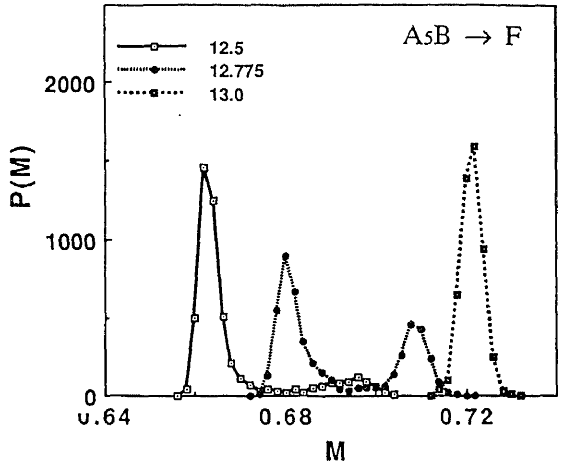

Figure 7. Plots of the distribution function $P(M)$ vs M for $J_2 = 0{\cdot}4$ and $k_B T/J_1 = 0{\cdot}7$ for the F to A_5B transition for three different values of the field H/J_1. The magnitudes of H/J_1 are indicated against the plot symbol. The lattice size for these simulations was $L = 12$.

to the CVM phase diagram for $\alpha = 0{\cdot}45$ with the following differences. In the CVM phase diagram, the A_2B_2 to F phase boundaries (co-existence region) appears to be the broadest around $k_B T/J_1 \sim 0{\cdot}8$ to $0{\cdot}9$ region and narrows down considerably with the decreasing temperature. In addition, this phase extends below $c_B = 0{\cdot}4$ at low temperatures and finally joins the A_2B phase. The Monte Carlo results, which were computed above $k_B T/J_1 = 0{\cdot}5$, due to the increased scatter in data at low temperatures, do not show this narrowing of co-existence region and also indicate a smaller region of stability for the A_2B_2 phase. The transition temperature at $c_B = 0{\cdot}5$

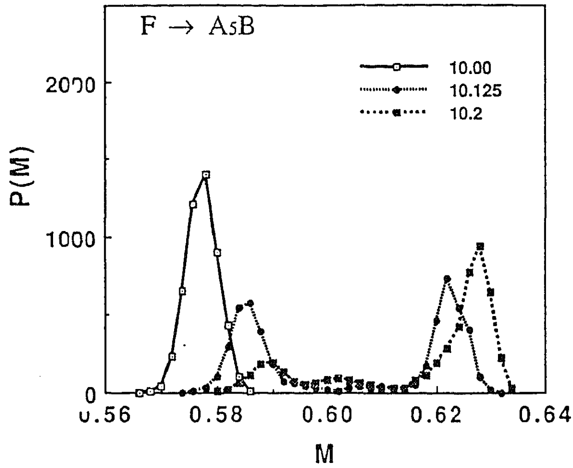

Figure 8. Plots of the distribution function $P(M)$ vs M for $J_2 = 0{\cdot}4$ and $k_B T/J_1 = 0{\cdot}7$ for the A_5B to F transition for three different values of the field H/J_1. The magnitudes of H/J_1 are indicated against the plot symbol. The lattice size for these simulations was $L = 12$.

appears to be identical in both simulations. The boundaries for A_2B and A_5B phases are similar in both cases apart from the fact that the region of stability of these phases is over-estimated in the CVM phase diagram. Also, the transition temperature for the A_5B phase is lower in our Monte Carlo results. In addition, the CVM results indicate the presence of an A_3B phase at very low temperatures.

As the second neighbour repulsion (α) decreases, the CVM phase diagrams tend to become fairly complicated. Main feature of these phase diagrams appears to be the gradual disappearance of the A_3B phase as α approaches 0·5. Canonical ensemble Monte Carlo simulations of Binder *et al* [11] at $\alpha = 0{\cdot}25$ indicated the presence of an A_3B phase at $c_B = 0{\cdot}25$ ($k_B T/J_1 = 1{\cdot}116$). Our simulations at $\alpha = 0{\cdot}4$ in the temperature range $k_B T/J_1 > 0{\cdot}5$ show a complete absence of the A_3B phase. A more complete investigation of the A_3B phase as a function of α by Monte Carlo methods is in progress. The other three superstructures A_2B_2, A_2B and A_5B are, however, stable in the entire parameter range ($0 < \alpha < 0{\cdot}5$).

We have considered here a very simple model, which cannot be expected to represent faithfully any real alloy system. We find that the behaviour of stoichiometric alloys is rather insensitive to the parameters of the model. Observing the ordering behaviour in the non-stoichiometric region would be a much more sensitive tool for checking whether a model correctly represents a real system. Many body interactions, concentration dependence of interaction strengths and contributions from more distant neighbours are expected to make simulation results more accurate. In addition, the Ising model in its present form cannot describe lattice-dynamical phase diagrams as one is looking only at the atomic ordering process and lattice relaxations/distortions are not allowed. There is still need for a lot of future work in this field.

References

[1] D P Landau and K Binder, *Phys. Rev.* **B17**, 2328 (1978)
[2] R Kikuchi, J M Sanchez, D de Fontaine and H Yamauchi, *Acta Metall.* **28**, 651 (1980)

[3] J Kanamori and Y Kakehashi, *J. Phys.* (*Paris*) **38 Suppl. C7**, 274 (1978)
[4] J M Sanchez and D de Fontaine, *Phys. Rev.* **B21**, 216 (1980)
[5] M Allan and J W Cahn, *Acta Metall.* **20**, 423 (1972)
[6] J M Sanchez and D de Fontaine, *Phys. Rev.* **B25**, 1759 (1982)
[7] M S Richards and J W Cahn, *Acta Metall.* **19**, 1263 (1971)
[8] R Khanna, T R Welberry and R L Withers, *J. Phys.* **C5**, 4251 (1993)
[9] K Binder and D P Landau, *Phys. Rev.* **B30**, 1477 (1984)
[10] K Binder, *Z. Physik* **B45**, 61 (1981)
[11] K Binder, J L Lebowitz, M K Phani and M H Kalos, *Acta Metall.* **29**, 1655 (1981)
[12] K Binder, in *Monte Carlo methods in statistical physics* (Springer, Berlin, 1979) vol. 1
[13] O G Mouritsen, in *Computer studies of phase transitions and critical phenomenon* (Springer Verlag, New York, 1984) p. 18

PRAMANA
— journal of
physics

© Printed in India

Vol. 41, No. 1,
July 1993
pp. 51–60

Field-cooled measurements of harmonic generation in magnetization of high-T_c superconductors

S B ROY, SHAILENDRA KUMAR, A K PRADHAN, P CHADDAH,
RAM PRASAD*, N C SONI* and KALYAN ADHIKARY*
Low Temperature Physics Group, Centre for Advanced Technology, Indore 452013, India
*Metallurgy Division, Bhabha Atomic Research Centre, Bombay 400085, India

MS received 24 February 1993

Abstract. We present measurements of harmonic generation in the magnetization of sintered pellets of $YBa_2Cu_3O_7$ and $Bi_{1\cdot7}Pb_{0\cdot3}Sr_2Ca_2Cu_3O_{10}$ as a function of DC field. The DC field is applied in the field-cooled mode. Measurements are made at 77 K for various values of the AC field amplitude. A comparison is made with calculations done within the critical state model.

Keywords. Harmonic generation; magnetization; superconductors; critical state model; field-cooled mode.

PACS Nos 74·30; 74·60

1. Introduction

The magnetic response of a sintered pellet of a high-temperature superconductor (HTSC), to a time-varying magnetic field $B(t) = B_{dc} + B_{ac}\cos\omega t$, has been studied in detail in the last few years [1–6]. When B_{dc} is zero, higher odd harmonics ($(2l+1)\omega$) are observed in the magnetisation with their magnitude increasing as B_{ac} is increased. The absence of even harmonics indicates the symmetry of the hysteresis loop. When B_{dc} is non-zero a response is also observed at higher even harmonics. This observation, and the consequent asymmetry of the minor hysteresis loop, was stressed [1] to be a signature of a field-dependent critical current density $J_c(B)$. The dependence of the harmonic magnitudes (M_n) on B_{dc} is again understood [7] as a signature of a field-dependent $J_c(B)$. Calculations of the dependence of various harmonics on B_{dc} and B_{ac}, as predicted by the critical state model with various forms of $J_c(B)$, have been reported in recent literature [1, 4, 8–10].

The transport $J_c(B)$ measured in sintered HTSC samples has been found to depend on the history of application of the magnetic field [11–13]. This, and related history effects in microwave measurements [7], have been understood by realising that a sintered pellet consists of grains and of intergrain regions and the transport $J_c(B)$ is dictated by the response of the intergrain region. The effective magnetic field in the intergrain region (say B_{eff}) has contributions from the externally applied field B_{ext} as well as the field generated by the magnetized grains. The magnetization of the grain depends on the history of application of B_{ext}, and B_{eff} mimics this history effect. The measured $J_c(B)$ is dictated by B_{eff} in the intergrain region, and must depend on the history of application of the external field. The minor hysteresis loop for small B_{ac}

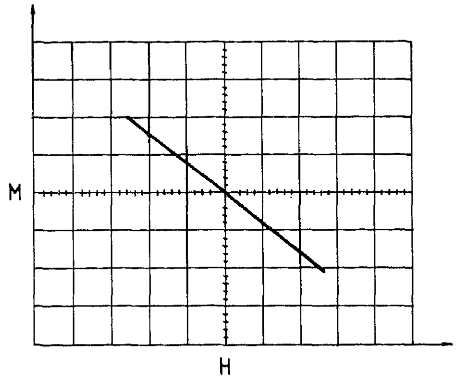

Figure 1a. M vs B loop, as seen on the oscilloscope for a YBaCuO pellet measured at $B_{ac} = 4$ G. Though the vertical scale is arbitrary for magnetization units, the oscilloscope was used in a 5·0 mV/cm configuration for the Y axis.

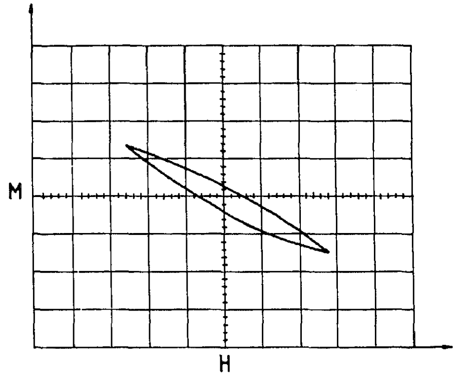

Figure 1b. Same as 1 (a) except that the pellet was momentarily exposed to $B_{dc} = 1$ kG (at 77 K) before measurement.

is attributed mainly to the intergrain region and, being dictated by B_{eff}, its shape should also depend on the history of application of B_{ext}. We have recently confirmed this by careful measurements on various sintered HTSC pellets [14], and figure 1 shows a typical result. Both the hysteresis loops shown are measured, with $B_{dc} = 0$ (earth's field) and $B_{ac} = 4$ G, on a YBaCuO pellet at 77 K. The only difference is that for figure 1 (b) the pellet was momentarily exposed to $B_{dc} = 1$ kG (at 77 K) before measurement in earth's field. This clearly shows that the shape of the minor hysteresis loop depends on the history of application of B_{dc}. The opening up of the hysteresis loop in figure 1 (b) indicates a power loss not seen in figure 1 (a), and provides a caution for accelerator cavity applications since accidental momentary exposure to a DC field can make the cavity show loss.

Since the shape of the minor hysteresis loop is history dependent, this dependence must also be seen in the harmonics. We have systematically demonstrated such history effects [15–17]. We have argued that only those measurements of harmonics in which B_{dc} was varied at $T > T_c$ (referred to as field-cooled data) could be readily compared with theory as only in this case is the DC part of $B_{eff}(t)$ equal to the applied B_{dc}. To our knowledge all reported measurements of M_n vs B_{dc} on HTSC pellets have so far been made with B_{dc} varied isothermally at $T < T_c$. In this paper we report the *first field-cooled data* on M_n vs B_{dc}. The measurements are made at 77 K on pellets of $YBa_2Cu_3O_7$ and $Bi_{1\cdot7}Pb_{0\cdot3}Sr_2Ca_2Cu_3O_{10}$. In the next section we present experimental details and results. We then present a qualitative comparison with theoretical calculations [10].

2. Experimental details and results

Measurements were made on sintered pellets of $YBa_2Cu_3O_7$ and $Bi_{1\cdot7}Pb_{0\cdot3}Sr_2Ca_2 \cdot Cu_3O_{10}$ (Bi-2223). The pellets were prepared by the standard solid state sintering route. For the former, Y_2O_3, $BaCO_3$ and CuO were calcined in air at 900°C (15 h) and 920°C (15 h) interspersed with grinding and mixing. The compacted (10 TS1) pellet was sintered in oxygen at 940°C (15 h) and was held at 400°C (15 h) during cooling. XRD showed no second phase, and oxygen was estimated by iodometry as 6·95. The sample had a resistive T_c of 91 K (confirmed by ZFC magnetization), and a 9 mm dia pellet was thinned to 0·25 mm thickness for the measurements discussed below. (The data shown in figure 1 are with a pellet of thickness 1 mm). For preparation of Bi-2223, $CaCO_3$, $SrCO_3$ and CuO were calcined twice in air at 950°C (15 h each) interspersed with grinding and mixing. $Sr_2Ca_2Cu_3O_7$ was then mixed with Bi_2O_3 and PbO in the right proportion and calcined at 800°C for 2 h followed by grinding and mixing. Pellet compacted at 10 TS1 was flash-heated at 915°C to obtain surface melting. It was crushed, pelletized and sintered at 855°C for 130 h. It was again crushed, pelletized and sintered at 865°C for 140 h. XRD showed no 2212 phase, and the sample has a resistive T_c of 107 K (confirmed by ZFC magnetization). The pellet used had a diameter of 9 mm and thickness of 0·7 mm.

The magnetization of these pellets was measured using a low-field hysteresis loop tracer [18], with a driving frequency of 317 Hz and with B_{ac} variable up to 18 G. The dc bias field was applied by a splitpair Helmholtz coil coaxial with the primary coil of the hysteresis-loop tracer. B_{ac} and B_{dc} were applied perpendicular to the plane of the pellet which was mounted in a glass dewar inside the pick-up coil. The magnetization signal from the output of the hysteresis loop tracer is fed to an HP 3582 A spectrum analyser where the magnitude of various harmonics is recorded. No attempt was made to cancel earth's field. All measurements were made at 77 K with B_{dc} applied with the sample at room temperature, and the sample field-cooled to 77 K. B_{ac} was kept $\leqslant 4$ G ($\leqslant 6$ G) for Bi-2223 (YBaCuO) pellet during field-cooling, and its magnitude was raised to the appropriate values at 77 K. No data were taken by reducing B_{ac} at $T < T_c$, due to associated history effects [14].

We now present the magnitude of various harmonics, as a function of B_{dc}, for various values of B_{ac}. Figures 2 to 5 show the results for Bi-2223, and figures 6 to 9 for YBaCuO. We outline below the salient features seen in these figures.

(i) We note that the second harmonic signal $2f$ (we denote the nth harmonic by nf) has its lowest value at $B_{dc} = 0$. This is also true for the $4f$ signal. This is consistent with the critical state model which requires that all even harmonics vanish for $B_{dc} = 0$. The small signal we observe in figures 2, 4, 6 and 8 can be attributed to the earth's field.
(ii) From figures 3 and 7 we note that $3f$ has a minimum as B_{dc} is raised, and this minimum occurs at higher values of B_{dc} as B_{ac} is raised.
(iii) $2f$ vs B_{dc} for YBaCuO (figure 6) has a small shoulder at 2 G, in addition to the main peak at 10 G, for $B_{ac} = 6$ G. This shoulder gains in intensity as B_{ac} is raised and

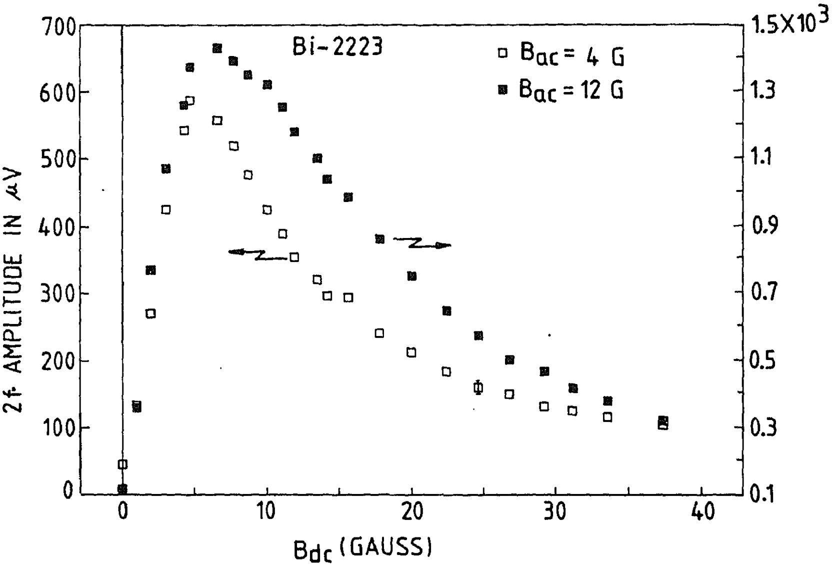

Figure 2. Second harmonic amplitude (2f) of Bi-2223 as a function of DC magnetic field (B_{dc}), the ac field (B_{ac}) being fixed at 4 and 12 G.

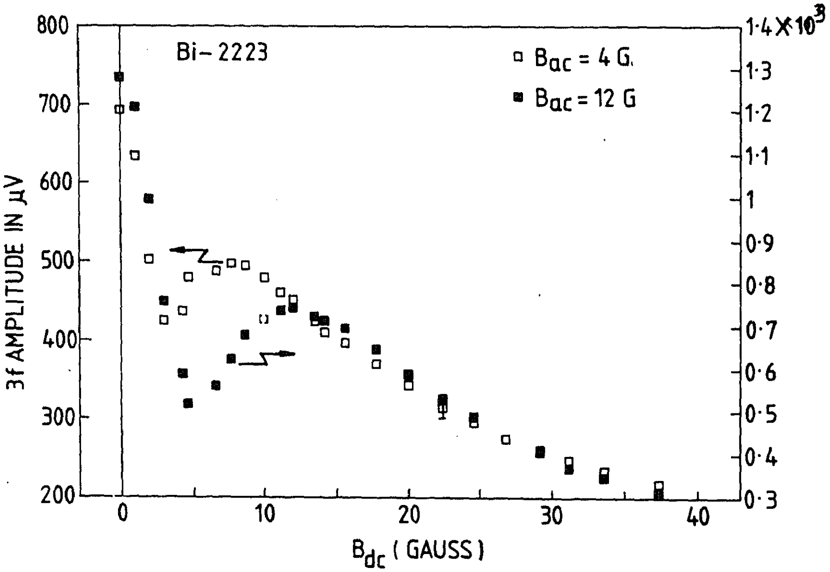

Figure 3. Third harmonic amplitude (3f) of Bi-2223 as a function of DC magnetic field (B_{dc}), the ac field (B_{ac}) being fixed at 4 and 12 G.

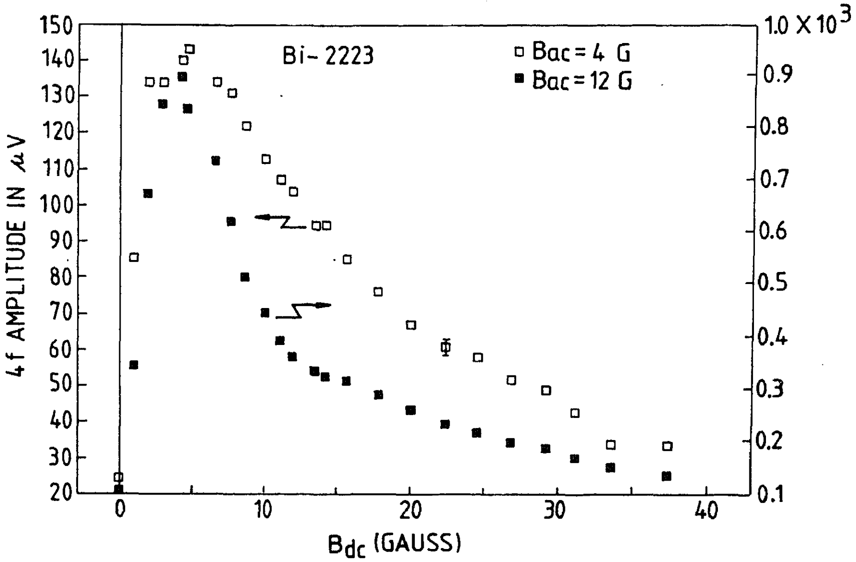

Figure 4. Fourth harmonic amplitude (4*f*) of Bi-2223 as a function of DC magnetic field (B_{dc}), the ac field (B_{ac}) being fixed at 4 and 12 G.

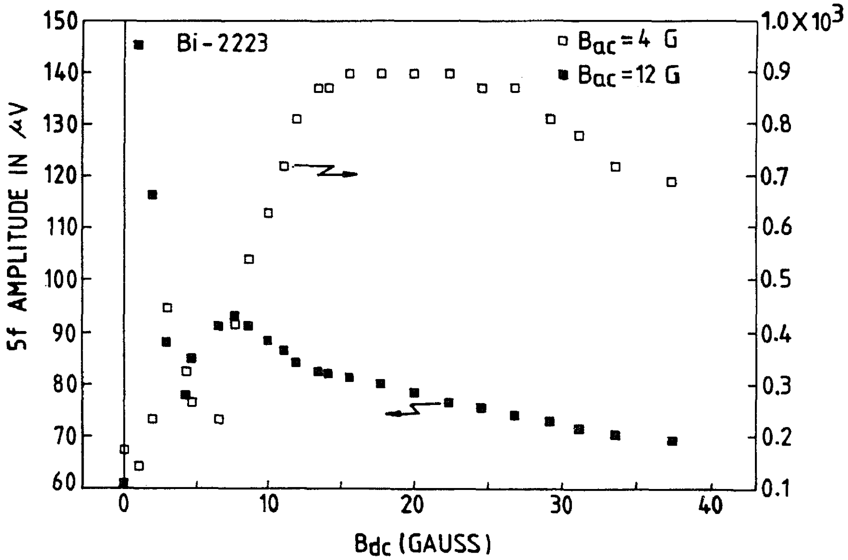

Figure 5. Fifth harmonic amplitude (5*f*) of Bi-2223 as a function of DC magnetic field (B_{dc}), the ac field (B_{ac}) being fixed at 4 and 12 G.

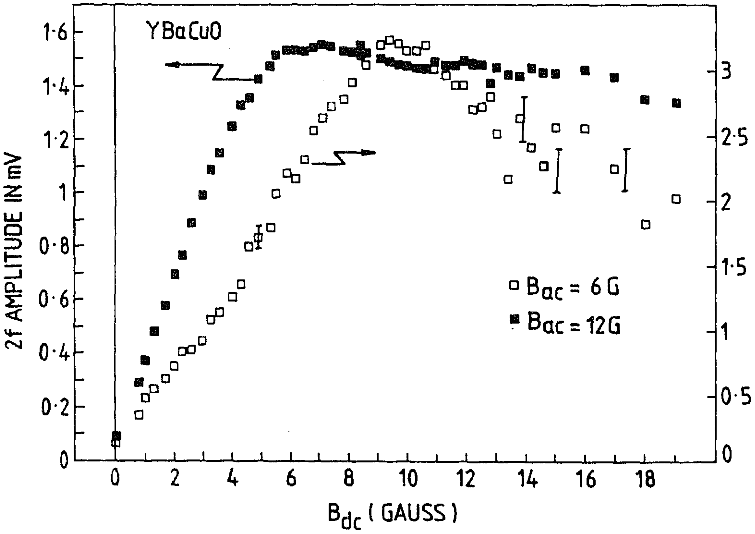

Figure 6. Second harmonic amplitude (2*f*) of YBaCuO as a function of DC magnetic field (B_{dc}), the ac field (B_{ac}) being fixed at 6 and 12 G.

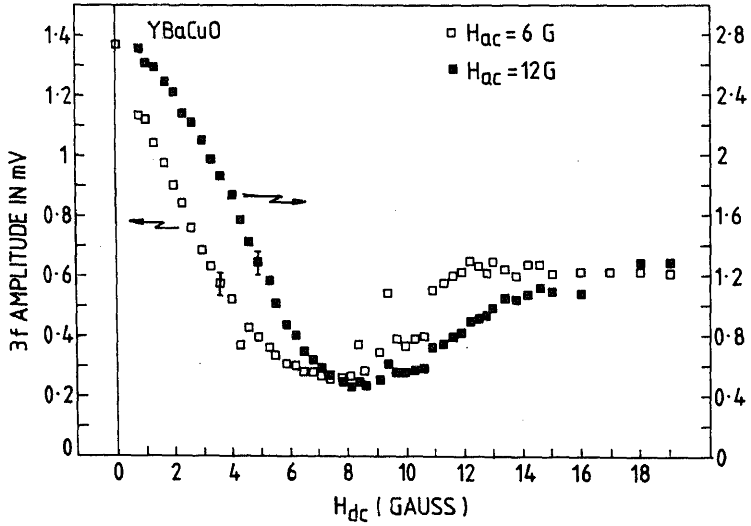

Figure 7. Third harmonic amplitude (3*f*) of YBaCuO as a function of DC magnetic field (B_{dc}), the ac field (B_{ac}) being fixed at 6 and 12 G.

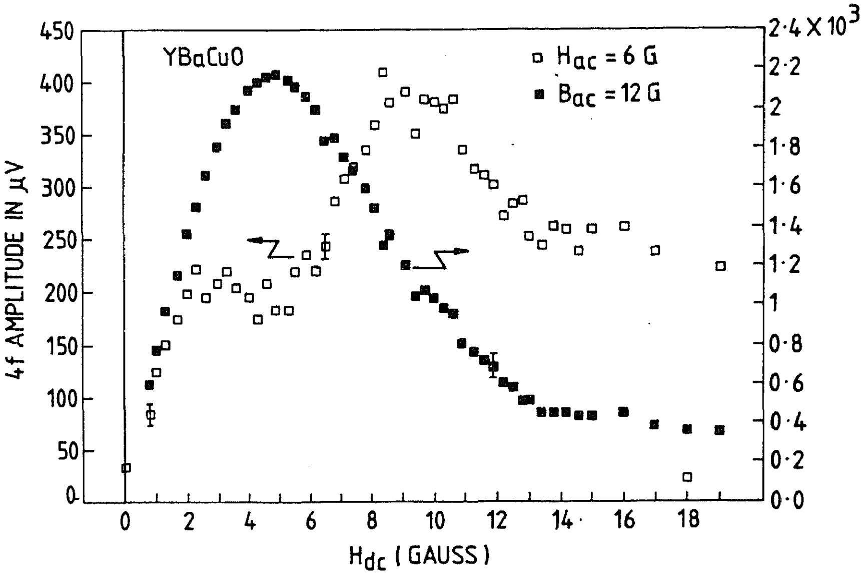

Figure 8. Fourth harmonic amplitude (4*f*) of YBaCuO as a function of DC magnetic field (B_{dc}), the ac field (B_{ac}) being fixed at 6 and 12 G.

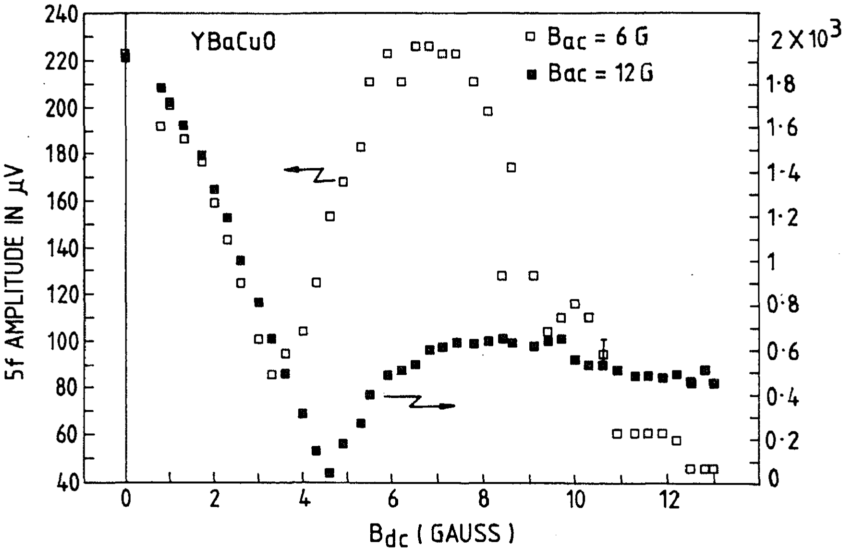

Figure 9. Fifth harmonic amplitude (5*f*) of YBaCuO as a function of DC magnetic field (B_{dc}), the ac field (B_{ac}) being fixed at 6 and 12 G.

also moves to larger values of B_{dc} (indicated by arrows). The clear double-peak observed in ZFC data [17] is however, smudged in this FC data.

(iv) The 5*f* data (figure 5 and 9) shows the existence of multiple minima at the lowest value of B_{ac}, but this sharp structure gets smudged for both Bi-2223 and YBaCuO as B_{ac} is raised.

3. Comparison with calculations

As discussed in the introduction, calculations of harmonic magnitude, as a function of B_{dc}, have been performed within the critical state model. One general result [1, 10] is that if the magnitude of *nf* is plotted as B_{dc} is varied from $-B_{ac}$ to B_{ac}, there should be $(n-1)$ minima. This is consistent with the data in figures 2, 3 and 5 (for

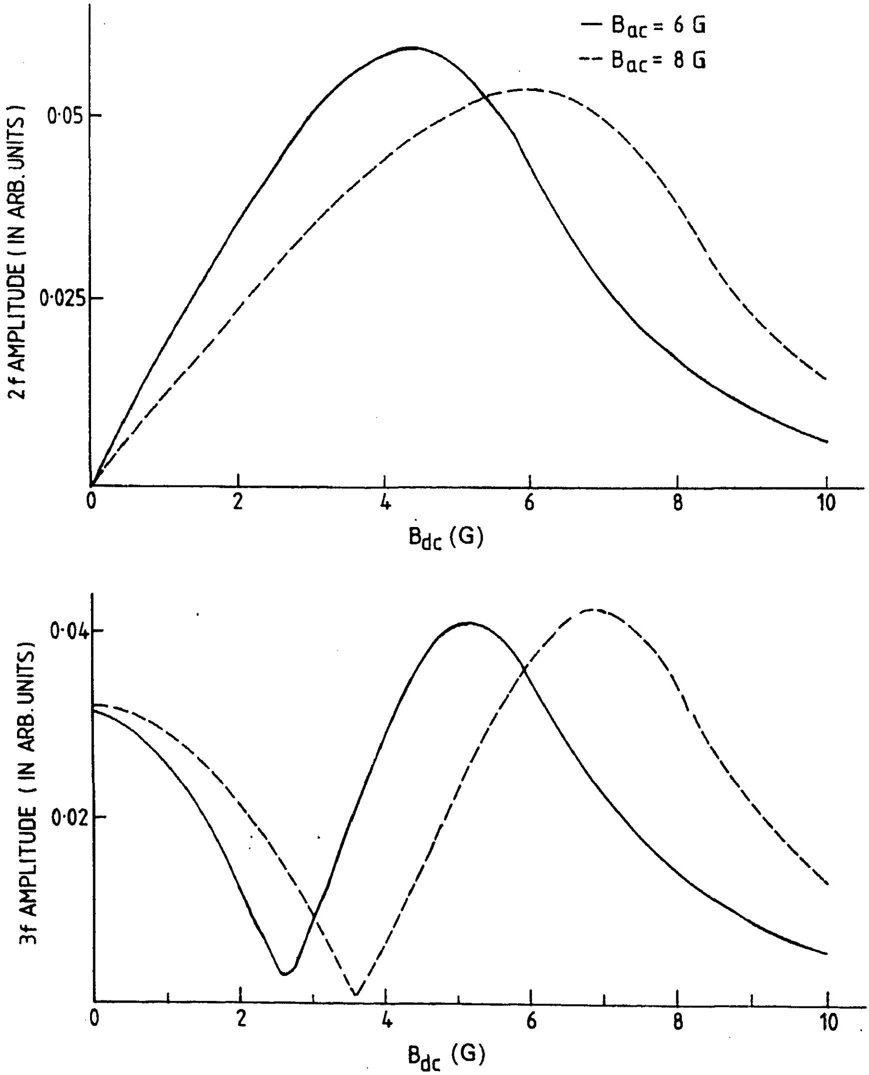

Figure 10. Calculated values of second (2*f*) and third (3*f*) harmonic amplitudes as a function of DC magnetic field (B_{dc}), the ac field (B_{ac}) being fixed at 6 and 8 G.

lowest B_{ac}) for Bi-2223 and with figures 6 and 7 for YBaCuO, but not for the other harmonics. The experimental observation (i) is, nevertheless, explained.

We show in figure 10 the calculated values of $2f$ and $3f$ as B_{ac} is raised. We assume in the calculation that $J_c(B) = J_c(0)\exp[-|B|/2]$. The calculations assume that Bean's parametric field [10] $B^* = 1$, and all fields in the calculation scale linearly with B^*. The peak in $2f$, and the minimum in $3f$, move to larger values of B_{dc} as B_{ac} is raised. This is consistent with the data in figures 2, 3 and 7 but the $2f$ data for YBaCuO in

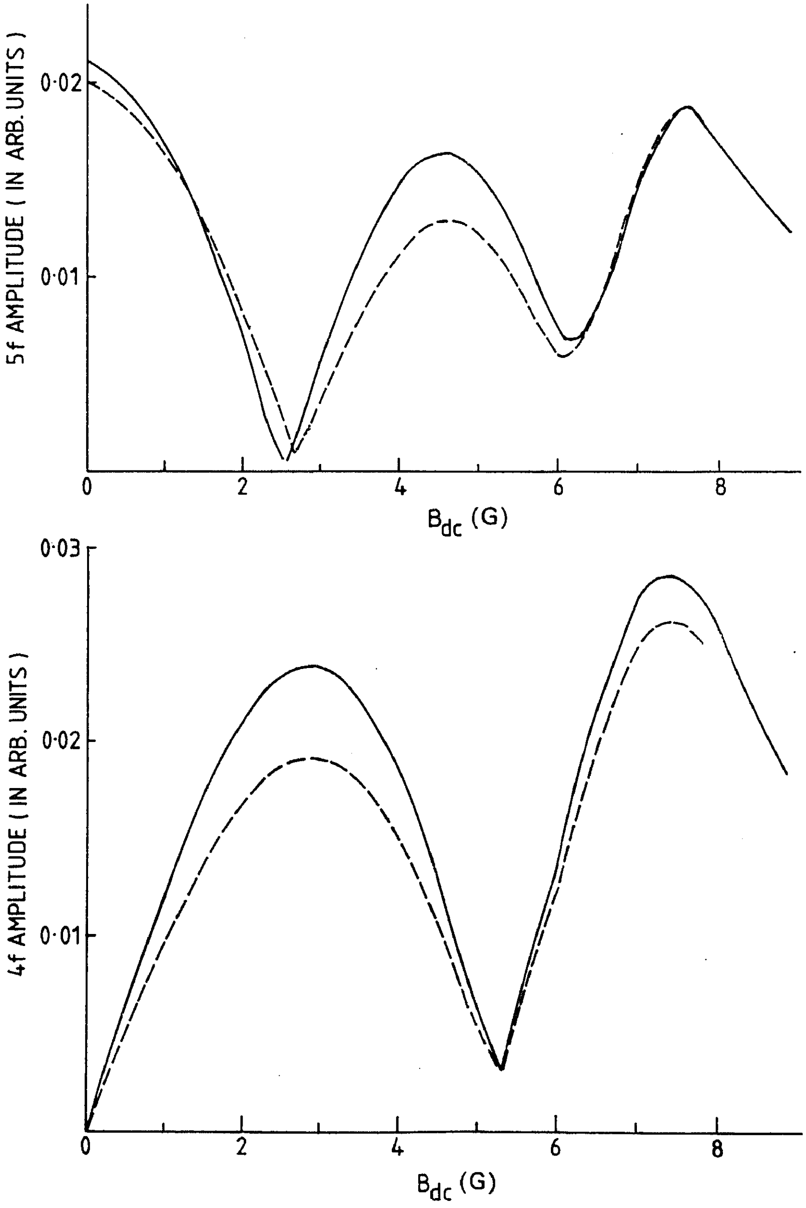

Figure 11. Calculated values of fourth ($4f$) and fifth ($5f$) harmonic aplitude as a function of DC magnetic field (B_{dc}) for two forms of $J_c(B)$ viz. $J_c(0)\exp(-|B|/2)$ (solid line) and $J_c(0)\,[1+|B|/3]^{-2}$ (dotted line).

figure 6 exhibits a shoulder that is not predicted by the calculation. The measured shoulder, as discussed by Roy *et al* [17], may be due to two parallel intergrain components. This is a complexity beyond the scope of existing calculations.

We show in figures 11 calculations of $4f$ and $5f$ for two forms of $J_c(B)$ viz. $J_c(0)\exp(-|B|/2)$ and $J_c(0)[1+|B|/3]^{-2}$. The latter form decays slower with B, and results in a smaller peak-to-valley ratio [10] in nf vs B_{dc}. This ratio is however still much larger than the experimental data presented in figures 4, 5, 8 and 9.

4. Conclusions

We have presented measurements of harmonic generation in sintered pellets of Bi-2223 and YBaCuO, with B_{dc} applied in the field-cooled mode. Qualitative features seen in the $2f$ and $3f$ data are consistent with the predictions of the critical state model. The behaviour of the higher harmonics calls for further refinements in the theoretical model.

Acknowledgements

One of the authors (PC) was introduced to the hysteresis loop tracer [18] in Prof. C Radhakrishnamurty's laboratory in 1987. The authors have used this versatile unit as the heart of their magnetization measurements. As Prof. Radhakrishnamurty nears the age of sixty, we wish to gratefully acknowledge the impact of his instrument on our work.

References

[1] L Ji, H Sohn, G C Spalding, C J Lobb and M Tinkham, *Phys. Rev.* **B40**, 10936 (1989)
[2] K H Muller, J C Macfarlane and R Driver, *Physica* **C158**, 366 (1989)
[3] T Ishida and R B Goldfarb, *Phys. Rev.* **B41**, 8937 (1990)
[4] Q H Lam, Y Kim and C D Jeffries, *Phys. Rev.* **B42**, 4846 (1990)
[5] R Novarro, F Lesa, C Rillo and J Bartolome, *Physica* **C167**, 549 (1990)
[6] S F Wahid and N K Jaggi, *Physica* **C170**, 395 (1990)
[7] P Chaddah, *Pramana – J. Phys.* **36**, 353 (1991)
[8] S F Wahid and N K Jaggi, *Physica* **C184**, 88 (1991)
[9] S F Wahid and N K Jaggi, *Physica* **C194**, 211 (1992)
[10] P Chaddah, S B Roy, Shailendra Kumar and K V Bhagwat, *Phys. Rev.* **B46**, 11737 (1992)
[11] J E Evetts and R A Glowacki, *Cryogenics* **28**, 641 (1988)
[12] M Majoros, M Polak, V Strbik, S Benacka, S Chromik, F Hanic and V Plechacek, *Super. Sci. Tech.* **3**, 227 (1990)
[13] P K Mishra, G Ravikumar, P Chaddah, Shailendra Kumar and B A Dasannacharya, *Jpn. J. Appl. Phys.* **29**, L1612 (1990)
[14] S B Roy, Shailendra Kumar, A K Pradhan, P Chaddah, Ram Prasad and N C Soni, 1993 (to be published)
[15] Shailendra Kumar, S B Roy, P Chaddah, Ram Prasad and N C Soni, *Physica* **C191**, 450 (1992)
[16] Shailendra Kumar, S B Roy, A K Pradhan, P Chaddah, Ram Prasad and N C Soni, *J. Appl. Phys.* **73**, 1539 (1993)
[17] S B Roy, Shailendra Kumar, P Chaddah, Ram Prasad and N C Soni, *Physica* **C198**, 383 (1992)
[18] C Radhakrishnamurty, S D Likhite and P W Sahasrabudhe, *Proc. Indian. Acad. Sci.* **A87**, 245 (1978)

PRAMANA
— journal of
physics

© Printed in India

Vol. 41, No. 1,
July 1993
pp. 61–66

Critical current density of a sample of melt grown $Y_{1\cdot2}Ba_{1\cdot8}Cu_{2\cdot4}O_x$

V GANESAN, R SRINIVASAN, R GOPALAN* and T RAJASEKARAN*
Inter University Consortium, University campus, Khandwa road, Indore 452001, India
*Defence Metallurgical Research Laboratory, Kanchanbagh, Hyderabad 500258, India

MS received 21 May 1993

Abstract. Melt grown samples of $Y_{1\cdot2}Ba_{1\cdot8}Cu_{2\cdot4}O_x$ have been prepared and studied for their current carrying capacity. The composition was chosen to include Y_2BaCuO_5 (211) particles in the $YBa_2Cu_3O_x$ (123) phase. The critical current density (J_c) of these samples was studied as a function of magnetic field using magnetization technique. The micrographic investigation shows well aligned grains in this material. The magnetic hysteresis measurements were done using a MPMS SQUID magnetometer up to the fields of 5·5 T. The J_c was estimated from the remanent magnetization using Bean model. Isothermal magnetization hysteresis loops at low fields reveal the presence of only one kind of hysteresis loops (corresponding to intragrain magnetizations). This is a valid proof that the weak links are greatly eliminated in these samples prepared by MG process. The J_c behaviour as a function of magnetic field has two components, a rapidly decaying exponential function of field and the other component that predominates at higher fields. This could be explained if we assume that the sample contains two phases of superconductors, one having a low H_{c_2} becoming normal at fairly medium fields of the order of a few kilogauss will act as pinning centres for the other phase having higher H_{c_2} and hence higher J_c at high fields.

Keywords. Critical currents; high temperature superconductors; melt growth.

PACS Nos 74·30; 74·70

1. Introduction

Advent of high T_c superconductivity above the liquid nitrogen temperature [1–3], stimulated interest in the applications of these materials. Ability for carrying high currents in the presence of magnetic fields of the order of few tesla is very important for many applications. Since the high T_c materials are granular their J_c is limited by the weak links, presence of secondary phases at the grain boundaries and the lack of texture etc. It was believed that elimination of weak links and grain alignment will improve the J_c. Grain alignment has been achieved by the controlled solidification [4–12]. One such process was Quench and Melt Growth (QMG) process successfully employed by Murakami *et al* [7] to obtain J_c of the order of 10^5 A/cm^2 or so. Transport measurements of J_c are not always possible because of the larger magnitude of J_c. Alternate way of obtaining J_c is by magnetization measurements using the famous Bean model [12]. Another advantage of this method is that the low field magnetization studies will provide information on the weak link nature of these materials. The development of two kinds of hysteresis loops (inter and intra grain) at low fields is well known in the granular superconducting materials [13–18]. The evidence for the elimination of weak links in the melt grown process can be had from micrographic studies [4–10] or from low field magnetization studies in which only one kind of hysteresis loops will present [13–18]. In this paper the J_c measurements of a sample of YBCO prepared by MG process was discussed for its magnetic field dependence.

2. Experimental

The samples of $Y_{1\cdot 2}Ba_{1\cdot 8}Cu_{2\cdot 4}O_x$ were prepared by conventional solid state reaction using nitrate precursors and the grain alignment was achieved by following the method of Murakami *et al* [5]. This composition was chosen to yield 211 particles in the 123 phase. Murakami *et al* [8] has described in his review that 211 inclusions dispersed in the 123 matrix can be controlled by changing the initial composition. It also contains the details of all types of melt grown processes and microstructure of typical composition of Y:Ba:Cu = 1·6:2·3:3·3 which shows a clear 211 inclusions in 123 matrix. Our composition is also nearly equal to the Murakami's ratio if properly normalized. However the method of initial quenching from 1400 C was bypassed by the quenching from 1200 C to liquid nitrogen temperature. Other processes are essentially the same as that of Murakami *et al.* The samples were prepared at DMRL, Hyderabad, India and the details of preparation have been reported by Rajasekaran *et al* [19]. The material was characterized by optical micrograph, XRD, electrical resistance and DC magnetization measurements. A rectangular piece was cut out of this sample for magnetization measurements.

3. Results

Optical micrograph of the sample showed the grain alignment clearly. The powder X-ray diffraction results of this sample indicate that all the (001) reflections were pronounced and having higher intensities is a valid proof for this alignment.

Electrical resistance of this sample was measured as a function of temperature using standard four-probe technique. The resistance drops to zero at 88 K. The details of characterization and the results of melt grown YBCO will be published elsewhere. In this paper we report the magnetization studies on $Y_{1\cdot 2}Ba_{1\cdot 8}Cu_{2\cdot 4}O_x$.

The DC magnetization measurements were carried out on MPMS SQUID magnetometer of quantum design. Figure 1 gives the variation of field cooled DC magnetic susceptibility as a function of temperature for this sample measured at a field of 100 G. It can be seen that the diamagnetic transition was quite sharp with the onset at 88 K.

The isothermal magnetization hysteresis loops were measured at 75 K for this sample at various maximum fields like 5, 10, 20, 30, 50, 100, 200, 300, 500, 1000, 10000, 55000 G etc.. Figure 2 gives the low field hysteresis loops showing only one kind of growth of loops justifying the elimination of weak links to a greater extent in these melt grown samples. Hence the use of Bean model as followed by Murakami *et al* [11] for the estimation of J_c in these MG samples is valid and more appropriate than ordinary sintered ceramic materials and the use of bulk sample dimension instead of grain dimension will yield the bulk J_c in these samples. Figure 3 gives the high field hysteresis loop of this sample from which we estimate the J_c of the material. Figure 4 gives the variation of J_c as a function of magnetic field obtained from 5·5 T hysteresis loop.

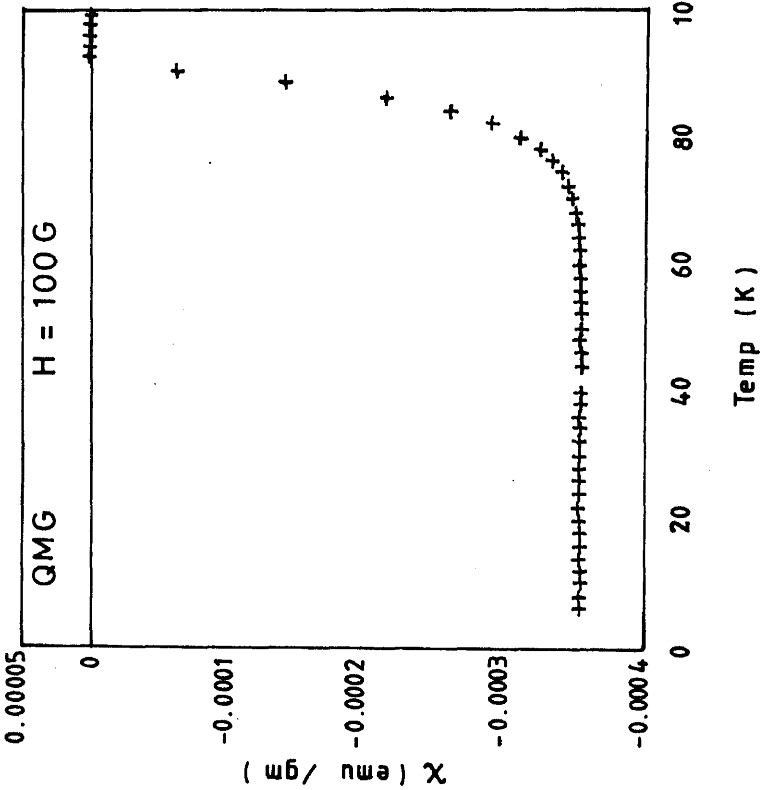

Figure 1. Field-cooled DC magnetic susceptibility as a function of the temperature.

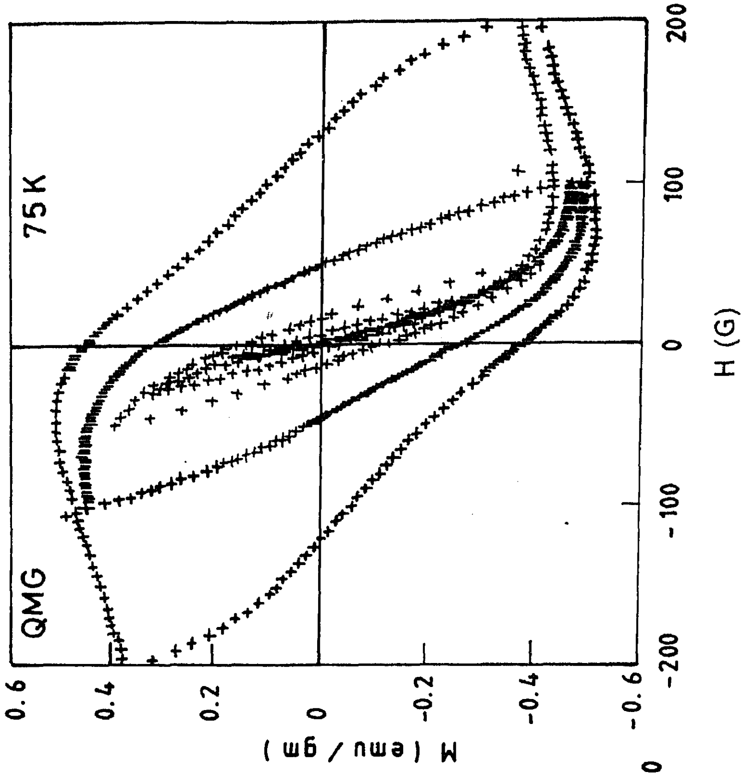

Figure 2. Low field magnetic hysteresis loops.

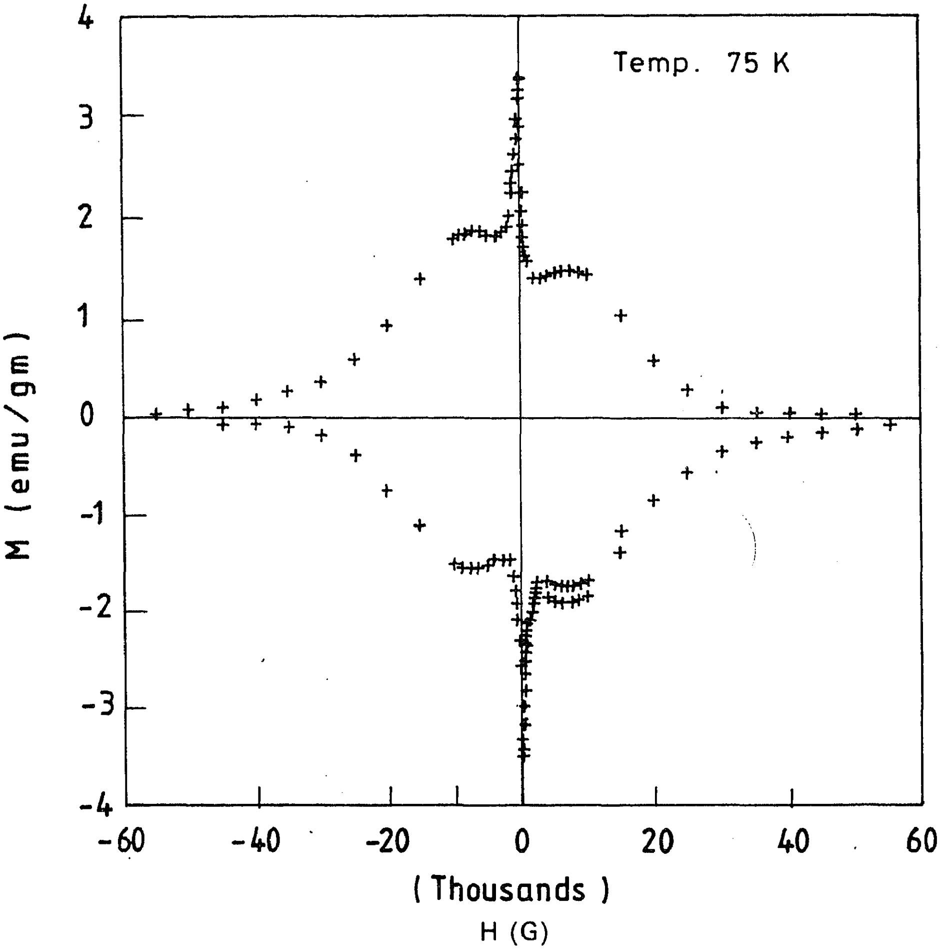

Figure 3. High field magnetic hysteresis loop.

The experimental data could be fitted as a sum of two current components, one a rapidly decaying exponential function of magnetic field and the other which predominates at high fields. [$J_c = J_{c_1} + J_{c_2}$, where $J_{c_1} = A_1 * \exp(-gB)$ and $J_{c_2} = A_2 + A_3 * B + A_4 * B^{0\cdot 5}$ and A_1 to A_4 and g are constants and B is the magnetic field. At least up to the fields we measured, (because the second component J_{c_2}, which increases with B may give physically meaningless results at very high fields, we restrict our discussion up to the fields we measured) the fit is reasonably good and this behaviour could be explained on the basis of a model that the sample contains two phases of superconductor, one having lower H_{c2} becoming normal at fairly intermediate fields like 10–20 kG and acting as a pinning site for the other superconducting phase having higher H_{c_2}. This may be attributed to the oxygen inhomogeniety in the interior of the bulk sample because of the higher density of the MG sample.

Similar variations of J_c with B can be found in the melt processed and textured samples of YBCO [9, 20]. Matsumoto *et al* [9] analysed the behaviour of J_c vs B using Kramer's plot and attributed it to the nature of saturated pinning properties.

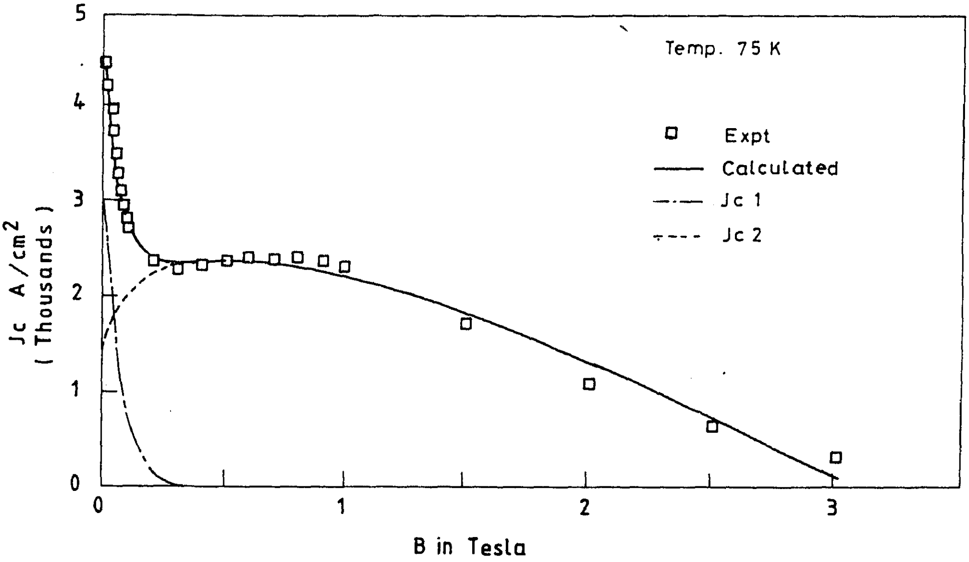

Figure 4. Variation of J_c as a function of the applied field.

According to them the field dependence of the pinning force can be expressed as $F_p \alpha b^p(1-b)^q$ where $b = B/B_{c_2}$, $p < 1$ and $q = 2$ and this type of variation is quite common even in conventional superconductors like Nb_3Sn in which crystal grain boundaries are the major pinning sites. These types of analysis on our samples were also made and reported by Ganesan *et al* [21]. These results along with the nature of J_{c_1} suggests that in these samples the grain alignment is still insufficient. The presence of cracks as well as the absence of sufficient 211 precipitates to act as pinning centres are the reasons of the low critical currents as compared to Murakami *et al* [7, 8, 11]. We are trying to prepare the samples of high J_c by controlling the microstructure of the phases and changing the preparation techniques.

Acknowledgements

This work was carried out through a grant sanctioned by the Program Management Board on Superconductivity of the Government of India. This is gratefully acknowledged. The experimental work was done at the low temperature laboratory of the Indian Institute of Technology, Madras.

References

[1] M K Wu, J Ashburn, C J Torng, P H Meng, L Gao, Z J Huang, U Q Wang and C W Chu, *Phys. Rev. Lett.* **58**, 908 (1987)
[2] H Maeda, Y Tanaka, M Fukutomi and T Asano, *Jpn. J. Appl. Phys.* **27**, L209 (1988)
[3] Z Z Sheng and A M Herman, *Nature* (*London*) **332**, 138 (1988)
[4] S Jin, R C Sherwood, E M Gyorgy, T H Tiefel, R B van Dover, S Nakahara, L F Schneemeyer, R A Fastnacht and M E Davis, *Appl. Phys. Lett.* **54(6)**, 584 (1989)
[5] M Murakami, *Mod. Phys. Lett.* **4**, 163 (1990)
[6] H Kupfer, C Keller, K Salama and V Selvamanickam, *Appl. Phys. Lett.* **55**, 1903 (1989)
[7] M Murakami, S Gotoh, N Koshizuka, S Tanaka, T Matsuhita, S Kambe and K Kitazawa, *Cryogenics* **30**, 390 (1990)

[8] M Murakami, *Supercond. Sci. Technol* (Preprint)
[9] K Matsumoto, H Kikuchi, N Uno and Y Tanaka, *Cryogenics* **30**, 5 (1990)
[10] K Yamaguchi, M Murakami, H Fujimoto, S Gotoh, N Koshizuka and S Tanaka, *Jpn. J. Appl. Phys.* **29**, L1428 (1990)
[11] M Murakami, M Morita and N Koyama, *Jpn. J. Appl. Phys.* **28**, L1125 (1989)
[12] C P Bean, *Phys. Rev. Lett.*, **8**, 250 (1962), *Rev. Mod. Phys.* **36**, 31 (1964)
[13] S Senoussi, C Aguillon and S Hadjoudj, *Physica C* **175**, 215 (1991)
[14] A K Grover, C Radhakrishnamurty, P Chaddah, G Ravi Kumar and G V Subba Rao, *Pramana – J. Phys.* **30**, 569 (1988)
[15] P Chaddah, *Pramana – J. Phys.* **36**, 353 (1991)
[16] Y Xu, W Guan and K Zeibig, *Solid State Commun.* **68**, 47 (1988)
[17] G Blatter, H Dersch, T Dupre, J Rhyner and H R Zeller, *Mod. Phys. Lett.* **B3** 375 (1989)
[18] G E Gough, M S Colclough, D A O'Connor, F Wellhofer, N McN Alford and T W Button, *Cryogenics* **31**, 119 (1991)
[19] T Rajasekharan, R Gopalan and T Roy, *Pramana – J. Phys.* **37**, L173 (1991)
[20] H Kupfer, I Apfelstedt, R Flukiger, C Keller, R Meier Hirmer, B Runtsch, A Turowski, U Wiech and T Wolf, *Presented at the discussion meeting "Critical currents in High T_c Superconductors"*, 16 May 1988, University of Birmingham, UK (preprint)
[21] V Ganesan, R Srinivasan, R Gopalan and T Rajasekaran, *Proceedings of the DAE symposium on Solid State Physics*, Vol. 35C, 320, 28 Dec 1992-1 Jan 1993

PRAMANA
— journal of
physics

© Printed in India

Vol. 41, No. 1,
July 1993
pp. 67–73

Electronic structure of a superconducting Bi2212 crystal by angle resolved ultra violet photoemission

N L SAINI, J KANSKI[+], P SRIVASTAVA, L ILVER[+], K B GARG and S DURCOK*

Department of Physics, University of Rajasthan, Jaipur 302 004, India
[+]Department of Physics, Chalmers University of Technology, S-412 96 Göteborg, Sweden
*Institute of Physics CSAV, Cukrovarnicka 10016200 PRAHA 6, Czechoslovakia

MS received 15 February 1993; revised 29 April 1993

Abstract. The electronic structure of a high quality superconducting $Bi_2Sr_2CaCu_2O_{8+\delta}$ (Bi2212) single crystal is studied by angle resolved ultra violet photoemission (ARUPS) using He I (21·2 eV). Our results appear to show two bands crossing the Fermi level in ΓX direction of the Brillouin zone as reported by Takahashi *et al.* The bands at higher binding energy do not show any appreciable dispersion. The nature of the states near the Fermi level is discussed and the observed band structure is compared with the band structure calculations.

Keywords. Electronic structure; superconductivity; photoemission spectroscopy.

PACS No. 74·25; 74·72

1. Introduction

Photoemission spectroscopy has successfully established the existence of a significant density of states (DOS) near the Fermi level in the high T_c superconducting compounds [1]. The angle resolved photoemission spectroscopy (ARPES) on the other hand, has been able to provide direct observation of energy bands crossing the Fermi level [2–5] as predicted by band structure calculations [6–8]. There exist, however, some discrepancies in the ARPES results reported so far on Bi2212 system. Manzke *et al* [5] and Olson *et al* [3] suggest that there is only one band crossing the Fermi level in ΓX direction which originates from O 2*p* of the Cu–O plane. However, the position of the crossing is different in two cases. On the other hand, Takahashi *et al* [2, 9] have been able to show that there are two bands crossing the Fermi level rather than one. In this short communication, we report our angle resolved ultraviolet photoemission (ARUPS) measurements on a well characterized superconducting Bi2212 single crystal in the high symmetry direction Γ(X). The observed band structure has been compared with the existing band structure calculations.

2. Experimental

The superconducting Bi2212 single crystal was grown by a self-flux method i.e. using starting materials as a flux, in our case CuO and Bi_2O_3. High purity Bi_2O_3, $SrCO_3$, $CaCO_3$ and CuO were mixed in the ratio 0·8 Bi_2O_3: 1·0 $SrCO_3$: 1·0 $CaCO_3$: 1·6 CuO, melted in an alumina crucible and soaked at 1050°C, step-cooled to 980°C, then slowly cooled (1·5 K/h) down to 850°C before reaching the room temperature by switching off the furnace. Black shiny crystals were mechanically seperated from the frozen melt. The T_c of the selected crystal was found to be 84 K by resistivity and a.c. susceptibility measurements.

The photoemission measurements were made with an ADES 400 system in which the analyser can be moved in one plane. The He I (21·2 eV) resonance line was used for excitation. The sample was mounted on a Ta foil by UHV compatible silver epoxy. A good surface was produced by cleavage of the single crystal ($5*4*0{\cdot}2\,\mathrm{mm}^3$) in ultra high vacuum chamber ($\sim 10^{-11}$). The symmetry direction was determined by low energy electron diffraction (LEED) which shows a sharp pattern, indicative of a single crystalline surface. The 1*5 structure was observed with long range ordering of superstructure along the b-axis (ΓY direction of Brillouin zone) as reported earlier [10–11]. The spectra were recorded for various emission angles along a high symmetry direction ΓX, to avoid any possible interference by the superstructure along the ΓY direction, in the surface Brillouin zone with an angular resolution of 2°. However, no difference is reported in the spectra in two (ΓX and ΓY) directions in the earlier studies [2–5]. The overall energy resolution for our measurements was $\sim$ 0·1 eV. The $Bi_2Sr_2CaCu_2O_{8+\delta}$ is known to always cleave along the a-b plane with Bi–O plane

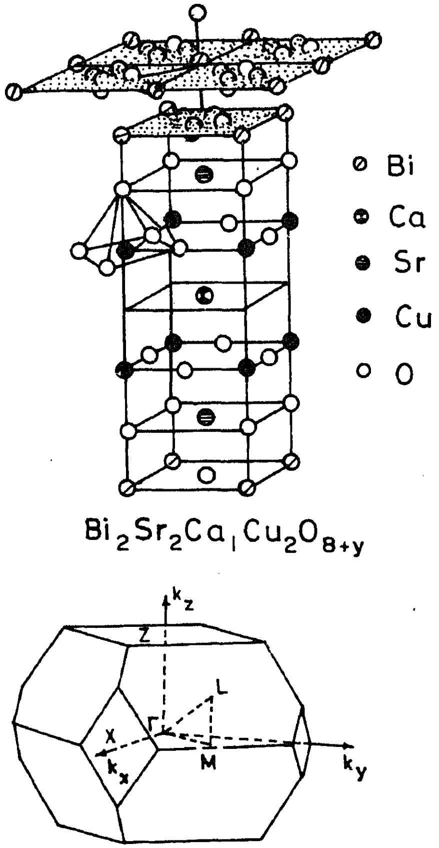

Figure 1. Crystal structure of $Bi_2Sr_2CaCu_2O_{8+\delta}$ system with Bi-O layer. The surface Brillouin zone of the compound is also shown.

as the top layer. We have shown the crystal structure of this compound and the most commonly accepted Bi-O surface construction alongwith the surface Brillouin zone in figure 1. The light incidence angle was kept constant at 47° relative to the surface normal. The pressure in the chamber was $8*10^{-10}$ Torr during operation of the He lamp. No signature of surface contamination, as monitored in situ by XPS, was however observed during the measurements.

3. Results and discussion

Figure 2 shows the angle resolved valence band photoemission spectra of the $Bi_2Sr_2CaCu_2O_{8+\delta}$ crystal in a high symmetry direction of Brillouin zone ΓX measured by us. To obtain the final spectra a background recorded on the Ta foil at each of the respective angles has been subtracted from the corresponding set of raw data. Our final spectra appear to be quite similar to that reported with a photon energy 21·2 eV by others [4, 12, 13]. The spectra are truncated at 0 eV as we will discuss the DOS near the E_F later in figure 3. The present spectra show several features including the prominent feature at ~ 3·4 eV which is ascribed to the main valence band of this system. The various features are marked K, L, M and N in the spectra. Almost all these features are either independent of angular variation or show a very small angular dependence as reported earlier [2, 4, 14]. Due to large size of the unit-cell of the compound and in addition the presence of very flat bands throughout the Brillouin zone one may expect that the relative contribution to the spectra from the strongly dispersive bands is negligible. However band L appears to show a small dispersion towards lower binding energy while moving from Γ to X point in the Brillouin zone. The other bands, except the N which shows almost similar dispersion as L in the ΓX direction, are more or less angular independent.

Figure 3 shows the angular dependence of the photoemission (the original data) spectra of the Bi2212 sample in vicinity of the Fermi level (in ΓX direction of Brillouin zone). The weak structures A and B show small but clear dispersion. Both the structures A and B tend to move towards the Fermi level with increasing emission angle, and appear to cross E_f at ~ 10° (~ 0·2ΓX) and 20° (~ 0·6ΓX) respectively. The precise crossing positions are, however, difficult to locate due to the weakness of these structures. Also, the increase in density of states at the Fermi level at around 10° (figure 3) confirms the crossing of the band A. The small increase in density of states at ~ 20° may similarly be due to the possible crossing of band B. However, we cannot rule out the possibility of a strong dispersion of band B without its crossing the Fermi level as the increase in DOS at the Fermi level around 20° is quite small.

We have compared the calculated band structure from our ARUPS results with the one-electron band structure calculation of Massida *et al* [6] in figure 4. The agreement in respect of the high energy bands is rather poor. The experimental bands do not show any appreciable dispersion while calculations show that a large number of these ought to show a strong dispersion. It is also difficult to rule out that some amount of three-dimensional nature in the observed spectra, if any, may be responsible for this observed disagreement. The band structure calculations show that one band is crossing the Fermi level in ΓX direction and is of oxygen 2*p* nature. This band is derived from the oxygen in the Cu–O plane. Our spectra however, show two bands in the ΓX direction but there is lack of agreement in this regard amongst the experimental data from various workers itself. There is thus disagreement not only between experiment and calculations but also between experiment and experiment.

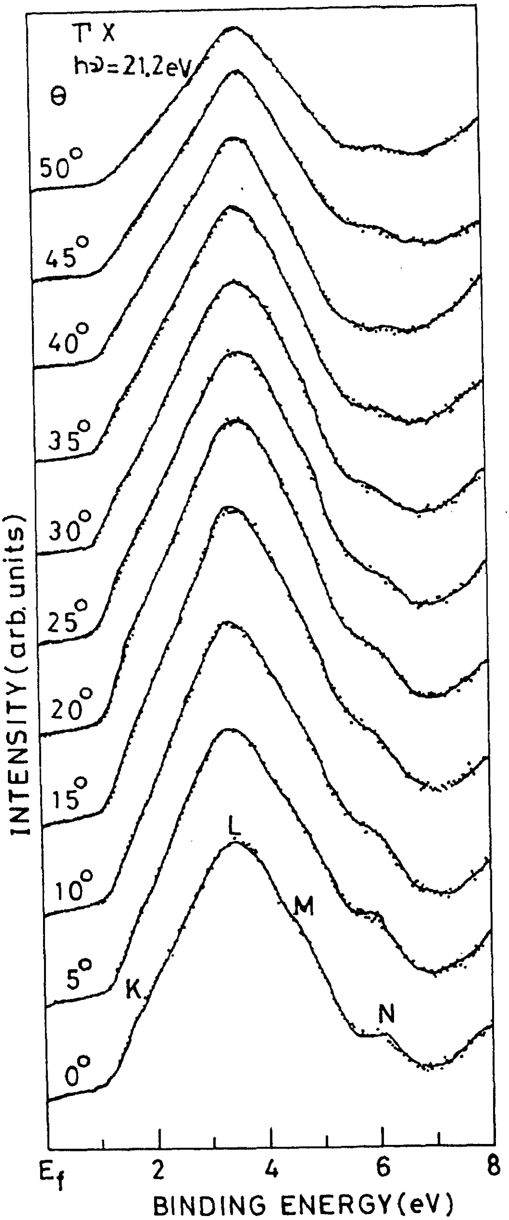

Figure 2. Angle resolved valence band spectra of Bi(2212) crystal recorded at $h\nu = 21{\cdot}2$ eV (He I) in ΓX direction of the surface Brillouin zone.

Manzke *et al* [5] and Olson *et al* [3] support only one band while Takahashi *et al* [2, 9] have been able to show that there are two bands crossing the Fermi level. Takahashi *et al* argue that the single band observed by Manzke *et al* (0·2 eV) corresponds to the band A in their spectra while the band observed by Olson *et al* (0·4 eV) may correspond to their band B. Our results appear to support those of Takahashi *et al* as can be seen from their positions in our spectra. The sample dependence of the bands however cannot be ruled out. It is possible that the difference

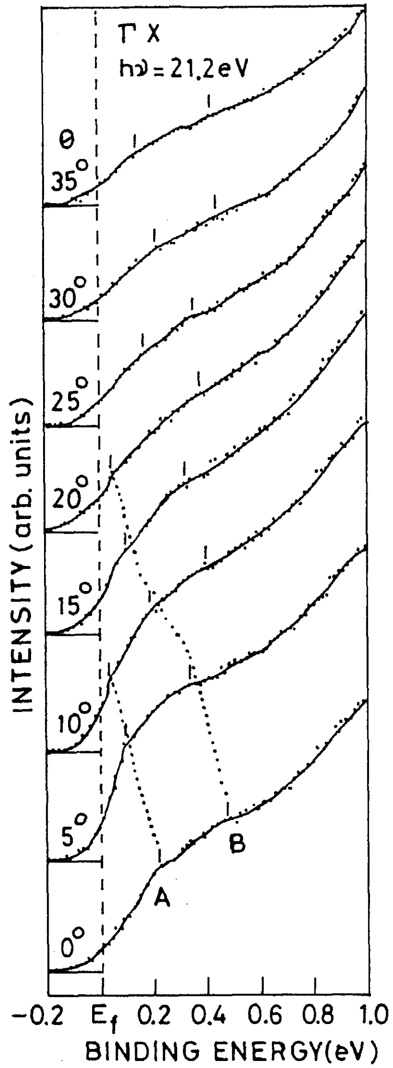

Figure 3. Angular dependence of density of states near the Fermi level of Bi2212 crystal (original data). Both the bands (A and B) are dispersing towards Fermi level (dots).

in surface reconstruction (Bi–O surface) in the case of different measurements may be responsible for the discrepancy in number of observed bands and their position in the Brillouin zone. Such differences in surface reconstructions for various crystals may be due to the differences in their synthesis conditions which is known to affect the oxygen content and the position of oxygens in them.

It is quite well-known that the states near the Fermi level are mainly of O 2*p* nature hybridized with Cu 3*d*. But due to strong correlation effects the Cu 3*d* states are pushed away from the Fermi level. Moreover, at this photon energy (21·2 eV) the O 2*p* photoemission cross-section is higher than Cu 3*d* [15]. Consequently, the bands crossing the Fermi level are more likely to be of O 2*p* nature. The question is whether both the bands are derived from the CuO_2 plane only. The possibility of Kondo-like

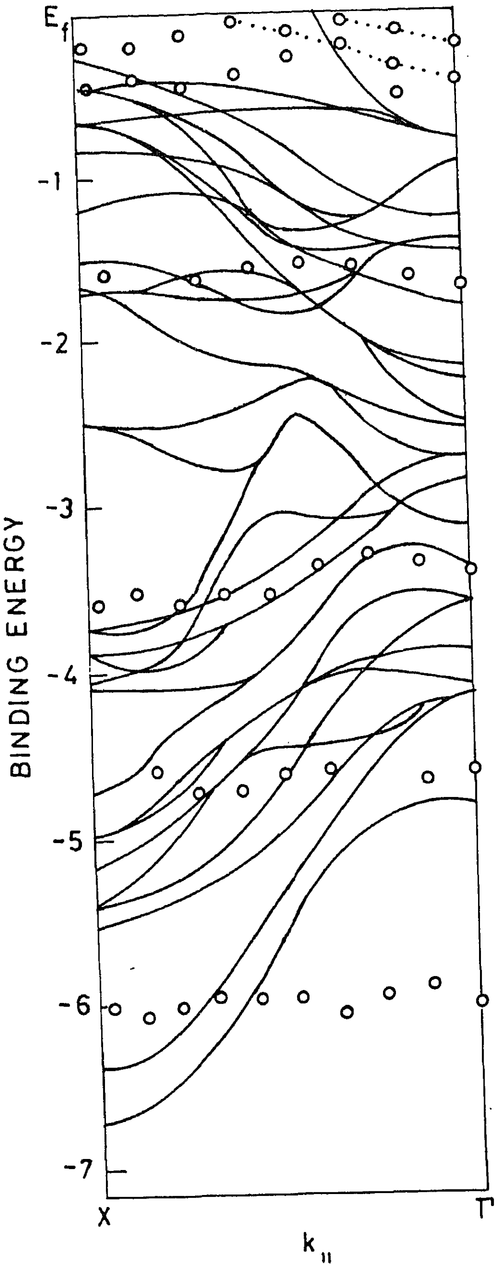

Figure 4. Comparison of the observed band structure (circles) with the one electron calculations of Massidda *et al* [6].

DOS at the Fermi level has already been ruled out by Fujimori *et al* [13]. Also, from the band structure calculations, there is no evidence of Bi-O band crossing in ΓX direction. Still, one cannot completely rule out the possibility of some contribution from the Bi–O plane to the band A as the crystal surface known to be a Bi-O plane. This is also suggested by Wells *et al* [16] who have evaporated a small amount of gold on an in-situ cleaved Bi2212 crystal surface and besides observing a drastic decrease in the DOS near the Fermi level in the ΓM direction of the Brillouin zone, observe a small decrease in DOS in the ΓX direction. The band structure calculations [6–8] also suggest that a Bi–O band does cross the Fermi level albeit in the ΓM direction of the Brillouin zone.

In summary, we have studied the electronic structure of a high quality superconducting Bi2212 crystal by angle resolved ultra violet photoemission spectroscopy. The measurements have been made on a well characterized crystal surface in a high symmetry direction ΓX of the Brillouin zone. Our ARUPS results appear to show that there are two bands crossing the Fermi level. The high energy bands structure observed by ARUPS show rather poor agreement with the band structure calculations.

Acknowledgements

We are grateful to Prof. P O Nilsson for his constant inspiration and helpful suggestions in completing the work. One of us (NLS) is thankful to IPPS, Uppsala for a fellowship in Sweden to do the work.

References

[1] P A P Lindberg, Z X Shen, W E Spicer and I Lindau, *Surface Sci. rep.* **11**, 1–137 (1990)

[2] T Takahashi, H Matsuyama, H Katayama-Yoshida, Y Okabe, S Hosoya, K Seki, H Fujimoto, M Sato and H Inokuchi, *Nature* (*London*) **334**, (25) 691 (1988); *Phys. Rev.* **B39**, (10) 6636 (1989)

[3] C G Olson, R Liu, D W Lynch, R S List, A J Arko, B W Veal, Y C Chang, P Z Jiang and A P Paulikas, *Phys. Rev.* **B42**, (1) 381 (1990)

[4] F Minami, T Kimura and S Takekawa, *Phys. Rev.* **B39**, (7) 4788 (1989)

[5] R Manzke, T Buslaps, R Claessen and J Fink, *Europhys Lett.* **9**, (5) 477 (1989); R Manzke, T Buslaps, R Claessen, M Skibowski and J Fink, *Phys. Scr.* **41**, 579 (1990)

[6] S Massidda, J Yu and A J Freeman, *Physica* **C152**, 251 (1988)

[7] H Krakauer and W E Pickett, *Phys. Rev. Lett.* **60**, 251 (1988)

[8] M S Hybersten and L F Mattheiss, *Phys. Rev. Lett* **60**, (16) 1661 (1988)

[9] T Takahashi, T Watanabe, T Kusunoki and H Katayama-Yoshida, *J Phys. Chem. Solids* **52**, (11/12) 1427 (1991)

[10] P A P Lindberg, Z X Shen, B O Wells, D B Mitzi, I Lindau, W E Spicer and A Kapitulnik, *Appl. Phys. Lett.* **53**, 2563 (1988)

[11] H Tokutaka, S Kishida, H Fujimoto, K Nishimori and N Ishihara, *Surface Sci.* **242**, 50 (1991)

[12] J W Imer, F Patthey, B Dardel, W D Schneider, Y Baer, Y Petroff and A Zettl, *Phys. Rev. Lett.* **62**, (3) 336 (1989)

[13] A Fujimori, Y Tokura, H Eisaki, H Takagi, S Uchida and M Sato, *Phys. Rev.* **40**, (10) 7303 (1989)

[14] P A P Lindberg, Z X Shen, D S Dessau, B O Wells, D B Mitzi, I Lindau, W E Spicer and A Kapitulnik, *Phys. Rev.* **B40**, (7) 5169 (1989)

[15] J J Yeh and I Lindau, *Atomic data and Nucl. data Tables* **32**, 1–55 (1985)

[16] B O Wells, Z X Shen, D S Dessau, W E Spicer, C G Olson, D B Mitzi, A Kapitulnik, R S List and A Arko, *Phys. Rev Lett.* **65**, (24) 3056 (1990)

[redacted]

PRAMANA
— journal of
physics

© Printed in India

Vol. 41, No. 1,
July 1993
pp. L75–L81

Symmetry breaking in quantum chaotic systems

AKHILESH PANDEY, RAMAKRISHNA RAMASWAMY and
PRAGYA SHUKLA
School of Physical Sciences, Jawaharlal Nehru University, New Delhi 110067, India

MS received 29 May 1993

Abstract. We show, using semiclassical methods, that as a symmetry is broken, the transition between universality classes for the spectral correlations of quantum chaotic systems is governed by the same parametrization as in the theory of random matrices. The theory is quantitatively verified for the kicked rotor quantum map. We also provide an explicit substantiation of the random matrix hypothesis, namely that in the symmetry-adapted basis the symmetry-violating operator is random.

Keywords. Quantum chaos; symmetry breaking; intermediate ensembles.

PACS Nos 05·45; 03·65; 24·60

There is considerable evidence that depending on the exact symmetries, the spectral behavior of chaotic systems can be modeled by one of the various universality classes of random matrices. Most common among these are the Gaussian orthogonal and unitary ensembles, GOE and GUE, and the analogous circular ensemble models COE and CUE [1, 2]. The former pertain to autonomous systems, whereas the latter have application in the study of non-autonomous systems such as quantum maps.

For systems with partly violated symmetry, one requires intermediate ensembles. Dyson [3] introduced Brownian motion ensembles of random matrices for studying small symmetry violations in complex systems. There are many examples in this regard, two of which are considered here, namely the transition from COE to CUE for partial time reversal (T) violation, and the transition from a direct sum of two independent COE's to a single COE of larger dimensionality for partial parity (P) violation. The assumption underlying this theory is that the symmetry violating part of the matrix (the Hamiltonian for autonomous systems and time evolution operator for quantum maps) is random when expressed in a representation in which the symmetry preserving part is diagonal [4, 5]. An important consequence of this is that the spectral correlations undergo a rapid transition from one universality class to another as a (global) symmetry breaking parameter is varied. The speed of the transition is determined by the effective dimensionality (N) of the matrix (N being energy dependent for autonomous systems). The transition itself is smooth when the parameter is scaled by some power of N [4–8]. These results have provided sensitive tests of time-reversal [5] and isospin symmetries in complex nuclei [8, 9], and the LS coupling scheme [10] in complex atoms. Aspects of the transition in spectral correlations have been the subject of some earlier studies on T-violation in quantum chaotic billiards [11–14] and kicked tops [15].

Transitions between universality classes themselves have a universal classification and the purpose of this letter is to establish this fact. We elucidate how features of these ensembles manifest in quantum maps, and provide a semiclassical calculation of the dependence of spectral correlations on symmetry-breaking parameters. Application is made to the case of the kicked rotor [16, 17],

$$H=\frac{(p+\gamma)^2}{2}+\alpha\cos(\theta+\theta_0)\sum_{n=-\infty}^{\infty}\delta(t-n) \tag{1}$$

where α is the stochasticity parameter. The parameters γ and θ_0 are introduced in the Hamiltonian in order to mimic the effects of time-reversal and symmetry-breaking in the quantum system. Our choice of this system is dictated by the fact that predictions of the transition for circular and Gaussian ensembles are identical [7]. In addition we also verify directly the above random-matrix hypothesis which pertains to the symmetry-breaking part of the evolution operator.

By application of Floquet's theorem, the quantum dynamics can be described by a discrete time evolution operator $U=\mathrm{BG}$ where $B=\exp(-i\alpha\cos(\theta+\theta_0)/\hbar)$ and $G=\exp(-i(p+\gamma)^2/2\hbar)$. The nature of the transition in the spectrum due to violation of symmetries will also depend on α and $\hbar$. We employ torus boundary conditions; both p and θ then have discrete eigenvalues and U can be reduced to a finite N-dimensional matrix of the form

$$U_{mn}=\frac{1}{N}\exp\left[-i\frac{\alpha}{\hbar}\cos\left(\frac{2\pi m}{N}+\theta_0\right)\right]\sum_{l=-N_1}^{N_1}\exp\left[-i\left(\frac{\hbar}{2}l^2-\gamma l-l\frac{(m-n)}{N}\right)\right] \tag{2}$$

where $N_1=(N-1)/2$ and $m,n=-N_1,-N_1,+1,\ldots,N_1$. For $\alpha^2\gg N\hbar$, the spectrum of U with parameters γ and θ_0 chosen to preserve an exact symmetry, can be modeled by random matrix theories [17]; this suggests that in the same limit Brownian-motion ensemble type behavior can be expected in the case of partly-broken symmetry as well.

Four transitions obtain from the two symmetries, time reversal $T(p\to-p,t\to-t)$ and parity $P(q\to-q,p\to-p)$: (i) P "fully" broken but T only "partly", (ii) P and T both fully broken but TP (an antiunitary symmetry like T) partly, (iii) T preserved but P partly broken, and (iv) TP preserved but T and P partly broken. In each case a single parameter (γ or θ_0) can be identified to govern the partial symmetry breaking. The Brownian motion theory predicts COE → CUE for (i, ii) and 2COE → COE for (iii, iv) under the random matrix hypothesis. Cases (i) and (iii) are dealt with here.

First we consider the case of T violation in detail. This is realized by choosing $\theta_0=\pi/2N$ (fully broken P) and varying the $T-$ violation parameter slightly $(0\ll\gamma\ll\hbar)$. A manifestly T-invariant form of U for $\gamma=0$ can be obtained by transforming it to $U_1=B^{1/2}GB^{1/2}$ with appropriate changes in the matrix elements given in (2). This then identifies $\exp(-i\gamma p/\hbar)$ as the T-violating part of U. In the $U_1(\gamma=0)$-diagonal representation p is an imaginary antisymmetric matrix. We show in figure 1 that in the "strongly" chaotic case $(\alpha^2\gg N\hbar)$ all distinct matrix elements of (ip), which are now *real* in this representation, are independent zero-centered Gaussian random variables with the same variance, $\mathrm{Tr}[p^2/N(N-1)]\simeq\hbar^2N/12$. We have also verified that in the $U_1(\gamma\neq0)$-diagonal representation the matrix p eventually becomes a typical member of the GUE. This, for the first time, gives a direct verification of a random matrix in a quantum chaotic system and, in particular, strongly suggests that the COE → CUE transition theory [7] should apply.

When $(\alpha^2\leqslant N\hbar)$, the weakly chaotic case, (ip) is a banded matrix [18] with significant

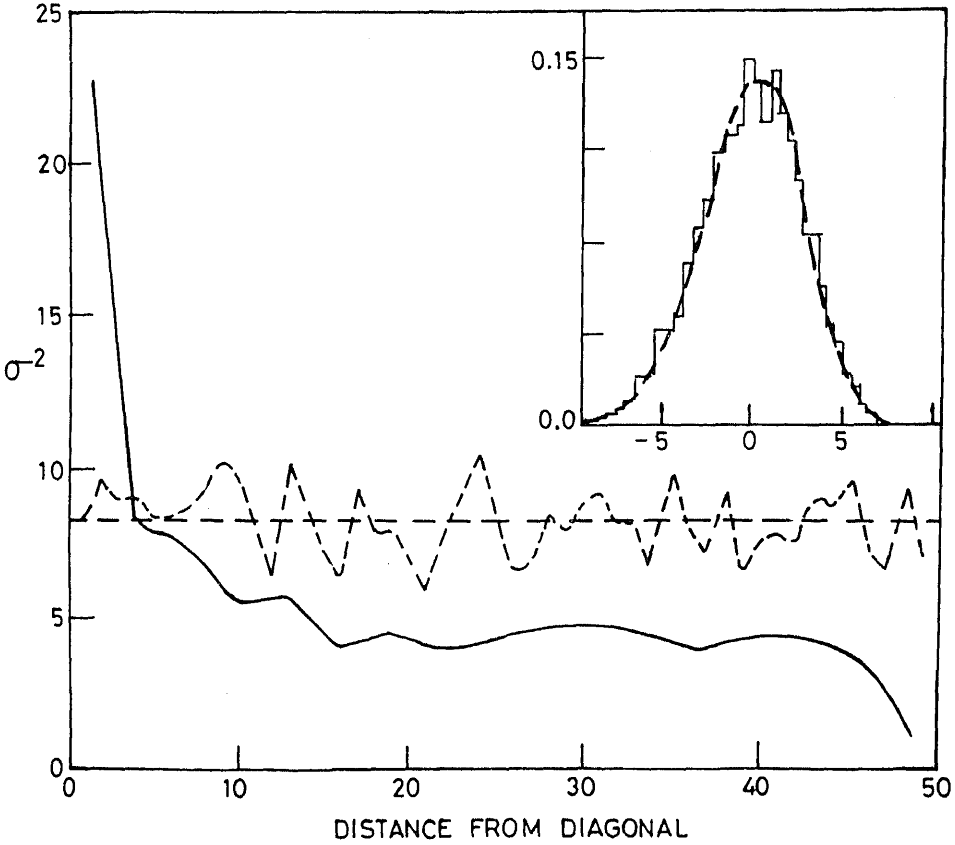

Figure 1. Variance σ^2 for off-diagonal matrix elements $\{ip_{jk}\}$ as a function of the distance from the diagonal, which is here the lower of $|j-k|$ and $N-|j-k|$; the latter takes into consideration that the eigenvalues of U are on a circle. In the $U(\gamma=0)$ diagonal representation used here, ip is real antisymmetric, and we fix $\hbar=1$, $N=99$ and $\theta_0=\pi/2N$. The horizontal dashed line is at $\sigma^2=N\hbar^2/12$, the case of uniform variance. Results are shown for a single matrix, with $\alpha=10$ (solid curve), the weakly chaotic case, and $\alpha=20000$ (dashed curve), the strongly chaotic case. Local smoothing is applied to eliminate finite sample effects. The inset compares the distribution of the matrix elements themselves with the Gaussian predicted for the strongly chaotic case.

variances only for the near-diagonal matrix elements (see figure 1). In fact it can be shown that the variance is

$$\operatorname{Var} p_{\mu\nu}=\frac{N\hbar^2}{12}\sum_{m=-\infty}^{\infty}\exp(im(E_\mu-E_\nu))C(m) \tag{3}$$

where the quasienergies E_μ are the eigenangles of U and $C(m)$ is the correlation coefficient between p and its mth iterate $p^{(m)}$ in the corresponding classical map. In the strongly chaotic limit $C(m)\to\delta_{m0}$, giving the above E-independence of the variance. The transition theory for the spectrum may also apply for cases with large band widths. In the opposite limit of very small band widths, the spectrum will be Poissonian for all γ[17].

In Dyson's theory, eigenvalues are treated as particles which perform a Brownian motion under a mutual two-body repulsive logarithmic potential as a parameter is varied; see refs. [3, 7] for details. This is a random-matrix result, and derives from, for example, parameter-dependent circular ensembles of unitary matrices $U(\tau)$ in which an infinitesimal random perturbation—in the present application a symmetry-breaking—is applied at each τ. Here τ can be thought of as "time": in our problem, $\tau = 0$ is the symmetry preserving case and $\tau = \gamma^2$ or $\tau = \theta_0^2$ the symmetry-breaking case. Stationarity is achieved in the $\tau \to \infty$ limit, when the appropriate universality class of the circular ensembles is attained. As verified above, the hermitian matrix corresponding to the symmetry-breaking random perturbation belongs to a universality class of the Gaussian ensembles which in turn fixes the $\tau \to \infty$ limit.

T-violation, as displayed by the COE → CUE transition, gives rise to stronger level repulsion and stronger long-range spectral rigidity. Both features can be seen from the analysis of the two-level cluster function $Y_2(r)$ where $r = (E_\mu - E_\nu)/D$ is the distance between any two levels in units of the average spacing $D = 2\pi/N$. Its Fourier transform $b_2(k)$ is given in the random-matrix theory by [6, 7].

$$\begin{aligned} 1 - b_2(k) &\equiv \int_{-\infty}^{+\infty} \exp(2\pi i k r)(\delta(r) - Y_2(r))\mathrm{d}r \qquad (4)\\ &= |k| + \frac{1}{2}\int_{1-2|k|}^{1} \mathrm{d}p \frac{p}{p+2|k|}\exp(-8\pi^2 p|k|\Lambda - 8\pi^2 k^2\Lambda), \quad |k| \leqslant 1\\ &= 1 + \frac{1}{2}\int_{-1}^{1} \mathrm{d}p \frac{p}{p+2|k|}\exp(-8\pi^2 p|k|\Lambda - 8\pi^2 k^2\Lambda), \quad |k| \geqslant 1. \end{aligned}$$

Here $\Lambda = \tau v^2/D^2$ with τv^2 the mean square of the T-violating matrix elements. This gives rise to a discontinuous transition with respect to τ. In the limit $|k| \ll 1$, which pertains to the long-range spectral rigidity, this reduces to

$$1 - b_2(k) = |k|\{1 + \exp(-8\pi^2|k|\Lambda)\}. \qquad (5)$$

The semiclassical calculation of $1 - b_2(k)$ for U shows similar behavior in the limit of small $|k|$. In the numerical analysis below we use the number variance $\Sigma^2(r)$, namely the variance of the number of levels in intervals of length rD, which derives from Y_2 and hence (4). For $r \geqslant 1$, the approximate expressions can be obtained from (5); see ref [5]. For the strongly chaotic rotor, $\Lambda = \gamma^2 N^3 \hbar^2/48\pi^2$.

For a semiclassical calculation of $1 - b_2(k)$, we write the spectral density of U as

$$\rho(E) = (2\pi)^{-1} \sum_{n=-\infty}^{\infty} \exp(inE)\mathrm{tr}(U^n). \qquad (6)$$

In the semiclassical limit, $\mathrm{Tr}(U^n)$ can be expressed as a sum over periodic orbits [19] (along the same lines as Gutzwiller trace formulae [20]) in classical phase space $(r \equiv (q, p))$

$$\mathrm{tr}(U^n) = \sum_j n_j A_j \exp(i m_j W_j/\hbar), \quad A_j = |\partial(\mathbf{r}_n - \mathbf{r}_0)/\partial\mathbf{r}_0|^{-1/2}_{\mathbf{r}_n=\mathbf{r}_0}, \qquad (7)$$

The amplitude A_j of the contribution from each (multiply-traversed) periodic orbit j with period n depends on the stability of the orbit, W_j is the action for one traversal of the orbit, m_j is the number of traversals and $n_j = n/m_j$ is the period of the orbit with single forward traversal. While considering the long-range correlations which are mainly affected by the long periodic orbits, it is sufficient to consider $|m_j| = 1$ (and therefore $n_j = |n|$).

Since the *spectral* b_2 function can be obtained from (6) for $k \neq 0$ as

$$1 - b_2(k) = N^{-1}|\mathrm{tr}(U^{kN})^2| \tag{8}$$

it becomes important to study the distribution of amplitudes A_j and actions W_j. In the absence of any symmetry in a chaotic system, almost all periodic orbits are non-degenerate and then, in the evaluation of $|\mathrm{tr}(U^n)|^2$ for small $\hbar$, only the "diagonal" periodic orbit sum contributes. Invoking the principle of uniformity [21, 22], we find $|\mathrm{tr}(U^n)|^2 = n^2\Sigma_j A_j^2 = |n|$ which, along with (8), gives the CUE result ($\Lambda \to \infty$) of (5). Note that the sum rule applies only to $|n| \gg 1$ in the weakly chaotic case but can be extended to $|n| = 1$ in the strongly chaotic case. Moreover the validity of (7) only for $|n| \ll N$ gives the constraint $|k| \ll 1$ on (5).

When T is preserved, almost all periodic orbits are doubly degenerate ($A_j^+ = A_j^-$, $W_j^+ = W_j^-$ with ± denoting a pair of degenerate orbits). In this case [22] $|\mathrm{tr}(U^n)|^2 = 4n^2\Sigma(A_j^+)^2 = 2|n|$ giving eq. (5) for COE (i.e. $\Lambda = 0$).

When T is weakly violated, the actions of nearly-degenerate periodic orbits can affect the spectral correlations significantly, although the $A^\pm$ can still be treated as nearly equal since they do not depend on $\hbar$[11]. We find

$$|\mathrm{tr}(U^n)|^2 = 2n^2[1 + \langle\cos\theta_j\rangle]\Sigma(A_j^+)^2 = |n|[1 + \exp(-8\pi^2\Lambda|n|/N)] \tag{9}$$

and then eqs (8), (9) give (5) for all Λ. Here the phase $\theta_j = (W_j^+ - W_j^-)/\hbar$ is a Gaussian variable with zero mean and variance $16\pi^2\Lambda|n|/N$, and we use the fact that the phase space average $\langle\cos\theta_j\rangle = \exp(-\mathrm{var}(\theta_j)/2)$. The Gaussian behavior comes from an extension of the central limit theorem since θ_j is the sum of n differences of single step actions with a pair correlation coefficient falling off exponentially (abruptly in the strongly chaotic case). Λ turns out to be the local symmetry breaking parameter, given by $\gamma^2N^3\hbar^2/48\pi^2$ in our case and brings out a smooth transition in $N \to \infty$ limit. This gives a semiclassical derivation of the COE to CUE type transition in T-violating cases of chaotic quantum maps for the long range correlations ($|k| \ll 1$). Numerical results of the behavior of the number variance $\Sigma^2(1)$ and $\Sigma^2(5)$ for this transition are in excellent agreement with the transition theory; see figure 2. A detailed corroboration, involving other measures, will be given elsewhere [23].

In dealing with other symmetries, the procedure detailed above (with T replaced by the appropriate symmetry and ± labels by the appropriate set of degenerate orbits) can be followed. Approximate random matrix theories are given in [5].

Now the case of parity breaking can be dealt with in brief. For the transition 2COE → COE, the approximate result [5] for Σ^2 gives

$$1 - b_2(k) = 2|k|\{1 + \exp(-4\pi^2|k|\Lambda)\} \tag{10}$$

for small $|k|$. Here Λ, as in eqs (4), (5), has an analogous definition for P-violation; for the strongly chaotic kicked rotor, $\Lambda = \theta_0^2N\alpha^2/4\hbar^2\pi^2$. In our semiclassical theory (note that orbits initially have a 4-fold degeneracy) an identical expression for b_2 is obtained. The rapidity of the transition here derives from the α dependence of Λ. To study this transition numerically, the same number of matrices was taken, with $\gamma = 0$

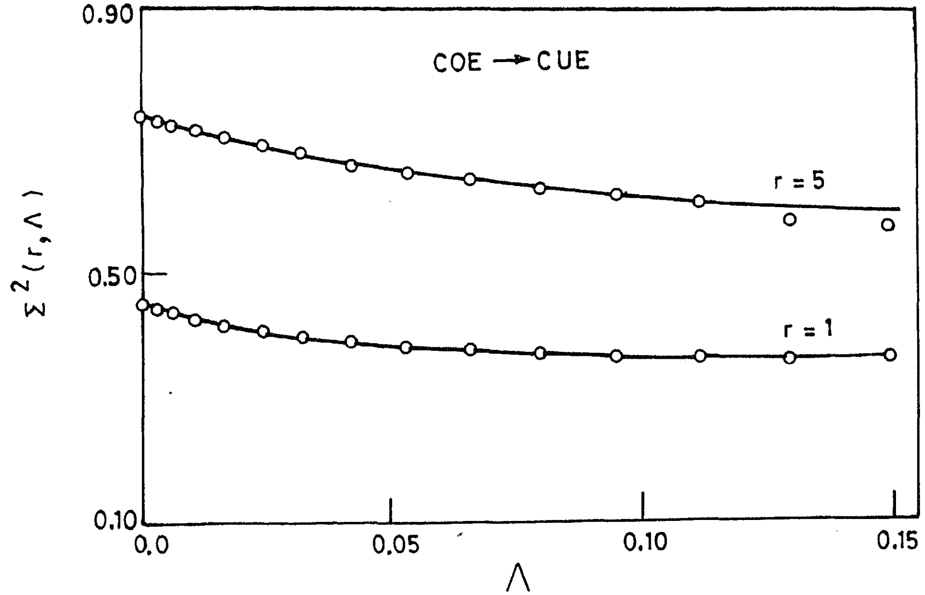

Figure 2. $\Sigma^2(r;\Lambda)$ vs Λ at $r=1$ and $r=5$ for T violation. The solid curve is the random-matrix prediction (Ref. [5]), or equivalently, the Brownian motion prediction. Calculated values (the open circles) are for 50 matrices with, as in Ref. [17], α around 20000, $N=199$, $\hbar=1$, $\theta_0=\pi/2N$ and varying γ.

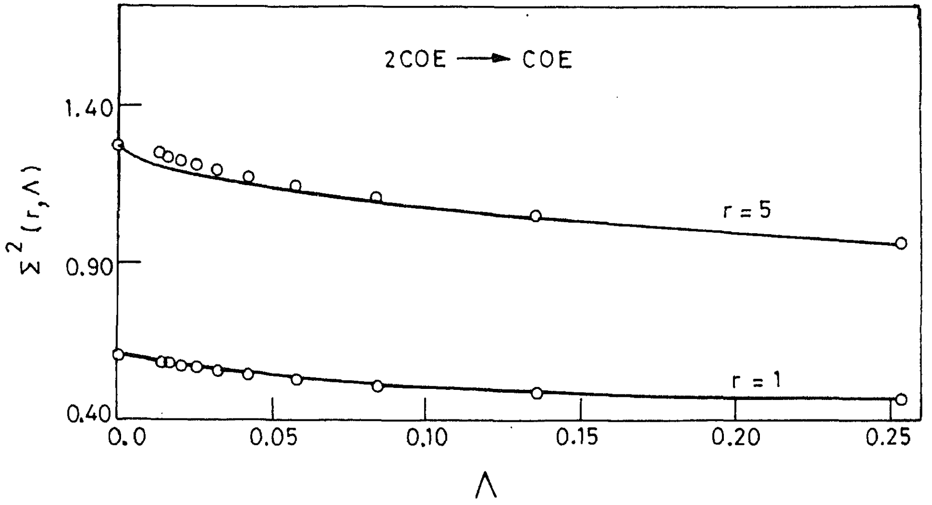

Figure 3. As in figure 2, for the case of P-violation. Now $\gamma=0$ and θ_0 varies.

and θ_0 varied. We again find excellent agreement between theory and numerical results for Σ^2 for this transition; see figure 3.

We conclude with a summary of our principal results. We have shown that the transitions between universality classes in quantum chaotic systems are rapid and have a universal classification. The Brownian motion model for spectra has been verified through semiclassical as well as numerical calculations. Finally, we have explicitly demonstrated the existence of a random matrix in the quantum mechanics of chaotic systems. We believe that such random matrices arise under *any* parametric variation (not necessarily only under symmetry breaking). This lends credence to the very existence of universality classes as well as to the universal nature of the transitions among them.

References

[1] M L Mehta, *Random matrices*, (Academic Press, New York) (1990)
[2] F Haake, *Quantum signatures of chaos*, (Springer, Berlin 1991)
[3] F J Dyson, *J. Math. Phys.* (*N.Y.*) **3**, 1191 (1962)
[4] A Pandey, *Ann. Phys.* (*N.Y.*) **134**, 110 (1981)
[5] J B French, V K B Kota, A Pandey and S Tomsovic, *Ann. Phys.* (*N.Y.*) **181**, 198, 235 (1988)
[6] A Pandey and M L Mehta, *Commun. Math. Phys.* **87**, 449 (1983)
M L Mehta and A Pandey, *J. Phys.* **A16**, 2655, L601 (1983)
[7] A Pandey and P Shukla, *J. Phys.* **A24**, 3907 (1991)
[8] T Guhr and H A Widenmüller, *Ann. Phys.* (*N.Y.*) **199**, 412 (1991)
[9] G E Mitchell, E G Bilpuch, P M Endt and J F Shriner Jr., *Phys. Rev. Lett.*, **61**, 1473 (1988)
[10] N Rosenzweig and C E Porter, *Phys. Rev.*, **120**, 1648 (1960)
[11] M V Berry and M Robnik, *J. Phys.*, **A19** 649 (1986)
[12] O Bohigas, M J Giannoni and C Schmit, in *Quantum chaos and statistical nuclear physics*, Eds T H Seligman and H Nishioka (Springer, Berlin, 1986), p 18
[13] A M O de Almeida, in *Quantum chaos*, Eds H Cerdeira, R Ramaswamy, G Casati and M Gutzwiller, (World Scientific, Singapore, 1990)
[14] N Dupuis and G Montambaux, *Phys. Rev.*, **B43**, 4390 (1991)
[15] G Lenz and F Haake, *Phys. Rev. Lett.*, **67**, 1 (1991)
[16] G Casati and L Molinari, *Prog. Theor. Phys. Suppl.*, **98**, 287 (1989)
[17] F M Izrailev, *Phys. Rev. Lett.*, **56**, 541 (1986)
[18] G Casati, L Molinari and F Izrailev, *Phys. Rev. Lett.*, **64**, 1851 (1990)
[19] M Tabor, *Physica*, **D6**, 195 (1983)
[20] M C Gutzwiller, *J. Math. Phys.* (*N.Y.*) **12**, 343 (1971)
[21] J Hannay and A M O de Almeida, *J. Phys.* **A17**, 3429 (1984)
[22] M V Berry, *Proc. R. Soc.* (*London*) **A400**, 299 (1985)
[23] P Shukla and A Pandey, (in preparation)

PRAMANA
— journal of
physics

© Printed in India

Vol. 41, No. 2,
August 1993
pp. 83–123

Resolved photon processes

MANUEL DREES[1]* and ROHINI M GODBOLE[2]
[1] Tata Institute of Fundamental Research, Homi Bhabha Road, Bombay 400005, India
* Permanent address: Department of Physics, University of Wisconsin, 1150 University Avenue, Madison WI 53706, USA
[2] Physics Department, University of Bombay, Vidyanagari, Bombay, 400098, India

MS received 3 February 1993; revised 31 May 1993

Abstract. We review high-energy scattering processes that are sensitive to the hadronic structure of the photon, describing theoretical predictions as well as recent experimental results. These processes include deep-inelastic electron–photon scattering at e^+e^- colliders; and the production of jets, heavy quarks and isolated photons in the collision of real photons at e^+e^- colliders, as well as in photon–photon collisions at ep colliders. We also comment on minijet based calculations of total γp and $\gamma\gamma$ cross-sections, and discuss the possibility that future linear e^+e^- colliders might produce very large photon fluxes due to the beamstrahlung phenomenon; in the most extreme cases, we predict more than one hadronic $\gamma\gamma$ event to occur at every bunch crossing.

Keywords. Photon structure functions; minijets; ep colliders; linear e^+e^- colliders.

PACS Nos 13·65; 13·87; 13·60; 12·38

Table of contents

1. Introduction
2. The photon structure function F_2^γ
3. Real $\gamma\gamma$ scattering at e^+e^- colliders
    3.1 $e^+e^- \rightarrow \text{jets} + X$
    3.2 Heavy quark production
    3.3 J/Ψ production
    3.4 Direct photon production
    3.5 Beamstrahlung and hard $\gamma\gamma$ processes at linear colliders
4. Resolved photon reactions in γp scattering
    4.1 $ep \rightarrow \text{jets} + X$
    4.2 Heavy quark production
    4.3 Direct photon production
    4.4 J/Ψ production
    4.5 Other processes
5. Minijets and total cross-sections
6. Summary and conclusions
7. Acknowledgements
8. References

1. Introduction

Among the quarks, leptons and gauge bosons now thought to be truly elementary particles, the photon occupies a special place. Together with the electron it was the first elementary particle correctly identified as such; the understanding of reactions involving these two particles spawned the theory of gauge interactions, now thought to describe all observed (electroweak, strong and gravitational) interactions. In view of this long, distinguished history, it may come as a surprise that there is one large class of photonic interactions about which only relatively little is known: The interaction of real (on-shell) photons with hadrons (or other real photons).

Such reactions can proceed in two quite different ways: The photon can couple directly to a quark or gluon in the struck hadron; in this case the whole energy of the photon goes into the hard (partonic) scattering process. Alternatively, the photon can undergo a transition into a (virtual) hadronic state before encountering the target hadron. In this case a quark or gluon "in" the photon can react, via strong interactions, with partons in the struck hadron. Notice that now only a fraction of the photon's energy goes into the partonic scattering; the rest is carried away by a "spectator jet" produced by the break-up of the photon. (In both cases the break-up of the struck hadron will also produce such a spectator or remnant jet, at least in the photon–hadron centre-of-mass frame.) In this article we generally refer to the first kind of reaction as *direct processes*, while those of the second kind are termed *resolved photon processes*. Cross sections for direct processes are computable from perturbative QCD (assuming the reaction is "hard" enough, i.e. involves a sufficiently large momentum exchange) in terms of parton densities inside the hadron. Similarly, the cross sections for resolved photon processes depend on the parton densities "inside" the photon.

Since the pioneering SLAC measurement [1] of deep-inelastic eletron–nucleon scattering, a large body of data on the parton distributions inside nucleons has been accumulated [2]. Further constraints on nucleonic parton densities are imposed by several sum rules, which can be derived directly from QCD. In comparison the picture looks much more sketchy where the parton content of the photon is concerned. Until very recently, the only relevant data were measurements of the electromagnetic structure function F_2^γ in deep-inelastic $e\gamma$ scattering; as we will see in more detail in § 2, these measurements suffer from large theoretical and/or experimental uncertainties. Moreover, they only cover a limited kinematical range. Finally, they are not sensitive to the gluon content of the photon, which plays an important role in many resolved photon processes. During the last year experimental analyses of jet production in $\gamma\gamma$ collisions in terms of resolved photon processes have started to appear [3, 4]. Even more recently, the *ep* collider HERA has started operations; photoproduction processes, including resolved photon reactions, play an important role in its physics programme [5, 6]. It seems therefore timely to review what is known about resolved photon processes and the parton content of the photon, and what we can hope to learn in the near future. We will see in § 5 that this information might be crucial for assessing the physics potential of future linear e^+e^- supercolliders.

This article is organized as follows. In § 2 we give a short introduction to the photon structure function, describing the theoretical understanding of as well as experimental data on F_2^γ. We also briefly compare existing parametrizations of photonic parton densities. In § 3 we discuss hard $\gamma\gamma$ processes at existing and planned e^+e^- colliders, while § 4 is devoted to hard γp reactions. We will see in both cases that the relative importance of resolved photon processes steadily increases with the available centre-of-mass energy. As a result, at existing e^+e^- colliders one can probably only study processes with large partonic cross sections, i.e. jet and heavy quark production; in contrast, at HERA and certain e^+e^- supercolliders a large variety of final states that receive contributions from resolved photon processes can be produced with detectable rates. In § 5 we discuss to what extent "minijet" calculations allow us to predict total γp and $\gamma\gamma$ cross sections. We will show that even if the total pp cross section and the parton densities in the photon were known, sizable theoretical uncertainties would remain due to our insufficient understanding of multiple parton scattering. Finally, § 6 contains a summary of our results.

2. The photon structure function F_2^γ.

As we know, information about the proton structure is obtained by studying deep inelastic scattering (DIS) of high energy leptons of energy E off proton targets.

$$e^- + p \to e^- + X \tag{2.1}$$

shown in figure 1a. The structure of the proton as revealed to a photon probe of invariant mass $-Q^2$ depends on the value of Q^2. In the DIS regime the process of (2.1) is characterised by two independent kinematic variables, $y = \nu/E$ where ν is the energy carried by the probing photon in the laboratory frame, and $x = Q^2/(2M\nu)$ where M is the proton mass. We also know that the double differential cross-section for this process factorises in the quark parton model (QPM) as,

$$\frac{\mathrm{d}^2\sigma^{ep\to X}}{\mathrm{d}x\mathrm{d}y} = \frac{2\pi\alpha^2 s}{Q^4} \times [(1+(1-y)^2)F_2^p(x) - y^2 F_L^p(x)], \tag{2.2}$$

where

$$F_2^p(x) = \sum_q e_q^2 x q^p(x);$$

$$F_L^p(x) = F_2^p(x) - 2xF_1^p(x) \tag{2.3}$$

are the two electromagnetic structure functions of the proton. The longitudinal structure function $F_L^p(x)$ is zero in QPM, $q^p(x)$ the probability for quark q to carry a momentum fraction x of the proton and e_q denotes the electromagnetic charge of quark q in units of the proton charge. This factorisation of the x and Q^2 dependence in (2.2) is of course only approximate. In general F_2^p depends on x as well as Q^2 and $F_L^p(x)$ is nonzero. QCD predicts the Q^2 dependence of the structure functions, given by the Gribov–Lipatov–Altarelli–Parisi (GLAP) [7] equations but does not say anything about the shape of hadronic structure functions. According to QCD

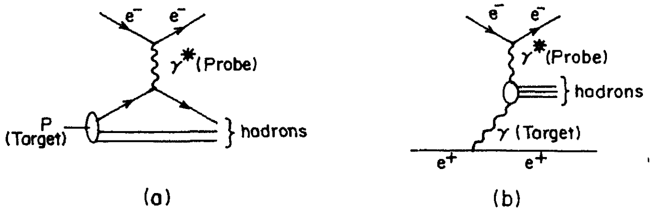

Figure 1. Deep inelastic scattering for the proton and photon.

predictions all the hadronic structure functions shrink to lower values of x as Q^2 increases.

The idea that photons behave like hadrons when interacting with other hadrons dates back to the early days of strong interaction physics and is known to us under the name of the Vector Meson Dominance (VMD) picture. This essentially means that at low 4-momentum transfer, the interaction of a photon with hadrons is dominated by the exchange of vector mesons which have the same quantum numbers as the photon. While this picture works reasonably well for "soft" processes (i.e., reactions characterized by small 4-momentum transfer), it is not at all clear that it should describe the whole story of interactions of photons with hadrons at high energies as well.

Since a photon is known to behave like a hadron, it seems reasonable that it should be possible to probe its structure also in a DIS experiment. Such an experimental situation is provided at e^+e^- colliders in $\gamma^*\gamma$ reactions as shown in figure 1b. Here the virtual photon with invariant mass square $-Q^2$ probes the structure of the real photon. If the VMD picture were the whole story then one would expect that such an experiment will find

$$F_2^\gamma \simeq F_2^{\gamma,\mathrm{VMD}} \propto F_2^{\rho^0} \simeq F_2^{\pi^0}. \tag{2.4}$$

Then with increasing Q^2, the structure function F_2^γ will behave just like a hadronic proton structure function. However, there is a very important difference in case of photons, i.e., photons possess pointlike couplings to quarks. This has interesting implications for $\gamma^*\gamma$ interactions as first noted in the framework of the QPM by Walsh [8]. It essentially means that $\gamma^*\gamma$ scattering in figure 1 contains two contributions as shown in figure 2. The contribution of figure 2a can be estimated by (2.4), whereas that of figure 2b was calculated in the QPM [8]. This is done by considering the cross-section for the reaction

$$\gamma + \gamma^* \to q + \bar{q}.$$

Due to t and u channel poles this can be calculated only when one considers quarks with finite masses. The result can be recast in a form equivalent to (2.2):

$$\begin{aligned}\frac{\mathrm{d}^2\sigma^{e\gamma\to X}}{\mathrm{d}x\,\mathrm{d}y} &= \frac{2\pi\alpha^2 s_{e\gamma}}{Q^4} \times \frac{3\alpha}{\pi} \\ &\quad \sum_q e_q^4 \left\{ (1+(1-y)^2) \times [x(x^2+(1-x)^2) \times \ln\frac{W^2}{m_q^2} \right. \\ &\quad \left. + 8x^2(1-x) - x] - y^2[4x^2(1-x)] \right\},\end{aligned} \tag{2.5}$$

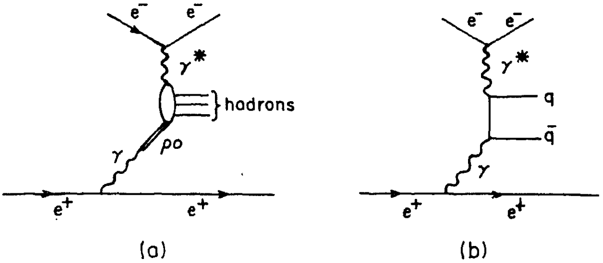

Figure 2. Two contributions to F_2^γ.

where $W^2 = Q^2(1-x)/x$. On comparing (2.2) and (2.5) we see that the factors in square brackets in the above equation have the natural interpretation as photon structure functions F_2^γ and F_L^γ and one has

$$F_2^{\gamma,\mathrm{pointlike}}(x,Q^2) = 3\frac{\alpha}{\pi}\sum_q e_q^4\left[x(x^2+(1-x)^2)\times\ln\frac{W^2}{m_q^2} + 8x^2(1-x) - x\right]$$
$$= \sum_q e_q^2 x q^{\gamma,\mathrm{pointlike}}(x,Q^2). \tag{2.6}$$

Two points are worth noting: the function $F_2^{\gamma,\mathrm{pointlike}}(x,Q^2)$ can be completely calculated in QED and secondly this contribution to F_2^γ increases logarithmically with Q^2. So in this simple "VMD + QPM" picture, F_2^γ consists of two parts, $F_2^{\gamma,\mathrm{pointlike}}$ and $F_2^{\gamma,\mathrm{VMD}}$, with distinctly different Q^2 behaviour and with the distinction that for one part both the x and the Q^2 dependence can be calculated completely from first principles.

This QPM prediction received further support when it was shown by Witten [9] that at large Q^2 and at large x, both the x and Q^2 dependence of the quark and gluon densities in the photon can be predicted completely even after QCD radiation is included. An alternative way of understanding this result is to consider the evolution equations [10] for the quark and gluon densities inside the photon. These contain an inhomogeneous term on the r.h.s. proportional to α, which describes $\gamma \to q\bar{q}$ splitting, i.e. the pointlike coupling of photons to quarks. In the 'asymptotic' limit of large Q^2 and large x, the $q_i^\gamma(x,Q^2)$ have the form

$$q_i^{\gamma,\mathrm{asymp}}(x,Q^2) \propto \alpha\times\ln\left(\frac{Q^2}{\Lambda_{\mathrm{QCD}}^2}\right)F_i(x)$$
$$\simeq \frac{\alpha}{\alpha_s}F_i(x), \tag{2.7}$$

where Λ_{QCD} is the usual QCD scale parameter and the x dependence of the $F_i(x)$ is completely calculable. Comparing (2.6) and (2.7) we see that the essential change, apart from the different x dependence, between the leading order (LO) QCD and QPM predictions is the replacement of $m_q^2 \to \Lambda^2$. We then have

$$F_2^{\gamma,\mathrm{asymp}} = \sum_q e_q^2 x q^{\gamma,\mathrm{asymp}}. \tag{2.8}$$

The asymptotic form of $G^\gamma(x,Q^2)$ can also be uniquely calculated. These asymptotic predictions, however, show unphysical divergences as $x \to 0$ indicating thereby that at small x the "hadronic" part of F_2^γ can not be neglected, and is not adequately described by a regular, VMD-inspired ansatz. The initial enthusiasm that this completely calculable prediction can be used as a test of QCD and also for a high precision measurement of α_s, suffered a big set back by the observation [11] that the degree of the $x \to 0$ pole becomes larger in higher orders of perturbation theory; we therefore have to conclude that the separation of F_2^γ in two parts $F_2^{\gamma,\mathrm{VMD}}$ and $F_2^{\gamma,\mathrm{asymp}}$ is not physical. One way out of this is to add a hadronic contribution to $F_2^{\gamma,\mathrm{asymp}}$ with similar divergence so as to get a finite result at small x [12]. This involves arbitrary parameters, but keeps the hope of being able to use the calculable pointlike contribution for QCD tests. An alternative suggestion is to use the experimental data on F_2^γ to fit a finite input distribution for $\mathbf{q}^\gamma$ at a scale $Q_0^2 \simeq 1\,\mathrm{GeV}^2$, thus retaining the predictability only of the Q^2 dependence but gaining the ability to calculate physically meaningful quantities for all combinations of x and $Q^2 \geqslant Q_0^2$ [13]. The theoretical debate on the subject is still not completely closed [14].

By now several parametrizations of the parton densities inside the photon $\mathbf{q}^\gamma(x, Q^2) \equiv (q_i^\gamma, G^\gamma)(x, Q^2)$ exist. The oldest parametrizations [15, 16] are based on the "asymptotic" LO predictions. However, these parametrizations are even more singular as $x \to 0$ than the exact "asymptotic" prediction. Care must therefore be exercised if these parametrizations are to be used at small x.

The first parametrization that followed the suggestion of ref. [13] to fit input distributions at some low scale Q_0^2 such that data at higher Q^2 are reproduced is the "DG" parametrization of ref. [17]. In 1984, when this parametrization was constructed, only a single set of data on F_2^γ existed [18]. Since then, more data have become available [19, 4]. Most of these newer data were taken into account in the "LAC" fits of ref. [20]. Indeed, taken at face value, low-Q^2 data from the TPC/2γ collaboration [21] at PEP disfavour the older DG parametrization compared to the LAC fits. However, the interpretation of these data is not entirely straightforward. A general problem of the measurement of the x dependence of F_2^γ is that, unlike in deep-inelastic ep scattering, x has to be determined from the hadronic final state, since the energy of the target photon is not known [22]. Unfortunately some of the final state particles are usually lost in the beam pipe. One therefore needs fairly sophisticated "unfolding" techniques in order to determine the true value of x from the observed final state. Notice that some model of F_2^γ has to serve as an *input* for this unfolding procedure. Usually a simple "QPM + VMD" description is used for this purpose, even though we have seen above that this picture is not very meaningful within QCD.

Low-Q^2 data suffer from two additional problems. First of all, higher twist contributions might be quite important. Often only the region $W \geqslant 2\,\mathrm{GeV}$ is used for QCD comparisons, i.e. the region of large x is discarded; it is not clear, however, whether this is sufficient to really make higher twist contributions negligibly small. Secondly, at low x and low Q^2 one actually has $W^2 \gg Q^2$; in this case it is not clear that Q^2 is indeed the relevant scale in the process. Ideally one would like a unified treatment of real $\gamma\gamma$ (no-tag) and $\gamma^*\gamma$ (single-tag) data, allowing for a smooth transition from one to the other. Work along these lines is in progress [23]. At present we do not think it advisable to base the exclusion of a parametrization of $\mathbf{q}^\gamma(x, Q^2)$ on these low-Q^2 data alone.

The parametrizations of refs. [17, 20] are the only ones that allow an arbitrary form at least of the quark densities at scale Q_0^2; this leads to a fairly large number of free parameters which, in view of the paucity of good data, cannot be determined very precisely. The authors of ref. [24] have therefore used theoretical considerations (or prejudices) to fix the shape of the input distributions, reducing the number of free fit parameters to one. They assume that (2.4) is valid at the rather low input scale $Q_0^2 = 0{\cdot}25\,\mathrm{GeV}^2$; this scale has been taken from the "dynamical" fits to proton structure functions by the same authors [25]. Similarly, their pionic structure functions [26] were used to fix the shape of the input distributions. The only free parameter is then the overall size of the input distributions; the idea is that this parameter describes the contribution of vector mesons beyond the ρ.

Finally, for the "GS" parametrization of ref. [27] an intermediate approach has been taken. In order to avoid the ambiguities of low-Q^2 data, rather high input scale

$Q_0^2 = 5{\cdot}3\,\mathrm{GeV}^2$ has been chosen. At this scale, F_2^γ is assumed to be described by the "QPM + VMD" model; however, the gluon and sea-quark distributions in the pion, the overall size of the VMD (pionic) contribution, as well as the quark masses in eq. (2.6) are all allowed to vary within reasonable limits.

In figure 3a we compare various parametrizations for $F_2^\gamma(x, Q^2 = 5{\cdot}3\,\mathrm{GeV}^2)$ with each other and with experimental data from the PLUTO collaboration [18]. Since only the contributions from u, d and s quarks have been included in the calculation, charm-subtracted data have been used. We observe that all shown parametrizations describe the data reasonably well, although none of the fits is perfect. The differences between the various parametrizations only amount to typically 20% in the region $x \geqslant 0{\cdot}05$. Due to the inhomogeneous term in the evolution equation, these differences tend to be even smaller at higher Q^2; statistical errors are also larger for these theoretically cleaner high-Q^2 data. The best possibility to discriminate between different parametrizations using data on F_2^γ therefore seems to lie in high-statistics measurements at intermediate values of Q^2 and small x.

In figure 3b we compare the parametrizations of the gluon density at the same value of Q^2. Obviously the various parametrizations differ much more strongly here than for the quark densities that determine F_2^γ. The extreme behaviour of the LAC parametrizations is especially noticeable; this is because in these parametrizations no theoretical assumptions about $G^\gamma(x, Q_0^2)$ were made. The very hard gluon density of LAC3 is necessary to explain the rapid increase of $F_2^\gamma(x \simeq 0{\cdot}1, Q^2 \leqslant 4\,\mathrm{GeV}^2)$ with Q^2 seen in the data [21]; at $Q^2 > Q_0^2$, some of the gluons at large x are converted into $q\bar{q}$ pairs, leading to the maximum of $F_2^\gamma(x \simeq 0{\cdot}1)$ shown in figure 3a for this parametrization. These low-Q^2 data were ignored for the LAC2 fit, which uses $Q_0^2 = 4\,\mathrm{GeV}^2$; now a very soft gluon density is favoured. It should be noted, however, that the LAC3 parametrization also describes the high-Q^2 data adequately; this shows that F_2^γ is not very sensitive to G^γ.

For the other three parametrizations the gluon input is essentially fixed from the quark input. We already saw that the GRV fit only contains a single free parameter, which is fixed from data on F_2^γ. In the DG parametrization it is assumed that gluons are only produced radiatively from quarks, i.e. there is no truly intrinsic (VMD-like or otherwise) gluon content of the photon; as a result, the DG gluon density falls below that of the other parametrizations, except for very small x where it resembles the GRV and LAC3 gluons. Note, however, that the DG parametrization has been obtained using a rather large value for the QCD scale parameter $\Lambda = 400\,\mathrm{MeV}$, while all other parametrizations assume $\Lambda = 200\,\mathrm{MeV}$. The same value of Λ should also be used in the factors of α_s that occur in resolved photon cross-sections. As a result, the DG parametrization sometimes leads to larger predictions for such cross-sections, in spite of its smaller gluon content. Finally, in the GS2 parametrization, $G^\gamma(x, Q_0^2)$ receives contributions both from a VMD-like (pionic) term, and from radiation off the (QPM) quarks [28].

There are also versions of the GRV and GS parametrizations that include higher order effects, i.e. where the 2-loop evolution equations [11] have been used. However, in view of the large uncertainties at least in the gluon densities, this seems at present an unnecessary refinement. Moreover, full higher order calculations do not yet exist for most resolved photon processes; we will come back to this point later.

This concludes our discussion of deep-inelastic $e\gamma$ scattering. While theoretically relatively clean, since one computes a fully inclusive cross section, we have seen that this is probably not the best way to give us detailed information about the partonic

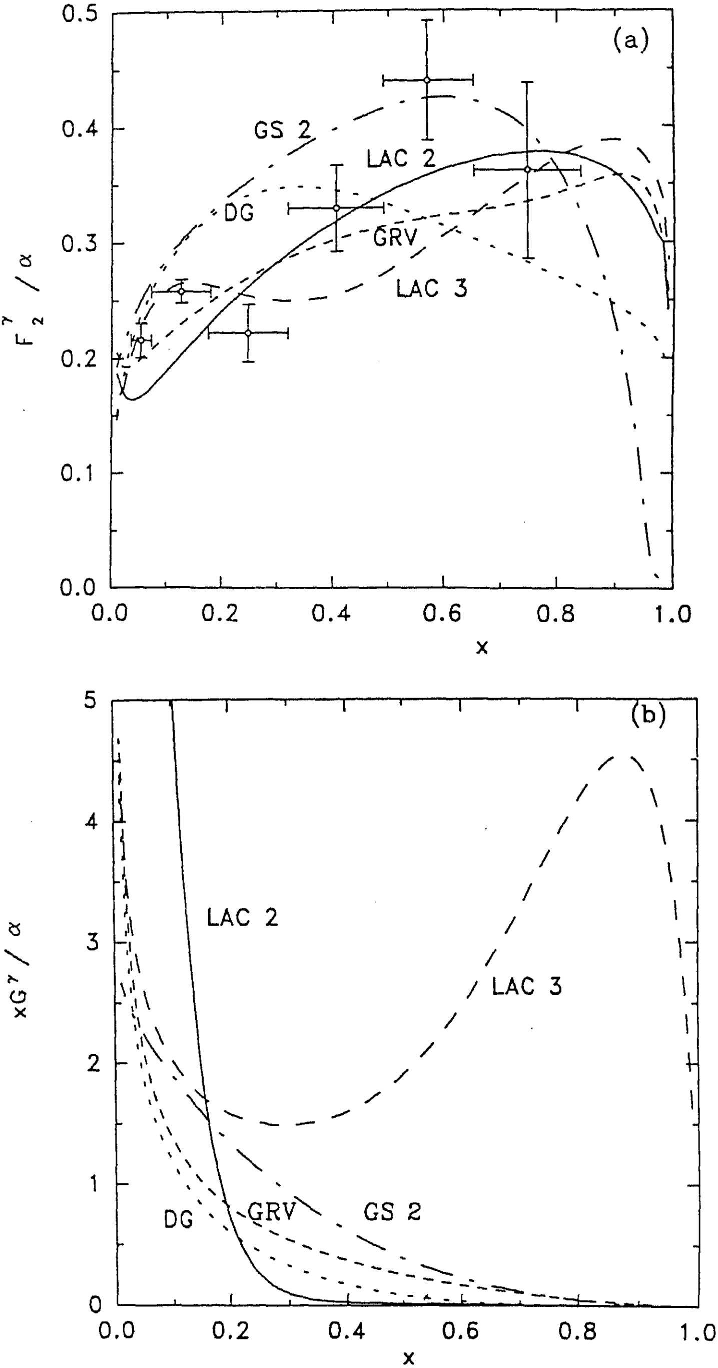

Figure 3. Comparison of existing parametrizations of $\mathbf{q}^\gamma$. The data are from [18].

structure of the photon, as witnessed by the large differences between parametrizations of the gluon density. As we will see in the following sections, this information might be provided by resolved photon processes involving only real photons.

3. Real $\gamma\gamma$ scattering at e^+e^- colliders

Effects of the photon structure and especially the gluon component of the photon are best studied in processes involving real photons. In this section we will discuss only the possibilities of probing the photon structure at e^+e^- colliders. Possible effects of the hadronic component of the photon at *ep* colliders and at fixed target photoproduction experiments will be discussed in the next section. At e^+e^- colliders processes other than DIS which could yield information about the photon structure function are jet production, heavy flavour production and prompt production initiated by partons in the photon. Compared to DIS (single-tag) processes, real $\gamma\gamma$ reactions have cross-sections which are enhanced by a factor $(\ln s/(4m_e^2)) \simeq 20$ at existing colliders. The scale at which the parton densities in the photon $\mathbf{q}^\gamma(x, Q^2)$, will be probed is decided by the p_T^2 of the jets, which is comparable to the higher end of Q^2 values accessible to DIS experiments at present colliders.

3.1 $e^+e^- \rightarrow jets + X$

Jet production in $\gamma\gamma$ collisions can receive contributions from three different types of diagrams [29] as shown in figure 4. The 'direct process' of figure 4a is due to $\gamma\gamma \rightarrow q\bar{q}$ production, present already in the naive quark–parton model. Figure 4b depicts the case where only one photon is resolved into its partonic components, which then interact with the other photon; we call these the 'once-resolved' processes ('1-res' for short). Finally, figure 4c shows the situation where both photons are resolved, so that the hard scattering is a pure QCD $2 \rightarrow 2$ process; we call these the 'twice-resolved' contributions ('2-res' for short). It is very important to note here that every resolved photon will produce a spectator jet of hadrons with small transverse momentum relative to the initial photon direction, which for (quasi-) real photons coincides with

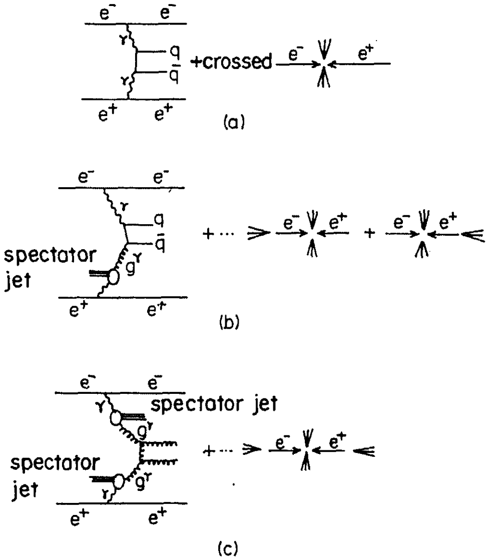

Figure 4. Different contributions to the production of high p_T jets in e^+e^- collisions with the associated topologies.

the beam direction. The resolved contributions of figure 4b and c can therefore be separated if one can tag on these spectator jets.

The cross-section for jet production in $\gamma\gamma$ collisions for the '2-res' processes can be written schematically as [30, 31]

$$d\sigma = f_{\gamma/e}(x_1)\mathbf{q}^{\gamma}(x_2, Q^2) f_{\gamma/e}(x_3)\mathbf{q}^{\gamma}(x_4, Q^2) d\hat{\sigma}, \tag{3.1}$$

where the $\hat{\sigma}$ are the cross-sections for the hard $2 \to 2$ subprocesses [32, 15], $\mathbf{q}^{\gamma}(x, Q^2)$, $f_{\gamma/e}$ denote parton densities inside the photon and photon fluxes inside the electron respectively; we include non-leading contributions to $f_{\gamma/e}$, following [33]. For the '1-res' (direct) processes, one (both) of the parton density functions $\mathbf{q}^{\gamma}(x, Q^2)$ have to be replaced by $\delta(1-x)$, and the proper hard sub-process cross-sections have to be inserted [15]. Recall (2.7) for $\mathbf{q}^{\gamma}$. This makes it clear that all three classes of diagrams are of the same order in α and α_s.

While it is clear that our present knowledge of $\mathbf{q}^{\gamma}$ is not precise enough to make absolute predictions, one can check how sensitively the predicted cross-sections depend on the choice of $\bar{\mathbf{q}}^{\gamma}$. The DG parametrization will usually give us the most conservative prediction of the available parametrizations, as can be seen from figure 3.

In figure 5 we show the energy dependence of the cross-section for the production of two jets with $p_T = 3$ GeV, as predicted [31] by the DG parametrization, in the range covered by the PETRA and TRISTAN colliders. For this choice of p_T the cross-section is quite sizable; recall that the total luminosity collected at PETRA amounts to several hundred pb^{-1} per experiment, while as of this writing, TRISTAN has collected about $100\,\text{pb}^{-1}$. The cross-section is also well above the background from annihilation events with hard initial state radiation (dotted curve). We also note that the twice-resolved contribution grows faster than $\sqrt{s}$ with increasing machine energy and, for this choice of p_T, begins to dominate the cross-sections in the energy range of TRISTAN. Notice that "jets" with smaller transverse momentum can even originate from the poorly understood soft (VMD) contribution to the $\gamma\gamma$ cross-section; this contribution is essentially negligible if $p_T \geqslant 2$ to 3 GeV. Thus TRISTAN is in a unique position to probe the structure of the photon through jet production. Our detailed studies [31] do indeed indicate that studying the production of high p_T jets and heavy flavour (charm) at TRISTAN should be able to probe the hadronic content of photon in some detail.

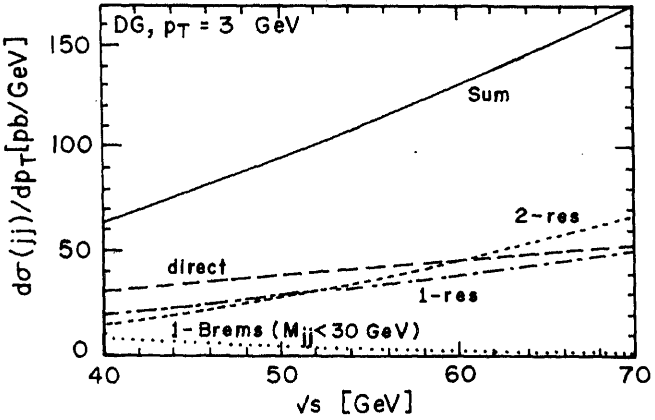

Figure 5. $d\sigma/dp_T$ at $p_T = 3$ GeV as a function of $\sqrt{s}$ [31].

This is demonstrated in figure 6, where we compare the p_T spectrum of jets produced in $\gamma\gamma$ collisions at $\sqrt{s}(e^+e^-) = 60\,\text{GeV}$, as predicted by the DG (a) and LAC3 (b) parametrizations. We already saw in the previous figure that the DG parametrization predicts the three classes of processes to contribute roughly equally at $p_T = 3\,\text{GeV}$. At larger values of p_T the direct process starts to dominate. The reason is simply

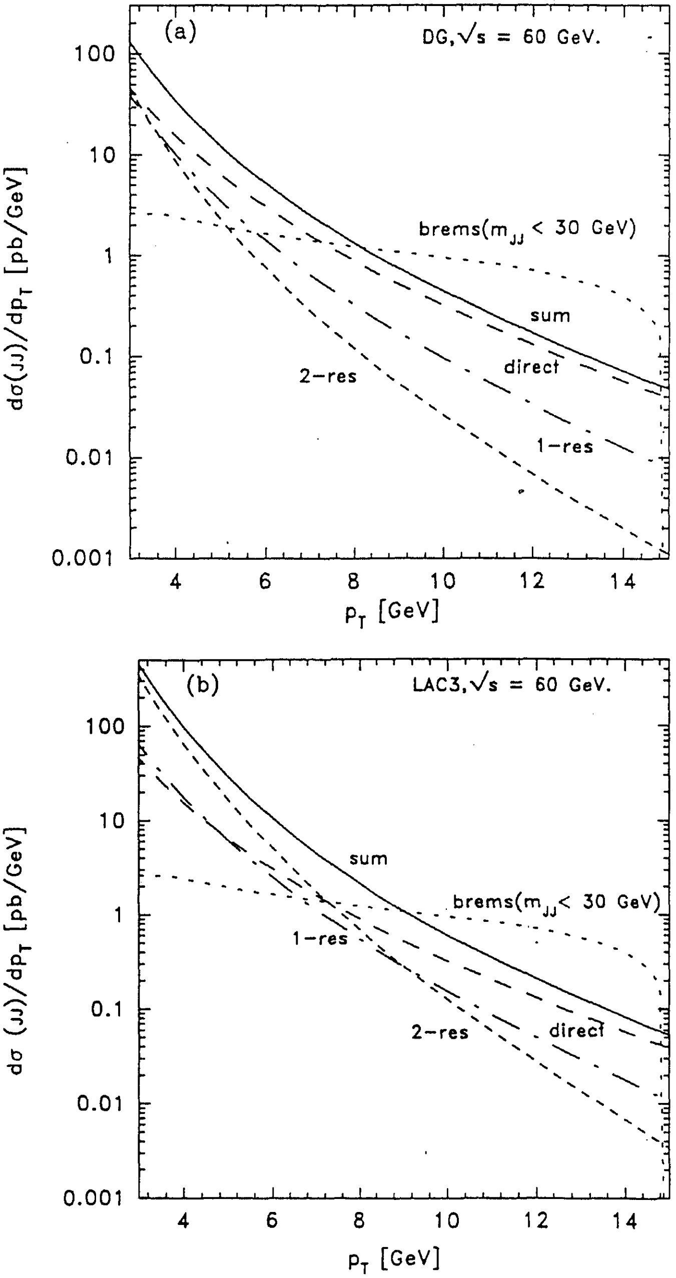

Figure 6. The transverse momentum spectrum of jets produced in real $\gamma\gamma$ scattering at $\sqrt{s} = 60\,\text{GeV}$, for (a) DG and (b) LAC3 parametrizations.

that a resolved photon has to split its energy between the parton participating in the hard scattering on the one hand, and a spectator jet on the other; therefore the cross-section for resolved photon processes will depend more strongly on the available phase space, i.e. will have a steeper p_T spectrum. Nevertheless, even for the DG parametrization the sum of once and twice resolved contributions exceeds the direct contribution out to $p_T \simeq 4{\cdot}5$ GeV.

The extremely hard gluon density of the LAC3 parametrization (see figure 3b) greatly enhances the cross-section for twice resolved processes compared to the predictions of the DG parametrization. Note that out of the eight $2 \to 2$ QCD scattering matrix elements, that for $gg \to gg$ scattering is the largest, followed by the one for $qg \to qg$ [32]. As a result, LAC3 predicts the 2-res contribution to be almost an order of magnitude larger than DG; it also predicts an approximately two times larger 1-res contribution. The LAC3 parametrization therefore predicts the high-p_T jet cross-section to be dominated by resolved photon contributions up to $p_T \simeq 9{\cdot}5$ GeV.

What is the experimental situation? Note that even at the lower end of the curves in figure 5, at PEP/PETRA energies, one expects a sizable contribution to the jet cross-section from resolved processes in addition to the 'direct' process. In this context it is interesting to note that almost all the groups at PEP/PETRA observed [34] such an excess of jet events. These experiments compared data with a two component model where they added to the direct process a soft component (with exponential p_T spectrum) expected from the VMD picture and always *failed* to reproduce the data. The data always had yet another 'third component' with a p_T spectrum softer than QPM but broader than VMD and thrust distribution broader than the QPM prediction. Both features are expected for resolved contributions.

The first experimental analysis including resolved photon contributions has recently been performed by the AMY collaboration at TRISTAN [3]. They modelled the three classes of hard contributions to high-p_T jet production using eq. (3.1), but included the full machinery of initial and final state parton showers predicted by QCD, as well as parton $\to$ hadron fragmentation. They conclude that inclusion of resolved photon processes as predicted using the DG parametrization greatly improves the agreement between Monte Carlo predictions and data.

An example is shown in figure 7 [35], which shows the p_T spectrum of their data

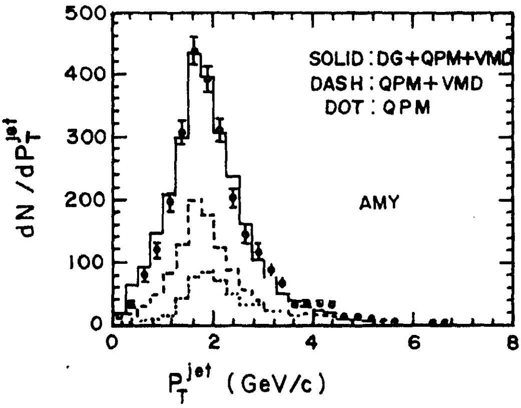

Figure 7. Data on $\gamma\gamma \to$ jets and predictions with and without 'res' contributions [35].

sample. It should be noted that, like previous analyses of $\gamma\gamma$ scattering [34], AMY does not use a jet finding algorithm. Rather, the entire event is divided into two hemispheres, perpendicular to the thrust axis; the p_T shown in the figure is then simply the sum over the transverse momenta of all particles in one hemisphere. Notice also that the AMY trigger requires the event to contain at least one charged particle with $p_T \geqslant 1{\cdot}0\,\mathrm{GeV}$. This suppresses events with very small p_T per hemisphere, and further complicates the relation between the partonic and hemispheric transverse momentum.

The agreement between QCD MC predictions (solid histogram) and data (points) shown in figure 7 is indeed quite impressive, in particular when compared to the prediction of the traditional "QPM + VMD" model (dashed histogram). It should be noted that the AMY Monte Carlo contains a number of free parameters beyond those determining the $\mathbf{q}^{\gamma}(x, Q^2)$. The most important one is the cut-off $p_{T,\min}$, which is the smallest partonic transverse momentum allowed in the hard scattering diagrams of figure 4. Of course, these diagrams diverge badly as $p_T \to 0$; QCD does not tell us, however, just how large the partonic p_T has to be for its predictions to become trustworthy. AMY thus simply fits $p_{T,\min}$ from their data with $p_T^{\text{thrust}} \geqslant 1{\cdot}5\,\mathrm{GeV}$; they find $p_{T,\min} = 1{\cdot}6\,\mathrm{GeV}$ for the DG parametrization, if only the three light flavours of quarks are assumed to be present in the photon. The same value of $p_{T,\min}$ also leads to a good description of the p_T^{thrust} spectrum in the theoretically cleaner region beyond 3 GeV. Other free parameters include the amount of intrinsic p_T allowed for the partons inside the photon, and parameters describing the hadronization process. The experimental observables that have been studied so far, in particular the thrust distribution, do not seem to depend much on the former, but are quite sensitive to the latter. More detailed analyses of higher statistics data taken with an upgraded AMY detector are now being carried out. However, the existing data are already good enough to rule out the LAC3 parametrization; the data are clearly incompatible [35] with the huge rate of resolved photon events predicted by this parametrization, see figure 6. In contrast, the LAC1 or LAC2 parametrizations, with $p_{T,\min} = 2{\cdot}0\,\mathrm{GeV}$, seem to describe the recent AMY data slightly better than the DG parametrization does [36]. On the other hand, a toy-model with zero gluon content of the photon falls short of the data, even if $p_{T,\min}$ is allowed to be as small as $1{\cdot}0\,\mathrm{GeV}$ [3]. Finally, by comparing their own data with data taken at the PETRA collider, AMY could show that the importance of the resolved photon processes increases with energy [3], as expected from figure 5.

More recently, other experimental groups have also entered the fray. In particular, the TOPAZ collaboration at TRISTAN has presented a preliminary analysis [37] of their data. Compared to the AMY detector, TOPAZ has the advantage of a lower trigger threshold, which merely requires the presence of 2 charged tracks with $p_T \geqslant 0{\cdot}3\,\mathrm{GeV}$ in the event; for a given luminosity, this leads to an approximately two times larger $\gamma\gamma$ data sample than at AMY. This should allow for a more detailed study of the region with low and intermediate p_T, which is however difficult to interpret theoretically. The p_T distribution presented by TOPAZ is in good agreement with the AMY result, while the thrust distributions seem to differ somewhat.

Very recently TOPAZ has also presented [38] preliminary results of an analysis which, for the first time in $\gamma\gamma$ physics, actually requires jets to be reconstructed, using an algorithm familiar from hadron collider studies of jets. They used an unfolding procedure to extract the *partonic* cross-section from the measured jet rates. The results for the cross-section integrated over 2·5 GeV $\leqslant p_T$ (parton) $\leqslant$ 8 GeV are:

$$\sigma(|y_1|, |y_2| \leqslant 0{\cdot}7) = 23{\cdot}4 \pm 2{\cdot}7 \pm 1{\cdot}7\,\mathrm{pb}$$
$$\sigma(|y_1| \leqslant 0{\cdot}7, y_2 \text{ anywhere}) = 96{\cdot}7 \pm 3{\cdot}7 \pm 8{\cdot}5\,\mathrm{pb}. \tag{3.2}$$

The first result corresponds to the situation where both high-p_T jets are reconstructed, while the second result includes events where only one high-p_T jet is seen. Notice that these are e^+e^-, not $\gamma\gamma$, cross-sections. The systematic errors include an estimate of the effect of varying $p_{T,\min}$ between 1·6 and 2 GeV. An additional 7% uncertainty is included in the single jet cross-section; this is the estimate for the contribution from soft processes. (Their contribution to the di-jet cross-section is negligible.) These numbers are preliminary; in particular, the error caused by fragmentation uncertainties has not yet been included. These numbers are reproduced equally well by the DG and LAC1, 2 parametrizations; e.g., DG predicts 21·4 and 90·9 pb for the first and second cross-section in (3.2), respectively. The predictions of the LAC3 parametrization are almost three times too large, so that this parametrization is clearly excluded; the DO + VMD parametrization is also disfavoured. The extraction of a partonic cross-section is an important step, since this allows to directly compare the predictions of theoretical models of $\mathbf{q}^\gamma(x, Q^2)$ with their data; it also simplifies the comparison of experimental data from different groups.

Finally, it should be mentioned that two LEP groups, ALEPH and DELPHI, have also presented first preliminary results on $\gamma\gamma$ scattering [39, 40]. The size of their data samples is only about 20% of those of the TRISTAN groups; in addition, the very large annihilation cross-section at $\sqrt{s} \simeq m_Z$ poses special background problems [41]. Nevertheless, both groups confirm that traditional "QPM + VMD" models are in conflict with their data, while the inclusion of resolved photon contributions, as predicted from the DG parametrization, leads to satisfactory agreement between MC results and data. Notice that the good angular coverage of LEP detectors can give them an advantage when trying to find direct evidence for spectator jets, which so far have only been observed in $\gamma\gamma$ collisions via their contribution to the thrust distribution. Good angular coverage is also necessary for the study of events where one or both high-p_T jets emerge at small angles, which would allow to extend the range of x values probed by a given experiment.

We have seen that the jet cross-sections and especially the resolved photon contributions fall off sharply with increasing p_T; e.g. in figure 6a the '2-res' processes dominate only up to $p_T \simeq 3$ GeV. However, if we consider $\mathrm{d}\sigma(jj)/\mathrm{d}m_{jj}$ where m_{jj} is the invariant mass of the two high-p_T jets, then the resolved processes dominate to higher values. This can be understood from the fact that only 2-res processes receive contributions from diagrams where a gluon is exchanged in the t- or u- channel, leading to a more singular dependence of the hard subprocess cross-section on the square of momentum transfer $\hat{t}$ for these contributions. Thus the study of invariant mass distributions, as well as rapidity distributions, can help us to get more detailed information on $\mathbf{q}^\gamma$ [31]. If one can measure the spectator jet energy instead of only using the spectator jet activity to 'tag' the 'res' contributions, it may be possible to separate gluon initiated events from quark initiated ones. Since $G^\gamma(x, Q^2)$ is peaked at smaller values of x as compared to $\mathbf{q}_i^\gamma(x, Q^2)$, the spectator jet energies will be higher for events initiated by gluons in the photon.

3.2 *Heavy quark production*

As already stressed at the end of §2, at present we have much less information about the gluon content of the photon than about its quark content. Unfortunately, the production of central jets with $p_T \geqslant 3$ GeV is sensitive mainly to the region $x \geqslant 0{\cdot}15$ at TRISTAN and LEP1 energies [42]. As a result, the study of high-p_T jet production at these colliders is unlikely to discriminate between different ansätze for G^γ, provided only that it is "soft" (this rules out LAC3, as we have seen). The production of open or hidden charm might offer better opportunities to get information about the gluon content of the photon. First of all, there is no need of a p_T cut to get rid of a "soft" component, since there is none. The invariant energy going into the hard scattering can therefore be almost a factor of 2 smaller than for the clean sample of high-p_T jets, and correspondingly smaller values of x can be probed. Secondly, even if it turns out that some p_T cut has to be imposed to allow for the identification of charm events, the sensitivity to G^γ is still greater than for inclusive jet production, because there is less background from resolved photon events initiated by quarks: The only 1-res contribution comes from γg fusion, and the 2-res contribution from $q\bar{q}$ annihilation is predicted to be very small. Any nonzero signal for $c\bar{c}$ production via resolved photon processes would therefore allow a direct measurement of G^γ.

In figure 8 we compare predictions [31] for the total $c\bar{c}$ cross-section as calculated from the DG and LAC1 parametrizations, in the energy range covered by TRISTAN and LEP. For this and the following figures of this section, we have modified the estimate of the flux of resolved bremsstrahlung photons. The standard expression of ref. [33] has been derived by integrating the photon propagator $\propto 1/P^2$ over the full kinematically allowed range of the photon virtuality $-P^2$. However, if P is larger than the scale Q characterizing the hard scattering process, the picture of real (on-shell) partons residing "in" the photon is no longer valid. Therefore the upper limit of the

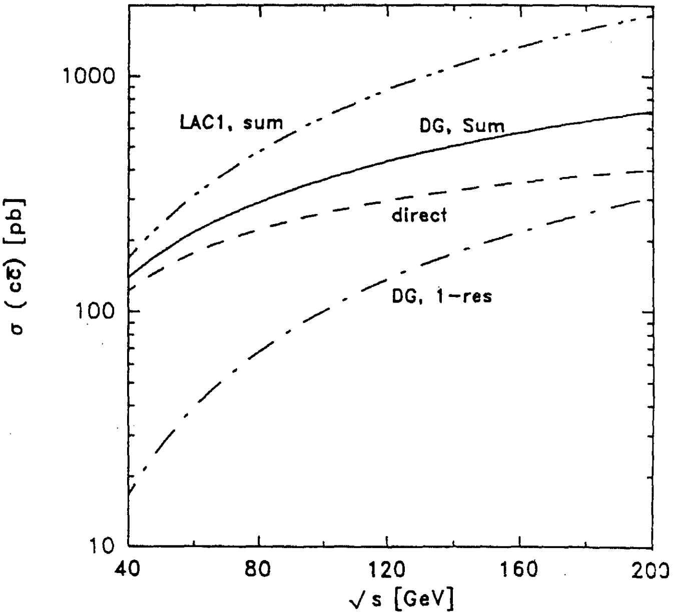

Figure 8. The total cross-section for $e^+e^- \rightarrow e^+e^- c\bar{c}X$ as a function of $\sqrt{s}$.

P^2 integration should be of order Q^2. Moreover, it has been known for some time [43] that the parton content of virtual photons with $\Lambda_{\rm QCD}^2 < P^2 < Q^2$ is suppressed compared to the parton content of on-shell photons. We attempt a crude estimate of this effect by introducing a further suppression factor of 0·85 for the bremsstrahlung flux of resolved photons; this number has been estimated from numerical results of Rossi [43]. Altogether we thus have:

$$f_{\gamma/e}^{\rm brems}(x) = 0{\cdot}85\frac{\alpha}{2\pi}[1+(1-x)^2]\ln\frac{Q^2}{m_e^2}. \tag{3.3}$$

The effect of this refinement will obviously be larger for larger ratio s/Q^2; this is why we did not introduce it in our predictions for jet production at TRISTAN energies and below. Of course, the formula of [33] is still applicable for the flux of bremsstrahlung photons interacting directly. It may be noted here that as has been pointed out [44] recently the abovementioned suppression ought to be different for quarks and gluons. Since in perturbation theory gluons can only be radiated off quarks, which are themselves off-shell if $P^2 \neq 0$, their density in the photon drops faster with increasing virtuality of the photon than the quark content does.

We see that, with the exception of the immediate vicinity of the Z pole, the two-photon cross section is *larger* than the one for the corresponding annihilation process $e^+e^- \to c\bar{c}$, by a factor of at least 8 (200) at $\sqrt{s} = 60$ (200) GeV. Secondly, just as in case of jet production, the contributions from resolved photon processes grow substantially faster with energy than that of the direct $\gamma\gamma \to c\bar{c}$ process. However, at least for the more conservative DG parametrization, the direct contribution still dominates the total cross-section even at $\sqrt{s} = 200$ GeV. Cuts on the transverse momentum or angle of the produced charm quarks will further reduce the importance of the resolved photon contribution, since it has a softer p_T spectrum and a more asymmetric angular distribution than the direct contribution. If the actual gluon content is indeed described by the DG parametrization, $c\bar{c}$ production can therefore only be used to measure G^γ if the direct contribution can be suppressed by detecting the spectator jet from the resolved photon, either directly or via the total thrust distribution. The GRV parametrization even predicts slightly (by 5 to 10%) smaller resolved photon contributions, due to the smaller value of α_s that has to be used with this parametrization; note that at the rather low energy scales characteristic for charm production, α_s depends quite sensitively on $\Lambda_{\rm QCD}$.

On the other hand, the LAC1 parametrization predicts the resolved photon contribution to dominate already for $\sqrt{s} \geqslant 55$ GeV; at $\sqrt{s} = 200$ GeV it predicts an almost 3 times larger total $c\bar{c}$ cross-section than the DG parametrization does. (Similar results also hold for the LAC2 parametrization.) If the LAC1 predictions turn out to be close to the truth, isolation of the resolved photon contribution to $c\bar{c}$ production should not be very difficult. However, even in this extreme case the 2-res contribution only amounts to 1·5% of the total at the highest LEP energy; any resolved photon signal in $c\bar{c}$ production can therefore safely be identified as stemming from 1-res photon-gluon fusion process.

3.3 *J/Ψ Production*

Another interesting process at existing e^+e^- colliders is the production of J/Ψ mesons in the reaction

$$e^+ + e^- \to \gamma + \gamma \to J/\Psi + X. \tag{3.4}$$

In this case the relevant hard scattering process is $\gamma + g \to J/\psi + g$, which can be estimated from the colour singlet model [45]. Notice that this requires one of the photons to be resolved; in leading order in α and α_s, there is *no* direct contribution. Moreover, as in case of open charm production, the 2-res contribution is negligible. As a result the process is an extremely clean probe of $G^\gamma(x, Q^2)$ for $x \sim 0{\cdot}01$–$0{\cdot}05$. The main problem in this case is the rather small total cross section; the DG parametrization predicts the cross-section to grow from 0·5 pb at $\sqrt{s} = 60\,\mathrm{GeV}$ to 4·0 pb at $\sqrt{s} = 200\,\mathrm{GeV}$ [31]. The LAC1, 2 parametrizations again lead to more than 3 times larger cross-sections. However, almost certainly only the 12% of all J/ψ mesons that decay into e^+e^- or $\mu^+\mu^-$ pairs will be detectable. Moreover, there are indications from the photoproduction of J/ψ, which proceeds via the *same* hard scattering process, that the LO prediction of the colour singlet model might be too low by as much as a factor of 5 [46]. While this is good news as far as the observability of the J/ψ signal at e^+e^- colliders is concerned, this large theoretical uncertainty means that at present this process cannot be used for a reliable measurement of the absolute size of the gluon component of the photon [47].

3.4 *Direct photon production*

Given a sufficiently large data sample, one might even attempt to look for $\gamma\gamma$ processes that occur only in higher orders in α. An example is the study of the production of prompt photons in $\gamma\gamma$ collisions via the processes,

$$\begin{aligned} &q^\gamma + \gamma \to q + \gamma \\ &q^\gamma + \bar{q}^\gamma \to \gamma + g \\ &g^\gamma + q^\gamma \to q + \gamma \end{aligned} \tag{3.5}$$

These processes, though suppressed by a factor of α compared to the case of jet production, have the advantage of having a cleaner final state. In the PEP to TRISTAN energy range the 1-res contribution clearly dominates [48]; requiring $p_T^\gamma (= p_T^{\mathrm{jet}}$ in leading order) to be larger than 1·5 GeV (a value very close to the value of $p_{T,\min}$ as determined from the AMY jet analysis [3] described above), the DG parametrization predicts a total γ + jet cross-section of about 1 pb at $\sqrt{s} = 60\,\mathrm{GeV}$. At LEP energies the 2-res contributions become more significant, and might allow to extract additional nontrivial information about the parton content of the photon [48].

3.5 *Beamstrahlung and hard $\gamma\gamma$ processes at linear colliders*

We have seen repeatedly that, for fixed transverse momenta of the particles produced in the hard scattering process or fixed invariant mass of the system produced in that scattering, the importance of resolved photon events increases quite rapidly with increasing beam energy; under the same circumstances, the ratio of $\gamma\gamma$ to annihilation events also grows rapidly with $\sqrt{s}$, as we have seen for the example of the total charm production cross-section. At future e^+e^- colliders it might therefore no longer be possible to consider $\gamma\gamma$ events as a background that can be suppressed easily.

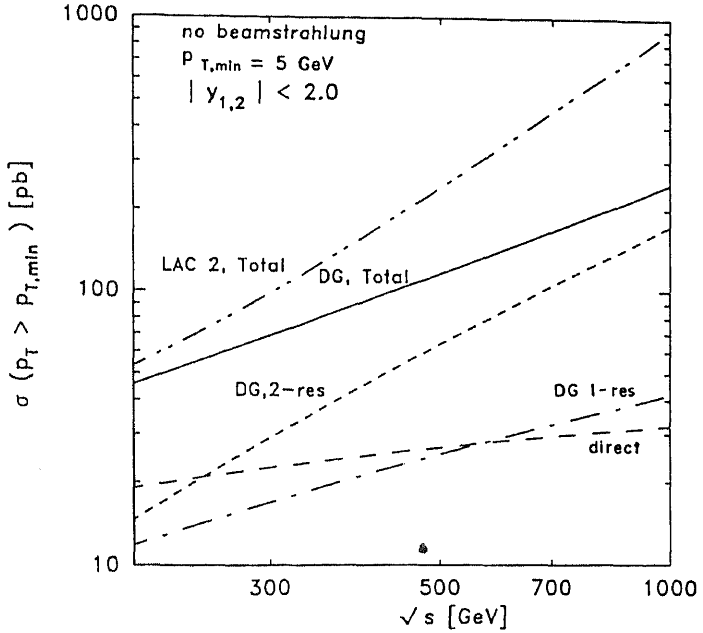

Figure 9. Cross-section for $\gamma\gamma \rightarrow$jets as a function of $\sqrt{s}$ for $p_{T,\min} = 5\,\mathrm{GeV}$.

This is demonstrated in figure 9, where we show the energy dependence of the total cross-section for the production of a pair of central jets (with rapidity $|y_{1,2}| \leqslant 2$) with $p_T \geqslant 5\,\mathrm{GeV}$ in $\gamma\gamma$ collisions at high energy e^+e^- colliders. Here we have conservatively ignored all effects of beamstrahlung (see below), and have used (3.3) for the flux of resolved photons. Nevertheless, even the DG parametrization predicts resolved photon contributions to be dominant already at $\sqrt{s} = 200\,\mathrm{GeV}$; at $\sqrt{s} = 500\,\mathrm{GeV}$, which is now foreseen as the likely operating energy of the next (linear) e^+e^- collider, resolved photon processes are predicted to dominate the direct one by a ratio of 6:1. Once again the LAC2 parametrization predicts both a more rapid increase with energy, and a considerably larger absolute value, of the $\gamma\gamma \rightarrow$jets cross-section. Notice finally that the annihilation cross-section at $\sqrt{s} = 500\,\mathrm{GeV}$ only amounts to 0·4 pb for $\mu^+\mu^-$ pairs, and 8 pb for W^+W^- pairs; this is to be compared to a $\gamma\gamma$ cross-section of at least 150 pb at the same energy, even using the relatively strong cuts of figure 9; this cross-section is as large as 500 pb if the photon structure is better described by the LAC1 parametrization.

In figure 9 we have only included the bremsstrahlung contribution to the photon spectrum. However, it is well known that synchrotron radiation makes the construction of e^+e^- storage rings with $\sqrt{s}$ significantly beyond the reach of LEP2 prohibitively expensive; one will therefore have to use linear colliders (linacs) if higher energies are to be reached in e^+e^- collisions. In such linacs, each electron or positron bunch has only a single chance to produce a reaction; at the same time, the total luminosity of the machine has to grow $\propto s$ if a useful rate of annihilation events is to be maintained. These two constraints imply that the luminosity per bunch crossing has to be much larger than at present storage rings; this in turn necessitates the use of very dense bunches, with transverse dimensions of the order of a few dozen nm. This leads to a large charge density, which produces very strong electromagnetic fields. Immediately before and during bunch collisions the particles in one bunch feel the field produced by the other bunch, and are accelerated. The radiation produced by this acceleration is known as beamstrahlung [49].

This qualitative discussion shows that machines with large luminosity per bunch crossing generally produce more beamstrahlung [50]. The necessary luminosity per bunch crossing is obviously inversely proportional to the number of bunch collisions per second; this number in turn depends on the design of the accelerating structures.

Some typical examples of beamstrahlung spectra for e^+e^- colliders operating at $\sqrt{s} = 500\,\mathrm{GeV}$ are shown in figure 10 [52]; these curves have been computed using approximate analytical expressions given in ref [53]. The acronyms P-G, P-F, D-D and T stand for the Palmer-G, Palmer-F, DESY-Darmstadt and TESLA designs, respectively, while wbb (nbb) denotes the wide (narrow) band beam option of the D-D design. We see that machines that utilize accelerating RF fields with wavelength in the "X band" region (P-G, P-F as well as the Japanese Linear Collider JLC, whose first stage is somewhat similar to the Palmer-F design) have harder beamstrahlung spectra than designs using the longer wavelengths of the "S band" (D-D), or the TESLA design, which is based on superconducting cavities. For comparison we also show the Weizsacker–Williams (WW) bremsstrahlung spectrum (dotted curve). For large fractional photon momentum x, the beamstrahlung contribution is exponentially suppressed; this end of the spectrum is therefore still dominated by the bremsstrahlung contribution. However, at smaller values of x beamstrahlung photons are more abundant; the cross-over point between the regions dominated by beam- and bremsstrahlung depends sensitively on the machine parameters.

Finally, it has been pointed out [54] that an e^+e^- collider can be converted into a $\gamma\gamma$ collider by shining very intense laser light on the particle beams; some laser photons then undergo Compton backscattering. The dash-dotted curve in figure 10 shows the spectrum that results if the laser energy is chosen such that the invariant mass of a laser and a backscattered photon is just below $2\,m_e$, and both laser and electron beam are unpolarized. Notice that these backscattered photons, as well as beamstrahlung photons, are truly on-shell, unlike bremsstrahlung photons.

Obviously beamstrahlung can greatly enhance rates of two-photon events. For

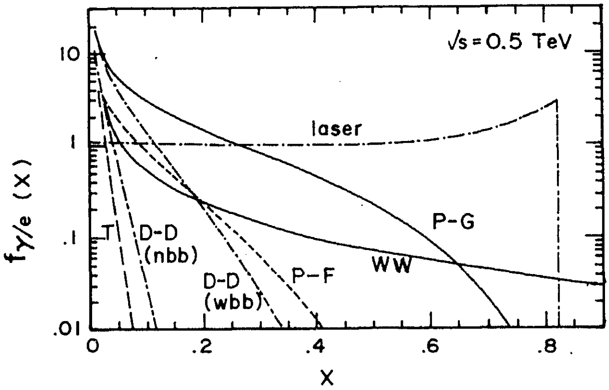

Figure 10. The beamstrahlung photon spectrum of 4 typical designs of 500 GeV e^+e^- linacs, as well as of bremsstrahlung photons (dotted) and of backscattered laser photons (dot-dashed). From [52].

example, had we included the beamstrahlung contribution to $f_{\gamma/e}$ in figure 9, the cross-section would have grown [52] to between 180 pb (for TESLA) and 4·5 nb (for Palmer-G). Since the luminosity of those designs is 2 (6)$\cdot 10^{33}\,\mathrm{cm}^{-2}\,\mathrm{s}^{-1}$, this corresponds to approximately 4 (250) *million* events with total hard $E_T > 10$ GeV per year for the TESLA (Palmer-G) collider! Of course, in principle one can get rid of most of these events by setting a rather high trigger threshold on the transverse momentum of the jets, or the total E_T in the event [55]. However, then one risks to lose interesting annihilation events containing massive stable neutral particles, as predicted e.g. by supersymmetric theories. Moreover, the $\gamma\gamma$ events are interesting in their own right. In our view it is therefore preferable to use a low trigger threshold, even if this means that the amount of data to be handled is rather large for e^+e^- colliders; it is still small compared to the amount of information that has to be manipulated at typical LHC or SSC detectors.

Beamstrahlung also changes the electron spectrum [53]; obviously an electron will lose some of its energy when emitting a hard photon. This effect has to be added to the smearing of the beam energy due to the machine parameter independent initial state radiation. For designs with hard beamstrahlung spectrum (e.g., Palmer-G), the e^+e^- luminosity spectrum is distorted by beamstrahlung even for energies far below the nominal $\sqrt{s}$ of the collider. At small invariant masses one thus generally has a competition between $\gamma\gamma$ and e^+e^- events. This is demonstrated in figure 11, where we show the invariant mass spectrum of events with two central jets with $p_T \geqslant 20$ GeV [52]. The annihilation contribution exhibits a prominent peak at $\sqrt{s} = M_Z$; by comparing events in that peak with events with $M_{jj} \simeq \sqrt{s}$, one can hope to study the QCD evolution of the hadronic system with increasing invariant mass in a single detector, thereby reducing experimental (systematic) errors. However, this figure shows that at this collider it would be very difficult to extract a clean sample of annihilation events with $M_{jj} \simeq M_Z$; in spite of the rather severe cut on p_T which reduces the $\gamma\gamma$ contribution considerably, the Z peak will hardly stand out in the total sample of di-jet events once detector resolution effects are included. In colliders with soft

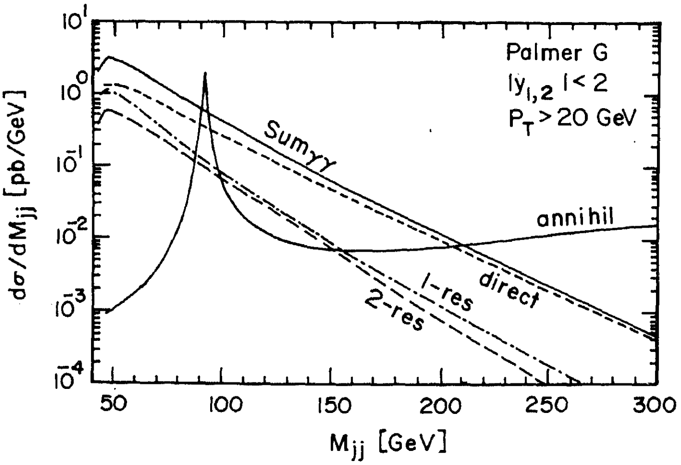

Figure 11. The invariant mass distribution of events with two central jets with $p_T \geqslant 20$ GeV. The resolved $\gamma\gamma$ contributions have been estimated [52] using the DG parametrization.

Table 1. Total $c\bar{c}$ cross-sections from two-photon processes at the 4 e^+e^- colliders of figure 10, as well as for a $\gamma\gamma$ collider made from an e^+e^- collider with $\sqrt{s} = 500$ GeV. We have used the DG parametrization to estimate the resolved photon contributions. $\sigma(q\bar{q})$ and $\sigma(gg)$ stand for the 2-res $q\bar{q}$ annihilation and gluon fusion cross-sections, $\sigma(\gamma g)$ for the 1-res photon gluon fusion contribution, and $\sigma(\gamma\gamma)$ for the direct contribution; $\sigma(J/\psi)$ is the 1-res $\gamma + g \rightarrow J/\psi + g$ cross-section in the color singlet model. All cross-sections are in nb.

Collider	$\sigma(q\bar{q})$	$\sigma(gg)$	$\sigma(\gamma g)$	$\sigma(\gamma\gamma)$	$\sigma(\text{tot})$	$\sigma(J/\psi)$
T	0·010	0·038	1·8	2·2	4·0	0·014
D-D (wbb)	0·041	0·11	7·0	6·4	13·5	0·053
P-F	0·017	0·08	4·0	2·4	6·4	0·030
P-G	0·14	1·1	38	9·9	49	0·28
$\gamma\gamma(500)$	0·13	7·6	130	0·14	140	0·89

beamstrahlung spectrum (TESLA or the nbb option D-D) the annihilation cross-section at $M_{jj} = M_Z$ is reduced by a factor of 3, but the $\gamma\gamma$ contribution is almost 30 times smaller than at Palmer-G, enabling one to isolate a rather clean sample of annihilation events from the Z peak.

As a final example of the importance of beamstrahlung we list in table 1 estimates of total $c\bar{c}$ and J/ψ production cross-sections, using the DG parametrization. Since these processes are sensitive to the region of small x, even the soft beamstrahlung spectrum of the TESLA collider leads to a sizable enhancement of the rate. This is especially true for the direct contribution, whose cross-section decreases with increasing $W_{\gamma\gamma}$, unlike those for the resolved photon contributions; without beamstrahlung the direct and 1-res total $c\bar{c}$ cross-sections would only amount to 0·6 and 0·85 nb, respectively. Due to the different dependence on $W_{\gamma\gamma}$, resolved photon events are more important at colliders with harder beamstrahlung spectrum. However, even for the Palmer-G design we find [52] that the cross-section for the production of central $c\bar{c}$ pairs with $p_T > 5$ GeV is dominated by the direct contribution. This is because the 1-res contribution has a softer p_T spectrum and, due to the asymmetric initial state, is peaked at small angles. If, on the other hand, the e^+e^- collider is converted into a $\gamma\gamma$ collider, even the 2-res contribution will be larger than the direct one; notice that in this case the 2-photon luminosity actually falls at small $W_{\gamma\gamma}$.

Qualitatively similar results hold for total $b\bar{b}$ production, except that the cross-sections are smaller by a factor between 100 and 200. It has been claimed [56] that at future linacs total $t\bar{t}$ production might also be dominated by the $\gamma\gamma$ contribution. We find [52], however, that even at the Palmer-G collider the $\gamma\gamma$ contribution amounts to at most 5% of the total; for the other designs of 500 GeV linacs this number is closer to 1%. Even for the third stage of the JLC, which operates at $\sqrt{s} = 1{\cdot}5$ TeV and also has a rather hard beamstrahlung spectrum, the annihilation contribution is still dominant if $m_t > 130$ GeV. At such very high energy colliders, beamstrahlung and initial state radiation also increase the annihilation contribution by as much as 60%, due to the reduction of the average centre-of-mass energy of e^+e^- pairs. In principle one could increase beamstrahlung even further, e.g. by using round beams. However, we will argue in § 5 that in this case one will have to deal with qualitatively new beamstrahlung induced backgrounds, including the existence of an "underlying event" which will make experiments at such e^+e^- linacs similar to those at hadron colliders, so that the detailed study of $t\bar{t}$ events will become very difficult. In contrast, most of the e^+e^- colliders discussed here could quite easily accumulate a clean sample of $t\bar{t}$ events from e^+e^- annihilation. We therefore see no advantage of operating future linacs in the domain of high beamstrahlung.

Of course, at present predictions for total $c\bar{c}$ and $b\bar{b}$ production cross-sections at high energy linacs suffer from large uncertainties, since, one is probing the parton content of the photon at values of x as small as 10^{-3}, where no experimental information exists so far. With the advent of the ep collider HERA this is expected to change soon, however, as we discuss in the next section.

4. Resolved photon reactions in γp scattering

The discussion in earlier sections indicates that we need to probe the parton content of the photon, especially the gluon content, at small values of x and large Q^2. For reasons discussed earlier, DIS experiments are limited by statistics in the region of large Q^2 and probe G^γ only indirectly. Jet production in $\gamma\gamma$ collisions at TRISTAN and LEP will certainly provide useful information. But the only other possibility to go to higher values of $\sqrt{s}$ for photon interactions and hence increase the range of x and Q^2 values at which the photon can be probed, is at present the high energy ep collider HERA.

The suggestion to use γp collisions to study $\mathbf{q}^\gamma$ is not new [57]. Theoretically the situation is actually somewhat simpler than for real $\gamma\gamma$ scattering, since we only have to deal with two classes of contributions: Direct ones, where the photon directly interacts with the partons in the photon; and resolved photon reactions, where the partons in the photon scatter off partons in the proton. The low energy of photon beams available at fixed target experiments reduces the contribution of 'res' processes in current experiments but it still plays an important role [57, 15, 58]. At the high energy HERA collider with an ep centre-of-mass energy ~ 300 GeV, the situation is quite different. In a large number of QCD processes such as high p_T jet production [59, 60, 61], heavy flavour production [59, 62], direct photon production [63] and Drell Yan lepton pair production [64] the hadronic structure of the photon not only plays an extremely important role but even dominates in some cases. The cross-section for the various QCD processes is given by expressions very similar to (3.1), where one replaces one photon by the proton and includes the partonic subprocesses corresponding to the QCD process under consideration. We now describe some reactions in more detail.

4.1 $ep \to jets + X$

We start with a discussion of inclusive jet pair production, which offers the highest cross-section of all hard scattering processes at HERA. Here the direct processes are the same as the 1-res processes of $\gamma\gamma$ scattering, and the resolved photon reactions correspond to the 2-res contributions to $\gamma\gamma$ collisions.

In figure 12 we show the ratio R_σ of the cross-sections of the resolved and direct processes as a function of the transverse momentum p_T of the jets [59]. We see that even the DG parametrization predicts the resolved photon contribution to be larger than the direct one out to $p_T \simeq 35$ GeV. In γp collisions we have to pay the price (in terms of reduced phase space) of producing an additional spectator jet only once

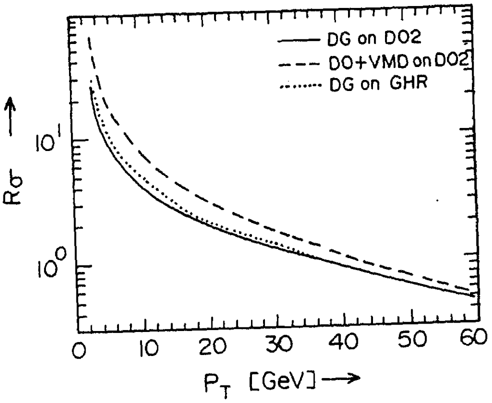

Figure 12. Ratio of resolved and direct contributions for $d\sigma(ep \to \text{jets})/dp_T$ as a function of p_T [59].

when we want to gain access to the QCD $2 \to 2$ scattering processes, whose matrix elements are enhanced by gluon exchange in the t- or u-channel, as discussed earlier; in $\gamma\gamma$ collisions this price has to be paid twice, since both photons have to be resolved. Moreover, the proton has a relatively larger gluonic component than the photon, at least if the DG parametrization is close to the truth. This further favours resolved photon processes over direct ones, since the QCD $2 \to 2$ matrix elements containing gluons in the initial and final state are enhanced by colour factors, while the direct γg fusion process is actually colour-suppressed (by a factor of 3/8) compared to γq scattering. These two observations explain why at HERA resolved photon processes dominate jet production out to larger values of $x_T \equiv 2p_T/\sqrt{s}$ than at e^+e^- colliders: see figure 6. Figure 12 also illustrates that existing parametrizations of proton structure functions (DO2 [65] vs. GHR [66]) differ much less than those for the photon, at least in the region $x \geqslant 0{\cdot}01$ relevant for the production of high-p_T jets.

In figure 13a, b we show the p_T spectrum in absolute units. In these figures, we also show the contributions from different final states separately; for most events the parton composition of the initial and final states are identical. We see that, unlike at hadron colliders, the gg final state dominates only at very low values of p_T, below 3 GeV for the DG parametrization. This is because the difference in shape between quark and gluon distribution functions is larger for photons than for nucleons. In the latter case all parton densities fall with increasing x, while $x \cdot q^\gamma$ has a maximum at $x \simeq 0{\cdot}9$, as shown in figure 3.

For most of the p_T range where resolved photon contributions dominate, the largest contribution comes from the mixed qg final state. The DG parametrization predicts that in most cases the quark comes from the photon and the gluon from the proton; this is again a result of the relative softness of G^γ and the large gluon content of nucleons. Finally, figure 13b shows that the direct contribution is only dominated by photon-gluon fusion for values of p_T where the total di-jet cross-section is dominated by res contributions; this might make it difficult to extract the gluon density of the nucleon from measurements of jet production at HERA.

Of course, in principle direct and res events can be distinguished by the presence of the spectator jet from the photon going in the electron beam direction, which is the hallmark signature of resolved photons. However, while there are arguments suggesting [59] that this jet should be rather broad and hence easily detectable in

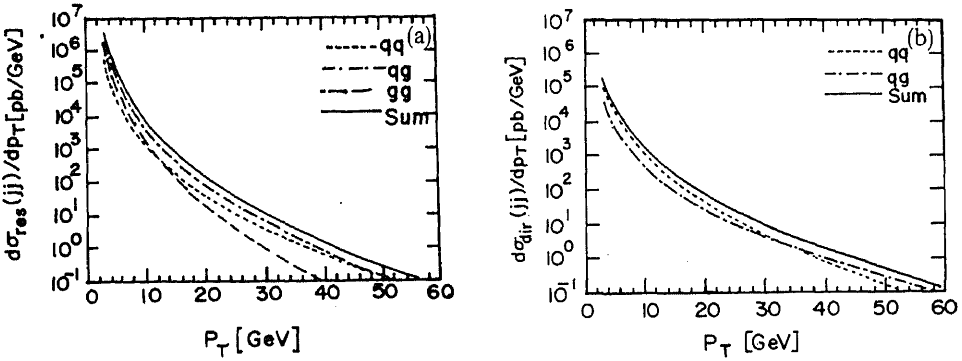

Figure 13. Resolved (a) and direct (b) contribution to two-jet production at HERA, where the different final states are shown separately; q denotes a quark or anti-quark of any flavour. We have used the DO2 and DG parametrizations for the proton and the photon, respectively. From ref. [59].

most cases, the exact value of the efficiency for tagging on this jet clearly depends on the details of the jet formation model (i.e., it is not an "infrared safe quantity"), as well as on the detector acceptances. It is therefore tempting to try and find differences between direct and res contributions in the distributions of the high-p_T jets themselves, which can be predicted directly from perturbative QCD.

One possibility [61] is to look at the cross-section as a function of the centre-of-mass scattering angle. Due to the presence of diagrams with gluon exchange in the t- or u-channel the resolved photon contribution will be more strongly peaked at small angles than the direct contribution.

Another possibility [59] is to study the triple-differential cross-section $d\sigma/dp_T dy_1 dy_2$, where the y_i are the rapidities of the two high-p_T jets. The results of figure 13 show that the cross-section should be large enough to allow such detailed studies even with less than the full HERA design luminosity of about $100\,\mathrm{pb}^{-1}$/yr. In this case we can make use of purely kinematical considerations to separate the two classes of contributions. Obviously a parton "in" a photon will have less energy than the photon itself. For a given invariant mass of the produced partonic system, the parton from the proton will therefore have to supply more energy in resolved photon events than in direct ones; this results in a boost of the partonic system in the direction of the proton beam. Since, as we have emphasized repeatedly, G^γ is expected to be much softer than the q_i^γ [67], this boost will be stronger if the parton that is "pulled out" of the photon is a gluon. Parametrizations with larger G^γ will thus tend to predict a rapidity distribution that is more strongly peaked at larger rapidities.

This is demonstrated in figure 14, which shows the shape of the rapidity distributions (for $y_1 = y_2 \equiv y$) at $p_T = 10\,\mathrm{GeV}$. In order to avoid "k-factor" uncertainties, all curves have been normalized to give the same single-differential cross-section $d\sigma/dp_T = 8{\cdot}8\,\mathrm{nb/GeV}$ at $p_T = 10\,\mathrm{GeV}$. The DO + VMD distribution with its rather large gluon content leads to a much more pronounced peak at $y \simeq 2{\cdot}2$ than the DG parametrization does, although the position of the peak is not shifted very much; note that $y \to y_{\max}$ corresponds to $x_p \to 1$, where $\mathbf{q}^p$ vanishes. On the other hand, a toy model with zero gluon content predicts the peak in the rapidity distribution to be shifted towards smaller y by about 1·5 units. We have already seen that AMY data require [3] a

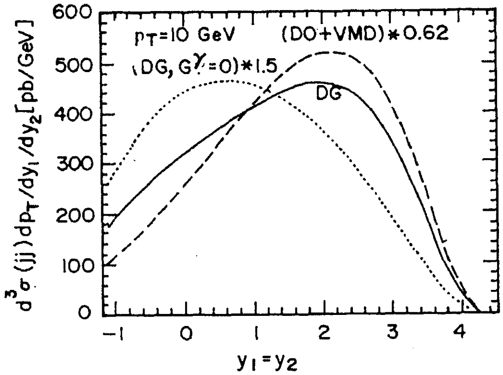

Figure 14. Comparison [59] of the shape of the rapidity distribution of jets produced at HERA. Note that the dotted and dashed curves have been normalized, as described in the text.

nonzero G^γ, but they cannot distinguish between the DG and DO + VMD parametrizations; from figure 14 we can conclude that jet studies at HERA should allow much more detailed analyses, due to the large event rates even at rather large values of p_T, where the choice of $p_{T,\min}$ becomes irrelevant and the analysis is less sensitive to the details of the jet fragmentation scheme. Finally, it should be mentioned that the direct contribution actually peaks at the smallest possible value of y. Here x_p approaches its kinematical minimum ($= x_T^2$), while nearly the whole electron energy has to be transmitted to the photon; this is quite unlikely, but the rapid increase of $\mathbf{q}^p$ at small x_p over-compensates this suppression factor.

We thus see that the presence of resolved photon contributions leads to 3 qualitative predictions [59] that ought to be testable quite easily: Large jet production cross sections; spectator jets from the photon; and a rapidity distribution that is peaked at positive y (corresponding to the proton beam direction). Even though HERA experiments so far have only taken a few nb^{-1} of data, they are already starting to confirm these predictions.

In figure 15 we show the transverse energy spectrum of the photoproduction events identified by the ZEUS collaboration [5] in the first (pilot) run of HERA. For $E_T > 10\,\mathrm{GeV}$ the soft (VMD) contribution is found to be negligible; the events in this region therefore have to be explained by hard scattering processes. The dashed curve shows the prediction of the HERWIG generator [68] using the DG parametrization with $p_{T,\min} = 1{\cdot}5\,\mathrm{GeV}$; we see that it describes the data quite well. Recall that almost the same value of $p_{T,\min}$ has been found to describe the TRISTAN data. From their data sample ZEUS extracts a total cross-section for the production of events with $E_T > 10\,\mathrm{GeV}$ of $2{\cdot}4 \pm 0{\cdot}1 \pm 0{\cdot}7\,\mu\mathrm{b}$. A glance at figure 13 shows immediately that a cross-section of this size cannot be explained from direct processes alone; indeed, the detailed MC study of the ZEUS group shows that without the resolved photon contributions theory falls short of the data by at least one order of magnitude. Similar results have been reported by the H1 collaboration [6].

Both groups also find evidence for the spectator jet from the photon in their data. As an example we show in figure 16 the energy flow measured [6] in the H1 calorimeter as a function of the angle ($\theta = 0$ is the direction of the proton beam); only events where both high-p_T jets emerge at $\theta \leqslant 100°$ have been included. At small angles a

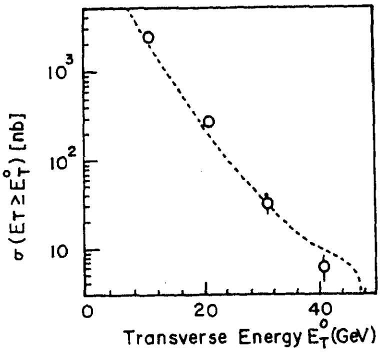

Figure 15. The total *ep* cross-section measured [5] for transverse energies larger than E_T^0. The curve is the HERWIG prediction, using the DG parametrization with $p_{T,\min} = 1{\cdot}5\,\mathrm{GeV}$.

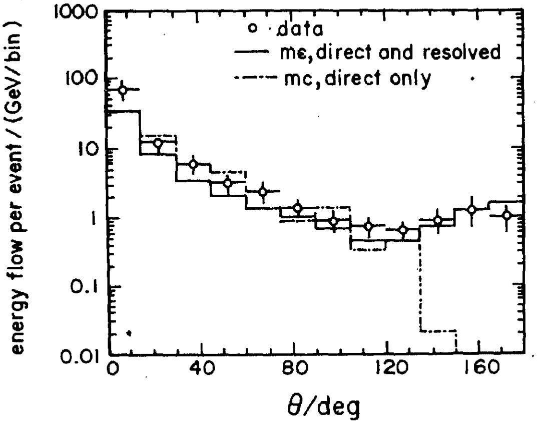

Figure 16. Histogram of energy flow per event versus polar angle. The open points represent the data, while the full and dotted lines give the MC prediction with and without resolved photon contributions. From ref. [6].

large amount of energy is deposited by the proton remnants. At intermediate angles both soft and hard processes contribute. However, direct events are unable to populate the region around the electron beam direction, in conflict with the data, which show a constant or even slowly rising energy deposition at $\theta \simeq 180°$. This is well described by the MC generator once resolved photon contributions are included. ZEUS also finds [5] evidence for the spectator jet in their sample of reconstructed jet events: Some events have sizable energy deposit around the electron beam direction even though all high-p_T jets are 2 or more units of rapidity away. Their data indicate that the efficiency for tagging on this spectator jet should be around 40%, in qualitative agreement with earlier MC studies [69].

Finally, H1 also finds [6] that their jets populate a quite different angular (or rapidity) region than what one would expect from direct events. In particular, they find that a large fraction of their events have one or both jets relatively close to the proton beam direction; we have seen in figure 14 that direct γp scattering produces jets preferably at large angles. Our three main predictions are therefore all borne out at least qualitatively by the data; we are looking forward to more detailed analyses of higher statistics data samples.

Before closing this subsection we should point out that recently first results of next-to-leading order calculations of the photoproduction of jets at HERA energies have become available. NLO corrections to the direct processes have been computed already some time ago by Aurenche *et al* and independently by Baer *et al* [58]; they have recently been re-done and applied to HERA in ref. [70]. The production of three jets in direct and resolved photon interactions has been studied in ref. [61]. Full NLO corrections to the resolved photon contribution have been computed in ref. [71]. Finally, so far the only paper that includes a full next-to-leading order calculation of all contributions to jet production is ref. [72]. Such a comprehensive analysis is necessary since some divergent corrections to the direct process have to be absorbed in the parton distribution functions of the photon, thereby blurring the distinction between direct and resolved photon contributions. These studies indicate that inclusion of NLO corrections reduces the artificial dependence of the cross-section on factorization and renormalization scales. However, if these scales are chosen to be equal to the transverse momentum of the jets and a cone size $\Delta R = 0{\cdot}7$ is chosen in the jet definitions, NLO corrections appear to be quite modest. The results of this subsection, which have been obtained from leading order calculations, should therefore retain their validity also in NLO.

4.2 *Heavy quark production*

We have seen in the last subsection that inclusive jet production at HERA will probably only allow a rather indirect determination of G^γ due to the large background from quark-initiated resolved photon events. Just as in case of $\gamma\gamma$ scattering, one can enhance the importance of gluon-initiated processes by studying specific final states. Among those, the production of a pair of heavy quarks offers the largest cross-section. We focus here on b-quarks, which should be easier to identify than c quarks, and where fragmentation effects should be smaller.

The total $b\bar{b}$ cross-section at HERA as predicted from the DG parametrization is [59, 62] about 1 nb, which corresponds to 100,000 $b\bar{b}$ pairs per year. Unfortunately the resolved photon contribution only amounts to about 20% of the total; a separation of the two classes of contributions thus becomes mandatory if bb production is to be used to determine G^γ. Fortunately we have seen at the end of the previous subsection that it seems to be possible to tag spectator jets from the photon with reasonable effciency; this should allow to accumulate a rather clean sample of resolved $b\bar{b}$ events.

In figure 17 we show the p_T spectrum of the b (or $\bar{b}$) quark for the symmetric configuration $y_1 = y_2 \equiv y$; the res contribution has again been estimated from the DG parametrization. We see that the slope of the spectrum at high p_T depends quite sensitively on y; recall that large y correspond to large x_p, where the parton densities in the nucleon decrease rapidly. One can also conclude that a detailed study of the resolved photon contribution will only be possible if b quarks with p_T below 10 GeV can be identified efficiently and reliably; otherwise the rate will be too small.

Figure 17 also shows that resolved photon contributions are much more important at large y. After the discussion of the rapidity distribution of jets in the previous subsection this should not be surprising; since the res contribution to $b\bar{b}$ pair production is dominated by gg fusion, res $b\bar{b}$ events will usually undergo a strong

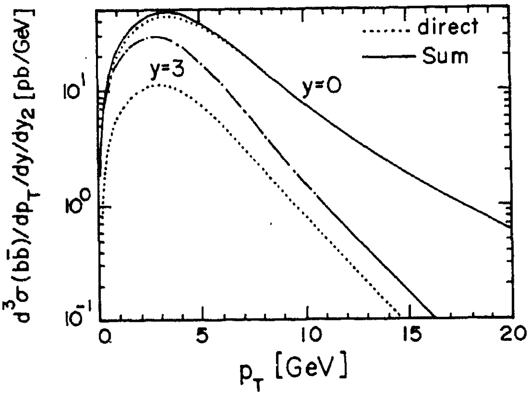

Figure 17. p_T distribution of the b (or $\bar{b}$) quark produced in photoproduction events at HERA as predicted [59] from the DG parametrization, for $y_1 = y_2 \equiv y$.

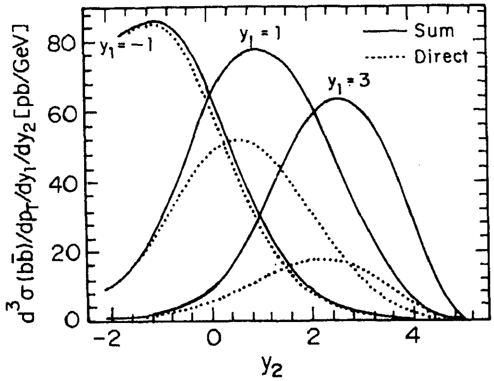

Figure 18. Rapidity distribution of the b(or $\bar{b}$) quark produced in photoproduction events at HERA as predicted [59] from the DO + VMD parametrization, for fixed value of the other rapidity and $p_T = 5$ GeV.

boost in the proton beam direction. This is further illustrated in figure 18, where we show the $b\bar{b}$ cross-section as a function of y_2 for fixed y_1, at $p_T = 5$ GeV. Notice that in this figure the res contribution has been computed from the DO + VMD parametrization, which predicts a ratio of direct to resolved contributions of about 2:1, as opposed to 4:1 for the DG parametrization. We have seen above that the efficiency for tagging the photonic spectator jet might be around 40 to 50% for generic high-p_T jet events; it might be somewhat smaller for the more spherical $b\bar{b}$ events. Simply requiring the absence of such a tag would thus leave a $b\bar{b}$ sample that still contains 20 to 30% resolved photon events, if G^γ is similar to the DO + VMD parametrization; this could complicate the extraction of the gluon content of the nucleon from studies of $b\bar{b}$ pair production at HERA. Fortunately figure 18 shows that even the large res contribution predicted by the DO + VMD parametrization can be suppressed to an insignificant level by requiring either the b or the $\bar{b}$ to emerge at small (negative) rapidity; this restriction still allows to probe $G^p(x_p)$ for x_p between $2\cdot 10^{-3}$ and 1 by varying y_2 within its kinematically allowed limits. The same conclusion holds for all parametrizations of $q^\gamma(x, Q^2)$ that predict $G^\gamma(x)$ to be soft, as seems to be required by TRISTAN data. By separating the total $b\bar{b}$ sample into events with and without a photonic spectator jet, and studying the rapidity distribution in each sample, it should therefore be possible to extract important information about both G^p and G^γ from $b\bar{b}$ pair production at HERA.

Finally, we remark that so far only partial NLO calculations for the photoproduction of heavy quark pairs exist [62, 73, 74]. In these papers the corrections to the direct process are included, but the resolved photon contribution, which occurs at the same order in α_s, has only been included at tree level.

4.3 *Direct photon production*

Another process that can be studied at HERA is the production of hard direct photons in $ep \to e\gamma X$ [75]. Of course, the cross-section is now $\mathcal{O}(\alpha^3)$ and thus approximately two orders of magnitude smaller than the jet cross-section. On the other hand, the direction and energy of a hard photon can be determined much more precisely than those of a jet; this should help in the reconstruction of the Bjorken-x variables of the partons participating in the hard scattering.

In [63] a fairly comprehensive study of this reaction has been presented for HERA energies. NLO corrections to the direct process $\gamma q \to \gamma q$ [76] are included, but the resolved photon contributions ($gq \to \gamma q$ and $q\bar{q} \to \gamma g$) are treated at the Born level. If a hard photon within a jet can be detected, one can also study the fragmentation of a parton into a photon, which is the inverse of $\gamma \to$ parton splitting described by the parton densities in the photon. Even if these contributions are included, resolved photon processes dominate the total cross-section only for $p_T^\gamma \leqslant 15\,\text{GeV}$, according to the DG parametrization. The reason is that again one has to produce two additional jets (the spectator jet from the photon, and the remnants of parton → photon fragmentation) before the QCD $2 \to 2$ processes become accessible.

Nevertheless the study of photons with $p_T \simeq 5\,\text{GeV}$ or so should yield information about $\mathbf{q}^\gamma$, especially G^γ. Kinematics again implies that events of the type $q^p g^\gamma \to q\gamma$ should be strongly boosted in the proton direction; in addition, the hard matrix

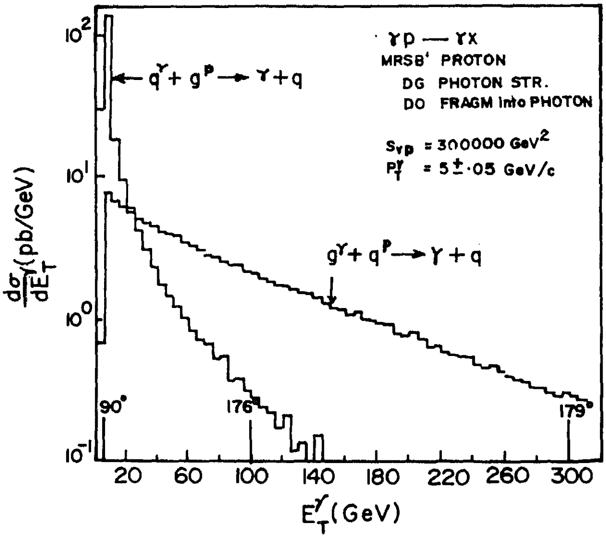

Figure 19. Energy spectrum of photons produced in γp scattering at $s = 30{,}000\,\text{GeV}^2$, as predicted [77] from the DG parametrization.

element favours the photon to emerge close to the direction of the incident quark. The combination of these two effects implies [77] that res contributions dominate at small angles relative to the proton beam direction, as shown in figure 19. Here a fixed energy of the incoming photon has been assumed, $E_\gamma = 9\,\mathrm{GeV}$; experimentally this means that the ongoing electron has to be tagged in a forward spectrometer, which is also used for luminosity measurements. Since the transverse momentum of the outgoing photon has been fixed to 5 GeV, there is a one-to-one relation between the energy and the angle of the photon, with small angles corresponding to large energies. The coverage of the electromagnetic calorimeter of HERA experiments starts approximately 4 degrees from the proton beam pipe [77]; this means that photons with energy as large as 110 GeV should be detected with sizable rates. Notice also that at this angle even the DG parametrization predicts the resolved photon contribution to be a full order of magnitude above the direct one. Even if the outgoing electron is not tagged, i.e. after integration over the Weizsäcker–Williams spectrum, at this angle res contributions are at least two times bigger than direct ones.

The proximity of the spectator jet from the proton should not compromise the observability of this signal, since this jet is not expected to contain photons of this very high energy. Finally, due to the softness of G^γ, almost the whole energy of the incoming photon will go into the spectator jet. If the energy of the photon is known (by measuring the energy of the outgoing electron), this information can be used to study a sample of photonic spectator jets with known energy, which might provide valuable information for the study of other resolved photon processes.

4.4 J/ψ Production

Just like the production of heavy quark pairs, the process $ep \to eJ/\psi X$ has originally been proposed [78] as a way to determine the gluon density of the proton; results from such analyses have been reported from fixed-target photoproduction experiments [46]. It was realized later [64], however, that at the much higher energies which can be achieved at HERA this final state also receives sizable contributions from resolved photon processes. J/ψ mesons can be produced from $\gamma g \to J/\psi g$ (direct process) as well as $gg \to J/\psi g$ (res process); in addition, they can be produced in the decay of χ mesons or b quarks. Indeed, this latter process dominates [79] for $p_T > 5\,\mathrm{GeV}$; moreover, the cross-section becomes quite small in this region. Most studies of J/ψ production at HERA therefore focus on the region $1\,\mathrm{GeV} \leqslant p_T \leqslant 5\,\mathrm{GeV}$.

Although the total resolved photon contribution estimated from the DG parametrization amounts to about 0·5 nb, extraction of the signal may not be trivial. First of all, only the leptonic decays will be detectable at HERA, which reduces the signal by a factor of 7. Since most J/ψ's produced via res processes emerge at large rapidity, i.e. small angle to the proton beam, requiring both leptons to be detected further degrades the signal; in this case there is no rapidity region left where the res contribution clearly dominates [80]. Of course, requiring the spectator jet from the photon to be detected will suppress the direct contribution, while J/ψ's produced with negative rapidity will overwhelmingly come from direct processes, as in case of open heavy flavour production.

Another possibility is to tag the outgoing electron [81]. This selects events with incident photon energy $E_\gamma > 7\,\mathrm{GeV}$, since otherwise the outgoing electron is too energetic to be bent out of the beam, which is necessary for its detection in the forward spectrometer. As shown in figure 20, this is sufficient to suppress the direct contribution

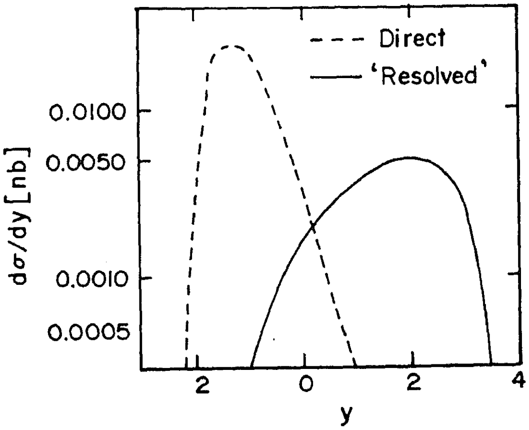

Figure 20. Rapidity distribution [81] of J/ψ mesons produced at HERA in events where the outgoing electron is tagged, as estimated using the DO2 and DG parametrizations for the proton and photon, respectively.

at positive rapidities to an insignificant level. The price is the reduction of the overall signal by a factor of 10 or so; on the other hand, the analysis is no longer sensitive to the details of the spectator jet formation.

Finally, it has been pointed out in ref. [80] that there is no direct contribution if the J/ψ is produced in association with a hard photon; this process has subsequently been studied in ref. [82]. The main problem is again the small event rate; after mild acceptance cuts, the DG parametrization predicts an observable cross-section of only 0·08 pb. However, as already mentioned in connection with J/ψ production at e^+e^- colliders, the "colour singlet" model [45], which has been used in all cross-section calculations, might underestimate the rate by as much as a factor of 5 [46]. While this would make the detection of the signal easier, the presence of a k-factor of this magnitude casts doubt on the leading order analyses presented here. Nevertheless, J/ψ production at HERA has the potential to probe gluon densities down to very small values of x, of order 10^{-3} or less.

4.5 *Other processes*

We close this section with a brief survey of other processes that receive contributions from resolved photon reactions, although limitations of space do not allow to discuss them in detail.

Of great theoretical interest is the production of W and Z bosons at HERA. In leading order only the resolved photon (Drell–Yan) process $q\bar{q}' \rightarrow W$ contributes [83]; note that the corresponding cross-section is $\mathcal{O}(\alpha^3/\alpha_s)$, since $\mathbf{q}^\gamma \propto 1/\alpha_s$. On the other hand, the direct process $\gamma q \rightarrow Wq'$, while formally of higher order in $\alpha_s(\sim \alpha^3)$, is sensitive to the γWW coupling [84]. In order to study this dependence the $p_T \rightarrow 0$ divergent pieces of the direct contribution, which are already included in the res part, have to be subtracted to avoid double-counting. Several subtraction procedures have been suggested recently [85]. The resulting cross-section in the standard model is about 0·5 pb for W bosons, but probably only the leptonic decay mode can be identified; the cross-section for Z bosons is even smaller.

In § 4.3 we have discussed the production of real (on-shell) photons at HERA. The same processes can also give rise to off-shell photons, and hence to lepton pairs; this has been studied in refs [64, 74]. As expected from our previous discussions, resolved photon contributions are quite important at small transverse momentum and/or small invariant mass of the dilepton system. However, compared to direct photon production the cross-section is down by another factor of α. This process can therefore only yield useful information about parton densities after a large amount of data has been accumulated.

It has also been suggested [86] to study the production of a photon whose transverse momentum is balanced by a charm quark as a means to constrain the heavy flavour content of the proton as well as the photon. The charm quark is detected via its decay into a muon. The total cross-section after acceptance cuts is expected to be a few pb; the exact number depends on the way mass effects are included in heavy flavour density distributions.

As a last process we mention the production of two hard photons at HERA [87]. The cross-section is rather small, being of order α^4, so that only a limited range of transverse momenta can be studied experimentally. On the other hand, this process receives important contributions from *gg* fusion, via a box diagram which (up to trivial coupling and colour factors) is equivalent to the famous light-by-light scattering diagram; although first studied more than 50 years ago [88], the effect of this diagram has still not been detected experimentally.

5. Minijets and total cross-sections

So far we have only discussed "hard" processes, where the applicability of perturbative QCD is not in doubt. However, we have already seen in § 3 that one has to introduce at least one parameter that cannot be predicted from perturbative QCD if one wants to describe existing $\gamma\gamma$ data in the intermediate region where both soft and hard processes contribute; this parameter is the cut-off $p_{T,\min}$, which parametrizes the applicability of perturbative QCD. TRISTAN data indicate that this parameter has to be chosen around 1·5 (2·0) GeV if data are to be described by the DG (LAC1) parametrization. However, with such values of $p_{T,\min}$, the total jet pair cross-section grows very rapidly with energy, and eventually even exceeds the value of the total cross-section measured at lower energies.

The rapid growth of the inclusive jet cross-section due to the copious production of "minijets" with $p_T \simeq p_{T,\min}$ via resolved photon processes has first been pointed out in ref. [89] for the case of γp scattering; an example is shown in figure 21, for $p_{T,\min} = 2\,\text{GeV}$ and various parametrizations of $\mathbf{q}^\gamma$. It was conjectured in that paper that this increase of the cross-section might help to explain the mysteriously large number of muons observed [90] in photon-induced cosmic air showers. Later detailed Monte Carlo calculations [91] showed that, while resolved photon processes might boost the muon yield by a factor of 2–3, they are not sufficient to explain the data by themselves.

Of course, the total cross-section cannot grow indefinitely at the rate shown in figure 21; some mechanism will have to unitarize it. This problem is well known for hadronic (*pp* or $p\bar{p}$) collisions; indeed, it was suggested almost 20 years ago [92] that minijet production might contribute to the growth of total hadronic cross-sections. In this case unitarization is usually achieved by eikonalization. The crucial observation here is that LO QCD predictions for cross-sections, like those shown in figure 21, refer to *inclusive* jet cross-sections; in other words, they differ from the jet production contribution to the total cross-section by a factor of the average jet pair multiplicity

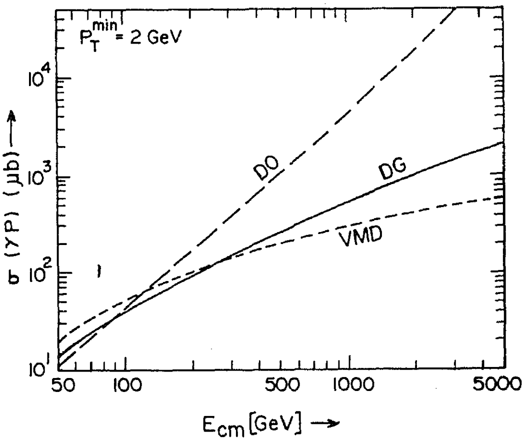

Figure 21. Predictions [89] of the increase of the inclusive (mini) jet cross-section in γp collisions with $\sqrt{s}$, for $p_{T,\rm min} = 2\,\rm GeV$ and various parametrizations for $\mathbf{q}^\gamma$.

$\langle n_{\rm jet}\rangle$. Formally one writes [93]

$$\sigma_{pp}^{\rm inel} = \int d^2b\{1 - \exp[-(\sigma_{pp}^{\rm hard}(s) + \chi_{pp}^{\rm soft})A(b)]\}, \tag{5.1}$$

Here $\mathbf{b}$ is the two-component impact parameter, $A(b)$ described the transverse distribution of partons in nuleons, $\sigma_{pp}^{\rm hard}$ is the perturbative QCD prediction for the minijet cross-section (obtained by integrating $d\sigma/dp_T$ in the region $p_T \geqslant p_{T,\rm min}$), and $\chi_{pp}^{\rm soft}$ is the non-perturbative (soft) contribution to the eikonal, which is fitted from low-energy data. In (5.1) it has been assumed that the transverse distribution is independent of x and Q^2, and that different partonic scatterings are uncorrelated, i.e. obey Poisson statistics. Eikonalized minijet models with $p_{T,\rm min}$ around 1·5 to 2 GeV and standard parametrizations for $\mathbf{q}^p$ not only reproduce the rise of the total and inelastic pp and $p\bar{p}$ cross-sections [93], but also correctly describe many details of "minimum-bias" events as well as events containing hard jets [94].

However, as pointed out by Collins and Ladinsky [95], (5.1) will have to be modified before it can be applied to photonic cross-sections. This can easily be seen [96] by expanding the exponential; one finds that the cross-section for the production of 2 jet pairs is proportional to the square of the hard QCD cross-section. In case of γp scattering this hard cross-section is of $\mathcal{O}(\alpha\alpha_s)$, so that (5.1) would predict σ(2 pairs) $\sim \mathcal{O}(\alpha^2\alpha_s^2)$. On the other hand, once the photon has undergone its transition into a (virtual) hadronic state, no additional factor of α is necessary to produce additional jet pairs; rather, one would expect σ(2 pairs) $\sim \mathcal{O}(\alpha\alpha_s^3)$. Similar arguments hold for even larger number of jet pairs. This can be achieved by introducing a parameter $P_{\rm had}$ describing the probability that the photon goes into a hadronic state; clearly $P_{\rm had} \sim \mathcal{O}(\alpha)$. Equation (5.1) then becomes [95]

$$\sigma_{\gamma p}^{\rm inel} = \int d^2b P_{\rm had}\{1 - \exp[-(\sigma_{\gamma p}^{\rm hard}(s) + \chi_{\gamma p}^{\rm soft})A(b)/P_{\rm had}]\}, \tag{5.2}$$

A similar expression can be derived for $\gamma\gamma$ collisions, but here $P_{\rm had}$ has to be replaced by $P_{\rm had}^2$ [97].

Unfortunately there are many unknown quantities in (5.2). First of all, we cannot predict the hard scattering cross-section, since we do not (yet) know the parton densities in the photon at sufficiently small values of x. TRISTAN data give some indication what $p_{T,\min}$ should be, but it is not clear that the same value should be used in γp scattering, or that it should be independent of energy (although first HERA data do seem to point in that direction). Finally, it is not clear how $P_{\rm had}$ and $A(b)$ are to be determined. In most papers [95, 97, 98] VMD ideas are used to estimate these quantities. In particular, $P_{\rm had}$ is taken to be the $\gamma \to \rho$ transition probability $\simeq 1/300$, and $A(b)$ is computed from the Fourier transform of some pionic form factor. However, it should be stressed that these are *assumptions* which are *not* inherent to perturbative QCD or even to the idea that minijets drive the increase of hadronic cross-sections. Recall, for example, that in the GRV parametrization the "naive" VMD estimate of $\mathbf{q}^{\gamma}(x, Q_0^2)$ had to be doubled [24] in order to describe data at higher Q^2. Finally, if one estimates [96] $P_{\rm had}$ as $\int_0^1 \mathrm{d}x x\, \mathbf{q}^{\gamma}(x, p^2_{T,\min})$, one finds a value around 1/150 even for the DG parametrization. We therefore have to conclude that theoretical considerations at present only allow to estimate $P_{\rm had}$ up to a factor of 2 or so. The uncertainty in $A(b)$ has so far not been discussed in the literature, but might be of similar magnitude.

In view of these ambiguities it is not surprising that predictions [95, 96, 97, 99, 100] for the total γp cross-section at HERA energies differed quite widely prior to its measurement. Some examples are shown in figure 22, together with low-energy data and the recent ZEUS measurement [101]; a very similar value has been reported by the H1 collaboration [102]. The two solid curves show fits to low-energy data based on Pomeron phenomenology. The two dot-dashed curves show minijet predictions [100] using the DG parametrization with $p_{T,\min} = 1{\cdot}4$ (upper) and $2{\cdot}0$ (lower curve) GeV, while the dotted and dashed curves have been obtained from the LAC1 parametrization using the same values of $p_{T,\min}$. The LAC parametrization seems disfavoured, but in view of the theoretical and experimental uncertainties it might be premature to exclude it altogether. The DG minijet prediction with $p_{T,\min} = 2\,\mathrm{GeV}$ is certainly in agreement with the data. Notice, however, that all minijet calculations

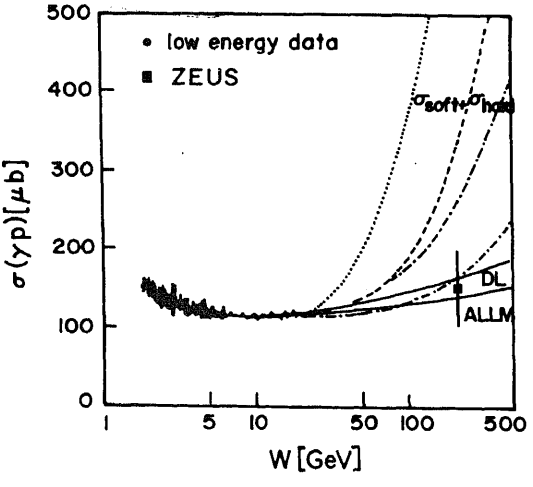

Figure 22. Comparison of various predictions of total γp cross-sections with low-energy data and the recent ZEUS measurement [101].

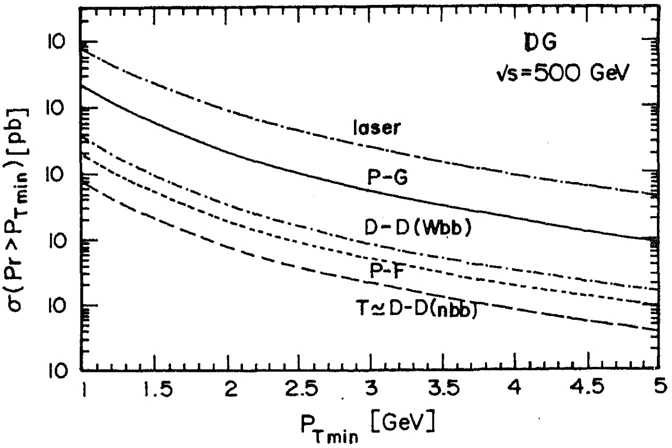

Figure 23. Integrated two jet cross-section for $p_T \geqslant p_{T,\min}$ as a function of $p_{T,\min}$ for the photon spectra of figure 10, as predicted [52] from the DG parametrization.

predict a substantially larger slope of the cross-section than the Pomeron-based fits do; a measurement of the energy-dependence of the total γp cross-section at HERA might therefore help to distinguish these models [103]. Finally, we have already seen that, in the case of hadronic collisions, minijet models also reproduce details of event shapes, e.g. multiplicity fluctuations and various correlations [94]. The measurement of similar quantities at HERA should help to distinguish between models.

Minijets are also expected to play an important role in $\gamma\gamma$ collisions at e^+e^- colliders [104, 52]. Indeed, the minijet cross-section at e^+e^- colliders rises even faster than at hadron colliders, since not only the $\gamma\gamma$ cross-section but also the γ flux increases with energy, especially once beamstrahlung becomes important. Some examples of the resulting minijet cross-sections are shown in figure 23 [52], for the same photon spectra introduced in figure 10. We see that the DG parametrization with $p_{T,\min} \simeq 1{\cdot}6$ GeV predicts a cross-section between about 20 and 500 nb, depending on the machine parameters; at a $\gamma\gamma$ collider this cross-section would be as large as 2 μb. For the Palmer-G (Palmer-F) design this corresponds to about 25(0·5) minijet pairs per bunch train collision; for the wbb option of the D-D and TESLA designs one expects 0·02 and 0·004 minijet pairs, respectively, in a 100 nanosecond interval. Of course, the minijet cross-section is sensitive to the parton content at small x values, where so far no experimental data exist. On the other hand, "shadowing" effects, which can be important for $x < 10^{-3}$, are not expected to be relevant for colliders with $\sqrt{s} \leqslant 1$ TeV.

We have just seen that (inclusive) jet cross-sections can be larger than the total cross-section. However, with the possible exception of the Palmer-G design whose hard beamstrahlung spectrum implies that the average $W_{\gamma\gamma}$ and hence $\sigma(\gamma\gamma \to \text{jets})$ averaged over the photon spectrum is quite large, eikonalization effects are not expected to change the number of hadronic (minijet) events at 500 GeV e^+e^- colliders significantly even if a conservative, VMD-based eikonalization scheme is used. This can be seen from the fact [52] that the minijet cross-section (as predicted from the DG parametrization) is smaller than or of the same order of magnitude as the total $e^+e^- \to e^+e^- + \text{hadrons}$ cross-sections estimated using a constant $\gamma\gamma \to \text{hadrons}$ cross-section of 250 nb for $W_{\gamma\gamma} > 5$ GeV. We thus have to face the unpleasant fact that some designs for e^+e^- colliders predict several hadronic events to occur at each bunch train collision already at $\sqrt{s} = 500$ GeV. It is usually accepted that a 500 GeV collider should be designed such that it can be upgraded to $\sqrt{s} \geqslant 1$ TeV; of course, beamstrahlung and hadronic 2-photon backgrounds become worse at higher energies.

This problem might be alleviated somewhat if detectors achieve a very good time resolution. E.g., at Palmer-F or -G, a bunch train consists of 10 bunches in time intervals of 1·4 ns. A time resolution of about 2 ns seems achievable at least for the tracking system, so that this part of the detector would "see" at most two superimposed bunch crossings; this would obviously reduce the number of minijets in the smallest time unit measureable by the detector by a factor of 5. On the other hand, it seems unlikely that similarly fast calorimeters can be built. Notice that about 35 to 40% of the energy of a hadronic jet is carried by neutral particles, which are only detectable in calorimeters.

What are the consequences of "always" having > 1 minijet event present in the detector? Basically it means that one now has an "underlying event"; i.e. every annihilation event (and every hard $\gamma\gamma$ event) will be accompanied by several minijet events. *Every* event will thus have some hadronic activity. This situation is of course well known from hadron colliders, but the absence of an underlying event, i.e. the "cleanliness" of the experimental environment, is usually considered to be one of the main advantages of e^+e^- colliders. The presence of a few (or even a few dozen) soft hadrons does usually not affect the possibility to detect "new physics" signals very much, although some care has to be taken when defining what is meant by an isolated lepton or photon, or by a hadronically quiet event; and it has to be kept in mind that fluctuations in the underlying event might fake elements of a signal, e.g. missing p_T. However, the ability of future linacs to study new particles in detail might be compromised severely by the presence of a large underlying event. First of all, the beam energy constraint would no longer be applicable, since the visible energy can be larger than $\sqrt{s}$. This already excludes the possibility of precision measurements of the mass of a hadronically decaying particle at energies far above threshold. An underlying event would also make it more difficult to discriminate between hadronically decaying W and Z bosons. Moreover, a large multiplicity of soft particles might make it impossible to operate a microvertex detector, which is deemed necessary for efficient b and c quark tagging. We estimate that one minijet event will deposit between 6 and 10 GeV of transverse energy in the detector (from both the minijets itself and the outer fringes of the spectator jets), corresponding to a charged multiplicity of about 8. Finally, an underlying event would also complicate the study of hard $\gamma\gamma$ events, since there would always be some spectator jet activity in the forward and backward directions, making it much more difficult to distinguish between hard, direct and resolved photon events.

It therefore seems much preferable to us to construct future e^+e^- linacs and their detectors such that an underlying event can be avoided. This ought to be relatively easy at $\sqrt{s} = 500$ GeV, but might prove challenging [52] for colliders operating at $\sqrt{s} \geqslant 1$ TeV.

6. Summary and conclusions

The measurement of F_2^γ in deep-inelastic $e\gamma$ scattering at present e^+e^- colliders does not yield sufficient information for decisive tests of QCD, nor for a discrimination of different ansätze for the parton content of real photons (§ 2). This is partly due to rather poor statistics (which is 3 or 4 orders of magnitude worse than for typical fixed-target deep-inelastic lepton-nucleon scattering experiments), partly due to kinematical constraints (which do not allow measurements at small Bjorken-x), and partly because F_2^γ is not very sensitive to G^γ. The situation might improve at future colliders, where smaller values of x become accessible in DIS; in this "sea" region, gluons do contribute to F_2^γ. The ideal experiment of this type could be performed [105] if an e^+e^- linac can be converted into an $e\gamma$ collider by backscattering laser photons.

In the last year the existence of resolved photon contributions had evolved from a theoretical prediction into an experimental fact. Their presence has first been demonstrated by the AMY group at TRISTAN, and has been confirmed by TOPAZ at TRISTAN and by the LEP experiments ALEPH and DELPHI (§ 3). Very recently the HERA experiments H1 and ZEUS have also reported that their data from the first (pilot) run show clear evidence of resolved photon events. The three main theoretical predictions [59]—large jet cross-sections at small and moderate transverse, momentum; jet rapidity distribution peaked at large values; and the presence of a photonic spectator jet—have already been confirmed experimentally.

This first analyses of resolved photon events have already contributed to our understanding of the hadronic structure of the photon. TRISTAN data clearly exclude one parametrization of photonic parton densities (LAC3); the measurements of the total γp cross-section at HERA are in conflict with predictions from the more extreme variety of minijet models. TRISTAN and LEP data will improve due to increased statistics, improved angular coverage of the detectors (at TRISTAN) and increased beam energy with less annihilation backgrounds (at LEP). The next year should see the HERA data sample grow by at least 3 orders of magnitude. The number of resolved photon events detected at HERA will then greatly exceed that of all e^+e^- colliders combined, allowing for detailed studies of jet production as well as searches for many other final states (§ 4). Nevertheless, e^+e^- data will continue to play an important role. On the one hand, these lower energy (in the $\gamma\gamma$ or γp centre-of-mass system) machines can probe the parton densities in the photon at large x but moderate Q^2, while at higher energies large x usually imply large Q^2. Recall that all models converge towards the asymptotic prediction if both x and Q^2 are large, while there are sizable differences at large x and moderate Q^2. Moreover, e^+e^- colliders also allow to study events with rather small invariant mass, which are usually boosted out of the detector at HERA; this should help us in understanding the transition between soft and hard interactions.

Soft and semihard (minijet) $\gamma\gamma$ events can lead to an "underlying event" at future e^+e^- supercolliders, spoiling the traditional cleanlines of e^+e^- colliders (§ 5). The main question here is whether beamstrahlung can be kept under control. Existing designs indicate that this should be fairly easy at centre-of-mass energies up to 500 GeV, but can become increasingly difficult at higher energies.

Our general conclusion is that the importance of resolved photon contributions increases with beam energy, and thus with time. We therefore expect great progress to be made in this field over the next few years. This is the heroic age of resolved photons!

Acknowledgements

We thank our experimental colleagues, G d'Agostini from ZEUS, A Finch from ALEPH, H Hayashii from TOPAZ and T Nozaki from AMY, for keeping us informed about the latest stage of the analyses of their data. MD thanks the theory group of the TIFR for their kind hospitality during his stay.

References

[1] See e.g. J I Friedman and H W Kendall, *Ann. Rev. Nucl. Sci.* **22**, 203 (1972) and references therein

[2] For a recent review, see J F Owens and W-K Tung, *Rev. Nucl. Part. Sci.* **42**, 291 (1992)

[3] AMY Collab., R Tanaka *et al.*, *Phys. Lett.* **B277**, 215 (1992)

[4] *Proceedings of the IX International Workshop on Photon–Photon Collisions*, San Diego California. March 1992; in particular the contributions by A Finch, H Hayashii, F Kapusta and R Tanaka.

[5] ZEUS collab., M. Derrick *et al*, *Phys. Lett* **B297**, 404 (1992)

[6] H1 Collab., T Ahmed *et al*, *Phys. Lett.* **B297**, 206 (1992)

[7] G Altarelli and G Parisi, *Nucl. Phys.* **B126**, 298 (1977)
V N Gribov and V N Lipatov, *Sov. J. Nucl. Phys.* **15**, 78 (1972)

[8] T F Walsh, *Phys. Lett.* **B36**, 121 (1971)
S M Berman, J D Bjorken and J B Kogut, *Phys. Rev.* **D4**, 3388 (1971)
P Zerwas and T Walsh, *Phys. Lett.* **B44**, 195 (1973)

[9] E Witten, *Nucl. Phys.* **B120**, 189 (1977)

[10] R J deWitt, L M Jones, J D Sullivan, D E Willen and H W Wyld Jr., *Phys. Rev.* **D19**, 2046 (1979)

[11] W A Bardeen and A J Buras, *Phys. Rev.* **D20**, 166 (1979); erratum, **D21**, 2041 (1980)
D W Duke and J F Owens, *Phys. Rev.* **D22**, 2280 (1980)
G Rossi, *Phys. Lett.* **B130**, 105 (1983)
M Fontannaz and E Pilon, *Phys. Rev.* **D45**, 382 (1992)
M Glück, E Reya and A Vogt, *Phys. Rev* **D45**, 3986 (1992)

[12] I Antoniadis and G Grunberg, *Nucl. Phys.* **B213**, 445 (1983)

[13] M Glück and E Reya, *Phys. Rev.* **D28**, 2749 (1983)

[14] I Antoniadis and L Marleau, *Phys. Lett.* **B161**, 163 (1985)
J H Field, K Kapusta and E Poggioli, *Phys. Lett.* **B181**, 362 (1986); *Z. Phys.* **C36**, 121 (1987)
M Glück and E Reya, *Nucl. Phys.* **B311**, 519 (1988)

[15] D W Duke and J F Owens, *Phys. Rev.* **D26**, 1600 (1982)

[16] A Nicolaidis, *Nucl. Phys.* **B163**, 156 (1980)

[17] M Drees and K Grassie, *Z. Phys.* **C28**, 451 (1985)

[18] PLUTO Collab., Ch. Berger *et al*, *Phys. Lett.* **B142**, 111 (1984)

[19] Ch Berger and W Wagner, *Phys. Rep.* **146**, 1 (1987)
J Olsson, *Nucl. Phys.* B, Proc. Suppl **3**, 613 (988)

[20] H Abramowicz, K Charchula and A Levy, *Phys. Lett.* **B269**, 458 (1991)

[21] TPC/2γ Collab., D Bintiger *et al.*, *Phys. Rev. Lett.* **58**, 97 (1987)

[22] Recall that in the "single-tag" experiments we are discussing here, one of the electrons emerges at too small an angle to be detected.

[23] F Kapusta (Private communication)

[24] M Glück, E Reya and A Vogt, *Phys. Rev.* **D46**, 1973 (1992)

[25] M Glück, E Reya and A Vogt, *Z. Phys.* **C53**, 127 (1992)

[26] M Glück, E Reya and A Vogt, *Z. Phys.* **C53**, 651 (1992)

[27] L E Gordon and J K Storrow, *Z. Phys.* **C56**, 307 (1992)

[28] We do not show results for the LAC1 and GS1 parametrizations, since they are qualitatively similar to the LAC2 and GRV parametrizations, respectively.

[29] C H Llewellyn Smith, *Phys. Lett.* **B79**, 83 (1978)

[30] S J Brodsky, T A deGrand, J F Gunion and S Weis, *Phys. Rev. Lett.* **41** 672 (1978); *Phys. Rev.* **D19**, 1418 (1979)
K Kajantie and R Raitio *Nucl. Phys.* **B159**, 528 (1979)
S F Li and H C Liu, *Phys. Lett.* **B143**, 489 (1984)

[31] M Drees and R M Godbole, *Nucl. Phys.* **B339**, 355 (1990)

[32] See for example, B L Combridge, J Kripfganz and J Ranft, *Phys. Lett.* **B70**, 243 (1977)

[33] S J Brodsky, T Kinoshita and H Terazawa, *Phys. Rev.* **D4**, 1532 (1971)

[34] R Kofler, in ref. [4]

[35] R Tanaka for the AMY Collab., in ref. [4]

[36] T Nozaki for the AMY Collab., Talk presented at the *Workshop on e^+e^- Collider Physics*, KEK, Tsukuba, Japan, December 1992; to appear in the Proceedings

[37] H Hayashii for the TOPAZ Collab., in ref. [4]

[38] H Hayashii for the TOPAZ Collab., as in ref. [36]

[39] A Finch for the ALEPH Collab., in ref. [4]

[40] F Kapusta for the DELPHI Collab., in ref. [4]

[41] M Drees and R M Godbole, *Phys. Lett.* **B234**, 375 (1990)

[42] Recall that the $\gamma\gamma$ cms energy $W_{\gamma\gamma}$ is usually much smaller than $\sqrt{s}$, since $f_{\gamma/e}(x) \propto 1/x$.

[43] T Uematsu and T F Walsh, *Nucl. Phys.* **B199**, 93 (1982)
G Rossi, *Phys. Rev.* **D29**, 852 (1984)

[44] F Borzumati and G A Schuler, DESY preprint 92-078

[45] E L Berger and D Jones, *Phys. Rev.* **D23**, 1521 (1981)

[46] N M Collab., D Allasia *et al*, *Phys. Lett.* **B258**, 493 (1991)

[47] The large size of the "k-factor" is not only due to the usual HO corrections, but presumably also includes corrections to the treatment of the J/ψ meson as a non-relativistic $c\bar{c}$ bound state. Already in a "hybrid" treatment, where the 1-loop corrected leptonic decay width of J/ψ is used to determine the wave function at the origin which also determines the cross-section, about 50% higher rates are predicted.

[48] M Drees and R M Godbole, *Phys. Lett.* **B257**, 425 (1991)

[49] For a review, see K Yokoya and P Chen, Lecture at the *1990 US-CERN School on Particle Accelerators*, Hilton Head, SC, KEK preprint 91-2

[50] Beamstrahlung can be reduced while keeping the luminosity fixed if elliptic bunches with large aspect ratio (the ratio between the semi-major and semi-minor axis) are employed [51]. However, the steering of very flat beams is expected to be even more difficult than for round beams, which puts an upper limit on the aspect ratio. Typical aspect ratios for present designs range from a few dozen to about 100.

[51] R Blanckenbecler and S D Drell, *Phys. Rev. Lett.* **61**, 2324 (1988)

[52] M Drees and R M Godbole, *Bombay Univ. preprint* BU 92/1, DESY Preprint 92-044 (to appear in *Z. Phyik C*)

[53] P Chen, *Phys. Rev.* **D46**, 1186 (1992)

[54] I F Ginzburg, G L Kotkin, V G Serbo and V I Telnov, *Nucl. Instrum Method* **205**, 219 (1983), and **219**, (1984) 5;
V I Telnov, *Nucl. Instrum Method* **294**, 72 (1990)

[55] A cut on the visible energy E_{vis} would be less effective; $\gamma\gamma$ events often have $E_{vis} \gg E_T$, since jets are often produced at small angles, and since spectator jets contribute to E_{vis} but only little to E_T

[56] F Halzen, C S Kim and M L Stong, *Phys. Lett.* **B274**, 489 (1992)

[57] J F Owens, *Phys. Rev.* **D21**, 54 (1979); Other early references are: T-S Tu, *Nucl. Phys.* **B161**, 417 (1979); I Kang and C H Llewellyn Smith, *Nucl. Phys.* **B166**, 413 (1980); M Fontannaz, A Mantrach, D Schiff and B Pire, *Z. Phys.* **C6**, 241 (1980)

[58] P Aurenche, R Baier, A Douiri, M Fontannaz and D Schiff, *Nucl. Phys.* **B286**, 553 (1987)
H Baer, J Ohnemus and J F Owens, *Phys. Rev.* **D40**, 2844 (1989)

[59] M Drees and R M Godbole, *Phys. Rev. Lett.* **61**, 683 (1988); *Phys. Rev.* **D39**, 169 (1989)

[60] W J Stirling and Z Kunszt, in *Proc. HERA workshop*, DESY 1987, (ed) R D Peccei p. 331

[61] H Baer, J Ohnemus and J F Owens, *Z. Phys.* **C42**, 657 (1989)

[62] R K Ellis and Z Kunszt, *Nucl. Phys.* **B303**, 653 (1988)
[63] A C Bawa, W J Stirling and M Krawczyk, *Z. Phys.* **C50**, 293 (1991)
[64] Z Kunszt and W J Stirling, *Phys. Lett.* **B217**, 53 (1989)
[65] D W Duke and J F Owens, *Phys. Rev.* **D30**, 49 (1984)
[66] M Glück, E Hoffman and E Reya, *Z. Phys.* **C13**, 119 (1982)
[67] It is worth mentioning that the validity of this statement rests on the fact that analyses of TRISTAN data have already ruled out the LAC3 parametrization, as discussed in the previous section
[68] G Marchesini *et al.*, *Comp. Phys. Commun.* **67**, 465 (1992)
[69] G d'Agostini and D Monaldi, *Proc. of the Workshop on HERA physics*, DESY 1991, (eds) W Buchmüller and G Ingelmann; see also the contributions by G Knies and A Valkarova, ibid.
[70] D Bödeker, *Phys. Lett.* **B292**, 164 (1992)
[71] G Kramer and S Salesch, in ref. [69]
[72] L E Gordon and J K Storrow, *Phys. Lett.* **B291**, 320 (1992)
[73] J Smith and W L van Neerven, *Nucl. Phys.* **B374**, 36 (1992)
S Riemersma, J Smith and W L van Neerven, *Phys. Lett.* **B282**, 171 (1992)
[74] M Glück, E Reya and A Vogt, *Phys. Lett.* **B285**, 285 (1992)
[75] J D Bjorken and E A Paschos, *Phys. Rev.* **185**, 1975 (1969)
T-S Tu and C-M Wu, *Nucl. Phys.* **B156**, 493 (1979)
K Iguchi and A Niegawa, *Z. Phys.* **C9**, 135 (1981)
P Aurenche *et al.*, *Z. Phys.* **C24**, 309 (1984), and in ref. [60]
A C Bawa and W J Stirling, *J. Phys.* **G14**, 1353 (1988)
[76] M Krawczyk, *Acta Phys. Polon.* **B21**, 999 (1990)
[77] A C Bawa and M Krawczyk, *Phys. Lett.* **B262**, 492 (1991)
[78] T Weiler, *Phys. Rev. Lett.* **44**, 304 (1980)
A D Martin, C-K Ng and W J Stirling, *Phys. Lett.* **B191**, 200 (1987)
J Abraham, *Phys. Lett.* **B240**, 224 (1990)
[79] Z Kunszt, *Phys. Lett.* **B207**, 103 (1988)
[80] R S Fletcher, F Halzen and R W Robinett, *Phys. Lett.* **B225**, 176 (1989)
[81] R S Fletcher, F Halzen, S Keller and W H Smith, *Phys. Lett.* **B266**, 183 (1991)
[82] M Drees and C S Kim, *Z. Phys.* **C53**, 673 (1992)
[83] M Drees, *Mod. Phys. Lett.* **A2**, 573 (1987)
[84] U Baur and D Zeppenfeld, *Nucl. Phys.* **B325**, 253 (1989), and references therein
[85] U Baur, J A M Vermaseren and D Zeppenfeld, *Nucl. Phys.* **B375**, 3 (1992)
A C Bawa, C S Kim and W J Stirling, *Durham preprint DTP*-91-38 (1992);
F Borzumati and G Schuler, in ref. [69]
[86] M Drees and C S Kim, *Z. Phys.* **C52**, 503 (1991)
[87] A C Bawa, *Z. Phys.* **C57**, 647 (1993)
[88] H Euler and B Kockel, *Naturwiss.* **23**, 246 (1935)
[89] M Drees and F Halzen, *Phys. Rev. Lett.* **61**, 275 (1988)
[90] See e.g., B L Dingus, *Phys. Rev. Lett.* **61**, 1906 (1988)
[91] T K Gaisser, F Halzen, T Stanev and E Zas, *Phys. Lett.* **B243**, 444 (1990)
[92] D Cline, F Halzen and J Luthe, *Phys. Rev. Lett.* **31**, 491 (1973)
[93] T K Gaisser and F Halzen, *Phys. Rev. Lett.* **54**, 1754 (1985)
L Durand and H Pi, *Phys. Rev. Lett.* **58**, 303 (1987)
[94] T Sjostrand and M van Zijl, *Phys. Rev.* **D36**, 2019 (1987)
X-N Wang and M Gyulassy, *Phys. Rev.* **D44**, 3501 (1991), and **D45**, 844 (1992)
[95] J C Collins and G A Ladinsky, *Phys. Rev.* **D43**, 2847 (1991)
[96] R S Fletcher, T K Gaisser and F Halzen, *Phys. Rev.* **D45**, 377 (1992); erratum -ibid. **D45**, 3279 (1992)
[97] J R Forshaw and J K Storrow, *Phys. Lett.* **B268**, 116 (1991); erratum, **B276**, 565 (1992); *Phys. Rev.* **D46**, 4955 (1992)
[98] R S Fletcher, T K Gaisser and F Halzen, *Phys. Lett.* **B298**, 442 (1993)
[99] R Gandhi and I Sarcevic, *Phys. Rev.* **D44**, R10 (1991)

[100] G A Schuler, in ref. [69]

[101] ZEUS Collab., M Derrick *et al.*, *Phys. Lett.* **B293**, 465 (1992)

[102] H1 Collab., T Ahmed *et al.*, *Phys. Lett.* **B299**, 374 (1992)

[103] The total cross-section can only be determined from events where the outgoing electron is tagged. That means that only the region 180 GeV $\leqslant \sqrt{s}(\gamma p) \leqslant$ 240 GeV is available for such a measurement. At least in the minijet calculations the cross-section should vary substantially even in this limited region

[104] M Drees and R M Godbole, *Phys. Rev. Lett.* **67**, 1189 (1991)

[105] A C Bawa and W J Stirling, *Z. Phys.* **C57** 165 (1993)

PRAMANA
— journal of
physics

© Printed in India

Vol. 41, No. 2,
August 1993
pp. 125–137

q-Deformation of algebraic structures of quantum and classical mechanics

DEBENDRANATH SAHOO and M C VALSAKUMAR
Theoretical Studies Section, Materials Science Division, Indira Gandhi Centre for Atomic Research, Kalpakkam 603 102, India

MS received 6 April 1993

Abstract. There exists a coassociative and cocommutative coproduct in the linear space spanned by the two algebraic products of a classical Hamilton algebra (the algebraic structure underlying classical mechanics [1]). The transition from classical to quantum Hamilton algebra (the algebraic structure underlying quantum mechanics) is an $\hbar$-deformation which preserves not only the Lie property of the classical Hamilton algebra but also the coassociativity and cocommutativity of the above coproduct. By explicit construction we obtain the algebraic structures of the q-deformed Hamilton algebras which preserve the said properties of the coproduct. Some algorithms of these structures are obtained and their implications discussed. The problem of consistency of time evolution with the q-deformed kinematical structure is discussed. A characteristic distinction between the parameters $\hbar$ and q is brought out to stress the fact that q *cannot* be regarded as a fundamental constant.

Keywords. Classical Hamiltonian algebra; quantum Hamiltonian algebra; quantum mechanics; classical mechanics.

PACS Nos 02·20; 03·65

1. Introduction

It was Dirac who first realized that the Poisson bracket in classical mechanics is a Lie bracket. As is well known, in setting up his quantum theory, Dirac replaced Poisson bracket by the commutator bracket (divided by $i\hbar$), thus preserving the Lie-algebraic structure. After Moyal [2] gave the phase space representation of quantum mechanics it became transparent that quantum mechanics may structurally be viewed as a deformation of classical mechanics with $\hbar$ as the deformation parameter. The Moyal sine and cosine brackets of quantum mechanics are respectively the deformations of the Poisson bracket and of the ordinary product of classical mechanics. The former products reduce to the latter in the limit $\hbar \to 0$. Inspired by the development of quantum groups [3, 4] and that of noncommutative geometry [5, 6, 7], recently, a second deformation (called the q-deformation) is being discussed in the literature [8, 9] wherein both classical as well as quantum mechanics are once more deformed.

From an algebraic point of view, these deformations fall into two distinct classes. In the first, the algebraic structure of mechanics is *undeformed*, but the Hamiltonian corresponding to the specific mechanical system under consideration is deformed. The work on q-deformation of oscillators [10, 11], the free particle [12], the rigid rotor [13], the hydrogen atom [14] and on q-deformation of the Schrödinger equation

[15, 16] and of the Heisenberg equation [17, 18] may be cited in this connection. Spiridonov [19] has proposed a deformation of conformal and supersymmetric quantum mechanics in the same perspective.

On the other hand, it is natural to ask if the underlying algebraic structure (of mechanics) also can be consistently deformed. Gelfand and Fairlie [20] have proposed such a q-deformation of quantum mechanics by replacing the Heisenberg commutation relation $PQ - QP = i\hbar$ with its q-deformed version $PQ - qQP = i\hbar$. They have obtained the algebra of q-symmetrized polynomials in P and Q and have attempted to q-deform the Moyal bracket. Fairlie [21] and Fletcher [22] have also considered the possibility of a q-Moyal bracket. These works prompt for a detailed investigation of the q-deformation of the full algebraic structure of quantum and also of classical mechanics. The existence of such deformations of mechanics should be examined carefully in view of the celebrated theorem of Falk [23] according to which exactly two associative algebras admit a product satisfying the axioms of the Poisson bracket (in fact, the Jacobi identity is *excluded* from the set of axioms): the algebra of commuting functions of phase space variables, and the algebra of noncommuting functions whose generators satisfy Heisenberg's commutation relations. Another variation of this theorem is contained in a similar result of Mehta [24] and in more recent results due to Arveson [25] and Bayen *et al* [26]. A generalization of Falk's theorem to encompass nonsymplectic systems such as the one described by the spin variables was achieved by Grgin and Petersen [27] and is also contained in the thesis of Sahoo [28]. In these works the algebraic structures of classical and quantum mechanics were abstracted and introduced in the names of classical and quantum Hamilton algebras (abbreviated as CHA and QHA respectively). The results of Sahoo [28, 29], Grgin and Petersen [27] imply the following

a) the QHA is a $\hbar$-deformation of the CHA
b) the tensor product of two CHA's is again a CHA
c) the above property persists in the QHA

Thus in addition to Dirac's insistence that the Lie structure of the Poisson bracket be preserved in the transition to quantum theory, the second property in the above list also needs to be preserved while going over to quantum theory. The physical justification for the stability of structure under tensor product composition is that interacting classical (quantum) systems should also find a description in the same classical (quantum) structural framework. In this paper, the assignment of the algebraic products to their respective forms in the tensor product space is further sharpened by recognizing that a coassociative and cocommutative coproduct is induced in the two dimensional linear space spanned by the two products in the Hamilton algebra. This coproduct structure is preserved in the deformation CHA → QHA.

Having noted the above basic feature of the $\hbar$-deformation process, it is natural to enquire whether in the process of q-deformation of a CHA (QHA), the above mentioned coproduct still maintains the property of being cocommutative and coassociative. An explicit construction of a q-QHA is then done by examining the properties of the q-commutator bracket $fg - qgf$ (of two operators f and g). The $\hbar \to 0$ limit of the q-QHA leads to a q-CHA.

We then find (by inspection) two sets of solutions for realization of the q-CHA and the q-QHA. Some results obtained in the literature are seen to correspond to our solutions.

The successful q-deformation of the kinematical structures naturally raises the question of q-dynamics. If the time evolution of an observable is given by the q-Lie bracket, then it is seen to be inconsistent with some of the identities defining the QHA. The requirement of consistency of the algebraic structure with dynamics—known to be satisfied in conventional classical and quantum mechanics (also in the Hamilton algebra framework)—calls for drastic changes in our framework. This question is discussed further in the concluding section.

2. Algebraic structure of classical mechanics

2.1 *Classical Hamilton algebra*

It is easy to obtain the algebraic structure of classical mechanics: Given two functions f and g in phase space, we can form a third function either by taking their Poisson bracket $\{f, g\}$ or by taking their usual product $f \cdot g$. The Poisson bracket $\{\cdot, \cdot\}$ operation is known to satisfy the following identities:

$$\{f,g\} = -\{g,f\} \text{ (antisymmetry).} \tag{1}$$

$$\{f,\{g,h\}\} + \{g,\{h,f\}\} + \{h,\{f,g\}\} = 0 \text{ (Jacobi identity).} \tag{2}$$

The usual product (called the observable product) "$\cdot$", on the other hand, is associative and commutative:

$$(f \cdot g) \cdot h = f \cdot (g \cdot h) \text{ (associativity).} \tag{3}$$

$$f \cdot g = g \cdot f \text{ (commutativity).} \tag{4}$$

These two products are inter-related: This comes about by noting that the time evolution law of f is governed by the Hamilton's equation

$$\frac{\mathrm{d}f}{\mathrm{d}t} = \{f, h\}, \tag{5}$$

where h is regarded as a Hamiltonian function. If we require that

$$\frac{\mathrm{d}}{\mathrm{d}t}(f \cdot g) = \frac{\mathrm{d}f}{\mathrm{d}t} \cdot g + f \cdot \frac{\mathrm{d}g}{\mathrm{d}t}, \tag{6}$$

then using (5), one must have the relation

$$\{(f \cdot g), h\} = \{f, h\} \cdot g + f \cdot \{g, h\}. \tag{7}$$

Thus the Poisson bracket is a *derivation* with respect to the observable product. The Jacobi identity too may be viewed as a consistency condition for time evolution of the Poisson bracket of two variables. Consider the time evolution of $\{f, g\}$ and require that

$$\frac{\mathrm{d}}{\mathrm{d}t}\{f,g\} = \left\{\frac{\mathrm{d}f}{\mathrm{d}t}, g\right\} + \left\{f, \frac{\mathrm{d}g}{\mathrm{d}t}\right\}. \tag{8}$$

Now using (5) in the above equation and then using (1) leads to the Jacobi identity (2). The abstract algebraic structure can now be extracted by assuming that the observables of *all* classical systems $f, g, h, \cdots$ form a linear space $\mathscr{H}$ over $\mathbf{R}$. The

Poisson bracket and the observable product are now replaced by their abstract counterparts

$$\alpha:\mathscr{H}\otimes\mathscr{H}\to\mathscr{H},$$
$$\sigma:\mathscr{H}\otimes\mathscr{H}\to\mathscr{H},$$

which are *bilinear* products satisfying the following relations:

$$f\alpha g=-g\alpha f \text{ (antisymmetry).} \tag{9}$$

$$f\sigma g=g\sigma f \text{ (commutativity of } \sigma). \tag{10}$$

$$(f\alpha g)\alpha h+(g\alpha h)\alpha f+(h\alpha f)\alpha g=0 \text{ (Jacobi identity).} \tag{11}$$

$$f\alpha(g\sigma h)=(f\alpha g)\sigma h+g\sigma(f\alpha h) \text{ (derivation law).} \tag{12}$$

$$[f,g,h]_\sigma\equiv(f\sigma g)\sigma h-f\sigma(g\sigma h)=0 \text{ (associativity of } \sigma). \tag{13}$$

The two product algebra $\{\mathscr{H},\sigma,\alpha,\mathbf{R}\}$ satisfying the above identities will be referred to as a CHA. We now turn to an important property of the above algebra.

2.2 *Tensor product composition of CHA*

When two classical systems interact, they form a single classical system. This implies that the composite system must be describable in the same way as the component systems themselves. In keeping with this fact, the CHA is characterized by an important property that the tensor product composition of two such algebras $\{\mathscr{H}',\sigma',\alpha',\mathbf{R}\}$ and $\{\mathscr{H}'',\sigma'',\alpha'',\mathbf{R}\}$ is again a CHA, $\{\mathscr{H}^{(',")},\sigma^{(',")},\alpha^{(',")},\mathbf{R}\}$. More explicitly, let $f',g',h'\in\mathscr{H}'$ and $f'',g'',h''\in\mathscr{H}''$ so that $(f'\otimes f''),(g'\otimes g''),(h'\otimes h'')\in\mathscr{H}^{(',")}$. Then analogous to equations (9)–(13), we have

$$(f'\otimes f'')\alpha^{(',")}(g'\otimes g'')=-(g'\otimes g'')\alpha^{(',")}(f'\otimes f'') \tag{14}$$

$$(f'\otimes f'')\sigma^{(',")}(g'\otimes g'')=(g'\otimes g'')\sigma^{(',")}(f'\otimes f'') \tag{15}$$

$$\begin{aligned}&[(f'\otimes f'')\alpha^{(',")}(g'\otimes g'')]\alpha^{(',")}(h'\otimes h'')+[(g'\otimes g'')\alpha^{(',")}(h'\otimes h'')]\alpha^{(',")}(f'\otimes f'')\\&\quad+[(h'\otimes h'')\alpha^{(',")}(f'\otimes f'')]\alpha^{(',")}(g'\otimes g'')=0\end{aligned} \tag{16}$$

$$\begin{aligned}&(f'\otimes f'')\alpha^{(',")}[(g'\otimes g'')\sigma^{(',")}(h'\otimes h'')]=[(f'\otimes f'')\alpha^{(',")}(g'\otimes g'')]\sigma^{(',")}(h'\otimes h'')\\&\quad+(g'\otimes g'')\sigma^{(',")}[(f'\otimes f'')\alpha^{(',")}(h'\otimes h'')]\end{aligned} \tag{17}$$

etc. In refs [27, 28] explicit forms of the composition laws of the σ and α products are defined

$$\sigma^{(',")}=(\sigma'\otimes\sigma'')\circ S \tag{18}$$

$$\alpha^{(',")}\doteq(\alpha'\otimes\sigma''+\sigma'\otimes\alpha'')\circ S \tag{19}$$

where S is the switching operator

$$S:(\mathscr{H}'\otimes\mathscr{H}'')\otimes(\mathscr{H}'\otimes\mathscr{H}'')\to(\mathscr{H}'\otimes\mathscr{H}'')\otimes(\mathscr{H}'\otimes\mathscr{H}'')$$

defined by the action of switching the "middle two" elements:

$$S[(f'\otimes f'')\otimes(g'\otimes g'')]=(f'\otimes g')\otimes(f''\otimes g'').$$

Thus for example, the α product of $(f'\otimes f'')$ and $(g'\otimes g'')\in\mathscr{H}^{(','')}$ is

$$\begin{aligned}
&\alpha^{(','')}[(f'\otimes f'')\otimes(g'\otimes g'')]\\
&\quad=(\alpha'\otimes\sigma''+\sigma'\otimes\alpha'')\circ S[(f'\otimes f'')\otimes(g'\otimes g'')]\\
&\quad=(\alpha'\otimes\sigma''+\sigma'\otimes\alpha'')(f'\otimes g')\otimes(f''\otimes g'')\\
&\quad=(f\alpha g)'\otimes(f\sigma g)''+(f\sigma g)'\otimes(f\alpha g)''
\end{aligned}$$

where for brevity we have denoted $f'\sigma' g'=(f\sigma g)'$, etc.

Consider now the linear space $\mathscr{L}$ over the reals spanned by the products α and σ themselves. This is clearly possible since the combination $a\alpha+b\sigma\,(a,b\in\mathbf{R})$ is well defined, i.e.,

$$(a\alpha+b\sigma):(f\otimes g)\to a(f\alpha g)+b(f\sigma g)$$

for any $f\otimes g\in\mathscr{H}\otimes\mathscr{H}$. The assignment

$$\Delta:\begin{pmatrix}\sigma\\ \alpha\end{pmatrix}\to\begin{pmatrix}\sigma^{\otimes}=\sigma\otimes\sigma\\ \alpha^{\otimes}=\alpha\otimes\sigma+\sigma\otimes\alpha\end{pmatrix}$$

where $\sigma^{\otimes}$, $\alpha^{\otimes}$: $(H\otimes H)\otimes(H\otimes H)\to(H\otimes H)$ are products defined on the tensor product of identical algebras defines a coproduct Δ. This coproduct is obviously cocommutative since it is symmetric in the interchange of the left and right components, i.e., it satisfies the property $\Delta=T\circ\Delta$ where T is the transposition map which interchanges the left and right components. A straightforward calculation shows that Δ is coassociative too. The cocommutativity of Δ is expressed by the following commutative diagram:

$$\begin{tikzcd}
\mathcal{L} \arrow[r, "\Delta"] \arrow[d, "\Delta"'] & \mathcal{L}\otimes\mathcal{L} \\
\mathcal{L}\otimes\mathcal{L} \arrow[ur, "T"'] &
\end{tikzcd}$$

Figure 1. Cocommutativity of Δ.

and the coassociativity property is expressed by the diagram:

$$\begin{tikzcd}
\mathcal{L} \arrow[r, "\Delta"] \arrow[d, "\Delta"'] & \mathcal{L}\otimes\mathcal{L} \arrow[d, "1\otimes\Delta"] \\
\mathcal{L}\otimes\mathcal{L} \arrow[r, "\Delta\otimes 1"'] & \mathcal{L}\otimes\mathcal{L}\otimes\mathcal{L}
\end{tikzcd}$$

Figure 2. Coassociativity of Δ.

This result is the restatement of the postulate of the semigroup property of the composition class [27].

3. $\hbar$-Deformation of CHA

From the work done in [27, 28] it follows that the algebra QHA of observables of quantum mechanics is obtained by generalizing (deforming) a CHA. In this deformation process, the Lie property of the α product is preserved, but the associativity property (13) is relaxed. It is postulated that the commutative diagrams of figures 1 and 2 still hold good. Then it is shown that (13) needs to be replaced by the following:

$$[f,g,h]_\sigma = a[f,g,h]_\alpha = ag\alpha(h\alpha f), \tag{20}$$

where $a \in \mathbf{R}$ is a constant and $[f,g,h]_\alpha \overset{\text{def}}{=} (f\alpha g)\alpha h - f\alpha(g\alpha h)$ is the α-associator. The identities defining a QHA are eqn (9)–(12), and (20). Following results are known [27, 28]:

1. The σ composition law (18) is deformed whereas the α composition law (19) is *not*.

$$\sigma^{(','')} = (\sigma' \otimes \sigma'' - a\alpha' \otimes \alpha'')\circ S.$$

$$\alpha^{(','')} = (\alpha' \otimes \sigma'' + \sigma' \otimes \alpha'')\circ S.$$

2. The composition of two QHA's $\{\mathscr{H}', \sigma', \alpha', \mathbf{R}\}^{a'}$ and $\{\mathscr{H}'', \sigma'', \alpha'', \mathbf{R}\}^{a''}$ characterized by quantum constants a' and a'' is also a QHA $\{\mathscr{H}' \otimes \mathscr{H}'', \sigma^{(','')}, \alpha^{(','')}, \mathbf{R}\}^{a}$ if and only if $a' = a'' = a$ – a property which clearly brings out the fundamental nature of 'a' (i.e., of the Planck's constant $\hbar$).
3. Although both σ and α products are nonassociative, their linear combination $\tau \overset{\text{def}}{=} \sigma + i\sqrt{a}\alpha$ is an associative product defined in the complex extension $\mathscr{A}$ of $\mathscr{H}$.
4. The substructures $\{\mathscr{H}, \sigma\}$ and $\{\mathscr{H}, \alpha\}$ are derived algebras of the algebra $\{\mathscr{A}, \tau, \mathbf{C}\}$, i.e.,

$$f\sigma g = \frac{1}{2}(f\tau g + g\tau f). \tag{21}$$

$$f\alpha g = \frac{1}{2i\sqrt{a}}(f\tau g - g\tau f). \tag{22}$$

$\{\mathscr{H}, \sigma\}$ is a special Jordan algebra and $\{\mathscr{H}, \alpha\}$ is a Lie algebra. The product τ is the more familiar noncommutative and associative product of quantum mechanics and a has to be assigned the value $\hbar^2/4$ for making contact with the conventional quantum mechanics. When $a \to 0$, QHA reduces to a CHA. Thus a QHA is a a-deformed (or $\hbar$-deformed) CHA in which the Lie property of α product as well as the commutative diagrams of figures 1 and 2 are all preserved.

For these results it is obvious that the map $\Delta: \mathscr{H} \to \mathscr{H} \otimes \mathscr{H}$ is a-deformed:

$$\Delta: \begin{pmatrix} \sigma^a \\ \alpha^a \end{pmatrix} \to \begin{pmatrix} \sigma^{a,\otimes} = \sigma^a \otimes \sigma^a - a\alpha^a \otimes \alpha^a \\ \alpha^{a,\otimes} = \alpha^a \otimes \sigma^a + \sigma^a \otimes \alpha^a \end{pmatrix}. \tag{23}$$

There exists an interesting structural relation between the CHA and the QHA [27, 28]. Let the products (σ, α) of the CHA be relabelled with superscripts zero to emphasize that these are obtained from their respective quantum counterparts in the limit $a \to 0$. If one assumes the *same* underlying space $\mathscr{H}$ to support the algebraic structures of both the QHA and the CHA, then it can be shown [27, 28] that the following

$$\begin{tikzcd}
\mathcal{H}\otimes\mathcal{H} \arrow[r, "\alpha^0"] \arrow[d, "\Omega"'] & \mathcal{H} \\
\mathcal{H}\otimes\mathcal{H} \arrow[ur, "\sigma^0"'] &
\end{tikzcd}$$

Figure 3. Factorization of the bilinear product α^0.

essentially *unique* structural relation hold between (σ^a, α^a) and (σ^0, α^0):

$$\alpha^a = \sigma^0 \circ \frac{\sin(\sqrt{a}\Omega)}{\sqrt{a}}. \tag{24}$$

$$\sigma^a = \sigma^0 \circ \cos(\sqrt{a}\Omega). \tag{25}$$

Here Ω is a linear operator $\Omega: \mathscr{H} \otimes \mathscr{H} \to \mathscr{H} \otimes \mathscr{H}$ satisfying the following commutative diagram:
It is interesting to note that this relation (24) has reappeared in the recent work of Drinfeld [30] (see also [31, 32]) in connection with quantization of Poisson–Hopf algebras. We now proceed to discuss our main results on the q-deformed Hamilton algebras.

4. q-Deformation of Hamilton algebras

4.1 *The q-QHA*

In the literature [9, 20, 33], a q-deformed commutator $FG - qGF \overset{\text{def}}{=} [F, G]_q$ of operators has been introduced in the context of q-generalization of quantum systems/mechanics, but the associative operator product τ is assumed to be undeformed. The relations (21), (22) suggest the following deformed decomposition of τ:

$$f\tau g = f\sigma(q)g + i\sqrt{a} f\alpha(q)g \tag{26}$$

$$f\sigma g = \frac{1}{2}(f\tau g + qg\tau f) \tag{27}$$

$$f\alpha g = \frac{1}{2i\sqrt{a}}(f\tau g - qg\tau f). \tag{28}$$

The $\alpha(q)$ and $\sigma(q)$ are seen to satisfy the relations

$$f\sigma(q)g = q[g\sigma(\bar{q})f] \tag{29}$$

$$f\alpha(q)g = -q[g\alpha(\bar{q})f] \tag{30}$$

where $\bar{q} \overset{\text{def}}{=} q^{-1}$ (thus $q \neq 0$). The most general form of the q-deformed Jacobi identity consistent with definition (22) can be easily seen to be the following [34]:

$$f\alpha(q_2)[g\alpha(q_1)h] + q_2 g\alpha(q_1\bar{q}_2\bar{q}_3)[h\alpha(q_3)f] + q_1\bar{q}_3 h\alpha(\bar{q}_1 q_3)[f\alpha(q_2 q_3)g] \equiv 0. \tag{31}$$

Note that the above deformation results in loss of cyclicity property of the Jacobi identity.

Now (31) can be written in the form of a (deformed) self-derivation:

$$f\alpha(q_2)[g\alpha(q_1)h] = [f\alpha(q_2q_3)g]\alpha(q_1\bar{q}_3)h + q_2q_3g\alpha(q_1\bar{q}_2\bar{q}_3)[f\alpha(\bar{q}_3)h]. \tag{32}$$

It can also be written in the form of an (deformed) associator:

$$[f\alpha(q_2q_3)g]\alpha(q_1\bar{q}_3)h - f\alpha(q_2)[g\alpha(q_1)h] = q_2g\alpha(q_1\bar{q}_2\bar{q}_3)[h\alpha(q_3)f]. \tag{33}$$

The q-deformed version of the derivation relation (12) can be written simply by changing $f\alpha(q_2)[g\alpha(q_1)h] \to f\alpha(q_2)[g\sigma(q_1)h]$ in the LHS of (32) and then making corresponding changes in the RHS. (It could also be independently worked out.):

$$f\alpha(q_2)[g\sigma(q_1)h] = [f\alpha(q_2q_3)g]\sigma(q_1\bar{q}_3)h + q_2q_3g\sigma(q_1\bar{q}_2\bar{q}_3)[f\alpha(\bar{q}_3)h]. \tag{34}$$

The q-deformed version of the associator relation (20) can be obtained by replacing the α's occurring in the LHS of (33) by the corresponding σ's so as to obtain the deformed σ-associator and then making use of the proportionality of the two associators as given in (20). This leads to the relation

$$[f\sigma(q_2q_3)g]\sigma(q_1\bar{q}_3)h - f\sigma(q_2)[g\sigma(q_1)h] = aq_2g\alpha(q_1\bar{q}_2\bar{q}_3)[h\alpha(q_3)f]. \tag{35}$$

Relations (29, 30, 31, 34, 35) define the q-QHA and can be checked to hold good for the realization $\sigma(q) = \{,\}_q$ and $\alpha(q) = [,]_q$.

Consider two QHA's $\{\mathscr{H}', \sigma'(q'), \alpha'(q'), \mathbf{R}\}^a$ and $\{\mathscr{H}'', \sigma''(q''), \alpha''(q''), \mathbf{R}\}^a$. Let $f' \otimes f''$ and $g' \otimes g'' \in \mathscr{H}' \otimes \mathscr{H}''$. Then the composition laws for the product laws in $\mathscr{H}' \otimes \mathscr{H}''$ are given by

$$(f' \otimes f'')\sigma^{\otimes}(q', q'')(g' \otimes g'') = (f\sigma(q)g)' \otimes (f\sigma(q)g)'' - a(f\alpha(q)g)' \otimes (f\alpha(q)g)''$$

$$(f' \otimes f'')\alpha^{\otimes}(q', q'')(g' \otimes g'') = (f\alpha(q)g)' \otimes (f\sigma(q)g)'' + (f\sigma(q)g)' \otimes (f\alpha(q)g)''$$

where for brevity we have written $(f\alpha(q)g)' \overset{\text{def}}{=} f'\alpha'(q')g'$, etc. By lengthy algebraic manipulations involving all the q-deformed identities, it is possible to show that the characteristic property of the QHA—the composition property—is preserved by the proposed q-deformation. The resulting algebra is again a deformed QHA $\{\mathscr{H}' \otimes \mathscr{H}'', \sigma^{\otimes}(q', q''), \alpha^{\otimes}(q', q''), \mathbf{R}\}^a$. The symmetry properties are expressed by the relation:

$$(f' \cdot f'')\sigma^{\otimes}(q', q'')(g' \cdot g'') = q'q''[(g' \cdot g'')\sigma^{\otimes}(\bar{q}', \bar{q}'')(f' \cdot f'')] \tag{36}$$

$$(f' \cdot f'')\alpha^{\otimes}(q', q'')(g' \cdot g'') = -q'q''[(g' \cdot g'')\alpha^{\otimes}(\bar{q}', \bar{q}'')(f' \cdot f'')] \tag{37}$$

and the Jacobi identity is expressed by the relation:

$$\begin{aligned}
&(f' \cdot f'')\alpha^{\otimes}(q_2', q_2'')[(g' \cdot g'')\alpha^{\otimes}(q_1', q_1'')(h' \cdot h'')] \\
&\quad + q_2'q_2''(g' \cdot g'')\alpha^{\otimes}(q_1'\bar{q}_2'\bar{q}_3', q_1''\bar{q}_2''\bar{q}_3'')[(h' \cdot h'')\alpha^{\otimes}(q_3', q_3'')(f' \cdot f'')] \\
&\quad + q_1'\bar{q}_3'q_1''\bar{q}_3''(h' \cdot h'')\alpha^{\otimes}(\bar{q}_1'q_3'q_2''\bar{q}_1''q_3'')[(f' \cdot f'')\alpha^{\otimes}(q_2'q_3', q_2''q_3'')(g' \cdot g'')] = 0.
\end{aligned} \tag{38}$$

Similar relations for the derivation and the associator identities follow. Explicit calculation shows that the cocommutativity and coassociativity of the coproduct Δ

holds; infact, like the product τ, Δ remains undeformed. No new identities (like the associator identity (20) in the $\hbar$-deformation) are implied. We now obtain the $a \to 0$ limit of the q-QHA.

4.2 *The q-CHA*

The CHA being the $a \to 0$ limit of the QHA, it is natural to consider the $a \to 0$ limit of the q-QHA. By setting $a = 0$ in the identities (29, 30, 31, 34) and (35), we obtain the identities which define the q-CHA. Note that it is the q-QHA which provides the clue to the q-deformation of the CHA in our analysis. It was not possible for us to straightaway arrive at the identities defining a q-CHA. We now discuss some representations of the q-Hamilton algebras.

5. Algorithms for *q*-Hamilton algebra

For the purpose of simplicity, we consider the special case of the q-Hamilton algebras corresponding to the special choice of the parameters $q_1 = q_3 = q$ and $q_2 = 1$. The q-QHA is then denoted by the somewhat more pleasing form of the identities:

$$f\alpha[g\alpha(q)h] + g\alpha[h\alpha(q)f] + h\alpha[f\alpha(q)g] = 0. \tag{39}$$

$$f\alpha[g\sigma(q)h] = [f\alpha(q)g]\sigma h + qg\sigma[f\alpha(\bar{q})h]. \tag{40}$$

$$\begin{aligned}[f\sigma(q)g]\sigma h - f\sigma[g\sigma(q)h] &= qa\{[f\alpha(q)g]\alpha h - f\alpha[g\alpha(q)h]\}\\ &= qa\{g\alpha[h\alpha(q)f]\}.\end{aligned} \tag{41}$$

Notice the restoration of cyclicity property in the q-Jacobi identity. The classical limit of (41) is

$$[f\sigma(q)g]\sigma h - f\sigma[g\sigma(q)h] = 0. \tag{42}$$

We consider first a rather trivial looking solution for the q-CHA in the usual phase space.

$$f\alpha(q)g = \sqrt{q}\{f\overleftrightarrow{\nabla}g\}, \tag{43}$$

$$f\sigma(q)g = \sqrt{q}\{f\cdot g\}, \tag{44}$$

Here f and g are functions of commuting phase space variables, $\overleftrightarrow{\nabla}$ denotes the usual Poisson bracket operation and the dot "$\cdot$" represents the usual multiplication of functions. We note that these solutions conform to the q-deformed Poisson bracket obtained from consideration of the action functional in the path-integral for the q-deformed oscillator [35]. By invoking the structural relation (24), we obtain:

$$f\alpha(q)g = f\left\{\frac{2}{\hbar}\cdot\sin\left[\frac{\hbar\sqrt{q}}{2}\overleftrightarrow{\nabla}\right]\right\}g. \tag{45}$$

$$f\sigma(q)g = f\left\{\sqrt{q}\cos\left[\frac{\hbar\sqrt{q}}{2}\overleftrightarrow{\nabla}\right]\right\}g. \tag{46}$$

Here it is important to note that while (45) and (46) are consistent with the q-QHA structure described above, we have $f\alpha(q)g = \sqrt{q}[f, g]$ and $f\sigma(q)g = \sqrt{q}\{f, g\}$ which is of a form different from that described by (27, 28).

Another solution is found by considering first the phase space realization of the q-QHA [defined by (29, 30, 31, 34), and (35)] and subsequently taking the classical limit $\hbar \to 0$. Since the associative product τ is undeformed, we may choose to work in the phase space representation where $\tau = \exp[(i\hbar/2)\overleftrightarrow{\nabla}]$. Then we obtain

$$f\sigma(q)g = \left(\frac{1+q}{2}\right) f\left[\cos\left(\frac{\hbar}{2}\overleftrightarrow{\nabla}\right)\right] g + i\left(\frac{1-q}{2}\right) f\left[\sin\left(\frac{\hbar}{2}\overleftrightarrow{\nabla}\right)\right] g, \tag{47}$$

$$f\alpha(q)g = \left(\frac{1-q}{2i\hbar}\right) f\left[\cos\left(\frac{\hbar}{2}\overleftrightarrow{\nabla}\right)\right] g + \left(\frac{1+q}{2}\right)\frac{2}{\hbar} f\left[\sin\left(\frac{\hbar}{2}\overleftrightarrow{\nabla}\right)\right] g. \tag{48}$$

In the limit $\hbar \to 0$, it is possible to find a solution corresponding to a q-CHA. Let q be of the form $q = 1 - 2ib\hbar + O(\hbar^2)$ with b being a real parameter. Then in the limit $\hbar \to 0$, we obtain

$$f\sigma(q)g = f \cdot g, \tag{49}$$

$$f\alpha(q)g = b(f \cdot g) + f\overleftrightarrow{\nabla} g. \tag{50}$$

This solution leads to a nontrivial deformation of the classical Hamilton algebra.

If we assume the time evolution of an observable f to be given by the deformed bracket (50) then one would obtain

$$\frac{\mathrm{d}f}{\mathrm{d}t} = bhf + \{f, h\}, \tag{51}$$

where h is the Hamiltonian. For a harmonic oscillator, i.e., for the choice $h = \frac{1}{2}(x^2 + p^2)$, the equations of motion for x and p would have the form

$$\frac{\mathrm{d}x}{\mathrm{d}t} = bx\left(\frac{x^2 + p^2}{2}\right) + p,$$

$$\frac{\mathrm{d}p}{\mathrm{d}t} = bp\left(\frac{x^2 + p^2}{2}\right) - x,$$

the solutions of which are given by:

$$x = \frac{r_0}{\sqrt{1 - r_0^2 bt}} \cos(t + \theta_0),$$

$$p = -\frac{r_0}{\sqrt{1 - r_0^2 bt}} \sin(t + \theta_0),$$

where r_0 and θ_0 are fixed by the initial condition. This solution is interesting in that it exhibits *damped* behaviour (for $b < 0$), thereby creating an impression that dissipation can be introduced by q-deformation. However, as per the defining axiom (see (40)), time evolution given by (51) is *not* consistent with the usual derivation property. Therefore (51) is *not* a differential equation with the usual topology for t. It is also not the so-called q-differential equation described by Exton [36]. Elucidation of the nature of (51) is an outstanding problem.

On the other hand, the time evolution

$$\frac{\mathrm{D}f}{\mathrm{D}t} = bhf + \{f, h\}, \tag{52}$$

where

$$\frac{\mathrm{D}f}{\mathrm{D}t} \overset{\mathrm{def}}{=} \exp(-bth)\frac{\mathrm{d}}{\mathrm{d}t}(\exp(bth)f)$$

$$= bhf + \frac{\mathrm{d}f}{\mathrm{d}t}.$$

removes the "extra" term involving b and we get the usual dynamical equation of classical mechanics. This shows that we are then working with just *another* representation of classical mechanics. More discussion on the question of time evolution is included in the next section where we summarize our findings and end with our conclusions.

6. Summary and conclusion

We considered $\hbar$-deformation of the algebraic structure of classical mechanics and emphasized the preservation of two basic features—one, the Lie algebraic properties of the Poisson bracket and two, the cocommutative and coassociative property of the coproduct defined on the linear space spanned by the observable product and the Lie product of the algebra of observables. The former result is well known. The latter is an abstraction of the synthesis of the algebraic structure of Hamilton algebra and the semigroup structure of composition class discussed in the earlier work. [27, 28]. A clue to the structure of the q-deformed algebra of observables of quantum mechanics is provided by the decomposition of the noncommutative and associative product $f\tau g \overset{\mathrm{def}}{=} fg$ into a q-deformed anticommutator $\frac{1}{2}(fg + qgf)$ and a q-deformed commutator $(1/i\hbar)(fg - qgf)$. We have abstracted the properties of these deformed brackets and shown that the resulting q-deformed quantum algebra of observables still maintains the cocommutative, coassociative nature of the deformed coproduct, while the Lie property gets deformed. No new identities need to be introduced in this process of q-deformation. The q-deformed algebraic structure of classical mechanics is then obtained as the $\hbar \to 0$ limit of the q-deformed quantum mechanics. Thus the algebraic structures of both classical and quantum mechanics are shown to admit a consistent q-deformation.

An important point to note is the fact that although the transition CHA → QHA is a deformation where the constant a plays the role of the deformation parameter, there is much more to the significance of a—*it is a fundamental constant characterizing a given QHA*. Thus two QHA's with two different a's—say a' and a''—do not compose under the tensor product unless $a' = a'' = a$ and the composed algebra is again a QHA characterized by the *same* a. This is *not* so for the q-deformation as is reflected in eqs (36, 37, 38). A q-QHA characterized by the parameter q' can be tensor producted with another q-QHA with parameter q'' to lead to a composed q-QHA with the parameter $q'q''$ and even when $q' = q'' = q$, the resulting q-QHA is *not* characterized by the *same* parameter (i.e., q). Similar property holds good for the general q-QHA obtained earlier. Thus although the transition CHA → QHA is an a-deformation, it is distinguished from q-deformation QHA → q-QHA by invariance of the deformation parameter. Viewed this way, *q parameter does not appear to have any fundamental physical significance.*

Our result that the Hamilton algebras can be consistently q-deformed is *not* at variance with our second result that the parameter q is devoid of any fundamental physical significance. The first result simply refers to the Hamilton algebra structure and shows that the tensor-product composition preserves the Hamilton algebra structure. It makes no reference at all to the value of the parameter q. The second result points out the distinctive nature of the $\hbar$-deformation wherein the value of $\hbar$ is also preserved during the composition process.

The concept of time evolution is known [17, 18] to be problematic in q-deformed quantum mechanics. In the framework of the q-QHA also this difficulty persists. Assume for example, a time evolution of an "observable" f generated by a "hamiltonian" $h(f, h \in \mathscr{H})$ as given by the Heisenberg equation of motion

$$\frac{\mathrm{d}f}{\mathrm{d}t} = f\alpha(q)h.$$

Unlike in the conventional quantum mechanics, time evolution of an observable such as $g\alpha(q)k$ or $g\sigma(q)k(g, k \in \mathscr{H})$ is *not* preserved, i.e.,

$$\frac{\mathrm{d}}{\mathrm{d}t}(g\alpha(q)k) \neq \frac{\mathrm{d}g}{\mathrm{d}t}\alpha(q)k + g\alpha(q)\frac{\mathrm{d}k}{\mathrm{d}t} \quad \text{for } q \neq 1,$$

and

$$\frac{\mathrm{d}}{\mathrm{d}t}(g\sigma(q)k) \neq \frac{\mathrm{d}g}{\mathrm{d}t}\sigma(q)k + g\sigma(q)\frac{\mathrm{d}k}{\mathrm{d}t} \quad \text{for } q \neq 1,$$

if the operation $\mathrm{d}/\mathrm{d}t$ is interpreted in the usual sense, i.e., $\mathrm{d}t^n/\mathrm{d}t = nt^{n-1}$. Note that the above comment is applicable to a q-CHA as well. This problem is *not* solved by replacing the ordinary time derivative by a q-derivative, defined by $\mathrm{d}t^n/\mathrm{d}t = [n]t^{n-1}$, where $[n]$ is a suitably defined q-number ([36]). Elucidation of the action $\mathrm{d}/\mathrm{d}t$ so as to have the q-deformed time evolution (51) consistent, is an open problem.

In our opinion further changes in the Hamilton algebra structure have to be made in order to accommodate other aspects of dynamics such as dissipation. It seems that the Lie structure (especially the Jacobi identity) has to be completely abandoned to achieve this. More work on this line is obviously called for.

It is worth pointing out that in this work we have *not* attempted to incorporate the quantum space nature of the phase space in our q-deformation. Gelfand and Fairlie [20] have taken a step in this direction, but they have not completed the q-deformation of quantum mechanics. However, we believe that incorporation of quantum space nature of the phase space in our formalism will *not* restore fundamental status to the parameter q. It would be of interest to first incorporate the quantum space into classical mechanics by q deforming the Poisson bracket and then making transition to q-quantum mechanics by an appropriate Moyal quantization.

Acknowledgement

This paper is dedicated to Dr G Venkataraman, who has been a great source of inspiration to us, on the occasion of his sixtieth birthday.

References

[1] E Grgin and A Petersen, *J. Math. Phys.* **15**, 764 (1974)

[2] J Moyal, *Proc. Cambridge Philos. Soc.* **45**, 99 (1949)

[3] H D Doebner and J D Hennig (eds), *Quantum groups proceedings, Clausthal, FRG 1989, Lecture notes in physics*, (Springer-Verlag, Berlin, 1990) **370**

[4] T Curtright, D Fairlie and C Zachos (eds), *Quantum groups: Proceedings of Argonne workshop* (World Scientific, Singapore, 1991)

[5] A Connes, *Geometrie non-commutative* (Inter Editions 1990)

[6] Yu I Manin, *Quantum groups and non-commutative geometry*, Montreal Univ Rep CRM-1561 (1988)

[7] S L Woronowicz, *Commun. Math. Phys.* **111**, 613 (1987); **122**, 125 (1989)

[8] I Ya Aref'eva and I V Volovich, *Phys. Lett.* **268**, 179 (1991)

[9] B Zumino, *Mod. Phys. Lett.* **6**, 1225 (1991)

[10] L C Bidenharn, *J. Phys.* **A25** L 873 (1989)

[11] A J Macfarlane, *J. Phys.* **A22** 4581 (1989)

[12] I Ya Aref'eva, *Quantum group gauge fields* preprint CERN-TH 66207/91; see also ref. [8]

[13] Z Chang, *Phys. Rev.* **A45**, 4303 (1992)

[14] X C Song and L Liao, *J. Phys.* **A25**, 623 (1992)

[15] S Chaturvedi, R Jagannathan, R Sridhar and V Srinivasan, *preprint: imsc*-92/45 (1992)

[16] U Carow-Watamura, M Schlieker and S Watamura, *Z. Phys.* **C49**, 439 (1991)

[17] A Chodos and D G Caldi, *J. Phys.* **A24**, 5505 (1991)

[18] R Ubriaco, *Phys. Lett.* **A163**, 1 (1992)

[19] V Spiridonov, *Mod. Phys. Lett.* **A7**, 1241

[20] I M Gelfand and D B Fairlie, *Commun. Math. Phys.* **136**, 487 (1991)

[21] D B Fairlie, *Quantum groups* eds T Curtright, D Fairlie and C Zachos, (World Scientific, Singapore, 1991) p. 133

[22] P Fletcher, *Quantum groups* eds T Curtright, D Fairlie and C Zachos (World Scientific, Singapore, 1991) p. 143

[23] G Falk, *Math. Ann.* **123**, 379 (1951)

[24] C L Mehta, *J. Math. Phys.* **5**, 5 (1964)

[25] W Arveson, *Commun. Math. Phys.* **89**, 77 (1983)

[26] F Bayen, M Flato, C Fronsdal, A Lichnerowicz and D Sternheimer, *Ann. Phys. (N.Y.)* **111**, 61, 111 (1978)

[27] E Grgin and A Petersen, *Commun. Math. Phys.* **50**, 177 (1976)

[28] D Sahoo, *Some algebraic aspects of the relationship between classical and quantum mechanics* Ph.D. thesis, Yeshiva University, New York; University Microfilms Inc (Ann Arbor, Michigan, 1972)

[29] D Sahoo, *Pramana – J. Phys.* **8**, 545 (1977)

[30] V G Drinfeld, "Quantum Groups" *Proc. Int. Cong. of mathematicians* (Berkeley, 1986) (American Mathematical Society, 1987), p 798

[31] H D Doebner, J D Hennig and W Lücke in *Quantum groups proceedings*, edited by H D Doebner and J D Hennig Clausthal, FRG 1989, lecture notes in physics **370**, (Springer-Verlag, Berlin, 1990)

[32] L A Takhtajan, in *Introduction to quantum group and integrable massive models of quantum field theory* edited by M Ge and B-H Zhao (World Scientific, Singapore, 1990) p. 69

[33] M Chaichian, P Kulish and J Lukierski, *J. Phys. Lett.* **B237**, 401 (1990)

[34] Note that if the commutator is deformed with two parameters (p, q), then the most general (p, q)-deformed Jacobi identity will contain six parameters $(p_1, p_2, p_3; q_1, q_2, q_3)$.

[35] S Iida and H Kuratsuji, *Phys. Rev. Lett.* **69**, 1833 (1992)

[36] H Exton, *q*-Hypergeometric functions and applications (Ellis Horwood, Chichester, 1983)

PRAMANA
— journal of
physics

© Printed in India

Vol. 41, No. 2,
August 1993
pp. 139–144

Inflation driven by energy and curvature dependent bulk viscosity

C WOLF
Department of Physics, North Adams State College, North Adams, MA 01247, USA

MS received 4 November 1992; revised 1 February 1993

Abstract. We study the relative rates of expansion in cosmologies admitting curvature dependent and energy dependent bulk viscosity. It is conjectured that curvature dependant bulk viscosity may be a phenomenological way of representing gravitational vacuum polarization around the time of the Planck era.

Keywords. Inflation; Planck era; bulk viscosity.

PACS No. 98·80

1. Introduction

Inflationary cosmology has become a practical way of resolving the flatness and horizon problems of observational cosmology [1]. It was Guth's [2] great insight in observing that the radiative corrected Coleman and Weinberg potential [3] could serve as an effective cosmological constant to drive the early universe to a period of exponential expansion. Old inflation [2], new inflation [4], chaotic inflation [5], and extended inflation [6] are all confronted with the problem of just how large scale structure can be seeded from primordial fluctuations during the inflationary period. Extended inflation offers us the most plausible solution to the problem of how the false vacuum makes the transition to the true vacuum by allowing sufficient inflation for small times to resolve the horizon and flatness problems and a slowing down of the expansion rate at greater time to allow the true vacuum to percolate. In theories of extended inflation a scalar field of a Brans–Dicke type theory provides a catalyst for the above cosmological transition. In addition to the above theories of inflation driven basically by a scalar field displaced from the minimum of the potential, there are other mechanisms to drive inflation such as bulk viscosity driven inflation [7] and higher curvature driven inflation [8]. Bulk viscosity in particular has been shown to be a phenomenological way of representing the conversion of massive string modes in the early universe to massless modes as well as representing a general form of dissipation associated with particle creation [9]. In addition to stringy interconversions, curvature dependent bulk viscosity has been shown to be equivalent to particle creation through gravitational vacuum polarization [10]. In a separate note [11] we have shown that curvature dependent bulk viscosity leads to inflation, and in this note, we extend these studies to the case when the bulk viscosity coefficient depends on the curvature squared and the energy density. After a brief discussion based on microphysics justifying the functional dependence of the bulk viscosity coefficient on the energy density and curvature squared, we demonstrate that both of these cases lead to inflation in a spatially flat universe and derive the relative expansion rates in each case. It could very well be that extended inflation can be realized as a combination of these two cases with rapid inflation at the outset and a diminished inflation rate for later times. With the interest in demonstrating that inflation exists under a variety of circumstances and the speculation that there exists a cosmic-no hair theorem [12, 13, 14] for inflation, the two cases of inflation discussed in this paper add to the list of inflationary like cosmologies. Also, since inflation might be independent of initial conditions and be an attractor in initial condition space [15], bulk viscosity driven inflation might suggest that quantum effects through vacuum polarization washes out any dependence of the initial conditions. Certainly if all models of inflation contain a portion of the true initial state of the universe then the cases in this paper only substantiate our belief in a cosmic no-hair theorem and the "attractor" theory of inflation.

2. Bulk viscosity driven inflation

We begin our analysis of assuming a homogeneous, isotropic Robertson–Walker metric

$$(\mathrm{d}S)^2 = \mathrm{d}t^2 - R^2\left(\frac{\mathrm{d}r^2}{1-Kr^2} + r^2(\mathrm{d}\theta)^2 + r^2\sin^2\theta(\mathrm{d}\phi)^2\right) \tag{1}$$

where $K = 0, +1, -1$, $C = 1$ and R is the scale factor.

For the Ricci components we have

$$R_{00} = 3\frac{R''}{R} \tag{2}$$

$$R_{ij} = \left[\frac{R''}{R} + 2\left(\frac{R'}{R}\right)^2 + \frac{2K}{R^2}\right]g_{ij}.$$

The matter content we assume is described by a viscous fluid [16] wherein

$$T_{\mu\nu} = (\bar{P} + \varepsilon)U_\mu U_\nu - g_{\mu\nu}\bar{P} \tag{3}$$

where

$$\bar{P} = P - \xi U^a_{;a} \tag{4}$$

Here ξ is the bulk viscosity coefficient and $U^a_{;a}$ is the expansion.

For the Einstein equations we have

$$R_{\mu\nu} = -k\left[T_{\mu\nu} - \frac{1}{2}Tg_{\mu\nu}\right]\left(k = \frac{8\pi G}{C^4}, C = 1\right). \tag{5}$$

The components of (3) are

$$T_{00} = \varepsilon, \tag{6}$$

$$T_{ij} = -\bar{P}g_{ij} = -\left(P - \frac{\xi 3R'}{R}\right)g_{ij}.$$

For the trace of $T_{\mu\nu}$ we have

$$T = T_{\mu\nu}g^{\mu\nu} = \varepsilon - 3\bar{P} = 9\xi\frac{R'}{R}. \tag{7}$$

Here we have assumed the radiative equation of state to be

$$P = \frac{\varepsilon}{3}.$$

The Einstein equations corresponding to (5) are for $K = 0$ (spatially flat)

$$3\frac{R''}{R} = -k\left[\varepsilon - \frac{1}{2}\left(9\xi\frac{R'}{R}\right)\right] \tag{8}$$

$$\frac{R''}{R} + 2\left(\frac{R'}{R}\right)^2 = -k\left[-P + 3\xi\frac{R'}{R} - \frac{1}{2}\left(9\xi\frac{R'}{R}\right)\right] \tag{9}$$

To study the implications of (8) and (9) using the radiative question of state we now insert the functional dependence of ξ on factors that are phenomenological representations of the underlying microphysics. In this regard Barrow [17] has pointed out that particle production due to the non-adiabatic decaying of the field driving slow rollover inflation can macroscopically be described by the viscous cosmological model of Murphy [18] with a bulk viscosity coefficient proportional to the energy density ($\xi \propto \varepsilon$). Along a somewhat similar line of reasoning Turok [19] has proposed a bulk viscosity coefficient proportional to $\varepsilon^{3/2}$ to model string loop production in the early universe and Barrow [20] has discussed the general case $\xi = C\varepsilon^n$ with the result that for $n > 1/2$ the solutions for a Friedman–Walker flat universe start out in a deSitter phase and evolve into a power law expansion in t for late times. As mentioned in [10], Gurovich and Starobinsky have shown that vacuum polarization in a gravitational field can be modelled by a bulk viscosity coefficient dependent on the curvature squared. Such a process would be significant when the curvature is large, in particular near the Planck era. We will in what follows study the two cases (energy density dependent, curvature squared dependent bulk viscosity) and derive the inflation rates in each case for a spatially flat universe. We thus write for the two cases

$$\xi = C_1(R_S)^2, \quad \xi = C_2\varepsilon \text{ for a spatially flat universe } (K = 0)$$

and study the evolution of the scale factor for a flat universe for each case.

(Here R_s = curvature scalar.)

Case I

From (8) and (9) we have

$$6\frac{R''}{R} + 6\left(\frac{R'}{R}\right)^2 = \frac{k9\xi R'}{2R} - \frac{9\xi kR'}{R} + \frac{27k\xi R'}{2R} = 9\xi k\frac{R'}{R} \tag{10}$$

From (2) we have

$$R_S = R_{\mu\nu}g^{\mu\nu} = 6\frac{R''}{R} + 6\left(\frac{R'}{R}\right)^2. \tag{11}$$

Setting $\xi = C_1(R_s)^2$ (C_1 = constant) and inserting the inflationary solution $R = R_0e^{\alpha t}$ into (10) we have

$$12\alpha^2 = 9kC_1(144\alpha^4)\alpha \tag{12}$$

$$\alpha = \left(\frac{1}{108C_1k}\right)^{1/3} \tag{13}$$

Case II

Upon dividing (9) by (10) we have using

$$P=\frac{\varepsilon}{3},\quad \xi=C_2\varepsilon,$$

$$\frac{\dfrac{3R''}{R}}{\dfrac{R''}{R}+2\left(\dfrac{R'}{R}\right)^2}=\frac{1-\dfrac{1}{2}9C_2\dfrac{R'}{R}}{-\dfrac{1}{3}+3C_2\dfrac{R'}{R}-\dfrac{9}{2}C_2\dfrac{R'}{R}}. \tag{14}$$

Inserting $R=R_0e^{\alpha t}$ into (14) we have

$$\frac{3\alpha^2}{3\alpha^2}=\frac{1-\dfrac{9C_2\alpha}{2}}{-\dfrac{1}{3}-\dfrac{3}{2}C_2\alpha},$$

$$\alpha=\frac{4}{9C_2}. \tag{15}$$

Equations (13) and (15) can be written in CGS units as

$$\alpha_1=\left[\frac{C^7}{8\pi G(108C_1)}\right]^{1/3},\quad \alpha_2=\frac{4C}{9C_2}. \tag{16}$$

The dimensional dependence of C_1, C_2 on the fundamental units of mass, length and time can be computed using

$$[R_S]=\left[\frac{1}{L^2}\right],\quad [\varepsilon]=\left[\frac{mL^2}{T^2L^3}\right],\quad [U^a_{;a}]=\left[\frac{1}{L}\right],$$

as

$$[C_1]\left[\frac{1}{L^5}\right]=\left[\frac{mL^2}{T^2L^3}\right],\quad [C_1]=\left[\frac{mL^4}{T^2}\right], \tag{17}$$

in a like manner

$$[C_2]=[L]. \tag{18}$$

Numerically we have no way to date of calculating C_1, C_2. We would expect however that if the bulk viscosity coefficients could be calculated from a quantum gravitational microphysical model that C_1, C_2 would differ greatly due to the fact that the energy scale is so high (Planck scale) and any microphysical calculation based on quantum gravity may generate large corrections due to possible wormhole effects [21] and instanton effects that would cause large differences in C_1, C_2.

3. Conclusion

The above analysis has demonstrated that the two cases ($\xi=C_1R_S^2, \xi=C_2\varepsilon$) possess inflationary-like solution for a radiative equation of state for a spatially flat universe

($K = 0$). Actually the existence of such solutions can be traced to the homogeneous nature of the equations in the spatially flat case. As mentioned above, it would be of interest to ask if C_1 C_2 could be calculated from a quantum gravitational model of particle creation, string creation and gravitational vacuum polarization around the Planck era. The problem with any such calculation would be that it would be subject to the same scrutiny that all quantum gravitational calculations are subjected to because of the lack of a firm basis of quantum gravity based on unitarity, renormalizability and convergence of perturbative approach [22]. Actually, Padmanabhan and Chitre [23] have previously studied a bulk viscous universe with $K = 0$ and demonstrated that inflation results for a constant bulk viscosity coefficient. They also make the point, that in a microphysical sense, bulk viscosity can phenomenologically represent the viscous drag on superconducting strings in a magnetic field, the drag brought about in monopole-monopole interactions, the dissipative force due to particle creation, and the viscous drag from photon viscosity and neutrino viscosity. It would also be of interest to ask if the above inflationary solutions that we derived are stable to higher order curvature corrections to the action since certainly the curvature is high near the Planck era. [24] Lastly the subject of 'fragility' has recently surfaced in general relativity as a probe to the general problem of general relativistic stability and it would be of interest to ask if the above inflationary solutions are stable in this sense [25].

Acknowledgement

The author would like to thank the Physics Departments at Williams College and Harvard University for the use of their facilities.

References

[1] E W Kolb and M S Turner, The early universe (Addison Wesley, Reading, MA 1990) 261
[2] A Guth, *Phys. Rev.* **D23**, 347 (1981)
[3] A Coleman, *Phys. Rev.* **D15**, 2929 (1977)
[4] P J Steinhardt and M S Turner, *Phys. Rev.* **D29**, 2162 (1984)
[5] A D Linde, *Phys. Lett* **B129**, 177 (1983)
[6] E W Kolb, D S Salopek and M S Turner, *Phys. Rev.* **D42**, 3925 (1990)
[7] T A Verwimp and D K Callebaut, *Proc. of 26th Liege Int. astrophysics colloquium* (The Univ. of Liege, Belgium) July 1–4, (1986)
[8] W M Swen, *Proc. of 26th Liege Int. astrophysics colloquium* (The Univ. of Liege, Belgium) July 1–4, 1986
[9] C Wolf, *Hadronic J.* **10**, 59 (1987)
[10] V Z Gurovich and A Starobinsky, *Sov. Phys.* (JETP) **50**, 844 (1979)
[11] C Wolf, *Phys. Lett.* **A127**, 129 (1988)
[12] F Hoyle and J V Narlikar, *Proc. R. Soc.* **A273**, 1 (1963)
[13] G W Gibbons and S W Hawking, *Phys. Rev.* **D15**, 2783 (1977)
[14] S W Hawking and I Moss, *Phys. Lett.* **B110**, 35 (1982)
[15] D S Goldwirth, *Phys. Lett.* **B243**, 41 (1990)
[16] A Banerjee, S B Duttachoudhury and S B Sanyal, *Gen. Relativ. Gravit.* **18**, 461 (1986)
[17] J D Barrow, *Phys. Lett.* **B180**, 335 (1986)
[18] G L Murphy, *Phys. Rev.* **D48**, 4231 (1973)
[19] N Turok, *Phys. Rev. Lett.* **60**, 549 (1988)
[20] J D Barrow, *The formation and evolution of cosmic strings*, edited by G Gibbons, S Hawking and T Vachaspati (Cambridge Univ. Press, 1990)

[21] P F Gonzales-Diaz, *Nuovo Cimento* **B106**, 335 (1991)
[22] N D Birrell and P C W Davies, *Quantum fields in curved space* (Cambridge Univ. Press, Cambridge, MA 1982)
[23] T Padmanabhan and S M Chitre, *Phys. Lett.* **A120**, 433 (1987)
[24] E W Kolb and M S Turner. *The early universe* (Addison Wesley, Reading, MA 1990) p. 447
[25] A A Coley and R K Tavakol, *Gen. Relativ. Gravit.* **24**, 835 (1992)

PRAMANA
— journal of
physics

© Printed in India

Vol. 41, No. 2,
August 1993
pp. 145–149

${}^{6}_{\Lambda\Lambda}$He hypernucleus in $\alpha + 2\Lambda$ cluster model

MAHMOOD MIAN
Department of Applied Physics, Guru Nanak Dev University, Amritsar 143 005 India

MS received 7 October 1992; revised 12 April 1993

Abstract. The binding energy of the double hypernucleus ${}^{6}_{\Lambda\Lambda}$He is calculated in $\alpha + 2\Lambda$ cluster model using the method of translation invariant basis TIMO. As regards the required interaction potentials we use a density dependent effective ΛN force and a gaussian form for $\Lambda\Lambda$ potential. With these interactions a very reasonable value of $B_{\Lambda\Lambda}$ is obtained if the oscillator states up to the excitation quantum number $N = 12$ are taken into account in the expansion of wavefunction of the hypernucleus. This value of N is much smaller than that obtained in an earlier study. This lowering in N value is attributed to a much better choice of ΛN potential used in the present study.

Keywords. Double hypernucleus; translation invariant basis; ΛN interaction.

PACS No. 21·80

The binding energies of two double hypernuclei ${}^{10}_{\Lambda\Lambda}$Be and ${}^{6}_{\Lambda\Lambda}$He have been the only source of information on $\Lambda\Lambda$ interaction. A large number of binding-energy calculations [1–7] have been made to obtain information about $\Lambda\Lambda$ interaction which is essential for a general understanding of baryon–baryon interactions. The determination of $\Lambda\Lambda$ interaction obviously needs an accurate method of investigating the structure of hypernuclei and a better knowledge of ΛN and NN interactions. The required interactions [8, 9] are now known to some accuracy. Dzhibuti *et al* have studied the $\Lambda\Lambda$ hypernucleus ${}^{6}_{\Lambda\Lambda}$He in $\alpha + 2\Lambda$ model using the method of translational-invariant oscillator basis TIMO and employing the gaussian form for both the $\Lambda\Lambda$ and the ΛN interaction potentials. Their conclusion is that the wavefunction of this system converges much faster than for nuclei and the states up to the excitation quantum number $N = 20$ are needed to obtain the correct value of $B_{\Lambda\Lambda}$. The fast convergence of the wavefunction is attributed to much shorter range of ΛN interaction. We do agree with this conclusion but we strongly feel that in order to check the convergence of the basis, a more realistic ΛN interaction should be used.

Keeping this in mind we calculate the binding energy of ${}^{6}_{\Lambda\Lambda}$He in the same approach and with the same $\Lambda\Lambda$ potential. For ΛN interaction, however, we use a more realistic density dependent effective ΛN potential. The mathematical formulation is exactly the same as in ref. [7] and is presented here again in the subsequent paragraphs. Even our notations are the same as those in ref. [7].

The mutual motion of three particles of unequal masses m_1, m_2 and m_3 in the field of a harmonic oscillator of frequency ω is described by the Jacobi coordinates

$$X_1^{(i)} = (-1)^{i+k}\left[\frac{m_i\mathbf{r}_i + m_j\mathbf{r}_j}{m_i + m_j} - \mathbf{r}_k\right],$$

$$X_2^{(i)} = (-1)^{i+j}(\mathbf{r}_j - \mathbf{r}_i), \quad (i,j,k) = (1,2,3). \tag{1}$$

These coordinates are converted into dimensionles Jacobi coordinates:

$$x_1^{(i)} = X_1^{(i)} \Big/ \sqrt{\frac{\hbar}{\mu_1^{(i)}\omega}} \quad x_2^{(i)} = X_2^{(i)} \Big/ \sqrt{\frac{\hbar}{\mu_2^{(i)}\omega}} \tag{2}$$

where

$$\mu_1^{(i)} = \frac{m_i(m_i + m_j)}{M}, \quad \mu_2^{(i)} = \frac{m_i m_j}{m_i + m_k}$$

$$M = m_i + m_j + m_{k'} \quad (i,j,k) = (1,2,3).$$

We can go from set $(x_1^{(i)}, x_2^{(i)})$ to the set $(x_1^{(j)}, x_2^{(j)})$ by means of the following unitary transformation:

$$\begin{aligned} x_1^{(i)} &= a_{ij} x_1^{(j)} + b_{ij} x_2^{(j)}, \\ x_2^{(i)} &= (-1)^{i+j+1} b_{ij} x_1^{(j)} + (-1)^{i+j} a_{ij} x_2^{(i)}, \end{aligned} \tag{3}$$

where $a_{ij}^2 + b_{ij}^2 = 1$, and a_{ij} and b_{ij} are related with the particle masses by following relations

$$\begin{aligned} a_{ij} &= (-1)^{j+k+1} \left[\frac{m_i m_k}{(m_i + m_j)(m_j + m_k)} \right]^{1/2}, \\ b_{ij} &= \left[\frac{m_j M}{(m_i + m_j)(m_j + m_k)} \right]^{1/2}, \quad (i,j,k) = (1,2,3). \end{aligned} \tag{4}$$

The Hamiltonian of the system is

$$H = \frac{\hbar\omega}{2} \sum_{s=1}^{2} [\mathbf{p}_{x_s^{(i)}}^2 + (x_s^{(i)})^2]$$

The wavefunction $\psi(x_1^{(i)}, x_2^{(i)})$ which is the solution of equation

$$H\psi(x_1^{(i)}, x_2^{(i)}) = (N+3)\hbar\omega\psi(x_1^{(i)}, x_2^{(i)}) \tag{5}$$

where

$$N = 2\,(n_1 + n_2) + l_1 + l_2 \tag{6}$$

is the number of the oscillator exitation quanta, is characterized by L and m.

$$\begin{aligned} \psi(x_1^{(i)}, x_2^{(i)}) &= [\langle x_1^{(i)} | n_1 l_1 m_1 \rangle \langle x_2^{(i)} | n_2 l_2 m_2 \rangle]_m^L \\ &= |n_1 l_1 (x_1^{(i)}) n_2 l_2 (x_2^{(i)}) : Lm\rangle = [n_1 l_1 n_2 l_2]_m^L, \end{aligned} \tag{7}$$

where $\langle x_s^{(i)} | n_s l_s m_s \rangle = R_{n_s} l_s(x_s^{(i)})\, Y_{l_s} m_s(\hat{x}_s^{(i)})$, $s = 1, 2$, $i = 1, 2, 3$ are single particle oscillator functions.

The wavefunctions $\psi(x_1^{(i)}, x_2^{(i)})$ transform under unitary transformation (3) with Talmi–Moshinsky–Smirnov coefficients (TMSC) [10, 11]

$$\begin{aligned} |n_1 l_1 (x_1^{(i)}) n_2 l_2 (x_2^{(i)}) : Lm\rangle &= \sum_{\gamma'} \left\langle n_1 l_1 n_2 l_2 : L \left| \frac{a_{ij}^2}{b_{ij}^2} \right| n'_1 l'_1 n'_2 l'_2 : L \right\rangle \\ &\quad |n'_1 l'_1 (x_1^{(j)}) n'_2 l'_2 (x_2^{(j)}) : Lm\rangle, \end{aligned} \tag{8}$$

where

$$\left\langle n_1 l_1 n_2 l\colon L \left| \frac{a_{ij}^2}{b_{ij}^2} \right| n'_1 l'_1 n'_2 l'_2\colon L \right\rangle = \left\langle \gamma\colon L \left| \frac{a_{ij}^2}{b_{ij}^2} \right| \gamma'\colon L \right\rangle - \text{TMSC},$$

These orbital functions are coupled to spin-isospin functions of the three particles to obtain the complete set of translation-invariant oscillator functions:

$$|NLSJTM_T\rangle = [[n_1 l_1 n_2 l_2]^L [[\sigma_1 \sigma_2]^{S_{12}} \sigma_3]^S]]^J [[\tau_1 \tau_2]^{T_{12}} \tau_3]^T. \tag{9}$$

The wavefunction of hypernucleus designated by the quantum numbers J^Π, T and M_T can be expanded in terms of TIMO basis functions

$$\psi(\mathbf{r}_1, \mathbf{r}_2, \mathbf{r}_3) = |J^\Pi T M_T\rangle = \sum_{\substack{NLSn_1 l_1 \\ n_2 l_2}} C_{NLS}^{n_1 l_1 n_2 l_2} |NLSJTM_T\rangle$$

$$= \sum_{NLS\gamma} C_{NLS}^{\gamma} |NLSJTM_T\rangle = \sum_i C_i |i\rangle. \tag{10}$$

The expansion coefficients C_{NLS}^{γ} are determined variationally. For the ground state of $^{6}_{\Lambda\Lambda}$He, $J^\Pi = 0^+$, $S = T = M = M_T = 0$.

To determine the binding energy we diagonalize the energy matrix constructed in the above basis:

$$\langle i|H|k\rangle = \langle i|T|k\rangle + \langle i|V|k\rangle \tag{11}$$

where T and V are the kinetic and potential energy operators, respectively.

The potential energy matrix elements is expressed as

$$\langle \Psi(\mathbf{r}_1, \mathbf{r}_2, \mathbf{r}_3)| V |\Psi(\mathbf{r}_1, \mathbf{r}_2, \mathbf{r}_3)\rangle = \sum_{\substack{NLS\gamma \\ N'L'S'\gamma'}} C_{NLS}^{\gamma} C_{N'L'S'}^{\gamma'}$$

$$\times \sum_{\gamma''\gamma'''j} \left\langle \gamma\colon \left| L \left| \frac{a_{ij}^2}{b_{ij}^2} \right| \gamma''\colon L \right. \right\rangle \left\langle \gamma'\colon L' \left| \frac{a_{ij}^2}{b_{ij}^2} \right| \gamma'''\colon L' \right\rangle$$

$$\times \langle [|n''_1 l''(\mathbf{x}_1^{(j)}) n''_2 l''_2(\mathbf{x}_2^{(j)})\colon Lm\rangle [S_{12}\sigma_3]^S]^J [T_{12}\tau_3]^T$$

$$\times V(r_0^{(j)} x_2^{(j)}) | [|n'''_1 l'''_1(\mathbf{x}_1^{(j)}) n'''_2 l'''_2(\mathbf{x}_2^{(j)})\colon L'm'\rangle [S'_{12}\sigma_3]^S]^j [T_{12}\tau_3]^T\rangle. \tag{12}$$

We write the potential energy function as

$$V(r_0^{(j)} x_2^{(j)}) = \sum_{\lambda=0,1,2} V_\lambda^{l_3}(r_0^{(j)} x_2^{(j)}) (L^{(\lambda)} S^{(\lambda)}). \tag{13}$$

Then the right hand side of the above equation becomes

$$\langle [|n_1 l_1(\mathbf{x}_1^{(j)}) n_2 l_2(\mathbf{x}_2^{(j)})\colon Lm\rangle [S_{12}\sigma_3]^S]^J [T_{12}\tau_3]^T|$$

$$\times \sum_\lambda V_\lambda^{l_3}(r_0^{(j)} x_2^{(j)}) (L^{(\lambda)} S^{(\lambda)}) | [|n'_1 l'_1(\mathbf{x}_1^{(j)}) n'_2 l'_2(\mathbf{x}_2^{(j)})\colon L'm'\rangle$$

$$\times [S'_{12}\sigma_3]^S]^J [T_{12}\tau_3]^T\rangle$$

$$
\begin{aligned}
&= \delta_{l_1 \cdot l'_1} \delta_{S_{11} S_{12'}} \delta_{n_1 n_{1'}} [(2L+1)(2L'+1)(2S+1)(2S'+1)]^{1/2} \\
&\quad \times \sum_{\lambda=0,1,2} (-1)^{\lambda} W(JSL'\lambda|LS')\, W(l'_1 l l'_2 \lambda|l_2\, L')\, W(\sigma_3 S' S_{12} \lambda|S'_{12} S) \\
&\quad \times \langle l_2 \| L^{(\lambda)} \| l'_2 \rangle \langle S_{12} \| S^{(\lambda)} \| S'_{12} \rangle \\
&\quad \times \langle n_2 l_2 (\mathbf{x}_2^{(j)}) | V_{\lambda}^{l_s}(r_0^{(j)} x_2^{(j)}) | n'_2 l'_2 (\mathbf{x}_2^{(j)}) \rangle, \qquad (14)
\end{aligned}
$$

Where W (abcd|ef) are the Racah coefficients.

The ground state $B_{\Lambda\Lambda}$ of ${}^{6}_{\Lambda\Lambda}$He is obtained by diagonalizing the energy matrix. For $\Lambda\Lambda$ interaction potential we use the same gaussian potential which was used in [7]. For ΛN interaction however we use a density dependent effective ΛN force [8].

$$
V_{\Lambda N}(|\mathbf{r}-\mathbf{r}'|;\rho) = \bar{V}_0 \frac{1}{(\Pi d^2)^{3/2}} \exp[-(\mathbf{r}-\mathbf{r}')^2/d^2] \left[1 - \beta\rho^{2/3}\left(\frac{\mathbf{r}+\mathbf{r}'}{2}\right)\right]
$$

The $\Lambda - \alpha$ potential $V_{\Lambda}(r)$ is obtained by folding this potential into the density of α particle [8] $\rho(\mathbf{r})$

$$
V_{\Lambda}(r) = \bar{V}_0 \int \frac{\exp[-(\mathbf{r}-\mathbf{r}')^2/d^2]}{(\Pi d^2)^{3/2}} \left[1 - \beta\rho^{2/3}\left(\frac{\mathbf{r}+\mathbf{r}'}{2}\right)\right] \rho(\mathbf{r}')\mathrm{d}\mathbf{r}'. \qquad (15)
$$

This integral is evaluated in momentem space. The $V_{\Lambda}(r)$, after reverting it back to coordinate space, reads as

$$
V_{\Lambda}(r) = \frac{\bar{V}_0}{2\Pi^2} \int F(q) \exp\left[-\frac{q^2 d^2}{4}\right] q^2 j_0(q_0 r)\mathrm{d}q. \qquad (16)
$$

where $j_0(qr)$ is the spherical based function of order zero and

$$
F(q) = \int \exp(i\mathbf{q}\cdot\mathbf{r})\rho(\mathbf{r})[1 - \beta\rho^{2/3}(\mathbf{r})]\mathrm{d}\mathbf{r}. \qquad (17)
$$

The best fitted values of parameters $\bar{V}_0$, β and d are $\bar{V}_0 = 297{\cdot}86$ MeV fm^3, $\beta = 1{\cdot}92$ fm^2, $d = 0{\cdot}729$ fm.

Using the above potentials we compute the ground state binding energy of ${}^{6}_{\Lambda\Lambda}$He by varying $\hbar\omega$ for a fixed value of N and then repeating the calculations for different values of N until the system becomes bound. We find that for smaller N (say $N = 6$) the system is unbound and the energy is dependent on $\hbar\omega$. With increasing N, however, this dependence of energy on $\hbar\omega$ becomes weaker and weaker and at $N = 12$, the system becomes bound and the energy of system becomes almost independent of $\hbar\omega$. The predicted energy at $N = 12$ is about 10·72 MeV which compares well with the experimental [refs 12–14] value 10·9 ± 0·6 MeV.

Thus we see that the TIMO basis converges much faster with a density dependent effective ΛN interaction than with a gaussian interaction. This study also indicates that in order to further investigate the features of this model one should use a range of phenomenological $\Lambda\Lambda$ potentials based on meson exchange models and take into account the internal structure of α particle.

References

[1] R H Dalitz and G Rajasekaran, *Nucl. Phys.* **50**, 450 (1964)
[2] Y C Tang and R C Herndon, *Phys. Rev.* **138**, B637 (1965)
[3] A R Bodmer and S Ali, *Phys. Rev.* **138**, B644 (1965)
[4] S Ali and A R Bodmer, *Phys. Lett.* **B24**, 343 (1967)
[5] A R Bodmer, Q N Usmani and J Carlson, *Nucl. Phys.* **A422**, 510 (1984)
[6] R I Dzhibuti and M Tsiklauri Sh, *Yad. Fiz.* **39**, 1115 (1984)
[7] R I Dzhibuti, T Ya Mikhelashvili and K V Shitikova, *Yad. Fiz* **45**, 670 (1987)
[8] Mahmood Mian, *Phys. Rev.* **C35**, 1463 (1987)
[9] A R Bodmer, Q N Usmani and J Carlson, *Phys. Rev.* **C29**, 684 (1984)
[10] Yu F Smirnov, *Nucl. Phys.* **27**, 177 (1961)
[11] V G Neudachin and Yu F Smirnov, *Nuclear clusters in light nuclei* (in Russian), Moscow, Nauka (1969)
[12] M Danysz *et al*, *Nucl. Phys.* **49** 121 (1963)
M Danysz *et al*, *Phys. Rev. Lett.* **11**, 29 (1963)
[13] J Prowse, *Phys. Rev. Lett.* **17**, 782 (1966)
[14] K Paniewski and D Zieminska, *Proc. conf. on kaon-nuclear interaction and hyperceli Zvenigorod* 1977 (Moscow, 1979) p. 33

PRAMANA
— journal of
physics

© Printed in India

Vol. 41, No. 2,
August 1993
pp. 151–162

Deuteron-induced reaction studies of the nuclear structure of ^{178}Hf

RAYMOND K SHELINE, MICHAEL M MINOR, PRAKASH C SOOD* and DENNIS G BURKE†
Departments of Chemistry and Physics, Florida State University, Tallahassee, FL 32306, USA
*Department of Physics, Banaras Hindu University, Varanasi, India 221 005
†Department of Physics and Astronomy, McMaster University, Hamilton, Ontario, L8S 4M1, Canada

MS received 11 March 1993; revised 30 June 1993

Abstract. The level structure of ^{178}Hf is interpreted on the basis of the population of the states following ^{178}Hf (d, d'), ^{177}Hf (d, p) and ^{179}Hf (d, t) reactions. Evidence for quadrupole and octupole vibrational bands and unmixed and intermixed two-quasiparticle configurations is presented.

Keywords. ^{178}Hf, vibration band; two quasiparticle configurations; deuteron-induced reaction studies.

PACS Nos 25·45; 27·70

1. Introduction

The nucleus ^{178}Hf has been studied extensively especially by thermal neutron capture and by average resonance neutron capture [1]. This has led to a detailed set of levels with assigned spins and parities which have been grouped into rotational bands [2]. Often vibrational or configurational assignments for these bands are lacking or uncertain. This work attempts to remedy this situation by reporting on ^{178}Hf (d, d') studies to look especially for collective vibrations, and ^{177}Hf (d, p) and ^{179}Hf (d, t) reactions to look for the characteristic differential cross-sections ("finger prints") of various configurations.

It is interesting and probably unique to this region of the nuclear periodic table that almost all of the low-lying two quasineutron configurations have corresponding low-lying two quasiproton configurations with the same pairs of Gallagher–Moszkowski K values. As shown in table 1 even the energy ordering of K values is the same. This implies that often the low-lying rotational bands will be admixtures of two quasineutron and two quasiproton configurations. Evidence for this was first observed by Gallagher *et al* [3] who found two excited states in ^{178}Hf at 1148 and 1480 keV following the decay of the high spin 2·1 h ^{178}Ta activity. The spins and parities were determined to be 8^- for both levels and the states were interpreted as highly admixed two-proton and two-neutron configurations.

Table 1. Similar Gallagher–Moszkowski doublets resulting from the low lying two-quasiproton and two-quasineutron configurations in ^{178}Hf. The identical band quantum numbers K_S (for the singlet with antiparallel spins) and K_T (for the triplet with parallel spins) of each Gallagher–Moszkowski doublet with the lower lying K_S underlined is shown in the centre.

Two-quasiproton configurations	K_S, K_T	Two-quasineutron configurations
$\pi\pi[404\downarrow] \pm [514\uparrow]$	$\underline{8}^-, 1^-$	$\nu\nu[514\downarrow] \pm [624\uparrow]$
$\pi\pi[404\downarrow] \pm [402\uparrow]$	$\underline{6}^+, 1^+$	$\nu\nu[514\downarrow] \pm [512\uparrow]$
$\pi\pi[404\downarrow] \mp [541\downarrow]$	$\underline{3}^-, 4^-$	$\nu\nu[514\downarrow] \pm [651\downarrow]$
$\pi\pi[404\downarrow] \mp [411\downarrow]$	$\underline{3}^+, 4^+$	$\nu\nu[514\downarrow] \mp [521\downarrow]$
$\pi\pi[404\downarrow] \pm [523\uparrow]$	$\underline{7}^-, 0^-$	$\nu\nu[514\downarrow] \mp [633\uparrow]$
$\pi\pi[514\uparrow] \mp [402\uparrow]$	$\underline{2}^-, 7^-$	$\nu\nu[624\uparrow] \mp [512\uparrow]$
$\pi\pi[514\uparrow] \pm [411\downarrow]$	$\underline{5}^-, 4^-$	$\nu\nu[624\uparrow] \pm [521\downarrow]$
$\pi\pi[514\uparrow] \mp [523\uparrow]$	$\underline{1}^+, 8^+$	$\nu\nu[624\uparrow] \mp [633\uparrow]$
$\pi\pi[514\uparrow] \pm [541\downarrow]$	$\underline{5}^+, 4^+$	$\nu\nu[624\uparrow] \pm [651\downarrow]$

2. Experimental methods and results

Deuteron-induced reactions were studied by bombarding thin vacuum-evaporated or isotope-separated targets (prepared on the Florida State University Isotope Separator) with well collimated 12 MeV deuterons from the Florida State University Tandem van de Graaff Accelerator. A list of the various reactions and the corresponding targets used in these experiments is given in table 2. Beam currents varied from 0·3 to 1·5 μA. The light outgoing reaction particles were momentum analyzed with the 6/5 scale Florida State University Browne-Beuchner magnetic spectrograph. Charged particles of a given focused momentum were detected by sets of four Kodak NTA 50 micron nuclear plates affixed to the focal curve of the spectrograph by a removable plate holder. The plates were covered with aluminium foil during the (d, p) exposures to stop inelastically scattered deuterons. The developed plates were scanned under a microscope in 1/2 mm × 8 mm strips. The numbers of tracks per 1/2 mm strip were recorded as a function of the distance along the calibrated focal curve of the spectrograph.

2.1 *Inelastic deuteron scattering experiments*

The reaction ^{178}Hf (d, d') was studied at laboratory angles of 60°, 70°, 80° and 100°. These spectra were accumulated simultaneously with the ^{178}Hf (d, t) spectra. The elastic and inelastic deuteron spectrum taken at 100° is shown in figure 1. The corresponding excitation energies and their respective intensities are given in table 3. The excitation energies quoted in table 3 correspond to the more accurate energies given by Browne [2]. Elastic deuteron groups from light impurities (e.g. ^{37,35}Cl) have been identified by their large kinematic shifts.

2.2 *Stripping and pick-up reactions*

The reaction ^{177}Hf (d, p) was studied at laboratory angles 35°, 45°, 55°, 65°, 85° and 95°. The spectrum at 65° with respect to the incident beam is shown in figure 2. The

Table 2. Nuclear reactions, angles and targets used in studying ^{178}Hf.

Reaction	Angle	Target
^{177}Hf (d, p)	55° 65°	Evaporated Oxide ~ 75 μg/cm^2 on C ^{176}Hf 0·76% ^{177}Hf 91·67% ^{178}Hf 4·85% ^{179}Hf 0·92% ^{180}Hf 1·80%
^{177}Hf (d, p)	35° 45° 85° 95°	Direct deposition on F.S.U. Isotope Separator ~ 30 μg/cm^2 on C ~ 99% ^{177}Hf
^{179}Hf (d, t)	75° 85° 95°	Isotope separated ~ 10 μg/cm^2 on C ~ 99% ^{179}Hf
^{178}Hf (d, d)	60° 70° 80° 100°	Evaporated Oxide ~ 100 μg/cm^2 on C ^{177}Hf 2·1% ^{178}Hf 95·5% ^{179}Hf 1·2% ^{180}Hf 1·2%

a) Isotopic composition of the targets was furnished by the Isotopes Division of the Oak Ridge National Laboratory, Oak Ridge, Tennessee.

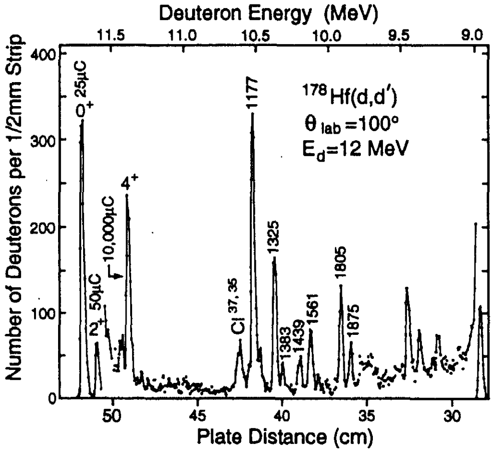

Figure 1. The deuteron spectrum observed at 100° with respect to the beam direction in the reaction ^{178}Hf (d, d') using 12·0 MeV deuterons. The energies of prominent peaks below 2 MeV are labeled by their energies in keV. Different total exposures are shown in microcoulombs (μC).

Table 3. Levels, assignments and differential cross-sections observed in the ^{178}Hf(d,d'), ^{177}Hf(d,p) and ^{179}Hf(d,t) reactions.

		(d,d') differential		(d,p) differential						(d,t) relative	
Excitation energy[a] (keV)	Assignment KJ^π	Cross-section (μb/sr)		Cross-section (μb/sr)						Cross-section	Configuration
		80°	100°	35°	45°	55°	65°	85°	95°	95°	
0	$0\,0^+$	$1{\cdot}35\times10^5$	$4{\cdot}5\times10^4$				~1				G.S. Band
93·2	$0\,2^+$	9700	4400	3			8	5	11	~3	G.S. Band
306·6	$0\,4^+$	94	72	4	9		5	4	6	7	G.S. Band
632·2	$0\,6^+$	~8	~6				3			5	G.S. Band
1058·6	$0\,8^+$						~1	~1			G.S. Band
1147·4	$8\,8^-$					~4	~3	3		5	$\nu\nu[514\downarrow]+[624\uparrow]_8+\pi\pi[404\downarrow]+[514\uparrow]_{8^-}$
1174·6	$2\,2^+$	220	120	b	15	26	29	13	12		γ-band
1199·4	$0\,0^+$			~5		~2	~3?	3			$K=0^+$ two-quasiparticle?
1260·3	$2\,2^-$									25	$K=2^-$; Oct.; $\nu\nu[624\uparrow]-[512\uparrow]_{2^-}$
1268·5	$2\,3^+$			24	31	31	21	14	14		γ-band
1276·7	$0\,2^+$	9									2^+ on 1199·4 keV $K=0^+$
1310·1	$1\,1^-$					7	3	~2	~2		$K=1^-$; Oct.; $\nu\nu[514\downarrow]-[624\uparrow]_{1^-}$
1322·5	$2\,3^-$	130	62							30	3^- on 1260·3 keV $K=2^-$
1362·6	$1\,2^-$					~2	5	4	6		2^- on 1310·1 keV $K=1^-$ and
1364·1	$8\,9^-$									20	9^- on 1147·1 keV $K=8^-$
1384·5	$2\,4^+$	18	15	10	11	15	14	7	11		γ-band
1409·4	$2\,4^-$									30	4^- on 1260·3 keV $K=2^-$
1433·6	$1\,3^-$	15	20	25?		3	4	4	3	23	3^- on 1310·1 keV $K=1^-$
1450·4	$0\,4^+$			~8			~2				4^+ on 1199·4 keV $K=0^+$
1479·0	$8\,8^-$						5	17	3	5	$\pi\pi[404\downarrow]+[514\uparrow]_{8^-}+\nu\nu[514\downarrow]+[624\uparrow]_{8^-}$
1496·5	$0\,2^+$	13									$K=0^+$, $\beta+$ pairing vib.?
1512·6	$2\,5^-$									(13)	5^- on 1260·3 keV $K=2^-$
1513·6	$0\,2^+$	17									$K=0^+$, $\beta+$ pairing vib.?
1513·8	$4\,4^+$			160	200	170	150	91	98		$\nu\nu[514\downarrow]+[510\uparrow]_{4^+}$
1533·2	$2\,5^+$			~15	~40	27	23	11	10		γ-band
1538·8	$1\,4^-$									10	4^- on 1310·1 keV $K=1^-$

1554·0	6 6^+		6		7	12	4			$\nu\nu[514\downarrow]+[512\uparrow]_{6^+}$
1561·5	(2) 2^+	28								2^+ unassigned
1601·5	8 10^+			10	7	9	5	3		10^- on 1147·1 keV $K=8^-$
1636·7	5 5^-								180	$\nu\nu[624\uparrow]+[521\downarrow]_{5^-}$
1640·5	4 5^+		110	110	120	100	69	70		5^+ on 1513·8 keV $K=4^+$
1648·8	2 6^-								~ 10	6^- on 1260·3 keV $K=2^-$
1697·5	8 9^-				7	6	3	8		9^- on 1479·0 keV $K=8^-$
1758·1	3 3^+		12	8	14	12	8	8		$\nu\nu[514\downarrow]-[521\downarrow]_{3^+}$
1781·3	5 6^-								25?	6^- on 1636·7 keV $K=5^-$
1788·6	4 6^+		14	38	17	c	21	18		6^+ on 1513·8 keV $K=4^+$
1803·4	3 3^-	42								$K=3^-$ Oct. Band
1808·3	(2) 2^+		24	24	26	29	18	22	20	2^+ unassigned
1862·2	3 3^+		150	170	240	150	150	120	40	$\nu\nu[514\downarrow]-[510\uparrow]_3$
1875[d]	(0 3)	24								tentative $K=0^-$ $J=3^-$ Oct.
1891·3	? 2^+		9	21	23	33	17	8		2^+ unassigned
1913·6	3 4^-		9	4	15	15				4^- on 1803·4 $K=3^-$
1953·1	3 4^+		130	160	230	150	120	110		$\{$ 4^+ on $K=3^+$ and 7^+ on $K=4^+$
1953·7	4 7^+									at 1862·2 and 1513·6 keV
2068·0	3 5^+		49	47	65	58	40	43		5^+ on 1862·2 keV $K=3^-$
2139[d]	(4 8^+)		15		23	18	3	6		tentative 8^+ on 1513·6 keV $K=4^+$

a. Ref. 1;
b. Obscured by impurity;
c. Partially obscured by edge of plate;
d. Energy uncertainty 5 keV

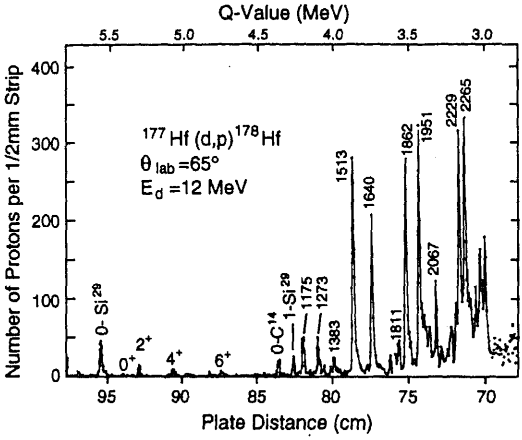

Figure 2. The proton spectrum observed in the reaction ^{177}Hf (d, p) ^{178}Hf using 12·0 MeV deuterons. The angle of observation was 65° with respect to the beam direction. Prominent peaks are labeled by their energies in keV. The ground state band is also labeled with the appropriate spins, and impurities are indicated.

excitation energies (corresponding to ref. 2) and differential cross-sections at each of the angles are given in table 3. The (d, p) Q-value to the ground state of ^{178}Hf is determined to be 5397 ± 10 keV which is in good agreement with the neutron separation energy of $7626{\cdot}34 \pm 0{\cdot}30$ keV [1] measured using the thermal neutron capture reaction.

The (d, t) reaction leading to ^{178}Hf has been studied at angles 75°, 85° and 95°. The ^{179}Hf target was prepared on the Florida State University Isotope Separator using natural $HfCl_4$. The ion source production efficiency was very poor resulting in an exceedingly thin target. No attempt was made to extract absolute cross-sections. The states observed at all three angles and the relative intensities at 95° are given in table 3. The ^{179}Hf (d, t) ^{178}Hf ground state Q-value is determined to be 153 ± 10 keV.

3. The ^{178}Hf level scheme and discussion

A level scheme for ^{178}Hf is presented in figure 3. It utilizes the extensive level structure observed in a large number of previous studies and summarized in Nuclear Data Sheets [2], but interprets the levels in terms of vibrational bands and two-quasiparticle configurations largely deduced from this research. No attempt is made to plot all levels previously observed unless they are part of rotational bands observed in this study, and no levels above ~2200 keV are considered. The levels populated in this research are shown bold with a triangle above the line to the right representing (d, p) population, below the line (d, t) population, and above the line to the left, (d, d') population. The level structure will be described in what follows in terms of the ground state rotational band, collective vibrational states and two-quasiparticle configurations, in that order.

The ground state rotational band is observed through spin 6^+ in the (d, d') reaction and tentatively through 8^+ in the (d, p) reaction.

The 2^+ gamma vibrational band head at 1174·6 keV is the most strongly populated state in the inelastic deuteron spectrum (figure 1), except for some members of the

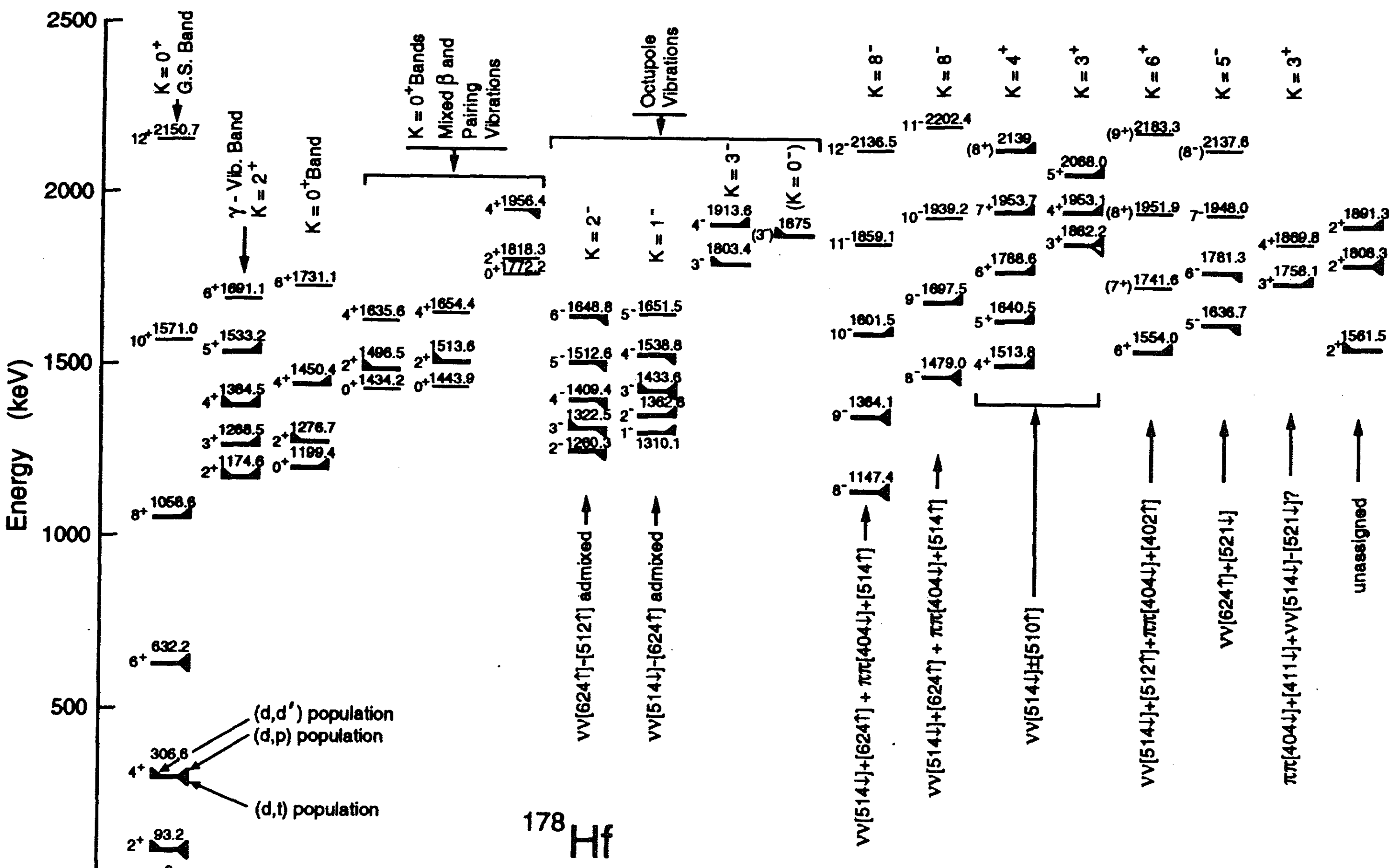

Figure 3. Level structure of ^{178}Hf as populated in (d, d'), (d, p) and (d, t) reactions. Only levels with flags on them were populated in this study. All other levels and the energies, rounded to 1 decimal, were taken from ref. [2].

Table 4. Differential cross-sections in the population of the gamma vibrational band in the (d,p) reaction in ^{178}Hf.

		Differential cross-sections (μb/sr)			
	I^{π}	2^+	3^+	4^+	5^+
Angle	Energy (keV)	1176	1269	1384	1532
45° Theory[a]		17·6	16·1	9·3	3·3
Expt.		15	31	11	~40[b]
65° Theory[a]		17·4	17·0	10·2	3·8
Expt.		29	21	14	23[b]

[a] Reference [4]; [b] see text

ground state rotational band. The 4^+ member of this band is also populated in the inelastic deuteron experiment, but, as expected for states of unnatural parity, there is no evidence for the 3^+ and 5^+ members of this band. All members of the gamma vibrational band from spins 2^+ to 5^+ are observed in the (d,p) reaction, as expected because of the importance of the $\nu\nu[514\downarrow]$–$[512\downarrow]$ configuration in the gamma vibration. Furthermore, their differential cross-sections agree moderately well with the calculations of Kern *et al* [4], although in general the experimental cross-sections are 35–40% higher than the calculations. This is shown in table 4. The level at 1532 keV, assigned as the 5^+ member of the gamma band, appears as a shoulder on the strong 1513 keV (d,p) peak, and therefore may be weaker than that indicated in table 4. It might also be pointed out that the experimental cross-sections to the gamma band are approximately twice as strong as the most recent calculations of Soloviev [5]. Perhaps the experimental data reflect that their calculated admixture of the $\nu\nu[514\downarrow]$–$[512\downarrow]$ configuration is too small.

The first $K^{\pi}=0^+$ band beginning at 1199·4 keV, which has been assigned as a beta vibrational band [6], is only populated sporadically and very weakly in these experiments. Thus, the inelastic deuteron experiment populates only the 2^+ member of this band, while the (d,p) experiment populates very weakly the 0^+ and 4^+ members of this band. It is also significant that the ^{180}Hf (p,t) experiment [7] which is known to pick out $K^{\pi}=0^+$ states does not populate this band. This may imply that the $K^{\pi}=0^+$ band at 1199·4 keV is neither the beta vibration, which should have been populated more strongly in the inelastic deuteron experiment, nor the pairing vibration which should have been populated strongly in the (p,t) reaction.

Two more $K^{\pi}=0^+$ bands are observed at 1434·2 and 1443·9 keV, respectively. The 2^+ members of each of these bands are populated in the deuteron inelastic scattering reaction, but are not populated in the (d,p) reaction. Furthermore, the 1443·9 and possibly the 1434·2 keV states are strongly populated in the (p,t) reaction [7]. In view of the 10 keV resolution in the (p,t) experiment, it is difficult to differentiate between these states which are only 9·7 keV apart. The combination of the nuclear reaction spectroscopic data suggests that the beta and pairing vibrations are highly mixed and occur at about 1·4 MeV as predicted by the calculations of Mikoshiba *et al* [8]. A fourth $K^{\pi}=0^+$ band is observed at 1772·2 keV and is strongly populated in the (p,t) reaction [7]. Presumably a part of the pairing strength is also present in this rotational band. It is quite clear from the above discussion that the four excited $K^{\pi}=0^+$ bands in ^{178}Hf below 2 MeV need to be better understood and require additional experimental and theoretical characterization.

The octupole vibrations are particularly prominent in the nuclear reaction spectroscopy of ^{178}Hf. The band head of the 2^- octupole is observed at 1260·3 keV and, as expected, the 3^- member at 1322·5 keV is strongly populated in the deuteron inelastic scattering reaction. Population of this rotational band is not observed in the (d, p) reaction. However, all members of the band from spin 2^- through 6^- are observed in the (d, t) reaction. This suggests that the $K^\pi = 2^-$ octupole band may have an appreciable two quasineutron component from the configuration $\nu\nu[624\uparrow]$–$[512\uparrow]$. The character of this configuration implies that it would be populated by the (d, t) reaction, but not by the (d, p) reaction. Indeed the most recent calculation of Soloviev [5] suggests a 79% admixture of the $\nu\nu[624\uparrow]$–$[512\uparrow]$ configuration in the 2^- octupole vibration. The $K^\pi = 1^-$ octupole vibrational band begins at 1310·1 keV. The 1433·6 keV 3^- member of this band is populated in the inelastic deuteron scattering experiment, but much more weakly than the 3^- member of the $K^\pi = 2^-$ octupole band. The $J^\pi = 1^-, 2^-$ and 3^- members of this band are populated in the (d, p) reaction but only the 3^- and 4^- states are populated in the (d, t) reaction. This suggests that the $K^\pi = 1^-$ octupole band may have an important contribution from the two-neutron quasiparticle state $\nu\nu[514\downarrow]$–$[624\uparrow]$ which should be populated by both (d, p) and (d, t) reactions. Although Soloviev [5] suggested that the 1^- octupole band is dominated by the two-proton configuration $\pi\pi[404\downarrow]$–$[514\uparrow]$, in a more recent publication [9] he has suggested the two-neutron configuration suggested above. The $K^\pi = 3^-$ octupole band head is observed at 1803·4 keV. It is strongly populated in the inelastic deuteron scattering experiment, but not in the (d, p) reaction. However, the 4^- state is indicated in the (d, p) reaction. A state at 1875 keV is populated in the (d, d') reaction and also in the (p, t) reaction [6] which may be the 3^- member of the $K^\pi = 0^-$ octupole vibration.

The calculations of Neergård and Vogel [10] for the energies and $B(E3)$ values for the octupole vibrations in ^{178}Hf are shown in table 5. It is clear that their calculations have reproduced, in a reasonable way, the systematics of the experimentally observed octupole bands in ^{178}Hf. Specifically the calculated energies agree reasonably well and the predicted larger $B(E3)$ values for the $K = 2^-$ and 3^- bands are reflected in the much larger inelastic deuteron cross-sections to the 3^- members of these bands.

The lowest two-quasiparticle states in ^{178}Hf occur as a result of the mixing of the

Table 5. The experimental and theoretical energies and the theoretical $B(E3)$ values for the octupole vibrational bands in ^{178}Hf.

	E(MeV)		B(E3)^b
K^π	Expt^a	Theor^b	$(10^{-74}\,\mathrm{cm}^6\cdot e^2)$
2^-	1·26	1·32	6·2
1^-	1·31	1·40	0·6
3^-	1·80	1·74	7·0
0^-	(1·77)^c	1·89	0·8

a. These results; b. Reference [10]; c. Energy of the $K^\pi = 0^-$, $J^\pi = 1^-$ state calculated assuming $\hbar^2/2\mathscr{I} = 10{\cdot}4$ keV and the observed 1875 keV state assumed to be the $K^\pi = 0^-$, $J^\pi = 3^-$ state.

two-quasiparticle neutron configuration $\nu\nu[514\downarrow]+[624\uparrow]$ and the two-proton configuration $\pi\pi[404\downarrow]+[514\uparrow]$, both of which yield $K=8^-$. The lowest 8^- state is observed at 1147·4 keV. The 8^-, 9^- and 10^- members of this rotational band are seen weakly in the (d,p) reaction, and the 8^- and 9^- members are observed in the (d,t) reaction. The second 8^- band head is observed at 1479·0 keV and is populated in both (d,p) and (d,t) reactions. The 9^- member of this $K=8^-$ band is also observed in the (d,p) reaction. Since the stripping and pick-up reactions can only populate the two-neutron quasiparticle states, the intensities of these two bands populated in such reactions can, in principle, provide a measure of their configuration mixings. Unfortunately the statistics on the population of these two states are inadequate to deduce a quantitative measure of this high degree of mixing.

The next two quasiparticle states observed in these studies result from the two-neutron configuration $\nu\nu[514\downarrow]\pm[510\uparrow]$. This configuration gives rise to a $K=4^+$ band expected to lie low and a $K=3^+$ band expected to lie somewhat higher in energy. Both of these bands are prominently observed in the data with the (d,p) populations going from a 4^+ state at 1513·8 keV all the way through a tentative 8^+ state at 2139 keV, not previously observed. Using the simple $I(I+1)$ dependent rotational energy formula, the observed 7^+-6^+ energy separation yields a moment of inertia parameter value of 11·8 keV; this, in turn, predicts the 8^+ level to occur around 2142 keV. Accordingly the observed peak at (2139 ± 5) keV in the (d,p) spectrum is tentatively identified as the 8^+ level of this band. The $K=3^+$ band beginning at 2862·2 keV is populated through the 5^+ state at 2068 keV. The apparent population of the 3^+ state at 1862·2 keV in the (d,t) reaction must be questioned. Presumably another state or an impurity must be involved since there is no reasonable $K=3^+$ configurational component which can be strongly (d,t) populated. Table 6 shows the comparison between the experimental and theoretical (d,p) cross-sections observed for these two bands taken from the thesis of Minor [11]. In view of the agreement we are quite confident in the assignment of this configuration. However, it should be noted that in the Nuclear Data Sheets [2] and in [1], all the levels of this $K=3^+$ band are shown as members of a $K=2^+$ band beginning at 1808·3 keV with no configurational assignment. We have summarized a number of arguments including the agreement between the experimental and theoretical differential cross-sections [12] which show conclusively that the 1808 keV 2^+ state is not a part of this band. The additional confirmation for the $K=3^+$ assignment comes from the connection (evidenced by strong inter-band M1 transitions) with the 1513·8 keV

Table 6. Differential cross-sections in the transfer of $1/2^-[510]$ neutron in ^{178}Hf.

	$K^\pi=3^+\ \nu\nu[514\downarrow]–[510\uparrow]$		$K^\pi=4^+\ \nu\nu[514\downarrow]+[510\uparrow]$	
I^π	dσ/dΩ(μb/sr) 45° Predicted	exp	dσ/dΩ(μb/sr) 45° Predicted	exp
3^+	173	170		
4^+	134	160	212	200
5^+	51	47	128	110
6^+	12	—	27	38
Sum	370	377	367	348

$K=4^+$ band having confirmed $\nu\nu[514\downarrow]+[510\uparrow]$ configuration, branching ratios for these inter-band transitions in agreement with Alaga rule predictions, and similar rotational parameters for the $K=3$ and $K=4$ bands In consequence the 2^+ state at 1808·3 keV, as also the 2^+ states at 1561·5 and 1891·3 keV, are shown as unassigned in Figure 3.

The next rotational band observed in ^{178}Hf is the $K=6^+$ band with the tentative two quasineutron configuration $\nu\nu[514\downarrow]+[512\uparrow]$. The band head is observed at 1554·0 keV with tentative rotational members observed through the 11^+ at 2700·4 keV [2]. The 6^+ band head is weakly populated in the (d,p) reaction, but none of the higher rotational levels is populated. There is no evidence for this band in the (d,t) reaction. Unpublished data from the ^{181}Ta (p,α) reaction [13] suggest that an important part of the $K=6^+$ band of ^{178}Hf is the two quasiproton $\pi\pi[404\downarrow]+[402\uparrow]$ configuration. Khoo and Løvhøiden [14] have given the configuration of this $K=6^+$ band as 69% $\pi\pi[404\downarrow]+[402\uparrow]$ and 31% $\nu\nu[514\downarrow]+[512\uparrow]$. It seems as if both the (d,p) and (p,α) data are consistent with this description.

A $K=5^-$ rotational band beginning at 1636·7 keV with rotational members through the tentative 8^- state at 2137·6 keV has been observed. The two lowest members of this band are strongly populated in the (d,t) reaction although possible interference from nearby bands makes this experimental finding less certain. If these strong populations are correct, the most reasonable assignment is $\nu\nu[624\uparrow]+[521\downarrow]$.

Finally, a $K=3^+$ rotational band has been suggested [2] consisting of only 3^+ and 4^+ rotational members. A possible two quasineutron configuration for this band is $\nu\nu[514\downarrow]$–$[521\downarrow]$. Only the band head at 1758·1 keV is populated in the (d,p) reaction. This band has also been strongly populated in the ^{181}Ta (p,α) reaction [13], and the dominant configuration has been shown to be $K=3^+$, $\pi\pi[404\downarrow]$–$[411\downarrow]$. It might also be mentioned that the (d,p) population of this $K=3^+$ band head may also have a contribution from a possible admixture of the $K=3^+$ band at 1862·2 keV.

4. Conclusions

Considerable portions of the fairly extensive level structure of ^{178}Hf have been studied using the (d,d'), (d,p) and (d,t) reactions. The specificity of the reactions and the "finger print" pattern of the differential cross-sections have allowed us to identify a number of the vibrational and two-quasiparticle configurations in the level structure. A part of the spectra at the highest energies remains unassigned. Clearly high resolution nuclear reaction studies can lead to considerable additional information.

Acknowledgements

We wish to thank the National Science Foundation for support, the Natural Sciences and Engineering Research Council of Canada for support to McMaster University, and the Department of Atomic Energy, Government of India, for support to Banaras Hindu University.

References

[1] A M I Hague, R F Casten, I Förster, A Gelberg, R Rascher, R Richter, P von Brentano, G Berreau, H G Börner, S A Kerr, K Schreckenbach and D D Warner, *Nucl. Phys.* **A455**, 231 (1986)

[2] E Browne, *Nucl. Data Sheets* [*N.Y.*] **54**, 199 (1988)

[3] C J Gallagher, Jr, H L Nielsen and O B Nielsen, *Phys. Rev.* **123**, 564 (1961)

[4] J Kern, O Mikoshiba, R K Sheline, T Udagawa and S Yoshida, *Nucl. Phys.* **A104**, 642 (1967)

[5] E P Grigoriev and V G Soloviev, *Structure of even deformed nuclei*, (Moscow: Nauka 1974) (in Russian)

[6] H L Nielsen, K Wilsky, J Zylicz and G Sørensen, *Nucl. Phys.* **A93**, 385 (1967)

[7] M A Oothoudt and N M Hintz, *Nucl. Phys.* **A213**, 221 (1973)

[8] O Mikoshiba, R K Sheline, T Udagawa and S Yoshida, *Nucl. Phys.* **A101**, 202 (1967)

[9] V G Soloviev and N Yu Shirikova, *Z. Phys.* **A334**, 149 (1989)

[10] K Neergård and P Vogel, *Nucl. Phys.* **A145**, 33 (1970)

[11] M M Minor, Doctoral dissertation, Florida State University, Tallahassee, FL (1968)

[12] R K Sheline, D G Burke, M M Minor and P C Sood, *Phys. Rev.* **C48**, (August 1993)

[13] D G Burke, unpublished data, 1992

[14] T I Khoo and G Løvhøiden, *Phys. Lett.* **B67**, 271 (1977)

PRAMANA
— journal of
physics

© Printed in India

Vol. 41, No. 2,
August 1993
pp. 163–169

Neutron flow or collective degrees of freedom for near barrier heavy-ion fusion

S KAILAS and A NAVIN
Nuclear Physics Division, Bhabha Atomic Research Centre, Bombay 400085, India

MS received 30 March 1993

Abstract. Various models have been proposed in order to understand the near barrier heavy-ion fusion data. Amongst others the coupled channel approach of Dasso and Landowne and the neutron flow picture of Stelson are two of the mechanisms which describe well a large body of near barrier fusion data. From an analysis of ^{16}O induced fusion reaction around the barrier for various targets an attempt has been made to identify which out of the above two mechanisms is more appropriate to explain these data.

Keywords. Fusion reactions near Coulomb barrier; ^{16}O projectile; targets with A values between 120 and 186.

PACS No. **25·70**

1. Introduction

The study of heavy-ion fusion reactions near the Coulomb barrier continues to be of considerable interest [1]. Out of the many theoretical prescriptions proposed to describe the near barrier fusion cross-sections, the coupled channel approach [2, 3] and the neutron flow picture [4–6] are the most successful. The former is based on the fact that couplings of the incident channel to other non-elastic channels e.g. inelastic and transfer modify (both lower and raise) the barrier height and lead to an enhancement of the fusion cross-section near the 1-dimensional barrier. The Stelson model attributes the enhancement of the fusion cross-section to the onset of neutron flow due to the exchange of neutrons between the interacting nuclei (eventually leading to fusion) at a distance larger than the barrier radii. These two models also predict different barrier distributions.

Recently Vandenbosch [7] has made a comparison of these two models for the systems analyzed by Stelson and his collaborators and concluded that from the data analyzed one cannot choose between these models. The data used in that work were for different projectiles and targets. In the present work an attempt has been made to determine as to which out of the two mechanisms proposed for near barrier fusion is more appropriate, by choosing for an analysis, data for a single projectile ^{16}O, interacting with several targets having mass numbers ranging from 120–186. Thus it is ensured that the effect of the projectile is a common factor in all the systems studied.

2. Models for fusion

2.1 *The neutron flow model of Stelson*

Stelson [4, 5, 6] suggested that near barrier fusion cross-section is dominated by neck formation initiated by neutron flow between the colliding nuclei at distances typically 1 to 2 fm larger than the mean barrier distance. He showed that if one assumed a flat distribution of barriers $D(B)$, symmetric about a mean barrier B and having a sharp lower cut-off at T (which is determined by the distance of approach at which the least bound neutrons may flow from one nucleus to the other), the usual expression for fusion cross-section (for energies greater than the barrier B)

$$\sigma_{\text{fus}}(E) = \pi R_b^2 \left(1 - \frac{B}{E}\right), \tag{1}$$

becomes for near barrier energies

$$\sigma_{\text{fus}}(E) = \frac{\pi R_b^2}{4E} \frac{(E-T)^2}{4E(B-T)}, \tag{2}$$

where R_b is the barrier radius.

Assuming a neutron shell-model potential centered on each of the interacting nuclei he calculated the maximum value of the merged neutron potential $V_n(\text{max})$ at a distance R_t which is the distance at which the threshold barrier T is reached. (The mean barrier B is reached at a distance R_b in the total potential versus relative distance plot). According to Stelson, if the maximum of the merged neutron shell model potential $V_n(\text{max})$ is deeper than the binding energy of the valence neutron $S_{2n}/2$ of the two interacting nuclei the neutron flow is possible from the target to projectile and vice versa. As can be seen from figure 1, for both ^{144}Sm and $^{154}\text{Sm} + {}^{16}\text{O}$ systems the neutron flow is possible only from the target to projectile. This point is further discussed in § 3.3. From a systematic study of near barrier fusion data, he found a correlation between the T values and the average neutron separation energy $S_n = S_{2n}/2$ (to take into account the odd-even effect in the neutron separation energy) and $V_n(\text{max})$. It is conceivable then that the extent of the barriers i.e. $B-T$ values are also correlated with $VSN = V_n(\text{max}) - S_{2n}/2$.

2.2 *Coupled channel model*

It has been pointed out [2, 3] that the coupling of the incident channel to other channels such as inelastic and transfer can modify the barriers. By calculating the transmission through the new barriers (with their appropriate weights) the fusion cross-section can be obtained. The change in height and the weights of these new barriers depend on the strength of the couplings ($F_i(r)$) of the ith state coupled to the ground state and the Q value of that state. To simplify calculations they have made use of the constant coupling approximation i.e. the r dependence of $F_i(r)$ is neglected and is replaced by its representative value $F_0 = F(R_b)$, where R_b is the barrier radius for a given system. The coupling strength for inelastic excitations to collective states is calculated from the deformation parameter $\beta_{\lambda k}$ as [assuming

Coulomb and nuclear deformation parameters to be the same],

$$F_k(r) = \frac{\beta_{\lambda k}}{\sqrt{4\pi}}\left[-R_k\frac{\mathrm{d}V_n(r)}{\mathrm{d}r} + \frac{3Z_1Z_2e^2}{(2\lambda+1)}\frac{R_k^{\lambda}}{r^{\lambda+1}}\right], \tag{3}$$

where λ is the multi-polarity of the transition and k is the nuclei being excited (target or projectile). R_k is the radius of the nucleus ($1{\cdot}2A^{1/3}$ where A is the mass number) which is excited and V_n is the nuclear potential. The extraction of the radial dependence and strength of the form factor for the transfer channels is not so straightforward and involves the measurement of transfer angular distributions and their cross-sections for a particular system. There have been some attempts at obtaining the form factor for the transfer channels [8, 9]. However in the present work, only inelastic couplings have been considered. As the couplings (F) lead to the barrier being lowered (or increased) it is expected in this model that the B–T values will be related to F.

3. Correlation between B–T versus F and VSN

3.1 *Extraction of B, T and R values from the data*

In the present work we have used the fusion data available for the following systems: $^{16}O + {}^{120}Sn$ [10], ^{144}Nd [11], $^{148,150}Nd$ [12], ^{144}Sm [13], $^{148,150,152,154}Sm$ [14], $^{182,184,186}W$, $^{176,180}Hf$ [15], ^{166}Er, ^{176}Yb [16]. The B and R_b values for the above system were obtained by fitting the fusion data at the above barrier energies using (1). The T values were determined by considering the data at near barrier energies (values lying between 10 and 150 mb) using (2).

3.2 *Determination of an effective F′*

The quantity F (eq. (3)) has been determined for each system considering the inelastic excitation channels which include the low lying 2^+ and 3^- states in both the target and the projectile, with no inter-couplings between them. The values of $\beta_{\lambda k}, \lambda, Q$ were obtained from the literature [17, 18]. For each system the corresponding effective value of the coupling F' has been calculated as follows; At deep sub-barrier energies the extraction of an effective value of F' gets simplified [19]. We calculate the fusion cross-section with and without coupling and equate this ratio to $e^{F'/\varepsilon}$ where ε is the barrier curvature. For each system the quantity F' has been determined using the code CCDEF [20, 21].

3.3 *Calculation of VSN*

From the T values obtained as mentioned earlier the R_t values were determined using the approximate relation

$$R_t = \frac{Z_t Z_p e^2}{T}, \tag{4}$$

where Z_p, Z_t are charges of the projectile and the target respectively. For each target-projectile combination the maximum value (V_n(max)) of the sum of the shell model neutron potentials centered on the projectile and the target has been obtained by examining the potential energy at various positions along the internuclear axis

Table 1. Summary of near barrier fusion analysis projectile ^{16}O. The error in $B-T$ is given in the brackets.

Target	R_b fm	B MeV	R_t fm	T MeV	$B-T$ MeV	F' MeV	V_n(max) MeV	$S_{2n}/2$ MeV	VSN MeV
^{120}Sn	9·6	49·5	12·4	46·5	3·0(0·5)	0·67	9·1	7·8	1·3
^{144}Nd	10·0	56·7	12·6	54·7	2·0(0·4)	0·96	9·8	7·0	2·8
^{148}Nd	9·7	57·4	12·6	54·9	2·5(0·5)	1·35	10·5	6·3	4·2
^{150}Nd	9·4	57·3	12·8	54·1	3·2(0·4)	1·53	9·5	6·2	3·3
^{144}Sm	11·0	60·0	12·3	57·9	2·1(0·3)	0·90	12·0	9·5	2·5
^{148}Sm	10·3	59·3	12·8	55·8	3·5(0·5)	1·14	9·3	7·3	2·0
^{150}Sm	10·4	58·9	12·9	55·4	3·5(0·5)	1·28	8·8	7·0	1·8
^{152}Sm	9·4	57·8	13·1	54·5	3·3(0·4)	1·65	7·8	7·0	0·8
^{154}Sm	9·9	58·5	13·1	54·5	4·0(0·5)	1·75	7·9	6·9	1·0
^{166}Er	10·3	63·5	13·2	59·3	4·2(0·3)	1·93	8·3	7·6	0·7
^{176}Yb	12·6	64·1	13·4	60·2	3·9(0·5)	1·84	8·0	6·4	1·6
^{176}Hf	9·0	66·3	13·1	63·4	2·6(0·6)	1·82	9·9	7·5	2·4
^{180}Hf	9·4	65·9	13·2	63·0	2·9(0·5)	1·66	9·6	6·8	2·8
^{182}W	10·6	69·2	13·2	64·4	4·8(0·4)	1·62	9·3	7·4	1·9
^{184}W	10·7	68·8	13·3	64·2	4·6(0·4)	1·59	9·3	6·8	2·5
^{186}W	10·0	67·4	13·2	64·4	3·0(0·5)	1·47	10·0	6·5	3·5

keeping the interaction distance fixed at R_t following the procedure of Stelson [5]. The average separation energy $S_{2n}/2$ values for the target have been obtained from the mass table [22]. The neutron flow initiated from the projectile ^{16}O has not been considered here as the separation energy ($S_{2n}/2$) is 14·4 MeV in this case and is much higher than the V_n(max) values for all the targets considered here (see table 1). This is illustrated in figure 1, where the result of this type of calculation is shown for the $^{16}\mathrm{O} + {}^{154}\mathrm{Sm}$ and $^{16}\mathrm{O} + {}^{144}\mathrm{Sm}$ systems. It can be clearly seen that $S_{2n}/2$ is larger than (V_n(max)) and hence it is not possible for neutron flow to take place from ^{16}O to the target. Finally the quantity

$$VSN = V_n(\mathrm{max}) - S_n \tag{5}$$

has been computed.

3.4 *Comparison with the data*

In table 1 we have collected the various quantities B, R_b, T, R_t extracted along with the F', $S_{2n}/2$, V_n(max) and VSN values calculated in this work. It is interesting to compare the R_t values (obtained from the onset of fusion at the threshold barrier due to exchange of neutrons) with the D value obtained from heavy-ion single neutron transfer studies. The average value of R_t obtained from this work is

$$R_t = 1{\cdot}65(A_t^{1/3} + A_p^{1/3}).$$

This value compares very well with the average value of D obtained from single neutron transfer studies which varies from 1·54 to 1·83 $(A_t^{1/3} + A_p^{1/3})$ [23]. In figure 2a the $B-T$ values have been plotted as a function of VSN. It is noticed that the $B-T$

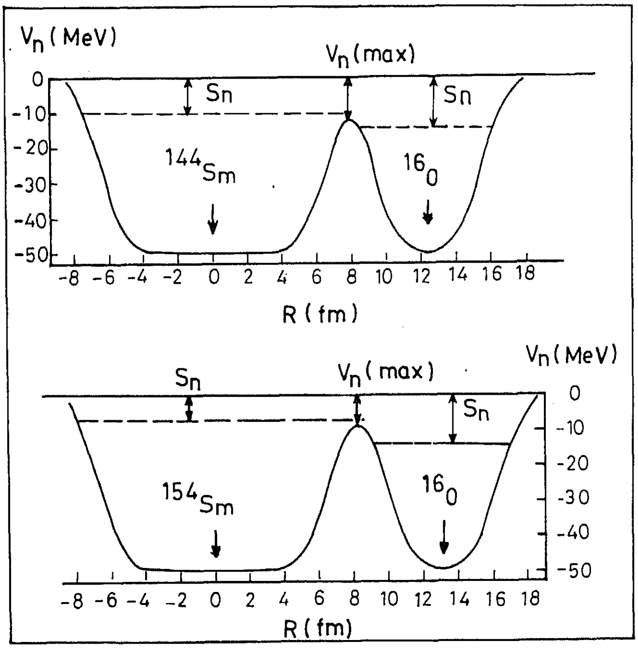

Figure 1. Merged neutron potentials at R_t for ^{144}Sm and ^{154}Sm + ^{16}O systems. The V_n(max) and the target/projectile S_n values are marked in the figure.

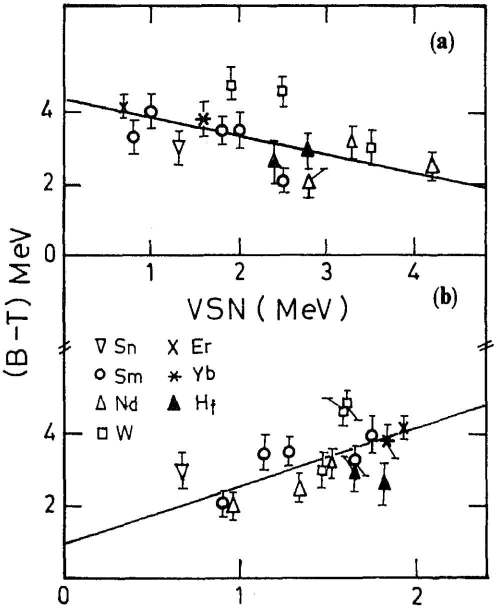

Figure 2. The B–T values determined for the various systems plotted against (**a**) VSN and (**b**) F'. The straight lines represent the best linear fits to the data.

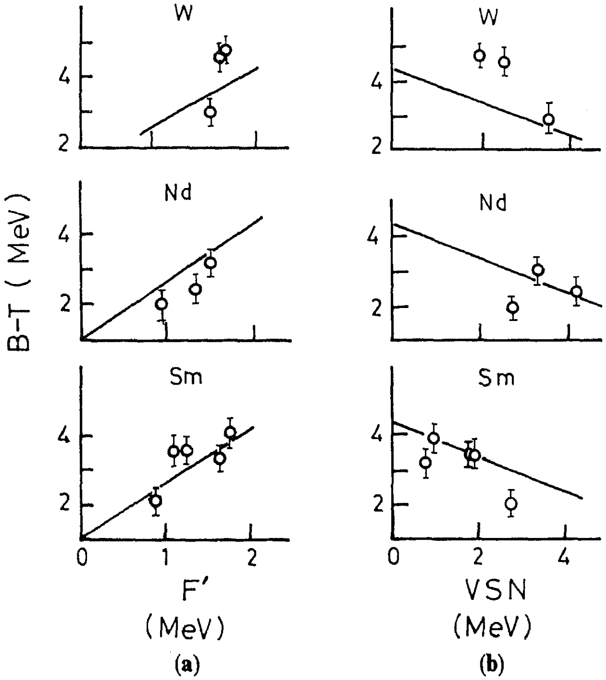

Figure 3. The $B-T$ values obtained for Nd, Sm and W isotopes are plotted against F' and VSN. The straight lines are obtained using the global fit parameters of figure 2.

values on the average decreased with increase of VSN values but the correlation is not as striking as found between $B-T$ and F'. Shown in figure 2b is the plot of $B-T$ versus F'. From the figure one can observe a good correlation between the two quantities, an increasing value of $B-T$ with increasing F'. Assuming a linear relationship between F' and $B-T$ a fit to the data was made. A straight line adequately describes the data. A similar fit is made for the VSN versus $B-T$ data. The χ^2 per degree of freedom for the latter fit was 30% worse than that obtained for the former one. In order to bring out the sensitivity of the models to the data, we have shown in figure 3 the $B-T$ values for a range of isotopes for a given Z and compared them with F' and VSN estimates. The straight lines in this figure are obtained using the parameters determined in the earlier global fit. In general, both the models describe the trend of $B-T$ variation. However the coupled channel approach is superior in describing the $(B-T)$ data.

4. Summary

In the present work, from an analysis of near barrier fusion data available for ^{16}O interacting with several targets with mass numbers ranging from 120 to 186, it is found that the deduced $B-T$ values are better correlated with the variable F' (related to collective degrees of freedom) than with VSN (related to the neutron flow picture). The present results are suggestive that for ^{16}O as projectile interacting with various targets, the collective degrees of freedom are more important than the neutron flow in influencing the near barrier fusion phenomenon. It will be interesting to make this kind of comparison for other projectiles as well.

Acknowledgement

The authors thank Prof. R Vandenbosch for his interest in this work and helpful comments.

References

[1] C Signorini, S Skorka, P Spolaore and A Vitturi, (eds) *Proc. Int. Symp. on heavy ion interactions around the Coulomb barrier, Legnaro* (Italy) (1988)
[2] C H Dasso, S Landowne and A Winther, *Nucl. Phys.* **A407**, 221 (1983)
[3] R A Broglia, C H Dasso, S Landowne and G Pollarolo, *Phys. Lett.* **B133**, 34 (1983)
[4] P H Stelson, in *Int. Symp. on heavy-ion reaction dynamics in tandem energy region*, Hitachi (Japan) August 1–3 (1988)
[5] P H Stelson, *Phys. Lett.* **B205**, 190 (1988)
[6] P H Stelson, H J Kim, M Beckerman, D Shapira and R L Robinson, *Phys. Rev.* **C41**, 1584 (1990)
[7] R Vandenbosch, *Proc. eighth winter workshop on nuclear dynamics*, Jacksonhole Wyoming, USA Edited by W Bauer and B Back (World Scientific, USA) (1992)
[8] L Corradi, S J Skorka, U Lenz, K E G Lobner, P R Pascholati, U Quade, K Rudolph, W Schomburg, M Steinmayer, H G Thies, G Montagnoli, D R Napoli, A M Steffanini, S Beghini, F Scarlassara, C Signorini and F Soramel, *Z. Phys.* **A334**, 55 (1990)
[9] C H Dasso and G Pollarolo, *Phys. Lett.* **B155**, 223 (1985)
[10] P Jacobs, Z Fraunkel, G Mamane and I Tserruya, *Phys. Lett.* **B175**, 271 (1986)
[11] M di Tada (Private Communication 1992)
[12] R Broda, M Ishihara, B Herskind, H Oeschler, S Ogaze and H Ryde, *Nucl. Phys.* **A248**, 357 (1975)
[13] D Di Gregario, J O Fernandez Niello, A J Pacheco, D Abriola, S Gil, A O Macchivelli, J E Testoni, P R Pascholati, V R Vanin, Neto R Liguori, N Calin Filho, M M Coimbre, P R Silveira Gomes and R G Stokstad, *Phys. Lett.* **B176**, 322 (1986)
[14] R G Stokstad, Y Eisen, S Kaplanis, D Pelte, U Smilansky and I Tserruya, *Phys. Rev.* **C21**, 2427 (1980)
[15] J R Leigh, J J M Bokhosrt, D J Hinde and J O Newton, *J. Phys.* **G14**, L55 (1988)
[16] J Fernandez Niello, M di Tada, A O Macchivelli, A J Pacheco, D Abriola, M Elgue, A Etchegoyen, M C Etchegoyen, S Gil and J E Testoni, *Phys. Rev.* **C43**, 2303 (1991)
[17] S Raman, C H Malarkey, W T Milner, C W Nestor Jr and P H Stelson, *At. Nucl. Data. Tables.* **36**, 1 (1987)
[18] R H Spear, *At. Nucl. Data Tables* **42**, 55 (1988)
[19] S Landowne and S C Pieper, *Phys. Rev.* **C29**, 1352 (1984)
[20] C H Dasso and S Landowne, *Comput. Phys. Commun.* **46**, 187 (1987)
[21] J Fernândez Niello, C H Dasso and S Landowne, *Comput. Phys. Commun.* **54**, 409 (1989)
[22] A H Wapstra and R Hoekstra, *At. Data and Nucl. Data Tables* **39**, 281 (1988)
[23] W Frahn and R H Venter, *Nucl. Phys.* **59**, 651 (1964)

PRAMANA
— journal of
physics

© Printed in India

Vol. 41, No. 2,
August 1993
pp. 171–174

Momentum space distribution of electrons in an atom using hydrogenic wave functions

NAZAKAT ULLAH
Tata Institute of Fundamental Research, Homi Bhabha Road, Bombay 400005, India

MS received 1 February 1992; revised 28 April 1993

Abstract. A formulation is developed to derive exact analytic expressions for electron–electron correlation and density of electrons in momentum space using hydrogenic wave functions. It is shown that for large atoms the expression for density of electrons has a simple form.

Keywords. Momentum space; electron–electron correlations; density of electrons; hydrogenic wave functions.

PACS Nos 02·90; 31·90

1. Introduction

The momentum space representation of a many-particle wave function provides an alternative formulation to the usual coordinate space formulation. The study of density and correlations in this space for certain potentials like the Coulombic potential provides new insights into certain aspects of a many-particle system. Since momentum space representation is obtained by taking Fourier transform of coordinate space, as far as mathematical formulation goes the harmonic oscillator potential is quite straight-forward as the Fourier transform of a Gaussian is again a Gaussian. But for the Coulombic potential which is used for the motion of electrons in an atom this is quite a challenging problem. It is precisely because of this reason that while extensive developments in the past have taken place to study, e.g; Wigner transform [1] using harmonic oscillator potential, no such studies have ever been undertaken to study this transform when Coulomb potential is involved.

Even though fairly accurate values of wave functions of electrons in an atom are available at present, it is difficult to work out analytic expressions for density and correlations using them. In order to simplify the problem we have used hydrogenic wave functions. The basic idea is first to derive exact results using these wave functions and later improve the analytic results by either introducing parameters or using the theory of probability to modify the results to make them suitable for fitting the experimental data. It is shown that by employing hypergeometric functions [2] and their properties one could derive analytic expressions for density and correlations.

The mathematical formulation is described in § 2. Using this formulation an expression for momentum density of electrons is given in § (3). Concluding remarks are presented in § 4.

2. Formulation

Let us consider an atom having Z electrons which fully occupy the states $m_s = \pm\frac{1}{2}$, $-l \leqslant m_l \leqslant l$, $l = 0, \cdots, n-1$ and $n = 1, \cdots, N$. For simplicity we are considering here the closed shell atoms only. Our aim is to find an expression for $g(\bar{k}_1, \bar{k}_2)$ which is defined by

$$g(\bar{k}_1,\bar{k}_2) = \frac{1}{(2\pi)^3}\int \mathrm{d}\bar{r}_1\,\mathrm{d}\bar{r}_2 \exp(-i\bar{k}_1\cdot\bar{r}_1 + i\bar{k}_2\cdot\bar{r}_2)\sum_\alpha \phi_\alpha^*(\bar{r}_1)\phi_\alpha(\bar{r}_2), \tag{1}$$

where the single electron wave function $\phi_\alpha(\bar{r})$ is a product of a spin wave function, a spherical harmonic and a radial wave function $R_{nl}(r)$.

The theoretical quantity $g(\bar{k}_1, \bar{k}_2)$ plays a key role in the study of many physical quantities of interest like the momentum distribution of electrons. Since the many electron wave function is an antisymmetric wave function, the two particle correlation has both a direct as well as exchange part. However both of them can be expressed knowing the quantity $g(\bar{k}_1, \bar{k}_2)$.

Using the expansion of plane waves in spherical harmonics [3] and integrating over the angular variables in expression (1) we get

$$g(\bar{k}_1,\bar{k}_2) = \frac{1}{2\pi^2}\sum_{n=1}^{N}\sum_{l=0}^{n-1}(2l+1)P_l(\cos(\hat{k}_1,\hat{k}_2))I_{nl}(k_1)I_{nl}(k_2), \tag{2}$$

where P_l is the Legendre polynomial and I_{nl} denotes the integral

$$I_{nl}(k) = \int_0^\infty \mathrm{d}r\, r^2 j_l(kr) R_{nl}(r), \tag{3}$$

j_l being the spherical Bessel function.

In writing (2) we have left out a factor arising due to summation over spin states. It will be added later when we take the specific example of density of electrons.

We shall employ the hydrogenic type of radial wave functions R_{nl}, which are given by [4]

$$R_{nl}(r) = \left[\frac{(n+l)!}{(2n)(n-l-1)!}\left(\frac{2\alpha}{n}\right)^3\right]^{1/2}\frac{1}{(2l+1)!}\left(\frac{2\alpha}{n}r\right)^l {}_1F_1\left(-n+l+1; 2l+2; \frac{2\alpha}{n}r\right)\exp\left(-\frac{\alpha}{n}r\right), \tag{4}$$

where ${}_1F_1$ is the confluent hypergeometric function and α is a parameter.

In applications to atomic problems the parameter α can be obtained by using a variational calculation using the Hamiltonian which is a sum of single particle kinetic energy operator and Coulomb attraction between electrons and the nucleus and the two electron interaction e^2/r_{ij}.

Expressing confluent hypergeometric function in terms of associated Laguerre polynomial and using its generating function, the integral in (3) can be written as

$$I_{nl} = \sqrt{\frac{(n-l-1)!}{(n-l)!}}(l+1)!\frac{4n}{\alpha^{3/2}}\left(\frac{4nk}{\alpha}\right)^l$$

$$\left[1+\frac{n^2k^2}{\alpha^2}\right]^{-l-2}\frac{1}{2\pi_i}\oint\frac{\mathrm{d}z}{z^{n-l}}(1-z^2)\left[(1+z^2)+2z\left(\frac{1-(n^2k^2/\alpha^2)}{1+(n^2k^2/\alpha^2)}\right)\right]^{-l-2}. \tag{5}$$

From (5) we see that the contour integral is a sum of two parts because of the factor $(1-z^2)$. Consider first the term arising from 1. After carrying out some algebra it can be written as

$$(-1)^{n-l-1}\frac{n!}{(n-l-1)!(l+1)!}\left[\frac{2(1-(n^2k^2/\alpha^2))}{(1+(n^2k^2/\alpha^2))}\right]^{n-l-1}$$
$${}_2F_1\left(-\frac{n}{2}+\frac{l}{2}+1,-\frac{n}{2}+\frac{l}{2}+\frac{1}{2};-n;\left(\frac{1+(n^2k^2/\alpha^2)}{1-(n^2k^2/\alpha^2)}\right)^2\right).$$

A similar expression can be written from the second term (z^2). We first make the quadratic transformation [2] to get rid of factors of $\frac{1}{2}$ in the hypergeometric function and then use contiguous relations of Gauss to combine the two hypergeometric functions. This finally gives the following expression for I_{nl},

$$I_{nl}=\frac{\sqrt{\pi}}{2^{2l-1}}(-1)^{n-l-1}\frac{n^2}{\alpha^{3/2}}\sqrt{\frac{(n+l)!}{(n-l-1)!}}\frac{1}{\Gamma(l+\frac{3}{2})}$$
$$\left[1+\frac{n^2k^2}{\alpha^2}\right]^{-n-1}\left(\frac{4nk}{\alpha}\right)^l{}_2F_1\left(-n+l+1,-n+\frac{1}{2};l+\frac{3}{2};-\frac{n^2k^2}{\alpha^2}\right). \tag{6}$$

Putting (6) in (2) and noting that $\cos(\hat{k}_1,\hat{k}_2)=\dfrac{(k_1^2+k_2^2)-|\bar{k}_1-\bar{k}_2|^2}{2k_1k_2}$, we find that $g(\bar{k}_1,\bar{k}_2)$ can be written as

$$g(\bar{k}_1,\bar{k}_2)=\frac{8}{\pi^2\alpha^3}\sum_{n=1}^{N}n^5\left[\left(1+\frac{n^2k_1^2}{\alpha^2}\right)\left(1+\frac{n^2k_2^2}{\alpha^2}\right)\right]^{-2}$$
$${}_2F_1\left(-n+1,n+1;\frac{3}{2};\frac{\left(\frac{n}{\alpha}\right)^2|\bar{k}_1-\bar{k}_2|^2}{\left(1+\frac{n^2k_1^2}{\alpha^2}\right)\left(1+\frac{n^2k_2^2}{\alpha^2}\right)}\right). \tag{7}$$

Expression (7) gives the analytic form of $g(\bar{k}_1,\bar{k}_2)$ for a given closed shell atom.

3. Momentum density distribution

Since there is considerable interest in heavy atoms, we shall now describe an approximate form of $g(\bar{k}_1,\bar{k}_2)$ for this case. By expanding the hypergeometric function and keeping the leading order terms in summation over n, we get

$$g(\bar{k}_1,\bar{k}_2)=\frac{8N^6}{\pi^2\alpha^3}\int_0^1\mathrm{d}v\,v^5\left[\left(1+\frac{N^2v^2k_1^2}{\alpha^2}\right)\left(1+\frac{N^2v^2k_2^2}{\alpha^2}\right)\right]^{-2}$$

$$j_0\left[\frac{2|\bar{k}_1-\bar{k}_2|N^2v^2}{\alpha\sqrt{\left(1+\frac{N^2k_1^2v^2}{\alpha^2}\right)\left(1+\frac{N^2k_2^2v^2}{\alpha^2}\right)}}\right]. \tag{8}$$

Expression (8) is valid for small values of k_1, k_2 only.

Next we derive an expression for momentum density of electrons by putting $k_1 = k_2 = p$ in the exact expression (7). Replacing the sum over n by an integral, we get for large values of N the following expression for the density $\rho(\bar{p})$

$$\rho(\bar{p}) = \frac{8N^6}{3\pi^2\alpha^3}\left[\left(1+\frac{N^2p^2}{\alpha^2}\right)^{-3} - \frac{1}{N^6}\left(1+\frac{p^2}{\alpha^2}\right)^{-3}\right]. \tag{9}$$

In writing expression for $\rho(\bar{p})$ we have multiplied expression (8) by a factor two to take care of the two possible spin states.

As (9) is valid for all values of p, we find that the density of electrons for large p goes as p^{-8}, same as for H atom.

4. Conclusions

Before we conclude we would like to pass two remarks. The first is that many of the new expressions which have been derived here like the integral I_{nl} given by equation [6] can be easily checked by using specific values of n, l. The second is that the exact momentum density for light atoms can be calculated by putting $N = 1, 2, \ldots$ in (7).

Several applications of the present formulation like the calculation of correlation coefficients in momentum space [5] and Wigner transform for closed shell atoms is intended to be taken up later.

We would also like to point out here that momentum space wave functions for H atom in terms of Gegenbauer polynomials have recently been given by Hey [6] and analytic functions for atomic momentum density have been studied by Chen *et al* [7].

References

[1] M Hillery, R F O'Connel, M O Scully and E P Wigner, *Phys. Rep.* **106**, 121 (1984)

[2] M Abramowitz and I Stegun, *Handbook of mathematical functions* (Dover, New York, 1965) Ch. 15

[3] A R Edmonds, *Angular momentum in quantum mechanics* (Princeton, Princeton University Press, 1957) Ch. 5

[4] E Merzbacher, *Quantum mechanics* (New York, Wiley, 1984)

[5] K E Banyard and J C Moore, *J. Phys.* **B10**, 2781 (1977)

[6] J D Hey, *Am. J. Phys.* **61**, 28 (1993)

[7] Y F Chen, C M Kwei and C J Tung, *Phys. Rev. Abst.* **24**, 11 (1983)

PRAMANA
— journal of
physics

© Printed in India

Vol. 41, No. 2,
August 1993
pp. 175–184

L-shell/subshell ionization of Au, Pb and Bi by low energy proton impact

K N PANDEY, D N TRIPATHI, R N CHAKRABORTY and D K RAI
Department of Physics, Banaras Hindu University, Varanasi 221 005, India

MS received 13 October 1992; revised 8 February 1993

Abstract. Proton induced X-ray emission has been used to measure L-subshell and total ionization cross-sections of Au, Pb and Bi in the energy range of 200–350 keV. The ionization cross-sections have been extracted using the X-ray spectra and other quantities like fluorescence yields, transition probabilities, relative widths and Coster–Krönig fraction etc. involved in the process. The results have been compared with the cross-sections measured before and discussed in the light of known theories regarding the ion-atom collisions.

Keywords. L-shell/subshell ionization; PWBA theory; RPWBA-BC theory; ECPSSR theory

PACS No. 34·50

1. Introduction

Inner shell ionization cross-section for atoms due to charged particle impact are of interest to investigators in radiation damage of biological and other materials, traces in nuclear emulsion, auroral and other atmospheric phenomena as well as to those studying the basic mechanisms of ionization and secondary electron production. Studies regarding the characteristics of the said processes by detecting the emitted X-rays in the bombardment of solid targets with different ions have been carried out extensively in the past few years. Most of these studies are, however, limited to only K-shell ionization. Previous work regarding L-shell ionization is scarce, as it is more complex comparatively. L-shell consists of three sub-shells and the X-rays that are emitted are experimentally not well resolved. The accuracy of the ionization cross-sections are based upon the validity of a set of radiative transition probabilities, fluorescence yields and Coster–Krönig fractions which can be affected by multiple excitation of the target atom. Therefore, a careful analysis of the ion induced X-ray is essential in order to determine the inner shell ionization cross-sections due to ion impact.

In the case of slow moving projectiles which produce inner shell ionization by Coulomb excitation, the theoretical interpretation has undergone a sustained evolution. Corrections for Coulomb deflection, increased binding energy, energy loss and relativistic effects gradually incorporated into these theories have resulted in better agreement with experimental results. Several authors have reported the results of their measurements of X-ray production cross-sections for different elements [1–7] including Au and Pb in the low energy range. The shell/subshell ionization cross-sections have also been measured earlier [8–11].

Measurements in the low energy range, however, show large discrepancies with the theory especially for the heavier elements [12]. Therefore, accurate measurements are necessary to clarify the behaviour of the inner shell ionization cross-sections in the low velocity limit.

In the present work we measure and analyze the L-subshell and total ionization cross-sections of Au, Pb and Bi due to proton impact in the energy range 200–350 keV. The results have been interpreted in the light of earlier experimental [9, 11, 13] and theoretical [14, 15, 16] studies.

2. Experimental procedure

The beam of proton was extracted from the 400 kV Van de Graff accelerator. The well collimated beam (diameter ~ 1·5 mm) was allowed to fall on thin target of Au Pb and Bi (density ~ 200 μg/cm^2) and mounted at 45° to the beam direction at the centre of the evacuated (~ 10^{-6} torr) scattering chamber [17]. The Au target was self-supporting; while the Pb and Bi targets were deposited on mylar backing (~ 700 μg/cm^2 thick). The L X-rays, emitted as a result of the inelastic collision, passed through a 6 μm hostaphane foil window and 2 cm air gap. The L X-rays were detected by a Si(Li) detector (having a energy resolution of ~ 200 eV FWHM at 5·9 keV) placed at 90° to the beam axis. Proton beam current (maximum) up to 160 nA were employed for bombarding the targets. The spectrum of the emitted X-rays for each element at 300 keV proton energy is shown in figures 1–3.

3. Determination of L-shell and subshell ionization cross-sections

The L X-ray energy spectrum may be divided into three main groups: the L_α, L_β and L_γ. The L_α has weaker L_l and L_η lines in its tail. The L_β lines are resolved into their

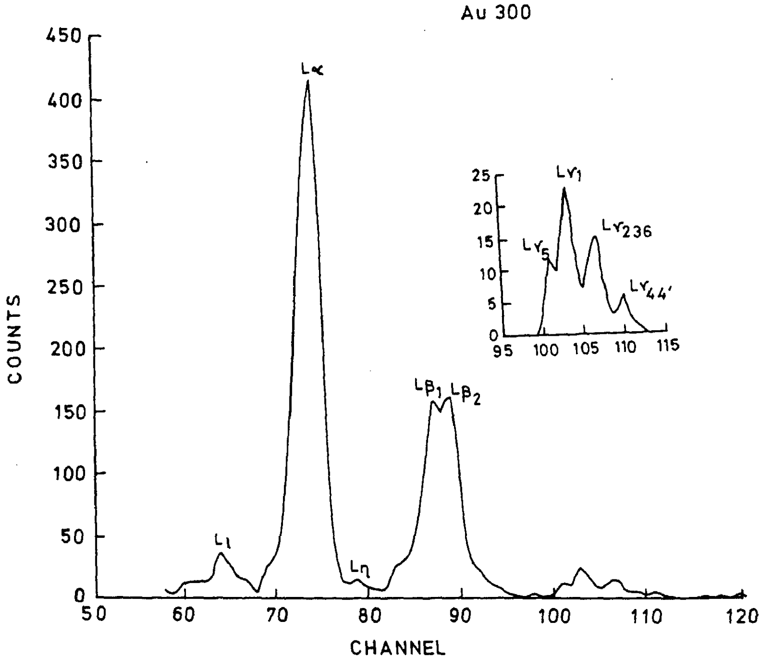

Figure 1. Proton impact L-shell X-ray sepctrum of Au at 300 keV.

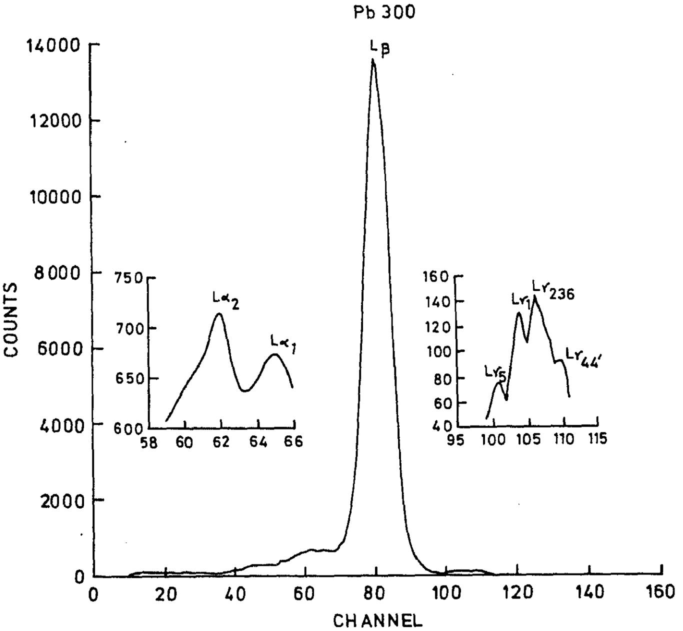

Figure 2. Proton impact L-shell X-ray spectrum of Pb at 300 keV.

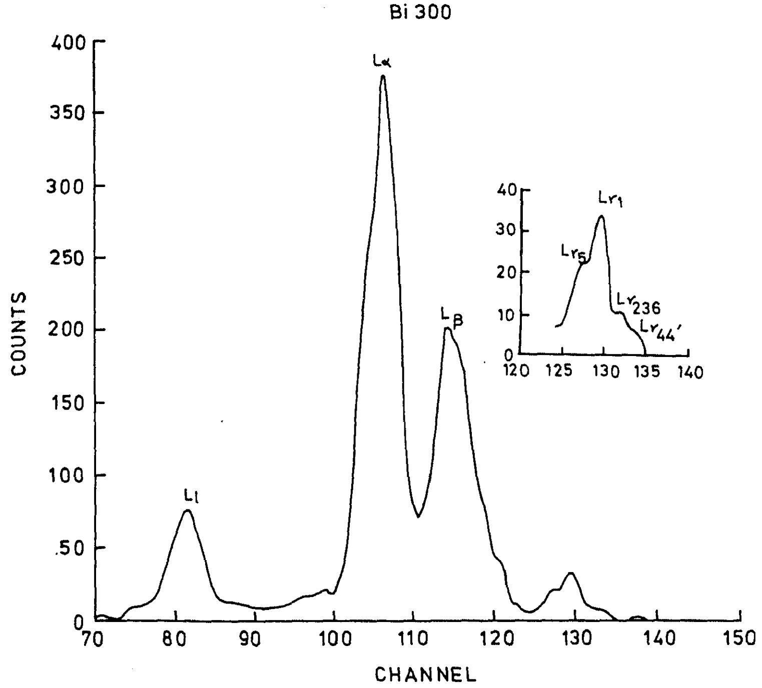

Figure 3. Proton impact L-shell X-ray spectrum of Bi at 300 keV.

components for lower impact energies only, while L_γ lines could not be resolved into their components. L X-ray emission has been taken to be isotropic [10].

Experimental L_j X-ray production cross-sections $\sigma^x_{L_j}$ were determined from the expression given below [18]

$$\sigma^x_{L_j} = Y_{L_j} A_2 4\pi / N_p N_0 (\rho t) \Omega 2^{1/2} \varepsilon_{L_j} C_{L_j}, \tag{1}$$

where Y_{L_j} is the L_j X-ray yield, A_2 is the target mass, N_p is the number of charged particles to which the target has been exposed, N_0 is the Avogadro's number, ρt is the areal density of the target, Ω is the solid angle of the Si(Li) detector, ε_{L_j} is the Si(Li) detector efficiency and C_{L_j} denotes the absorption correction for L_j X-rays in hostphane-foil chamber window and air. The mass absorption coefficient required for evaluating C_{L_j} has been obtained using the table of Storm and Israel [19].

The L_α, L_β, L_γ, L_l and L_η lines are clearly separated in the observed spectrum. (see figures 1–3). The measured L_α, L_{γ_1}, $L_{\gamma 236}$ and $L_{\gamma 44'}$ X-ray production cross-sections are related with L_i subshell ionization cross-sections $\sigma^{\text{exp}}_{L_i}$ $(i = 1, 2, 3)$ by the following relation [18];

$$\sigma^{\text{exp}}_{L_1} = S_1 \sigma^x_{L\gamma 2344'} / S_{1\gamma 2344'} \omega_1, \tag{2}$$

$$\sigma^{\text{exp}}_{L_2} = S_2 \sigma^x_{L\gamma 1} / S_{2\gamma 1} \omega_2 - f_{12} \sigma^{\text{exp}}_{L_1} \tag{3}$$

$$\begin{aligned}\sigma^{\text{exp}}_{L_3} = S_3/S_{3\alpha}\omega_3 [\sigma^x_{L_\alpha} - \omega_2 (f_{12}\sigma^{\text{exp}}_{L_1} + \sigma^{\text{exp}}_{L_2}) S_{2\eta}/S_2] \\ - \sigma^{\text{exp}}_{L_1}(f_{12}f_{23} + f_{13} + f'_{13}) - \sigma^{\text{exp}}_{L_2} f_{23}\end{aligned} \tag{4}$$

where $\omega_i (i = 1, 2, 3)$ are the L_i subshell fluorescence yields, $f_{ij} (i, j = 1, 2, 3$ with $i < j)$ are the non-radiative Coster–Krönig yields, f_{13} is the radiative Coster–Krönig yield, $S_i (i = 1, 2, 3)$ are the total L_i radiative rates and S_{ij} are the radiative rates of L_{ij} transitions. The value of ω_i and f_{ij} were extracted from the table of Krause [20] and S_{ij} from the table of Scofield [21]. The required $L_{\gamma 2344'}$ yield was obtained from the expression as given below:

$$Y_{L_{\gamma 2344'}} = Y_{L_{\gamma 23644'}} - Y_{L_{\gamma 1}} S_{2_{\gamma 6}} / S_{2_{\gamma 1}}. \tag{5}$$

A detailed description regarding the determination of quantum efficiency of the solid state detectors has been given by Buras and Gerward [22]. It is quite obvious from figure 15 (page 108) of that reference that in the X-ray energy range of interest in the present work viz; 3 to 15 keV, the efficiency is almost unity.

The major sources of experimental uncertainties included for determining the total experimental error in the total ionization cross-sections are the following,

(i) projectile energy (2·5%), (ii) target areal density (2·2%), (iii) absorption corrections (5–10%), (iv) solid angle (1·4%), and (v) counting statistics ($\leqslant 10\%$)

On combining these uncertainties quadratically, the final uncertainties in $\sigma^x_{L_i}$ were found to be 6–10, 6–11 and 6–14% for L_α, $L_{\gamma 1}$ and $L_{\gamma 2344'}$ respectively. The atomic parameters (ω_i, S_{ij} and f_{ij}) introduce systematic uncertainties into $\sigma^{\text{exp}}_{L_i}$ as has been pointed out by several authors (for example, [23, 24]). However, these are difficult to quantify and consequently, following normal practice, were excluded from the error calculations. The final uncertainties in $\sigma^{\text{exp}}_{L_i}$ for protons incident on Au are 6–14% for L_1, 13–14% for L_2 and 8–17% for L_3.

4. Results and discussion

Gold: The measured subshell (σ_{L_1}, σ_{L_2} and σ_{L_3}) and total (σ_L) ionization cross-sections due to proton impact in the energy range of 200–350 KeV are given in table 1 and shown in figure 4. The cross-sections measured by Datz *et al* [9], Kiss *et al* [11] and the available theoretical results due to Pandey *et al* [14] (PWBA), Cohen and Harrigan [15] (ECPSSR) and Chen and Crasemann [16] (RPWBA-BC) are also given for the sake of comparison. Our results of σ_{L_1} and σ_{L_2} at 250 keV are almost half of that due to Datz *et al* [9] but are in good agreement with the calculated values reported by Chen and Crasemann [16] (RPWBA-BC) as well as Cohen and Harrigan [15] (ECPSSR). Present results of σ_{L_3} are however, in close agreement with both earlier observed and theoretically calculated cross-sections. At 350 keV incident energy, our measured values for σ_{L_2} and σ_{L_3} are in good agreement with the results of Datz *et al* [9]. Present measurements regarding σ_{L_1} σ_{L_2} and σ_{L_3} at 200 keV energy are in quite good agreement with the previous results. The results of our total L-shell ionization cross-sections (σ_L) are in very good agreement ($\mp 15\%$) with the earlier results of experiment [9, 11] and theory (ECPSSR and RPWBA-BC) at 200 keV.

The subshell ionization cross-section ratios viz: $\sigma_{L_1}/\sigma_{L_2}$, $\sigma_{L_2}/\sigma_{L_3}$ and $\sigma_{L_1}/\sigma_{L_3}$ are listed in table 4. Our measured values of $\sigma_{L_1}/\sigma_{L_2}$ are in agreement with the calculated ratios in the entire energy range and with the earlier measurements in the 250–300 keV range. But for 200 keV and 300 keV incident energy our results deviate from the earlier measurements. For $\sigma_{L_2}/\sigma_{L_3}$ the present values are in good agreement with the previously reported results.

Lead: Measured L-subshell and total inner shell ionization cross-sections along with the other experimentally measured and calculated results are given in table 2 and also shown in figure 5. Our σ_{L_1} values are almost in agreement (lower by 20%) with that of the measured value due to Moheb *et al* [13]. Good agreement is seen between

Table 1. L-shell/subshell ionization cross-sections (in barn) of Au.

Energy (keV)		200	250	300	350
σ_{L_1}	P	0·0019	0·012	0·026	0·032
	E	0·0020*	0·024$^{\#}$	0·035$^{\#}$	0·065$^{\#}$
	T	0·0020^{++}	0·015^{+}	0·034^{++}, 0·26$^{\$}$	0·41$^{\$}$
σ_{L_2}	P	0·00025	0·0024	0·0081	0·023
	E	0·00020*	0·0050$^{\#}$	0·013$^{\#}$	0·025$^{\#}$
	T	0·00034^{++}	0·0028^{+}	0·0089^{++}, 0·12$^{\$}$	0·21$^{\$}$
σ_{L_3}	P	0·0029	0·017	0·064	0·11
	E	0·0020*	0·025$^{\#}$	0·060$^{\#}$	0·12$^{\#}$
	T	0·0035^{++}	0·019^{+}	0·069^{++}, 0·71$^{\$}$	1·25$^{\$}$
σ_L	P	0·0050	0·031	0·098	0·165
	E	0·0042*	0·054$^{\#}$	0·108$^{\#}$	0·210$^{\#}$
	T	0·0059^{++}	0·037^{+}	0·11^{++}, 1·09$^{\$}$	1·87$^{\$}$

P: Present measurement.
E: Measurement made earlier $*$ – Ref. [11]; # – Ref. [9]
T: Theoretical calculations + – (RPWBA-BC) Ref. [16]; + + – (ECPSSR) Ref. [15]; \$ – (PWBA) Ref. [14]

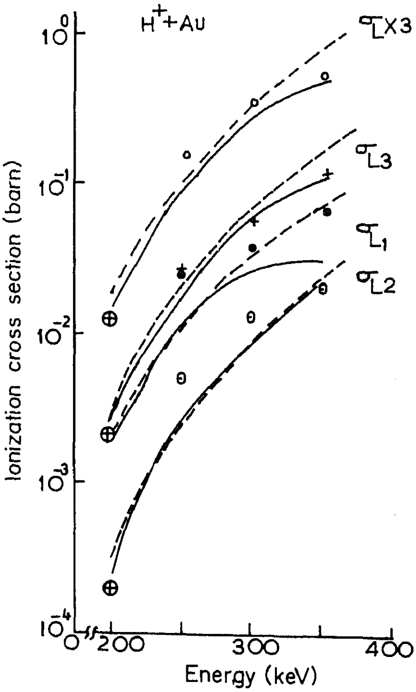

Figure 4. L-shell/subshell ionizations of Au due to proton impact. ——: Present results, ----: Ref. [15], (●) σ_{L_1}, (⊙) σ_{L_2}, (×) σ_{L_3}, (○) σ_L Ref. [9], (⊕) σ_L Ref. [11].

Table 2. L-shell/subshell ionization cross-sections (in barn) of Pb.

Energy (keV)		200	240	250	280	300	340	350
σ_{L_1}	P	0·0019		0·0071		0·018		0·033
	E		0·0069*		0·014*	0·021*	0·046*	
	T	0·00077^{++}				0·017^{++} 0·16$^{\$}$		0·26$^{\$}$
σ_{L_2}	P	0·00045		0·0011		0·0035		0·0054
	E		0·00087*		0·0020*	0·0023*	0·0059*	
	T	0·00011^{++}				0·0038^{++} 0·06$^{\$}$		0·12$^{\$}$
σ_{L_3}	P	0·0034		0·0075		0·019		0·042
	E		0·0040*		0·016*	0·028*	0·062*	
	T	0·0014^{++}				0·035^{++} 0·43$^{\$}$		0·79$^{\$}$
σ_L	P	0·0057		0·016		0·040		0·080
	E		0·0118*		0·032*	0·051*	0·1139*	
	T	0·0023^{++}				0·056^{++} 0·65$^{\$}$		1·17$^{\$}$

P: Present measurement.
E: Measurement made earlier $*$ – Ref. [13];
T: Theoretical calculations $++$ – (ECPSSR) Ref. [15]; \$ – (PWBA) Ref. [14]

the measurements and results reported by Cohen and Horigen [15] using the ECPSSR method for σ_{L_1} and σ_{L_2} cross-sections at 300 keV. The corresponding PWBA cross-sections [14] however, do not agree with our measured cross-sections. Present results for σ_{L_2} are in good agreement (though higher by 25%) with the cross-sections measured

Table 3. L-shell/subshell ionization cross-sections (in barn) of Bi.

Energy (KeV)		250	300	350
σ_{L_1}	P	0·0021	0·0029	0·0064
	T	0·0054^{+}	0·013^{++}	
σ_{L_2}	P	0·00098	0·0011	0·0034
	T	0·00084^{+}	0·0028^{++}	
σ_{L_3}	P	0·0045	0·0074	0·011
	T	0·0066^{+}	0·027^{++}	
σ_L	P	0·0076	0·011	0·021
	T	0·013^{+}	0·043^{++}	

P: Present measurement.
T: Theoretical calculations + –(RPWBA-BC) Ref. [16];
++ –(ECPSSR) Ref. [15]

Table 4. L-subshell ionization cross-section ratios for Au.

Energy (KeV)		200	250	300	350
$\sigma_{L_1}\sigma_{L_2}$	P	7·6	5·0	3·2	1·4
	E	10·0*	4·8#	2·7#	2·6#
	T	5·9^{++}	5·4^{+}	3·8^{++} 2·2$^{\$}$	1·9$^{\$}$
$\sigma_{L_2}\sigma_{L_3}$	P	0·09	0·14	0·13	0·21
	E	0·10*	0·20#	0·22#	0·21#
	T	0·097^{++}	0·15^{+}	0·13^{++} 0·17#	0·17$^{\$}$
$\sigma_{L_1}\sigma_{L_3}$	P	0·65	0·71	0·41	0·29
	E	1·0*	0·96#	0·58#	0·54#
	T	0·57^{++}	0·79^{+}	0·49^{++} 0·37$^{\$}$	0·33$^{\$}$

P: Present measurement.
E: Measurement made earlier * – Ref. [11]; # – Ref. [9]
T: Theoretical calculations + –(RPWBA-BC) Ref. [16]; ++ –(ECPSSR) Ref. [15]; \$ – (PWBA) Ref. [14]

by Moheb *et al* [13]. For the σ_{L_3}-subshell our values for the ionization cross-sections are close to the results of Moheb *et al* [13] but this agreement worsens as incident energy increases. Calculated σ_{L_3}cross-sections are two to three times lower at 200 keV but are larger by the same factor at 300 keV. Total inner shell ionization cross-section σ_L however, is found to be in good agreement with the earlier measured total cross-sections, though here also the agreement is poor towards higher incident energies.

The results of the subshell ionization cross-section ratios ($\sigma_{L_1}/\sigma_{L_2}$, $\sigma_{L_2}/\sigma_{L_3}$ and $\sigma_{L_1}/\sigma_{L_3}$) are given in table 5. It is found that our results are more or less similar to the values given by the ECPSSR theory [15]. Earlier measured values of $\sigma_{L_1}/\sigma_{L_2}$ ([13]) are approximately two times larger than the present results while our results for $\sigma_{L_2}/\sigma_{L_3}$ are two times larger than the corresponding values reported by Moheb *et al* [13]. In the case of $\sigma_{L_2}/\sigma_{L_3}$, the two sets of values are in reasonable agreement.

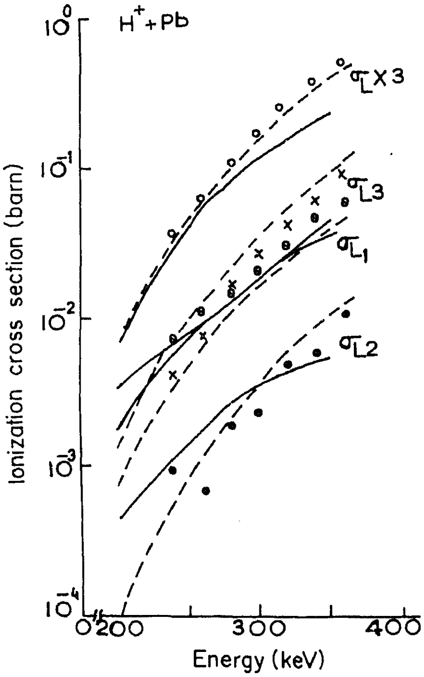

Figure 5. *L*-shell/subshell ionizations of Pb due to proton impact. ——: Present results, ----: Ref. [15] (○) σ_{L_1}, (●) σ_{L_2}, (×) σ_{L_3}, (○) σ_L Ref. [13].

Table 5. *L*-subshell ionization cross-section ratios for Pb.

Energy (KeV)		200	240	250	280	300	340	350
$\sigma_{L_1}/\sigma_{L_2}$	P	4·2		6·4		5·1		6·1
	E		7·9*		7·0*	9·1*	7·8*	
	T	7·0^{++}				4·47^{++} 2·67$^{\$}$		2·17$^{\$}$
$\sigma_{L_2}/\sigma_{L_3}$	P	0·132		0·147		0·184		0·128
	E		0·217*		0·125*	0·082*	0·095*	
	T	0·078^{++}				0·108^{++} 0·139$^{\$}$		0·152$^{\$}$
$\sigma_{L_1}/\sigma_{L_3}$	P	0·56		0·95		0·94		0·78
	E		1·72*		0·87*	0·75*	0·74*	
	T	0·55^{++}				0·48^{++} 0·37$^{\$}$		0·33$^{\$}$

P: Present measurement.
E: Measurement made earlier * – Ref. [13]
T: Theoretical calculations ++ –(ECPSSR) Ref. [15]; \$ – (PWBA) Ref. [14]

Bismuth: Results of our measurements of the *L*-shell ionization cross-sections due to proton impact regarding Bi are given in table 3 and shown in figure 6. No earlier measurements are available. Therefore, only theoretically calculated cross-sections are available for comparison. From the table as well as the figure it is seen that our results for various subshells as well as the total ionization cross-sections are satisfactorily reproduced by the ECPSSR [15] at 300 keV. The cross-section ratio obtained using the RPWBA-BC [16] method at 250 keV are also seen to be in

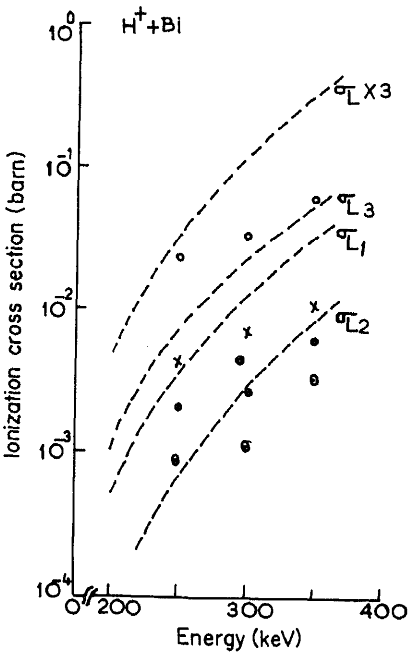

Figure 6. *L*-shell/subshell ionizations of Bi due to proton impact. (●), (⊙, ×, ○) Present results, ----: Ref. [15].

Table 6. *L*-subshell ionization cross-section ratios for Bi.

Energy (keV)		250	300	350
	P	2·1	2·6	1·9
$\sigma_{L_1}/\sigma_{L_2}$	T	$6{\cdot}43^+$	$4{\cdot}64^{++}$	
	P	0·22	0·15	0·31
$\sigma_{L_2}/\sigma_{L_3}$	T	$0{\cdot}13^+$	$0{\cdot}10^{++}$	
	P	0·47	0·39	0·58
$\sigma_{L_1}/\sigma_{L_3}$	T	$0{\cdot}81^+$	$0{\cdot}48^{++}$	

P: Present measurement.
T: Theoretical calculations + –(RPWBA-BC) Ref. [16]; + + –(ECPSSR) Ref. [15].

agreement with our measured values except for σ_{L_1} which is somewhat lower. Measured subshell ionization cross-sections (see table 6) are also in reasonable agreement with the calculated values except for $\sigma_{L_1}/\sigma_{L_3}$, in which case calculated values are comparatively large.

5. Conclusions

The agreement of the presently measured subshell and total inner shell ionization cross-sections for all the three systems with the previously measured and theoretically determined results are generally reasonable, considering the uncertainties in fluorescence yields, Coster Krönig transition probabilities and relative widths. Therefore, functioning of our experimental set-up seems to be fairly reliable. In the case of Bi the reported result is the first experimental one regarding the low energy proton impact inner-shell ionization cross-section. Efforts in the direction of measuring the cross-sections for a large number of systems, in the same energy range are in progress.

Acknowledgments

The authors acknowledge the help received from Profs H Ehrhardt, K Bergmann and Dr K Jung of the University of Kaiserslautern, Germany. Discussions with Prof. A K Nigam, Drs L Chaturvedi and V J Menon are also gratefully acknowledged. These targets were provided by Prof. S K Parthasarathy (VECC, Calcutta) and the financial assistance by VW-Stifftung (Germany) and UGC (India).

References

[1] D Bhattacharya, S K Bhattacherjee and S K Mitra, *J. Phys.* **B13**, 967 (1980)
[2] J R Chen, J D Reber, David J Ellis and Thomas E Miller, *Phys. Rev.* **A13**, 941 (1976)
[3] J J Chmielewski, J L Flinner, F W Inmann, B Sollenberger and N V Udeh, *Phys. Rev.* **A29**, 29 (1981)
[4] S Fast, J L Flinner, A Glick, F W Inmann, L Oolman, C Pearso and D Wickelgren, *Phys. Rev.* **A26**, 2417 (1982)
[5] E Rosato, P Cuzzocrea, N De Cesare, E Perillo and G Spadaccini, *IEEE. Trans. Nucl Sci.* **NS30**, 967 (1983)
[6] A R Zander, *Nucl. Instrum. Methods* **280**, 483 (1985)
[7] P S Singh, H Mohan, D Singh, H R Verma and C S Khurana, *Indian J. Phys.* **A62**, 674 (1988)
[8] F Abrath and Tom J Gray, *Phys. Rev.* **A10**, 1157 (1974)
[9] S Datz, J L Duggan, L C Feldman, E Laegsgaard and J U Andersen, *Phys. Rev.* **A9**, 192 (1974)
[10] W Jitschin, A Kaschuba, R Hippler and H O Lutz, *J. Phys.* **B15**, 763 (1982)
[11] K Kiss, T Papo, J Palinkas, L Sarkadi and B Schilenk, *Acta Phys. Hung.* **58(1–2)**, 69 (1985)
[12] T K Li D L Clatk and G W Greenless, *Phys. Lett* **37**, 1209 (1976)
[13] H Moheb, R Bigaouette and F W Inmann, *Phys. Rev.* **A32**, 3739 (1985)
[14] K N Pandey, U S Tiwari and D N Tripathi, *Indian J. Phys.* **B63**, 133 (1990)
[15] D D Cohen and M Harrigan, *At. Data Nucl. Data Tables* **33**, 255 (1985)
[16] M H Chen and B Crasemann, *At. Data Nucl. Data Tables* **33**, 217 (1985)
[17] K N Pandey, R Shanker D N Tripathi and D K Rai, *Indian J. Technol.* **25**, 393 (1987)
[18] R S Sokhi and D Crumpton, *J. Phys.* **B19**, 4193 (1986)
[19] E Storm and H I Israel, *Nucl. Data Tables* **A47**, 565 (1970)
[20] M O Krause, *J. Phys. Chem. Ref. Data* **8**, 307 (1979)
[21] J H Scofield, *At. Data Nucl. Data* **14**, 121 (1974)
[22] B Buras and L Jelward, *Progress in crystal growth and characterization* [Recent advances in X-ray characterization of materials-II, edited by P Krishna (Pergamon Press, Oxford-New York, 1988) Vol 18, p 108
[23] R S Sokhi and D Crumpton, *Nucl. Instrum. Methods* **181**, 5 (1981)
[24] W Jitschin, R Hippler, K Fink, R Schuch and H O Lutz, *J. Phys.* **B16**, 4405 (1983)

PRAMANA
— journal of
physics

© Printed in India

Vol. 41, No. 2,
August 1993
pp. 185–191

Kinetic properties of an acoustic-like mode in a two-ion quasi-neutral plasma

C B DWIVEDI*
Physical Research Laboratory, Navarangpura, Ahmedabad 380 009, India
*Present Address: Institute of Advanced Study in Science and Technology, Khanapara, Guwahati 781 022, India

MS received 15 December 1992; revised 22 April 1993

Abstract. Kinetic analysis of an acoustic-like mode in a plasma with hot and cold ion components has been carried out. Under the short wevelength approximation ($k\lambda_{De} \gg 1$), electrons are assumed to form a dynamic neutralising background and their contribution to the perturbation is neglected. The significant role of the hot ions to Landau damping of the acoustic-like mode is highlighted and a novel concept of plasma experiment is suggested.

Keywords. Kinetic property; acoustic-like mode; Landau damping; Maxwellian distribution; quasi-neutral.

PACS No. 52·35

1. Introduction

It is well established that the ion-acoustic wave (IAW) is the only low frequency mode in an unmagnetized plasma system wherein the dynamics of both, the electrons and ions, is involved. The IAW propagates as a normal mode when $T_e \gg T_i$ i.e. electrons are hotter than ions, otherwise the mode is heavily Landau damped. Moreover, only longer wavelengths ($k\lambda_{De} \ll 1$) of IAW propagates whereas the shorter wavelengths ($k\lambda_{De} \gg 1$) transform into an ion plasma oscillation. However, recently Dwivedi *et al* [1] (hereafter called as paper I) have shown that an acoustic-like mode (ALM) appears to propagate as a normal mode even for the shorter wavelength case in a plasma consisting of hot and cold ions with different masses, number densities and temperatures. Under the short wavelength approximation the role of electrons in the perturbation has been neglected and the linear and nonlinear behaviour of the aforesaid mode has been described using fluid model. The plasma system considered in paper I may be anticipated in thermalisation of the counter streaming ion beams [2] of appropriate energies with hot electrons or in fusion plasmas with selective heating of one ion species. Similar situation is likely to be achieved in dusty plasmas in laboratory. The practical realisation of required conditions for the existence of ALM may not be very easily achieved due to highly restrictive theoretical constraints. The present conceptual plasma model may provide a base to the experimentalists to produce ALM in the laboratory [3].

From the linear dispersion relation derived for ALM in paper I, one finds that the relative ion density and temperature are crucial parameters for deciding the existence of the mode. Fluid treatment is found to be valid for $\varepsilon_T \gg \varepsilon_n \gg 1$ and $\varepsilon_n \gg \varepsilon_m$ with

$\varepsilon_m > 1$ and $\varepsilon_z > 1$, where all the notations are defined in paper I. For $\varepsilon_m < 1$, the fluid approximations are very well satisfied. Unlike the usual IAW where only electron and ion temperature ratio is a responsible parameter for kinetic effects to be important, ALM involves more free parameters to decide its kinetic propreties. This provides more freedom to play with these parameters so as to allow the existence of the mode. Under the fluid approximations, the required conditions for the existence of a normal mode cannot be specified quantitatively. The fluid treatment ignores the wave-particle interaction which cannot always be true. This interaction becomes important when the phase velocity of a mode is of the order of thermal velocity of a plasma component and leads to the collisionless Landau damping. Consideration of the wave-particle interaction cannot be described within the framework of a fluid model and hence the kinetic approach becomes necessary. The Landau damping being a kinetic phenomenon decides the quantitative limitation of the fluid model. The basic motivation behind the present analysis is to look for the quantitative estimation of the plasma parameters for the existence of the ALM as a normal mode. Wide range variability of more free parameters creates curiosity to analyse their effect on the Landau damping and find appropriate values of these parameters for the normal mode behaviour of the ALM. With this idea in mind, the kinetic analysis of the ALM has been performed and the contribution of the hot ions to its Landau damping has been highlighted.

It is concluded that the hot ion component causes finite Landau damping with sensitive dependence on the charge states of the ions. The mass ratio of hot and cold ions also constitutes an important candidate to decide the normal mode behaviour of the ALM. It is emphasized that the hot and cold ions considered in the present plasma model are not the manifestation of double humped distribution with two maxima but these represent the two different species of ions with Maxwellian distribution at their respective temperatures.

2. Vlasov equation and Landau damping

Using standard Vlasov equation and following the usual treatment of collisionless Landau damping [4], the expression for the Landau damping of ALM has been derived and analysed. The hot and cold ions can be described by Vlasov equation;

$$\frac{\partial f_\alpha}{\partial t} + \mathbf{v}_\alpha \cdot \nabla f_\alpha + \frac{q_\alpha}{m_\alpha} \mathbf{E} \cdot \frac{\partial f_\alpha}{\partial v_\alpha} = 0. \tag{1}$$

Here f_α is the distribution function for the αth plasma species. Subscript α denotes different ion components, hot ions (ih) and cold ions (ic). Let us assume that the ambient electric field $\mathbf{E}_0 = 0$, $f_\alpha = f_{\alpha 0} + \tilde{f}_\alpha$ such that $\tilde{f}_\alpha / f_{\alpha 0} \ll 1$, where $f_{\alpha 0}$ is the equilibrium and $\tilde{f}_\alpha$ the perturbed distribution functions of αth plasma species. Now the linearized form of (1) can be written as

$$\frac{\partial \tilde{f}_\alpha}{\partial t} + \mathbf{v}_\alpha \cdot \nabla \tilde{f}_\alpha + \frac{q_\alpha}{m_\alpha} \tilde{\mathbf{E}} \cdot \frac{\partial f_{\alpha 0}}{\partial v_\alpha} = 0, \tag{2}$$

where v_α is an independent variable and $q_\alpha = Z_\alpha q$, q being the charge on the ions and Z_α the charge multiplicity of αth plasma species. Considering one dimensional case and assuming the perturbation to vary as $\exp(-i\omega t + ikx)$, (2) can be Fourier analysed to yield,

$$\tilde{f}_\alpha = -\frac{i}{\omega - kv_\alpha}\frac{q_\alpha}{m_\alpha}\tilde{\mathbf{E}}\cdot\frac{\partial f_{\alpha 0}}{\partial v_\alpha}. \tag{3}$$

Associated perturbed density can be written as,

$$n_\alpha = \int \tilde{f}_\alpha \mathrm{d}v_\alpha = -i\frac{q_\alpha}{m_\alpha}\tilde{E}\int\frac{\partial f_{\alpha 0}/\partial v_\alpha}{\omega - kv_\alpha}\mathrm{d}v_\alpha. \tag{4}$$

Let us consider the equilibrium to be characterized by a Maxwellian velocity distribution $f_{\alpha 0}$;

$$f_{\alpha 0} = \frac{n_{\alpha 0}}{\pi^{1/2}v_{t\alpha}}\exp(-v_\alpha^2/v_{t\alpha}^2), \tag{5}$$

where $v_{t\alpha} = (2T_\alpha/m_\alpha)^{1/2}$ is the thermal velocity of αth species of plasma. Substituting the perturbed density $\tilde{n}_\alpha$ from (4) in the Poisson's equation one can, after some algebraic manipulation, derive the dispersion relation as,

$$1 - \sum_\alpha(\omega_{p\alpha}^2/k^2 v_{t\alpha}^2)Z'(\zeta_\alpha) = 0, \tag{6}$$

where $Z(\zeta_\alpha)$ is the plasma dispersion function defined by

$$Z(\zeta_\alpha) = \pi^{-1/2}\int\frac{\exp(-s_\alpha^2)}{s_\alpha - \zeta_\alpha}\mathrm{d}s_\alpha. \tag{7}$$

Here $\zeta_\alpha = (\omega/k)/v_{t\alpha}$, $s_\alpha = v_\alpha/v_{t\alpha}$ and $\omega_{p\alpha}^2 = 4\pi n_{\alpha 0}q_\alpha^2/m_\alpha$. Equation (6) is the required dispersion relation of the ALM with $Z'(\zeta_\alpha) = \partial Z(\zeta_\alpha)/\partial\zeta_\alpha$.

Following Chen [4] or any other general book on plasma physics and considering power series expansion of $Z(\zeta_{ih})$ and asymptotic expansion of $Z(\zeta_{ic})$ for $\zeta_{ih} \ll 1$ and $\zeta_{ic} \gg 1$ respectively, the dispersion relation can be simplified to give

$$\omega^2/k^2 = (\varepsilon_T/\varepsilon_n\varepsilon_z^2)(1 + 3\varepsilon_n\varepsilon_z^2/\varepsilon_T)v_{tic}^2. \tag{8}$$

In deriving (8) the approximations $\varepsilon_T \gg \varepsilon_n \gg 1$ and $\varepsilon_n\varepsilon_z^2 \gg \varepsilon_m$ have been used. This is the dispersion relation for ALM [1] with $\gamma_{ic} = 3$. This is to note that by replacing hot ions with electrons and considering $\varepsilon_z = 1$, eq. (8) is reduced to the usual dispersion relation of an IAW.

Now retaining the Landau terms for hot and cold ions, (6) can be simplified to give;

$$\gamma = -(\mathrm{Im}\,\zeta_c/\mathrm{Re}\,\zeta_c) = -(\mathrm{Im}\,\omega/\mathrm{Re}\,\omega) = \left(\frac{\pi}{8}\right)^{1/2}(3+\theta)^{1/2}$$
$$\left(\theta + (\varepsilon_m/\varepsilon_T)^{1/2}\exp\left\{(1 - \varepsilon_m/\varepsilon_T)\frac{3+\theta}{2}\right\}\right)\exp\left(-\frac{3+\theta}{2}\right), \tag{9}$$

where

$$\theta = \left(\frac{1}{\varepsilon_n\varepsilon_z^2}\right)\varepsilon_T.$$

The second term inside the capital bracket arises due to the hot ion's contribution to the Landau damping. Replacement of hot ions by electrons reduces (9) to the usual expression of Landau damping for IAW wherein the contribution of electrons is negligibility small due to ε_m being a very small parameter. For very large values of θ ($\varepsilon_T \gg \varepsilon_n \gg \varepsilon_m$) the Landau damping is approximated by $\gamma \approx (\pi \varepsilon_m / 8\varepsilon_n \varepsilon_z^2)^{1/2}$ and is governed by the balance between increase in hot ion contribution and decrease in cold ion contribution to the Landau damping. The increase (decrease) of the Landau damping due to hot (cold) ions is associated with the deviation of the phase velocity of ALM closer to (away from) the thermal velocity of hot (cold) ions. In other words, one can say that the deficiency in wave-particle interaction due to the cold ions is compensated by hot ions at higher values of θ and hence a constant (plateau) but finite level of Landau damping is achieved. All the features of the plateau can be described by the above approximate form of the Landau damping. The ratio of Landau dampings with and without hot ions is given as

$$-(\gamma_{h+}/\gamma_{h-}) = 1 + \frac{1}{\theta}\left(\frac{\varepsilon_m}{\varepsilon_T}\right)^{1/2} \exp[0{\cdot}5\{(1 - \varepsilon_m/\varepsilon_T)(3+\theta)\}]. \tag{10}$$

It is obvious that for certain range of plasma parameters, the contribution of hot ions to the Landau damping of ALM can be significant and their role to decide its existence cannot be undermined. This can be attributed to the relative density of hot and cold ions which forms an important parameter to compete with their relative temperature to decide the kinetic effects (8). Charge multiplicity is also found to be a sensitive parameter.

3. Conclusions

In general the collisionless damping due to wave-particle interaction occurs if $\partial f_{\alpha 0}/\partial v_\alpha | v_\alpha = w/k \ll 0$ otherwise, in the opposite limit, growth is obtained. A favourable situation for the latter arises in a plasma system of hot and cold ions associated with two maxima in double humped ion distribution. However, this paper considers a plasma model wherein the hot and cold ions form two different species of ions which are Maxwellian at their respective temperatures. Consequently the possible existence of an instability and its analysis lie beyond the scope of the proposed plasma model. Such configuration of ion components may be realised in dusty plasma systems provided that all the characteristic plasma lengths and perturbational wavelengths be larger than the dust size otherwise the present mathematical formalism will not be valid. Accordingly, the present analysis falls in the first category wherein slow particles are more than the fast ones. From numerical calculations, it is inferred that the acoustic-like mode propagates as a normal mode with weak Landau damping provided that the temperature ratio of hot and cold ions (ε_T) is larger than their density ratio (ε_n) by about an order of a magnitude (figures. 1–6). The weak Landau damping is clearly due to hot ions which contribute significantly for $\varepsilon_z < 1$ (figure 5) and $\varepsilon_m > 1$ (figure 3). The collisionless Landau damping is less for $\varepsilon_z > 1$ (figure 6) and $\varepsilon_m < 1$ (figure 4). The maximum peak occurs at $\varepsilon_n \approx \varepsilon_T$; the variation of damping rate at peak is of the order of 10%. In brief one can say that the lighter hot ions in majority ($\varepsilon_n > 10$) with higher charge state is favourable for the existence of the ALM in a three component plasma. However, the numerical analysis suggests that the

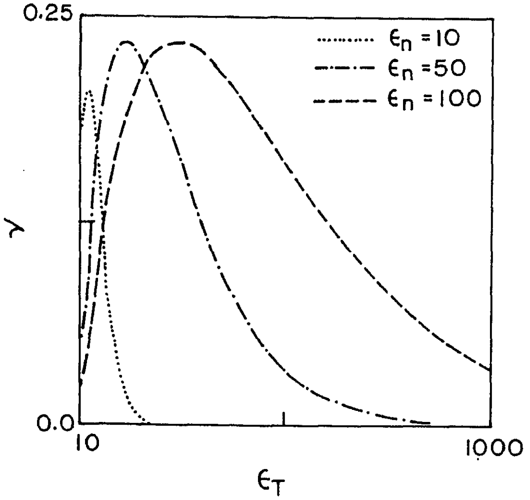

Figure 1. Variation of Landau damping (γ) with hot and cold ion temperature ratio (ε_T) without hot ions contribution for $\varepsilon_z = 1$, $\varepsilon_m = 1$.

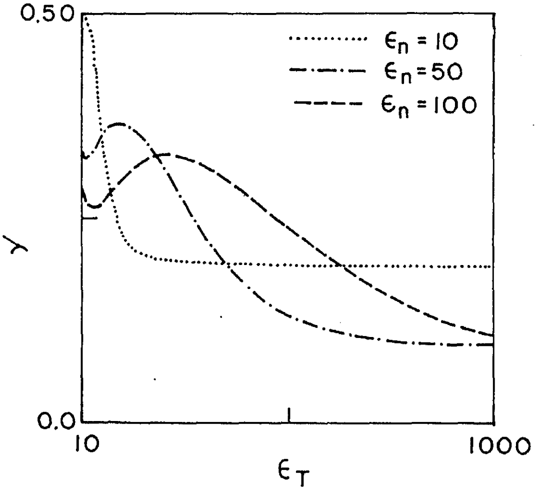

Figure 2. Variation of Landau damping with hot and cold ion temperature ratio with hot ions contribution for $\varepsilon_z = 1$, $\varepsilon_m = 1$.

mode will always be associated with finite but small Landau damping for any practical situation within the framework of the present theoretical constraints.

Thus the role of hot ions to the Landau damping of ALM in a two-ion species quasi-neutral plasma has been analysed and numerical calculations have been done for the appreciation of the results. Some calculations for the similar plasma parameters have been done by Farr and Budwine [5] for the study of high frequency flute like instability in multi-component plasmas. Their calculations involve electron's contribution to the perturbation whereas in this work electron's contribution is justifiably

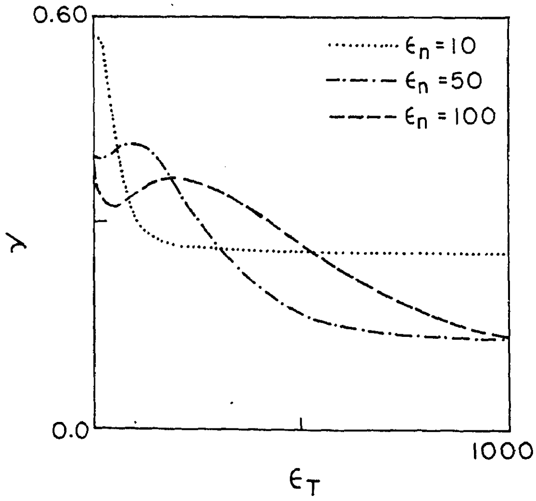

Figure 3. Variation of Landau damping with hot and cold ion temperature ratio with hot ions contribution for $\varepsilon_z = 1$, $\varepsilon_m = 2$.

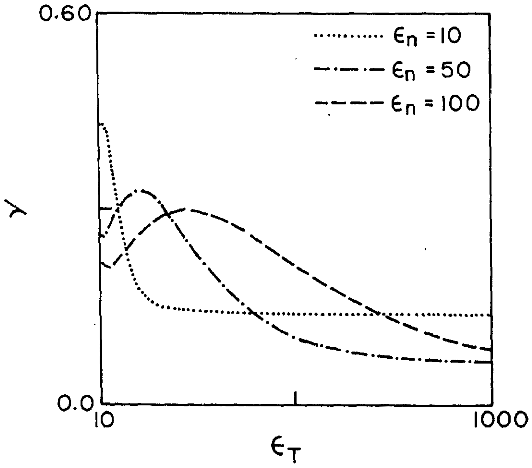

Figure 4. Variation of Landau damping with hot and cold ion temperature ratio with hot ions contribution for $\varepsilon_z = 1$, $\varepsilon_m = 0{\cdot}5$.

neglected. They argue that their calculations have some relevance for an experiment which involves injection of the hot ions into a cold background plasma like mirror confined plasmas.

Based on the present analysis a novel concept of plasma experiment is proposed wherein cold ions can be injected into a hot background plasma to produce a plasma system which can support ALM mode. This may provide an experimental idea to study the acoustic-like mode in the laboratory plasmas.

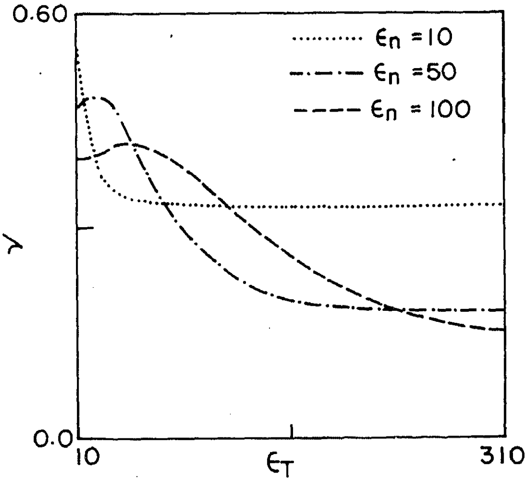

Figure 5. Variation of Landau damping with hot and cold ion temperature ratio with hot ions contribution for $\varepsilon_z = 0{\cdot}5$, $\varepsilon_m = 1$.

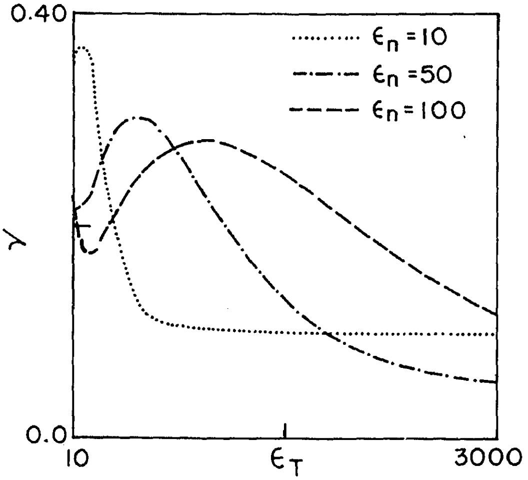

Figure 6. Variation of Landau damping with hot and cold ion temperature ratio with hot ions contribution for $\varepsilon_z = 2$, $\varepsilon_m = 1$.

Acknowledgements

Useful discussions with Prof. A C Das and the assistance of Dr S C Tripathy in the numerical calculations are thankfully acknowledged.

References

[1] C B Dwivedi, R S Tiwari, V K Sayal and S R Sharma, *J. Plasma Phys.* **41**, 219 (1989)
[2] K Abe, in Proceedings of topical meeting on particle beam fusion and its related problems (Nagoya University, Nagoya, 1986) Vol. 1, p. 174
[3] M J Gerver, *Phys. Fluids* **19**, 1581 (1976)
[4] F F Chen, *in Introduction to plasma physics and controlled fusion* (Plenum Press, New York, 1984) Vol. 1, II Edn
[5] W M Farr and R E Budwine, *Phys. Fluids* **11**, 833 (1968)

PRAMANA
— journal of
physics

© Printed in India

Vol. 41, No. 2,
August 1993
pp. L193–L198

Conservation laws in stochastic deposition–evaporation models in one dimension

DEEPAK DHAR and MUSTANSIR BARMA
Tata Institute of Fundamental Research, Homi Bhabha Road, Bombay 400005, India

MS received 3 June 1993; revised 9 July 1993

Abstract. An infinite number of conservation laws is identified for a stochastic model of deposition and evaporation of trimers on a linear chain. These laws can be encoded into a single nonlocal invariant, the irreducible string, which uniquely lables an exponentially large number of kinetically disconnected sectors of phase space. This enables the number and sizes of sectors to be determined. The effects of conservation laws on some thermodynamic properties are studied.

Keywords. Conservation laws; stochastic processes; deposition-evaporation models; slow kinetics.

PACS Nos 02·50; 05·50; 68·45; 82·20

Conservation laws are known to play a very important role in determining the behaviour of systems which evolve by stochastic dynamics. In this paper, we identify and study an infinite number of conservation laws for a recently introduced model of deposition and evaporation of trimers on a lattice [1, 2]. These laws have a number of interesting and useful consequences. They provide a labelling scheme to uniquely identify each of an exponentially large number of dynamically disconnected sectors of phase space; they clarify why steady states differ from the Gibbs state for a simple lattice gas, even though the transition rates satisfy the detailed balance condition for the lattice gas; and they shed light on the time-dependence of correlation functions.

The model is defined as follows. At each site i of a chain of L sites, there is a variable n_i which takes two possible values, say a if the site is occupied, and b if it is empty. The time evolution is Markovian: In a small time $\mathrm{d}t$ any three adjacent empty sites become occupied with a probability $\varepsilon \mathrm{d}t$ (trimer deposition). Any three adjacent occupied sites become unoccupied with a probability $\varepsilon' \mathrm{d}t$ (trimer evaporation). If three consecutive sites are not all empty, or all full, no deposition or evaporation takes place on those three sites. Note that the model allows for free reconstitution of trimers. If $\varepsilon' = 0$ (irreversible deposition only), the process reduces to the well-studied problem of random sequential adsorption [3, 4]. The higher-dimensional generalizations of this model are also of interest [5], but we restrict ourselves to the one-dimensional case in this paper. For simplicity, we consider open boundary conditions throughout.

It is natural to think of the line as made of three sublattices, A, B and C. If M_A, M_B and M_C are the numbers of occupied sites on each sublattice, it is clear that $(M_A - M_B)$ and $(M_B - M_C)$ are conserved under the stochastic dynamics [1, 2]. These conservation laws imply that the state-space breaks up into many disconnected sectors; evidently, the number of sectors increases at least as fast as L^2 for large L. As a matter of fact, however, the number increases much faster—exponentially with L [1, 2]. The additional conservation laws responsible for this further break up into smaller sectors in this model are not immediately obvious, and form the subject of this paper.

A configuration of the chain is specified by giving an L-bit string composed of letters a and b. We define a *reduction rule* for a string by looking for the occurrence of any triplet aaa or bbb. If any such triplet occurs, it is replaced by the null string ϕ, reducing the length of the string by 3 bits. This reduction procedure is applied repeatedly, until we are left with a string that cannot be further reduced. We call such a string *irreducible*. The irreducible string corresponding to the string S is denoted by $I(S)$. For example, $I(aabaab) = aabaab$, $I(abbbba) = aba$ and $I(abbbaa) = \phi$, the null string. The key observation that allows us to construct an infinite number of conservation laws corresponding to trimer dynamics is the following: If S is the string specifying a configuration of the chain, and S' is another string obtained by a time evolution of S, then $I(S) = I(S')$. This is because the elementary Markovian step of deposition or evaporation does not change I. Also, if two strings S and S' correspond to the same irreducible string, then it can be shown [6] that S can be obtained from S' in a finite number of steps using the rules of trimer dynamics, i.e. $aaa \rightarrow bbb$ and $bbb \rightarrow aaa$. Thus, treated as a dynamical variable, the irreducible string is a constant of motion and provides a unique label for each invariant subspace of the stochastic dynamical evolution operator.

The number N_L of distinct sectors is thus the number of distinct irreducible strings I obtainable from all possible L-bit strings. First consider strings S containing no triplets aaa or bbb, for which $I(S)$ is also of length L. These configurations are totally jammed, and cannot evolve at all. As shown earlier [1, 2], their number is $2F_L$, where F_L are the Fibonacci numbers defined by $F_1 = 1$, $F_2 = 2$, $F_{k+2} = F_{k+1} + F_k$, for $k \geqslant 1$. Thus F_L increases as μ^L, where μ is the golden ratio $(\sqrt{5}+1)/2 \approx 1{\cdot}618$. Since all possible irreducible strings I obtainable from strings of length L are either of length L or obtainable from strings of length $(L-3)$, the total number of sectors N_L corresponding to length L satisfies the recursion relation $N_L = N_{L-3} + 2F_L$. This has the solution

$$N_L = \sum_{m=0}^{[L/3]} 2F_{L-3m} \tag{1}$$

where $[x]$ is the largest integer less than x. Thus N_L also grows as μ^L for large L, and the ratio N_L/F_L tends to $2(1-\mu^{-3})^{-1} \approx 2{\cdot}618$. As a consequence, the number of unjammed sectors $(N_L - F_L)$ (for which only numerical results were available earlier [1, 2]) grows as μ^L as well.

Next we characterize the sizes of sectors. Let $D(I, L)$ be the size of sector (I, L), i.e. the number of L-site configurations in a sector labelled by the irreducible string I. It is convenient to introduce the generating function

$$g(I, x) = \sum_{L=l}^{\infty} x^L D(I, L) \tag{2}$$

where l is the length of the irreducible string I. First consider the sector Φ, which is comprised of all configurations which are reducible to the null string ϕ. (The all-sites-empty configuration clearly belongs to this sector.) It is useful to define a formal series $G(\phi)$ which is a sum over all distinct strings (of arbitrary length) which are reducible to ϕ. Thus

$$G(\phi) = \phi + aaa + bbb + aaaaaa + abbbaa + aaabbb + \cdots \tag{3}$$

A string S is said to be *indecomposable* if $I(S) = \phi$, and one cannot find strings $t_1, t_2 \neq \phi$ such that $s = t_1 \cdot t_2$ and $I(t_1) = I(t_2) = \phi$. For example, the string *aabbba* is indecomposable while *aaabbb* is decomposable. Then any string S which is reducible to ϕ has a unique decomposition of the form $S = t_1 \cdot t_2 \cdot t_3 \cdots t_r$, where $t_1, t_2, \cdots t_r$ are indecomposable substrings, and the product of strings is understood as the standard concatenation operation. If $G_{\text{in}}(\phi)$ is the sum over all non-null indecomposable substrings reducible to ϕ, equation (3) can be rewritten as

$$G(\phi) = \frac{\phi}{1 - G_{\text{in}}(\phi)} \tag{4}$$

where the right hand side of (4) is defined by its binomial expansion. If $G_a(G_b)$ consists of a sum over all non-null indecomposable strings which reduce to ϕ and start with the letter $a(b)$, then we have $G_{\text{in}}(\phi) = G_a + G_b$ and

$$G_a = a \frac{1}{1 - G_b} a \frac{1}{1 - G_b} a \tag{5a}$$

$$G_b = b \frac{1}{1 - G_a} b \frac{1}{1 - G_a} b. \tag{5b}$$

Equations (4) and (5) determine $G(\phi)$. The generating function $g(\phi, x)$ for sector sizes is obtained from the formal string sum $G(\phi)$ by substituting $\phi \to 1$, $a \to x$, $b \to x$ in the latter and treating the result as an ordinary polynomial. Under these substitutions, both G_a and G_b reduce to the same function $h(x)$, which, in view of (5), satisfies

$$h(1 - h)^2 = x^3. \tag{6}$$

Further, G_{in} reduces to $2h(x)$, so eq. (4) becomes

$$g(\phi, x) = \frac{1}{1 - 2h(x)}. \tag{7}$$

Of the three solutions of the cubic equation (6), the branch on which $h \to 0$ as $x \to 0$ is the physical branch. In view of (2) and (7), the rate of growth of $D(\phi, L)$ with L is governed by the singularities of $h(x)$ closest to the origin in the complex x^3-plane. This occurs when two roots of the cubic equation (6) coincide, i.e. when $h = 1/3$, corresponding to $x_c^3 = (4/27)$. Thus for large L, the size of null sector grows as $L^{-3/2}(27/4)^{L/3}$—an exponentially small fraction of the total number of configurations, 2^L.

Now consider non-null sectors, labelled by a given irreducible string $I = \alpha_1 \alpha_2 \alpha_3 \cdots \alpha_l$, where l is the length of I, and α_i are letters taking values a and b. Analogously to (4) and (5) we have

$$G(I) = \frac{1}{1 - H(\alpha_1)} \alpha_1 \frac{1}{1 - H(\alpha_2)} \alpha_2 \frac{1}{1 - H(\alpha_3)} \alpha_3 \cdots \alpha_l G(\phi) \tag{8}$$

where $H(a) = G_b$ and $H(b) = G_a$. As a result, we find

$$g(I, x) = \left[\frac{x}{1 - h(x)}\right]^l \frac{1}{1 - 2h(x)}. \tag{9}$$

Note that the only dependence of the generating function on the irreducible string I is through l, the length of I. So long as l is finite, $D(L, I)$ increases as $(27/4)^{L/3}$ as $L \to \infty$. If, however, l/L tends to a finite limit λ as $L \to \infty$, then $D(L, I)$ increases as $[\kappa(\lambda)]^L$ where $\kappa(0) = (27/4)^{1/3}$ and $\kappa(1) = 1$. The growth constant $\kappa(\lambda)$ can be determined explicitly for arbitrary λ, and is found to be

$$\kappa(\lambda) = 3[(1 - \lambda)^{1-\lambda}(2 + \lambda)^{2+\lambda}]^{-1/3}. \tag{10}$$

For a random string of length L, the corresponding irreducible string has an average length $\lambda_0 L$ where $\lambda_0 = 1 - 3\mu^{-2}/2$.

In random sequential adsorption (which is the $\varepsilon' = 0$ case of our model) it is known that the final state is not described by an equilibrium ensemble of a simple local Hamiltonian, and it is worthwhile to investigate whether this is true also of the dynamical steady state when both deposition and evaporation are allowed. In particular, consider the sector Φ, and let $W(S_1)$ and $W(S_2)$ be the steady state weights of configurations S_1 and S_2, where S_1 is obtained from S_2 by the deposition of a single trimer. Detailed balance then implies $W(S_1)/W(S_2) = \varepsilon/\varepsilon' \equiv z^3$ where z is the single a-particle fugacity. This condition is the same as would hold for a simple lattice gas with no constraint other than single occupancy of sites. The question is then whether thermodynamic properties of our model are the same as the lattice gas. The partition function associated with sector Φ is

$$Z_{L,\Phi} = \sum{}' z^{N_a(S)} \tag{11}$$

where the prime indicates that the sum is over all strings of length L which can be reduced to the null string ϕ, and $N_a(S)$ is the number of a's in S. The transform $\Sigma_L x^L Z_{L,\Phi}(z)$ can be found on making the substitutions $a \to xz$, $b \to x$ in (4) and (5). Then Z is found on inverting the transform, and the mean density n_a of a sites is obtained by differentiating with respect to z. In the low-density limit, the result [6] is $n_a \approx 2^{-1/3} z$. The significant point is that this differs from the answer which would result from the Gibbs state characterized just by fugacity z (as for the lattice gas) for which $n_a \approx z$ in the low density limit. Of course, there is no contradiction; we have demonstrated only that the constraints implied by the conservation laws for trimer dynamics restrict the ensemble to such a small portion of the full phase space that averages over this ensemble differ from those in the canonical ensemble.

It is clear that the construction of the irreducible string for a given configuration is a non-local operation, and three sites well-separated from each other may or may not form a reducible triplet depending on the substrings in between. However, it is possible to reexpress the constant of motion given by the irreducible string in a form which appears more local. To this end, we define two 2×2 complex matrices $A(0, x)$ and $A(1, x)$ depending on a real parameter x by

$$A(n, x) = \begin{pmatrix} \omega & nx \\ \bar{n}x & \omega^* \end{pmatrix}, \quad n = 0, 1 \tag{12}$$

where $\bar{n} = 1 - n$, and ω is a complex cube root of unity. It is easily checked that

$A^3(n,x)=I$, for $n=0,1$, for all x. Now, for any configuration $S=\{n_j\}$ on the linear chain, we associate with site i a 2×2 complex matrix $U_i(x)$ which is specified in terms of $\{n_j\}$ by the equation

$$U_i(x)=\prod_{j=1}^{i} A(n_j,x) \tag{13}$$

where the product is ordered so that larger values of j are to the left. Clearly, we can determine the configuration $\{n_i\}$ uniquely if we are given all the matrices U_i. A stochastic evolution of $\{n_i\}$ corresponds to a stochastic evolution of the $\{U_i\}$. While the definition of $\{U_i\}$ in terms of $\{n_i\}$ is non-local, the stochastic evolution rules for updating U_i are local: If $U_i(x)$ and $U_{i+3}(x)$ are equal, then $U_{i+1}(x)$ and $U_{i+2}(x)$ are changed together in a specified way with some given rate, otherwise not. In addition, $U_L(x)$ remains unchanged by the dynamics. If we define $U_{i=0}(x)$ as the identity matrix, the dynamics is tantamount to the stochastic evolution of a 'string' fixed at both ends, the 'displacement' of the string being the matrix variable U_i.

If we expand $U_L(x)$ in a power series in x

$$U_L(x)=\sum_m u_{L,m}x^m, \tag{14}$$

then the conservation of $U_L(x)$ implies that the coefficients $u_{L,m}$ which are functions of the configuration $\{n_i\}$, are constants of motion. This gives us an infinite number of conservation laws. The first member of this family of conserved quantities is $u_{L,1}$, which is of the form $\begin{pmatrix} 0 & V_1 \\ V_2 & 0 \end{pmatrix}$ where V_1 is a complex number given by

$$V_1=\omega^{L+1}\sum_{j=1}^{L} n_j\omega^j. \tag{15}$$

It is easy to see that the conservation of real and imaginary parts of V_1 corresponds to the conservation of M_A-M_B and M_B-M_C.

To identify a sector completely, we have to specify the function $U_L(x)$ for all x, or equivalently an infinite number of coefficients $u_{L,m}$. Let the value of $U_L(x)$ in two configurations C_1 and C_2 be $u_1(x)$ and $u_2(x)$. Let x^* be any transcendental number. Then $u_1(x^*)=u_2(x^*)$ implies that $u_1(x)=u_2(x)$ for all x (otherwise x^* would be the root of a polynomial equation). Thus, the full family of invariants $U_L(x)$ contains no more information than the single invariant $U_L(x^*)$. Indeed, we have seen that a simple integer invariant—the binary representation of which is the irreducible string—already gives the maximal decomposition of phase space into disjoint sectors. This can be understood in terms of a theorem of von Neumann [7, 8] which states that in quantum mechanics, any number of conservation laws can be encoded into a single conservation law which carries the same information. In our case here, the master equation for the evolution of probabilities is the analogue of the Schrödinger equation in quantum mechanics, and conserved quantities are operators which commute with the evolution operator. The single invariant, the irreducible string, here provides a compact representation which, moreover, is quite useful in a practical, computational sense. It is quite possible that similar invariants may also be constructed in other problems with an infinite number of conservation laws.

The existence of these conservation laws implies a slow decay of time-dependent correlation functions in this model. Let the irreducible string be $I = \alpha_1 \alpha_2 \cdots \alpha_l$. Then a general configuration in this sector is of the form $\xi_1 \alpha_1 \xi_2 \alpha_2 \xi_3 \alpha_3 \cdots \alpha_l \xi_{l+1}$, where ξ_i's are substrings reducible to the null string ϕ. If we treat the ξ strings as background, then the time evolution corresponds to a diffusive motion of α_i's on the line. These 'α-particles' cannot cross each other, and in this sense act like hard-core particles. For diffusion of hard core particles on a line, it is well known that with a finite density of particles, density fluctuations decay as $t^{-1/2}$ while the root-mean-square displacement of any given particle varies as $t^{1/4}$ for large times t due to the caging effects of other particles [9]. We have verified in Monte Carlo simulations that the same behavior is obtained for the diffusion of α_i's in our model in several sectors, for t between 10 and 10,000. We also studied the time dependence of the autocorrelation function of density fluctuations in the steady state, and found interesting variations from one sector to another, from power laws with different powers, to stretched exponentials. Details of this work will appear elsewhere [6].

We thank P Thomas for discussions, M Azam for bringing Ref. [8] to our notice, and the referee for his useful comments.

References

[1] M Barma, M D Grynberg, R B Stinchcombe, *Phys. Rev. Lett.* **70**, 1033 (1993)
[2] R B Stinchcombe, M D Grynberg, M Barma, *Phys. Rev.* **E47**, 4018 (1993)
[3] P J Flory, *J. Am. Chem. Soc.* **61**, 1518 (1939)
[4] J W Evans, submitted to *Rev. Mod. Phys.*
[5] N N Chen, M D Grynberg, R B Stinchcombe, preprint
[6] D Dhar and M Barma, to be published
[7] J von Neumann, *Ann. Math.* **32**, 191 (1931)
[8] S Wiegert, *Physica* **D56**, 107 (1992)
[9] T M Liggett, *Interacting particle systems* (Springer, New York, 1985)

PRAMANA
— journal of
physics

© Printed in India

Vol. 41, No. 2,
August 1993
pp. C199–C200

Comment on: Modified perturbation series for the anharmonic oscillator using linearization technique

BISWANATH RATH and K PATTNAYAK*
Physics Department, S.B. Women's College Cuttack 753 001, India
*Physics Department, Utkal University, Vanivihar, Bhubaneswar 751 004, India

MS received 4 July 1992; revised 19 December 1992

Abstract. Following the argument of Halliday and Suranyi (1980), we find that the perturbation series for the anharmonic oscillator using linearization technique of random phase approximation (Ullah 1985) will lead to divergent result. A remedy for this is also suggested.

Keywords. Perturbation series; anharmonic oscillator

PACS No. 03·65

From the review of literature on quantum mechanics of anharmonic oscillator in the context of perturbation theory, we find that Ullah [1] has suggested a model perturbation theory using random-phase-approximation with no discussion on convergency. However, following the argument of Halliday and Suranyi [2], it is easy to show that perturbation series, suggested earlier [1] will lead to divergent result for any value of coupling parameter.

Using linearization technique the Hamiltonian

$$H = \frac{P^2}{2} + \frac{X^2}{2} + \lambda X^4 \tag{1}$$

of the anharmonic oscillator is split as

$$H = H_0 + H_1 \tag{2}$$

where

$$H_0 = \frac{P^2}{2} + \frac{W^2 X^2}{2}, \tag{3}$$

$$H_1 = \lambda X^4 - \beta X^2, \tag{4}$$

with

$$W^2 = 1 + 2\beta. \tag{5}$$

The unknown parameter in (5) is determined by the condition [3]

$$2\beta^3 + \beta^2 = 9\lambda^2. \tag{6}$$

The analysis we present regarding convergency is as follows. The groundstate energy E_0 in terms of perturbation corrections can be expressed as

$$E_0 = E_0^{(0)} + E_0^{(1)} + E_0^{(2)} + \cdots + E_0^{(k)} + \cdots \tag{7}$$

where $E_0^{(k)}$ is the kth order correction. In this infinite series for each subsequent term we find an extra factor of the form $\langle n|H_1|k\rangle/E_0^{(0)} - E_n^{(0)} = \alpha$ where $k = n$, $n \pm 2$, $n \pm 4$ [2, 4–6]. For large n the ratio grows as $\alpha = n/W^3$. Thus for a given value of coupling parameter λ the denominator becomes a constant quantity whereas the numerator is not, thereby each term goes on increasing leading to divergence [4–6]. This can be explicitly stated as

$$E_0 = \text{Finite terms} + L(N)[1 - \alpha + \alpha^2 - \alpha^3 \cdots] \tag{8}$$

where $L(N)$ is a finite but large. One can see that (8) is a divergent series.

To rectify he above drawback we rewrite the (2) as

$$H = H(W) + H_P \tag{9}$$

with $H(W) = H_0 + H_{ID}$ as unperturbed Hamiltonian and $H_P = H_{IN}$ as perturbation term. In the above, subscript D stands for diagonal term N stands for non-diagonal term. One can see that above drawback [1] is rectified automatically [4, 7]. Now groundstate energy corrections up to second order are given below

$$E_0^{(0)} = \frac{W}{4} + \frac{1}{4W} + \frac{3\lambda}{4W^2}, \tag{10}$$

$$E_0^{(1)} = 0, \tag{11}$$

$$E_0^{(2)} = \frac{-3\lambda^2}{4W^5\left[1 + \dfrac{1}{W^2} + \dfrac{15\lambda}{W^3}\right]}. \tag{12}$$

Lastly we find for $\lambda = 1$ the groundstate energy using eqs. (10–12) is 0·805 which compares well with the exact value 0·80377 (up to five decimals; [8]. However, earlier reported value (from table 1 of [1]) is 0·80078.

References

[1] N Ullah, *Pramana – J. Phys.* **24**, 27 (1985)
[2] I G Halliday and P Suranyi, *Phys. Rev.* **D21**, 1529 (1980)
[3] R K Nesbet, *Proc. R. Soc.* (*London*) **A230**, 312 (1955)
[4] P K Patnaik, *Phys. Rev.* **D35**, 1234 (1987)
[5] B Rath, *Phys. Rev.* **A42**, 2520 (1990a)
[6] B Rath, *Eur. J. Phys.* **11**, 184 (1990b)
[7] B Rath and K Patnaik, *Proc. Indian Natl. Sci. Acad.* (1992) (accepted for publication)
[8] W E Caswell, *Ann. Phys.* (*NY*) **123**, 153 (1979)

PRAMANA
— journal of
physics

© Printed in India

Vol. 41, No. 2,
August 1993
pp. C201–C202

Reply to the comment on 'Modified perturbation series for the anharmonic oscillator using linearization technique'

NAZAKAT ULLAH
Tata Institute of Fundamental Research, Homi Bhabha Road, Bombay 400 005, India

MS received 11 January 1993

Abstract. It is pointed out that the value of the perturbed energy calculated in the comment by Rath and Pattnayak, is incorrect. When the coupling parameter has the value unity, the energy up to second order of perturbation theory is 0·801 compared to its exact value of 0·804. The suggested split of the Hamiltonian into an unperturbed and perturbed part does not seem to be of any use as the unperturbed part contains anharmonic terms.

Keywords. Perturbation theory; anharmonic oscillator.

PACS No. 02·90

In the last ten years several papers have appeared to modify ordinary perturbation theory to make it applicable to the anharmonic oscillator problem, particularly when the coupling parameter becomes large. In these papers [1–3] the modified form of perturbation theory was obtained by adding a potential term in the unperturbed part of the Hamiltonian and subtracting the same from the perturbed part. The unknown parameter in the added potential term was obtained using various physical pictures. The perturbed energies calculated up to various orders in perturbation had given excellent results.

Rath and Pattnayak [4] because of some error in their numerical calculation are led to believe that the results reported by Ullah [3] do not agree with the exact numerical values given by Hioe and Montroll [5].

Let us first discuss the case when the coupling parameter $\lambda = 1$. The unperturbed Hamiltonian is then given by

$$H_0 = -\frac{1}{2}\frac{\partial^2}{\partial x^2} + 2x^2, \tag{1}$$

this is obtained by putting $\beta = \frac{3}{2}$ in (13) of Ullah [3]. The parameter β is related to λ by

$$\beta^2(1+2\beta) - 9\lambda^2 = 0, \tag{2}$$

and the perturbation potential H_1 is given by

$$H_1 = x^4 - \tfrac{3}{2}x^2. \tag{3}$$

Table 1 then gives E_0 up to second order as

$$E_0 = 1 - \tfrac{3}{16} - \tfrac{3}{128} = 0{\cdot}801.$$

It also shows how the values decrease as one goes to higher orders of perturbation. The value wrongly calculated by Rath and Pattnayak is 0·080078, thereby misleading them to incorrect conclusions about modified perturbation series.

Now let us look at their eq. (9), where they propose a new split of the total Hamiltonian H as

$$H = H(W) + H_P, \tag{2}$$

where

$$H_W = \frac{p^2}{2} + \frac{1}{2} W^2 X^2 + H_{1D},$$

and

$$H_P = H_{1N},$$

H_{1D}, H_{1N} being diagonal and non diagonal parts of the operator $\lambda x^4 - \frac{1}{2}(W^2 - 1)X^2$. It is hard to understand how one will find the complete set of unperturbed energies and eigen functions if the X^4 term is included in the unperturbed Hamiltonian.

Finally one notes that the numerical calculations [1–3] which are done to second and higher orders of perturbation do not support any of the arguments put forth by Rath and Pattnayak below (7) of their paper and the value of the ground state energy obtained using their new prescription is much poorer than what has already been reported e.g. by Franchuk and Komarov [2] using the modified form of perturbation theory.

References

[1] J Killingbeck, *J. Phys.* **A14**, 1005 (1981)
[2] I D Franchuk and L I Komarov, *Phys. Lett.* **A88**, 211 (1982)
[3] Nazakat Ullah, *Pramana – J. Phys.* **24**, 27 (1985)
[4] B Rath and K Pattnayak, *Pramana – J. Phys.* 40 p. 000 (1993)
[5] F T Hio and E W Montroll, *J. Math. Phys.* **16**, 1945 (1975)

PRAMANA
— journal of
physics

© Printed in India

Vol. 41, No. 3,
September 1993
pp. 203–208

Anomalies in second order elastic constants and gyrotropic constants of triglycine sulphate near phase transition

B SUBRAMANYAM and K S VISWANATHAN
Department of Physics, Indian Institute of Technology, Madras 600036, India

MS received 28 June 1993

Abstract. The anomalies in second order elastic constants and gyrotropic constants have been considered for the phase transition of triglycine sulphate. Expressions have been derived for the equilibrium values of order parameter and strain variables in both phases. Using Landau–Khalatnikov equation the fluctuation in order parameter is expressed in terms of fluctuations in strain variables. Substitution of these in free energy gives anomalies arising from Landau and coupling energies in second order elastic constants. The real part of the anomalies decreases steeply across the transition temperature and thereafter flatly tend to ferroelectric values. The anomalies in the components of the gyrotropic tensor have been derived and their temperature variation discussed.

Keywords. Elastic anomalies; gyrotropic constants; phase transition; triglycine sulphate

PACS Nos 64·70; 62·20; 64·60

1. Introduction

Triglycine sulphate (TGS), isomorphous triglycine selenate (TGSe) and triglycine fluoberyllate are useful ferroelectrics. They follow the Curie–Weiss law. In TGS the spontaneous polarization decreases slowly with temperature and shows no discontinuity at the Curie temperature $T_c = 322\,\mathrm{K}$ indicating a second order phase transition. The ratio of slopes of inverse of dielectric constant versus temperature lines [1] taken just below and above the Curie point turns out to be about 2 to 3. Hoshino *et al* [2] measured the specific heat versus temperature for TGS. The pyroelectric coefficient [3] tends to infinity as the temperature tends to Curie point. The elastic constants [4] affected by phase transition are C_{11}, C_{22}, C_{33}, C_{66}, C_{12}, C_{13} and C_{23}. Westwanski and Fugiel [5] proposed a form of scaling function which gives a more accurate description of the critical properties of TGS and TGSe. Banan *et al* [6] discussed the application of modified TGS single crystal (with caesium impurity) for infrared detector applications. General laws of formation of domain structure in pure and impure crystals of TGS is presented by Dontsova *et al* [7].

The crystal class of TGS changes from $2/m(C_{2h})$ to $2(C_2)$ at the transition temperature. The order parameter (Q) is the electric polarization which is zero in high temperature phase and is directed along Y-axis in low temperature phase. There is an inversion symmetry in high temperature phase and the crystal cannot exhibit any gyrotropic effects in the paraelectric phase. Gyrotopic effects could appear in the ferroelectric (low temperature) phase where this symmetry element is destroyed. When spatial dispersion is present in the system the elastic constant matrix [8] acquires the structure

$$C_{ij}(\Omega k) = C_{ij}(\Omega) + i d_{ijl}(\Omega) k_1,$$

where k denotes the wave vector and Ω is the circular frequency of the acoustic wave. The gyrotropic constants d_{ijl} are components of a fifth rank tensor and satisfy the antisymmetry relations with respect to interchange of indices i and j. The number of gyrotropic constants for different classes of crystals has been worked out by Kumaraswamy and Krishnamurty [8].

In this paper we report the anomalies of TGS, near the phase transition in second-order elastic (SOE) constants and gyrotropic constants within the framework of the Landau theory. It is only valid for the equilibrium properties and does not apply to non-equilibrium conditions. The Landau theory has been first applied to the case of barium titanate by Devonshire [9]. While the equilibrium values of strains and order parameter in low temperature phase can be obtained from the stability conditions, the fluctuation in the order parameter has been derived by an appeal to the Landau–Khalatnikov equation. In §2 we derive equilibrium values in both the paraelectric and ferroelectric phases and obtain an expression for the fluctuation in order parameter about the equilibrium value. In § 3 we derive expressions for the SOE anomalies and discuss their temperature variation. In § 4, gyrotropic anomalies are derived and their variation with temperature is discussed.

2. Equilibrium values and fluctuations in order parameter

The free energy of the crystal is the sum of (i) elastic energy F_{ela} (ii) the Landau energy F_Q (iii) the coupling energy F_C between the order parameter and strains (iv) the gyrotropic energy F_{gc} involving order parameter, strains and the spatial derivatives of order parameter and strains

$$F = F_{\mathrm{ela}} + F_Q + F_C + F_{\mathrm{gc}} = F_0 + F_{\mathrm{gc}}. \tag{1}$$

Since the gyrotropic energy term F_{gc} is much smaller than F_C we neglect it in calculating elastic anomalies and use F_{gc} only for phenomena relating to gyrotropic effects. The elastic energy for the monoclinic class is given by

$$\begin{aligned} F_{\mathrm{ela}} = \frac{1}{2}\sum_{ii} C_{ii}\eta_i^2 + C_{12}\eta_1\eta_2 + C_{13}\eta_1\eta_3 \\ + C_{16}\eta_1\eta_6 + C_{23}\eta_2\eta_3 + C_{26}\eta_2\eta_6 + C_{36}\eta_3\eta_6 + C_{56}\eta_5\eta_6, \end{aligned} \tag{2}$$

where $\eta_i (i = 1 \text{ to } 6)$ are the components of the strain tensor and C_{ij} are the elastic constants. In the Landau theory F_Q is a power series in the order parameter square that develops near a phase transition and is given by

$$F_Q = \frac{1}{2}\alpha Q^2 + \frac{1}{4}\beta Q^4, \tag{3}$$

where $\alpha = \alpha'(T - T_c)$ and α' and β are constants. The coupling energy F_C that couples the order parameter with strains is of the form

$$F_C = Q^2(A_1\eta_1 + A_2\eta_2 + A_3\eta_3 + A_5\eta_5), \tag{4}$$

where A_1, A_2, A_3 and A_5 are constants. It can be verified that the strains η_1, η_2, η_3, η_4 and η_5 are invariant under the operations of all the elements of the group C_{2h}. Since $Q \rightarrow -Q$ in this phase, these strain coefficients couple with $Q^2 \cdot F_{\text{gc}}$ is of the form

$$\begin{aligned} F_{\text{gc}} &= a_{4x}\left(Q\frac{\partial\eta_4}{\partial x} - \eta_4\frac{\partial Q}{\partial x}\right) + a_{6x}\left(Q\frac{\partial\eta_6}{\partial x} - \eta_6\frac{\partial Q}{\partial x}\right) \\ &\quad + a_{4z}\left(Q\frac{\partial\eta_4}{\partial z} - \eta_4\frac{\partial Q}{\partial z}\right) + a_{6z}\left(Q\frac{\partial\eta_6}{\partial z} - \eta_6\frac{\partial Q}{\partial z}\right) \end{aligned} \tag{5}$$

where a_{4x}, a_{6x}, a_{4z} and a_{6z} are constants. It can again be verified that each of the term given in (5) is invariant under the symmetry group of the crystal in paraelectrical phase. The terms $\eta_i(\partial Q/\partial x)$ in (5) ensures that the antisymmetric relation in gyrotropic constants is satisfied.

To get the equilibrium values of the order parameter and the strains in the two phases, we neglect F_{gc} in comparison with other terms in F as it is of smaller order of magnitude. Using the stability conditions given by

$$\frac{\partial F}{\partial Q} = 0 \quad \text{and} \quad \frac{\partial F}{\partial \eta_i} = 0 \ (i = 1 \text{ to } 6), \tag{6}$$

it can be shown that the equilibrium values of the order parameter and strains in high temperature paraelectric phase ($T > T_c$) are given by

$$Q_0 = \eta_{i0} = 0 \quad \text{for} \quad (i = 1 \text{ to } 6). \tag{7}$$

For the low temperature ferroelectric phase ($T < T_c$) the equilibrium values are

$$Q_0^2 = \frac{\alpha}{(2X - \beta)}. \tag{8a}$$

$$\eta_{i0} = \frac{\Delta_i}{\Delta}(-Q_0^2) \quad \text{for} \quad (i = 1 \text{ to } 3 \text{ and } 6). \tag{8b}$$

$$\eta_{40} = A_5 C_{45}(C_{45}^2 - C_{44}C_{55})^{-1}(-Q_0^2). \tag{8c}$$

$$\eta_{50} = A_5 C_{44}(C_{44}C_{55}C_{45}^2)^{-1}(-Q_0^2). \tag{8d}$$

where

$$X = \frac{A_1\Delta_1 + A_2\Delta_2 + A_3\Delta_3}{\Delta} + \frac{A_5^2 C_{44}}{C_{44}C_{55} - C_{45}^2},$$

and Δ is the value of the determinant

$$\Delta = \begin{vmatrix} C_{11} & C_{12} & C_{13} & C_{16} \\ C_{12} & C_{22} & C_{23} & C_{26} \\ C_{13} & C_{23} & C_{33} & C_{36} \\ C_{16} & C_{26} & C_{36} & C_{66} \end{vmatrix}$$

Δ_1, Δ_2, Δ_3 and Δ_6 are obtained by replacing 1st, 2nd, 3rd and 4th columns of Δ by the column $(A_1 A_2 A_3 0)$ respectively.

The Landau–Khalatnikov equation expresses the fact that the regression $(\mathrm{d}Q/\mathrm{d}t)$ of the order parameter fluctuation towards equilibrium is proportional to the thermodynamic restoring force $(\partial F/\partial Q)$.

$$\dot{Q} = \frac{-1}{\mu}\frac{\partial F}{\partial Q} \tag{9}$$

where μ is the viscosity coefficient. Let us write $Q = Q_0 + Q^*$ and $\eta_i = \eta_{i0} + \eta_i^*$ where Q^* and η_i^* ($i = 1$ to 6) represent the fluctuations in the values of Q and η_i respectively. By expanding $(\partial F/\partial Q)$ about the equilibrium values of Q and strain variables and ignoring higher order terms we have

$$\frac{\partial F}{\partial Q} = \left(\frac{\partial F}{\partial Q}\right)_0 + \left(\frac{\partial^2 F}{\partial Q^2}\right)_0 Q^* + \sum_i \left(\frac{\partial^2 F}{\partial Q \partial \eta_i}\right)_0 \eta_i^* \tag{10}$$

By setting $Q^* = \exp(i\Omega t)$ and substituting (10) in (9) we get the fluctuation in order parameter as

$$Q^* = -(2X - \beta)^{1/2}(\alpha\beta)^{-1/2}(1 + i\Omega\tau)^{-1}\sum A_i \eta_i^* \tag{11}$$

i takes values from 1 to 3 and 5. The relaxation time $\tau = \mu(\partial F^2/\partial Q^2)_0^{-1}$. Equation (11) shows that Q^* is a linear function of the strain variables to a first order of approximation.

3. Second order elastic anomalies

Substituting $Q = Q_0 + Q^*$ and $\eta_i = \eta_{i0} + \eta_i^*$ in the expression for F_0 and considering only terms quadratic in strain variables we get

$$F_2 = \frac{1}{2}\sum C_{ij}^* \eta_i^* \eta_j^* = \frac{1}{2}\sum C_{ij}\eta_i^*\eta_j^* + \Delta F_2,$$

where

$$\Delta F_2 = \sum \frac{1}{2}\Delta C_{ij}^* \eta_i^* \eta_j^*,$$

$$= \sum A_i A_j \eta_i^* \eta_j^* [\beta^{-1}(1 + i\Omega\tau)^{-2} - 2\beta^{-1}(1 + i\Omega\tau)^{-1}]. \tag{12}$$

i and j take values 1 to 3 and 5.

The existence of anomalies in the SOE constants shows that the velocity of elastic waves undergo a change during phase transition, and further the waves are attenuated as ΔC_{ij}^* are complex. The real part of ΔC_{ij}^* is given by

$$\mathrm{Re}(\Delta C_{ij}^*) = \frac{-2}{\beta}(1 + 3\Omega^2\tau^2)(1 + \Omega^2\tau^2)^{-2} A_i A_j. \tag{13}$$

i and j takes values 1, 2, 3 and 5.

The temperature variation of τ is given by Lemanov as [10]

$$\tau = \frac{\tau_0}{T - T_c}, \tag{14}$$

with $\tau_0 = 10^{-11}$ sK. For numerical calculations we shall choose the experimental value of $\Omega = 10^9 \mathrm{s}^{-1}$. At the transition temperature $T = T_c$ $\Omega\tau \to \infty$ so that $R(\Delta C_{ij}^*) = 0$. Next $\Omega\tau$ reaches the value of unity when $T_c - T = \Omega\tau_0 = 10^{-2}$. For this value as well as for $\tau = 0$ we find that

$$\mathrm{Re}(\Delta C_{ij}^*) = -2\beta^{-1} A_i A_j. \tag{15}$$

Again the stationary values of the anomalies are reached when $\Omega\tau = 1/\sqrt{3}$ and for this value

$$\mathrm{Re}(\Delta C_{ij}^*) = \frac{-9}{4\beta} A_i A_j. \tag{16}$$

With the above numerical values, we notice that the SOE constants have uniform value in the paraelectric state, fall steeply within a range of order 10^{-2}K to the value $(-9/4\beta)A_i A_j$ and reach asymptotic value of $(-2/\beta)A_i A_j$ within a range of 10^{-1}K.

4. Gyrotropic anomalies

The high temperature (paraelectric) phase has inversion symmetry, hence all d_{ijl} are zero in this phase. In the low temperature (ferroelectric) phase inversion symmetry is absent and gyrotropic constants arise from the coupling of order parameter with the spatial derivatives of strain and order parameter. We can express F_{gc} in the form

$$F_{gc} = \sum_{ijl} d_{ijl} \eta_i^* \frac{\partial \eta_i^*}{\partial x_i}. \tag{17}$$

The gyrotopic anomalies are then given by

$$\Delta d_{ijl}^* = d_{ijl} = \frac{\partial^2 F_{gc}}{\partial \eta_i^* (\partial \eta_j^* / \partial x_l)}. \tag{18}$$

Substituting the value of Q^* in the expression for F_{gc} we can identify all the gyrotropic anomalies. The anomalies are:

$$d_{i41} = dA_i a_{4x}, \tag{19a}$$

$$d_{i61} = dA_i a_{6x}, \tag{19b}$$

$$d_{i43} = dA_i a_{4z}, \tag{19c}$$

$$d_{i63} = dA_i a_{6z}. \tag{19d}$$

where d is given by

$$d = -(2X - \beta)^{-1/2}(\alpha\beta^2)^{-1/2}(1 + i\Omega\tau)^{-1}. \tag{20}$$

In eqs (19a) to (19d) $i = 1$ to 3 and 5 so that the anomalies are present in 16 gyrotropic constants. The gyrotropic anomalies are complex, temperature dependent and characterized by $d_{ijl} = -d_{jil}$. We can see from (19) and (20) that the gyrotropic anomalies are proportional to $[(T - T_c)^{1/2}(1 + i\Omega\tau)]^{-1}$. The real part of the anomalies are proportional to $(T - T_c)^{3/2}[(T - T_c)^2 + \Omega^2\tau_0^2]^{-1}$. At $T = T_c$ the anomalies vanish. When $\Omega\tau_0 = T - T_c = 10^{-2}$ the anomalies are proportional to 10. In general the variation of the anomalies follow the variation of the term $(T - T_c)^{9/2}[(T - T_c)^2 + \Omega^2\tau_0^2]^{-1}$. The anomalies reach stationary value when $T - T_c = \sqrt{3}\,\Omega\tau_0$. For $(T_c - T) \gg \Omega\tau_0$ the anomalies are proportional to $(T_c - T)$.

References

[1] S Triebwasser, *Phys. Rev.* **118**, 100 (1960)
[2] S Hosino, F Mitsui, F Jona and R Pepinsky, *Phys. Rev.* **107**, 1225 (1957)
[3] A G Chynoweth, *Phys. Rev.* **117**, 1235 (1960)
[4] B A Strukov, K A Minaeva, N M Shirina, V I Teleshevskii and S K Khanna, *Izv. Akad. Nauk. SSR Ser. Fiz.* **39**, 180 (1975)
[5] B Westwanski and B J Fugiel, *Phys. Condens. Matter.* **3**, 2577 (1991)
[6] M Banan, K B Lal and A J Batra, *Mat. Sci.* **27**, 2291 (1992)
[7] L I Dontsova, N A Tikhomirova, L G Bulatova and R V Korina, *Sov. Phys. Cryst. Phys.* **33**, 265 (1988)
[8] K Kumaraswamy and N K Krishnamurty, *Acta Crystallogr.* **A37**, 760 (1980); *J. Acoust. Soc. Am.* **76**, 1522 (1984)
[9] A F Dovenshire, *Philos. Mag.* **40**, 1040 (1949)
[10] V V Lemanov, *Optical and acoustic waves in solids–Modern topics*, Proc. of the second int. conf. on condensed matter physics (1982)

PRAMANA
— journal of
physics

© Printed in India

Vol. 41, No. 3,
September 1993
pp. 209–217

Surface acoustic wave distribution and acousto-optic interaction in proton exchanged $LiNbO_3$ waveguides

P ANNACHELVI, A SELVARAJAN and G V ANAND
Department of Electrical Communication Engineering, Indian Institute of Science, Bangalore 560012, India

MS received 17 February 1993; revised 16 July 1993

Abstract. The efficiency of acoustooptic (AO) interaction in YZ-cut proton exchanged (PE) $LiNbO_3$ waveguides is theoretically analysed by determining the overlap between the optical and acoustic field distributions. The present analysis takes into account the perturbed SAW field distribution due to the presence of the PE layer on the $LiNbO_3$ substrate determined by the rigorous layered medium approach. The overlap is found to be significant upto very high acoustic frequencies of the order of 5 GHz, whereas in the earlier analysis by vonHelmolt and Schaffer [6] for diffused waveguides, it was shown that the overlap integral rolls down to nearly zero at this high frequency range.

Keywords. Acoustooptic interaction; $LiNbO_3$ waveguides; proton exchange.

PACS No. 42·82

1. Introduction

Integrated optical devices based on proton exchanged $LiNbO_3$ ($PE:LiNbO_3$) waveguides are being researched for various applications including signal processing, communication, etc. The devices based on the acoustooptic (AO) interaction in these waveguides are promising and have given rise to considerable activity in recent years. Technologically, proton exchange is a simpler and low temperature process, which is easy to perform. Immersion of $LiNbO_3$ in proton sources such as benzoic acid leads to a high index region of $H_xLi_{1-x}NbO_3$, with 77% of Li^+ replaced by protons [1]. The main advantages of PE waveguides are the large increase in the extraordinary refractive index, the nearly step index profile, and the high optical damage threshold [2]. Many AO experiments have been performed and devices realized [3, 4], taking advantage of the special optical and acoustic properties of these waveguides. Yet, a rigorous computation of the basic AO interaction in these waveguides has not been reported so far. In this paper, we present a theoretical analysis of the AO interaction in PE waveguides by rigorously calculating the perturbed SAW distribution and the optical field distribution in the $PE:LiNbO_3$. The analysis leading to the determination of SAW distribution in $PE:LiNbO_3$ is based on a recent work [5], wherein the material constants are determined for the PE medium.

2. Calculation of the SAW field

The Rayleigh wave propagation in a piezoelectric medium in governed by a set of four coupled differential equations [5]:

$$\rho \frac{\partial^2 u_j}{\partial t^2} - C'_{ijkl} \frac{\partial^2 u_k}{\partial x_i \partial x_l} - e'_{kij} \frac{\partial^2 \phi}{\partial x_i \partial x_k} = 0, \qquad i,j,k,l = 1,2,3, \tag{1}$$

$$e'_{ikl} \frac{\partial^2 u_k}{\partial x_i \partial x_l} - \varepsilon'_{ik} \frac{\partial^2 \phi}{\partial x_i \partial x_k} = 0, \qquad i,k,l = 1,2,3 \tag{2}$$

where u_i is the ith component of mechanical displacement, ϕ is the electric potential, C'_{ijkl}, e'_{ikl} and ε'_{ik} are the rotated components of the elastic stiffness, piezoelectric and dielectric permittivity tensors respectively, and summation over repeated indices is implied. Using the coordinate system shown in figure 1, solutions of (1) and (2) can be written as

$$u_i = a_i \exp(jk\alpha x_3)\exp[jk(x_1 - vt)], \qquad i = 1,2,3 \tag{3}$$

$$\phi = a_4 \exp(jk\alpha x_3)\exp[jk(x_1 - vt)], \tag{4}$$

where a_i are the amplitude coefficients, α is the propagation constant in the x_3 direction, and v is the SAW phase velocity. Substitution of (3) and (4) into (1) and (2) leads to the linear homogeneous matrix equation:

$$\mathbf{MA} = 0, \tag{5}$$

where $\mathbf{M}$ is a 4×4 matrix with elements involving the material constants and α, and $\mathbf{A}$ is a 4-dimensional column vector with elements a_i, $i = 1, \ldots, 4$. Nontrivial solutions of (5) exist if and only if

$$|\mathbf{M}| = 0, \tag{6}$$

where the determinant $|\mathbf{M}|$ is a polynomial in α of degree eight. For a given phase velocity, (6) is solved to get the eight propagation constants α_n and the corresponding amplitude coefficient vectors $\mathbf{A}_n$. The procedure has to be carried out for both the substrate and the layer. Since the field components of Rayleigh waves must decay exponentially into the substrate, only four propagation constants with negative imaginary parts may be used for the substrate. For the layer all the eight eigenvalues are allowed. Thus, superposition of the partial wave solutions and denoting the

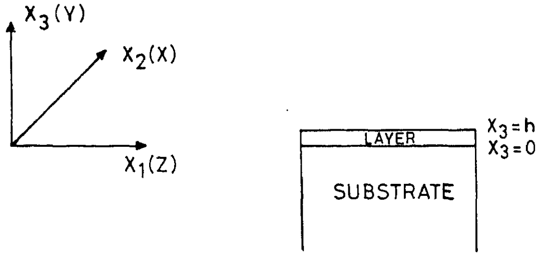

Figure 1. Schematic geometry of PE:LiNbO$_3$. X, Y, Z are the crystal axes.

potential by u_4 leads to the following solution for the Rayleigh wave in vector form:

$$\mathbf{u} = \sum_n \mathbf{B}_n \mathbf{A}_n \exp(jk\alpha_n x_3) \exp[jk(x_1 - vt)], \tag{7}$$

where $\mathbf{u}$ is a 4-dimensional column vector with elements u_i, $\mathbf{A}_n$ are 4-dimensional column vectors with elements a_{in} and B_n are the scalar quantities denoting partial wave amplitudes, with $n = 1, \ldots, 4$ for the substrate and $n = 5, \ldots, 12$ for the layer.

Formulation of the boundary conditions yields a linear homogeneous system of twelve equations, from which B_n can be found. The boundary conditions are:

(i) At the layer-substrate interface $x_3 = 0$, the mechanical displacement components u_1, u_2 and u_3, the electric potential ϕ, the stress components T_{13}, T_{23} and T_{33} and the electric displacement D_3 are continuous. The stress components T_{i3} and the electric displacement D_3 are given by,

$$T_{i3} = C'_{i3kl} S_{kl} + e'_{i3k} E_k, \qquad i = 1, 2, 3 \tag{8}$$

$$D_3 = e'_{3kl} S_{kl} - \varepsilon'_{3k} E_k \tag{9}$$

(ii) At the free surface $x_3 = h$, the stress components T_{13}, T_{23} and T_{33} vanish and the electric displacement D_3 is continuous. The twelve boundary conditions lead to the homogeneous equation,

$$\mathbf{RB} = 0, \tag{10}$$

where $\mathbf{R}$ is the boundary condition matrix of order 12×12, and $\mathbf{B}$ is the 12 dimensional column vector containing the 12 unknown partial wave amplitudes B_n.

For nontrival solutions of (10), the boundary condition determinant $|\mathbf{R}|$ should vanish, and this can be accomplished by variation of the only free parameter, kh. For a given phase velocity, the boundary condition determinant determines the parameter kh and this parameter describes the dispersive behaviour of SAW in the layered medium.

3. Application to PE:LiNbO$_3$

3.1 *Crystalline model*

The assumptions which we have adopted in the case of PE waveguides, following the earlier investigations [5], are:

(i) The PE region behaves like a homogeneous nonpiezoelectric medium.
(ii) For the exchange rate considered here, viz., $x \approx 0.7$, the crystalline structure of the PE medium ($H_xLi_{1-x}NbO_3$) can be taken as trigonal.
(iii) For the PE medium, $\varepsilon_{11} = \varepsilon_{22} = \varepsilon_{33} = 55\,\varepsilon_0$, and $\rho = 4500\,\mathrm{kgm}^{-3}$.
(iv) The set of material constants and the dispersion curve corresponding to the YZ-configuration are reliable for waveguides fabricated in diluted melts containing 0·25 to 2 mol%. of lithium benzoate.

3.2 *SAW field distribution*

The relevant material constants C_{ijkl}, e_{ijk} and ε_{ij} of LiNbO$_3$, v_{SAW} and the Euler angles used to find the rotated components, C'_{ijkl}, e'_{ijk} and ε'_{ij} are taken from [6] and

[7]. To check the correctness of matrix $\mathbf{M}$ in (5), α and $\mathbf{A}$ are calculated for the case of SAW in bulk $LiNbO_3$. The results agree well with the values reported by von-Helmholt and Schaffer [6]. For the PE layer, which is nonpiezoelectric, $e = 0$ and the other constants of the PE medium C_{ijkl} and ε_{ij} and the dispersion curve are taken from [5].

The scalar constants α_n and vectors $\mathbf{A}_n$ for a given v_{SAW} are determined for the substrate and the layer individually from (6). For different values of v_{SAW}, different sets of α_n and $\mathbf{A}_n$ are obtained. The value of kh corresponding to each v_{SAW} is taken from the dispersion curve in the calculation of B_n. In finding B_n, the 12 boundary condition equations reduce to 8 equations because of the following reasons:

(i) In the nonpiezoelectric layer and the piezoelectric substrate combination, the continuity of ϕ at the layer-substrate interface and the continuity of D_3 at the free surface are satisfied by taking the potential in the form given below [8]:

$$\phi = \phi_0 \exp(-ik''x_3)\left(\frac{\exp(k'x_3) + B\exp(-k'x_3)}{1+B}\right), \tag{11}$$

where

$$k' = k\left(\frac{\varepsilon_{11}\varepsilon_{33} - \varepsilon_{13}^2}{\varepsilon_{33}^2}\right)^{1/2},$$

$$k'' = k\frac{\varepsilon_{13}}{\varepsilon_{33}},$$

$$B = \left(\frac{k'\varepsilon_{33} + k\varepsilon_0}{k'\varepsilon_{33} - k\varepsilon_0}\right)\exp(2k'h),$$

ϕ denotes the potential in the layer and ϕ_0 denotes the substrate potential evaluated at $x_3 = 0$. For the present case of PE medium, $k'' = 0$; $k' = k$; $B = (\varepsilon_{33} + \varepsilon_0)/(\varepsilon_{33} - \varepsilon_0)$ $\exp(2kh)$.

(ii) In the YZ-cut trigonal crystals, the sagittal plane (X_1, X_3 plane in figure 1) is

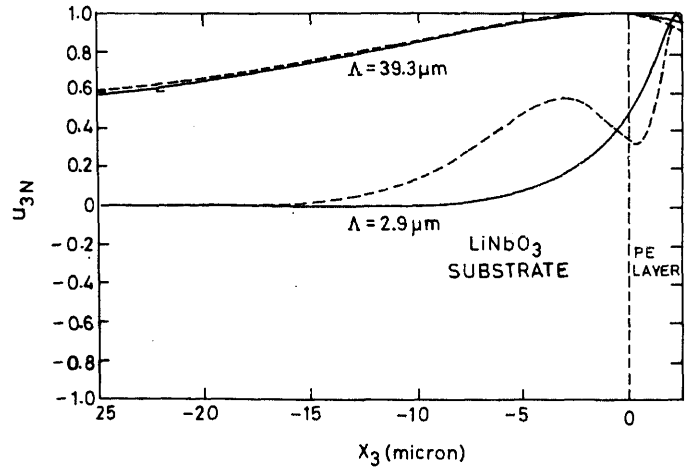

Figure 2. Normalized mechanical displacement distribution, u_{3N} in PE:$LiNbO_3$ through the present analysis (----) and in bulk $LiNbO_3$ using vonHelmolt't analysis (———); waveguide depth = 2·5 μm.

the mirror plane for elastic symmetry and therefore the mechanical displacement component $u_2 = 0$ and all the associated boundary condition matrix elements vanish.

Thus, in the case of the substrate, the solutions u_1, u_3 and ϕ contain linear combinations of four partial wave solutions with appropriate coefficients α_n and a_n. In the guiding layer, u_1 and u_3 are given by linear combinations of four partial wave solutions and ϕ is given by (11). The partial field amplitudes are normalized to a SAW power flow $P_{1m} = 1$ W/m and $\omega = 1$ rad/s. For very small values of kh (i.e., $\Lambda \gg h$), it is seen from figure 2 that the perturbation due to the presence of the PE layer is negligible and the SAW distribution resembles that in the bulk $LiNbO_3$ medium. The case of SAW in bulk $LiNbO_3$ is treated in the earlier analysis by vonHelmolt and Schaffer [6].

The strain component S_1 and the electric field component E_1 are continuous across the layer-substrate interface. The component S_3, which is along the depth direction, has different magnitudes at the interface owing to the different decay coefficients of the substrate and the layer media.

4. Optical field distribution

The steplike refractive index profile of the proton exchanged waveguides is considered. This index profile leads to the optical field for TE_0 mode given by [9],

$$U_m(x_3) = \cos[\kappa_f(-x_3 + h)] + \frac{\kappa_c}{\kappa_f}\sin[\kappa_f(-x_3 + h)] \quad 0 \leqslant x_3 \leqslant h \tag{12}$$

$$U_m(x_3) = \left[\cos(\kappa_f h) + \frac{\kappa_c}{\kappa_f}\sin(\kappa_f h)\right]\exp(\kappa_s x_3) \qquad x_3 \leqslant 0$$

where κ_f, κ_c and κ_s are the propagation constants in the film, cover and the substrate regions respectively and h is the waveguide depth.

5. Theory of guided wave acoustooptic interaction

In our geometry, the co-ordinate axes (x_1, x_2, x_3) coincide with the crystal axes (Z, X, Y). The acoustooptic diffraction efficiency of an optical guided wave perfectly phase matched to the SAW for the isotropic case, with incident and diffracted optical modes being the same with respect to polarization, is given by the well known formula [10]:

$$\eta = \sin^2\left(\frac{\pi n_{\text{eff}}^2 L}{2\lambda\cos\theta_B}|\Delta B_{\max}||\Gamma|\right), \tag{13}$$

where, n_{eff} is the effective modal refractive index, λ is the free space optical wavelength, Γ is the coupling function or the overlap integral, L is the interaction length or acoustic aperture and θ_B is the Bragg angle. The AO diffraction efficiency strongly depends on the overlap Γ between the optical and acoustic fields. Γ which depends solely on the waveguide parameters and the acoustic frequency is given by,

$$|\Gamma| = \left|\frac{\int_{-\infty}^{h}|U_m|^2 U_{aij}\,\mathrm{d}x_3}{\int_{-\infty}^{h}|U_m|^2\,\mathrm{d}x_3}\right|, \tag{14}$$

where,

$$U_{aij} = \frac{\Delta B_{ij}}{|\Delta B_{ij\max}|}, \tag{15}$$

$$\Delta B_{ij} = p^E_{ijkm} S_{km} + r^S_{ijk} E_k \quad i,j,k,m = 1,2,3 \tag{16}$$

where ΔB_{ij} is the change in the optical indicatrix created by SAW, $U_m(x_3)$ is the optical mode profile of the waveguide, p^E_{ijkm} is the strain optic tensor at constant E, S_{km} are the strain components of SAW, r^S_{ijk} is the electrooptic tensor at constant S and E_k are the electric field components of SAW.

6. Interaction in proton exchanged waveguide

The optical mode field as in (12) and the SAW field distribution as in (7) corresponding to the proton exchanged waveguides are used in (14) to determine the overlap integral. The integral is evaluated in the two regions (layer and substrate) using the appropriate functions, U_a and U_m. With the SAW propagating along x_1 and the TE polarized light along x_2, we have

$$\Delta B_1 = p_{33} S_1 + p_{31} S_3 + r_{33} E_1. \tag{17}$$

The coefficients p and r are referred to the crystal axes, $X = 1$, $Y = 2$, $Z = 3$. r_{33} in the PE region is $22{\cdot}6 \times 10^{-12}$ m/V [11] whereas, r_{33} in the $LiNbO_3$ substrate is $30{\cdot}8 \times 10^{-12}$ m/V. The proton exchanged waveguides considered in the present work are the annealed proton exchanged waveguides. The annealing process may involve migration of Li ions from adjacent regions of the substrate into the waveguiding region in addition to the removal of hydrogen bonded OH and the diffusion of free OH into the substrate. In this situation the distorted unit cell structure in the waveguide may tend to change back to that of virgin $LiNbO_3$. As a consequence, the electrooptic effect would be restored and propagation losses reduced [12].

The values of p_{33} and p_{31} for $LiNbO_3$ are 0·071 and 0·179 respectively. For the PE region, values of p_{33} and p_{31} are assumed to be the same as those in $LiNbO_3$. The optical wavelength λ is taken to be 0·83 μm and the value of Δn is chosen for a given waveguide depth such that the waveguide operates in the single mode region (for $d = 1{\cdot}33$, $\Delta n = 0{\cdot}01$). Since the substrate is piezoelectric, the contribution to ΔB is more due to the electrooptic effect (EO) than due to the acoustooptic effect (AO) in this region. In the nonpiezoelectric layer, the AO contribution dominates. The AO and EO contributions to ΔB are plotted in figure 3.

The overlap integral is plotted as a function of acoustic frequency for different waveguide parameters in figures 4 and 5. At very low and very high acoustic frequencies, when the waveguide depth h is not comparable to the acoustic wavelength Λ, the overlap integral decreases with increasing acoustic frequency. It is also seen that at high acoustic frequencies the overlap decreases with increasing waveguide depth. This is due to the fact that the penetration depth of SAW is inversely proportional to the acoustic frequency. The acoustic penetration depth (the depth at which the SAW amplitude is equal to $1/e$ times its surface value) is plotted as a function of acoustic frequency in figure 6. It is clear from figures 4 and 5 that, depending upon the waveguide depth, the frequency range of interest can be obtained. Secondly, for a given waveguide depth, when the optical penetration depth is increased, i.e., when the optical field becomes less concentrated in the waveguide, the overlap is less compared to the case of waveguides with smaller penetration depth. The optical

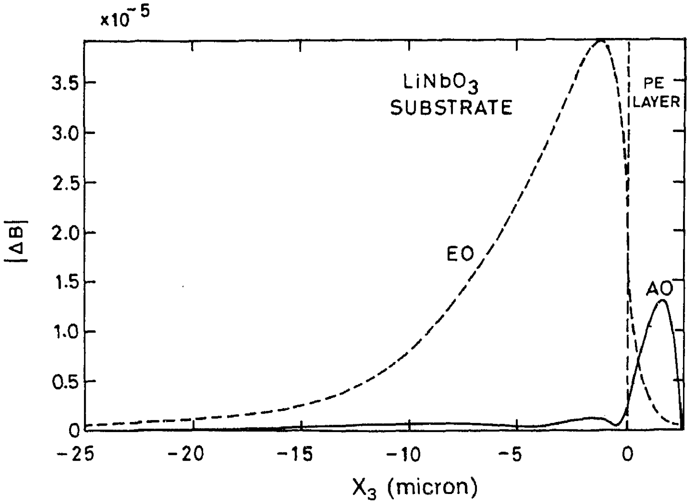

Figure 3. Normalized change in indicatrix ΔB due to electrooptic and acousto-optic effects; SAW frequency = 950 MHz.

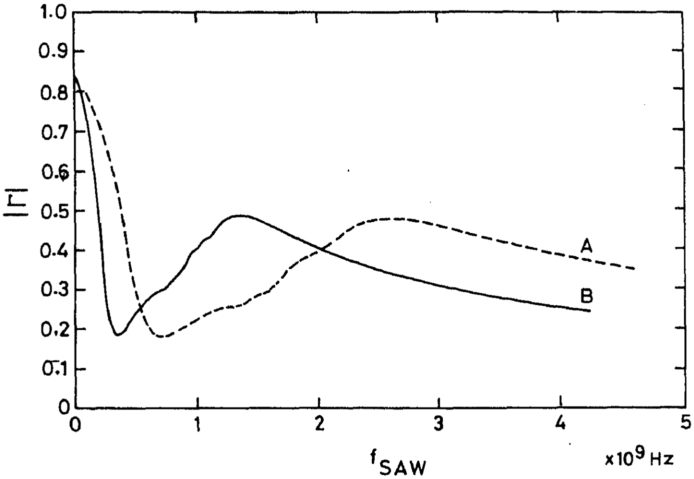

Figure 4. Overlap integral as a function of acoustic frequency; waveguide depth = 1·33 μm for curve A and 2·5 μm for curve B.

penetration depth is defined as the depth at which the optical field intensity is equal to $1/e^2$ times the maximum intensity. For a fixed waveguide depth, the different optical penetration depths may be obtained by changing Δn.

When h is comparable to Λ, there is no longer a monotonous decrease in the overlap with increase in frequency, but instead the overlap begins to increase as the frequency increases. In this intermediate frequency range, with h being comparable to Λ, the layer offers a characteristic dimension to the system and there is a considerable contribution to ΔB from both the layer and the substrate. The proximity of the maximum of ΔB in the substrate to the layer-substrate interface leads to the increase in the overlap with increase in frequency. Because the substrate is piezoelectric and the layer is nonpiezoelectric, the maximum of ΔB lies in the substrate region.

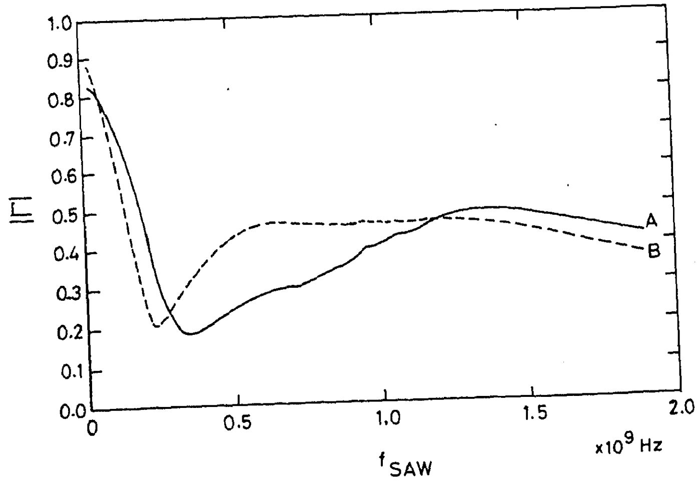

Figure 5. Overlap integral as a function of acoustic frequency for a given waveguide depth of 2·5 μm. The optical penetration depths are 6 μm (curve A) and 9 μm (curve B).

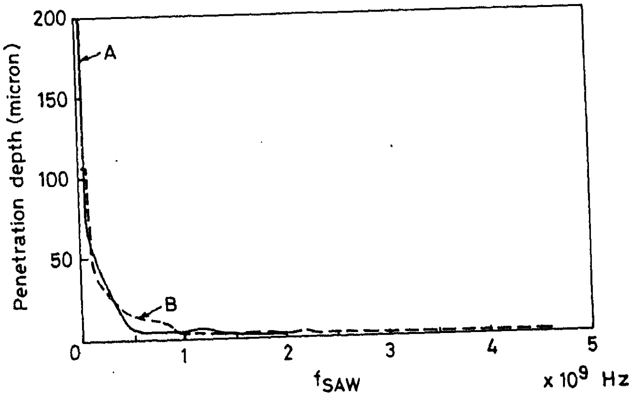

Figure 6. Acoustic penetration depth as a function of acoustic frequency for waveguide depth of A) 2·5 μm and B) 1·33 μm.

The earlier analysis by vonHelmolt and Schaffer [6] is also carried out for the present case of the PE waveguides, the step index profile of the waveguides being taken into account in determining the optical field distribution. The result is shown in figure 7 along with that of the present improved analysis of the PE waveguides. For the present case, since the maximum of ΔB lies in the substrate region, the overlap integral is always less than 1. In the earlier analysis, on the other hand, the maximum of ΔB is at, or, near the surface without an intermediate minimum and this leads to the overlap integral value of 1 at very low frequencies. The overlap is more at high frequencies in the present case.

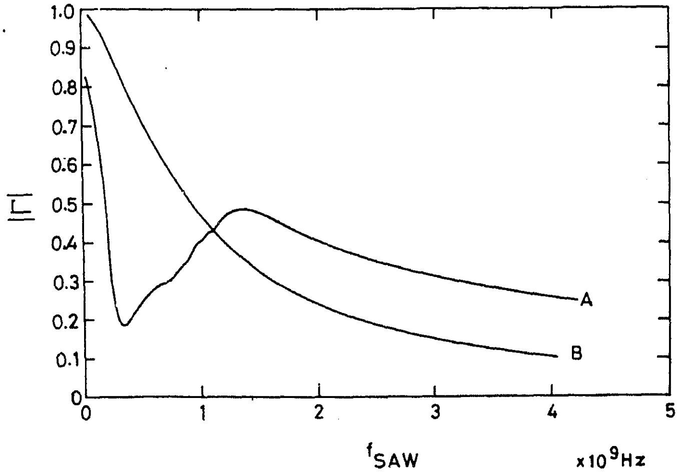

Figure 7. Frequency response of the overlap integral in the present case (curve A) and according to vonHelmolt's analysis (curve B).

7. Conclusion

The AO interaction in PE:$LiNbO_3$ is theoretically investigated using the improved calculation of SAW in these waveguides. The analysis presented here is more accurate since it takes into account the material constants of the PE medium and the dispersive behaviour of the waveguide. By the use of the modified SAW distribution and the improved calculation of the AO interaction, presented in this analysis, sophisticated design of guided SAW and AO devices based on $LiNbO_3$ can be achieved.

References

[1] J L Jackel, C E Rice and J J Veselka, *Appl. Phys. Lett.* **41**, 607 (1982)
[2] R A Becker, *Appl. Phys. Lett.* **43**, 131 (1983)
[3] M Miyawaki and S Ogura, *Appl. Phys. Lett.* **47**, 918 (1985)
[4] M Varasi, A Vannucci and S Reid, *Proc. SPIE* **1151**, 457 (1989)
[5] E M Biebl and P Russer, *IEEE Trans. Ultrason., Ferroelect. Freq. Control.* **39**, 330 (1992)
[6] C H vonHelmolt and C Schaffer, *J. Opt. Commun.* **8**, 49 (1987)
[7] A W Warner, M Onoe and G A Coquin, *J. Acoust. Soc. Am.* **42**, 1223 (1967)
[8] G W Farnell, *IEEE Trans. Sonics, Ultrason, Ferroelect. Freq. Control* **SU17** 229 (1970)
[9] A K Ghatak and K Thyagarajan, *Optical electronics* (Cambridge University Press, London, 1989) ch. 14, p. 427
[10] C S Tsai, M A Alhaider, L T Nguyen and B Kim, *Proc. IEEE* **64**, 318 (1976)
[11] S Mc Meekin and R M De la Rue, *Electron. Lett.* **25**, 853 (1989)
[12] A Loni, G Hay, R M De la Rue and J M Winfield, *IEEE J. Lightwave Technol.* **7**, 911 (1989)

PRAMANA
— journal of
physics

© Printed in India

Vol. 41, No. 3,
September 1993
pp. 219–232

Switching of partially switched $KNbO_3$ single crystals containing cooperatively ordered impurity dipoles

S G INGLE and R N KAKDE
Laxminarayan Institute of Technology, Nagpur University, Nagpur 440010, India

MS received 18 February 1993; revised 14 June 1993

Abstract. Switching studies have been carried out in partially switched $KNbO_3$ single crystals by observing switching transients and hysteresis loops. The crystals used contained ordered impurity dipoles that are active in nucleating domains around them. Partial initial switching was obtained by applying known compressive stress to the crystal by means of a spring. The partially switched nature was determined by recording the photograph of the crystal surface. The changed domain structure on the surface gave a clear idea of the extent of partial switching. As the compressive stress was gradually increased, the crystal showed increased initial mechanical switching through the mechanism of evaporation of domain walls associated with ordered impurity dipoles. The dipoles then switch systematically converting 90° domains with polar axes in the plane of plate into 60° domains with polar axes in the perpendicular pseudocubic {001} planes. The initial switching condition changes the switching characteristics as determined by hysteresis loops and switching transients. The results are interpreted in terms of domains in the crystal. If the dipole density is quite high, the effect of the dipoles becomes negligible, and the switching behaviour approximates that of a normal ferroelectric. The switching transients and the hysteresis loops in the crystals containing cooperatively ordered dipoles are basically different from the ones observed in normal ferroelectrics. The anomalous behaviour is detrimental to the use of material in device applications. Hence, it is shown that the switching transients and hysteresis loops provide a ready means of detecting the presence of these ordered impurity dipoles.

Keywords. Impurity dipoles; cooperative ordering; switching transients; hysteresis loops.

PACS No. 77·80

1. Introduction

Ingle and Dupare [1] recently reported that the switching mechanism in $KNbO_3$ single crystals containing cooperatively ordered defects is radically different from the one normally observed in ferroelectrics. This difference arises from the fact that the defects when they are ordered easily induce nucleation of domains around them, and the entire domain structure in the crystal may be formed by this mechanism (Ingle and Moon [2, 3]). The switching in such crystals involves evaporation and renucleation of these domains, and dP/dE is strongly time-dependent leading to anomalous hysteresis loops even at low frequencies. The distorted loops reported earlier by Fousek and Berezina [4] had their origin in the inability of the domains to follow the changes in the electric field, and this effect naturally occurred only at high frequencies. The distorted loops reported by Jaskiewicz [5], Maleshina [6], Boser [7], etc., were also modifications of regular hysteresis loops.

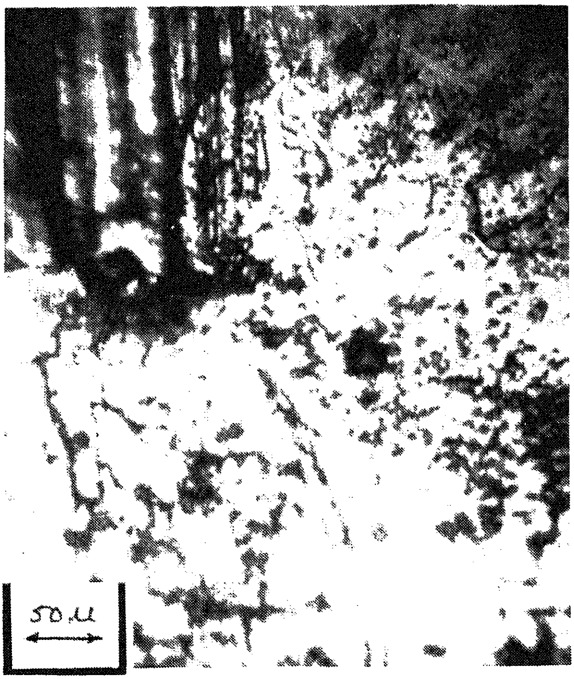

Figure 1. Photomicrograph of the surface of the crystal used for switching (487 ×).

the polarization throughout lies in the plane of the plate as shown in figure 3. Since the impurity dipole moments are parallel to P_s directions [3], the impurity dipoles lie in the plane of the plate.

The crystal was next subjected to compressive stress $33{\cdot}78 \times 10^3\ \mathrm{Nm}^{-2}$. The crystal surface seen in figure 2(a) now shows many changes [figure 4(a)]. In the top right hand region 60° domains are obtained. These domains are of two types: (1) with domain lines parallel to edge, and (2) with domain lines at 45° with the edge. The domain structures in the two cases are shown in figures 5(a) and 5(b) respectively. The impurity dipole moment directions being parallel to P_s directions, it is seen that many dipoles have now switched in response to the compressive stress. Even in lower right region, the dipoles are seen to have switched, 90° domains giving way to 60° domains of the type of figure 5(a). Thus, there is increase in the 60° domains in the crystal as a result of partial switching. This is corroborated by the hysteresis loop shown in figure 4(b). The loop now shows less severe kinks as compared to those seen earlier [see figure 2(b)]. Since a kink is associated with nucleation or evaporation of a large domain [1], reduction in the size of the kink means reduction in the size of the 90° domains on account of partial change of domain structure from the type in figure 3 to the type in figure 5(a). There are some small changes in the switching transient also [figure 4(c)]. The height of current pulse is somewhat reduced, and also the τ_s value. Thus, the overall area under the current pulse corresponding to the switched polarization $[\int(\mathrm{d}P/\mathrm{d}t)\cdot\mathrm{d}t]$ has decreased on account of initial mechanical switching. Indeed, it is seen that as further compressive stresses are applied the area under the current pulse goes on decreasing continually. The decrease in current pulse height is also seen to increase as the applied compressive stress is increased.

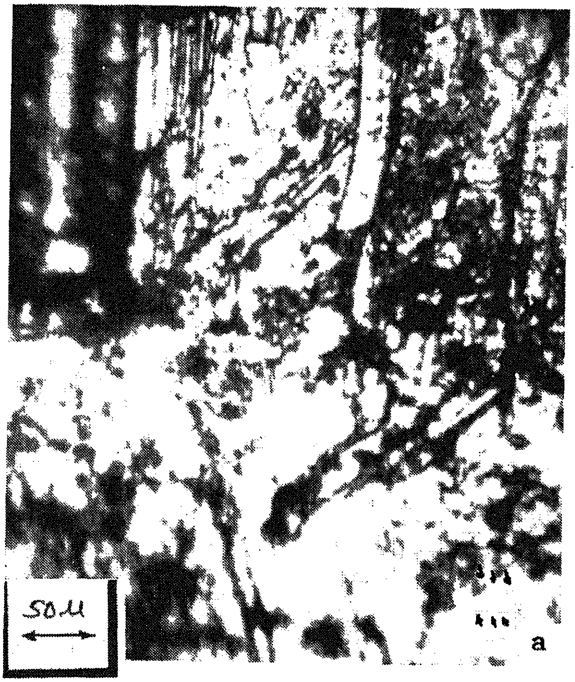

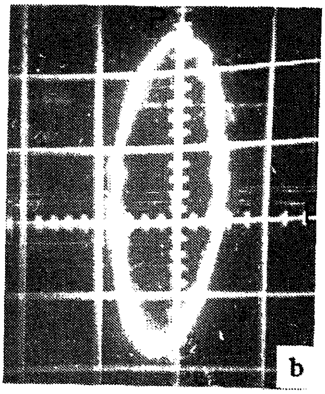

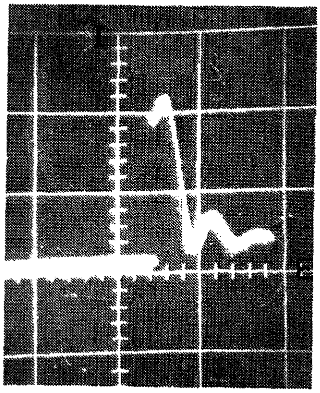

Figure 2(a). The photomicrograph of the crystal surface shown in figure 1 after compressive stress $12{\cdot}4 \times 10^3\,\mathrm{Nm}^{-2}$ was applied to the crystal (487 ×).
Figure 2(b). The hysteresis loop with the compressive stress $12{\cdot}4 \times 10^3\,\mathrm{Nm}^{-2}$ applied to the crystal. Scale: E axis (1 div = 650 v/cm), P axis (1 div = $3{\cdot}9\,\mu$c).
Figure 2(c). The switching transient with the compressive stress $12{\cdot}4 \times 10^3\,\mathrm{Nm}^{-2}$ applied to the crystal. Scale: E axis (1 div = 650 v/cm), I axis (1 div = 24×10^{-3} amp).

As the compressive stress was increased to a higher level $83{\cdot}5 \times 10^3\,\mathrm{Nm}^{-2}$, a lot of initial switching occurred as seen in the photomicrograph of figure 6(a). The hysteresis loop and the switching transient obtained in this case are shown in figures 6(b) and 6(c) respectively. The hysteresis loop now shows a double loop and the outer loop has only a few kinks. Such double loop formation can be due to weakening of bonds between two domains or two types of domains, 90° and 60°, or between domains formed by ordered impurity dipoles, and formed otherwise. In as much as both the loops show kinks the outer loop with a few kinks should correspond to small, newly formed 60° domains, while the inner loop with many kinks should correspond to 90° domains. Thus, the hysteresis loop in figure 6(b) shows increased participation of 60° domains which are formed by initial mechanical switching seen in figure 6(a). The switching transient in figure 6(c) also corroborates this. One can see here the changes of slopes in the switching current pulse at A and B [figure 6(c)], and these changes of slope are indicative of different rates of polarization change with respect to time, clearly corresponding to switching of different type of domains. This becomes clear

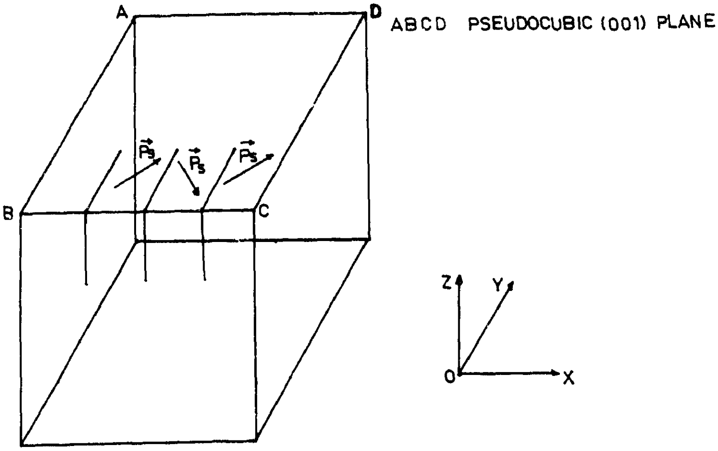

Figure 3. A sketch showing 90° domains with polar axes in the plane of plate.

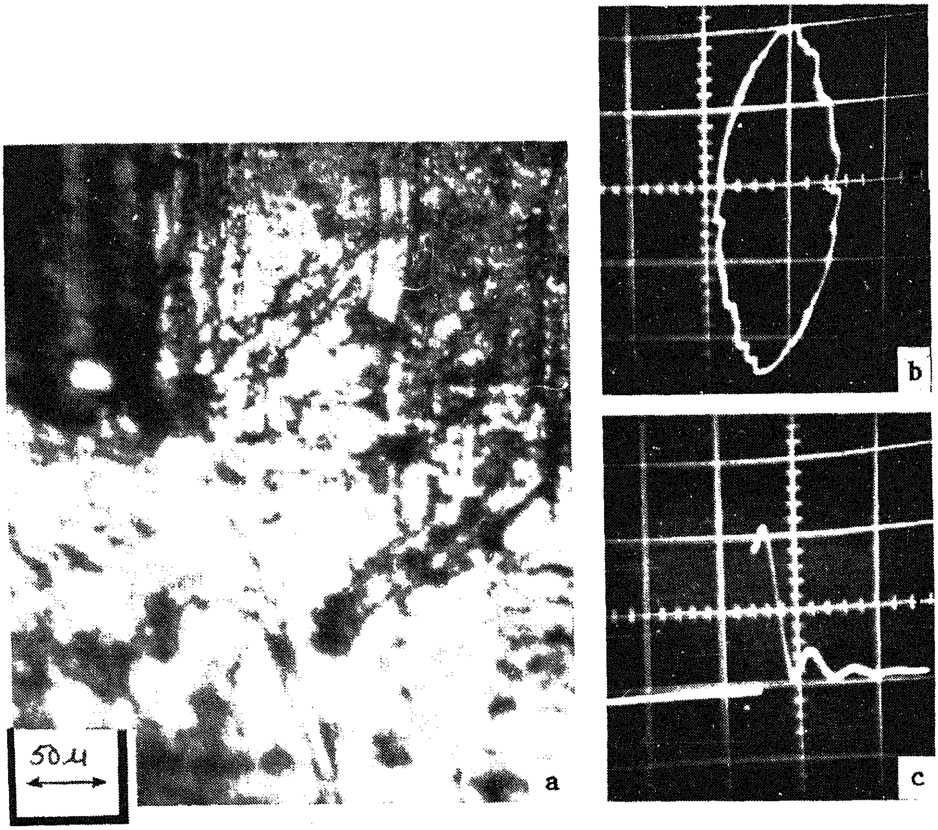

Figure 4(a). The photomicrograph of the crystal surface shown in figure 1 when compressive stress $33{\cdot}7 \times 10^3\,\mathrm{Nm}^{-2}$ is applied to the crystal (487 ×).
Figure 4(b). The hysteresis loop with the compressive stress $33{\cdot}7 \times 10^3\,\mathrm{Nm}^{-2}$ applied to the crystal. Scale: E axis (1 div = 650 v/cm), P axis (1 div = $3{\cdot}9\,\mu$c).
Figure 4(c). The switching transient with the compressive stress $33{\cdot}7 \times 10^3\,\mathrm{Nm}^{-2}$ applied to the crystal. Scale: E axis (1 div = 650 v/cm), I axis (1 div = 24×10^{-3} amp).

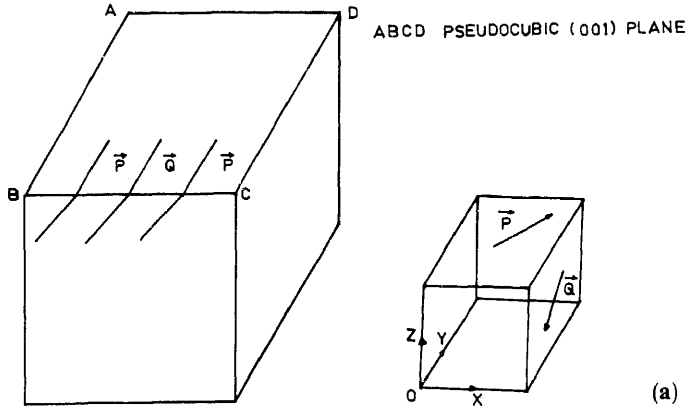

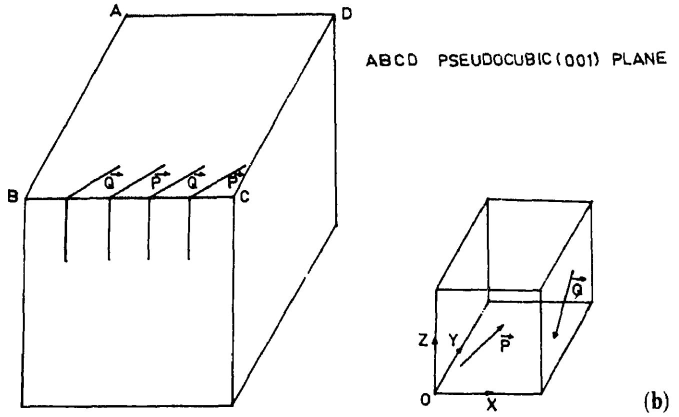

Figure 5(a). A sketch showing 60° domains when a domain line on pseudocubic $\{001\}$ surface is parallel to the edge.

Figure 5(b). A sketch showing 60° domains when a domain line on pseudocubic $\{001\}$ surface is at 45° with the edge.

if one compares the transient in figure 6(c) with the transient in figure 2(c), wherein one finds that there is no change of slope corresponding to B in figure 2(c), indicating the predominance of one type of domains in the crystal. The photomicrograph in figure 2(a) already shows only 90° domains, while the photomicrograph in figure 6(a) shows 90° as well as 60° domains. Thus, the information given by the photomicrographs can be suitably correlated with the hysteresis loops and the switching transients.

A very interesting situation arose as the compressive stress was increased to $104 \times 10^3\,\mathrm{Nm}^{-2}$. The ordered domain structure of figure 6(a) disappeared, and disorder set in [figure 7(a)]. It is because the domain structure shown in figure 5(a) has evaporated to usher in a more favourable structure in figure 5(b). The structure of figure 5(b) could not set in, however, leading to instability and lack of order. The hysteresis loop and the switching transient are shown in figures 7(b) and 7(c) respectively. We find in figure 7(c) that two successive switching transients have been obtained. After the first switching transient, the crystal switches again owing to inherent instability of the conditions existing in the crystal. The hysteresis loop in

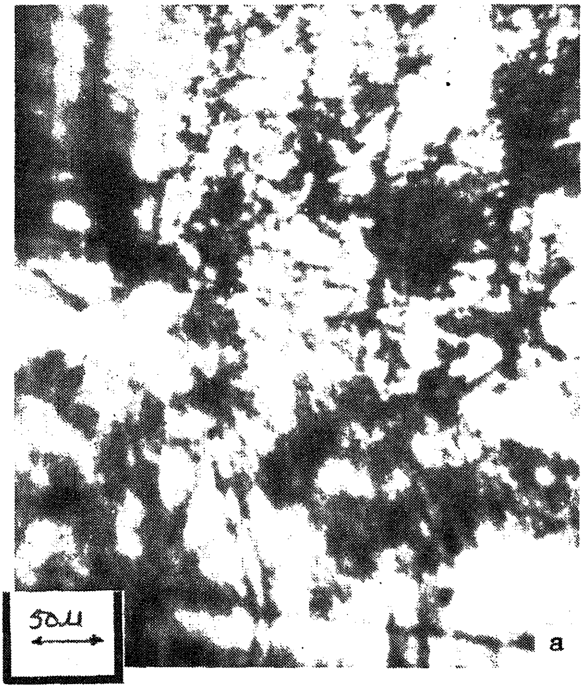

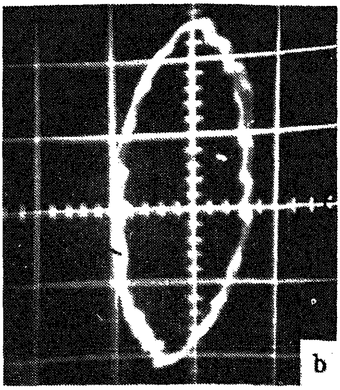

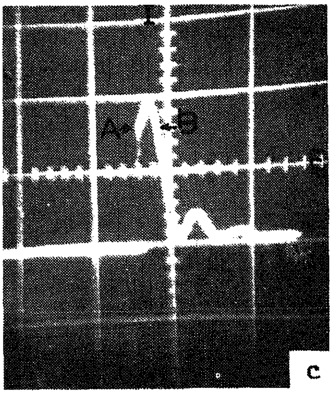

Figure 6(a). The photomicrograph of the crystal surface when the compressive stress $83{\cdot}5 \times 10^3\,\mathrm{Nm}^{-2}$ is applied to the crystal (487 ×).

Figure 6(b). The hysteresis loop when a compressive stress $83{\cdot}5 \times 10^3\,\mathrm{Nm}^{-2}$ is applied to the crystal. Scale: E axis (1 div = 650 v/cm), P axis (1 div = $3{\cdot}9\,\mu$c).

Figure 6(c). The switching transient when a compressive stress $83{\cdot}5 \times 10^3\,\mathrm{Nm}^{-2}$ is applied to the crystal. Scale: E axis (1 div = 650 v/cm), I axis (1 div = 24×10^{-3} A).

figure 7(b) shows this instability through the relative decrease in the number of large domains that is itself indicated by the presence of only a few kinks on the loop. The domains in question are 60°, as the initial switching converts at this stage most of the 90° domains into 60° domains. Further increase in the stress to the value $127 \times 10^3\,\mathrm{Nm}^{-2}$ succeeds in creating ordered structure [figure 8(a)] with the mixture of domain structures shown in figures 5(a) and 5(b). Correspondingly, we see now more kinks in the hysteresis loop [figure 8(b)] corresponding to more domains representing sudden changes of electric field and polarization. The change of the slope in current transient [figure 8(c)] during current fall as at B in figure 6(c) is absent, as 90° domains are mostly absent. Thus, we get a clear evidence of the fact that the change of slope corresponds to switching of different type of domains. Further increase in the stress again creates a disorder as explained above [figure 9(a)], and corresponding absence of kinks on hysteresis loop [figure 9(b)]. The absence of 90° domains is seen again in the switching transient [figure 9(c)] in the form of the absence of change of slope at B.

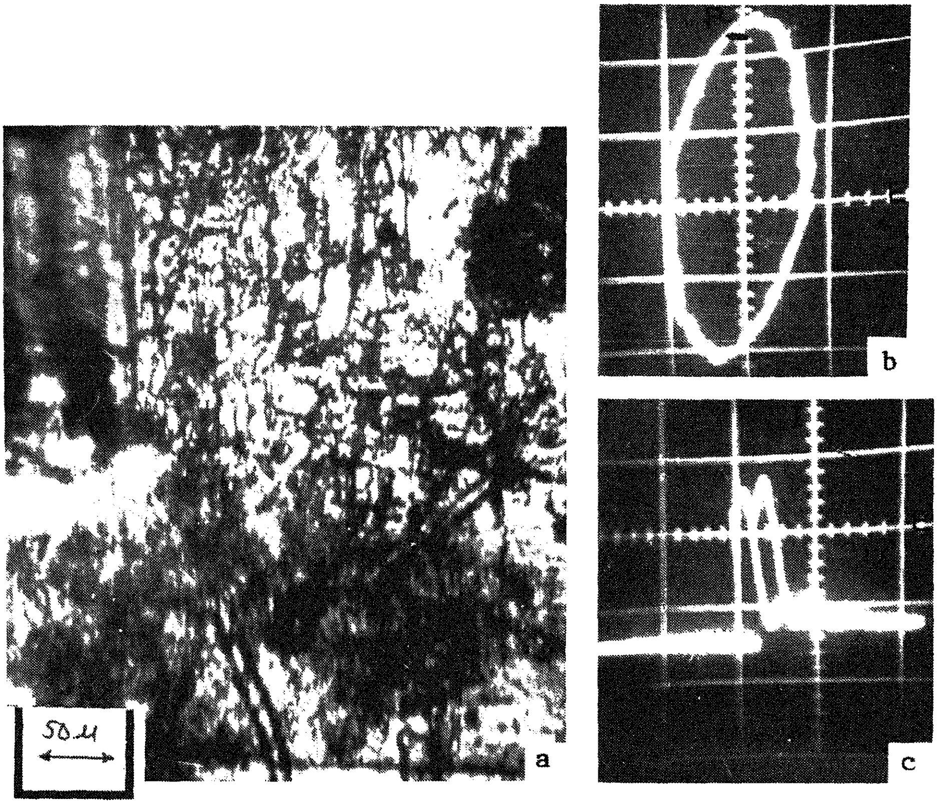

Figure 7(a). The photomicrograph of the crystal surface shown in figure 1 when a compressive stress $104 \times 10^3\,\mathrm{Nm}^{-2}$ is applied to the crystal (487 ×).
Figure 7(b). The hysteresis loop when a compressive stress $104 \times 10^3\,\mathrm{Nm}^{-2}$ is applied to the crystal. Scale: E axis (1 div = 650 v/cm), P axis (1 div = $3{\cdot}9\,\mu$c).
Figure 7(c). The switching transient when a compressive stress $104 \times 10^3\,\mathrm{Nm}^{-2}$ is applied to the crystal. Scale: E axis (1 div = 650 v/cm), I axis (1 div = 24×10^{-3} A).

Thus, we get here a systematic picture of the mechanical switching process, and also of how the various stages of initial switching are reflected in the hysteresis loops and switching transients. If we compare different hysteresis loops reproduced in above figures, we find that the coercive field is less when ordered domain structure exist, and vice versa. This is again easy to understand as it must be a lot easier to evaporate cooperatively a few ordered domains. Thus, the domain interpretation of the hysteresis loops and switching transients is seen to give a consistent picture under variety of situations.

It has been found by Ingle and Dupare [8] that the cooperative order of impurity dipoles exists for a limited range of dipole density. Hence, if the average dipole density in the crystal is high, the regions having cooperative ordering shall be relatively few. Consequently, the switching characteristics of such crystals shall be less dominated by the above discussed effects. To confirm this, the experiments were performed on crystals showing blue colouration that were known to have high content of oxygen vacancies [16].

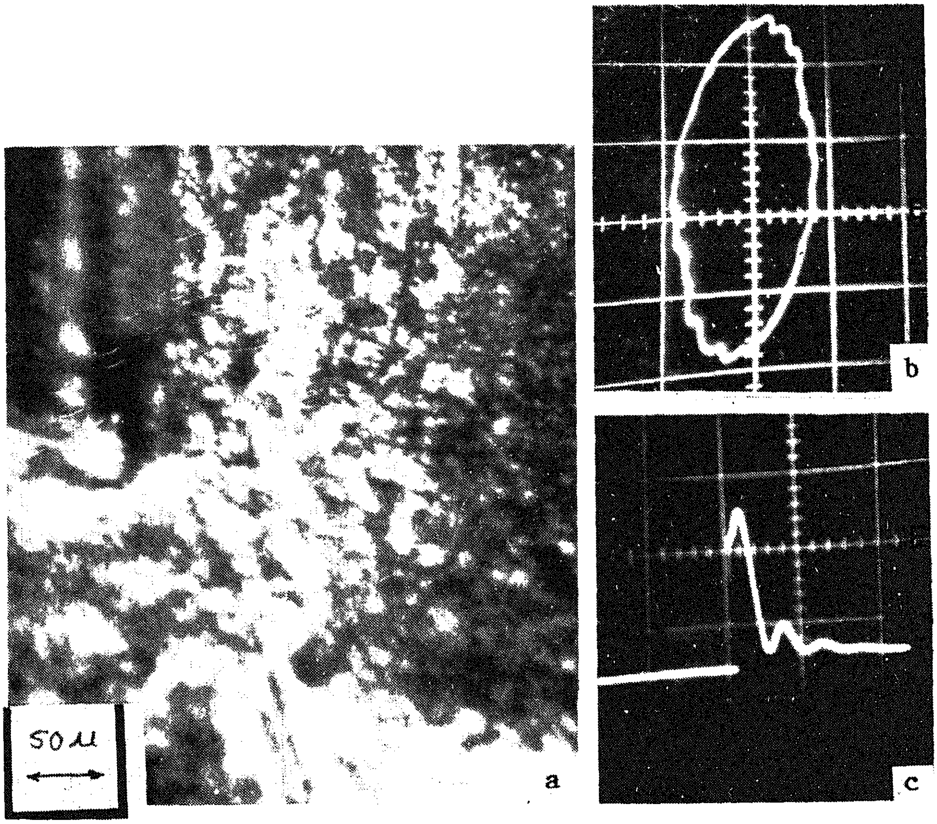

Figure 8(a). The photomicrograph of the crystal surface shown in figure 1 when a compressive stress $127 \times 10^3\,\mathrm{Nm}^{-2}$ is applied to the crystal (487 ×).
Figure 8(b). The hysteresis loop when a compressive stress $127 \times 10^3\,\mathrm{Nm}^{-2}$ is applied to the crystal. Scale: E axis (1 div = 650 v/cm), P axis (1 div = 3·9 μc).
Figure 8(c). The switching transient when a compressive stress $127 \times 10^3\,\mathrm{Nm}^{-2}$ is applied to the crystal. Scale: E axis (1 div = 650 v/cm), I axis (1 div = 24×10^{-3} A).

Figures 10(a) and 10(b) show respectively a typical hysteresis loop and switching transient in such type of crystals. The crystal has been subjected to a compressive stress $12{\cdot}44 \times 10^3\,\mathrm{Nm}^{-2}$. The following are the main points of difference between this current transient and the current transients shown earlier. (1) The trace is broad, showing loose bonding between domains. (2) The fall is steep without any change of slope, indicating absence of large domains associated with cooperatively ordered dipoles. (3) The fall in current does not reach the levels obtained earlier. This means that now $(\mathrm{d}P/\mathrm{d}t)$ is halted earlier and some polarization remains unreversed. Clearly, this unreversed polarization is not associated with cooperatively ordered dipoles. (4) The pulsation of the current after removal of voltage pulse is reduced. This is obviously due to the difficulty faced in nucleation and evaporation, as there are no cooperatively ordered impurity dipoles to assist these processes.

The effect of applying increased compressive stress before obtaining hysteresis loops and switching transients was also studied. The results agreed completely with the

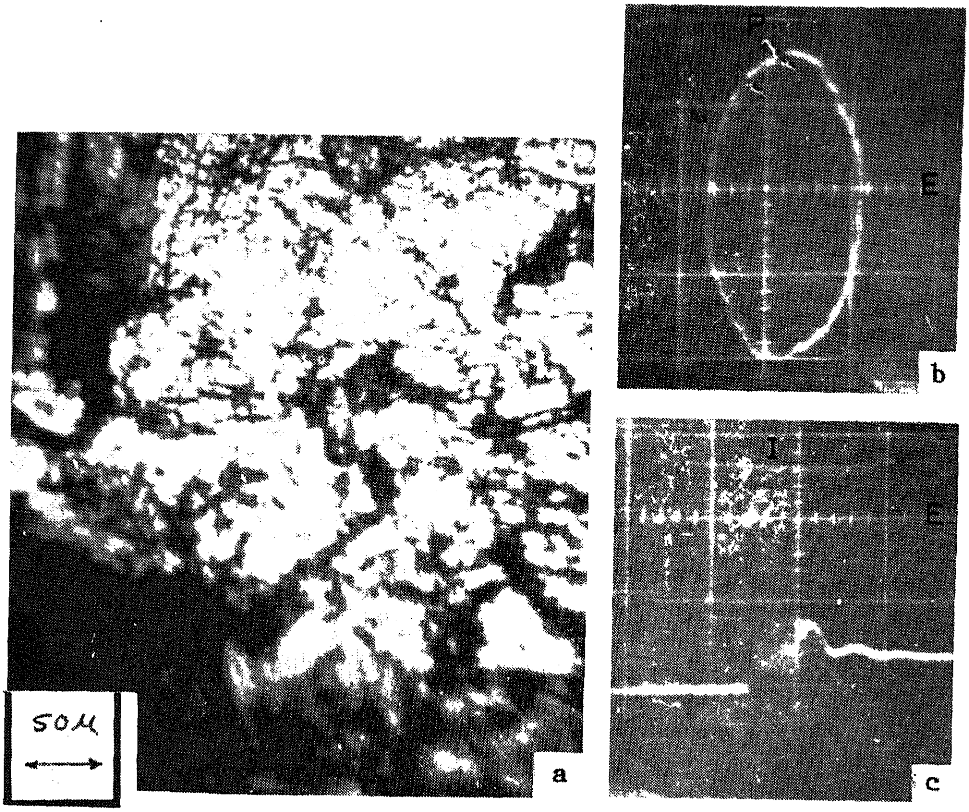

Figure 9(a). The photomicrograph of the crystal surface shown in figure 1 when a compressive stress $171 \times 10^3\,\mathrm{Nm}^{-2}$ is applied to the crystal (487 ×).
Figure 9(b). The hysteresis loop when a compressive stress $171 \times 10^3\,\mathrm{Nm}^{-2}$ is applied to the crystal. Scale: E axis (1 div = 650 v/cm), P axis (1 div = 3·9 μc).
Figure 9(c). The switching transient when a compressive stress $171 \times 10^3\,\mathrm{Nm}^{-2}$ is applied to the crystal. Scale: E axis (1 div = 650 v/cm), I axis (1 div = 24×10^{-3} A).

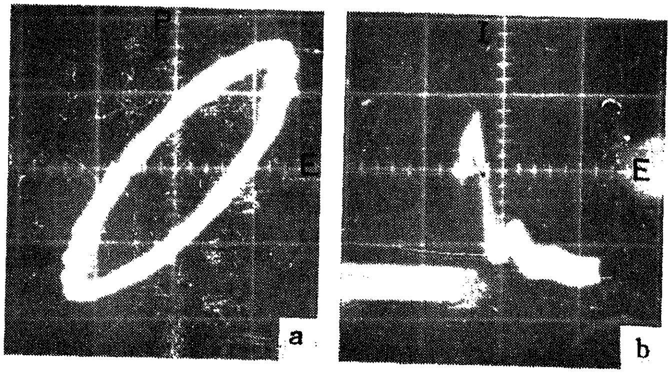

Figure 10(a). The hysteresis loop in a crystal containing high order of dipole density. Scale: E axis (1 div = 650 v/cm), P axis (1 div = 3·9 μc).
Figure 10(b). The switching transient in a crystal containing high order of dipole density. Scale: E axis (1 div = 650 v/cm), I axis (1 div = $26{\cdot}4 \times 10^{-3}$ A).

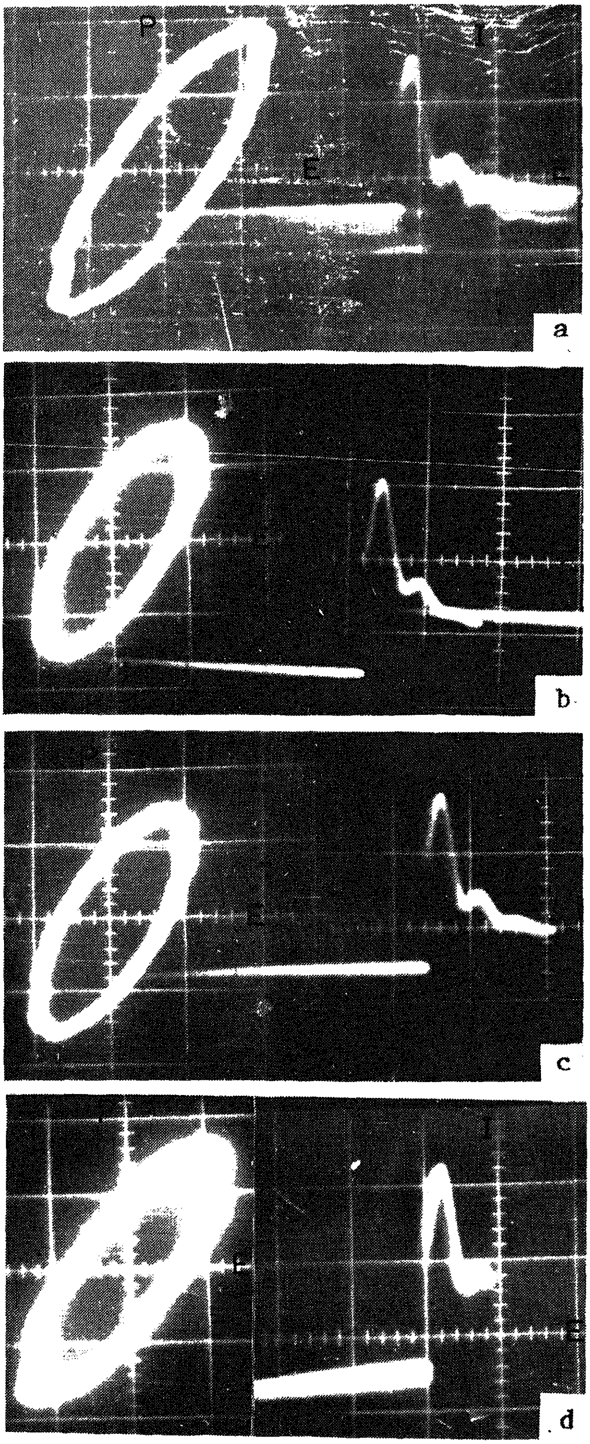

Figure 11. The hysteresis loop and the switching transient in the crystal used for figure 10 when a compressive stress (a) $23{\cdot}1 \times 10^3\,\mathrm{Nm}^{-2}$ (b) $67{\cdot}5 \times 10^3\,\mathrm{Nm}^{-2}$ (c) $150 \times 10^3\,\mathrm{Nm}^{-2}$ and (d) $200 \times 10^3\,\mathrm{Nm}^{-2}$ is applied to the crystal. Scale: E axis (1 div = 650 v/cm) P axis (1 div = $3{\cdot}9\,\mu$c) and I axis (1 div = $26{\cdot}4 \times 10^{-3}$ A).

ideas developed above. Particularly, two observations were significant: (1) The switching time $\tau_s = 0{\cdot}45$ ms remained more or less unaltered, showing less initial mechanical switching due to relative absence of domains with cooperative ordering of dipoles. (2) As the compressive stress is increased, the current pulse ended up earlier, and pulsations after removal of voltage pulse were also reduced. This is on account of the fact that the initial mechanical switching covers domains associated with impurity dipoles, and the increased compressive stress behaviour approaches the behaviour of a normal ferroelectric crystal.

Also, the current pulse height now increases as the compressive stress is increased, which is in contrast with the earlier observations with pale yellow crystals containing a large number of cooperatively ordered impurity dipoles. This again indicates less initial mechanical switching that is associated with domains with ordered impurity dipoles. The increase in height is due to generation of bias voltage that helps the voltage pulse. In the earlier transients, the initial switching effect more than compensated the bias voltage effect producing reduction in the current pulse height.

The various hysteresis loops and the switching transients at gradually increasing stress level are shown in figures 11(a), 11(b), 11(c) and 11(d). These observations have been obtained at stress levels $23{\cdot}11 \times 10^3\,\mathrm{Nm}^{-2}$, $67{\cdot}56 \times 10^3\,\mathrm{Nm}^{-2}$, $150 \times 10^3\,\mathrm{Nm}^{-2}$ and $200 \times 10^3\,\mathrm{Nm}^{-2}$ respectively. The relative absence of kinks can be noted in all the hysteresis loops. The reduction in switched polarization $\int(\mathrm{d}P/\mathrm{d}t)\cdot\mathrm{d}t$ can also be noted. It is interesting to find that in all the transients the current falls steeply without any change of slope indicating absence of domains with cooperatively ordered dipoles.

It follows that if one is interested to avoid the anomalous effects of cooperative ordering, one must have crystals where the kinks in the hysteresis loop are absent, and the switching transients do not show slopes and oscillations after removal of the voltage pulse. Thus, one obtained here a ready, nondestructive testing method to decide the suitability of crystals for applications. Since the crystals have high tendency to develop cooperative ordering through diffusion of impurity dipoles in the structure [1], the anomalous effects tend to be present even if the average density of dipoles in the crystal as a whole is low.

4. Conclusion

It is established that switching is dominated by the behaviour of impurity dipoles, and predominantly by the consideraton as to whether the dipoles are cooperatively ordered or not. When they are cooperatively ordered, nucleation and evaporation rates are much faster. The domains have their influence in the sense that 60° domains switch faster than the 90° domains. All these effects are reflected in the switching transients and the hysteresis loops, which hence serve as good indicators of the presence of cooperatively ordered impurity dipoles in the crystal. Since the cooperatively ordered dipoles lead to anomalous and unexpected behaviour during crystal application, their elimination is extremely necessary. It is possible to do so, since the cooperative ordering exists only within a limited range of dipole density. The mechanical switching is also seen to follow the same pattern as the electrical switching as regards the influence of impurity dipoles. Hence, for piezoelectric applications also, the elimination of cooperatively ordered dipoles is essential.

References

[1] S G Ingle and J G Dupare, *Phys. Rev.* **B45**, 2638 (1992)
[2] S G Ingle and K S Moon, *J. Phys.* **D24**, 1637 (1991)
[3] S G Ingle and K S Moon, *J. Phys. Chem. Solids* **53**, 61 (1992)
[4] J Fousek and B Berezina, *J. Phys. Soc. Jpn.* **19**, 830 (1964)
[5] A Jaskiewicz, *Acta Phys. Pol.* **27**, 637 (1965)
[6] V A Meleshina, *Kristallografiya* **16(3)**, 557 (1971)
[7] O Boser, *J. Appl. Phys.* **62(4)**, 1344 (1987)
[8] S G Ingle and J G Dupare, *Pramana – J. Phys.* **36**, 167 (1991)
[9] S G Ingle, K S Moon and R N Kakde, *Bull. Mater. Sci.* **15**, 251 (1992)
[10] K G Deshmukh and S G Ingle, *J. Phys.* **D4**, 124 (1971)
[11] S G Ingle and K S Moon, *Ferroelectrics* **119**, 107 (1991).
[12] Jai Prakash, A K Nishad and Rahul, *Jpn. J. Appl. Phys. Rev. I* **23**, 1403 (1984)
[13] S G Ingle and J G Dupare, *Philos. Mag.* **B67**, 117 (1993)
[14] S G Ingle and M V Kokate, *Philos. Mag.* **A61**, 543 (1990)
[15] W Merz, *Phys. Rev.* **95**, 690 (1954)
[16] S G Ingle and S C Joshi, *Phys. Rev.* **B34**, 4840 (1986)

PRAMANA
— journal of
physics

© Printed in India

Vol. 41, No. 3,
September 1993
pp. 233–237

Investigations on thermoelectric power of lanthanum oxide doped ferroelectric sodium vanadate

D V PAWAR, T S MAGDUM, S P RASAL and S H CHAVAN*
Ferroelectrics Laboratory, Department of Physics, Shivaji University, Kolhapur 416 004, India
*For correspondence

MS received 11 January 1993; revised 19 June 1993

Abstract. The thermoelectric power of ferroelectric sodium vanadate doped with different concentrations of lanthanum oxide has been measured in the temperature range covering their transition temperatures. It has been observed that the thermoelectric power increases with temperature, attains maximum value and with further increase in the temperature decreases to zero, indicating Curie temperature of the respective samples; however, it changes the sign for higher temperature. The thermoelectric power of sodium vanadate increases to maximum with increase in doping concentration of lanthanum oxide from 0·025 to 0·1 mol%; however, it decreases for higher concentrations. Pure as well as lanthanum oxide doped sodium vanadate samples show *p*-type behaviour in the ferroelectric region and *n*-type behaviour in the paraelectric region.

Keywords. Ferroelectrics; thermoelectric power; Curie temperature.

PACS No. 77·90

1. Introduction

In recent years, considerable advances have been made in the investigations on various properties of the ferroelectrics sodium vanadate, potassium vanadate and lithium vanadate, but the effect of doping on these properties has practically not been studied so far. The structural aspects of alkali metal vanadates were reported by Feigelson *et al* [1] who showed that $NaVO_3$ belongs to the monoclinic system with space group *Cc* at room temperature. The crystal chemistry of $M^+VO_3(M^+ = \text{Li, Na, K, Cs, Rb, NH}_4, \text{Tl})$ pyroxenes was studied by Hawthorne and Calvo [2]. The structural features of $NaVO_3$ single crystals and the variations in lattice parameters in the temperature range from room temperature to 500°C were reported by Ramani *et al* [3] and Shaikh *et al* [4]. Dielectric dispersion over a wide range of frequency, dielectric and pyroelectric properties for sodium vanadate at different temperatures were also investigated [5, 6]. The pyroelectric properties of ferroelectric $NaVO_3$, KVO_3, $LiVO_3$ and their solid solutions were studied by Patil *et al* [7].

The thermoelectric effects are utilized in a thermoelectric circuit to produce useful heating, cooling and/or power generation. The studies on thermoelectric power gives useful information regarding the nature, the number and the effective mass of charge carriers in solids. The thermoelectric power or Seebeck coefficient is defined as the emf developed when a unit temperature difference exists between the points of measurements. Saburi [8] studied the variation of the thermoelectric power with temperature in the doped $BaTiO_3$. Tennary and Cook [9] investigated the d.c. resistivity and thermoelectric power of rare-earth oxides doped $BaTiO_3$. Alder [10], Austin and Mott [11], Bosman and Daal [12] and Sumi [13] have studied the thermoelectric power and conduction mechanism in solids. The temperature variation of the thermoelectric power of $KNbO_3$ crystals doped with impurities was measured by Yanovskii [14]. Electrical conductivity and thermoelectric power of light and heavy rare earth vanadates were studied by Gaur and Lal [15, 16]. High temperature Seebeck coefficients on $YBa_2Cu_3O_{7-\delta}$ were carried out by Ramasesha *et al* [17].

The objective of the present communication is to study the effect of lanthanum oxide doping on the temperature dependence of thermoelectric power of ferroelectric sodium vanadate.

2. Experimental

2.1 *Preparation*

Polycrystalline alkali metal vanadate was prepared by the usual ceramic technique [1] which was grown from a stoichiometric mixture of AR grade alkali metal carbonate and vanadium pentoxide according to the reaction:

$$X_2CO_3 + V_2O_5 = 2XVO_3 + CO_2\uparrow \quad \text{where,} \quad (X = \text{Na}).$$

The alkali metal carbonate used was preheated at 200°C for 2 h before weighing, in order to minimize the moisture. The dried powder was then weighted and blended thoroughly with V_2O_5. This mixture was slowly heated in a platinum crucible inside a globar furnace up to 750°C and this temperature was maintained for 5 h and then melted and the furnace cooled.

La_2O_3 (purity 99% Loba Chemie Indoaustranal Co., Bombay) was used as an additive. The samples were prepared by weighing La_2O_3 in different percentages from 0·025 to 3 mol % in $NaVO_3$. Every batch was subsequently dry-mixed and then mixed wet with ethyl alcohol in an agate mortar. After the alcohol was completely evaporated, the batches were heated in a platinum crucible at 750°C for 5 h inside a globar furnace and then allowed to cool to room temperature. The prepared samples were then ground and passed through a 120 mesh sieve. The crystallinity was confirmed with X-ray diffraction. The pellets were pressed at $7{\cdot}6 \times 10^7\,\text{kg/cm}^2$ pressure, using hydraulic press, in discs of diameter 1 cm and thickness about 0·2 cm and were sintered on a platinum foil at 500° for 4 h in air inside a globar furnace. The two major faces were polished and silvered with air-drying silver paste to have good electrical contact.

2.2 *Apparatus and measurement*

The experimental set-up consists of an electrically heated furnace, a digital d.c. microvoltmeter (VMV 15 Vasavi Electronics) a temperature controller arrangement, digital multimeter and a specially designed sample holder. A typical sample holder was designed in our laboratory for the measurement of thermoelectric power as shown in figure 1. The thermoelectric power of these samples was measured by producing a constant thermal gradient ($\Delta T = 25$°C) across the sample pellets with the help of a small sub-heater, as shown in figure 1, attached to one of the hard electrodes of the sample holder. The ambient temperature was raised by the external heater. Silver electrodes were used for this measurement. The thermal gradient (ΔT)

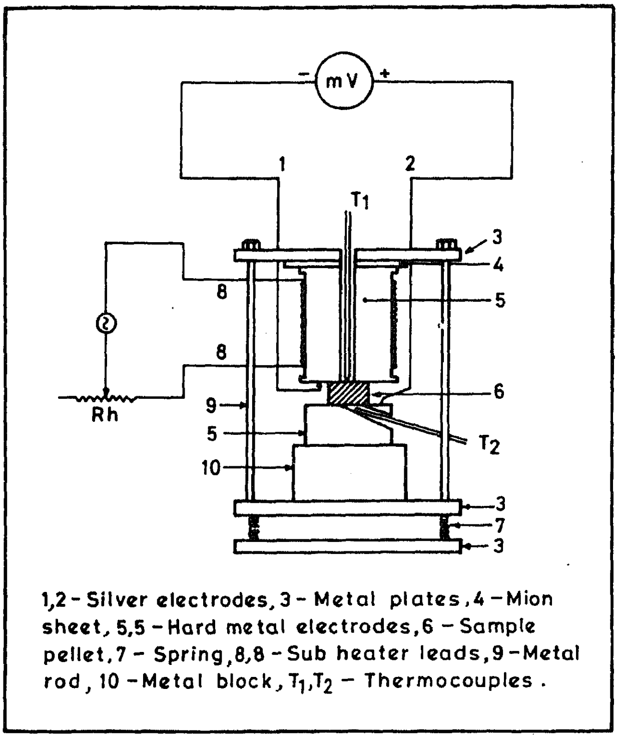
- mV +
1
2
T_1
3
4
5
8
8
6
9
5
10
T_2
3
7
3
Rh
1,2 - Silver electrodes, 3 - Metal plates, 4 - Mion sheet, 5,5 - Hard metal electrodes, 6 - Sample pellet, 7 - Spring, 8,8 - Sub heater leads, 9 - Metal rod, 10 - Metal block, T_1,T_2 - Thermocouples .

Figure 1. Typical sample holder for the measurement of thermoelectric power.

was measured using chromel–alumel thermocouples, T_1 and T_2. The thermo emf (ΔE) developed across the sample pellet was recorded by the digital d.c. microvoltmeter after thermal stability was reached. The thermoelectric power (S) was computed using the relation $S = \Delta E/\Delta T$.

3. Results and discussion

The variation of thermoelectric power with temperature of pure sodium vanadate and that doped with lanthanum oxide in ferroelectric and paraelectric regions is presented in figure 2. From figure 2, it is clearly seen that the thermoelectric power increases with increasing temperature and attains a maximum value. These after it starts decreasing with increasing temperature and becomes negative with further increase in temperature. The magnitude of the thermoelectric power of sodium vanadate doped with different concentrations of lanthanum oxide becomes zero at a particular temperature, indicating the Curie temperature of the respective samples and are in good agreement with those investigated by us using hysteresis loop method and dielectric constant measurements. From figure 2, it is also obvious that the sign of thermoelectric power is positive in ferroelectric region of the samples, representing that the majority charge carriers are positive charges and hence, the sample shows *p*-type behaviour. The negative sign of the thermoelectric power in the paraelectric region of the sample shows that the majority charge carriers are electrons indicating *n*-type behaviour.

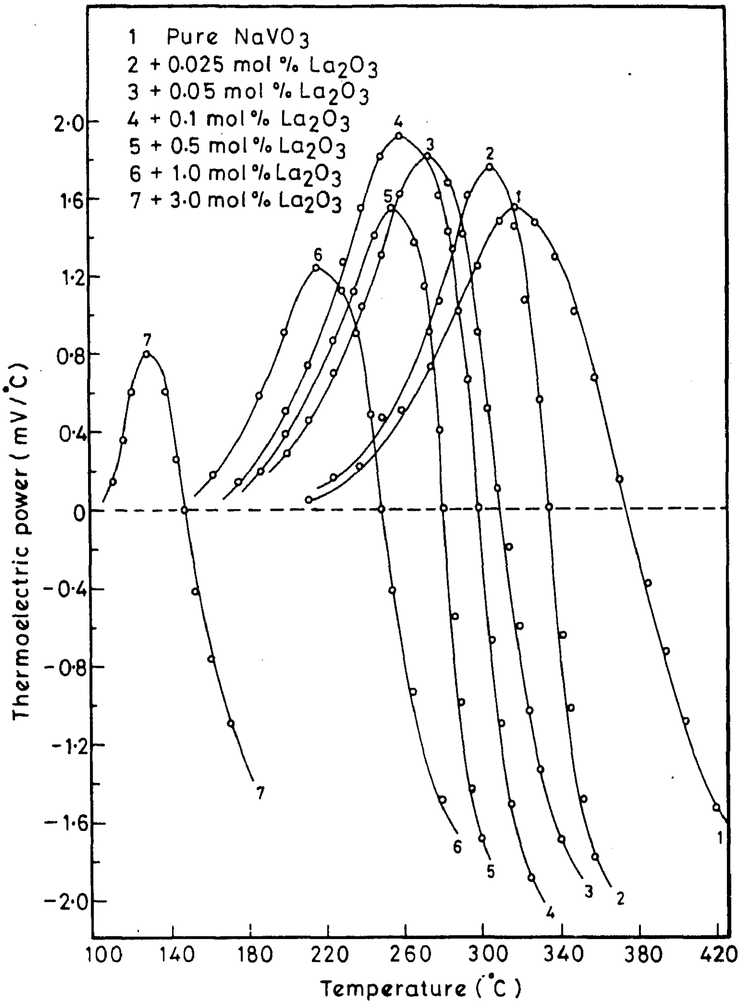

Figure 2. Variation of thermoelectric power with temperature for lanthanum oxide doped sodium vanadate.

The increase in thermoelectric power with increasing temperature of these samples in the ferroelectric region may be due to the increasing mobility of the charge carriers which increase exponentially with temperature. This increase in the mobility of charge carriers with temperature in ferroelectric region suggests a mechanism that deals with polaron hopping conduction. Similar results were also reported by Bosman and Daal [12] and Ansari *et al* [18]. In paraelectric region, the thermoelectric power decreases with increasing temperature, which is in the accordance with normal band conduction as explained by Methfessel and Mattis [19].

Figure 2 also shows that the thermoelectric power increases to maximum with increase in doping concentration of La_2O_3 from 0·025 to 0·1 mol%. However, for higher doping concentrations, it decreases. The increase in thermoelectric power is attributed to a rather more solid state interaction that takes place in the material. It is due to increase of density of $NaVO_3$ with increasing doping concentrations of La_2O_3 up to 0·1 mol%. The maximum densification at 0·1 mol% doping may represent the solubility limit of La_2O_3 in $NaVO_3$ lattice. Similar behaviour was observed for Fe_2O_3 doped PZT [20] and for Al-doped $BaTiO_3$ ceramics [21].

4. Conclusions

The thermoelectric power of pure sodium vanadate and that doped with different concentrations of lanthanum oxide changes its sign at transition temperature, indicating the Curie temperature of the respective samples. The pure as well as doped materials show that the conduction mode is *p*-type in the ferroelectric region and *n*-type in the paraelectric region. The thermoelectric properties of sodium vanadate are affected due to addition of lanthanum oxide. The thermoelectric power increases for 0·025, 0·05 and 0·1 mol % concentrations of La_2O_3; it, however, decreases for higher doping concentrations.

References

[1] R S Feigelson, G W Martin and B C Johnson, *J. Cryst. Growth* **13/14**, 686 (1972)
[2] F C Hawthorne and C Calvo, *J. Solid State Chem.* **22**, 157 (1977)
[3] K Ramani, A M Shaikh, B S Reddy and M A Viswamitra, *Ferroelectrics*, **9**, 49 (1975)
[4] A M Shaikh, M A Viswamitra and P S Narayanan, *Ferroelectrics*, **22**, 311 (1978)
[5] M Matsuda, *J. Phys. Soc. Jpn.*, **36**, 759 (1974)
[6] A Khan, D Ghare and P Narayanan, *Bull. Mater. Sci.*, **5**, 133 (1983)
[7] T A Patil, V M Jamadar and S H Chavan, *Indian J. Pure Appl. Phys.*, **26**, 456 (1988)
[8] O Saburi, *J. Phys. Soc. Jpn.*, **14**, 1159 (1959)
[9] V J Tennery and R L Cook, *J. Am. Ceram. Soc.* **14**, 187 (1961)
[10] D Alder, *Solid State Phys.* **21**, 1 (1968)
[11] I G Austin and N F Mott, *Adv. Phys.*, **18**, 41 (1969)
[12] A J Bosman and H J Daal, *Adv. Phys.*, **19**, 1 (1970)
[13] H Sumi, *J. Phys. Soc. Jpn.*, **33**, 327 (1972)
[14] V K Yanovskii, *Phys. Status Solidi.* **A51**, 399 (1984)
[15] K Gaur and H B Lal, *J. Mater. Sci.*, **20**, 3167 (1985)
[16] K Gaur and H B Lal, *J. Mater. Sci.*, **21**, 2289 (186)
[17] S K Ramasesha, T Mathews and K T Jacob, *Mater. Res. Bull.*, **25**, 149 (1990)
[18] T H Ansari, A K Pandit, M Prasad and R A Singh, *Indian J. Phys.*, **A63**, 784 (1989)
[19] S Methfessel and D Mattis, *Handbook of Physics* Springer-Verlag, Heidelberg (1968) p. 389
[20] T B Weston, A H Webster and N M McNamara, *J. Am. Ceram. Soc. (USA)* **52**, 253 (1969)
[21] A Tawfik, M M A Sekina and M K El-Nimr, *Indian J. Phys.*, **A52**, 164 (1978)

PRAMANA
— journal of
physics

© Printed in India

Vol. 41, No. 3,
September 1993
pp. 239–255

Electronic structure of hydrogen and muonium in Al, Mg and Cu

PAWAN SINGH and S PRAKASH
Department of Physics, Panjab University, Chandigarh 160014, India

MS received 22 March 1993; revised 19 May 1993

Abstract. The electronic structure of hydrogen and muonium in simple metals is investigated. The spherical solid model potential is used for the discrete lattice and the Blatt correction for lattice dilation. The proton and muon are kept at the octahedral sites in the fcc and hcp lattices and self-consistent non-linear screening calculations are carried out. The scattering phase shifts, electronic charge density, effective impurity potential, self-energy, charge transfer, residual resistivity and Knight shift are calculated. The spherical solid potential changes the scattering character of impurity. The phase shifts are found slowly converging. The scattering is more prominent in Al than in Mg and Cu. The virtual bound states of proton and muon are favoured in all the three metals. The calculated value of residual resistivity for CuH is in good agreement with the experimental value. The results for Knight shift for μ^+ in Cu and Mg are in reasonable agreement with the experimental values while those for μ^+ in Al are lower than the experimental value. The analytical expressions for effective impurity potential and electronic charge density are suggested.

Keywords. Hydrogen; muonium; Knight shift; resistivity

PACS Nos 71·50; 71·55

1. Introduction

Hydrogen atoms dissolved in a metal dissociate into protons and electrons. Protons being attractive centre are screened by conduction electrons. The first linear screening theory of proton in Cu was proposed by Friedel [1]. It was realized later that the proton-electron interaction is strong. The screening may not be linear and even the bound state may exist. Popovic *et al* [2] used Hohenberg–Kohn–Sham density functional formalism for the non-linear screening of the proton in the jellium model of the metal. Jena and Singwi [3] added the first gradient correction of exchange-correlation potential and found shallow *s* type bound state of the proton. Manninen and Nieminen [4] added the effect of discrete lattice through spherical solid model of the metal and calculated Knight shift, electric field gradient and heat of solution of hydrogen and muonium in simple metals.

When proton or muon is at an interstitial site it displaces host ions from the equilibrium positions. Therefore the positive charge density in the vicinity of the proton reduces, consequently the effective charge on the proton changes. The lattice dilation also introduces the strain field, therefore the total energy of the system also changes [5–6].

The above studies of non-linear screening of proton and muon are inconclusive because either the discrete lattice effect or the size effect is ignored. We thought it worthwhile to study the electronic structure of hydrogen and muonium in simple metals including both the effects. The discrete lattice effect and the size effect are included through the spherical solid model of the metal and Blatt correction [4–5] respectively. The self-consistent impurity potential, the induced charge density, charge transfer, residual resistivity and Knight shift are investigated.

The plan of the paper is as follows. The necessary formalism is presented in § 2. Calculations and results are presented in § 3 and are discussed in § 4.

2. Theory

2.1 *Size effect*

The screening cloud of conduction electrons and the zero point motion of proton and muon do not allow them to remain as static point charges. These impurities regain the finite size and displace the host ions away from the equilibrium positions. Therefore the positive charge density decreases and electronic charge density increases in the vicinity of the impurity. This changes the positive charge on the proton and the net protonic charge Z is given as [5]

$$Z = Z_\mathrm{I} - \frac{\delta V}{V} Z_\mathrm{H} \tag{1}$$

where Z_I and Z_H are the proton and the host atom ionicities respectively and $(\delta V/V)$ is the fractional change in atomic volume. If $(\delta V/V)$ is negative, Z becomes greater than Z_I. In the continuum model of the lattice $(\delta V/V)$ is taken as local dilation around the impurity and is given as

$$\frac{\delta V}{V} = \left(\frac{3}{\gamma_E}\right)\left(\frac{1}{a}\right)\left(\frac{\mathrm{d}a}{\mathrm{d}c}\right) \tag{2}$$

where $\gamma_E = [3(1-\sigma)/(1+\sigma)]$, σ is Poisson ratio, $(1/a)\,(\mathrm{d}a/\mathrm{d}c)$ is the relative change in the lattice parameter a in per cent per atomic per cent impurity and c is the concentration.

2.2 *Discrete lattice effect and non-linear screening*

We use Hohenberg–Kohn–Sham density functional formalism for non-linear screening [7]. A set of wave functions ψ_i with energy eigenvalues ε_i are generated through one particle Schrödinger equation [4]

$$\left[-\frac{1}{2}\nabla^2 + V(\mathbf{r})\right]\psi_i(\mathbf{r}) = \varepsilon_i \psi_i(\mathbf{r}). \tag{3}$$

The atomic units are used throughout. The first term on the left side is kinetic energy operator and the second term is the effective potential seen by an electron which is given

$$V(\mathbf{r}) = V_c(\mathbf{r}) + V_{xc}(n,\mathbf{r}) + V_{ss}(\mathbf{r}). \tag{4}$$

Here $V_c(\mathbf{r})$ is the electrostatic potential due to impurity induced electronic charge distribution. Explicitly it is given as

$$V_c(\mathbf{r}) = \int \frac{\mathrm{d}\mathbf{r}'[n(\mathbf{r}') - n_+(\mathbf{r}')]}{|\mathbf{r} - \mathbf{r}'|} \tag{5}$$

where

$$n(\mathbf{r}) = \sum_{\varepsilon_i < \mu} |\psi_i(\mathbf{r})|^2 \tag{6}$$

and for an interstitial impurity

$$n_+(\mathbf{r}) = n_0 + Z\delta(\mathbf{r}). \tag{7}$$

Here μ is chemical potential and is taken equal to Fermi energy. The origin is at the impurity site, $n_0(= 3/4\pi r_s^3)$ is uniform positive charge density of the host and r_s is interelectronic distance.

The second term in (4) is exchange-correlation potential which in the local density approximation is given as [8]

$$V_{xc}(n, \mathbf{r}) \simeq \varepsilon_{xc}(n(r)) + n\left(\frac{d\varepsilon_{xc}}{\mathrm{d}n}\right)_{n=n(r)} - V_{xc}(n_0, r_s). \tag{8}$$

The following parametrized form of the exchange-correlation energy $\varepsilon_{xc}(n(r))$ in eq. (8) is used [8]

$$\varepsilon_{xc}(n(r)) = -\frac{0{\cdot}9163}{r_s'} - 0{\cdot}112 + 0{\cdot}0335 \ln r_s' - \frac{0{\cdot}02}{0{\cdot}1 + r_s'}, \tag{9}$$

where $r_s' = [3/(4\pi n(r))]^{1/3}$. The potential $V_{xc}(n_0, r_s)$ in (8) is subtracted for convergence.

$V_{ss}(r)$, the last term of (4), is the spherical solid model potential. It is taken as the spherical average of the difference between the bare ion potential and electrostatic potential of the positive background of jellium. The explicit expression is

$$V_{ss}(\mathbf{r}) = -\frac{1}{4\pi}\int \mathrm{d}\Omega \sum_L w(\mathbf{r} - \mathbf{R}_L) + \int \frac{\mathrm{d}\mathbf{r}' n_0}{|\mathbf{r} - \mathbf{r}'|} \tag{10}$$

where $w(\mathbf{r})$ is the bare ion potential, $\mathbf{R}_L$ are the position vectors of the host atoms and $\mathrm{d}\Omega$ is the elementary solid angle. For simplicity we used Ashcroft model potential for bare ions i.e.

$$w(r) = -\frac{Z_\mathrm{H}}{r}\theta(r - r_c) \tag{11}$$

where r_c is potential parameter and $\theta(r)$ is unit step function. $V_{ss}(\mathbf{r})$ accounts for the discrete lattice of the host, however exact lattice symmetry is reduced to spherical symmetry due to angular averaging.

3. Calculation and results

3.1 *Effective charge on the proton and muon*

The effective charges on proton and muon in Al, Mg and Cu metals are estimated using (1) as described by Mahajan and Prakash [5]. The values of $(\delta V/V)$ and Z are given in table 1. The experimental value of $(\delta V/V)$ for hydrogen in Cu is taken from Katz *et al* [9] while for hydrogen in Al it is estimated from the data for hydrogen in Cu, Ni and Pd [10]. $\delta V/V$ for hydrogen in Mg is estimated from the ratio of moduli of rigidity of Al and Mg as both the metals have almost the same packing ratio.

Schilling *et al* [11] pointed out that muon, because of its smaller mass and larger zero point energy, causes 1·3 times more volume expansion than a proton in Cu. Therefore, in the absence of any other information $(\delta V/V)$ for muon in Al, Mg and Cu is obtained by multiplying the corresponding values of $(\delta V/V)$ for hydrogen in these metals by a factor of 1·3. The effective charge reduces by about 40% for proton and 50% for muon in Al and Mg metals. This reduction in charge is only 27% for proton and 35% for muon in Cu.

3.2 *Spherical solid model potential*

The two terms on the right side of (10) are calculated separately. The integral in the second term is separated into two parts: $r < r'$ and $r > r'$. These integrals are evaluated and the boundary condition that the potential vanishes as $r \to \infty$ is used. The detailed calculation gives this contribution as

$$V_1 = \frac{-2\pi n_0}{3} r^2. \tag{12}$$

The contribution of the first term on the right side of (10) is evaluated in the same coordinate system for Ashcroft model potential. This calculation is separated into three parts: the potential at the interstitial site, the potential in the region $|\mathbf{R}_i - \mathbf{r}_c| \leqslant r \leqslant |\mathbf{R}_i + \mathbf{r}_c|$ and $r > |\mathbf{R}_i + \mathbf{r}_c|$. The potential at origin is obtained by Ewald–Fuchs method and is equal to the negative of self-energy of the host ion i.e.

$$V_2 = \frac{Z_{\mathrm{H}}\alpha_{EW}}{R_{WS}} + \sum_i \frac{Z_{\mathrm{H}}}{|\mathbf{R}_i|}\theta(r - R_1 - r_c) \tag{13}$$

where α_{EW} is the Madelung constant for octahedral site in both the fcc and hcp lattices and $R_{WS}(=(Z_{\mathrm{H}}^{1/3})r_s)$ is the Wigner–Sejtz radius. $\mathbf{R}_i$ are the coordinates of host atoms with respect to the octahedral site. The potential at any point r in the Ashcroft sphere of radius r_c around each ion i.e. $|\mathbf{R}_i - \mathbf{r}_c| \leqslant r \leqslant |\mathbf{R}_i + \mathbf{r}_c|$ is

$$\begin{aligned} V_3 &= -\frac{1}{4\pi}\sum_i \int \frac{Z_{\mathrm{H}}}{|\mathbf{r} - \mathbf{R}_i|}\mathrm{d}\Omega \\ &= -\sum_i \frac{Z_{\mathrm{H}}}{2rR_i}(r + R_i - r_c); \quad |\mathbf{R}_i - \mathbf{r}_c| \leqslant r \leqslant |\mathbf{R}_i + \mathbf{r}_c| \end{aligned} \tag{14}$$

and the potential outside the Ashcroft sphere i.e. $r > |\mathbf{R} + \mathbf{r}_c|$

$$V_4 = -\sum_i \frac{Z_{\mathrm{H}}}{|\mathbf{r}|}; \quad r > |\mathbf{R}_i + \mathbf{r}_c|. \tag{15}$$

Table 1. The calculated results for AlH(μ^+), MgH(μ^+) and CuH(μ^+). ($\delta V/V$) is fractional change in atomic volume, Z is effective charge on impurity, β is potential parameter, n_s is net charge on impurity, E_s is self-energy, $\Delta\rho$ is residual resistivity and K is Knight shift.

Physical quantities	AlH	Alμ^+	MgH	Mgμ^+	CuH	Cuμ^+
$\delta V/V$	0·13	0·17	0·21	0·27	0·27	0·35
Z	0·61	0·49	0·58	0·46	0·73	0·65
β	1·22	1·18	1·12	1·07	1·20	1·15
$n_s(e)$	0·46	0·39	0·45	0·37	0·54	0·49
E_s(a.u.)	−0·042	−0·026	−0·035	−0·021	−0·060	−0·045
$\Delta\rho$($\mu\Omega$cm/at%) (exp)	—	—	—	—	1·5 ± ·05	—
(cal)	0·20	0·14	0·71	0·52	1·53	1·20
K(ppm) (exp)	—	79·6 ± 4·0	—	43·3 ± 3·5	—	60·3 ± 3·0
(cal)	44·39	33·41	38·01	30·14	54·90	48·24

Adding all the four contributions V_1, V_2, V_3 and V_4 and subtracting the constant potential $V_{ss}(r \to \infty) = 3r_c^2/2r_s^3$ for convergence purpose one finds

$$V_{ss}(r) = V_{ss}(0) - \frac{2\pi n_0 r^3}{3} - \left[\begin{array}{ll} \sum_i \left(\frac{Z_{\mathrm{H}}}{2rR_i}(r + R_i - r_c) - \frac{Z_{\mathrm{H}}}{|\mathbf{R}_i|} \right) & ; \quad |\mathbf{R}_i - \mathbf{r}_c| \leqslant \mathbf{r} \leqslant |\mathbf{R}_i + \mathbf{r}_c| \\ \sum_i \left(\frac{Z_{\mathrm{H}}}{|\mathbf{r}|} - \frac{Z_{\mathrm{H}}}{|\mathbf{R}_i|} \right) & ; \quad r > |\mathbf{R}_i + \mathbf{r}_c| \end{array}\right. \tag{16}$$

where

$$V_{ss}(0) = \frac{Z_{\mathrm{H}} \alpha_{EW}}{R_{WS}} - \frac{3r_c^2}{2r_s^3}. \tag{17}$$

The potential parameter r_c, Madelung constant α_{EW}, octahedral coordinates and R_{WS} for Al, Mg and Cu are given in table 2. The potential $V_{ss}(r)$ is terminated at $r = 8$, 10 and 7 a.u. for Al, Mg and Cu respectively because it becomes negligibly small for larger values of r.

The calculated $V_{ss}(r)$ for Al, Mg and Cu are shown in figure 1. The number of nearest neighbours and their positions with respect to octahedral site are also indicated there. We find that Mg is more uniformly packed as compared to Al and Cu. $V_{ss}(r)$ has the maxima around the nearest neighbour sites and minima between the two sites. It does not show exact periodicity of the lattice, therefore it can be regarded just as a correction term for the discrete nature of the lattice in $V(r)$ in (4). The potentials depend on Z_{H} and r_c, however their relative magnitudes are affected by the convergence correction term $3r_c^2/2r_s^3$. This is the reason that magnitude of $V_{ss}(r)$ for Cu and Mg is smaller than that for Al. Thus the discrete lattice effects become more dominant in Al than in Mg and Cu.

3.3 *Phase shifts and impurity potential*

The procedure due to Manninen *et al* [12] is used to solve eqs (3) to (9) self-consistently. The bound states are also included. The radial part of the Schrödinger equation is solved numerically in the steps of 0·1 a.u. up to a radius $R_0 = 19{\cdot}5$ a.u. using Fox

Table 2. The host parameters used in the calculations. r_s is the inter-electronic distance, Z_{H} is the ionicity, r_c is Ashcroft potential parameter, χ_e is the electronic susceptibility and α_{EW} is Modelung constant for octahedral site. The coordinates of the octahedral sites.are given in the last row.

Parameter	Al	Mg	Cu
r_s	2·07	2·66	2·67
Z_{H}	3	2	1
r_c	1·12	1·39	0·81
$\chi_e(\times 10^{-6})$	1·77	1·58	1·36
α_{EW}	0·42586	0·42732	0·42586
Oct. site	$\left(\frac{1}{2}, \frac{1}{2}, \frac{1}{2}\right)$	$\left(-\frac{1}{3}, \frac{2}{3}, \frac{\bar{1}}{3}, \frac{1}{4}\right)$	$\left(\frac{1}{2}, \frac{1}{2}, \frac{1}{2}\right)$

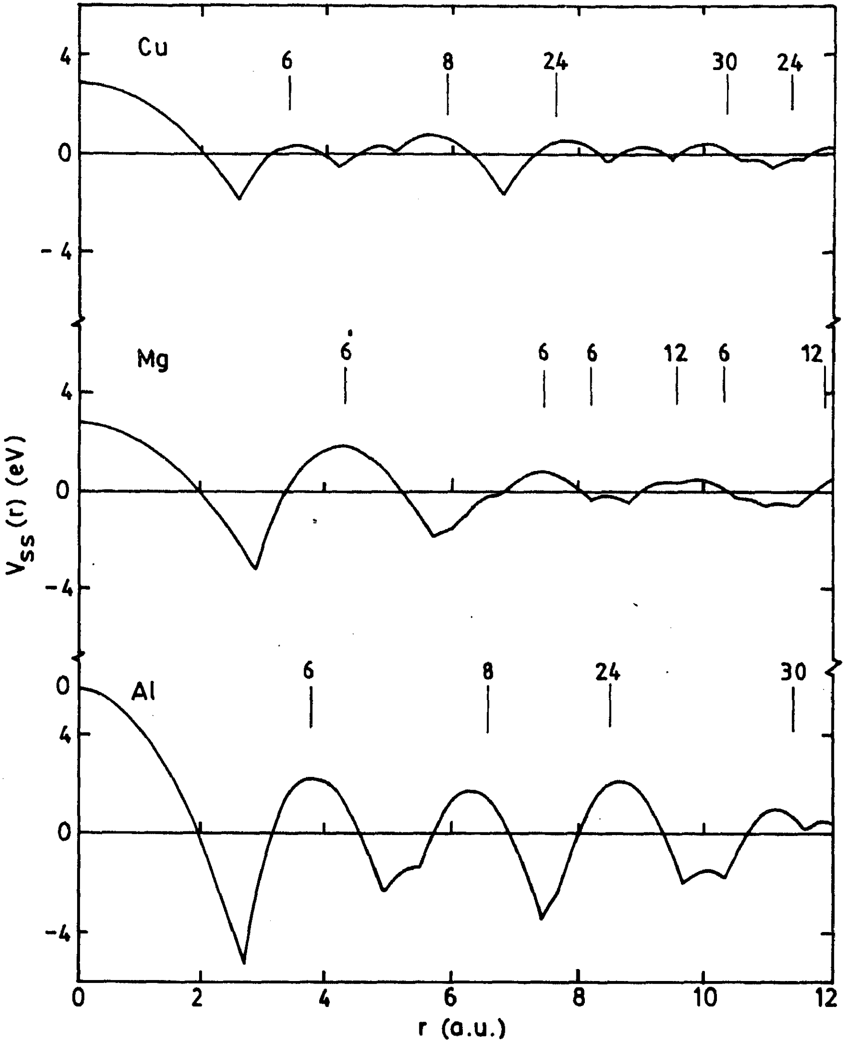

Figure 1. The spherical solid potential $V_{ss}(r)$ vs r for Al, Mg and Cu around octahedral site. The position and number of nearest neighbours are also indicated.

and Goodwin VI method. The phase shifts are calculated by matching the numerical solution with the asymptotic solution at R_0. The self-consistency is checked by satisfying the Friedel sum rule

$$Z = \frac{2}{\pi} \sum_{l=0}^{14} (2l+1)\delta_l(E_F) \tag{18}$$

where l is an orbital quantum number and $\delta_l(E_F)$ are scattering phase shifts at the Fermi energy E_F. The phase shifts are summed up to $l = 14$. Higher order shifts are found negligibly small. The charge density is found accurate within 0·01% in the vicinity of the impurity.

In the first step the calculations are done for the perfect crystal by putting $n(r) = n_{\mathrm{H}}(r)$, $Z = 0$ and $\delta n(r) = n_{\mathrm{H}}(r) - n_0$ in (6), (7) and (18). The self-consistently calculated $V_{\mathrm{H}}(r)$

Table 3. The scattering phase shifts $\delta_l(E_F)$ for proton (H^+) and muon (μ^+) in Al, Mg and Cu. $l = 0, 1, 2\ldots$ are $s, p, d\ldots$ phase shifts

δ_l	Al		Mg		Cu	
	H^+	μ^+	H^+	μ^+	H^+	μ^+
δ_0	0·4646	0·3521	0·6968	0·5760	0·7623	0·6639
δ_1	0·1429	0·1248	0·0454	0·0281	0·1319	0·1255
δ_2	0·0660	0·0628	0·0077	0·0056	−0·0249	−0·0260
δ_3	−0·0614	−0·0619	0·0284	0·0280	0·0174	0·0172
δ_4	−0·0125	−0·0125	0·0008	0·0008	0·0137	0·0136
δ_5	0·0544	0·0545	−0·0044	−0·0044	−0·0008	−0·0009
δ_6	0·0286	0·0287	−0·0027	−0·0027	−0·0025	−0·0025
δ_7	−0·0023	−0·0023	−0·0011	−0·0011	−0·0009	−0·0009
δ_8	−0·0065	−0·0064	−0·0003	−0·0003	−0·0002	−0·0002
δ_9	−0·0030	−0·0030	0·0000	0·0000	0·0000	0·0000
δ_{10}	−0·0008	−0·0008	0·0000	0·0000	0·0000	0·0000

and $\delta n_H(r)$ are obtained. In the next step the calculations are repeated with impurity at the octahedral site by putting $n(r) = n_I(r)$, $\delta n_I(r) = n_I(r) - n_0$ in (6), (7) and (18). The self-consistently calculated $V_I(r)$ and $\delta n_I(r)$ are obtained. The differences

$$\delta V_i(r) = V_I(r) - V_H(r), \tag{19}$$

$$\delta n_i(r) = \delta n_I(r) - \delta n_H(r), \tag{20}$$

give the impurity interaction potential and impurity induced charge density respectively.

The phase shifts which satisfy (18) are tabulated in table 3 for $\underline{\mathrm{Al}}\mathrm{H}(\mu^+)$, $\underline{\mathrm{Mg}}\mathrm{H}(\mu^+)$ and $\underline{\mathrm{Cu}}\mathrm{H}(\mu^+)$. The s and p phase shifts are leading. The magnitude of higher order phase shifts is oscillatory. Their signs also change and these are slowly converging. This is due to $V_{ss}(r)$ in $V(r)$. We also calculated the phase shifts without $V_{ss}(r)$ (not shown in the table), the magnitudes of phase shifts are reduced by an order of magnitude and rapidly decreasing [5]. Therefore $V_{ss}(r)$ changes the scattering character of impurity at Fermi surface. The size effect is found to reduce the magnitudes of the phase shifts. A relative comparison shows that s phase shifts in Al, Mg and Cu are in increasing order while higher order phase shifts do not show such a trend. The phase shifts converge slowly in Al and faster in Mg and Cu. Thus scattering is more prominent in denser than in rarer electronic medium. The lattice effects are also larger in Al than in Mg and Cu.

The bound states of proton and muon are not found in any of these metals. This is in agreement with the experimental information on the μ^+ in Cu [13]. If the size effect is ignored ($Z = 1$) the shallow s type bound states of energy −0·007 a.u. and −0·0026 a.u. are found in Cu and Mg respectively. However bound state is not favoured in Al due to predominant scattering.

The impurity potentials $\delta V_i(r)$ for $\underline{\mathrm{Al}}\mathrm{H}(\mu^+)$, $\underline{\mathrm{Mg}}\mathrm{H}(\mu^+)$ and $\underline{\mathrm{Cu}}\mathrm{H}(\mu^+)$ are shown in figures 2, 3 and 4 respectively. The potentials are strongly attractive in the vicinity of the impurity and consists of Friedel oscillations at large distance. A comparison with $\delta V_i(r)$ without $V_{ss}(r)$ [5] shows that the magnitude of maxima and minima is reduced. This is essentially the lattice effect. A relative comparison shows that the magnitudes of $\delta V_i(r)$ in Al, Mg and Cu are in the increasing order. The Ashcroft

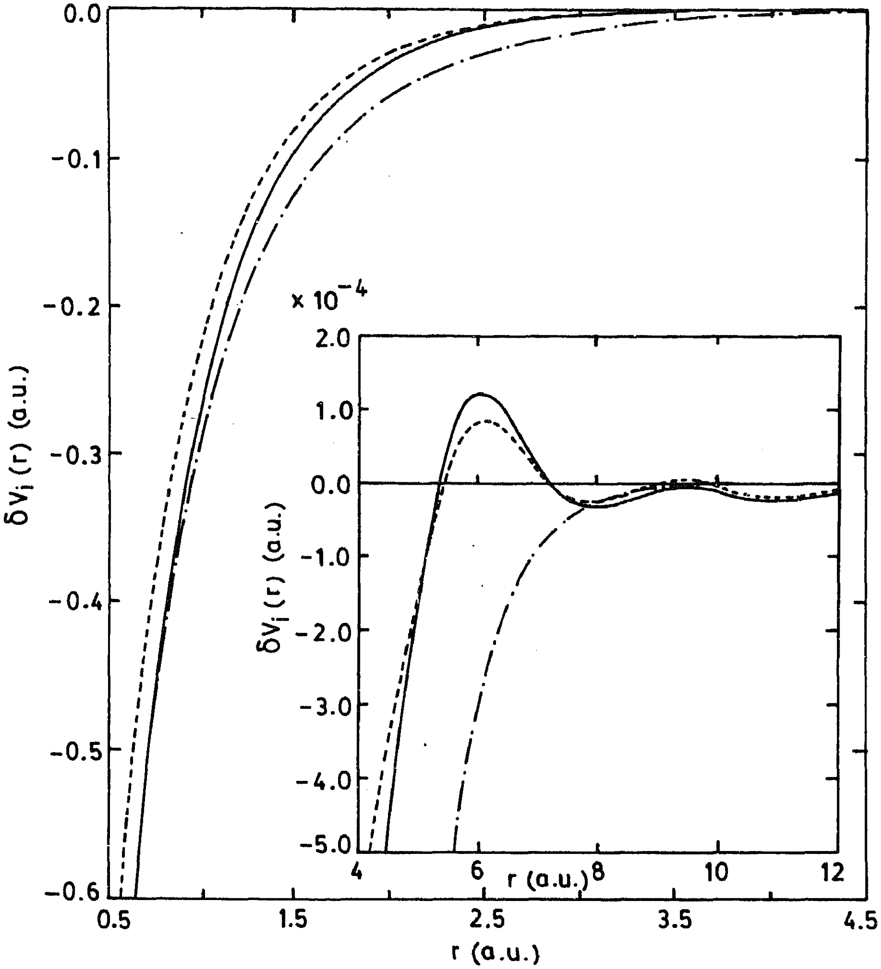

Figure 2. The proton and muon induced self-consistent potential $\delta V_i(r)$ vs r in Al. The solid line represents $\delta V_i(r)$ for proton and dashed line for μ^+. The dash-dot line shows $\delta V_i(r)$ given by equation (21) for proton.

model potential is nonunique within the radius of sphere r_c around each ion. Therefore $\delta V_i(r)$ is found very sensitive to r_c although it explicitly depends on other parameters Z, Z_H and r_s. If the Ashcroft potential is replaced by a more approriate potential $\delta V_i(r)$ will change.

Popovic *et al* [2] suggested the parametrized screened Coulomb potential i.e. $\delta V_i(r) = (-Z/r)\exp(-\alpha' r^{\beta'})$ for hydrogen in metal. α' and β' are determined by satisfying the Friedel sum rule. α' is found in general greater than unity. Sholl and Smith [14] suggested an improved one parameter potential which consists of screened Coulomb term and an exponential term i.e.

$$\delta V_i(r) = -Z\left(1 + \frac{\beta r}{2}\right)\frac{\exp(-\beta r)}{r}. \tag{21}$$

This potential is long-ranged as compared to Popovic potential and gives an exact

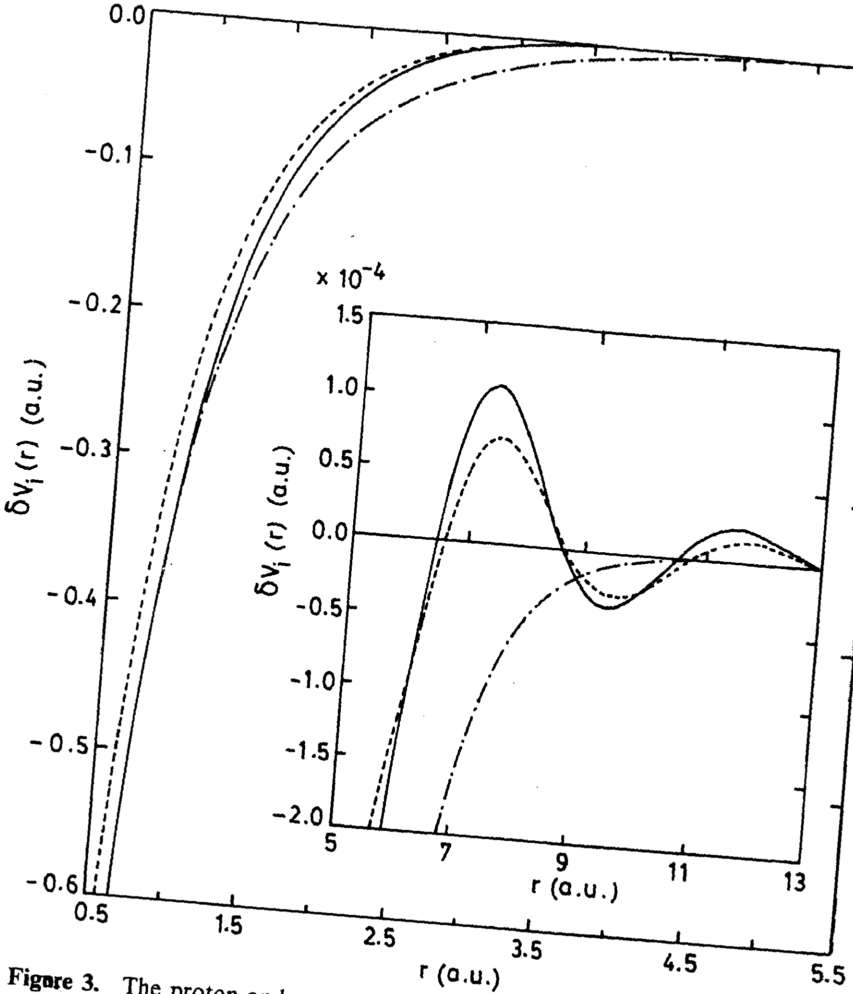

Figure 3. The proton and muon induced self-consistent potential $\delta V_i(r)$ vs r in Mg. The description is the same as that of figure 2.

solution of Poission equation for charge density i.e.

$$\delta n_i(r) = \frac{Z\beta^3}{8\pi} \exp(-\beta r), \tag{22}$$

Equations (21) and (22) are used to describe hydrogen impurity in both the electron gas and transition metals [14]. Therefore we represented our self-consistently calculated $\delta V_i(r)$ in the form of eq. (21) using the method of least square fit. The estimated values of β are given in table 1. For comparison $\delta V_i(r)$ of (21) is also shown in figures 2, 3 and 4. Equation (21) is in good agreement with the self-consistently calculated $\delta V_i(r)$ for smaller value of **r**, however at larger r (21) decreases rapidly while self-consistent $\delta V_i(r)$ is oscillatory. Therefore (21) is quite useful to investigate the short-ranged properties of the impurity.

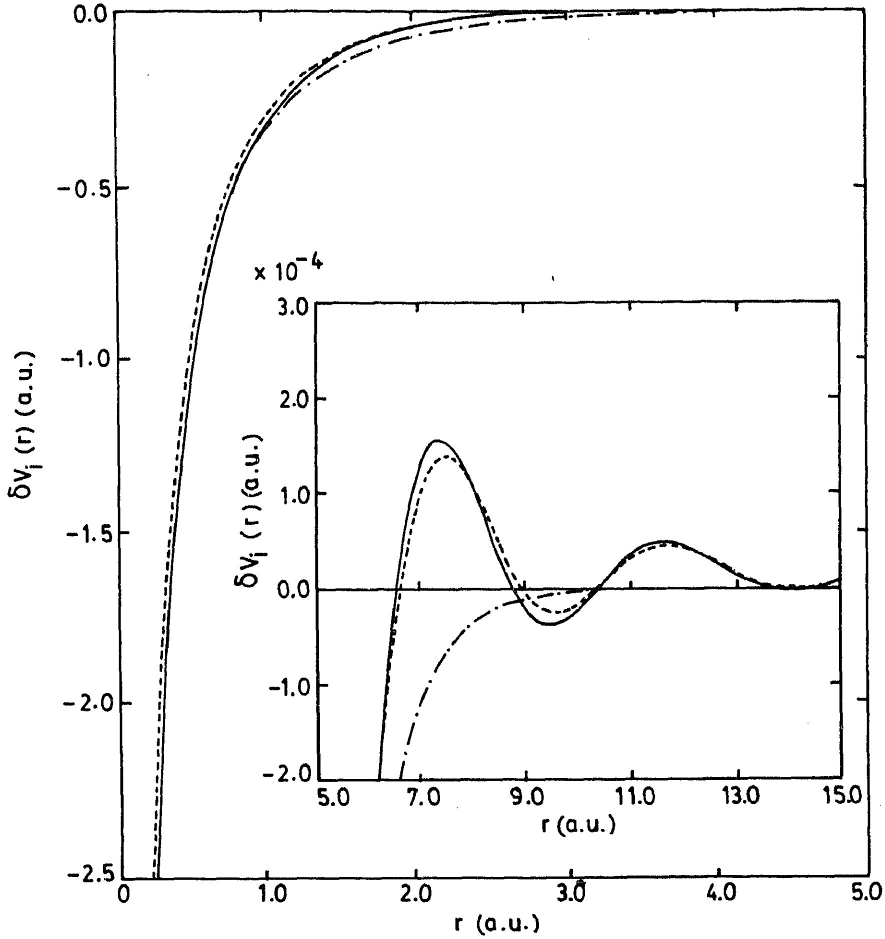

Figure 4. The proton and muon induced self-consistent potential $\delta V_i(r)$ vs r in Cu. The description is the same as that of figure 2.

3.4 *Electronic charge density and charge transfer*

The impurity induced charge density $\delta n_i(r)$ calculated using (20) in Al, Mg and Cu is shown in figures 5, 6 and 7 respectively. There is a pile up of charge on the impurity sites and it decreases rapidly with the increase of r and becomes oscillatory at large r. The charge density in the vicinity of proton is larger than in the vicinity of muon because of larger effective charge on the proton in all the metals. As compared to $\delta n_i(r)$ in jellium model [5] we found that the lattice effect and the size effect both reduce the magnitude of $\delta n_i(r)$. The positions of maxima and minima of $\delta n_i(r)$ also shift due to lattice scattering effects. The charge density given in eq. (22) is finite at the origin and is found smaller than the self-consistently calculated $\delta n_i(r)$.

Using eqs (21) and (22) the impurity induced self-energy is given as

$$
\begin{aligned}
E_s &= \frac{1}{2}\int \delta V_i(r)\delta n_i(r)\mathrm{d}r \\
&= \frac{-3}{32} Z^2 \beta. \qquad (23)
\end{aligned}
$$

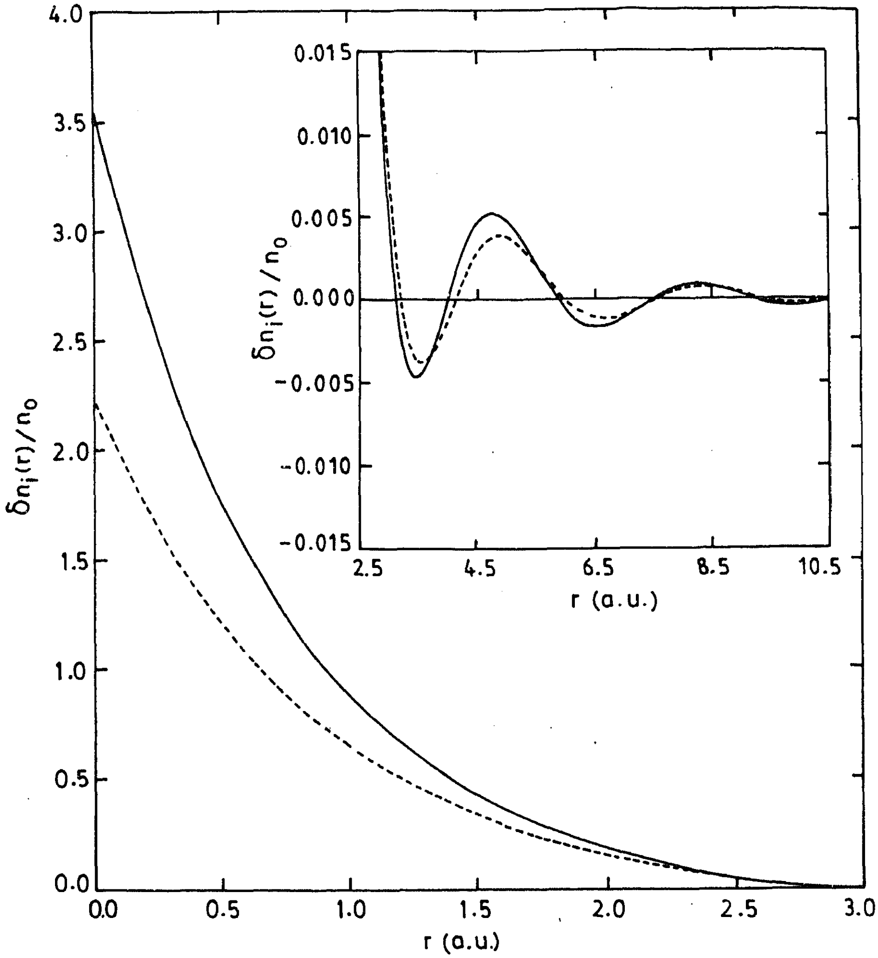

Figure 5. The proton and muon induced change in electronic charge density $\delta n_i(r)/n_0$ vs r in Al. The solid line represents the results for proton and the dashed line for muon.

The calculated E_s for $\underline{\text{Al}}\text{H}(\mu^+)$, $\underline{\text{Mg}}\text{H}(\mu^+)$ and $\underline{\text{Cu}}\text{H}(\mu^+)$ are tabulated in table 1. The self-energies of proton and muon in Al, Mg and Cu are in increasing order. This is due to the same character of $\delta V_i(r)$ and $\delta n_i(r)$ in these metals. Here E_s can be regarded as lower bound because $\delta n_i(r)$ is underestimated.

The electron charge density $\delta n_i(r)$ is integrated in the hydrogen and muon core radii (1 a.u.) and subtracted from the respective Z values. This gives the net protonic and muonic charges n_s which are also tabulated in table 1. The net charge on proton (muon) is 0·46e (0·39e), 0·45e (0·37e) and 0·54e (0·49e) in Al, Mg and Cu respectively. Thus the virtual bound states are favoured for proton and muon in these metals. The protonic and muonic charges in Cu are in agreement with the earlier calculations of Prakash [15] and Teichler [16]. Comparing with the results of Mahajan and Prakash in jellium model [5] we find that the lattice effects reduce the net charges on proton and muon due to enhanced scattering.

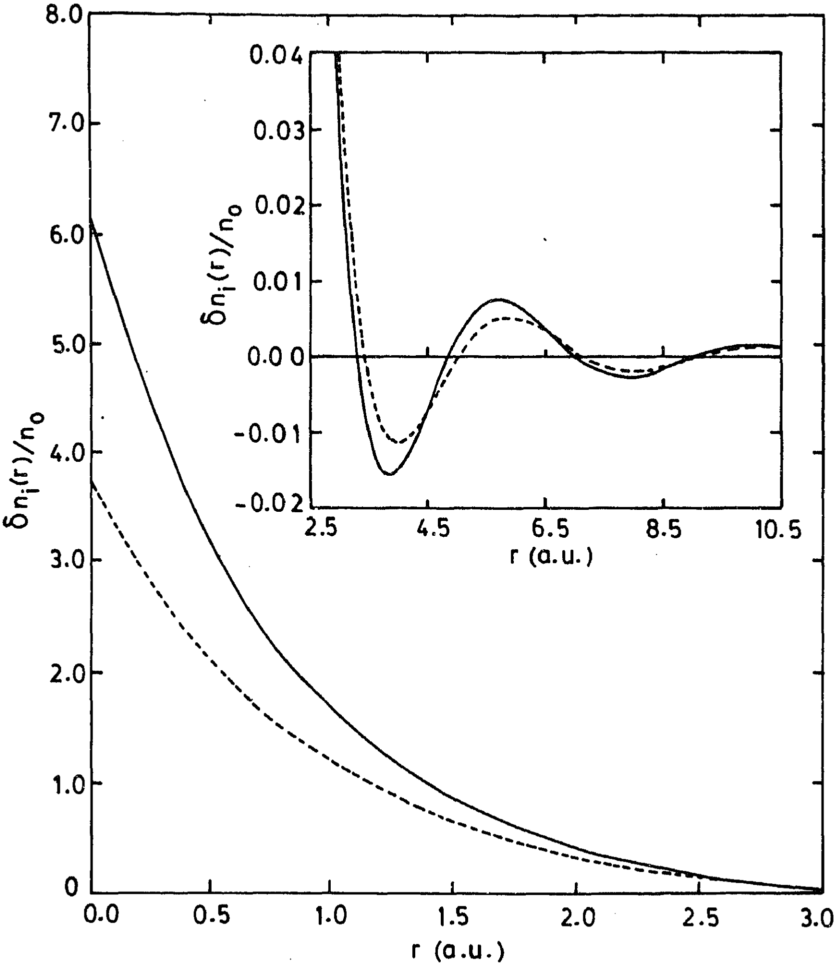

Figure 6. The proton and muon induced change in electronic charge density $\delta n_i(r)/n_0$ vs r in Mg. The description is the same as that of figure 5.

3.5 *Residual resistivity*

The residual resistivity $\Delta\rho$ for $\underline{\mathrm{Al}}\mathrm{H}(\mu^+)$, $\underline{\mathrm{Mg}}\mathrm{H}(\mu^+)$ and $\underline{\mathrm{Cu}}\mathrm{H}(\mu^+)$ is estimated using expression [1]:

$$\Delta\rho = \frac{2\cdot 732}{k_F Z_{\mathrm{H}}} \sum_{l=0}^{14} (l+1)\sin^2(\delta_l - \delta_{l+1}). \tag{24}$$

The phase shifts given in table 3 are used.

These calculated values are given in table 1. The residual resistivity for $\underline{\mathrm{Cu}}\mathrm{H}$ is in agreement with the experimental value [17]. The results for $\underline{\mathrm{Al}}\mathrm{H}(\mu^+)$ and $\underline{\mathrm{Mg}}\mathrm{H}(\mu^+)$ may be used for further investigations. The resistivity enhances from 5% to 25% if lattice effect $V_{ss}(r)$ is not included. Thus both the size and lattice effects are required to give the correct description of resistivity of these dilute metal hydrides.

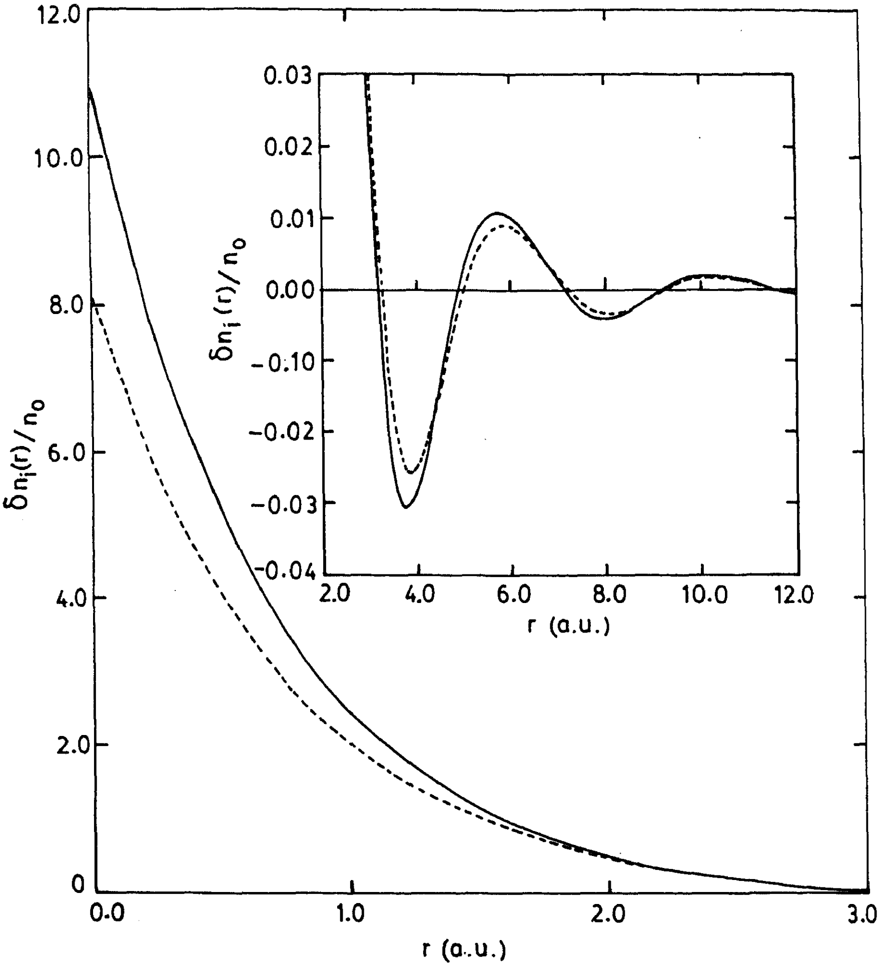

Figure 7. The proton and muon induced change in electronic charge density $\delta n_i(r)/n_0$ vs r in Cu. The description is the same as that of figure 5.

3.6 *Knight shift*

In eq. (4) $V(r)$ is spherically symmetric. Therefore, the Knight shift (the ratio between hyperfine field and the external magnetic field) can be written as the sum of three contributions i.e. [18]

$$K = K_c + K_d + K_z. \tag{25}$$

K_c is Fermi contact term and arises due to the presence of conduction electrons. K_d arises due to the diamagnetic shielding and accounts for the presence of other ions or the positive charge background. K_z is due to zero point motion of the impurity.

It is shown by Mishra *et al* [19] that K_d is smaller by an order of magnitude as compared to K_c and K_z is about 10% of K_c [18]. The proton and muon also do not have the core structure. Therefore the major contribution to K is expected from the

Fermi contact term which is given as

$$K \simeq K_c = \frac{8\pi}{3}\chi_e \frac{n_\uparrow(r) - n_\downarrow(r)}{n_{0\uparrow} - n_{0\downarrow}} \tag{26}$$

where χ_e is the electronic spin susceptibility, $n_\uparrow(r)$ and $n_\downarrow(r)$ are the spin up and spin down electronic densities at the muon site and $n_{0\uparrow}$ and $n_{0\downarrow}$ are the corresponding unperturbed background densities.

To calculate $n_\uparrow(r)$ and $n_\downarrow(r)$, eq. (3) is rewritten as

$$\left[-\frac{1}{2}\nabla^2 + V^\sigma(n,\zeta,\mathbf{r})\right]\psi_{i\sigma}(\mathbf{r}) = \varepsilon_{i\sigma}\psi_{i\sigma}(\mathbf{r}) \tag{27}$$

where the spin dependent potential

$$V^\sigma(n,\zeta,\mathbf{r}) = V_c(\mathbf{r}) + V^\sigma_{xc}(n,\zeta,\mathbf{r}) + V_{ss}(\mathbf{r}) \tag{28}$$

and the spin polarization parameters

$$\zeta(\mathbf{r}) = [n_\uparrow(\mathbf{r}) - n_\downarrow(\mathbf{r})]/[n_\uparrow(\mathbf{r}) + n_\downarrow(\mathbf{r})] \tag{29}$$

and

$$\zeta_0 = (n_{0\uparrow} - n_{0\downarrow})/n_0. \tag{30}$$

The procedure due to Manninen *et al* [4] is used for numerical solution of (27). $\zeta_0 = 0.05$ and the analytical expression for spin dependent exchange-correlation potential $V^\sigma_{xc}(n,\zeta,r)$ due to Gunnarson and Lundqvist [20] are used.

In the first iteration of the solution of (27) the spin independent $V(r)$ is used. $n_\uparrow(\mathbf{r})$ and $n_\downarrow(\mathbf{r})$ are calculated by summing over the allowed states in eq. (6) up to $E_{F\uparrow}$ and $E_{F\downarrow}$ which are determined by the relation

$$E_F\uparrow(\downarrow) = k_F^2\uparrow(\downarrow)/2 \tag{31}$$

where

$$k_{F\uparrow} = (1+\zeta_0)^{1/3}(9\pi/4)^{1/3}(1/r_s) \tag{32}$$

and $k_{F\downarrow}$ is obtained replacing $(1+\zeta_0)$ by $(1-\zeta_0)$ in (32). These values of $n_\uparrow(\mathbf{r})$ and $n_\downarrow(\mathbf{r})$ are used in (29) to determine $\zeta(r)$ and hence the $V^\sigma(n,\zeta,r)$ which is explicity used in later iterations in the self-consistent calculation. $n_\uparrow(\mathbf{r})$ and $n_\downarrow(\mathbf{r})$ are calculated separately and the Friedel sum rule is satisfied by adding the phase shifts for both the calculations i.e.

$$Z = \sum_\sigma Z^\sigma = \frac{2}{\pi}\sum_\sigma\sum_l (2l+1)\eta_l^\sigma(E_F^\sigma). \tag{33}$$

These values of $n_\uparrow(r)$ and $n_\downarrow(r)$ are used in (26). $(n_{0\uparrow} - n_{0\downarrow})$ is taken from (30) and χ_e from the tabulation of Gygax *et al* [21]. The calculated values of K_c are further enhanced by 10% for zero point motion correction. These final values of Knight shift are tabulated in table 1. The experimental values [20] are also tabulated there.

The calculated values of Knight shift are consistently lower than the experimental values. In the present calculations the size effect is included in the elastic continuum model of the lattice. If the size effect is ignored the calculated radius are 88·96, 112·42 and 92·93 (ppm) for μ^+ in Al, Mg and Cu respectively. These values are consistently higher than the experimental values. Therefore we conclude that the size effect is important in the determination of the Knight shift. The size effect is known accurately for μ^+ in Cu [11] therefore calculated K is closer to the experimental value for $\underline{\mathrm{Cu}\mu}^+$. The deviation is larger for $\underline{\mathrm{Mg}\mu}^+$ and $\underline{\mathrm{Al}\mu}^+$ as the size effect is just an extrapolated one. It is also noted that K is very sensitive to potential parameter r_c. If r_c is decreased by about 0·2 a.u., the calculated K agrees with the experimental values for Mg and Cu. A small change in r_c and size parameter can bring the calculated K in agreement with the experimental values. Such an attempt is not made in the present calculations as uncertainties are there in χ_e too and $V_{ss}(r)$ is also an approximate lattice potential.

4. Discussion

In these investigations of hydrogen and muonium in monovalent to trivalent metals the detailed electronic structure of metals is not considered. Only the spherically symmetric part of the periodic potential is included. The Fermi surface is assumed essentially spherical and conduction electron wave functions are taken as free particle like. These approximations are reasonable for Al and Mg but may not be justified for Cu as its energy band consists of narrow d-band below Fermi energy. A careful calculation by KKR-Green function method [22] may provide more information. However these involve heavy computational efforts.

The bound states and delocalized states are treated on the same footing using the same one particle potential and exchange-correlation potential. However these potentials may be different for these states. The use of different potentials may require supplementary renormalization procedure which will make the problem intractable.

In conclusion the non-linearity of screening of light impurities in simple metals is fully exploited. Although the discrete lattice and relaxation effects are included in an approximate manner, these effects alter significantly the effective charge, charge transfer, self-energy, residual resistivity and Knight shift of these impurities. The results agree with the experimental values whereever available.

Acknowledgements

The authors acknowledge financial support from the Department of Atomic Energy, Bombay. The authors are thankful to Dr S Mahajan for his help in the calculations of non-linear screening.

References

[1] J Friedel, *Philos. Mag.* **43**, 153 (1952)
[2] Z D Popovic, M J Stott, J P Carbotte and G R Piercy, *Phys. Rev.* **B13**, 590 (1976)
[3] P Jena and K S Singwi, *Phys. Rev.* **B17**, 3518 (1978)
[4] M Manninen and R M Nieminen, *J. Phys.* **F9** 1333 (1979)
[5] S Mahajan and S Prakash, *Nuovo Cimento* **2D**, 883 (1983)
[6] S Mahajan and S Prakash, *Phys. Status Solidi* (*b*) **126** 467 (1984)
[7] W Kohn and L J Sham, *Phys. Rev.* **A140**, 1133 (1965)
[8] P Vashishta and K S Singwi, *Phys. Rev.* **B6**, 8756 (1972)
[9] L Katz, M Guinàn and R J Borg, *Phys. Rev.* **B4**, 330 (1971)
[10] R A Oriani, in *Phase stability in metals and alloys,* edited by P S Rudman, J Stringer and R J Jaffe (New York) (1967)

[11] H Schilling, M Camani, F N Gygax, W Ruegg and A Schenck, *Hyperfine Int.* **8**, 675 (1981)

[12] M Manninen, R Nieminen, P Hautojärvi and J Arponen, *Phys. Rev.* **B12**, 4012 (1975)

[13] V G Grvebinnik, *JETP Lett.* **23**, 8 (1976)

[14] C A Sholl and P V Smith, *J. Phys.* **F8**, 775 (1978)

[15] S Prakash, *Phys. Rev.* **B18**, 3980 (1978);
S Prakash, J E Bonnet and P Lucasson, *Phys. Rev.* **B19**, 1976 (1979)

[16] H Teichler, *Phys. Lett.* **A67**, 313 (1978)

[17] R W Wampler and B Lengeler, *Phys. Rev.* **B15**, 4614 (1983)

[18] M Manninen, *Phys. Rev.* **B27**, 53 (1983)

[19] B Mishra, L K Das, T Sahu, G S Tripathi and P K Mishra, *Phys. Lett.* **A106**, 81 (1984)

[20] O Gunnarsson and B I Lundqvist, *Phys. Rev.* **B13**, 4274 (1976)

[21] F N Gygax, A Hinterman, W Rüegg, W A Schenck, W Studer and A J Van der wal, *J. Less Comm. Metals.* **101**, 97 (1984)

[22] J Deutz, P H Dederichs and R Zeller, *J. Phys.* **F11**, 1787 (1981)

[redacted]

PRAMANA
— journal of
physics

© Printed in India

Vol. 41, No. 3,
September 1993
pp. 257–269

Laser produced plasma: A pumping source for cadmium photo-ionization laser

REKHA TAMBAY and RAJ K THAREJA
Department of Physics and Centre for Laser Technology, Indian Institute of Technology, Kanpur 208 016 India

MS received 1 September 1992; revised 20 July 1993

Abstract. We report laser oscillations in Cd II on $4d^9 5s^2\ ^2D_{5/2} - 4d^{10} 5p^2 P_{3/2}$ transition at 441.6 nm using laser produced tungsten plasma as a pumping source. Mach Zehnder interferometer is used to measure electron density. Design and working of the crossed heat pipe used in the studies is discussed.

Keywords. Heat pipe; plasma; laser; photo-ionization; black body

PACS Nos **42.55; 52.50**

1. Introduction

The first proposal for observing population inversion in VUV and X-ray region was due to Duguay and Rentzepis [1]. The early experiments used X-ray filters to eliminate unwanted spectral components from the pumping source. Harris *et al* [2] suggested using a laser produced plasma (LPP) to excite the vapor or the gas. The scheme essentially reduces the separation between the source and the excitation region [3]. Silfvast *et al* [4], using the similar configuration, were the first to demonstrate photo-ionization laser. Since then there have been many reports [5, 6] on the observtion of population inversion using X-ray pumping. Lundberg *et al* [7] observed inversion densities in Zn^+ at 747.8 nm by photo ionizing inner *d* shell electron with a broad band soft X-ray source. Photo-ionization laser in cesium vapor in the range 665–800 nm using a single and multispot plasma has also been reported [8–10]. A 116 nm H_2 laser pumped by a travelling wave photo-ionization electron source has been reported by Benerofe *et al* [11]. Sher *et al* [12] have studied the saturation of Xe III 109 nm laser using travelling wave laser produced plasma excitation. Similar arrangement [13] has been used to study Auger pumped lasers in xenon (108.9 nm) and krypton (90.7 nm). The lasers are pumped by photo-ionization of inner shell electrons followed by Auger decay into excited states. Recently a magnesium photo-ionization laser at 24.7 nm has been proposed [14].

It is known that by focussing the laser radiation to a small area on to a solid target it is possible to create high temperature and high density plasma. Besides laser energy and wavelength the plasma characteristics depend on the physical properties of the target material. The plasma emission is primarily due to free-bound and line radiation. However, for a high *Z* solid target, the continuum emission dominates [15] over line radiation. The broadband emission in a thin layer close to the target surface can be approximated to a black body with temperature as that of the plasma. For lower intensities ($\sim 10^{10}\,\mathrm{W/cm^2}$) the temperature [16] of the plasma is given by,

$$T \approx (I\lambda^2)^{4/9}$$

while for higher intensities ($\sim 10^{13}\,\mathrm{W/cm^2}$) the temperature scales as,

$$T \approx 0.6(I\lambda^2)^{2/3}.$$

Studies on LPP of different target materials, in the intensity range 10^{11}–$10^{12}\,\mathrm{W/cm^2}$ have shown that for high Z elements the peak of the emission spectrum is shifted towards shorter wavelength [17]. Thus by choosing the target material we can match the emission spectrum with that of the photo-ionization cross section. The conversion efficiency of laser energy into photon flux in the soft X-ray region up to 50% has been reported [18]. The laser produced plasmas of a high atomic number transition element such as tungsten, tantalum etc. have been used as black body sources.

In the present work we have studied cadmium metal vapor plasma in a crossed heat pipe. The studies were done with and without a background LPP. A Nd:YAG (DCR-4G, Spectra Physics) laser and its harmonics delivering 1 J energy in 8.0 ns (FWHM) at fundamental was used for plasma production. Laser oscillations were observed in Cd II at 441.6 nm using tungsten plasma as a pumping source. Electron density was measured using a Mach Zehnder interferometer in which heat pipe formed one arm of the interferometer. The present report is organized as follows: In § 2 experimental set up and various diagnostics developed for this work are described. Section 3 contains the studies on metal vapor plasma in a heat pipe. In § 4 cadmium photo-ionization laser on $4d^9 5s^2\ {}^2D_{5/2} - 4d^{10} 5p^2 P_{3/2}$ transition at 441.6 nm is described. In § 5 we discuss various aspects of the present work.

2. Experimental techniques

Heat pipe is a well known device for producing homogeneous metallic vapors. The early experiments for generation of homogeneous metallic vapors used furnaces of different types; hot cathode diode, atomic beam devices, burner systems or other similar instruments. However, to get homogeneous temperature and density distribution, sophisticated radiation shields and heat baffles were used with most of these devices [19, 20]. Another difficulty was that of the windows. Since at high temperature many vaporized species are highly reactive, vapors were kept away from windows by means of traps. Even for nonreactive vapors, the temperature of the windows was kept higher in order to prevent vapor condensation on the windows. Either of the techniques introduces uncertainties in determining the number density of particles because of poorly defined boundary layers. This uncertainty can be reduced by using a 'heat pipe' [21]. The device has been successfully used in resonance fluorescence experiments on alkali molecules [22], harmonic generation in metal vapor gas mixture [23] and also for metal vapor lasers. However, the dynamics in a heat pipe oven cannot be worked out in a simple way, the optimum working conditions have been determined in an empirical way. It is observed that if the central part of the heat pipe is overheated the conditions are changed [24, 25].

Figure 1 shows a crossed heat pipe used for our studies. The crossed heat pipe was made using a stainless steel pipe of 2.5 cm diameter and of 2–3 mm wall thickness. The length of each arm of the pipe was 16 cm. An annular stainless steel plate with

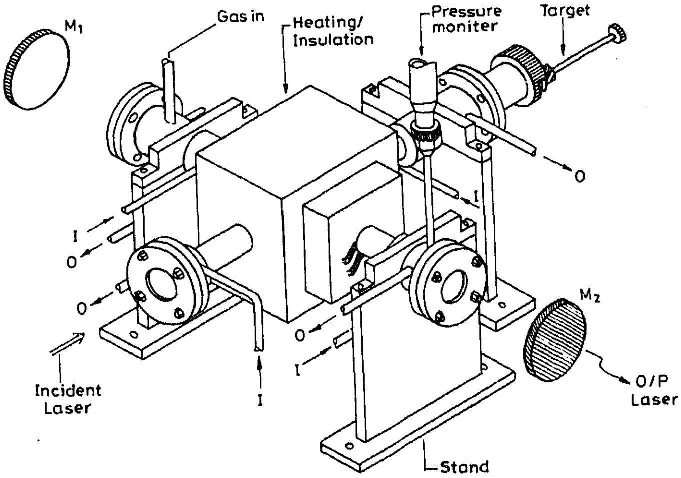

Figure 1. Design of crossed heat pipe.

O-ring groove was welded to each end of the pipe. Quartz windows were pressed on to the pipe by O-rings contained in the annular stainless steel flange plates. To avoid deposition of vapors on the windows, water jacket was provided at the ends of each of the four arms. To start with, the heat pipe was thoroughly cleaned with hydrochloric acid and acetone. Clean stainless steel mesh was rolled into layers and was inserted in the arms of the heat pipe. The heat pipe was connected to the vacuum system through copper tubing. The vacuum system consisted of a rotary pump and an oil diffusion pump giving vacuum better than 10^{-4} torr. Gas filling arrangement consisted of a He cylinder and a glass bulb which served as a reservoir. The bulb was first evacuated and then filled in with He at about 520 torr pressure. Heat pipe was evacuated to a pressure less than 10^{-4} torr, and then filled with the He gas at the desired pressure. An oil manometer was used to monitor pressure. The central zone was heated using a heating tape wrapped uniformly around the heat pipe and a fire brick structure covered the heated zone to reduce convection losses. A chromel alumel thermocouple was used to monitor temperature of the central zone. A temperature controller (Aplab, Type PTC-372) was used to control the temperature to a desired value. The temperature variation was maintained within ± 5°C. During this temperature variation the cadmium vapor pressure is nearly constant. The empty heat pipe (with mesh) was baked for several hours continuously at high temperature (about 500°C) under vacuum. Once the system was baked small pieces of pure cleaned cadmium metal were kept carefully at the center of the heat pipe. The system was then evacuated to $\leqslant 10^{-4}$ torr and then filled in with He gas at a desired pressure. The metal vapor plasma was generated by focussing Nd:YAG laser at the centre of the heat pipe. In order to study cadmium plasma in the presence of a high Z target, a tungsten target fixed to a rod was inserted into one of the arms of the heat pipe. The tungsten plasma was used as a pumping source to pump Cd vapors. To observe laser oscillations in Cd II at 441.6 nm a cavity was aligned normal to the direction of the incident (1.06 μm) laser beam. The pumping flux from the target is absorbed as it propagates through the vapor medium and hence affects the density and temperature of the vapor plasma. In order to account for the effect one needs to calculate plasma parameters viz. temperature and density.

2.1 *Temperature measurement*

The usually employed techniques to measure plasma temperature are a) Langmuir probes, b) measurement of intensity ratio of spectral lines. We have used line intensites of cadmium plasma to determine the electron temperature [26].

2.2 *Density measurement*

The electron density of a plasma is usually measured employing either the spectroscopic or an optical technique. In the former class the most widely used technique is to estimate Stark broadening of a particular transition [27]. For our present studies we have used optical technique to estimate density of the plasma. Optical diagnostics techniques are based on measuring the refractivity of a plasma by directly comparing the phase of a probe wavelength passing through the plasma with a reference. The measurement of phase shift provides us the density of electrons [28]. Studies on measurement of densities of electron and neutral atoms in a carbon plasma have been reported [29] using a two wavelength interferometry. In our studies we have used a Mach Zehnder interferometer [30] for measurement of plasma density. The experimental layout of Mach Zehnder interferometer is shown in figure 2. A $2\omega_0$ ($0.532\,\mu$m) radiation was used as a probe beam. The collimated probe was split into two beams to equal intensity at beam splitter BS_1 and were recombined at the beam splitter BS_2. The dispersive element, plasma in a heat pipe oven in our case, is kept in one arm of the interferometer and a compensating glass plate is inserted in the

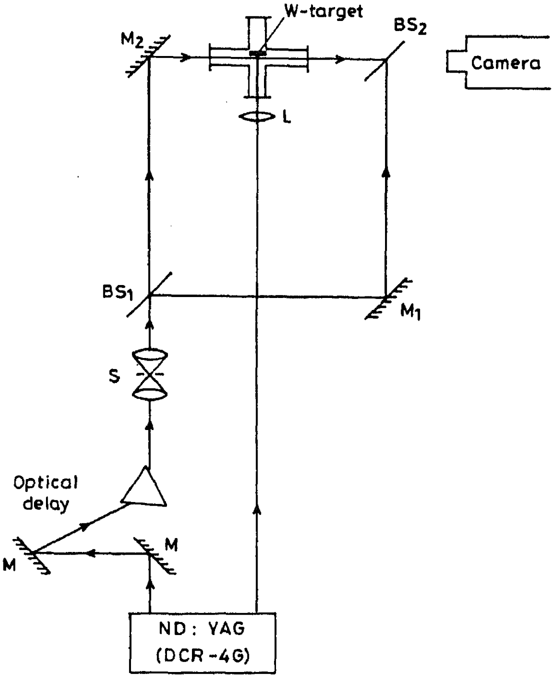
W-target
M_2
BS_2
Camera
L
BS_1
M_1
S
Optical delay
M
M
ND : YAG (DCR-4G)
M_1, M_2 - reflecting mirror; BS_1, BS_2 - beam splitter
S - spatial filter and collimator ; L - lens

Figure 2. Mach Zehnder interferometer for density measurement.

other arm of the interferometer. The phase difference between the two beams is given by,

$$\Delta\varphi = \frac{2\pi}{\lambda_p}\int_0^{r_0}(1-\mu)\mathrm{d}y \tag{1}$$

where μ is the refractive index of the plasma, λ_p the probe wavelength, and r_0 is the size of the plasma. The phase difference $\Delta\varphi$ given by (1) produces a shift in the fringes. The interferograms thus obtained are analysed using Abel inversion technique [31]. The technique is used for finding the radial dependence of a quantity $\varepsilon(r)$ e.g. refractive index, emission coefficient etc. when measurements of the line integral of $\varepsilon(r)$ are made along the chords of an axially symmetric plasma or other dielectric medium. If the measured quantity is $N(x)$ for a chord distant x from the axis we have

$$N(x) = 2\int_0^{(r_0^2 - x^2)^{1/2}} \varepsilon(r)\mathrm{d}y \tag{2}$$

$\varepsilon(r)$ is given by the Abel integral [31]

$$\varepsilon(r) = -\frac{1}{\pi}\int^{r_0} \frac{N'(x)}{(x^2 - r^2)^{1/2}}\mathrm{d}x. \tag{3}$$

The integral (3) is evaluated numerically with $N'(x) = \partial N/\partial x$ being found [32] from the experimental data $N(x)$. Following Bockasten [31] the integral can be written as a series

$$\varepsilon_j = \frac{1}{r_0}\sum_{k=0}^{n-1} a_{jk}N_k \tag{4}$$

a_{jk}'s are the Abel coefficient, r_0 is the size of the plasma and N_k is the value of $N(x)$ for which $x = \{kr_0/n\}$, n is the number of channels. A computer programme was developed to calculate the Abel coefficients and also to calculate the radial dependence of electron density. From eqs (1), (2) and (4), we have

$$n_e(r) = \frac{4\pi^2 m\varepsilon_0 c^2}{e^2\lambda_p}\frac{1}{\Delta}\varepsilon_j \tag{5}$$

where Δ is the fringe spacing. Equation (5) gives the radial dependence of electron density.

Mach Zehnder interferometer has been used for measuring densities of various atomic and ionic levels in the laser excited barium vapor [33]. A 1 μs long dye laser pulse tuned at wavelength of 553.5 nm was used to excite Ba vapor. The probe beam used for interferometric studies was a 1 ns long broad band (417–608 nm) dye laser. Interferometric studies of laser induced surface heating and deformation of metal and semiconductor have also been carried out [34]. Time resolved electron density measurements in an ArF excimer laser discharge have been reported [28] using He–N_2 laser (337.1 nm) as a probe beam. Recently density measurement of Ti atoms, in laser produced Ti vapor plasma has also been reported [35]. The plasma was produced using a YAG laser of 1.5 ns duration, and a N_2 laser (337.1 nm) of 10 ns pulse duration was used as a probe beam. Other techniques like Schliren [36] and

Shadowgraphy [37] have also been employed for density measurement. These techniques depend on deviation of the beam which is proportional to the first and second derivatives of the electron density. In these techniques no separate reference beam is used; the intensity variations arise by virtue of local intensification of the probe beam due to refraction. Such systems are easy to align compared to interferometers but the analysis of the results is difficult.

3. Studies on cadmium metal vapor plasma

In this section studies on cadmium metal vapor plasma in the presence of a high Z LPP are presented. The laser beam from a Nd:YAG laser was focussed at the center of the heat pipe using a quartz lens. The temperature was slowly raised to 450°C with He gas pressure of 7 torr, no cadmium plasma was observed visually. However, when the buffer gas pressure was increased to 52 torr and the temperature kept at 400°C a weak cadmium plasma was observed. Increasing temperature further at the same buffer gas pressure increased the intensity of the plasma. An intense green ball of cadmium plasma could be seen on viewing through one of the side arms when the heat pipe was operated at 500°C. Figure 4 shows a Cd spectrum at temperature of 500°C and He pressure of 77 torr, recorded using a monochromator set up shown in figure 3. The laser energy was 900 mJ in 8 ns pulse. An estimate of the temperature of metal vapor plasma was made by taking ratio of the intensities of the spectral lines. The observed temperature is 0.5 eV. It was also observed that on increasing the temperature of the heat pipe beyond 500°C the intensity of the green blob decreased. This may be due to particulate formation [25, 38] the so-called 'fogging' in the heat pipe. To confirm and visually observe the formation of clusters, a weak He–Ne laser beam was sent close to the centre of the heat pipe. The pattern in transmitted laser beam was observed on a wall, about 4 m away from the heat pipe.

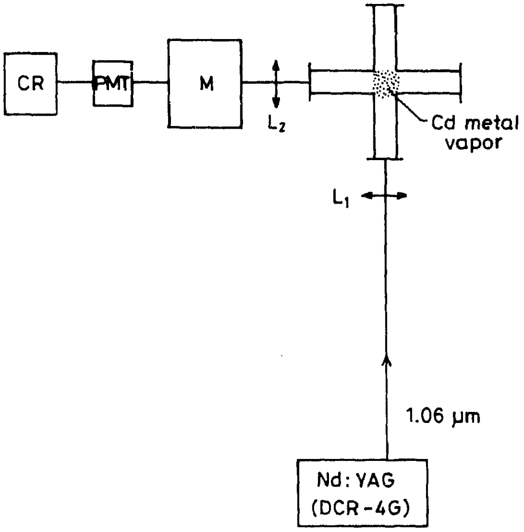

L_1, L_2 - Lenses; M - Monochromator; CR - Chart recorder; PMT - Photomultiplier tube

Figure 3. Experimental set-up for recording plasma emmision.

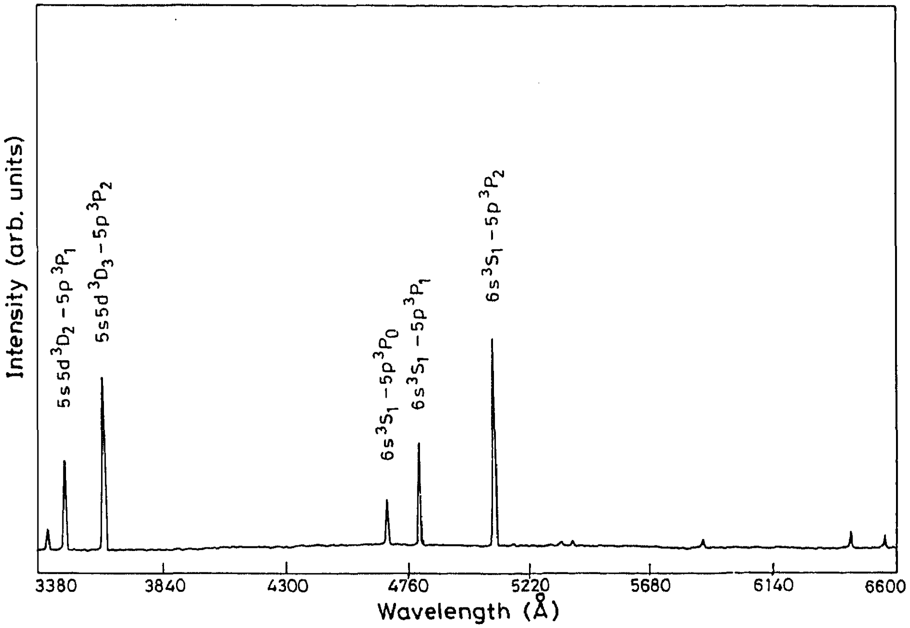

Figure 4. Visible spectrum of Cd metal vapor plasma at a He pressure of 77 torr.

The convective movement of the dust-like particles was clearly visible in the beam. We feel that this particulate formation is due to cadmium clusters created by condensation of the metal vapors in the cold zone at the boundary with the buffer gas. Similar effect was also observed if the central part of the heat pipe was suddenly overheated. Thus the poor conditions of operation for the heat pipe, result in cluster formation of the metal. Obtaining a high Cd density required for efficient plasma production appears to be the most difficult technical problem in the experiments, such as ours. Our experience shows that the temperature of the heat pipe should be increased very slowly and should not exceed the value at which the vapor pressure of the metal vapor and buffer gas pressure are equal [24].

In order to look at the possibility of using laser produced plasma as a pumping source for photo-ionization Cd^+ laser oscillating at 441.6 nm, a tungsten target fixed to a rod was inserted into one of the arms of the heat pipe opposite to the direction of the incident laser beam. The target rod was continuously rotated by an electric motor to avoid crater formation. The laser radiation was focussed to a spot of 100 μm onto the tungsten target with helium gas at a pressure of 7 torr. No heating of the heat pipe was done. A bluish white plasma of tungsten was visually seen at the target surface. The density of the laser produced tungsten plasma was estimated using a Mach Zehnder interferometer as described earlier in § 2.2. Figure 5 shows the radial density distribution of tungsten plasma at a distance of 1–2 mm from the target. The delay between the 1.06 μm beam and the probe beam was 19 ns. This was the optimum value of the delay. For lower values the plasma expansion was very fast and the fringes close to the target were quickly merged, while for higher value of delays the shift was very small.

In order to photo-ionize the cadmium metal vapor, the heat pipe temperature was raised to 420°C with a He pressure of 7 torr and the laser radiation was focussed onto the tungsten target. We observe a bluish white plasma very close to the target

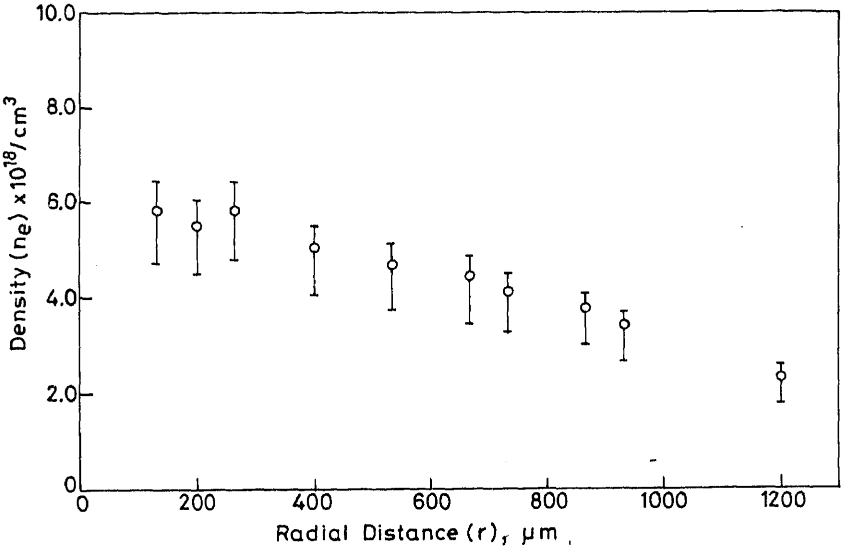

Figure 5. Radial density profile of tungsten plasma at 1–2 mm distance from the target.

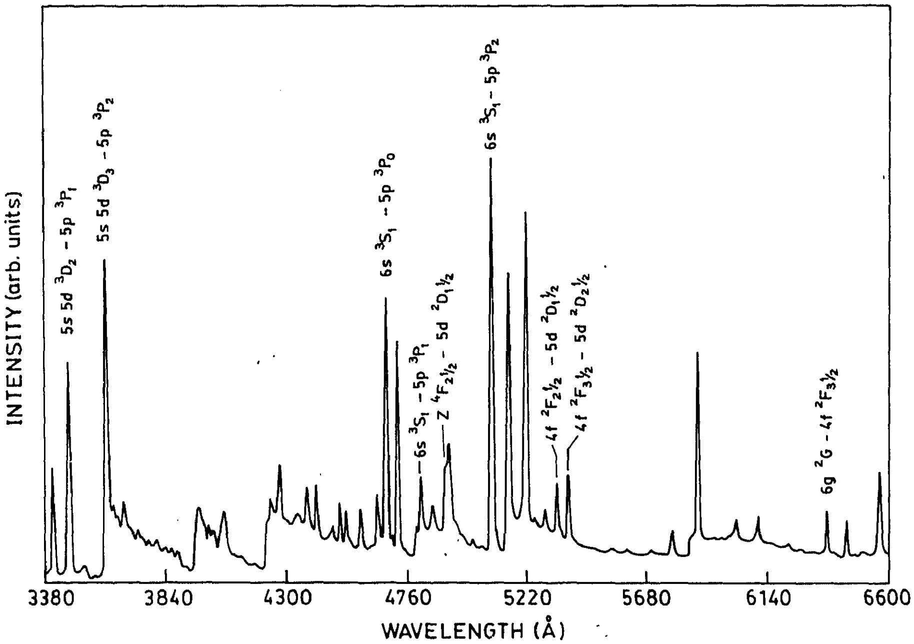

Figure 6. Visible spectrum of Cd metal vapor in the presence of tungsten plasma.

surface and green plasma due to cadmium vapor extending up to 8 mm away from the tungsten surface. The Cd emission spectrum shown in figure 6, recorded in the presence of tungsten target shows an increase in intensity of all lines and Cd II lines which were absent in figure 4 are also observed. Thus laser produced plasma can be a very effective source for getting higher ionic states. We estimate temperature of Cd plasma at 4 mm away from the surface of the target to be 0.3 eV.

4. Laser oscillations

Here we describe the laser oscillations on $4d^9 5s^2\ {}^2D_{5/2} - 4d^{10} 5p\ {}^2P_{3/2}$ transition at 441.6 nm using tungsten plasma as a pumping source. The population inversion occurs between the $4d^9 5s^2$ state and $4d^{10} 5p$ state. As said earlier, for high Z target continuum radiation dominates over the line radiation. The broad band soft X-ray emission from a laser produced plasma directly populates the upper laser level from the ground level. The pumping rate is essentially determined by the photon density of the pumping source. The fact that at short wavelength, inner-shell photo-ionization has a higher probability than ionization of a outer electron, the most probable process with the radiation peaked in the range 200–300 Å for high Z target is photo-ionization. The experimental set-up used by us for observing laser oscillations in Cd at 441.6 nm is shown in figure 7. A crossed heat pipe described in § 2 was used to produce homogeneous vapors of cadmium. The heat pipe was operated at 420°C with helium pressure of 7 torr. The cavity was formed using two He–Cd mirrors such that $g_1 g_2 \approx 0.65$. One of the mirrors was totally reflecting while the other had about 1% transmission at 441.6 nm, through which the laser output was monitored. The ends of the heat pipe along the axis of the resonator were fitted with windows set at Brewster angle. The optical axis of the resonator was parallel to the target (tungsten) surface. The output signal was sensitive to the alignment of the resonator axis, with a slight movement of either mirrors the stimulated emission fell to a very low value. The output was detected through a monochromator (HRS-2 Jobin-Yvon) using a photomultiplier tube (IP28, Hamamatsu, rise time 2.2 ns). To see the effect of the input laser energy (Nd:YAG) on the output of Cd II laser at 441.6 nm, experiment was performed at 100, 200 and 300 mJ of input energy. Figure 8 shows the variation of laser output with input laser (1.06 μm) energy. Because of target etching at high input energies we were not able to go beyond 300 mJ of input energy but it is expected that the laser output will increase with input energy. Although we observed laser oscillations close to the target surface, the optimum position of the resonator axis was found to be 4 mm away and parallel to the target surface. Since very close to the target surface the pumping flux is high, one expects high inversion densities but electron collisions depopulate the upper laser level. At larger distances the output is decreased due to the reduced pumping flux from the diverging X-rays. The coupling efficiency of the pumping flux and the lasing plasma depends on the configuration used for photo-ionizing source and metal vapor plasma. The emission from the laser

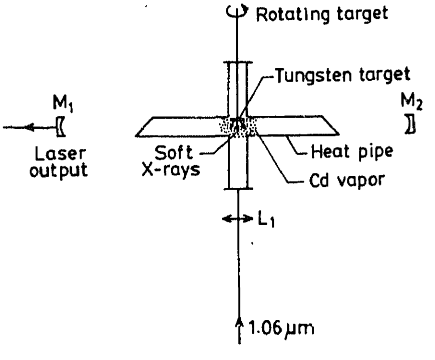

Figure 7. Experimental set-up for observing laser oscillations.

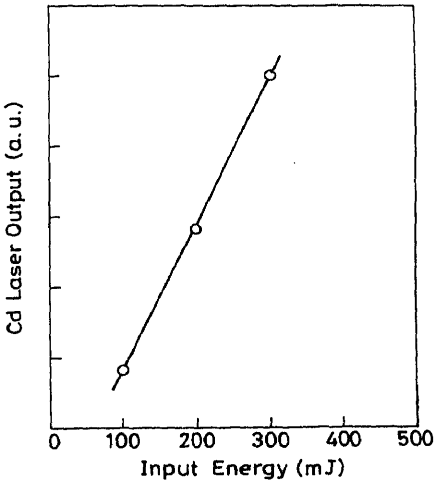

Figure 8. Variation of laser output with input laser (1·06 μm) energy.

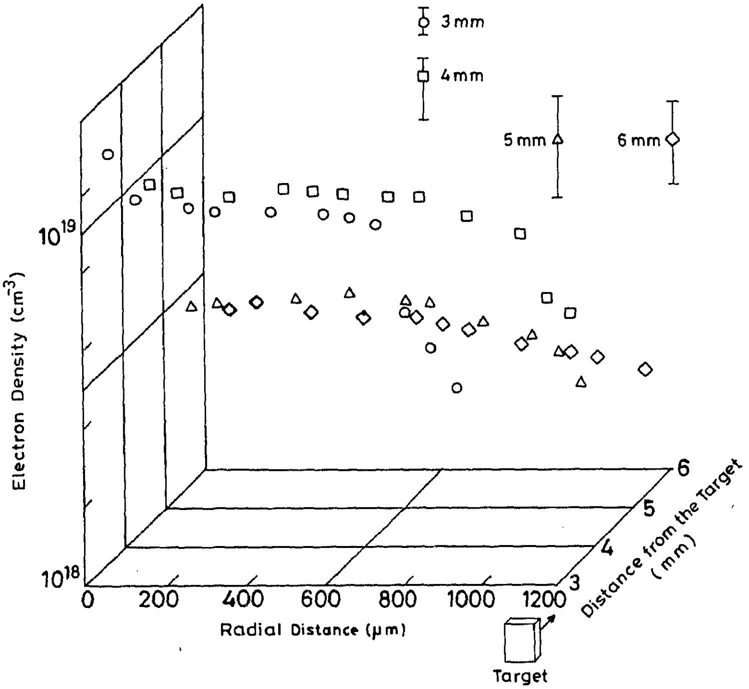

Figure 9. Radial density profiles of Cd plasma in the presence of tungsten target.

produced plasma source is absorbed as it propagates through the vapor medium and hence in our case affects the density and temperature of the medium. Thus the coupling between the background plasma and that of Cd plasma affects the pumping rate for a photo-ionization process. Figure 9 shows the radial profiles of electron density of cadmium plasma (in the presence of tungsten plasma) measured using the set-up shown in figure 2 at various distances from the target surface. The axial density can be obtained from the radial profiles and hence the effect of the density on the varying gain can be estimated. The high electron density observed close to the target surface shows the effect of plasma electrons. The influence of these electrons decreases as we move away from the target surface because for the given vapor pressure and within the excitation time these electrons penetrate only 2–3 mm into the vapor.

5.

Since our interest is in Cd II transitions, it is worthwhile to consider the possible routes for a Cd II transition at 441.6 nm (in particular). Although the process of inner-shell photo-ionization is dominant, one should also look at the effect of photoelectrons which are immediately present after photo-ionization. The energy distribution of the photoelectrons has a maxima around 40 eV and is determined by the photon energy distribution and wavelength dependence of the photo-ionization cross-section. If we compare the cross-sections [39, 40] for various levels of Cd we find that the cross-section for $5s^2$ levels are larger than $5p$ states in the region above 50 eV. Thus using a black body peaked in the range 200–300 Å one would expect that $5s^{2\,2}D$ states are formed almost exclusively by removal of innershell electron while the ordinary $5p$, $5d$, $6p$ states are formed by ionization of one electron and excitation of another electron.

Population inversion in photo-ionization lasers can be produced either by directly pumping the upper laser level or transferring population from a nearby directly pumped level to the upper laser level. It has been shown that the latter is less efficient possibly due to broadening of the laser transition during the transfer process [41]. Population inversion is also possible from states that are pumped by photo-ionization to lower lying bound or autoionizing states. The lower laser level being ground state of an ion. For such an inversion to occur the duration of the pumping source should be small so that efficient inversion is produced before electrons collide with neutral species and ionize them to produce ion ground state. The pumping rate depends on the density of photon from a laser produced plasma source interacting with metal vapor and σ_{pi} the photo-ionization cross-section to the upper laser level. The population of the upper level related to the ground state population can be written as

$$N_u = \frac{2W_p\sigma_{\mathrm{pi}}\exp(-\sigma_t Nr)\tau_P N}{h\nu_p \pi r^2} k_f \tag{6}$$

where W_p is the pumping power, N is the ground state population of the metal vapor and σ_t is the total absorption cross-section in the wavelength region that pumps the upper laser level. τ_P is the duration of the pumping X-ray pulse and is of same duration as that of the laser pulse used for creating soft X-rays, and k_f is the conversion efficiency of the incident flux into soft X-ray flux. It follows from (6) that for larger population of the upper state, the photon density N_ν should be large and the distance between active medium and the pumping source should be small. The gain length product GL can be written as

$$\mathrm{GL} \simeq N_u \sigma_{\mathrm{se}} L \tag{7}$$

where N_u is the population density of the upper level and, σ_{se} is the stimulated emission cross-section for the lasing wavelength (441.6 nm), L is the length of the gain medium. Using the values of various parameters and assuming $k_f \approx 1\%$, we get $\mathrm{GL} \sim 11$. The value of GL apart from other parameters depends on conversion efficiency k_f which depends on configuration, focussing condition, pulse width and wave-length of laser used for generation of photo-ionization source. The GL product can also be increased using a line pumping source. We have used single spherical plasma spot in our studies, however, using multifoci geometry to generate a multispot plasma one can increase total gain length.

In conclusion we studied the Cd metal vapor plasma in a crossed heat pipe. To study the effect of black body pumping, Cd metal plasma was studied in the presence of tungsten plasma. Laser oscillations were observed in Cd II on $4d^9 5s^2\ {}^2D_{5/2} - 4d^{10} 5p\ {}^2P_{3/2}$ transition at 441.6 nm using photo-ionization pumping scheme. The electron density was estimated using a Mach Zehnder interferometer.

Acknowledgement

This work is supported by the Department of Science and Technology, New Delhi.

References

[1] M A Duguay and P M Rentzepis, *Appl. Phys. Lett.* **10**, 350 (1967)

[2] S E Harris, J R Young, R W Falcone, J E Rothernberg, J R Willison and J C Wang in *Laser techniques for extreme ultraviolet spectroscopy*; edited by T J Mcllrath and R R Freeman (AIP, New York, 1982) p 147

[3] H W K Tom and O R Wood II, *Appl. Phys. Lett.* **54**, 517 (1989)

[4] W T Silfvast, J J Macklin and O R Wood II, *Opt. Lett.* **8**, 551 (1983)

[5] A J Mendelsohn and S E Harris, *Opt. Lett.* **10**, 128 (1985)

[6] W T Silfvast and O R Wood II, *J. Opt. Soc. Am.* **B4**, 609 (1987)

[7] H Lundberg, J J Macklin, W T Silfvast and O R Wood II, *Appl. Phys. Lett.* **45**, 335 (1984)

[8] M Hube, M Dieckmann, H Welling and B Wellegehausen, *J. Opt. Soc. Am.* **B6**, 1217 (1989)

[9] M Hube, R Brinkman, H Welling, R Beigang and B Wellegehausan, *Appl. Phys.* **B45**, 197 (1988)

[10] M Hube, J Michael and B Wellegehausen, *Opt. Lett.* **15**, 480 (1990)

[11] S J Benerofe, Yu Vin Guang, C P J Barty, J F Young, and S E Harris, *Phys. Rev. Lett.* **66**, 3136 (1991)

[12] M H Sher, J J Macklin, J F Young, and S E Harris, *Opt. Lett.* **12**, 891 (1987)

[13] H C Kapteyn and R W Falcone, *Phys. Rev.* **A37**, 2033 (1988)

[14] A M Weigold and J A Piper, *Opt. Lett.* **15**, 1209 (1990)

[15] O Sullivan, *J. Phys.* **B16**, 3291 (1983)

[16] T P Hughes, *Plasma and laser light* (Wiley, New York, 1975)

[17] J M Bridges, C L Cromer and T J Mcllrath, *Appl. Opt.* **25**, 2208 (1986)

[18] M D Rosen, D W Phillion, V C Rupert, W C Mead, W L Kruer, J J Thomson, H N Kornblum, V N Silvinsky, G J Caporaso, M J Boyle and K G Tirsell, *Phys. Fluids.* **22**, 2020 (1979)

[19] W R S Garton, K Codling, *Proc. Phys. Soc.* (*London*) **75**, 87 (1960)

[20] F S Tomkins and B Ercoli, *Appl. Opt.* **6**, 1299 (1967)

[21] G M Grover, T P Cotter and G F Erickson, *J. Appl. Phys.* **35**, 1990 (1964)

[22] C R Vidal, *J. Appl. Phys.* **44**, 2232 (1973)

[23] H Scheingraber and C R Vidal, *Rev. Sci. Instrum.* **52**, 1010 (1981)

[24] R Tambay, *Cadmium photo-ionization laser* Ph.D. Thesis, IIT Kanpur (1991)

[25] W Gawlik and R Neumann, *Opt. Commun.* **68**, 345 (1988)

[26] A Khare, V Kumar and R K Thareja, *Z Phys.* **D6**, 67 (1987)

[27] R Tambay, R Singh and R K Thareja, *J. Appl. Phys.* **72**, 1197 (1992)

[28] T Mochizuki, K Hirata, H Ninomiya, K Nakamura, K Maeda, S Horiguchi and Y Fujiwara, *Opt. Commun.* **72**, 30 (1989)

[29] C D David Jr, *Appl. Phys. Lett.* **11**, 394 (1967)

[30] W C Marlow, *Appl. Opt.* **6**, 1715 (1967)
[31] K Bockasten, *J. Opt. Soc. Am.* **51**, 943 (1961)
[32] R Illingworth and R K Thareja, *J. Phys.* **E14** 147 (1981)
[33] L Jahreiss and M C E Huber, *Phys. Rev.* **A28**, 3382 (1983)
[34] W K Lee and C C Davis, *IEEE J. Quantum Electron QE* **22** 3382 (1986)
[35] H Ninomiya, N Takashima and K Hirata, *J. Appl. Phys.* **69**, 67 (1991)
[36] T J Englert and M A Beik, *Rev. Sci. Instrum.* **61**, 3783 (1990)
[37] I H Hutchinson in *Principles of plasma diagnostics* (Cambridge University Press, 1987)
[38] M Allegrini, P Biechi, D Dattrino and L Moi, *Opt. Commun.* **49**, 39 (1984)
[39] T Goto, K Hane, M O Kuda and S Hattori, *Phys. Rev.* **A27**, 1844 (1983)
[40] W Lotz, *Z. Phys.* **220**, 466 1969
[41] W T Silfvast, O R Wood II, H Lundberg and J J Macklin, *Opt. Lett.* **10**, 122 (1985)

PRAMANA
— journal of
physics

© Printed in India

Vol. 41, No. 3,
September 1993
pp. 271–283

A translational energy spectrometer to probe interatomic potentials: Dissociation dynamics of CO_2^+ ions

M KRISHNAMURTHY, U T RAHEJA and D MATHUR
Atomic and Molecular Sciences Laboratory, Tata Institute of Fundamental Research, Homi Bhabha Road, Bombay 400 005, India

MS received 28 April 1993

Abstract. A new ion translational energy spectrometer has been developed to carry out low-energy, gas-phase ion-molecule collision experiments which aim to probe molecular potential energy surfaces. The collisional technique employed relates small changes in the kinetic energy of a projectile ion after it has undergone collision with a static neutral atom/molecule to changes in the overall potential energy of the collision system; information can be furnished about the interaction potential between the projectile and the target. First measurements are reported of a high resolution target excitation spectrum obtained in 1.8 keV collisions of H_2^+ ions with N_2. New results pertaining to collision-induced dissociation of CO_2^+ ions are presented and discussed in terms of potential functions of low-lying electronic states of the molecular ion.

Keywords. Ion-molecule collisions; translational energy spectrometer; dissociation; energy loss spectra.

PACS Nos 35·80; 34·50

1. Introduction

Quantitative insight into interatomic potentials which govern the dynamics of chemical transformation processes continues to elude physicists and chemists. Despite many far-reaching strides that have been made in development of experimental techniques in the course of the last decade, an active need continues to be felt to develop new methodologies for investigating the *dynamical* aspects of chemical transformation processes on a microscopic level, *collision by collision*. Ion translational energy spectrometry (TES) is an example of one such recent development. TES is a gas-phase collisional technique in which analysis of the changes in the kinetic energy of a projectile ion which has undergone collision with a neutral target atom or molecule furnishes information about the interaction potential between the projectile and the target. When the projectile is a charged species, ion-neutral reactions can be investigated whose dynamics are dominated by interactions which occur at large internuclear distances. In other words, only the long-range part of the overall potential energy surface on which a given reaction occurs need be considered in concomitant theoretical studies. This provides a distinct advantage insofar as quantitative understanding of reaction dynamics needs theoretical information of only a subset of the entire complex interatomic potential surface; conversely, experimental results forthcoming from TES measurements of ion-neutral reaction phenomena provide a stringent test of the effectiveness of contemporary quantal techniques of generating molecular potential energy surfaces.

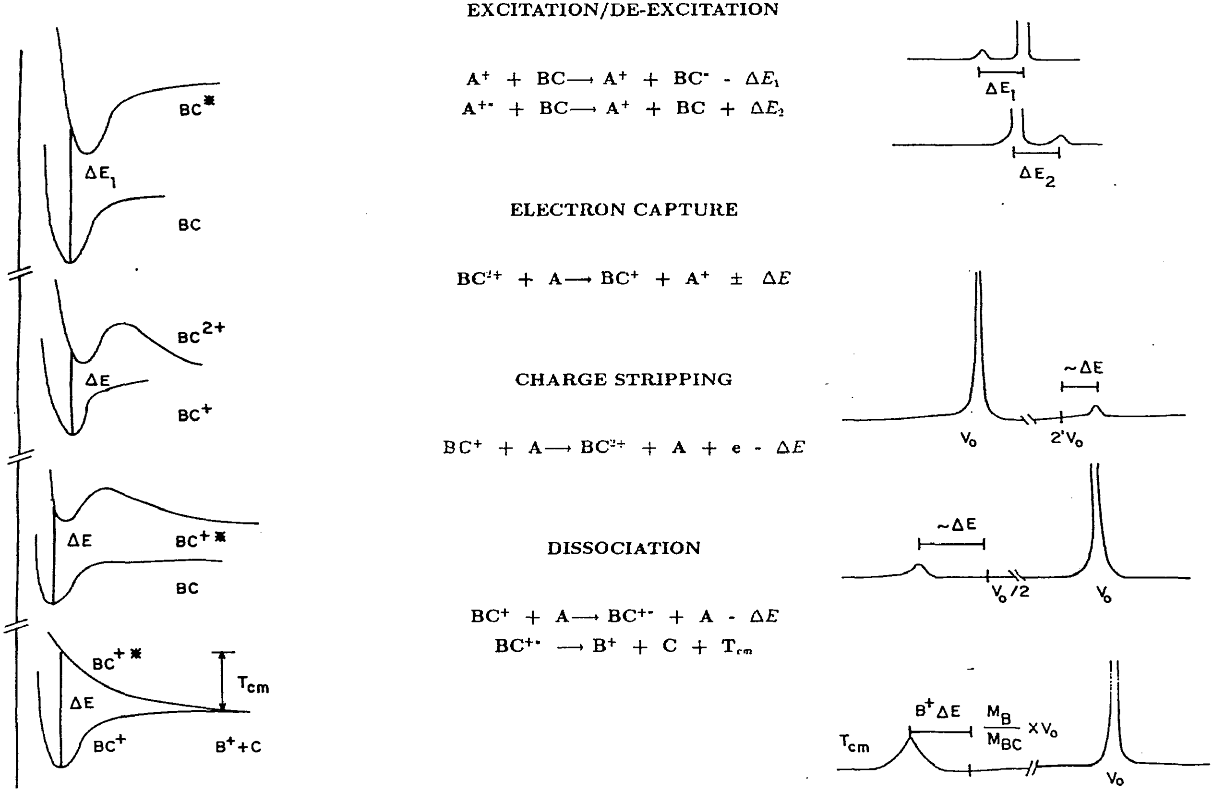

EXCITATION/DE-EXCITATION

$A^+ + BC \longrightarrow A^+ + BC^* - \Delta E_1$

$A^{+*} + BC \longrightarrow A^+ + BC + \Delta E_2$

ELECTRON CAPTURE

$BC^{2+} + A \longrightarrow BC^+ + A^+ \pm \Delta E$

CHARGE STRIPPING

$BC^+ + A \longrightarrow BC^{2+} + A + e - \Delta E$

DISSOCIATION

$BC^+ + A \longrightarrow BC^{+*} + A - \Delta E$

$BC^{+*} \longrightarrow B^+ + C + T_{cm}$

Figure 1. A summary of different ion-neutral collision processes that are assessible to translational energy spectrometry. The relationship of each collision process to transitions between different molecular potential energy curves is illustrated on the left side of the figure; the right side is a schematic representation of how each transition would manifest itself in the ion translation energy spectrum (V_0 represents the elastically scattered ion peak in all cases, and ΔE is the energy defect associated with each process.)

We describe here the development of a new, high-sensitivity, high-resolution, multi-sector ion translational energy spectrometer which is used to carry out experimental studies of atomic collision processes, particularly those involving low-energy, single collisions between gas-phase positive ions and neutral atoms or molecules. An entire gamut of reaction dynamics can be studied using our apparatus (see refs. [1, 2] for recent reviews of the application of the TES technique to experimental studies of molecular structure and dynamics). Figure 1 illustrates processes leading to single and multiple electron capture, charge stripping and dissociation; these provide examples of ion-neutral reactions which occur readily at large internuclear separations of reactant species and which are amenable to interpretation in terms of molecular potential energy functions which can be computed using contemporary ab initio molecular orbital techniques.

We present below details of our TES apparatus as well as new results on the dynamics of collision-induced dissociation of CO_2^+ ions. Apart from its significance to atmospheric chemistry and laser plasma physics, dissociation of CO_2^+ ions, leading to formation of $O^+ + CO$ or $CO^+ + O$ fragments, is of fundamental importance. The former fragmentation channel would be expected to be energetically favoured. However, our results indicate that the signal corresponding to the $CO^+ + O$ channel is several factors larger in intensity than the $O^+ + CO$ channel. Furthermore, contemporary quantum-mechanical wisdom does not permit the formation of either of the two fragment channels by direct dissociation of low-lying bound $X^2\Pi_g$, $A^2\Pi_u$ or $B^2\Sigma_u^+$ electronic states of CO_2^+ since the respective dissociation continua cannot be accessed via vertical, Franck–Condon transitions from the ground electronic state of CO_2. We interpret our results in terms of a curve-crossing picture involving excited electronic states of CO_2^+ in which the apparent suppression of the lowest-energy pathway to dissociation is accounted for.

2. Translational energy spectrometer

TES involves the determination of the energetics of a single collision reaction between a projectile ion and a target atom or molecule. When a monoenergetic beam of mass-selected projectile ions interacts with the neutral target, the energy balance of the reaction manifests itself as changes in the translational energy of the projectile ions under kinematic conditions of fast collision and forward scattering (large impact parameter collisions with nearly zero momentum transfer). The technique, therefore, requires formation of a monoenergetic beam of the appropriate ionic species and known translational energy, its interaction with a neutral gas target under conditions which ensure that only a single collision occurs (ultra high vacuum conditions leading to mean-free-paths which are very much larger than the dimensions of the apparatus). The post-collision translational energy has to be measured at zero degrees scattering angle with an adequate energy resolution. A schematic diagram of our TES apparatus which incorporates all these requirements is shown in figure 2.

The projectile ions in our apparatus are produced in a low pressure (*ca.* 10^{-6} torr) ion source with electrons of 70–100 eV energy. The ions formed in a field-free region are extracted by an electrostatic potential of 1·5–5 kV and focussed into a fine pencil beam by a three-element cylindrical einzel lens system. This beam then enters a region of crossed electric and magnetic fields (Wien filter), where momentum selection occurs. A suitable m/q of particles may be selected by suitably balancing the forces due to electric and magnetic fields in opposite directions. Mass selected ions are then energy

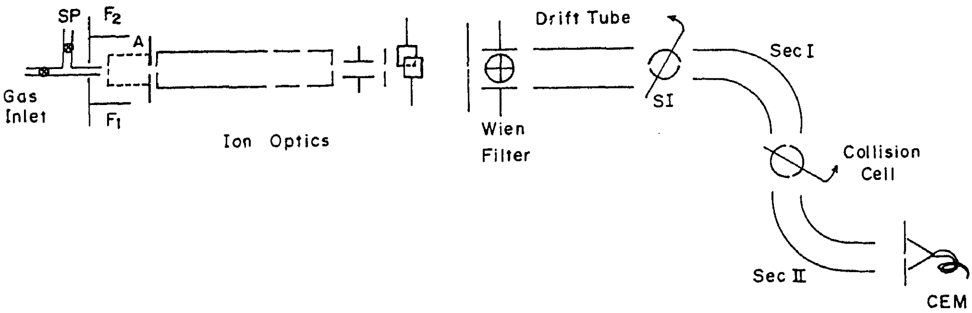

Figure 2. Schematic diagram of the ion translational energy spectrometer. $F_{1,2}$ and A are the two tungsten filaments and anode, respectively, which comprise the electron impact ion source; SI defines the entry slit into the first electrostatic energy analyser (Sec I); the rotating collision cell provides a continuously adjustable slit which acts as the entrance to the second energy analyser (Sec II); CEM is the channel electron multiplier detector. Details of the mechanical design of individual components are available from the authors.

monochromatized by a 90° cylindrical sector electrostatic analyser of mean radius 55 cm. The monoenergetic ions are then made to interact with a neutral gas target in a collision cell maintained at about 5×10^{-6} torr with gas load. The product ions formed in the projectile beam are energy analysed by a second, identical 90° electrostatic analyser. Ion detection is by a channel electron multiplier operating in the particle counting mode, coupled to conventional pulse counting electronics and a computerised data acquisition system. The overall background pressure in the apparatus is maintained in the 1×10^{-7} torr region; differential pumping is achieved by means of four oil diffusion pumps and one ion pump.

The sizes of the entry and the exit slits of the 90° cylindrical sector electrostatic analyser determine the energy resolution that can be obtained. We have designed variable width slits, whose widths can be varied on-line from 0 mm to about 1 mm. Taken together with the large radius of our energy analysers, our instrument is capable of energy resolving powers in excess of 2×10^4 in the laboratory frame. In the case of dissociation studies of the type reported below, the effective resolving power obtainable in the centre-of-mass frame is several orders of magnitude larger. Indeed, the TES technique has been utilized by us to study rotational resonances in ion-molecule collisions using another, lower-resolution apparatus in our laboratory [3, 4].

The total distance that an ion traverses from the ion source to the detector in the apparatus is of the order of 3 m.

2.1 *Ion injection system*

Electrons from a peripherally positioned hot thoriated tungsten filament are accelerated by a hollow cylindrical mesh anode to enter the field-free region perpendicular to the anode axis. The electron energy can be varied up to 500 eV. A gas jet is positioned along the anode axis. Ions are formed by electron impact ionization in the field-free region and are formed in the ground state as well as the excited states. The major advantages of this ion source lies in its stability and its simplicity.

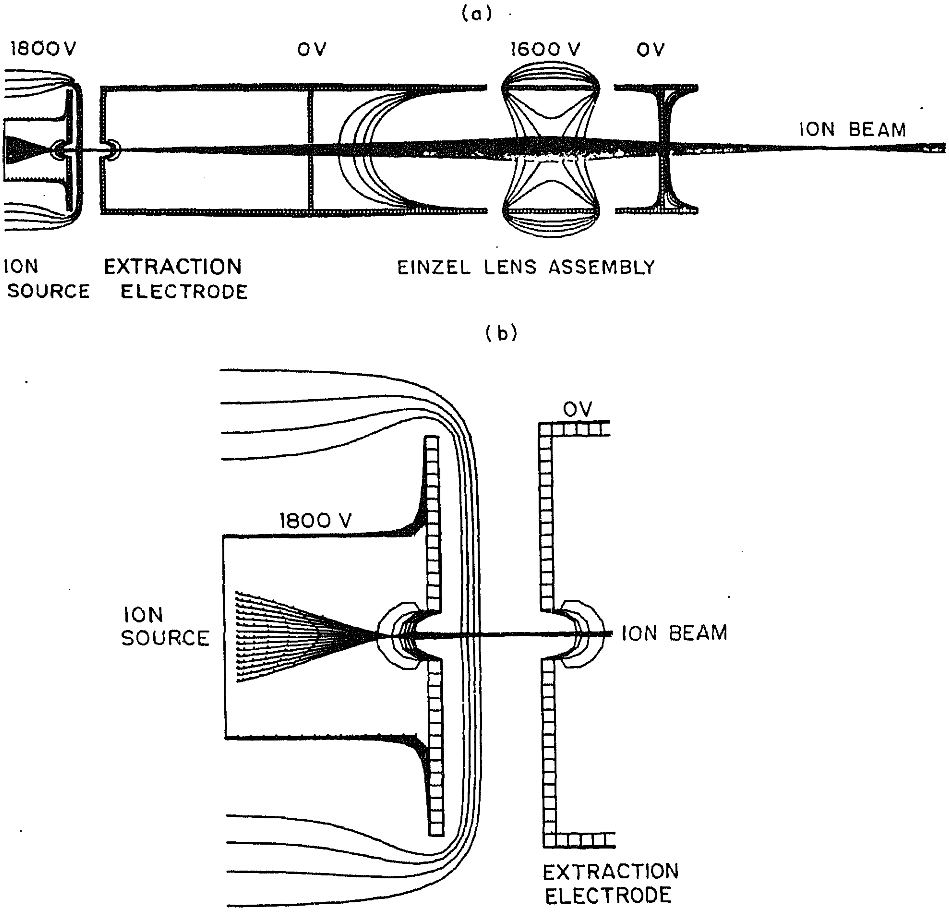

Figure 3(a). Computer simulations of N_2^+ ion (1·8 keV energy) trajectories in the ion source, extraction and focussing system. **(b)**. Expanded view of ion extraction from the ion source by a penetrating field. The dotted contours intersecting the ion beam trajectory within the source region represent ion transit time periods of 2 μs each; a typical residence time for N_2^+ ions within the source is estimated to be *ca* 16 μs.

Ions formed in the field free region are extracted by an electric field penetrating through a fine anode aperture. The field penetration into the anode mesh determines the energy spread in the extracted ion beam. In our design, considerable effort was expended to minimize the field penetration into the anode mesh by making the anode aperture smaller whilst, at the same time, ensuring that the efficiency of ion extraction is not reduced to unmanageable proportions. Figure 3 illustrates the field penetration pattern and the ion extraction efficiency of the optimised configuration that we arrived at after a large number of computer simulations were carried out using the ion trajectory method of Dahl *et al* [5] in the following manner.

The region of interest in the apparatus was notionally covered with a cartesian grid of points. Laplace's equation for the appropriate geometry, together with a Taylor series expansion of the potential at every adjacent point, is utilized to express the potential at an arbitrary point in the array in terms of the potential at the surrounding points. The grid points which correspond to ion source and extraction electrodes are held at the desired voltages, and the potential of each free point is calculated in terms of the surrounding points. Repeated iterations are performed; monitoring the change in potential at a point after each cycle shows when an adequate level of convergence has been achieved. Upon calculations of the potential array to a satisfactory degree of accuracy, the trajectories of a large number of ions in that field are calculated by numerical integration of the equations of motion for given initial position and velocity. The actual electrostatic field calculations is by means of the finite difference relaxation method [6].

In figure 3(b) we also show the results of calculations which offer an indication of the amount of time that molecular ions, of the type used in subsequent studies to be described below, take to traverse the ion source prior to extraction. The dotted lines shown within the ion source region indicate time separations of 2 μs. In the actual example shown in the figure N_2^+ ions, formed initially with only thermal energy, traverse through the source in a time period of about 16 μs. If the gas pressure within the source is sufficiently high, it may be possible to use the ion transit time information to deduce the degree of collisional de-excitation of the incident ion beam as it emerges from the source. Further work on this aspect of our design is under way.

Ions are electrostatically extracted by an accelerating potential of about 1–5 kV; the extracted ions are focussed by a three-element einzel lens system, whose design is identical to the one used in standard TV tube guns. The ion beam, further collimated mechanically by a fine aperture, enters a crossed electric and magnetic field analyser where the desired mass-to-charge (m/q) ratio of ions on the axis is selected by suitably balancing the forces exerted by the electric and magnetic fields in opposite directions.

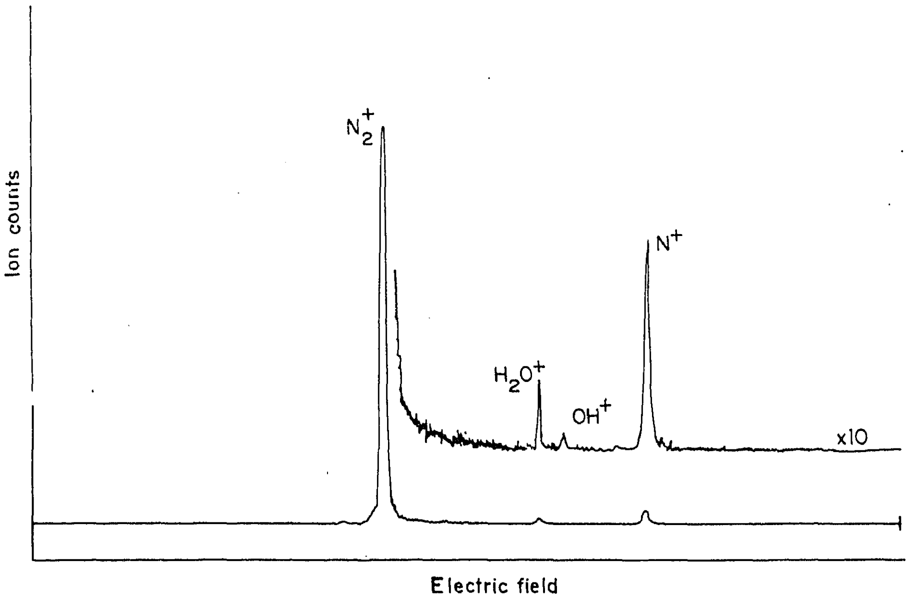

Figure 4. Typical mass spectrum obtained under focussing conditions such that unit mass resolution is obtained when a mixture of N_2 and H_2O are introduced into the ion source. The spectrum was obtained by varying the Wien filter's electric field over the range from 0 to 56 V cm^{-1} and keeping the magnetic field constant at 300 G.

The crossed field analyser used in the present apparatus is identical to that used in an earlier apparatus in our laboratory [7, 8] and will not be described here. It is, however, pertinent to point out the simple manner in which this device enables the mass resolution (and, correspondingly, the intensity of the ion signal that is transmitted) to be optimized for a given experimental situation by suitable choice of either electric field or magnetic field. A typical mass spectrum is shown in figure 4, illustrating unit mass resolution, which is more than adequate for the type of collision induced dissociation experiment which we report below.

2.2 *Energy monochromation and analysis*

The kinetic energy of the incident ion beam and post-collision energy analysis are both accomplished by means of two, large cylindrical electrostatic analysers. Both analysers are identical and consist of 55 cm mean radius 90° sectors with 2·0 cm radial gap. Factory-polished stainless steel sheets coated with colloidal graphite (to reduce surface space charge effects) are placed in 90° precision grooved holders on the top and bottom. Each analyser is assembled with the help of jigs to ensure the required gap, mean radius, parallelity, concentricity and exact 90° sector angle. There are locking devices incorporated which lock the sector assembly and prevent it from changing position when the jigs are dispensed with. The positions of all the mechanical fittings and supports for the sector elements inside each vacuum chamber are ensured by a right angle jig as the vacuum chamber (which consists of five segments) and the end flanges are welded with the jig and analyser assembly in the required position. Thus, all the critical parameters of mechanical design are kept under control and within the desired range by use of jigs throughout the fabrication and subsequent re-assembly stages.

The housing for the inter-sector slits also incorporates the gas target; by providing a gas flow in the variable sit assembly used in the present apparatus, the inter-sector slit has been converted into a gas target-cum-variable slit. The target region requires fast differential pumping. The position of the slits is dictated by the focal lengths of the two analysers. The first slit is positioned at the calculated focal length of the energy monochromator. The second, post-collision slit also needs to be positioned on a common tangent to the radial ion trajectories within the two analysers. The slit assembly is somewhat novel in that it consists of two 180° opposite parallel slits on the walls of a hollow cylinder. When the cylinder is rotated on its axis, the ion beam entering perpendicular to the axis and slits "sees" variations of area overlap between the entrance and exit slits with the change of angle of rotation. Any slit width from zero to the maximum (1 mm in the present design) can be obtained under dynamic conditions by rotating the cylinder under vacuum by means of a Wilson seal.

The post-collision energy analyzer is followed by a channel electron multiplier detector which is located at the focal length of the second analyzer. The detector is operated in the particle counting mode and is interfaced through a fast amplifier to conventional pulse counting electronics and to a microprocessor controlled data acquisition system.

2.3 *Some operational characteristics*

Figure 5 shows a typical energy loss spectrum obtained when H_2^+ ions with 1.8 keV translational energy collide with N_2. This spectrum is an example of the application of TES to studies of excitation/de-excitation reactions depicted in figure 1 and

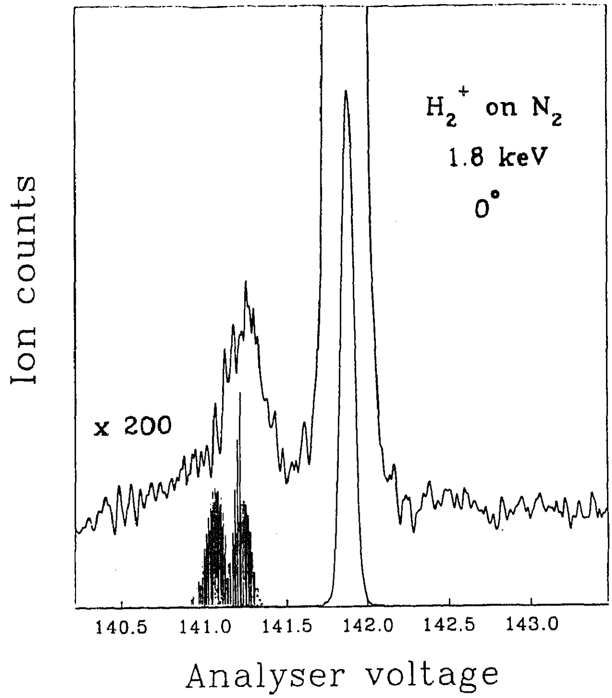

Figure 5. Translational energy spectrum of H_2^+ ions colliding with N_2 at 1·8 keV impact energy and 0° scattering angle. The peak in the vicinity of 142 V is the elastically scattered H_2^+ peak; the envelope of inelastic peaks in the region of 141·0 to 141·5 V are discussed in the text in terms of energy loss resulting from excitation of N_2 into various electronic states. The spectrum of vertical solid lines represents calculations of the transition probabilities for excitation to various N_2^+ excited electronic states.

represents the first such measurement of molecular target excitation induced by molecular projectile ion collisions reported to date. The elastically scattered H_2^+ ions give rise to the major peak in the spectrum; this peak has a full-width at half-maximum of 700 meV. This value represents an energy resolving power of just under 3000 which is obtained with ease and is adequate for purposes of illustrating the utility of the apparatus in studying collision-induced excitation processes involving singlet → triplet transitions which are forbidden by dipole selection rules.

The prominent peak observed at an energy loss of *ca.* 8 eV represents excitation of the target molecules in a composite process:

$$H_2^+ + N_2(^1\Sigma_g^+) \rightarrow H_2^+ + N_2^* - \Delta E \text{ eV}$$

where the N_2^{+*} states that are accessed are $A^3\Sigma_u^+$, $B^3\Pi_g$, $B'^3\Sigma_u^-$ and $a'^1\Sigma_u^-$. The relative transition probabilities for vertical excitation to each of these states from the ground state have been calculated by us using Franck–Condon factors obtained from the tabulated data of Lofthus and Krupenie [9]. The relative importance of each of these transitions in our spectrum is difficult to ascertain in a totally unambiguous fashion at present; a further, small enhancement in the resolving power is necessary and efforts are currently under way towards this end. For the purposes of this report, we wish to focus attention on the fact that this type of singlet-triplet excitation process would, of course, be inaccessible in conventional photon spectroscopic techniques. In H_2^+–N_2 collisions, however, the possibility of electron exchange permits the multiplicity of the target molecule to change while the electron spin angular momentum of the ion-molecule system as a whole is conserved. Essentially 50% of all the bound electronic states of molecular species would be triplet states, or states of higher multiplicity. Such states have hitherto not been studied with the care afforded to singlet states because of the quantum mechanical restriction that for molecules with singlet ground states, states of higher multiplicity have optically forbidden decay transitions. Ion induced excitations studied by means of TES are clearly of much utility in this type of electronic spectroscopy. Resolving powers of the order of 5000 or more are sufficient to enable resolution of vibrational structure, and the first TES experiments on ion-induced "vibrational spectroscopy" has recently been reported by Mathur *et al* [10].

The energy loss spectrum shown in figure 5 is by way of illustration; a more detailed report on excitation of N_2 and O_2 molecules by ion projectiles possessing different quantal properties will be presented elsewhere [11]. However, it is to be noted that the projectile energy range over which the present apparatus can operate is 300 eV to 3 keV. This is exactly the energy range which is difficult to access in accelerator-based experiments (the lower translational energy limit in such experiments is seldom below 10 keV) as well as in ion swarm and other plasma type of experiments (where the highest energies that can be attained do not exceed 100 eV or so). Figure 6 shows the transmission function of the apparatus for H_2^+ ions produced under three different ion source and extraction conditions.

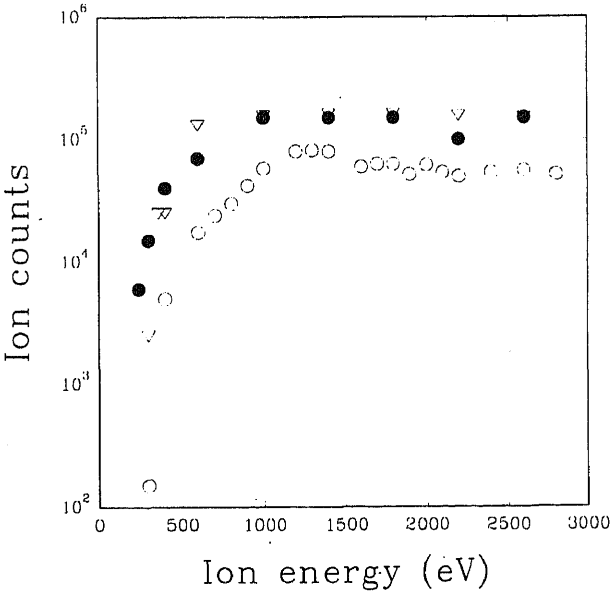

Figure 6. Transmission function for H_2^+ projectiles under different ion source conditions. Open circles: 3×10^{-6} torr; closed circles: 5×10^{-6} torr; triangles: 8×10^{-6} torr.

3. Collision-induced dissociation of CO_2^+ ions

Collision-induced dissociation of molecular ions may be understood in general terms as a two-step model within the framework of molecular potential energy surfaces. In the first step the projectile ion, AB^+, is collisionally excited to a higher electronic state:

$$AB^+ + M \rightarrow AB^{+*} + M - \Delta E.$$

In the second step, the ion in the excited state undergoes dissociation leading to the fragment ions:

$$\begin{aligned} AB^{+*} &\rightarrow A^+ + B + T_{cm} \\ &\rightarrow A + B^+ + T_{cm} \end{aligned}$$

A given excited state, AB^{+*}, may possess a potential energy (PE) curve which is either purely repulsive or the Franck–Condon transition from the ground state accesses that part of the PE curve which lies above the corresponding dissociation limit. A third alternative may involve an excited state which possesses a potential energy curve which has a minimum; such a state can undergo dissociation due to an avoided curve crossing involving a dissociative electronic state. This mode of

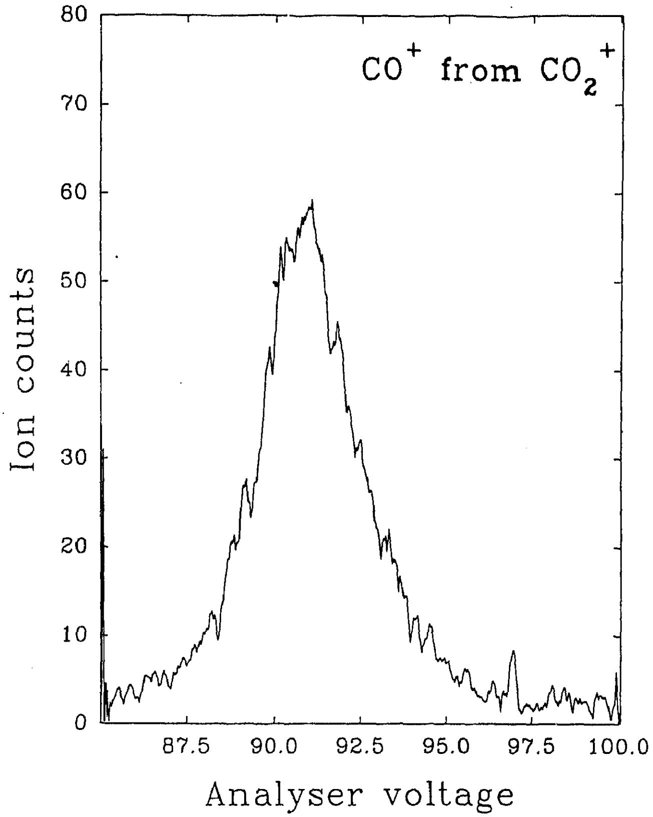

Figure 7. Translational energy spectrum of CO^+ fragment ions resulting from dissociation of CO_2^+ in 1·8 keV collisions with Ar.

dissociation is discussed below in the context of our results. The energy required for excitation, ΔE, in this inelastic process, is obtained by conversion of the projectile's kinetic energy into potential energy of the system.

Figure 7 shows a typical translational energy spectrum of CO^+ formed when CO_2^+ collides with neutral Ar at an impact energy of 1800 eV. Identical spectra are obtained when Ar is replaced by He or N_2 as the target gas. The projectile beam comprises mostly CO_2^+ in its ground $X^2\Pi_g$ state. As described in the two-step model the CO_2^+ molecule is initially excited to a higher electronic state which then dissociates to either $CO^+ + O$ or $CO + O^+$, releasing ε_{cm} energy in the centre-of-mass frame. This energy manifests itself as the kinetic energy of the fragment molecules and gives rise to the energy-broadened peak shown in figure 7 (compare with the energy width of the inelastic peak shown in the energy loss spectrum shown in figure 5). The measured energy in the laboratory frame, ε_{lab} can be obtained by the addition of collision velocities [1]:

$$\varepsilon_{lab} = \frac{M_{frag}}{M_{mol}} E + \frac{M_{frag}}{M_{mol}} \varepsilon_{cm} \cos^2\theta \pm \frac{M_{frag}}{M_{mol}} (\varepsilon_{cm} E)^{1/2} \cos\theta$$

where M_{frag} and M_{mol} are fragment and the projectile ion mass, respectively. θ is the angle of orientation of the molecular axis with respect to the beam axis and E is the energy of the projectile ion. Even though the numerical value of ε_{cm} may be small (of the order of a few hundred meV), ε_{lab} has a much larger value due to the addition of the velocity vectors. This energy 'amplification' which the TES method affords permits the study of the dissociation processes in considerable detail even with the instrument adjusted for modest energy resolution (and corresponding large ion intensities).

The $O^+ + CO$ dissociation channel was not measureable in our experiments, indicating that the excited electronic state of CO_2^+ that is initially accessed in the collision has quantal properties which give rise to only the $CO^+ + O$ dissociation limit. By measuring the half width of the CO^+ peak, we determine the average centre-of-mass kinetic energy release (KER_{cm}) value for the CO^+ fragment to be 170 ± 13 meV.

We correlate our energy spectrum of the CO^+ fragment to potential energy curves of CO_2^+ in the manner depicted in figure 8. CO_2^+ in its ground state ($X^2\Pi_g$) is collisionally excited to the $C^2\Sigma_g^+$ state. In the linear geometry this state correlates with CO^+ ($^2\Sigma^+$) + O (^3P), which is much above the C state. However the C state is predissociated by $^4\Pi_u$ state. So the dissociation of the molecule from the C state takes place through this quartet state. The CO_2^+ molecule in this state is more stable in the bent geometry, so it undergoes angular relaxation. At an OCO angle of 160° it undergoes another faster inter-system crossing to the X^2A_2 state, which corresponds to the $^2\Sigma_g$ state in the linear geometry. The molecule in the X state with large internal energy dissociates to $CO^+(^2\Sigma^+) + O(^3P)$ fragments.

Despite the apparent structural simplicity of the CO_2^+ molecular ion, there continues to be ambiguity regarding its proper quantal description. A number of high-level quantal calculations have been performed on the ground state and low-lying excited electronic states of this ion. In table 1 we draw attention to the divergent range of values of vertical excitation energy that have been computed for the $C^2\Sigma_g^+$ state as well as corresponding experimental data. Given that the C state is the electronic state that is responsible for formation of $CO^+ + O$ fragments, the amount of KER_{cm}

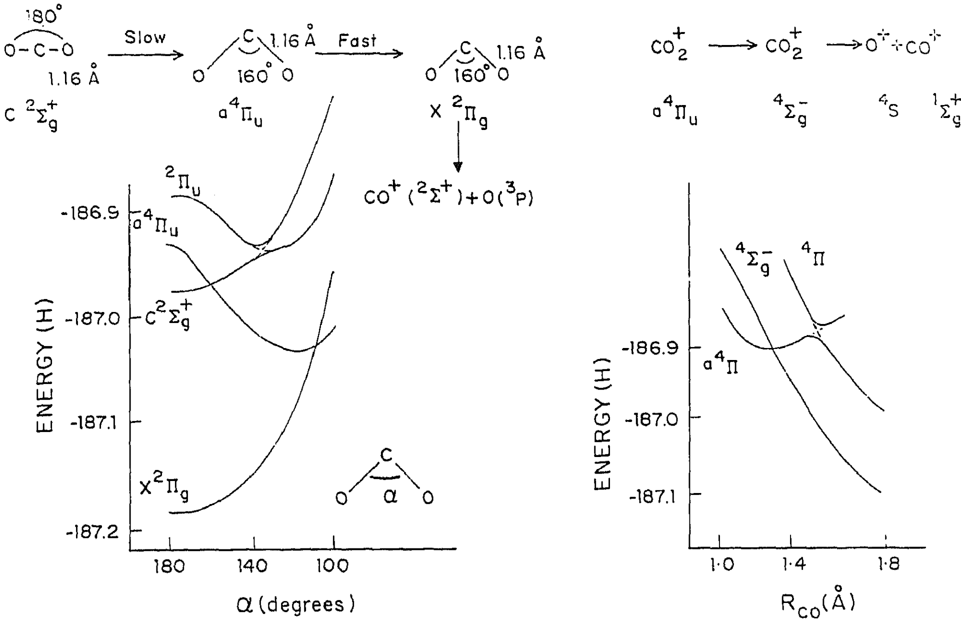

Figure 8. Schematic potential energy curves of low-lying excited electronic states of CO_2^+ (based upon the calculated results of Praet *et al* [13]) which take part in dissociation to $CO^+ + O$ fragments. The curves depicted on the left show variation of potential energy with the O–C–O angle; curves depicted on the right show the corresponding variation with C–O internuclear distance.

Table 1. Comparison of various contemporary values of the vertical excitation energy (in ev) of the $C^2\Sigma_g^+$ state of CO_2^+. All the values are results of large-scale ab initio calculation except the first which pertains to data from a He I photoelectron spectroscopy experiment.

Excitation energy	Reference
5·61	Potts and Fattahallah [12]
6·2	Roy *et al* [15]
5·69	Praet *et al* [13]
5·99	von Niessen *et al* [16]
5·49	Domcke *et al* [17]
7·25	England [14]
5·53	present work

obtained upon dissociation will be dependent upon the excitation energy: the larger the excitation energy, for a given (fixed-energy) dissociation limit, the larger will be the value of KER_{cm} that would be expected.

In view of the significant discrepancies that exist a calculation of the vertical excitation energy of the *C* state has been carried out by us using an all-electron, ab initio configuration interaction method [1, 2] with a 6-311G* basis set. Configuration interaction effects are accounted for by means of a coupled cluster formalism by a computational method known as QCISD (T)[1, 2]. The vertical excitation energy of the C state from the X state is determined from our calculation to be 5·53 eV, in excellent agreement with the experimental value [12] and with the value calculated by Praet *et al* [13]. On the other hand, calculations carried out England *et al* [14] and Roy *et al* [15] yield significantly larger values of C state excitation energy. On the basis of our calculations, the C state in the Franck–Condon region is found to lie 140 meV above the CO^+ $(^2\Sigma^+) + O(^3P)$ fragments, in good accord with the average KER_{cm} value determined from our measured energy spectrum.

It is also of interest to note that the $^4\Pi_u$ state also crosses the $^4\Sigma^-$ state. The $^4\Sigma^-$ state correlates with $O^+(^4S) + CO(^1\Sigma^+)$ fragments. At low internal energies of the molecule in the C state (population of the lower vibrational levels of the C state) dissociation must necessarily be into $O^+ + CO$ fragments on purely energetic grounds. At higher energies (population of higher vibrational levels of the C state). the $CO^+ + O$ fragmentation channel becomes more dominant. Experimentally, we observe that the O^+ fragment is much lower in intensity (by about two orders of magnitude) than the CO^+ fragment. Our observation indicates that collisional excitation from the ground state leads to population of the higher vibrational levels of the C state.

Acknowledgements

We are grateful to B S Prahallada Rao and S R Halbe of the Technical Physics and Prototype Engineering Division of Bhabha Atomic Research Centre (Bombay) for their skilful assistance and advice in the high-accuracy machining of large (> 1m) diameter stainless rings during the fabrication of the two energy analysers. We also acknowledge S V K Kumar's assistance in preliminary computer simulation studies of ion trajectories in the ion source and extraction region.

References

[1] D Mathur, *Physics of ion impact phenomena*, (Springer-Verlag, Berlin, 1991)
[2] D Mathur, *Phys. Reports* **225**, 193 (1993)
[3] V Krishnamurthi, D Mathur and G T Evans, *Rapid Commun. Mass Spectrom.* **5**, 557 (1991)
[4] G R Kumar, L Menon and D Mathur, *Phys. Rev.* A (in press)
[5] D A Dahl, J E Delmore and A D Appelhans, *Rev. Sci. Instrum.* **61**, 607 (1990)
[6] M Szilagyi, *Electron Optics* (Plenum Press, New York, 1988) Ch. 3
[7] D Mathur, F A Rajgara and V Krishnamurthi, *Proc. Indian Acad. Sci* (*Chem. Sci.*) **104**, 509 (1991)
[8] F A Rajgara, *Ion translational energy spectrometry*, M.Sc. Thesis (University of Bombay, 1992)
[9] A Lofthus and P H Krupenie, *J. Phys. Chem. Ref. Data* **6**, 113 (1977)
[10] D Mathur, A C R Wilkins and A G Brenton, *Rapid Commun. Mass Spectrom.* **6**, 479 (1992)
[11] M Krishnamurthy and D Mathur-(in preparation)
[12] A W Potts and G H Fattahallah, *J. Phys.* **B13**, 2545 (1980)
[13] M Th. Praet, J C Lorquet and G Raseev, *J. Chem. Phys.* **77**, 4611 (1982)
[14] W B England, *J. Chem. Phys.* **77**, 6609 (1982)
[15] P Roy, I Nenner, P Millie, P Morin and D Roy, *J. Chem. Phys.* **84**, 2050 (1982)
[16] W von Niessen, G H F Diercksen and L S Cederbaum, *J. Chem. Phys.* **67**, 4124 (1977)
[17] W Domcke, L S Cederbaum, J Schirmer, W von Niessen, C E Brion and K H Tan, *Chem. Phys.* **40**, 171 (1979)

PRAMANA
— journal of
physics

© Printed in India

Vol. 41, No. 3,
September 1993
pp. 285–289

Further studies on Ag/BPSCCO tapes using low purity materials

S R SHUKLA, Y S REDDY, N KUMAR, S K SHARMA and R G SHARMA
National Physical Laboratory, New Delhi 110012, India

MS received 12 March 1993; revised 15 May 1993

Abstract. Transmission electron microscopic (TEM) studies are reported on Ag-clad $Bi_{1\cdot7}Pb_{0\cdot4}Sr_{1\cdot8}Ca_2Cu_{3\cdot5}O_x$ tapes prepared by using low purity (98–99%) commercial grade materials. The self-field J_c values of these tapes viz. $6\cdot14 \times 10^3$ A.cm^{-2} at 77 K and $1\cdot4 \times 10^5$ A.cm^{-2} at 4·2 K, reported in an earlier publication, were significantly higher than the corresponding J_c values in tapes prepared with high purity (99·99%) materials. The TEM pictures on the low purity core material of the tapes reveal the presence of stacking faults and the intergrowth of the 2212 and 2223 phases which could be acting as flux pinning sites and responsible for enhanced J_c values. These defects can perhaps be traced back to the presence of 60 ppm iron in the low purity CuO as revealed by atomic absorption analysis reported earlier.

Keywords. Critical current density; Ag-clad BPSCCO tapes; structural inhomogeneities.

PACS No. 74·60

In an earlier paper, Shukla *et al* [1] reported a marked improvement in the critical current density (J_c) of Ag-clad $Bi_{1\cdot7}Pb_{0\cdot4}Sr_{1\cdot8}Ca_2Cu_{3\cdot5}O_x$ (BPSCCO) tapes when constituent oxides and carbonates of low purity (98–99%) were used. The highest J_c values obtained in these studies were $6\cdot14 \times 10^3$ A.cm^{-2} (77 K, 0T) and $1\cdot4 \times 10^5$ A.cm^{-2} (4·2 K, 0T). These values were significantly higher than those obtained in Ag-clad Bi (2223) tapes prepared using high purity (99·99%) materials [2] and processed in an almost identical manner. The motivation behind these studies [1] was two fold. Firstly, the use of low purity commercial grade material's being economical is important from the production point of view. Secondly, the small amount of impurities present in the low purity constituent oxides/carbonates could cause structural inhomogeneities which could act as flux pinning sites and enhance J_c values. It was also reported by us that CuO used in these studies contained 60 ppm iron as revealed by atomic absorption studies. It was conjuctured that this iron could be responsible for higher values of J_c through enhanced flux pinning.

In this brief communication we report our TEM studies carried out on some of these tape specimens. The studies showed some structural features which could be traced back to the presence of this small amount of iron impurity and a minor (2212) phase in an otherwise major 2223 phase.

The details of the tape fabrication have been described elsewere [1]. The core material with a composition $Bi_{1\cdot7}Pb_{0\cdot4}Sr_{1\cdot8}Ca_2Cu_{3\cdot5}O_x$ was prepared by the usual solid state diffusion method. The starting materials were Bi_2O_3 (99%), PbO (98%), $Sr(NO_3)_2$ (99%), $CaCO_3$ (99%) and CuO (99%), all of commercial grade purity. The

Table 1. Ag-clad $Bi_{1\cdot7}Pb_{0\cdot4}Sr_{1\cdot8}Ca_2Cu_{3\cdot5}O_x$ tape specimens with low purity starting materials.

Set no.	Specimen no.	Core size t(mm) × w(mm)	J_c(77 K) A.cm^{-2}	J_c(4.2 K) A.cm^{-2}
One	40	0·22 × 0·68	220	7700
	41	0·14 × 0·71	320	11000
	42	0·009 × 0·89	3750	131000
Two	45	0·18 × 0·71	580	8200
	46	0·08 × 0·80	1020	18300
	48	0·007 × 0·93	6140	149000

tapes were prepared by the usual powder-in-tube technique. Tapes of different thicknesses between 0·74 mm and 0·24 mm were prepared and sintered at 845°C for 20 h in air. These specimens are referred to as specimen nos 40, 41 and 42 shown as set no. 1 in table 1. Parts of these tapes were rolled again and sintered at 845°C for 20 h. These specimens are designated as specimens 45, 46 and 48 respectively and shown as set no. 2 in table 1. The specimen 48 is 0·14 mm thick with a core thickness of 7 μm. The grain structure as revealed by SEM has already been reported [1]. Successive rolling leads to an improved grain structure. The XRD spectra showed the presence of a predominantly 2223 phase with a 2212 phase as a minor fraction. The 2223 phase fraction increases with repeated rolling and sintering and the (001) reflections become sharp indicating grain alignment (c-axis texturing). Detailed microstructural analysis was carried out on a few specimens using a TEM model JCM 200 cx operating at 160–200 kV. The J_c of all the tape specimens was measured at 77 K and 4·2 K using a four-probe method and following a criterion of 1 μV/cm.

Table 1 gives the composition, sintering parameters, dimensions of the cores and the measured J_c values. These J_c values at 77 K and 4·2 K are plotted as a function of inverse of core thickness (t^{-1}) in figure 1. For comparison similar plots (J_c vs t^{-1}) for tape specimens with high purity (99·99%) starting materials which were earlier reported [2] are also shown in figure 1. As seen in the figure J_c increases with repeated rolling and sintering in conformity with earlier reports in the Bi-2223 system [2, 3, 4]. At 4·2 K J_c values of the tapes of set nos 1 and 2 lie on a single curve as both the phases of the Bi-system (2212 and 2223) are known [5] to carry identical currents at 4·2 K. J_c varies as t^{-1} similar to that reported earlier by Osamura *et al* [6] and Dersch and Blatter [7].

As mentioned earlier, 99% pure CuO was used while preparing the core material for the tapes. The atomic absorption spectroscopic analysis of CuO shows the presence of 60 ppm iron in it. To understand the role of iron in influencing the superconducting properties, it is important to know which site iron occupies in the Bi-system, superconducting properties being extremely sensitive to the Cu-sites. Mössbauer studies by Tang *et al* [8] carried out on a variety of BSCCO superconductors with the addition of 1·5% Fe in place of copper, show that iron substitutes the Cu (II) sites (square pyramidal) in the 2223 phase. This results in stacking faults and the intergrowth of different phases. These defects can enhance flux pinnings. Large intragranular pinning forces have indeed been reported by Wordenweber *et al* [9] in $YBa_2(Cu_{1-x}Fe_x)_3O_y$ (for $x \leqslant 0{\cdot}01$) which is isostructural to the BSCCO system. TEM micrograph on the core material of the tape specimen no. 48 indeed shows a typical lattice fringe

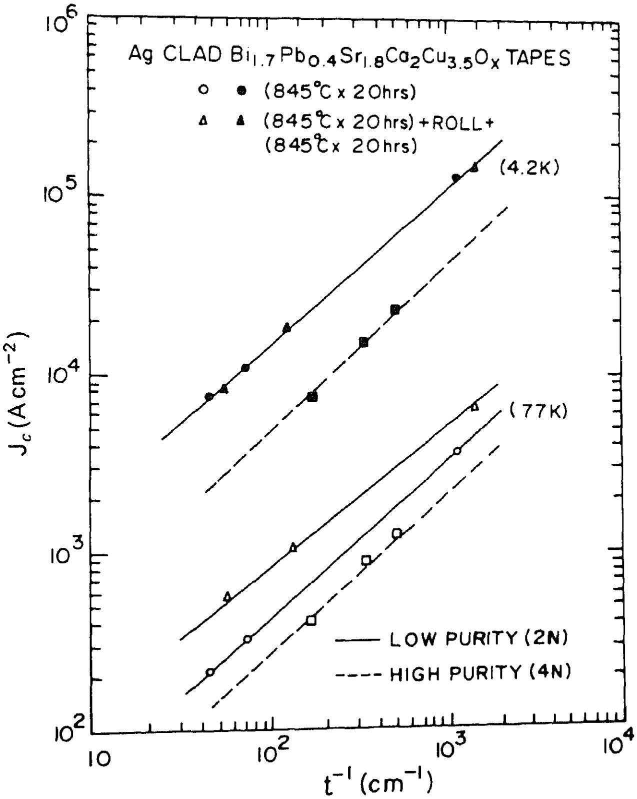

Figure 1. J_c at 77 K and 4·2 K of the tape specimens listed in table 1 plotted against inverse of core thickness (t^{-1}). For comparison J_c vs t^{-1} plots of the tape specimens prepared with high purity materials [2] are also included (dotted curves).

image displaying high density of stacking faults (figure 2). The micrograph reveals slight bending of the lattice fringes. The lattice spacing changes from one region to another. The lattice expansion occurring in one region causes a bent in the lattice, as seen in the TEM micrograph. The inset in figure 2 is the corresponding selected area electron diffraction pattern (SAEDP) showing an incommensurate structure.

In intergrowth of the two phases viz., 2212 and 2223 with two fringe spacing of 30·0 Å and 36·7 Å corresponding to the c-axis parameters of the two phases respectively are seen in the same specimen (figure 3). This is in conformity with the XRD studies which show the presence of the two phases (2223 and 2212) in the ratio 60:40 in the bulk material as determined by the relative intensities of the (002) reflections. Although the volume fraction of 2223 phases increases in the tapes of the second set yet the 2212 phase is still present (8% in specimen no. 48). The presence of the 2212 phase dispersed in the 2223 phase matrix must have beneficial effect on flux pinning. It has indeed been suggested [10] that the 2212 phase may act as potential flux pinning centres in these materials leading to high J_c values. The presence of the 2212 phase is however common to the tapes of the present studies as well as the tapes using high purity materials of the previous studies [2]. The significantly high values of J_c in low purity tapes can then be attributed to the stacking faults caused by the substitution of iron, present as an impurity in CuO, at the copper site. Systematic studies with

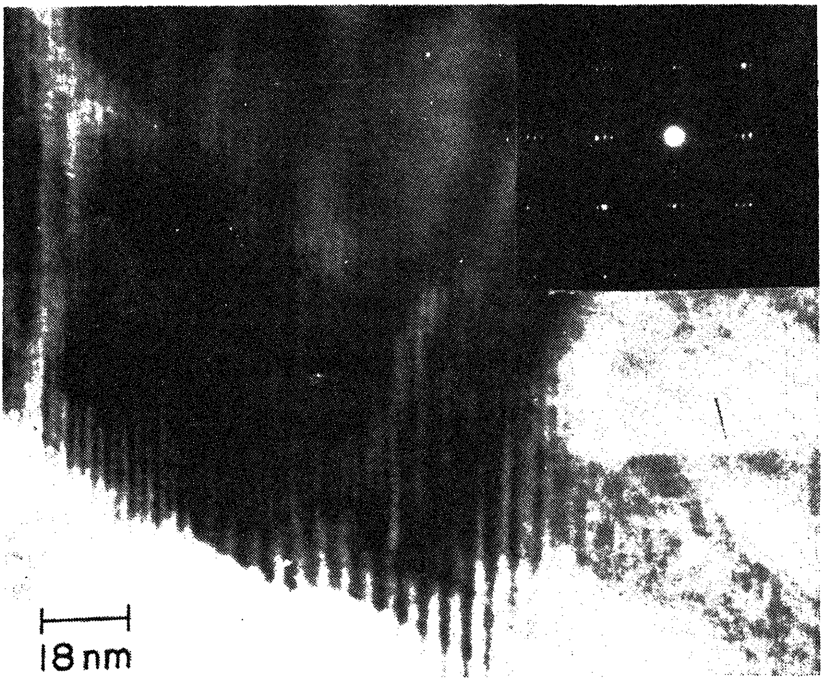

Figure 2. Lattice fringes image of tape specimen no. 48 showing high density of stacking faults. The picture shows slight bending of the lattice fringes and consequently the lattice spacing changes in different regions. The corresponding SAEDP reveal an incommensurate structure as seen in the inset.

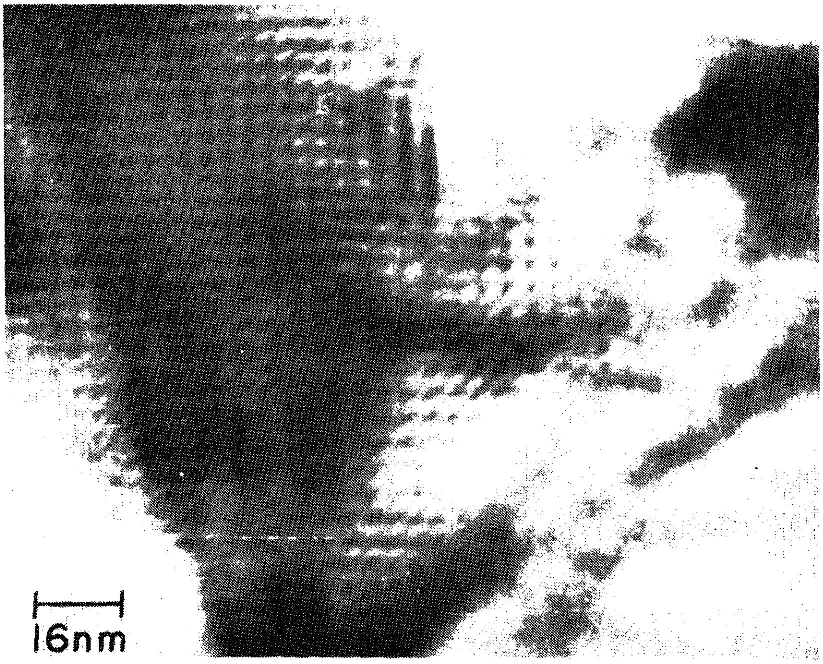

Figure 3. TEM micrograph of specimen no. 48 showing the intergrowth of two phases viz., low T_c (2212) and high T_c (2223) with a c-axis parameter equals to 30 Å and 36·7 Å respectively.

the addition of varying amounts of Fe in the B(P)SCCO materials are, however essential to confirm these conclusions. Such experiments are in progress.

Acknowledgements

The authors thank Prof. E S R Gopal for useful discussions, K D Kundra and U Dhawan for obtaining XRD data and S U M Rao for his help in SEM studies.

References

[1] S R Shukla, Y S Reddy and R G Sharma, *Pramana–J. Phys*, **38**, 179 (1992)

[2] S R Shukla, Y S Reddy D K Pandya, Y Tanaka and R G Sharma, *Pramana–J. Phys.* **37**, 333 (1991)

[3] T Asano, Y Tanaka, M Fukotomi, K Jikihara and M Maeda, *Jpn. J. Appl. Phys.* **28**, L595 (1988)

[4] K Togano, H Kumakura, H Maeda, E Yanagisiwa, N Irisawa, J Shimoyama and T Morimoto, *Jpn. J. Appl. Phys.* **28**, L95 (1989)

[5] H Kumakura, K Togano, H Maeda and M Mimura *J. Appl. Phys.* **67**, 3443 (1990)

[6] K Osamura, T Tokayama and S Ochiai, *Cryogenics* **29**, 430 (1990)

[7] H Dersch and G Blatter, *Phys. Rev.* **B38**, 11391 (1988)

[8] H Tang, Z Q Qiu, Y W Du and J C Walker, *J. Appl. Phys.* **67**, 4512 (1990)

[9] R Wordenweber, G V S Sastry, K Heinemann and H C Freyhardt, *J. Appl. Phys.* **65**, 1648 (1989)

[10] S X Dou, Y C Gou and H K Liu, *Physica* **C194**, 343 (1992)

PRAMANA
— journal of
physics

© Printed in India

Vol. 41, No. 3,
September 1993
pp. L291–L294

Influence of various gases on single bubble sonoluminescence

VIJAY H ARAKERI
Department of Mechanical Engineering, Indian Institute of Science, Bangalore 560 012, India

MS received 24 May 1993

Abstract. Influence of various gases on the intensity of single bubble sonoluminescence has been studied. The gases used were air, oxygen, nitrogen, argon and helium. Among these oxygen gave the brightest intensity with nitrogen giving the least.

Keywords. Sonoluminescence; bubble dynamics.

PACS Nos 78·60; 43·25; 42·50

Single bubble sonoluminescence (SBSL) [1,2] is the phenomenon of light emission from a single bubble driven into extreme nonlinear motion by an acoustic field. The light emitting bubble could be a source of picosecond flashes [2] if the SBSL intensity can be enhanced sufficiently. Towards this end we have investigated the influence of various gases on the intensity of SBSL. The apparatus used presently has been briefly described by Arakeri [3]. It basically consists of a 500 cc boiling flask driven into one of its resonant modes by a piezoelectric drive. A photomultiplier tube (RCA 4526) with a S–20 spectral response and a rise time of about 2 ns is used to measure SBSL intensity. The average of single pulse outputs of the PMT was recorded on a fast digital storage oscilloscope (Tekhind 2230) operated in repetitive sampling mode. The typical record obtained on the oscilloscope was presented earlier [3]. The area under the curve is directly related to the integrated charge output of the PMT and as described by Barber [4], this information can be used to obtain the number of photons emitted per flash. The present system was calibrated to give SBSL intensity in terms of the total number of photons emitted per flash. The maximum values attainable for each experimental condition are presented here.

With the exception of one series of tests, the others used distilled water as the liquid medium. The steps in the preparation of samples with various dissolved gases were to repeatedly degas the liquid to a low gas content value and expose it to the particular gas under study. The gas content was monitored with a Van Slyke apparatus. This repeated degassing and exposure was done to ensure that most (if not all) of the air which was originally present was driven out.

It was previously reported [3] that in air/water system, the SBSL intensity is strongly dependent on the extent of dissolved air content. Further studies indicated that the behaviour is more complex than suggested by the single set of experiments. Some additional results are presented in Figure 1. The behaviour in argon/water system is similar to that in air/water system at lower gas content (α) values. However, at higher α, the SBSL intensity in argon/water system seems to reach a constant value. Thus, near saturation conditions the light intensity with argon is higher than that with air. This has been the finding with sonoluminescence (SL) from multi-bubble

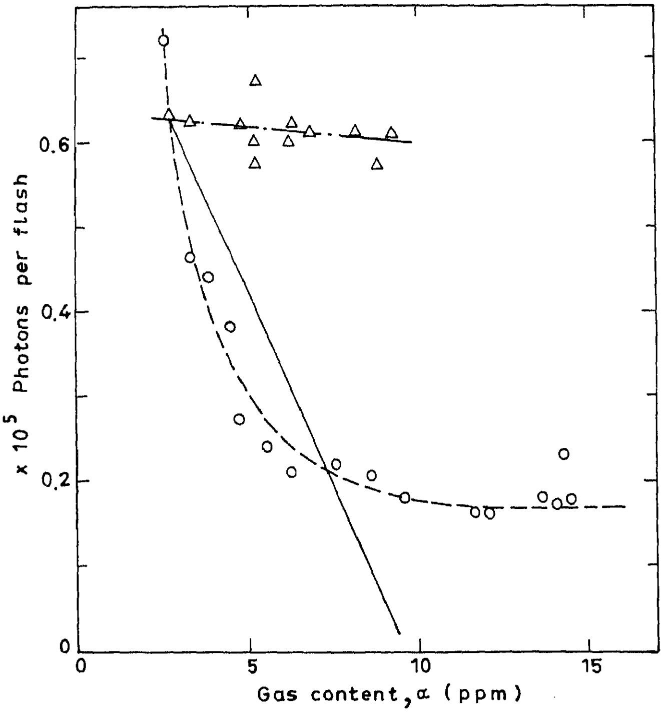

Figure 1. Effect of dissolved air concentration on single bubble sonoluminescence intensity. ——— air/water (Arakeri [3]), ○ argon/water, △ air/20% glycerine-water. $T = 20 \pm 1°C$.

cavitation fields [5, 6]. In contrast to air and argon/water systems a surprising finding was that with air/20 per cent glycerine-in-water-solution system, the SBSL intensity hardly changed with α (Figure 1). The presently measured SBSL intensity with this system is near $0{\cdot}6 \times 10^5$ photons per flash. In comparison, Barber and Putterman [2] have measured an intensity of about $0{\cdot}8 \times 10^5$ photons per flash in 25 per cent glycerine-in-water-solution at a frequency of about 30 kHz which is close to our operating frequency. Considering the differences in the apparatus including variations in PMT response, the agreement between the two measurements can be considered to be good. The presently observed difference in the behaviour of air/water and air/glycerine solution systems is quite puzzling. One observation could be relevant here; in the case of air/water system the SBSL was found to be absolutely steady; whereas, with air/glycerine solution system the SBSL would blink i.e. it would go on and off every few seconds. This fact has also been reported by Barber and Putterman [2]. In view of this, water was selected as the liquid medium for further tests.

It has already been noted that SBSL intensity depends on α; in addition, Hiller *et al* [7] have shown that SBSL intensity is also dependent on temperature, T. Comparison of results shows that the latter dependence is stronger than the former, in the sense that SBSL intensity can vary much more for 1°C change in T than for 1 ppm change in α. For this reason, the influence of various gases on SBSL intensity was studied by varying the sample temperature with a fixed initial value of dissolved gas content of about 5–6 ppm for all the tests. The results are presented in figure 2. It is clear that with oxygen, the SBSL intensity is the maximum and with nitrogen the minimum.

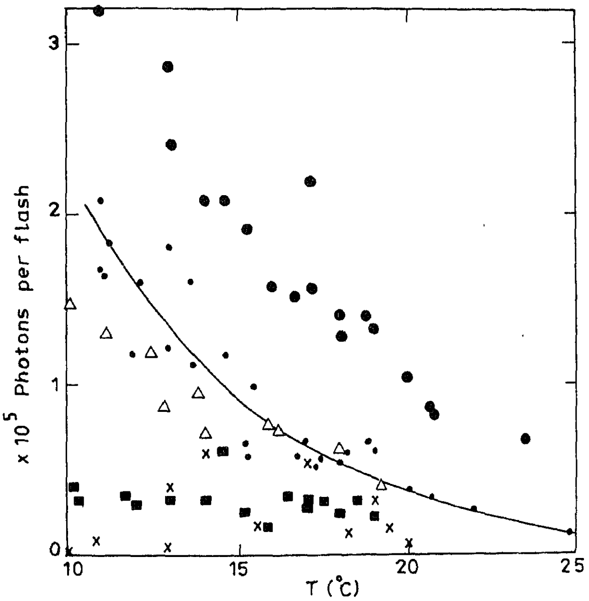

Figure 2. Influence of various gases on maximum single bubble sonoluminescence intensity in water at different temperatures. ● air, ● oxygen, △ argon, ■ helium, × nitrogen. Solid line is mean through air data. $\alpha = 5$–6 ppm. The intensity levels with air above are significantly lower than those reported in [7] since in the present apparatus most of the ultraviolet rays are cut-off.

The monoatomic gases argon and helium with higher γ values show lower intensities than air or oxygen. Close observation of bubble behaviour under light emitting conditions showed that the motion was steady and fixed with air, O_2 and N_2; whereas, it was unsteady with Ar and also with He bubbles. This may partly explain the observed relatively low values of SBSL intensity in the case of He. The intensity difference between the O_2 and N_2 bubbles is quite significant and is genuinely associated with internal dynamics since the bubble behaviour appeared very similar. In fact additional tests were carried out with O_2 and N_2 bubbles at higher dissolved gas concentration. In the case of O_2 with $\alpha = 14$ ppm, the intensity levels were similar to those for $\alpha = 5$–6 ppm and are presented in figure 2. On the other hand with N_2 and $\alpha = 9{\cdot}5$ ppm, *no* emission could be detected within a temperature range of 10 to 20°C of the liquid. It may be possible that the emission band was outside the S-20 spectral range. Present observations do suggest that closer examination of the O_2 and N_2 bubble behaviour with laser light scattering [1, 8] technique and SL spectrum measurement [7] could be very useful.

Previously, influence of various gases on SL from multi-bubble cavitation fields has been investigated [5], including detailed SL spectrum measurements by Sehgal *et al* [6]. However, all of these measurements have been limited to near saturation conditions and hence direct comparison of present finding in figure 2 with these may not be appropriate. In addition it is not clear whether the phenomenon of SBSL and SL from multi-bubble cavitation fields are similar.

Acknowledgement

The author would like to thank S Chakraborty for assistance in the initial phases of this study.

References

[1] D F Gaitan, L A Crum, C C Chruch and R A Roy, *J. Acoust. Soc. Am.* **91**, 3166 (1992)
[2] B P Barber and S J Putterman, *Nature* (*London*), **352**, 318 (1991)
[3] V H Arakeri, *Pramana – J. Phys.* **40**, L145 (1993)
[4] B P Barber, *Synchronous picosecond sonoluminescence* (Ph.D. Thesis, Univ. of California at Los Angeles (1992))
[5] A J Walton and G T Reynolds, *Adv. Phys.* **33**, 595 (1984)
[6] C Sehgal, R G Sutherland and R E Verrall, *J. Phys. Chem.* **84**, 388 (1980)
[7] R Hiller, S J Putterman and B P Barber, *Phys. Rev. Lett.* **69**, 1182 (1992)
[8] B P Barber and S J Putterman, *Phys. Rev. Lett.* **69**, 3839 (1992)

PRAMANA
— journal of
physics

© Printed in India

Vol. 41, No. 4,
October 1993
pp. 295–309

Controlling of chaos by weak periodic perturbations in Duffing–van der Pol oscillator

S RAJASEKAR
Department of Physics, Manonmaniam Sundaranar University, Tirunelveli 627 002, India

MS received 12 April 1993; revised 30 July 1993

Abstract. This paper investigates the possibility of controlling horseshoe and asymptotic chaos in the Duffing–van der Pol oscillator by both periodic parametric perturbation and addition of second periodic force. Using Melnikov method the effect of weak perturbations on horseshoe chaos is studied. Parametric regimes where suppression of horseshoe occurs are predicted. Analytical predictions are demonstrated through direct numerical simulations. Starting from asymptotic chaos we show the recovery of periodic motion for a range of values of amplitude and frequency of the periodic perturbations. Interestingly, suppression of chaos is found in the parametric regimes where the Melnikov function does not change sign.

Keywords. Duffing–van der Pol oscillator; chaos; controlling chaos; Melnikov method.

PACS Nos 05·45; 42·50; 42·65; 47·20

1. Introduction

The genericity and robustness of chaotic dynamics are now well established in typical nonlinear dynamical systems. In recent years, there has been growing interest to use chaos profitably by synchronizing chaotic orbits [1, 2] and design of mixing and transport processes [3]. At the same time there have been promising developments in controlling of chaos [4–12]. For example, adaptive control algorithm [5, 6], stabilization of unstable periodic orbits embedded in a chaotic attractor by a predetermined perturbation [4] and weak feedback signal [8] have been proposed. Suppression of chaos by weak periodic parametric perturbation [7] and addition of second periodic force [9] are also possible. In fact, shift in the period doubling bifurcations and the onset of chaos due to periodic perturbations have been reported earlier in the literature [13, 14]. In a recent paper, Rajasekar and Lakshmanan [12] numerically studied the applicability and efficacy of various control algorithms in Bonhoeffer–van der Pol oscillator.

In this paper, we investigate, analytically and numerically, the effect of periodic parametric and addition of second periodic force in Duffing–van der Pol (DVP) equation

$$\ddot{x} + p\dot{x}(1 - x^2) - \alpha^2 x + \beta x^3 = f\cos\omega t. \tag{1}$$

The motivation for our interest in this system is that it has wide range of applications in physics and biology. Equation (1) is an alternative form of Bonhoeffer–van der Pol oscillator [11, 12], driven magnetic oscillator [15] and also describes the dynamics of charge density in the plasma of a rf gas discharge. It exhibits well developed chaos in the parameter space [15–18]. Our objective here is to explore the possibility of controlling the horseshoe dynamics and asymptotic chaos using both analytical and numerical techniques. Horseshoe is the occurrence of transverse intersections of stable and unstable manifolds of saddle fixed point in the Poincaré map and is a global phenomenon [19, 20]. The appearance of which can be predicted analytically using the Melnikov technique [19]. It is well-known that the existence of horseshoe does not imply that the typical trajectories will be asymptotically chaotic. The asymptotically chaotic motion is characterized by positive maximal Lyapunov exponent. In our present analysis we use the Melnikov method to study the influence of periodic perturbations on horseshoe dynamics. Lyapunov exponents and Poincaré map are used to detect the suppression of chaos.

Firstly we investigate the effect of parametric perturbation $\beta\eta x^3 \cos\Omega t$ added in (1). The unperturbed part of the system (1) $(p=f=\eta=0)$ possesses two homoclinic orbits which we denote as W_+ and W_-. For $\eta=0$ we fixed the value of other parameters at a specific value so that the system shows both asymptotic chaos and transverse intersections of homoclinic orbits. From the Melnikov analysis we found that suppression of horseshoe is not possible in the (η, Ω) parameter space. However, we are able to identify the parametric regimes where intersections of stable and unstable branches of either W_+ or W_- alone occur. On the other hand, suppression of stable chaotic motion is found for range of values of amplitude and frequency of the perturbation. Secondly, we report our analytical and numerical studies on the DVP equation (1) with the second weak periodic force $\eta \cos\Omega(t+\phi)$ where ϕ is the initial phase shift. The most striking result is that horseshoe chaos is suppressed in various regimes in the (η, ϕ) parameter space. These regimes are predicted analytically using the Melnikov method. Analytical prediction is in good agreement with the numerical result. Another key observation is the recovery of periodic behaviour in the parametric intervals where the Melnikov function does not change sign.

The paper is organized as follows. In § 2 chaotic dynamics in DVP equation for a specific parametric choice is briefly reviewed. Then the effect of parametric perturbation on horseshoe dynamics is analysed using the Melnikov method. The analytical prediction is demonstrated through direct numerical simulations. Controlling of asymptotic chaos is also studied. Section 3 is devoted to the detailed study of DVP oscillator driven by second periodic force. Threshold curves in the (η, ϕ) space for the suppression of horseshoe is obtained. The analytical prediction is compared with the numerical results. Further, numerical simulations are performed to study the controlling of asymptotic chaos through maximal Lyapunov exponent. Finally, § 4 contains summary and conclusion.

2. Parametrically driven Duffing–van der Pol oscillator

2.1 *Preliminaries and calculation of Melnikov function*

We consider the DVP equation with a periodic parametric perturbation of the cubic term

$$\dot{x} = y, \tag{2a}$$

$$\dot{y} = \alpha^2 x - \beta x^3 (1 + \varepsilon\eta\cos\Omega t) - \varepsilon[p(1-x^2)y - f\cos\omega t], \tag{2b}$$

where η is the amplitude and Ω the frequency of the periodic perturbation. Because the Melnikov method is based on the perturbation theory we have introduced a small parameter ε into the equations of motion.

The unperturbed system of (2)($\varepsilon = 0$) has a saddle fixed point $(x^*, y^*) = (0,0)$ and two centre type fixed points $(\pm\alpha/\sqrt{\beta}, 0)$. The two homoclinic orbits which connects saddle to itself are given by

$$W_{\pm}(x_h(\tau), y_h(\tau)) = (\pm\alpha\sqrt{2/\beta}\operatorname{sech}\alpha\tau, \mp\alpha^2\sqrt{2/\beta}\operatorname{sech}\alpha\tau\tanh\alpha\tau), \quad \tau = t - t_0. \tag{3}$$

For $\varepsilon = 0$, the stable and unstable branches of homoclinic orbits join smoothly. When the dissipative perturbation is included the stable manifold W^s and the unstable manifold W^u do not join. However, above certain critical amplitude of the external periodic force, transverse intersections of W^s and W^u occur. The presence of such intersections implies that the Poincaré map has the so-called horseshoe chaos [19, 20]. Even though the orbits created by the horseshoe mechanism are unstable they can exert a dramatic influence on the behaviour of orbits which pass close to the point of intersection. These orbits will display an extremely sensitive dependence on initial conditions and exhibit a chaotic transient before settling to a periodic or strange attractors. The appearance of transverse intersections of homoclinic orbits can be predicted analytically by the Melnikov technique. For a system of the form

$$\mathrm{d}X/\mathrm{d}t = h_0(X) + \varepsilon h_1(X, t, \varepsilon), \tag{4}$$

where $X = (x, y)$, $h_0 = (f_0, g_0)$ and $h_1 = (f_1, g_1)$ the expression for the Melnikov function is given by [19, 20]

$$M(t_0) = \int_{-\infty}^{\infty} h_0(X_h(\tau)) \wedge h_1(X_h(\tau), t)\exp\left[-\int_0^{\tau}\operatorname{trace}[D_X(h_0(X_h(s)))]\mathrm{d}s\right]\mathrm{d}\tau. \tag{5}$$

Here X_h represents homoclinic orbit, $h_0 \wedge h_1 = f_0 g_1 - f_1 g_0$ and D_X denotes the partial derivative with respect to X.

For the DVP equation (2) the Melnikov function is

$$M(t_0) = \int_{-\infty}^{\infty} y_h[-py_h(1 - x_h^2) - \beta\eta x_h^3\cos\Omega(\tau + t_0) + f\cos\omega(\tau + t_0)]\mathrm{d}\tau. \tag{6}$$

Evaluating the integral using (3) we obtain

$$M(t_0) = \pm Af\sin\omega t_0 - B\eta\sin\Omega t_0 - C, \tag{7a}$$

where

$$A = \sqrt{2/\beta}\pi\omega\operatorname{sech}(\pi\omega/(2\alpha)),$$
$$B = (\pi/(6\beta))\Omega^2(4\alpha^2 + \Omega^2)\operatorname{cosech}(\pi\Omega/(2\alpha)),$$
$$C = 4p\alpha^3(5\beta - 4\alpha^2)/(15\beta^2). \tag{7b}$$

Before we go on to study the effect of parametric perturbation we briefly show the occurrence of chaotic dynamics for $\eta = 0$. For $\eta = 0$, the condition for transverse intersection of W^s and W^u is that $M(t_0)$ changes sign at some t_0 which occurs, from (7), for

$$|f| \geq f_M = 2\sqrt{2}p\alpha^3(5\beta - 4\alpha^2)\cosh(\pi\omega/(2\alpha))/(15\beta^{3/2}\pi\omega). \tag{8}$$

Equation (8) is the necessary condition for the occurrence of horseshoe. The sufficient condition requires the existence of simple zeros of $M(t_0)$. For our further analysis we fix $\alpha = 1$, $\beta = 5$ and $p = 0{\cdot}4$. For $\omega = 1$ the Melnikov analytical threshold value f_M is 0·1132. Figure 1 shows the numerically computed W^s and W^u of the saddle in the Poincaré map for $f = 0{\cdot}08$ and $f = 0{\cdot}125$. The unstable manifolds are obtained by integrating eq. (2) in the forward time for a set of 200 initial conditions chosen around the perturbed saddle point. The stable mainfolds are obtained by integrating the equations of motion in reverse time. For $f = 0{\cdot}08$ the two orbits are separated for which the Melnikov function is always negative. For $f = 0{\cdot}125$ from figure 1b we can clearly notice transverse intersections of orbits at four places. For $f < 0{\cdot}125$ asymptotically periodic motion is observed. Onset of chaotic motion is observed at $f = 0{\cdot}125$. For clarity, the chaotic orbit in the $x - y$ plane and the strange attractor

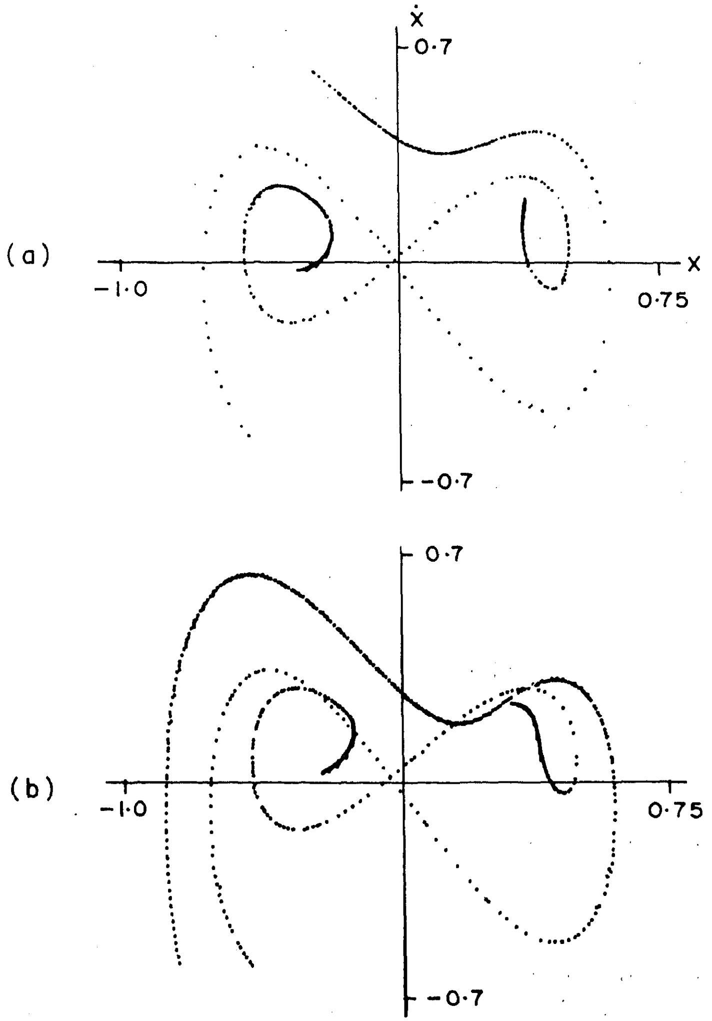

Figure 1. Numerically computed stable and unstable manifolds of saddle fixed point for $\alpha^2 = 1$, $\beta = 5$, $\omega = 1$, $\eta = 0$ and (**a**) $f = 0{\cdot}08$ and (**b**) $f = 0{\cdot}125$.

in the Poincare map are given in figure 2. We also study the effect of periodic perturbations on horseshoe dynamics and chaotic motion observed for $f = 0{\cdot}125$.

2.2 *Effect of weak parametric perturbation on homoclinic bifurcation*

For $\eta \neq 0$ the necessary condition for $M(t_0)$ to change sign is

$$\eta^{\pm} \leqslant \eta_M = \frac{6\beta(\pm Af - C)\sinh(\pi\Omega/2\alpha)}{\pi\Omega^2(4\alpha^2 + \Omega^2)}, \tag{9a}$$

or

$$\eta^{\pm} \geqslant \eta_M = \frac{6\beta(\pm Af + C)\sinh(\pi\Omega/2\alpha)}{\pi\Omega^2(4\alpha^2 + \Omega^2)}, \tag{9b}$$

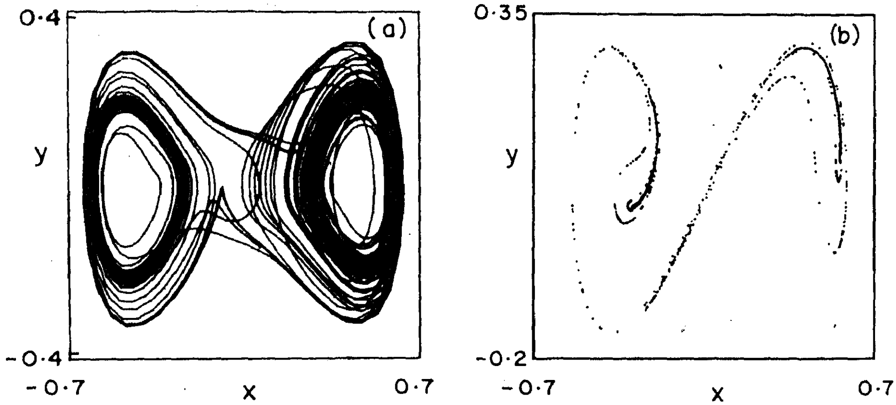

Figure 2. (**a**) Phase portrait and (**b**) Poincaré map of the chaotic attractor for $f = 0{\cdot}125$.

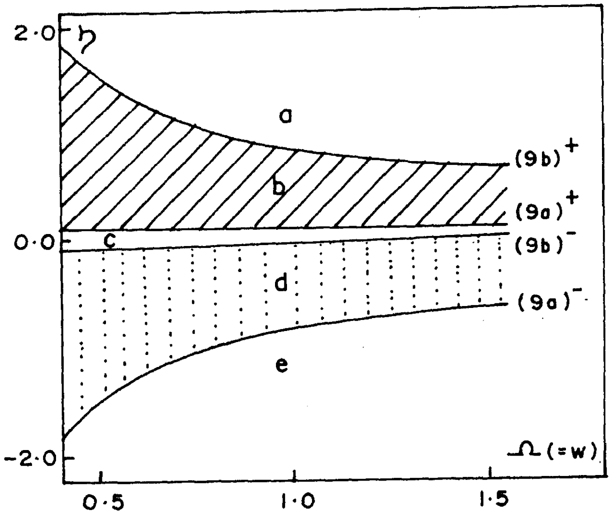

Figure 3. Melnikov threshold curves for horseshoe chaos in (η, Ω) plane.

where the superscripts '+' and '−' refer to the homoclinic orbits W_+ and W_- respectively. In general, for arbitrary values of ω and Ω, the above condition is not sufficient to ensure the existence of simple zeros of $M(t_0)$ in (7). However, the condition (9) is sufficient if the frequency Ω is in resonance with ω, that is, $p\Omega = q\omega$ where p and q are some positive integers. Figure 3 shows the threshold value of $\eta(\Omega)$ for $\Omega = \omega$. In the (η, Ω) parameter space tranverse intersections of W^s_+ and W^u_+ occur below the curve $(9a)^+$ and above the curve $(9b)^+$. While one can expect transverse intersections of W^s_- and W^u_- above the curve $(9b)^-$ and below the curve $(9a)^-$. Thus, horseshoe chaos occur in the entire (η, Ω) parameter space. However, in the shaded (dotted) region intersections of stable and unstable branches of W_+ (W_-) do not occur. We have verified the above analytical predictions by direct numerical simulations of the DVP equation (2). As an example, figure 4 shows the part of the stable and unstable orbits of saddle in the Poincaré map for $\Omega = 1$ and for four values of η chosen in the regions, *a*, *b*, *c* and *d*. Transverse intersections of stable and unstable branches of both the homoclinic orbits W_+ and W_- can be clearly seen in figure 4a for $\eta = 0{\cdot}85$ which falls in the region *a*. In figure 4b we see the intersections of W_- orbits alone at one place for $\eta = 0{\cdot}3$ (region *b*). While for $\eta = -0{\cdot}01$ (region *c*) intersections of both the homoclinic orbits has been found. This is shown in figure 4c. For $\eta = -0{\cdot}25$ (figure 4d), which correspond to the region *d*, branches of W_+ orbit alone found to intersect. These numerical results agree well with the theoretical predictions.

For $\Omega \neq \omega$ the appearance of horseshoe can be studied numerically measuring the time τ_M elapsed between two successive transverse intersections. τ_M, the first simple zero of $M(t_0)$, can be determined from (7). In figure 5 we have plotted $1/\tau_M$ as a function of Ω for $\eta = 0{\cdot}02$. Curve *a* corresponds to positive sign while curve *b* corresponds to negative sign in (7). Horseshoe chaos occur in the region where $1/\tau_M > 0$. Lower the $1/\tau_M$, higher is the number of iterates of Poincare map needed to guarantee a horseshoe. When Ω increases new intersection times suddenly appear which are responsible for the observed jumps of the function $1/\tau_M$ in figure 5. Further, we note that for Ω less than certain critical value the $1/\tau_M$ depicted by the curve *a* becomes zero, which indicates that in this Ω interval intersection of orbits of W_+ does not occur.

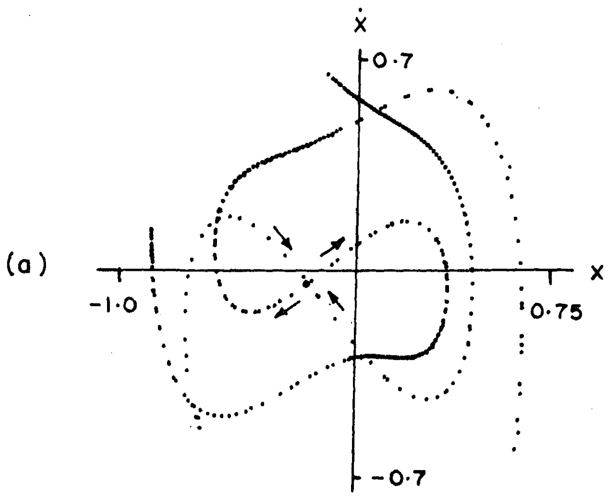

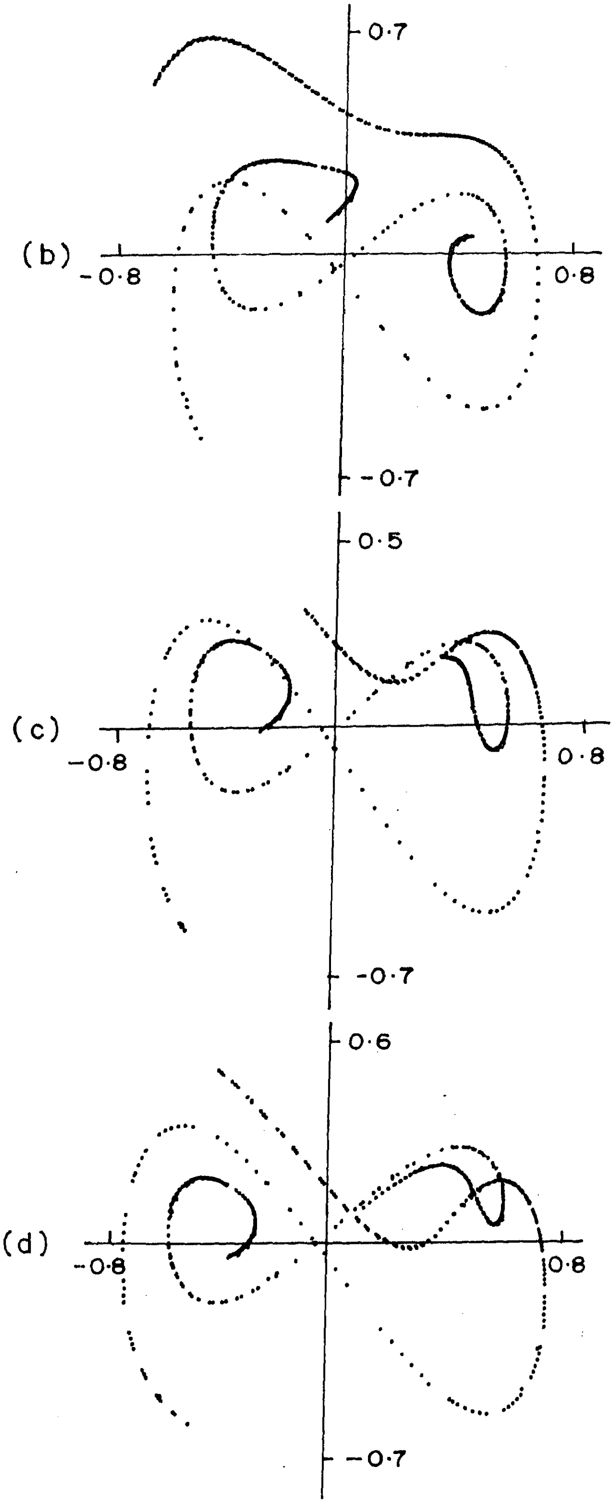

Figure 4. Parts of the stable and unstable manifolds of the saddle fixed point in the Poincaré map of (2) for (**a**) $\eta = 0{\cdot}85$, (**b**) $\eta = 0{\cdot}3$, (**c**) $\eta = -0{\cdot}01$ and (**d**) $\eta = -0{\cdot}25$.

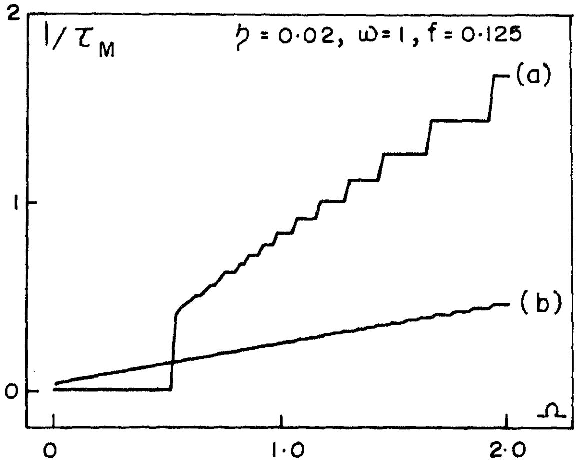

Figure 5. Variation of $1/\tau_M$ versus Ω for $\eta = 0{\cdot}02$. Curve a is for positive sign and curve b is for negative sign in equation (7).

2.3 *Controlling of asymptotic chaos*

In this subsection, starting from a chaotic region (figure 2) we explore the possibility of suppression of chaos for a range of values of η and Ω. A full-fledged phase diagram would be very valuable; however, with the limited computing facilities available we have investigated the dynamics in a restricted region, namely, (i) Ω fixed and η varying with increment $\Delta\eta = 0{\cdot}005$, (ii) η fixed and Ω varying with $\Delta\Omega = 0{\cdot}01$.

We confine our analysis in the parameter regime $\eta \in (0, 0{\cdot}2)$ and $\Omega \in (0, 3)$ only. For $\Omega = 0{\cdot}5$ chaotic behaviour persists for $\eta \leqslant 0{\cdot}13$ and period-$2T (T = 2\pi/\omega)$ motion is observed for $\eta \geqslant 0{\cdot}135$. For $\Omega = 1$ and 2 periodic motion with period-T occurs for $\eta \geqslant 0{\cdot}005$. Regular motion is recovered for Ω values near the resonance value to ω. For example, when $\Omega = 1{\cdot}1$ period $- 10T$ orbit is found for η values in the interval (0·055, 0·065), (0·085, 0·105) and (0·115, 0·2). Similarly, for fixed η values the nature of orbits for different Ω has been investigated. For small values of η regular motion is observed for very narrow regimes of Ω values. For $\eta = 0{\cdot}05$ periodic motion is found only at $\Omega = 1{\cdot}0(p-1)$, $2(p-1)$ and $3(p-4)$ and for $\eta = 0{\cdot}1$ suppression of chaotic behaviour is observed at $\Omega = 1(p-1)$, $1{\cdot}1(p-10)$ and $2(p-1)$. However, the width of the regular regime increases with increase in η. For example, for $\eta = 0{\cdot}18$ periodic motion is recovered at $\Omega = 0{\cdot}5(p-2)$, $0{\cdot}8(p-5)$, $1{\cdot}0(p-1)$, $1{\cdot}6(p-5)$, $1{\cdot}7(p-10)$, $1{\cdot}8(p-5)$, $2{\cdot}0(p-1)$, $2{\cdot}2(p-10)$, $2{\cdot}4(p-5)$, $2{\cdot}5(p-5)$, $2{\cdot}8(p-5)$ and $3(p-1)$.

3. Effect of second periodic force

One can also control the dynamics of a system by the addition of an external weak periodic force in the chaotic state. The DVP equation with second periodic force can be written as

$$\dot{x} = y, \tag{10a}$$

$$\dot{y} = \alpha^2 x - \beta x^3 - \varepsilon[p(1-x^2)y - f\cos\omega t - \eta\cos\Omega(t+\phi)], \tag{10b}$$

where ϕ is the phase shift. Here again we investigate controlling of chaotic dynamics using both Melnikov method and numerical techniques.

3.1 *Suppression of horseshoe chaos*

For system (10) the Melnikov function works out to be

$$M(t_0) = \pm Af \sin \omega t_0 \pm B\eta \sin \Omega (t_0 + \phi) - C, \tag{11a}$$

where

$$A = \sqrt{2/\beta}\pi\omega \operatorname{sech}(\pi\omega/2\alpha), \quad B = \sqrt{2/\beta}\pi\Omega \operatorname{sech}(\pi\Omega/2\alpha),$$
$$C = 4p\alpha^3(5\beta - 4\alpha^2)/(15\beta^2). \tag{11b}$$

First, we consider the case where the phase shift ϕ is zero. Now $M(t_0)$ becomes

$$M(t_0) = \pm Af \sin \omega t_0 \pm B\eta \sin \Omega t_0 - C. \tag{12}$$

Since the choice $\Omega = \omega$ is trivial we study the existence of horseshoe for $\Omega \neq \omega$. As mentioned earlier, we cannot write the Melnikov condition similar to (9) for arbitrary values of ω and Ω. So, we estimate the first intersection time τ_M and identify the parametric regime where $1/\tau_M \approx 0$. Figure 6 shows the plot of $1/\tau_M$ against Ω for $\eta = -0{\cdot}2$, $\omega = 1$ and $f = 0{\cdot}125$. Curve *a* represents the inverse of first intersection time of stable and unstable branches of the homoclinic orbit W_+. Curve *b* corresponds to the orbit W_-. $1/\tau_M$ is nonzero for the whole interval of Ω except at $\Omega = 1$. At $\Omega = 1$, $1/\tau_M$ is zero. This implies that horseshoe does not occur at $\Omega = 1$.

Now we describe what happens when ϕ is not zero. For $\phi > 0$ and $\omega = \Omega$ (which gives $A = B$) the Melnikov function is given by

$$M(t_0) = \pm (Af + A\eta \cos \omega\phi) \sin \omega t_0 \pm A\eta \sin \Omega\phi \cos \omega t_0 - C. \tag{13}$$

From the above equation, the condition for $M(t_0)$ to change sign is

$$\eta^2 + 2\eta \cos \Omega\phi + (f^2 - C^2/A^2) \geqslant 0. \tag{14}$$

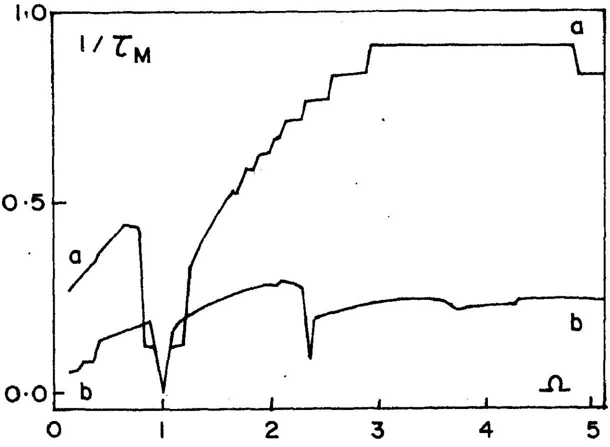

Figure 6. $1/\tau_M$ versus Ω for $\eta = -0{\cdot}2$. Curve *a* corresponds to positive sign while curve *b* corresponds to negative sign in equation (12).

When the equality is satisfied we have

$$\eta = -\cos\Omega\phi \pm [f^2\cos^2\Omega\phi + (C^2/A^2 - f^2)]^{1/2}. \tag{15$^\pm$}$$

From (14) and (15) we note that $M(t_0)$ changes sign, that is, the transverse intersection of homoclinic orbits, occur above and below the curves given by equations $(15)^+$ and $(15)^-$ respectively. These curves are shown in figure 7 for $\Omega = 1$. In the parametric regions *a*, *b* and *c* enclosed by the curves, $M(t_0)$ does not change sign and hence transverse intersections of homoclinic orbits do not occur. This is exactly what we observed numerically. As an example, figure 8 shows the numerical simulations for three η values. We fixed the value of ϕ at 1·0. For this choice from (14) we note that $M(t_0)$ changes sign and transverses intersections of homoclinic orbits occur for $\eta > -0{\cdot}026$ and $\eta < -0{\cdot}11$. This is shown in figures 8a and 8c for $\eta = -0{\cdot}02$ and $-0{\cdot}13$ respectively. Further, one can expect suppression of transverse intersections of orbits for $\eta \in (-0{\cdot}11, -0{\cdot}026)$. This is depicted in figure 8b for $\eta = -0{\cdot}05$ where both the orbits are well separated. Thus, suppression of horseshoe can be achieved for a range of values of η, Ω and ϕ.

3.2 *Controlling of asymptotic chaos*

Now we show the suppression of chaotic motion depicted in figure 2 by second periodic force. We have carried out analysis for Ω fixed and η varying with $\Delta\eta = 0{\cdot}005$. Table 1 summarizes the behaviour of the system as a function of the parameter η for five fixed values of Ω with $\phi = 0$. From this table we note that regular motion can be recovered for wide range of values of η and Ω. Here the suppression of chaos is by mode-locking.

Next, we consider the case $\phi > 0$. We have pointed out earlier that the Melnikov function $M(t_0)$ does not change sign and consequently no horseshoe dynamics occur in the regions *a*, *b* and *c* of figure 7. The striking result is that suppression of stable

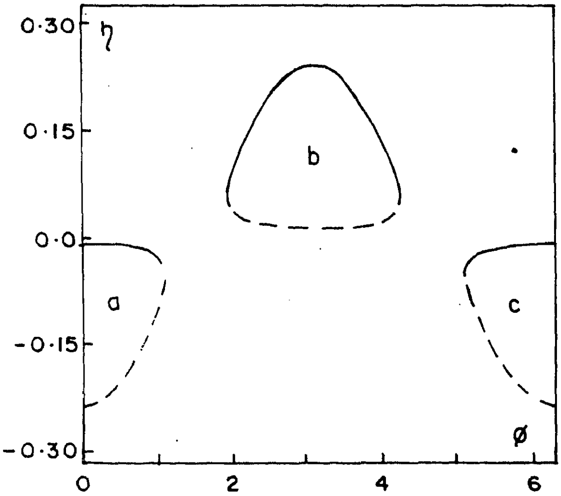

Figure 7. Graph of $(15)^\pm$. Horseshoe does not occur in the regions *a*, *b* and *c* enclosed by the curves. Continuous and dashed curves represent the solution of equation $(15)^+$ and equation $(15)^-$ respectively.

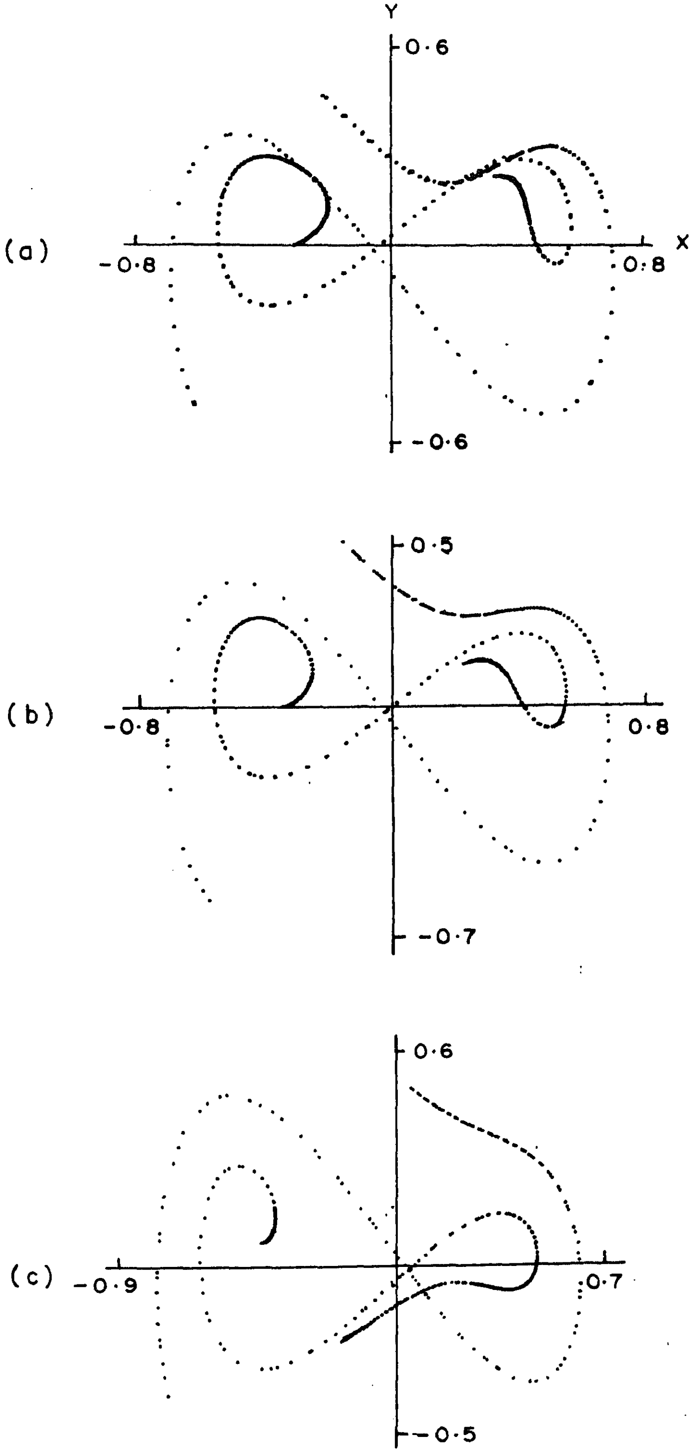

Figure 8. Numerically computed part of perturbed homoclinic orbits for **(a)** $\eta = -0{\cdot}02$, **(b)** $\eta = -0{\cdot}05$ and **(c)** $\eta = -0{\cdot}13$. The other parameters in equation (10) are fixed at $\alpha^2 = 1$, $\beta = 5$, $\omega = 1$, $f = 0{\cdot}125$, $\Omega = 1$ and $\phi = 1$.

Table 1. Dynamical behaviour of the DVP equation in the presence of second periodic force for five fixed values of Ω as a function of η.

Ω	η	behaviour
0·5	0 – 0·045	chaos
	0·05	period-6
	0·055 – 0·2	period-2
1·0	0 – 0·135	chaos
	0·14 – 0·2	period-1
1·4	0 – 0·045	chaos
	0·05 – 0·18	period-5
	0·185 – 0·2	chaos
1·5	0 – 0·08	chaos
	0·085 – 0·175	period-5
	0·18 – 0·19	period-8
2·0	0	chaos
	0·005 – 0·165	period-1
	0·17 – 0·2	chaos

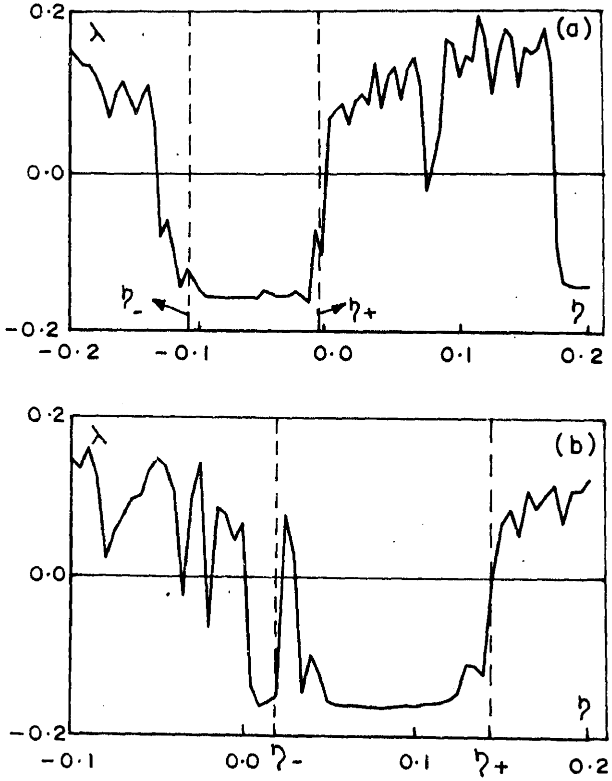

Figure 9. Estimated maximal Lyapunov exponent versus the parameter η for (**a**) $\phi = 1$ and (**b**) $\phi = 2{\cdot}2$. η_+ and η_- are the Melnikov threshold values given by the equation $(15)^{\pm}$.

chaotic motion is also found in these parametric regions. In figure 9 maximal Lyapunov exponent (λ) versus the parameter η is reported for $\Omega = 1$, $\phi = 1$ and 2·2. For $\phi = 1$ as shown earlier transverse intersections of homoclinic orbits do not occur for η values in the interval $(-0{\cdot}11, -0{\cdot}026)$. From figure 9a we find that λ is negative for $\eta \in (-0{\cdot}13, -0{\cdot}005)$. Similar result has been observed for various ϕ values in the regions a, b and c. For clarity, we summarize our results in table 2 for two values of ϕ. From our detailed analysis we infer that the Melnikov function $M(t_0)$ does not change sign for all t_0. This can serve as an analytical criterion to study the suppression of asymptotic chaos.

We have also performed our analysis outside the regions a, b and c of figure 7. In these regions horseshoe still persists. However, it is well known that the presence of horseshoe does not guarantee that typical long time motion is chaotic. In fact, in these regions we found regular behaviour for very narrow ranges of η and Ω values. This is evident from figure 10 where λ is negative only at six narrow ranges of η

Table 2. Details of theoretical and numerical predictions of the DVP system with second periodic force. $M(t_0)$ and λ denote the Melnikov function and maximal Lyapunov exponent respectively.

ϕ	η interval where the sign of $M(t_0)$ remain unchanged	η interval with $\lambda < 0$	η values	behaviour
1·0	$(-0{\cdot}11, -0{\cdot}026)$	$(-0{\cdot}13, -0{\cdot}02)$	$(-0{\cdot}2)-(-0{\cdot}13)$	chaos
			$(-0{\cdot}125)-(-0{\cdot}1)$	period-1
			$(-0{\cdot}095)-(-0{\cdot}03)$	period-2
			$(-0{\cdot}025)-(-0{\cdot}005)$	period-1
			$(0{\cdot}0)-(0{\cdot}2)$	chaos
2·2	$(0{\cdot}022, 0{\cdot}124)$	$(0{\cdot}005, 0{\cdot}02)$, $(0{\cdot}035, 0{\cdot}145)$	$(-0{\cdot}1)-(0{\cdot}0)$	chaos
			$0{\cdot}005-0{\cdot}02$	period-1
			$0{\cdot}025-0{\cdot}03$	chaos
			$0{\cdot}035-0{\cdot}045$	period-2
			$0{\cdot}05-0{\cdot}145$	period-1
			$0{\cdot}15-0{\cdot}2$	chaos

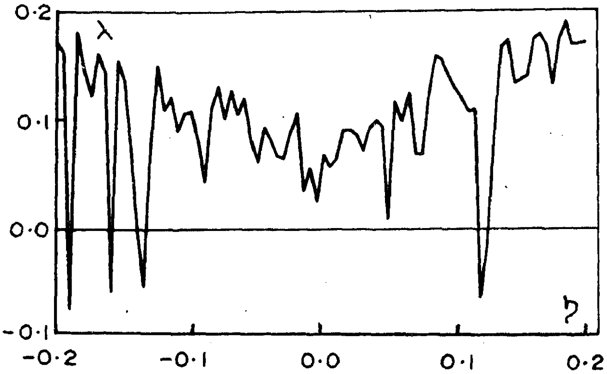

Figure 10. Variation of maximal Lyapunov exponent as a function of the parameter η for $\phi = 1{\cdot}5$.

values for $\phi = 1{\cdot}5$. For example, attractors with period-2 at $\eta = -0{\cdot}19$ and period-3 at $\eta = -0{\cdot}16$, $-0{\cdot}14$, $-0{\cdot}135$, $0{\cdot}12$ and $0{\cdot}125$ are found to occur.

The results presented in this section have shown how a relatively weak periodic force can change the global and local dynamics of the system in a drastic fashion; horseshoe and chaotic dynamics can be controlled.

4. Summary and conclusion

We have studied the effect of periodic perturbations on chaotic dynamics in the DVP oscillator. For typical parametric values we have shown that suppression of horseshoe is not possible by periodic parametric perturbation. However, suppression of horseshoe has been found for a range of amplitude of a second periodic force and phase shift between the two external forces. The system dynamics is sensitive to the initial phase shift. The effect of both types of periodic perturbations on stable chaotic motion is similar. In both the cases regular behaviour has been recovered for range of amplitude and frequency of the weak perturbations.

The other control mechanisms such as adaptive control algorithm [5, 6, 12], Ott-Grebogi-Yorke method [4] and feedback control mechanism [8] have the advantage of stabilizing a desired periodic motion. Whereas our analysis shows that chaotic motion can be converted to some regular motion by weak periodic perturbations. Further, the period of the controlled motion depends on η and Ω values. Thus, for a given chaotic system one has to carry out detailed numerical simulations in η, Ω space to identify the regular regime. However, for the DVP equation we have shown that most of the regular regime can be identified by the Melnikov method. With the good agreement obtained between theoretical and numerical predictions we emphasize that Melnikov analysis can be successfully used to predict the effect of weak periodic perturbations on chaos. In fact, for a large class of physical problems the calculation of Melnikov function is possible and hence the study of controlling of chaos by this analytical method will be of much interest.

Acknowledgements

It is a pleasure to thank Dr K P N Murthy for a critical reading of the manuscript. The author is indebted to Indira Gandhi Centre for Atomic Research, Kalpakkam for a visiting scientist fellowship.

References

[1] L M Pecora and T L Carroll, *Phys. Rev. Lett.* **64**, 821 (1990)
[2] M de Sousa Vieira, A J Lichtenberg and M A Lieberman, *Int. J. Bifur. Chaos* **1**, 691 (1991)
[3] J M Ottino *et al*, *Science* **257**, 754 (1992)
[4] E Ott, C Grebogi and J Yorke, *Phys. Rev. Lett.* **64**, 1196 (1990)
[5] B A Huberman and E Lumer, *IEEE Trans. Circuits Syst.* **37**, 547 (1990)
[6] S Sinha, R Ramaswamy and J Subba Rao, *Physica* **D43**, 118 (1990)
[7] R Lima and M Pettini, *Phys. Rev.* **A41**, 726 (1990)
[8] J Singer, Y Z Wang and H H Bau, *Phys. Rev. Lett.* **66**, 1123 (1991)
[9] Y Braiman and I Goldhirsch, *Phys. Rev. Lett.* **66**, 2545 (1991)
[10] E A Jackson, *Phys. Rev.* **A44**, 4839 (1991)
[11] S Rajasekar and M Lakshmanan, *Int. J. Bifur. Chaos* **2**, 201 (1992)
[12] S Rajasekar and M Lakshmanan, *Physica* **D67** 282 (1993)

[13] K Wiesenfeld and B McNamara, *Phys. Rev.* **A33**, 629 (1986)
[14] P Bryant and K Wiesenfeld, *Phys. Rev.* **A33** 2525 (1986)
[15] J Fang, *Phys. Lett.* **A146**, 35 (1990)
[16] S Rajasekar, S Parthasarathy and M Lakshmanan, *Chaos, Solitons and Fractals* **2**, 271 (1992)
[17] G P King and S T Gaito, *Phys. Rev.* **A46** 3092 (1992)
[18] M G M Gomes and G P King, *Phys. Rev.* **A46** 3100 (1992)
[19] S Wiggins, *Global bifurcations and chaos* (Springer, Berlin, 1988)
[20] J Guckenheimer and P Holmes, *Nonlinear oscillations, dynamical systems and vector fields* (Springer, Berlin, 1983)

PRAMANA
— journal of
physics

© Printed in India

Vol. 41, No. 4,
October 1993
pp. 311–327

Mathematical analysis of isobaric decay chain in alpha particle induced reactions

S MUKHERJEE, N L SINGH* and J RAMA RAO**
School of Studies in Physics, Vikram University, Ujjain 456 010, India
*Physics Department, MS University, Baroda 390 001, India
**Physics Department, Banaras Hindu University, Varanasi 221 005, India

MS received 15 February 1993; revised 20 July 1993

Abstract. A detailed mathematical formalism is developed from the first principles, to separate out the fractional contributions of the cross-section σ_g and σ_p for the production of the two isobaric precursor nuclei- grand parent and parent, respectively, to the cross-section σ_d for the formulation of the residual nucleus of interest. The analytical work of separating out such contributions gives a meaningful picture to the comparison with the theoretical predictions of hybrid model, using the initial exciton number $n_0 = 4(4p\,0h)$.

Keywords. Isobaric precursors; decay chain; Batemann's equations; hybrid model.

PACS No. 24·90

1. Introduction

During the last decade, a great deal of experimental studies and phenomenological modelling effort has been expended in order to explain the pre-equilibrium complex particle emission in the intermediate energy nuclear reactions [1, 2]. A large number of experimental measurements of the excitation functions has been made for a better understanding of the reactions involving complex particles [3, 4]. A detailed analysis of the experimental data [5] indicates that, even if the available measurements were accurate enough, the results disagree with the theory by several orders of magnitude. One of the reasons for this discrepancy is because the excitation functions represent the combined effects of two or more different reactions which produce beta decaying isobars, leading to the actually observed residual nucleus.

The above situation is often encountered in the activation method for the determination of excitation functions for (α, pxn) and $(\alpha, \alpha xn)$ type of reactions. For example, one can see that for a given target, the $[\alpha, (x+4)n]$, $[\alpha, p(x+3)n]$ and $[\alpha, \alpha xn]$ reactions lead to residual nuclei which are isobars of one another and form a beta-decaying chain. Thus, the growth and decay of the last residual nucleus are influenced by the contributions coming from its isobaric precursors. In such cases, the simple expression [6]

$$\sigma = \frac{\lambda A_i A_\gamma}{\phi P_i W_i P_\gamma \theta_\gamma \mathrm{Nav}(1-\exp(-\lambda t_i))\exp(-\lambda tw)(1-\exp(-\lambda\Delta))}$$

cannot be used to determine the cross-section of the residual (daughter) nucleus, since it does not take into account the contributions from the decaying parent and grandparent isobars (these include the contributions during their growth throughout the period of irradiation and also later due to their decay).

In the earlier reports on such inclusive excitation functions, no mention has been made about the possible isobaric precursor contributions [3] and no attempt has been made to account for them quantitatively. In the present work, a detailed formalism is developed from the first principles to separate out exactly, point-by-point, the isobaric precursor contributions from the measured excitation functions relevant to the particular reaction under study. This will enable a direct comparison of the theory and experiment for a single specified reaction.

With this end in view, the activation cross-section of four $(\alpha, xnypz\alpha)$ types of reactions on the target element niobium, in the energy range from threshold to 120 MeV, were adopted from our earlier measurements [5], for the analysis of isobaric precursor contributions, and to compare the results with the relevant theoretical calculations, on the basis of hybrid model [7].

2. Mathematical formalism

Let T be a target containing N_T nuclei per unit area and ϕ be the flux of α-particles incident on it for a period of time x. During this period of irradiation, three isobaric nuclei, G, P and D are produced through (α, xn), $(\alpha, px'n)$ and $(\alpha, \alpha x''n)$ reactions with cross-sections σ_g, σ_p and σ_d respectively. Also the isobaric nuclei are all radioactive with disintegration constants λ_g, λ_p and λ_d respectively and forming a radioactive decay chain

$$G \xrightarrow{\lambda_g} P \xrightarrow{\lambda_p} D \xrightarrow{\lambda_d}$$

to be designated by the notation that G stands for grandparent, P stands for parent and D for the daughter nucleus.

After a period of irradiation, x, the products are allowed to decay for a waiting time t_a and then the activity of the daughter nucleus D is measured up to the time t_b starting from t_a.

Treating T as a long-lived $(\lambda_T \simeq 0)$ leading member of a (fictitious) radioactive series

$$T \xrightarrow[\sigma_g]{\lambda_T} G \xrightarrow{\lambda_g} P \xrightarrow{\lambda_p} D \xrightarrow{\lambda_d}$$

the reaction yield of the grandparent G through (α, xn) reaction with cross-section σ_g can be simulated by using standard Batemann's equations [8] and making the substitutions,

$$T\lambda_T = \phi N_T \sigma_g$$

and

$$\lambda_T \simeq 0.$$

Similarly, the reaction yield of the parent P through $(\alpha, px'n)$ reaction with cross-section σ_p can be simulated by the (fictitious) radioactive series

$$T \xrightarrow[\sigma_p]{\lambda_T} P \xrightarrow{\lambda_p} D \xrightarrow{\lambda_g}$$

with the following substitutions in Batemann's equations:

$$T\lambda_T = \phi N_T \sigma_p$$

and

$$\lambda_T \simeq 0.$$

Likewise the direct production of the daughter nucleus D through the reaction $(\alpha, \alpha x''n)$ with a cross-section σ_d can be simulated by the (imaginary) radioactive series

$$T \underset{\sigma_d}{\overset{\lambda_T}{\rightarrow}} D \overset{\lambda_d}{\rightarrow}$$

with the following substitutions in Batemann's equations

$$T\lambda_T = \phi N_T \sigma_d$$

and

$$\lambda_T \simeq 0.$$

For simplicity of notation, let the letters T, G, P and D also stand for the numbers of radioactive nuclei of that kind, present at the instant of time under consideration.

The above described scenario can be schematically represented as follows:

$$\begin{tikzcd}
T \arrow[r, "\sigma_g"] \arrow[drr, "\sigma_p"] \arrow[ddrrr, "\sigma_d"] & G \arrow[r, "\lambda_g"] & P_1 \arrow[r, "\lambda_p"] & D_1 \arrow[r, "\lambda_d"] & {} \\
\lambda_T & & P_2 \arrow[r] & D_2 \arrow[r] & {} \\
 & & & D_3 \arrow[r] & {}
\end{tikzcd}$$

Stage 1: *Up to the end of irradiation* (x)

According to Batemann's equation,

$$G\lambda_g = (T\lambda_T)\frac{\lambda_g}{\lambda_g - \lambda_T}[1 - \exp(-(\lambda_g - \lambda_T)x)]$$

Substituting

$$\lambda_T = 0,$$

$$T\ \lambda_T = \phi N_T \sigma_g$$

One has

$$G_x = \frac{\phi N_T \sigma_g}{\lambda_g}(1 - \exp(-\lambda_g x)) \tag{1}$$

$$P_1\lambda_p = T\lambda_T\left[\frac{\lambda_g}{\lambda_g - \lambda_T}\frac{\lambda_p}{\lambda_p - \lambda_T}\frac{\lambda_g}{\lambda_T - \lambda_g}\frac{\lambda_p}{\lambda_p - \lambda_g}\exp(-(\lambda_g - \lambda_T)x)\right.$$
$$\left. + \frac{\lambda_g}{\lambda_g - \lambda_p}\frac{\lambda_p}{\lambda_T - \lambda_p}\exp(-(\lambda_p - \lambda_T)x)\right].$$

Substituting

$$\lambda_T = 0,$$

$$T\lambda_T = \phi N_T \sigma_g$$

One has,

$$P_1 = \frac{\phi N_T \sigma_g}{\lambda_p}\left[1 - \frac{\lambda_p}{\lambda_p - \lambda_g}\exp(-\lambda_g x) - \frac{\lambda_g}{\lambda_g - \lambda_p}\exp(-\lambda_p x)\right] \tag{2a}$$

$$P_2 \lambda_p = (T\lambda_T)\frac{\lambda_p}{\lambda_p - \lambda_T}[1 - \exp(-(\lambda_p - \lambda_T)x)]$$

Substituting

$$\lambda_T = 0,$$

$$T\lambda_T = \phi N_T \sigma_p$$

One has

$$P_2 = \frac{\phi N_T \sigma_p}{\lambda_p}(1 - \exp(-\lambda_p x)). \tag{2b}$$

Combining (2a) and (2b), one defines

$$P_x = P_1 + P_2$$

$$P_x = \frac{\phi N_T \sigma_g}{\lambda_p}\left(1 - \frac{\lambda_p}{\lambda_p - \lambda_g}\exp(-\lambda_g x) - \frac{\lambda_g}{\lambda_g - \lambda_p}\exp(-\lambda_p x)\right) + \frac{\phi N_T \sigma_p}{\lambda_p}(1 - \exp(-\lambda_p x)) \tag{3}$$

Similarly using Batemann's equations and making suitable substitutions, one gets

$$D_1 = \frac{N_T \phi \sigma_g}{\lambda_d}\left(1 - \frac{\lambda_p}{\lambda_p - \lambda_g}\frac{\lambda_d}{\lambda_d - \lambda_g}\exp(-\lambda_g x) - \frac{\lambda_g}{\lambda_g - \lambda_p}\frac{\lambda_d}{\lambda_d - \lambda_p}\exp(-\lambda_p x) - \frac{\lambda_g}{\lambda_g - \lambda_d}\frac{\lambda_p}{\lambda_p - \lambda_d}\exp(-\lambda_d x)\right) \tag{4a}$$

$$D_2 = \frac{N_T \phi \sigma_p}{\lambda_d}\left(1 - \frac{\lambda_d}{\lambda_d - \lambda_p}\exp(-\lambda_p x) - \frac{\lambda_p}{\lambda_p - \lambda_d}\exp(-\lambda_d x)\right) \tag{4b}$$

$$D_3 = \frac{N_T \phi \sigma_d}{\lambda_d}(1 - \exp(-\lambda_d x)) \tag{4c}$$

By adding (4a), (4b) and (4c), one defines

$$D_x = D_1 + D_2 + D_3$$

$$D_x = \frac{\phi N_T \sigma_g}{\sigma_d}\left(1 - \frac{\lambda_p}{\lambda_p - \lambda_g}\frac{\lambda_d}{\lambda_d - \lambda_g}\exp(-\lambda_g x) - \frac{\lambda_g}{\lambda_d - \lambda_p}\frac{\lambda_d}{\lambda_d - \lambda_p}\exp(-\lambda_p x) - \frac{\lambda_g}{\lambda_g - \lambda_d}\frac{\lambda_p}{\lambda_p - \lambda_d}\exp(-\lambda_d x)\right)$$

$$+\frac{\phi N_T\sigma_p}{\lambda_d}\left(1-\frac{\lambda_d}{\lambda_d-\lambda_p}\exp(-\lambda_p x)-\frac{\lambda_p}{\lambda_p-\lambda_d}\exp(-\lambda_d x)\right)$$

$$+\frac{\phi N_T\sigma_d}{\lambda_d}(1-\exp(-\lambda_d x)) \tag{5}$$

Stage 2: Irradiation ended, reaction is stopped. T is no longer present

$$G\xrightarrow{\lambda_g}P\xrightarrow{\lambda_p}D\xrightarrow{\lambda_d}$$

At the start of the series decay, $(t=0)$, $G=G_x$, $P=P_x$ and $D=D_x$.

$G=G_x\exp(-\lambda_g t)$ is the grandparent

To obtain P the rate equation is,

$$\frac{\mathrm{d}P}{\mathrm{d}t}=G\lambda_g-P\lambda_p$$

$$\exp(\lambda_p t)\left(\frac{\mathrm{d}P}{\mathrm{d}t}+P\lambda_p\right)=(G\lambda_g)\exp(\lambda_p t)$$

$$\frac{\mathrm{d}}{\mathrm{d}t}(P\exp(\lambda_p t))=G\lambda_g\exp(\lambda_p t)$$

Integrating above equation, one gets

$$P\exp(\lambda_p t)=G_x\lambda_g\int\exp(-\lambda_g t)\exp(\lambda_p t)\mathrm{d}t+K_p$$

$$=\frac{G_x\lambda_g}{\lambda_p-\lambda_g}\exp((\lambda_p-\lambda_g)t)+K_p$$

At $t=0$, $P=P_x$

$$P_x=\frac{G_x\lambda_g}{\lambda_p-\lambda_g}+K_p$$

$$K_p=P_x-\frac{G_x\lambda_g}{\lambda_p-\lambda_g}$$

$$P=\frac{G_x\lambda_g}{\lambda_p-\lambda_g}(\exp(-\lambda_g t)-\exp(-\lambda_p t))+P_x\exp(-\lambda_p t) \tag{6}$$

To solve for D, the rate equation is

$$\frac{\mathrm{d}D}{\mathrm{d}t}=\lambda_p P-\lambda_d D$$

$$\frac{\mathrm{d}D}{\mathrm{d}t}+\lambda_d D=\lambda_p P$$

$$
\begin{aligned}
D\exp(\lambda_d t) &= \int \lambda_p P \exp(\lambda_d t)\mathrm{d}t \\
&= \lambda_p \int \left\{ \frac{G_x \lambda_g}{\lambda_p - \lambda_g} [\exp((\lambda_d - \lambda_g)t) - \exp((\lambda_d - \lambda_p)t)] \right. \\
&\qquad \left. + P_x \exp((\lambda_d - \lambda_p)t) \right\} \mathrm{d}t \\
&= \lambda_p \left[\frac{G_x \lambda_g}{\lambda_p - \lambda_g} \left\{ \frac{\exp(\lambda_d - \lambda_g)t}{(\lambda_d - \lambda_g)} - \frac{\exp(\lambda_d - \lambda_p)t)}{(\lambda_d - \lambda_p)} \right\} \right. \\
&\qquad \left. + \frac{P_x}{\lambda_d - \lambda_p} \exp((\lambda_d - \lambda_p)t) \right] + K_d
\end{aligned}
$$

At $t = 0$, $D = D_x$

Therefore

$$
K_d = D_x - \lambda_p \left[\frac{G_x \lambda_g}{\lambda_p - \lambda_g} \left\{ \frac{1}{\lambda_d - \lambda_g} - \frac{1}{\lambda_d - \lambda_p} \right\} + \frac{P_x}{\lambda_d - \lambda_p} \right]
$$

Therefore

$$
\begin{aligned}
D = \lambda_p &\left[\frac{G_x \lambda_g}{\lambda_p - \lambda_g} \left\{ \frac{\exp(-\lambda_g t)}{\lambda_d - \lambda_g} - \frac{\exp(-\lambda_p t)}{\lambda_d - \lambda_p} \right\} \right. \\
&\left. + \frac{P_x}{\lambda_d - \lambda_p} \exp(-\lambda_p t) \right] + D_x \exp(-\lambda_d t) \\
&- \lambda_p \left[\frac{G_x \lambda_g}{\lambda_p - \lambda_g} \left\{ \frac{1}{\lambda_d - \lambda_g} - \frac{1}{\lambda_d - \lambda_p} \right\} + \frac{P_x}{\lambda_d - \lambda_p} \right] \exp(-\lambda_d t)
\end{aligned}
$$

$$
\begin{aligned}
D = \lambda_p &\left[\frac{G_x \lambda_g}{\lambda_p - \lambda_g} \left\{ \left(\frac{\exp(-\lambda_g t) - \exp(-\lambda_d t)}{\lambda_d - \lambda_g} \right) - \left(\frac{\exp(-\lambda_p t) - \exp(-\lambda_d t)}{\lambda_d - \lambda_p} \right) \right\} \right. \\
&\left. + \frac{P_x}{\lambda_d - \lambda_p} (\exp(-\lambda_p t) - \exp(-\lambda_d t)) \right] + D_x \exp(-\lambda_d t) \qquad (7)
\end{aligned}
$$

The number of radioactive daughter nuclei that have decayed in the time between t_a and t_b be designated as $[D_d]_{t_a}^{t_b}$. Then

$$
\begin{aligned}
&[D_d]_{t_a}^{t_b} = \\
&= \int_{t_a}^{t_b} \lambda_d D \,\mathrm{d}t = \left\{ \left[\frac{\lambda_d \lambda_p \lambda_g G_x}{\lambda_p - \lambda_g} \frac{1}{\lambda_d - \lambda_g} \left(\frac{\exp(-\lambda_g t)}{\lambda_g} - \frac{\exp(-\lambda_d t)}{\lambda_d} \right) \right. \right. \\
&\quad \left. - \frac{1}{\lambda_d - \lambda_p} \left(\frac{\exp(-\lambda_p t)}{\lambda_p} - \frac{\exp(-\lambda_d t)}{\lambda_d} \right) \right] + \\
&\quad \left. \frac{\lambda_p \lambda_d P_x}{\lambda_d - \lambda_p} \left(\frac{\exp(-\lambda_p t)}{\lambda_p} - \frac{\exp(-\lambda_d t)}{\lambda_d} \right) + \lambda_d D_x \left(\frac{\exp(-\lambda_d t)}{\lambda_d} \right) \right\}_{t_a}^{t_b}.
\end{aligned}
$$

Therefore

$$
\begin{aligned}
[D_d]_{t_a}^{t_b} = G_x\lambda_g\Bigg[&\frac{\lambda_p\lambda_d(\exp(-\lambda_g t_a)-\exp(-\lambda_g t_b))}{(\lambda_p-\lambda_g)(\lambda_d-\lambda_g)}\\
&+\frac{\lambda_p\lambda_d(\exp(-\lambda_p t_a)-\exp(-\lambda_p t_b))}{(\lambda_g-\lambda_p)(\lambda_d-\lambda_p)}\\
&+\frac{\lambda_p\lambda_d(\exp(-\lambda_d t_a)-\exp(-\lambda_d t_b))}{(\lambda_g-\lambda_d)(\lambda_p-\lambda_d)}\Bigg]\\
P_x\lambda_p\Bigg[&\frac{\lambda_d}{\lambda_d-\lambda_p}\Bigg\{\bigg(\frac{\exp(-\lambda_p t_a)-\exp(-\lambda_p t_b)}{\lambda_p}\bigg)\\
&-\bigg(\frac{\exp(-\lambda_d t_a)-\exp(-\lambda_d t_b)}{\lambda_d}\bigg)\Bigg\}\Bigg]\\
&+D_x\lambda_d\bigg(\frac{\exp(-\lambda_d t_a)-\exp(-\lambda_d t_b)}{\lambda_d}\bigg)
\end{aligned}
$$

$$
\begin{aligned}
[D_d]_{t_a}^{t_b} = \phi N_T\sigma_g(1-\exp(-\lambda_g x))\Bigg[&\frac{\lambda_p\lambda_d(\exp(-\lambda_g t_a)-\exp(-\lambda_g t_b)}{(\lambda_p-\lambda_g)(\lambda_d-\lambda_g)}\\
&+\frac{\lambda_p\lambda_d(\exp(-\lambda_p t_a)-\exp(-\lambda_p t_b))}{(\lambda_g-\lambda_p)(\lambda_d-\lambda_p)}\\
&+\frac{\lambda_p\lambda_d(\exp(-\lambda_d t_a)-\exp(-\lambda_d t_b))}{(\lambda_g-\lambda_d)(\lambda_p-\lambda_d)}\Bigg]\\
&+\phi N_T\sigma_g\bigg(1-\frac{\lambda_p}{\lambda_p-\lambda_g}\exp(-\lambda_g x)-\frac{\lambda_g}{\lambda_g-\lambda_p}\exp(-\lambda_p x)\bigg)\\
&\times\Bigg[\frac{\lambda_d}{\lambda_d-\lambda_p}\Bigg\{\bigg(\frac{\exp(-\lambda_p t_a)-\exp(-\lambda_p t_b)}{\lambda_p}\bigg)\\
&-\bigg(\frac{\exp(-\lambda_d t_a)-\exp(-\lambda_d t_b)}{\lambda_d}\bigg)\Bigg\}\Bigg]\\
&+\phi N_T\sigma_p(1-\exp(-\lambda_p x))\Bigg[\frac{\lambda_d}{\lambda_d-\lambda_p}\Bigg\{\bigg(\frac{\exp(-\lambda_p t_a)-\exp(-\lambda_p t_b)}{\lambda_p}\bigg)\\
&-\bigg(\frac{\exp(-\lambda_d t_a)-\exp(\lambda_d t_b)}{\lambda_d}\bigg)\Bigg\}\Bigg]\\
&+\phi N_T\sigma_g\bigg[1-\frac{\lambda_p}{\lambda_p-\lambda_g}\frac{\lambda_d}{\lambda_d-\lambda_g}\exp(-\lambda_g x)-\frac{\lambda_g}{\lambda_d-\lambda_p}\frac{\lambda_d}{\lambda_d-\lambda_p}\exp(-\lambda_p x)\\
&-\frac{\lambda_g}{\lambda_g-\lambda_d}\frac{\lambda_p}{\lambda_p-\lambda_d}\exp(-\lambda_d x)\bigg]\bigg(\frac{\exp(-\lambda_d t_a)-\exp(-\lambda_d t_b)}{\lambda_d}\bigg)\\
&+\phi N_T\sigma_p\bigg[1-\frac{\lambda_d}{\lambda_d-\lambda_p}\exp(-\lambda_p x)-\frac{\lambda_p}{\lambda_\beta-\lambda_d}\exp(-\lambda_d x)\bigg]
\end{aligned}
$$

$$\times\left(\frac{\exp(-\lambda_d t_a)-\exp(-\lambda_d t_b)}{\lambda_d}\right)$$

$$+\,\phi N_T\sigma_d(1-\exp(-\lambda_d x))\left(\frac{\exp(-\lambda_d t_a)-\exp(-\lambda_d t_b)}{\lambda_d}\right) \tag{8}$$

These $[D_d]_{t_a}^{t_b}$ nuclei that have decayed in the time interval between t_a and t_b, have emitted characteristic γ-rays of energy E_γ with an abundance of θ_γ per decay and these γ-rays are detected by a detector, with a photopeak efficiency P_γ corresponding to the energy E_γ and the given geometry and recorded as a full energy peak of area A_γ.

Therefore

$$A_\gamma=[D_d]_{t_a}^{t_b}\theta_\gamma P_\gamma$$

where

$$[D_d]_{t_a}^{t_b}=\frac{A_\gamma}{\theta_\gamma P_\gamma} \tag{9}$$

Also, N_T the number of target atoms per unit area is

$$N_T=\frac{w_i p_i N_{\mathrm{AV}}}{A_i} \tag{10}$$

where w_i is the weight of the target foil per unit area, P_i is the abundance of the target isotope, A_i is the mass number of the target and N_{AV} is the Avagadro number. Using (8), (9) and (10) and rearranging, one finally gets

$$\frac{A_i A_\gamma}{\phi w_i\theta_\gamma p_i P_\gamma N_{\mathrm{AV}}}=K$$

$$=\sigma_g(1-\exp(-\lambda_g x))\left[\frac{\lambda_p\lambda_d(\exp(-\lambda_g t_a)-\exp(-\lambda_g t_b))}{(\lambda_p-\lambda_g)(\lambda_d-\lambda_g)}\right.$$

$$+\frac{\lambda_p\lambda_d(\exp(-\lambda_p t_a)-\exp(-\lambda_p t_b))}{(\lambda_g-\lambda_p)(\lambda_d-\lambda_p)}$$

$$\left.+\frac{\lambda_p\lambda_d(\exp(-\lambda_d t_a)-\exp(-\lambda_d t_b))}{(\lambda_g-\lambda_d)(\lambda_p-\lambda_d)}\right]\Rightarrow g_1$$

$$+\,\sigma_g\left(1-\frac{\lambda_p}{\lambda_p-\lambda_g}\exp(-\lambda_g x)-\frac{\lambda_g}{\lambda_g-\lambda_p}\exp(-\lambda_p x)\right)$$

$$\times\left[\frac{\lambda_d}{\lambda_d-\lambda_p}\left(\frac{\exp(-\lambda_p t_a)-\exp(-\lambda_p t_b)}{\lambda_p}-\frac{\exp(-\lambda_d t_a)-\exp(-\lambda_d t_b)}{\lambda_d}\right)\right]$$

$$\Rightarrow g_{12}$$

$$+\,\sigma_g\left[1-\frac{\lambda_p}{\lambda_p-\lambda_g}\frac{\lambda_d}{\lambda_d-\lambda_g}\exp(-\lambda_g x)-\frac{\lambda_g}{\lambda_g-\lambda_p}\frac{\lambda_d}{\lambda_d-\lambda_p}\exp(-\lambda_p x)\right.$$

$$\left.-\frac{\lambda_g}{\lambda_g-\lambda_d}\frac{\lambda_p}{\lambda_p-\lambda_d}\exp(-\lambda_d x)\right]\left(\frac{\exp(-\lambda_d t_a)-\exp(-\lambda_d t_b)}{\lambda_d}\right)\Rightarrow g_{13}$$

$$+\sigma_p(1-\exp(-\lambda_p x))\left[\frac{\lambda_d}{\lambda_d-\lambda_p}\left(\frac{\exp(-\lambda_p t_a)-\exp(-\lambda_p t_b)}{\lambda_p}\right.\right.$$

$$\left.\left.-\frac{\exp(-\lambda_d t_a)-\exp(-\lambda_d t_b)}{\lambda_d}\right)\right]\Rightarrow g_2$$

$$+\sigma_p\left[1-\frac{\lambda_d}{\lambda_d-\lambda_p}\exp(-\lambda_p x)-\frac{\lambda_p}{\lambda_p-\lambda_d}\exp(-\lambda_d x)\right]$$

$$\times\left(\frac{\exp(-\lambda_d t_a)-\exp(-\lambda_d t_b)}{\lambda_d}\right)\Rightarrow g_{23}$$

$$+\sigma_d(1-\exp(-\lambda_d x))\left(\frac{\exp(-\lambda_d t_a)-\exp(-\lambda_d t_b)}{\lambda_d}\right)\Rightarrow g_3 \tag{11}$$

Therefore,

$$K=\sigma_g(g_1+g_{12}+g_{13})+\sigma_p(g_2+g_{23})+\sigma_d g_3 \tag{12}$$

Dividing throughout by g_3, one gets the experimentally measured cross-section σ_{exp} as

$$\sigma_{\text{exp}}=\frac{K}{g_3}=\sigma_g\frac{(g_1+g_{12}+g_{13})}{g_3}$$

$$+\sigma_p\frac{(g_2+g_{23})}{g_3}$$

$$+\sigma_d$$

$$\sigma_{\text{exp}}=\sigma_g C_g+\sigma_p C_p+\sigma_d$$

where C_g and C_p defined as above represent the relative cross-sectional contributions of the isobaric precursors to the daughter nucleus under study. In other words they represent the *legacy* of the grandparent and parent to the daughter isobar.

The physical significance of the terms g_1, g_{12}, g_{13}, g_2, g_{23}, and g_3 is understood by realizing that the activity of the daughter nucleus D at the final instant of time t_a just before activity measurement is contributed in six ways: Three isobars G, P and D contributing during two specific periods; (a) growth phase, from beginning to the end of irradiation ($t'=0-x$) and (b) decay phase, from the end of irradiation to the instant of counting ($t'=x-t_a$). These contributing factors are clearly explained in table 1.

3. Results and discussion

As mentioned above, the study of excitation functions is generally complicated by the possibility of isobaric precursors contributing to the cross-section of the formation of the residual nucleus of interest, particularly in the high energy region. This provides the motivation of separating out such contributions from four typical $(\alpha, xnypz\alpha)$ reactions, namely ^{93}Nb [$(\alpha,\alpha 3n)$, $(\alpha,\alpha p4n)$, $(\alpha,2\alpha n)$ and $(\alpha,2\alpha 2n)$], in order to show the applicability of the above formalism. The raw data of the experimentally measured excitation function for these reactions were taken from our earlier measurements [5].

Table 1. Growth and decay phases of the three isobars. Here the g-factors are the fractions contributing to the growth and decay of the isobars.

Term	Contributing isobar	Phases of the isobar(s)	Period of contribution	Mode of contribution
g_{13}	G	Growth of P Growth of D	$0-x$	$G \nearrow P \nearrow D$
g_{12}	G	Growth of P Decay of P	$0-x$ $x-t_a$	$G \nearrow P \searrow D$
g_1	G	Decay to P Decay to D	$x-t_a$	$G \searrow P \searrow D$
g_2	P	Growth of P Growth of D	$0-x$	$P \nearrow D$
g_{23}	P	Growth of P Decay to P	$0-x$ $x-t_a$	$P \searrow D$
g_3	D	Growth of D	$0-x$	D

3.1 $^{93}Nb(\alpha, \alpha 3n)\ ^{90}Nb$ *reaction*

As indicated in the inset of figure 1, there are two isobaric contributions to the residual nucleus ^{90}Nb under study. Using the present mathematical formulation, the isobaric precursor contributions, $C_g\sigma_g + C_p\sigma_p$, where C_g and C_p are the calculated coefficients and σ_g and σ_p are the experimentally measured cross-sections for the two reactions, were separated point by point. As shown in table 2, the sum of these contributions is about one third the measured cross-section around 110 MeV. The dotted curve in the figure shows the contributions which are subtracted from the experimental curve, shown by thick dashes, in order to obtain exclusively the cross-sections σ_d for the reaction under study, namely, ^{93}Nb($\alpha, \alpha 3n$) ^{90}Nb. Figure 9 shows a comparison between the experimentally measured cross-sections (σ_{exp}) with the exclusive cross-sections (σ_d) with the exclusive cross-sections (σ_d) obtained after separating the isobaric precursor contributions using the present mathematical formulation. Figure 9a shows that the exclusive cross-section (σ_d) is smaller by about a factor of 1·5 from the experimental cross-sections (σ_{exp}) at the peak position.

Figure 2, shows a comparison of the experimental excitation functions, so extracted, with the theoretically predicted curve on the basis of hybrid model [7, 9] using the initial exciton configuration $n_0 = 4$ ($4p\,0h$). As it is evident from the figure, the agreement between the theoretical predictions and the exclusive cross-sections (σ_d), shows a remarkable improvement as compared to the total experimental cross-sections (σ_{exp}), particularly in the high energy region.

3.2 $^{93}Nb(\alpha, \alpha p4n)\ ^{88}Zr$ *reaction*

The raw experimental data along with the two important isobaric precursor contributions for this reaction are shown in figure 3. It can be seen from table 2 that, these isobaric precursor contributions are about 20% of cross-section at the maximum, that is between 90 to 100 MeV. Figure 9b shows that at the peak position, the exclusive

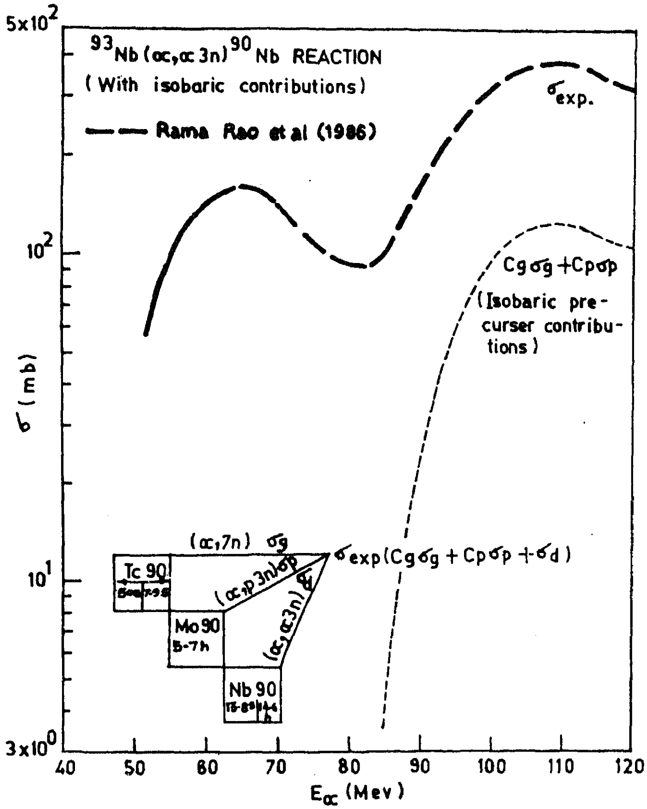

Figure 1. Experimental excitation function of ^{93}Nb$(\alpha, \alpha 3n)$ ^{90}Nb reaction. Dotted curve shows isobaric feeding of ^{93}Nb$[(\alpha, 7n) + (\alpha, p6n)]$ reactions.

Table 2. Relative contributions of the isobaric precursors in ^{93}Nb$(\alpha, xnypz\alpha)$ reactions. Here $C_g\sigma_g + C_p\sigma_p$ is the total isobaric precursor contributions in the experimentally measured cross-sections (σ_{exp}).

	^{93}Nb$(\alpha, \alpha 3n)^{90}$Nb	^{93}Nb$(\alpha, \alpha p4n)^{88}$Zr	^{93}Nb$(\alpha, 2\alpha n)^{88}$Y	^{93}Nb$(\alpha, 2\alpha 2n)^{87}$Y
E_α (MeV)	$\frac{C_g\sigma_g + C_p\sigma_p}{\sigma_{exp}}$	$\frac{C_g\sigma_g + C_p\sigma_p}{\sigma_{exp}}$	$\frac{C_g\sigma_g + C_p\sigma_p}{\sigma_{exp}}$	$\frac{C_g\sigma_g + C_p\sigma_p}{\sigma_{exp}}$
90	0·16	0·21	0·28	—
100	0·34	0·19	0·21	0·48
110	0·33	0·17	0·16	0·53
120	0·35	0·29	0·14	0·37

cross-sections (σ_d) is smaller by about a factor of 1·3 as compared to the experimentally measured cross-sections.

A comparison of the exclusive cross-section (σ_d) with the hybrid model predictions for this reaction is shown in figure 4. The theoretical excitation function for $n_0 = 4(4p\,0h)$ nearly reproduces the shape and also gives an agreement within a factor of 2. From the state of the art of pre-equilibrium model calculations, such a factor of two agreement is quite satisfactory for complex reactions like the present one.

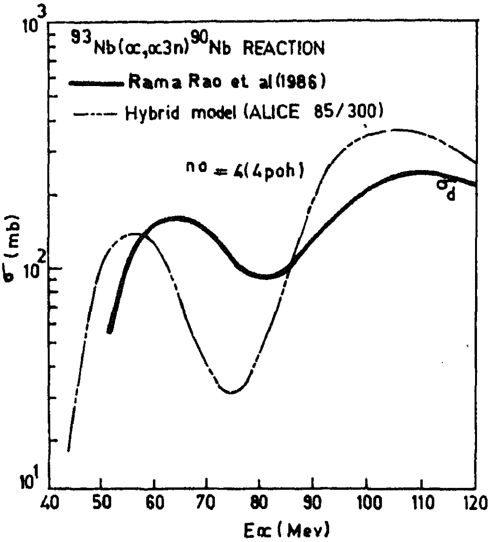

Figure 2. Comparison of theoretical results with the experimental results for ^{93}Nb$(\alpha, \alpha 3n)$ ^{90}Nb reaction.

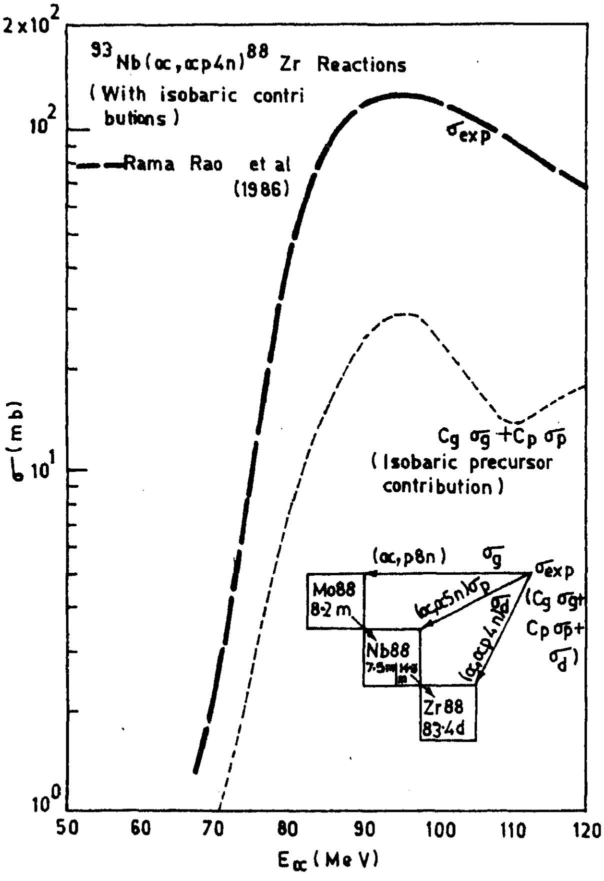

Figure 3. Experimental excitation function of ^{93}Nb$(\alpha, \alpha p4n)$ ^{88}Zr reaction. Dotted curve shows isobaric feeding of ^{93}Nb$[(\alpha, p8n) + (\alpha, \alpha 5n)]$ reactions.

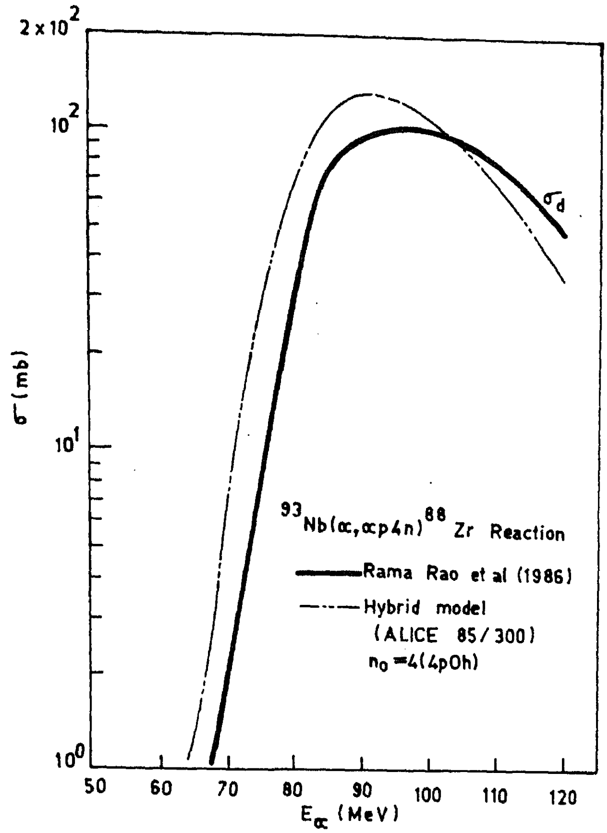

Figure 4. Comparison of theoretical results with experimental results for ^{93}Nb($\alpha, \alpha p4n$) ^{88}Zr reaction.

3.3 $^{93}Nb(\alpha, 2\alpha n)$ ^{88}Y *reaction*

The excitation function for the raw data is shown in figure 5, alongwith the isobaric precursor contributions. Table 2 shows that the isobaric precursor contribution varies between 15 and 30% in the high energy region, and exceeds the experimental errors of the measurements. Figure 9c further shows that the exclusive cross-sections (σ_d) is about a factor 1·2 smaller than the experimentally measured cross-sections (σ_{exp}).

Figure 6, shows a similar comparison between the exclusive experimental results and the hybrid model prediction for the reaction. There is a better agreement in the energy region between 80 and 120 MeV. In view of the increased alpha multiplicity, this improved agreement in the high energy region is praiseworthy.

3.4 $^{93}Nb(\alpha, 2\alpha 2n)$ ^{87}Y *reaction*

Figure 7, shows the excitation function for the raw data, alongwith the isobars contributing to the reaction as shown in the inset. Table 2, shows that the isobaric precursor contribution in this case is nearly 50% of the cross-section at maximum. This observation emphasizes the need for the analytical approach used in the present work. Further, it is shown in figure 9d that the exclusive cross-sections (σ_d) is almost half at the peak as compared to the experimentally measured cross-sections (σ_{exp}).

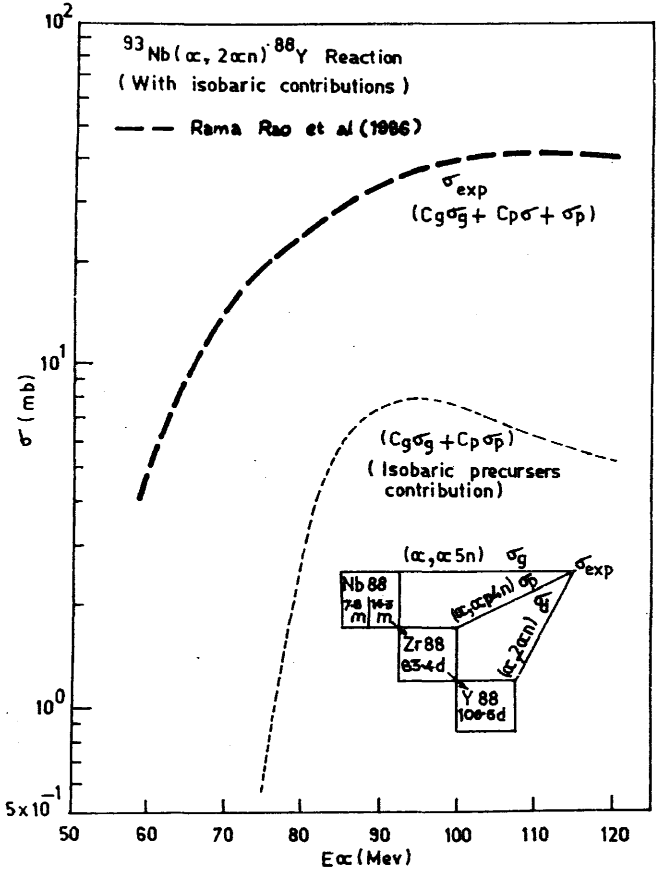

Figure 5. Experimental excitation function of ^{93}Nb(α, 2αn) ^{88}Y reaction. Dotted curve shows isobaric feeding of ^{93}Nb[(α, α5n) + (α, αp4n)] reactions.

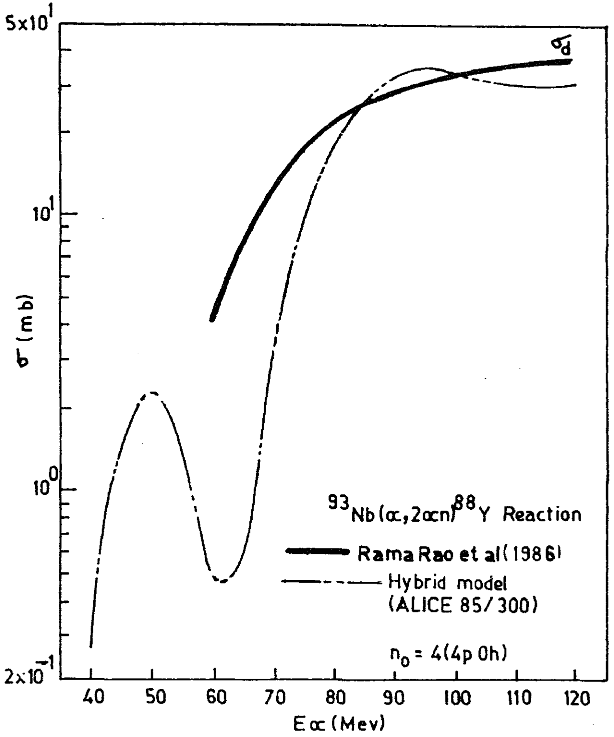

Figure 6. Comparison of theoretical results with the experimental results for ^{93}Nb(α, 2αn) ^{88}Y reaction.

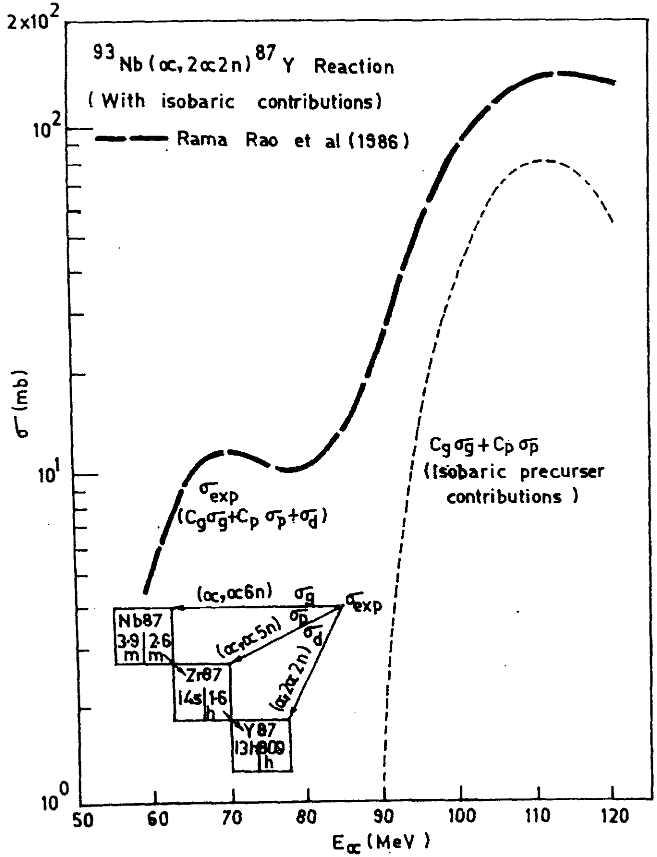

Figure 7. Experimental excitation function of ^{93}Nb(α, 2α2n) ^{87}Y reaction. Dotted curve shows isobaric feeding of ^{93}Nb[(α, α6n) + (α. αp5n)] reaction.

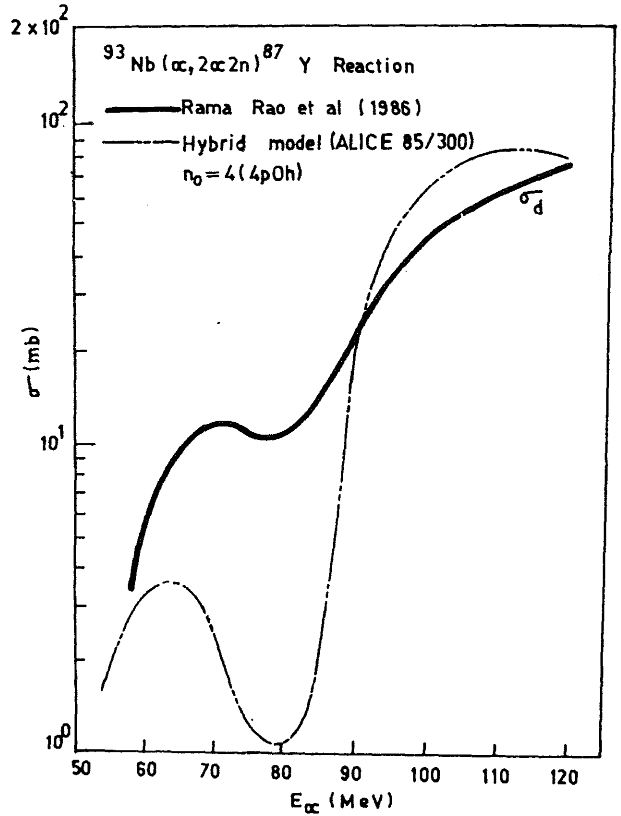

Figure 8. Comparison of theoretical results with the experimental results for ^{93}Nb(α, 2α2n) ^{87}Y reaction.

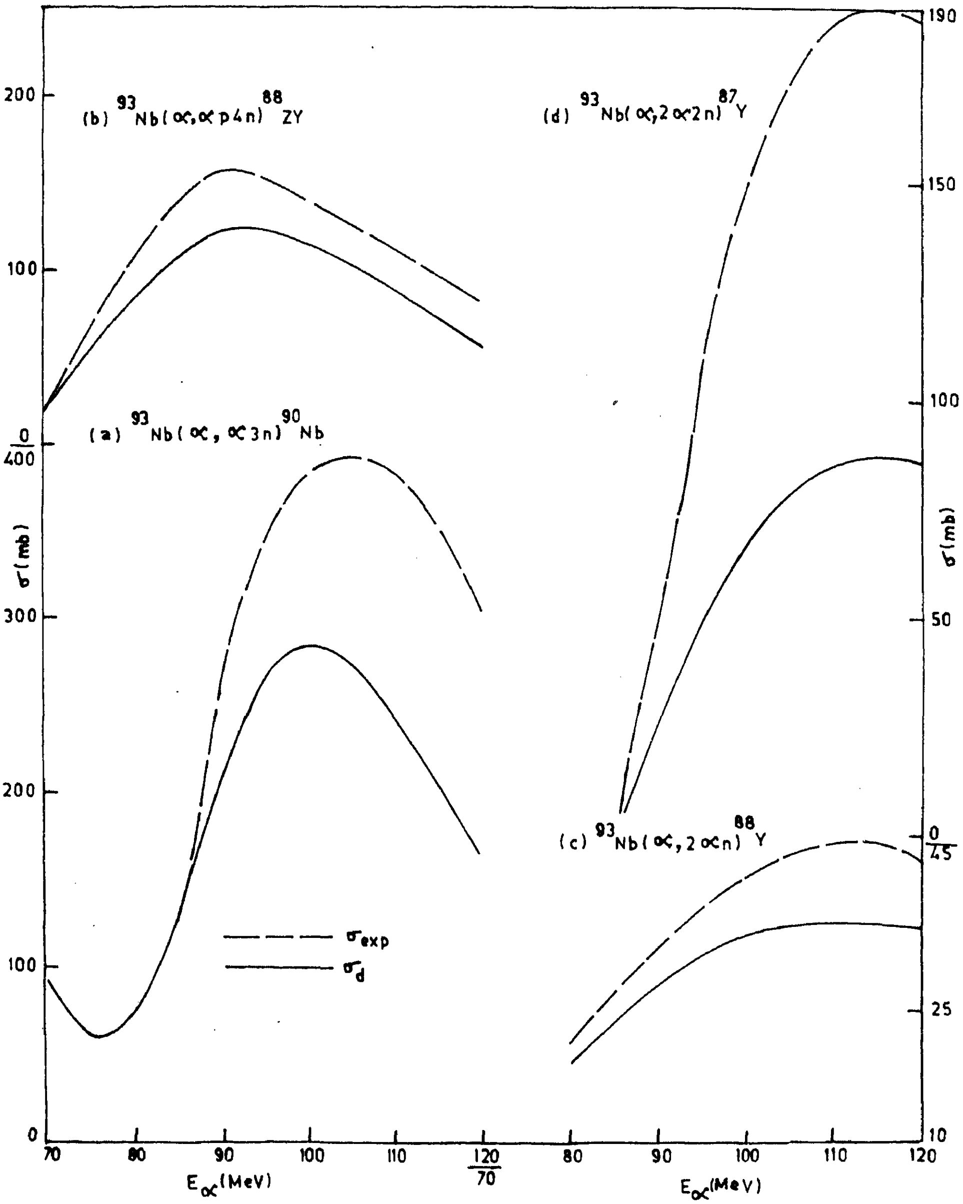

Figure 9. Comparison of the excitation functions of experimentally measured cross section (dashed curve) with the cross section excluding isobaric contributions (solid curve).

A comparison of the experimental results and the hybrid model predictions in figure 8, indicates the evidence for the emission of pre-equilibrium alpha particles around 80 MeV. At high energies beyond 90 MeV, the predicted values are reasonably close to the experimental values.

4. Conclusions

A detailed mathematical formalism is developed, to give a quantitative account of the fractional contributions of the cross-sections by the isobaric precursors, to the cross-section for the formation of the residual nucleus of interest. From the present analysis of the four reactions, namely, ^{93}Nb$[(\alpha,\alpha 3n), (\alpha,\alpha p4n), (\alpha,2\alpha n)$ and $(\alpha,2\alpha 2n)]$ it can be said in general, that the present analytical formalism, separates out effectively, the isobaric precursor contributions, if any, from the (α,pxn) and $(\alpha,\alpha xn)$ type of reactions, as it is quite evident from the relatively better agreement of exclusive experimental results with the theoretical predictions of the hybrid model, particularly in the high energy (70 to 120 MeV), where the isobaric precursor contributions are prominent.

Acknowledgements

The authors are thankful to Dr V J Menon and Dr A V Mohan Rao, BHU, Varanasi, for their help and useful suggestions at various stages of this investigation. One of the authors (SM) would like to thank the MAPCOST, Bhopal, for awarding the fellowship under *FTIYS Scheme*.

References

[1] H Machner, *Phys. Lett.* **868**, 129 (1979)
[2] H Machner, *Phys. Rev.* **C21**, 2695 (1980)
[3] J Ernst, R Ibowski, H Klampl, H Machner, T Mayer Kuckuk and R Schanz, *Z. Phys.* **A142**, 545 (1982)
[4] E Gadioli, E Gadioli-Erba, J J Hogan and B V Jacak, *Phys. Rev.* **C29**, 76 (1984)
[5] J Rama Rao, L Chaturvedi, A V Mohan Rao, S Mukherjee, R Upadhyay, N L Singh, S Agarwal and P P Singh, *Proceedings of Workshop on Utilization of future programme of variable energy cyclotron*, VECC, Calcutta (India), **19**, 11 (1986)
[6] S Mukherjee, A V Mohan Rao and J Rama Rao, *Il. Nuovo Cimento* **104**, 863 (1991)
[7] M Blann and H K Vonach, *Phys. Rev.* **C28**, 1475 (1983)
[8] H Batemman, *Proc. Cambridge Philos. Soc.* **15**, 423 (1910)
[9] M Blann, Code ALICE/85/300 UCID-20169 (1984)

PRAMANA
— journal of
physics

© Printed in India

Vol. 41, No. 4,
October 1993
pp. 329–338

Measurement and analysis of the excitation functions for alpha particle induced reactions on niobium

S MUKHERJEE, M H RASHID* and S N CHINTALAPUDI**
School of Studies in Physics, Vikram University, Ujjain 456010, India
*Variable Energy Cyclotron Centre, 1/AF, Bidhan Nagar, Calcutta 700064, India
**Inter University Consortium for DAEF, BJ–76, Bidhan Nagar, Calcutta 700091, India

MS received 11 November 1992; revised 11 May 1993

Abstract. Stacked foil activation technique and Ge(Li) gamma ray spectroscopy have been used for determining the excitation functions up to 45 MeV, of six reactions ^{93}Nb[(α, n), $(\alpha, 2n)^m$, $(\alpha, 2n)^g$, $(\alpha, 3n)$, $(\alpha, p3n)$ and $(\alpha, \alpha n)$]. Excitation functions were also calculated theoretically by means of the hybrid model with and without the inclusion of pre-equilibrium emission of particles. A general agreement was found in (α, xn) type of reactions.

Keywords. Excitation functions; stacked-foil activation technique; pre-equilibrium decay hybrid model.

PACS No. 24·00

1. Introduction

Nuclear reactions induced by medium energy projectiles (10–200 MeV), were studied to understand the equilibrium and pre-equilibrium processes. A priori knowledge of the excitation functions is essential to explain the equilibrium and pre-equilibrium emission of particles in $(\alpha, xnypz\alpha)$ reactions, and to test the adequacies of the various pre-equilibrium models, developed during the last few decades [1–9], in order to explain the underlying physics.

Niobium is a typical monoisotopic element situated in the middle of the periodic table and ideally suitable for such studies. Extensive measurements of alpha particle induced reactions are available over a wide region of energy using scintillation and germanium detectors [10–16]. However, a close scrutiny reveals that not only there are divergences beyond the experimental errors among the various reported values, but also a wide gap exists between 30 and 60 MeV [15].

Gadioli *et al* [16] studied these reactions in steps of 20MeV alpha particle energy, and there is only one energy point cross-section at 40 MeV available in each of these reactions, with no measurements in the low energy regions, where the transition from equilibrium to pre-equilibrium reaction mechanism takes place. Thus, the available Ge(Li) measurements for the above reactions at the low energy region (10 to 50 MeV) is still far from adequate.

In this context, the present investigations are undertaken with two aims: (i) to improve the quality of existing data, measured about a decade back and to add new energy point cross-sections wherever not available, and (ii) to compare the experimental results so obtained with one of the latest available theoretical codes

[17], for the first time, for these reactions, in the energy range between 10–45 MeV. Although, Ernst *et al* [15] have studied these reactions up to 170 MeV their data are not supported by any suitable theoretical calculations.

Thus, there is a strong motivation in the present work to measure the excitation functions of six reactions in the above mentioned energy range.

2. Experimental procedure

Six excitation functions for the reaction residues ^{96}Tc, ^{95m}Tc, ^{95g}Tc, ^{94}Tc ^{93}Mo and ^{92}Nb, in the alpha particle induced reaction on ^{93}Nb were measured using stacked-foil activation technique and Ge(Li) gamma ray spectroscopy.

Stacks of self-supporting niobium foils of thickness 11 mg/cm^2 each and purity greater than 99·99%, were interspersed with suitable aluminium degraders, to degrade the alpha particle energies from 45 MeV. At the front of the stack, an aluminium foil of thickness 20 mg/cm^2 was used as a flux monitor. The energy of alpha particles after they had traversed half of the thickness to each foil was determined from the range-energy tables of Williamson *et al* [18].

The alpha irradiation was performed at the Variable Energy Cyclotron Centre, Calcutta, India. Keeping in view the half lives and the yields, beam currents of the order of 200 nA was maintained throughout the irradiation. The flux monitor reactions used were $^{27}\mathrm{Al}(\alpha, \alpha 2pn)^{24}\mathrm{Na}$ and $^{27}\mathrm{Al}(\alpha, 2\alpha n)^{22}\mathrm{Na}$, for which well measured cross-sections are available in literature [19]. The reaction residues were identified by their characteristic gamma rays as mentioned in table 1 [20], and using Ge (Li) detector ($\sim$ 2·0 KeV FWHM for 1332 KeV photons of ^{60}Co) in conjunction with a 4 K multichannel analyser. The energy and efficiency calibration of the Ge(Li) detector was done by a ^{152}Eu standard source. The formula used in the cross-section measurement alongwith other details is given in literature [21].

3. Experimental results

The main sources of error in the present measurement of cross-section essentially include, uncertainties in the photopeak area, monitor cross-section, uniformity of the

Table 1. Reactions studied in the present work and the relevant decay characteristics of residual nuclei.

Reactions	Residual nucleus	Q value (MeV)	Half-life of residual nucleus $T_{1/2}$	Characteristic γ-ray energy E_γ(keV)	% abundance θ_γ(%)
$^{93}\mathrm{Nb}(\alpha, n)$	^{96}Tc	− 7·03	4·35 d	778	99·1
$^{93}\mathrm{Nb}(\alpha, 2n)$	^{95m}Tc	− 14·92	61·0 d	204·1	66·2
$^{93}\mathrm{Nb}(\alpha, 2n)$	^{95g}Tc	− 14·92	20·0 h	766	92·0
$^{93}\mathrm{Nb}(\alpha, 3n)$	^{94}Tc	− 24·84	4·88 h	871	100
$^{93}\mathrm{Nb}(\alpha, p3n)$	^{93}Mo	− 31·9	6·95 h	1477	99·1
$^{93}\mathrm{Nb}(\alpha, \alpha n)$	^{92m}Nb	− 8·96	10·14 d	934·5	99·2
Monitor reactions					
$^{27}\mathrm{Al}(\alpha, \alpha 2pn)$	^{24}Na	− 31·4	15·05 h	1369	100
$^{27}\mathrm{Al}(\alpha, 2\alpha n)$	^{22}Na	− 22·5	2·60 a	1275	100

Table 2. Experimental cross-section for the α-induced reaction on ^{93}Nb.

Reaction product nucleus E_α (MeV)	Cross section (mb) Nb(α, n) $^{96m+g}$Tc Present	Previous	Nb($\alpha, 2n$) ^{95g}Tc Present	Previous	^{95m}Tc Present	Previous
16·0	—	433 ± 33*	—	38 ± 3*	—	—
16·9	309 ± 24	—	—	—	—	—
21·2	276 ± 30	—	232 ± 28	—	93·4 ± 13·1	—
23·0	—	92 ± 7*	—	849 ± 66*	—	—
24·4	106 ± 15	—	489 ± 54	—	169 ± 22	—
29·0	—	22 ± 2·4*	—	913 ± 70*	—	—
29·5	22·6 ± 3·4	—	665 ± 67	—	203 ± 24	—
32·6	—	—	—	666*	—	—
34·1	—	—	—	387 ± 30*	—	—
34·3	20·5 ± 3·1	—	812 ± 81	—	223 ± 27	—
38·0	12·8 ± 1·9	—	349 ± 38	—	91·8 ± 12·8	—
38·8	—	—	—	184 ± 15	—	—
40·0	—	11·5 ± 0·1**	—	227 ± 3	—	—
42·0	9·98 ± 1·5	—	156 ± 22	—	—	—
43·2	—	—	—	104 ± 9*	—	—
	Nb($\alpha, 3n$) ^{94g}Tc		Nb($\alpha, p3n$) ^{93}Mo		Nb($\alpha, \alpha n$) ^{92m}Nb	
16·0	—	—	—	—	—	—
16·9	—	—	—	—	—	—
21·2	—	—	—	—	3·14 ± 0·47	—
23·0	—	—	—	—	—	—
24·4	—	—	—	—	14·6 ± 2·8	—
29·0	—	83 ± 6*	—	—	—	—
29·5	8·21 ± 1·20	—	—	—	26·4 ± 3·9	—
32·6	—	397*	—	—	—	—
34·1	—	518 ± 40	—	—	—	—
34·3	119 ± 15	—	2·24 ± 0·49	—	32·3 ± 3·9	—
38·0	485 ± 49	—	21·3 ± 3·2	—	39·6 ± 4·7	—
38·8	—	684 ± 53*	—	—	—	—
40·0	—	—	—	2·01 ± 0·05**	—	18·3 ± 0·5**
42·0	650 ± 65	—	32·1 ± 4·7	25 ± 2*	43·4 ± 4·8	—
43·2	—	609 ± 47*	—	—	—	—

*Ernst *et al* [15]; **Gadioli *et al* [16] foil thickness, detection efficiency and spectroscopic data. The overall projected error in the present work ranges between 9 and 14%.

The calculated values of cross-sections for the reactions measured in the present work alongwith the previous results wherever available are given in table 2.

The above mentioned reactions were earlier studied employing Ge(Li) detector spectroscopy by two groups of investigators about a decade back [15, 16]. The mutual disagreement between the two measurements are beyond the limits of error. Gadioli *et al* [16] measured the cross-sections for these reactions in steps of 20 MeV alpha particle energy, and there is only one energy point cross-section at 40 MeV in each reaction, with no measurements in the low energy region, where the transition from equilibrium to pre-equilibrium mechanism takes place, while Ernst *et al* [15] have reported their results with errors as high as 23% in some measurements. To the best of our knowledge, none of the above two authors have measured the ^{93}Nb(α, 2n) ^{95m}Tc reaction in the present energy range.

4. Comparison with the hybrid model

The observed excitation functions are characterized by a equilibrium peak followed by a high energy tail. Therefore the experimental cross-sections may be compared with the theoretical predictions based on Weisskopf–Ewing estimates giving the compound nucleus contribution as well as with the hybrid model in its latest form [9]. Basically, the hybrid model is semi-classical, hence invloves a large number of physical parameters alongwith a few adjustable parameters. A short description of the options chosen is given below. The nuclear masses were calculated from the Myers–Swiatecki mass formula [22] with the liquid drop having shell correction term without pairing, i.e. the level density pairing absorbed in binding energies. The inverse cross-sections were calculated by optical model subroutine included in the code. A level density parameter of A/8 MeV^{-1} was used. For the equilibrium part, the so called S-wave approximation is used which takes into account the full gamma, competition with particle emission. The initial exciton number $n_0(P_0 h_0)$ plays an important role because it governs the entire cascading process of binary collisions and thereby influence the shape of hard component in the particle spectra.

We have made the theoretical calculations using the initial excitation configurations 4(4p0h), 5(5p0h) and 6(5p1h). It was observed that the theoretical predictions of the hybrid model with 4(4p0h) gives better results, as compared to the predictions of the 5(p0h) and 6(5p1h) configurations. Therefore we have shown 4(4p0h) configuration in the comparison.

Figures 1 to 4 show the measured excitation functions for the reactions ^{93}Nb[(α, n), (α, 2n), (α, 3n), (α, p3n) and (α, α n)], alongwith the theoretical predictions of Weisskopf–Ewing estimates giving compound nucleus contributions alongwith the hybrid model calculations [17]. The (α, n) reaction proceeds through evaporation mode, roughly up to 30 MeV. The energy region 33 to 45 MeV for this reaction is almost completely dominated by the pre-equilibrium neutron emission. Thus, the hybrid model more or less gives a satisfactory agreement with the initial exciton configuration 4(4p0h). As suggested by the bell shaped curve of the Weisskopf–Ewing estimate, the (α, 2n) reaction, in the energy region 15–45 MeV, mainly proceeds through the well known compound nucleus mode. The onset of pre-equilibrium neutron emission starts only beyond 45 MeV. However, the excitation function underestimates the theoretical curves almost by a factor of 1·5. This is due to the fact that the angular

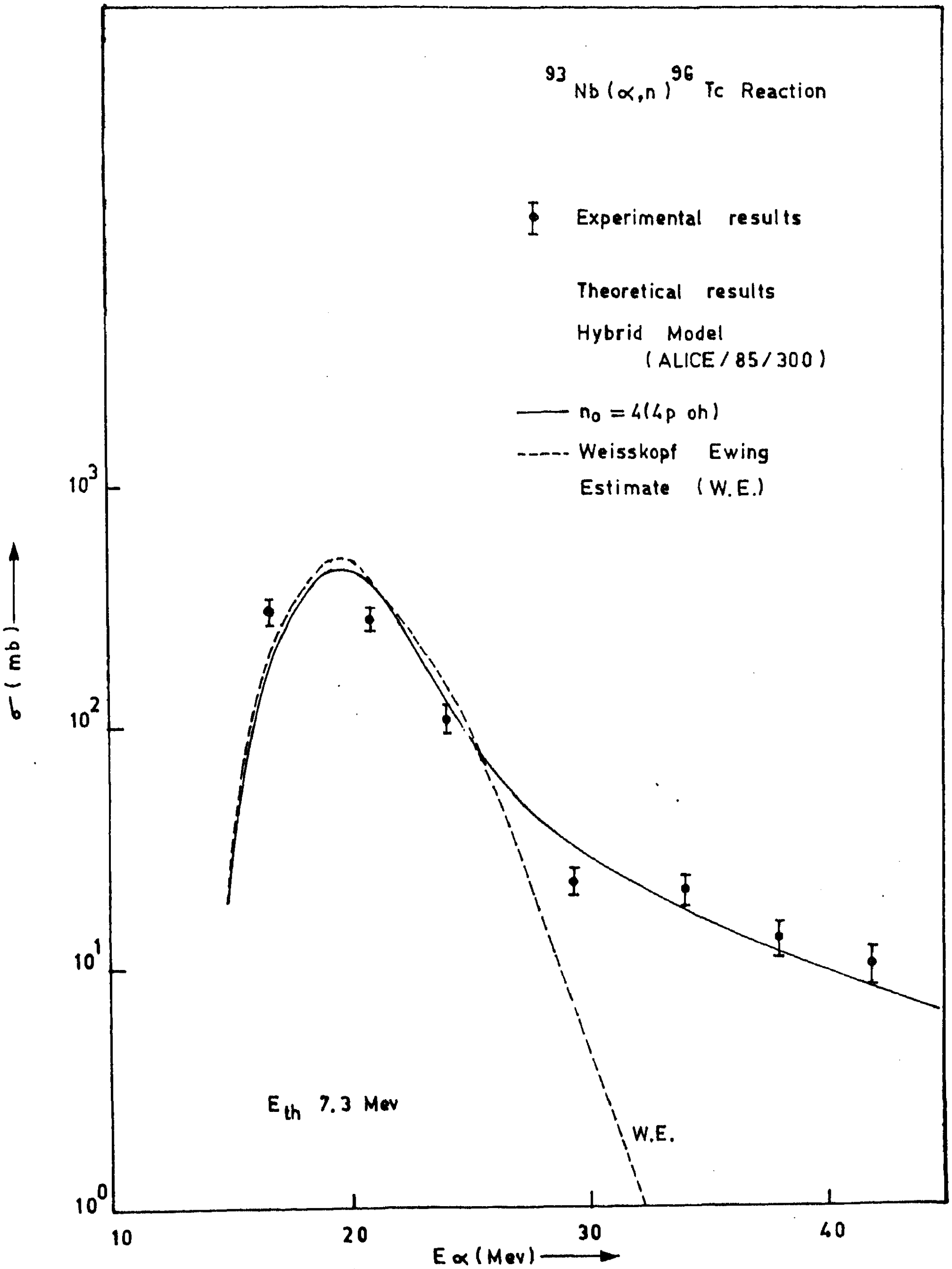

Figure 1. Comparison of theoretical and experimental excitation function of ^{93}Nb(α, n) ^{96}Tc reaction.

momentum effects are not properly accounted for in the code. More elaborate computing using the Hauser–Feshbach theory may bring about a better agreement.

The threshold energy for $(\alpha, 3n)$ reaction is rather large(25·9 MeV), as such we have only the rising part of the excitation function. However, the shape of the theoretical curve is reproduced within a factor of 2. There are only three points in the initial

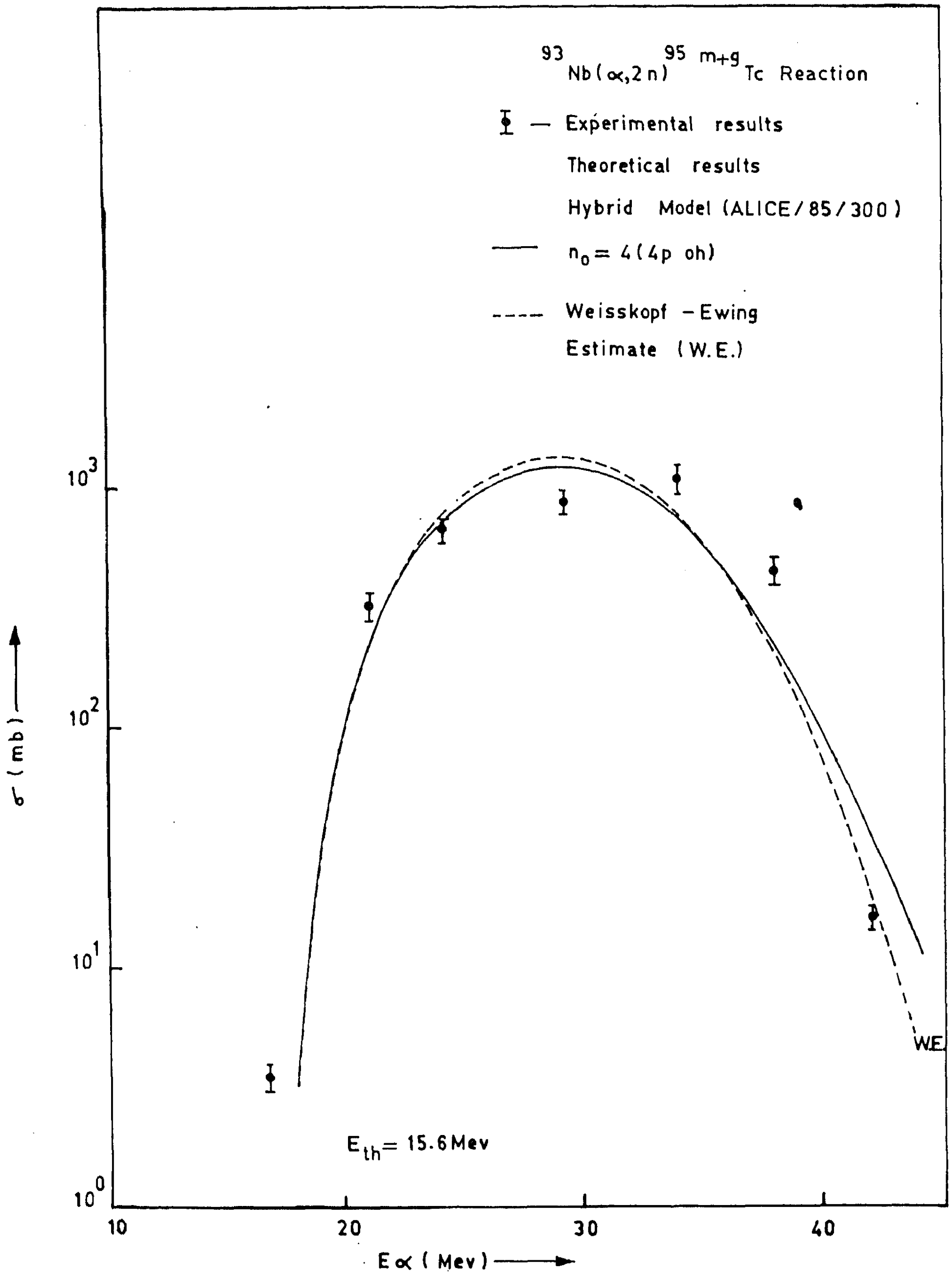

Figure 2. Comparison of theoretical and experimental excitation function of ^{93}Nb(α, 2n) $^{95m+g}$Tc reaction.

rising part of the experimental excitation function of (α, p3n) reaction. In this region there are no pre-equilibrium contributions.

In figure 4, the excitation function of ^{93}Nb(α, αn) is shown. The theoretical curves fail to reproduce even the shape of the excitation function. This is not surprising because the hybrid model is not designed to deal with the alpha emission in

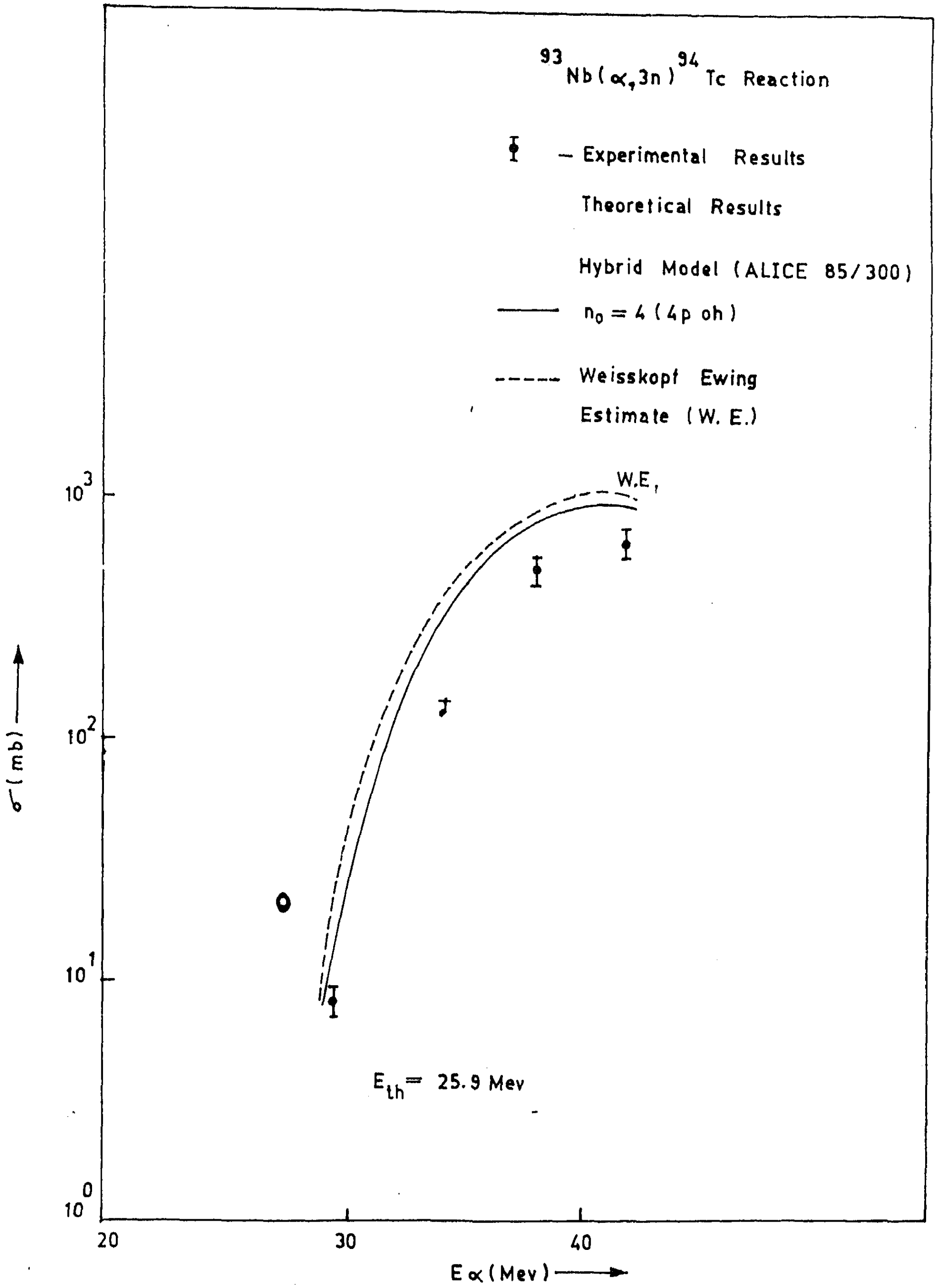

Figure 3. Comparison of theoretical and experimental excitation function of $^{93}Nb(\alpha, 3n)$ ^{94}Tc reaction.

pre-equilibrium phase. Moreover, the radical difference between the predicted and observed shape of the excitation function strongly suggests the influence of direct interaction effect in the emission of alpha particles. The observed slowly rising monotonic shape, which is common to all the $(\alpha, \alpha xn)$ type of reactions, points out to a possible inelastic scattering of the incident alpha particle, followed by neutron

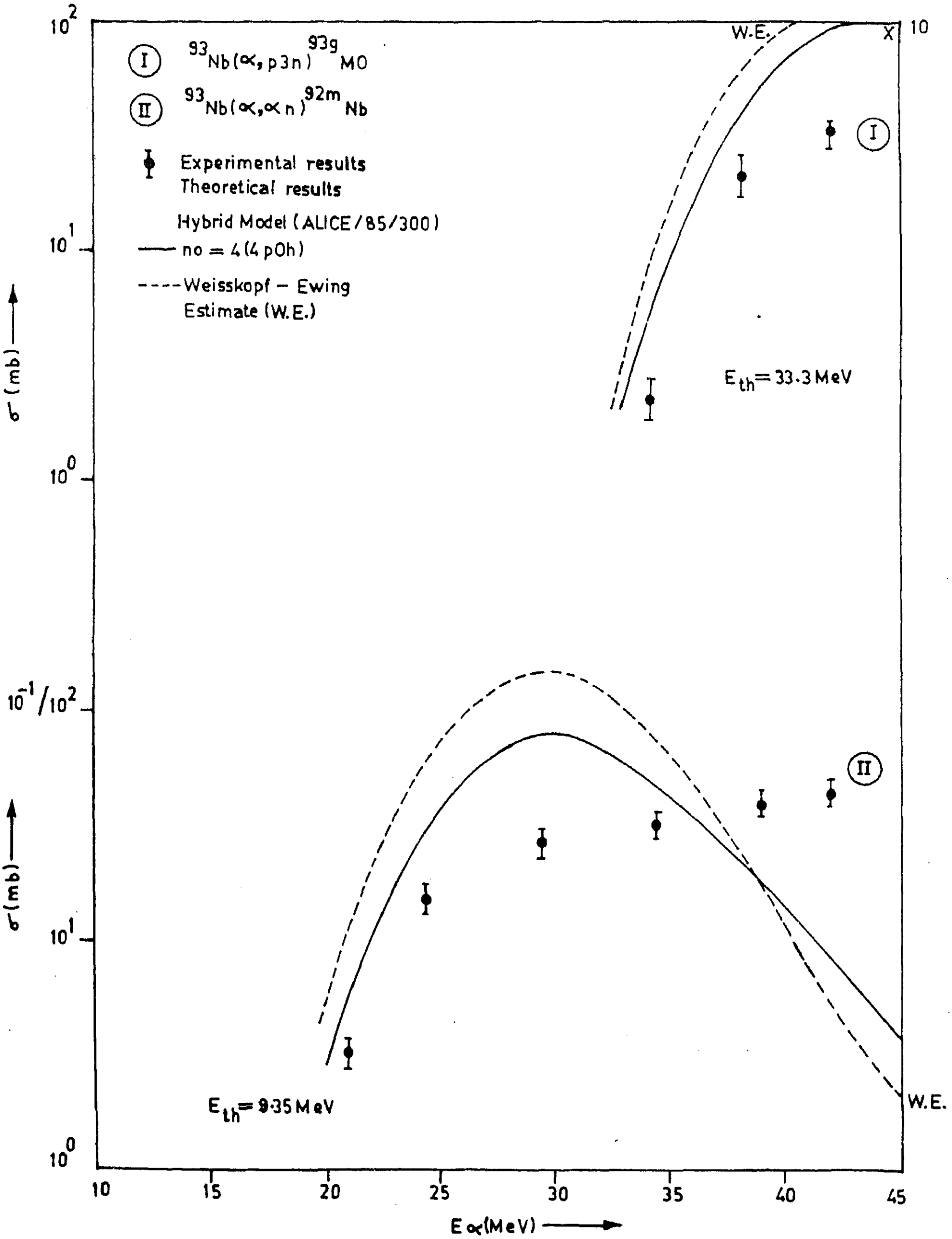

Figure 4. Comparison of theoretical and experimental excitation functions of ^{93}Nb[$(\alpha, p3n)$ and $(\alpha, \alpha n)$] reactions.

evaporation. Similar observations were made by Lanzafame and Blann [23], while studying alpha particle induced reactions on gold. They studied the recoil ranges of the residual nuclei in $(\alpha, \alpha xn)$ type of reactions and found that there is a very little momentum transfer to the recoiling nucleus, as expected for a direct interaction.

5. Conclusions

Excitation functions for six reactions of the type $(\alpha, xnypz\alpha)$ were studied in the present work. The present experimental results are systematic and more accurate over many of the previous measurements, adding several useful energy point cross-sections not measured earlier.

From an overall comparison between experimental results and theoretical predictions based on the compound nucleus Weisskopf–Ewing estimates as well as pre-equilibrium hybrid model one can infer that the model gives a fairly good account of nucleon emission in (α, xn) type of reactions in the medium mass region with an initial exciton configuration $n_0 = 4$ $(4\,p0h)$. The above initial configuration justifiably implies that, following the first projectile target interaction, only four excitons share the excitation energy and they being the four nucleons of the alpha particle of pre-equilibrium mechanism and only a few degrees of freedom are initially excited in a reaction at moderate energies.

However, the hybrid model fails to reproduce even the shapes of the excitation function of $(\alpha, \alpha xn)$ type of reactions. This is because, basically this model is not designed to handle complex (alpha) particle emission. It can treat only nucleon emission (either proton or neutron) in the pre-equilibrium phase. The alpha particle emission in the hybrid model is far from the level of the nucleon emission. The problem here is that the alpha particle in a nucleus does not exist on a semi-permanent basis as nucleons do. Recently, certain refinements have been reported [24, 25] in order to explain the emission of alpha particles in an approximate way. Further work in this direction is under progress, using more elaborate theoretical codes [26].

Acknowledgements

The authors wish to thank Dr Bikash Sinha and the entire staff of the Variable Energy Cyclotron Centre, Calcutta, India, for their co-operation. One of the authors (SM) would like to thank the Madhya Pradesh Council of Science and Technology, Bhopal, for awarding a fellowship. Thanks are also due to Professor J Rama Rao, Physics Department, Banaras Hindu University, Varanasi, India for his help and suggestions.

References

[1] J J Griffin, *Phys. Rev. Lett.* **17**, 478 (1966)
[2] C K Cline and M Blann, *Phys. Rev.* **A172**, 225 (1971)
[3] M Blann, *Phys. Rev. Lett.* **27**, 337, 700E, 1550E (1971)
[4] E Gadioli, E Gadioli-Erba and P G Sona, *Nucl. Phys.* **A217**, 589 (1973)
[5] M Blann, *Ann. Rev. Nucl. Sci.* **25**, 123 (1975)
[6] G Mantzouranis, D Agassi and H A Weidenmuller, *Z. Phys.* **A27**, 145 (1976)
[7] J Ernst and J Rama Rao, *Z. Phys.* **A281**, 129 (1977)
[8] H Machner, *Phys. Lett.* **B86** 129 (1979)
[9] M Blann and H K Vonach, *Phys. Rev.* **C28**, 1475 (1983)
[10] P H Stelson and F K McGowan, *Phys. Rev.* **B133**, 911 (1964)
[11] L F Hanson and M L Stelta, *Phys. Rev.* **B136**, 1000 (1964)
[12] I Matsuo, J M Matuszek, N D Dubey and T T Sugihara, *Phys. Rev.* **B139**, 886 (1965)
[13] P Bond and S Jha, *Phys. Rev.* **C2**, 1887 (1970)
[14] C L Brañouinho, S M A Hoffmann, G W A Newton, V J Robinson, H Y Wang, J S Grant and J A B Goodalo, *J. Inorg. Nucl. Chem.* **41**, 617, 791 (1979)

[15] J Ernst, R Ibowaki, H Klampfl, H Machner, T Mayer Kuckuk and R Schanz, *Z. Phys.* **A308**, 301 (1982)
[16] E Gadioli, E Gadioli-Erba, J J Hogan and B V Jacak, *Phys. Rev.* **C29**, 76 (1984)
[17] M Blann, Code ALICE/85/300 UCID-20169 (1984)
[18] C F Williamson, J P Boujot and J Picard, *CENS Report*, CEAR 3042 (1966)
[19] H J Probst, S M Qaim and R Weinreich, *Int. J. Appl. Radiat. Isotopes* **27**, 431 (1976)
[20] C M Lederer and V S Shirley, *Table of isotopes* (John Wiley, New York, 1978)
[21] S Mukherjee, A V Mohan Rao and J Rama Rao, *Il. Nuovo Cimento* **A104**, 863 (1991)
[22] R D Myers, *Droplet model of atomic nuclei* (Plenum, New York, 1977)
[23] F M Lanzafame and M Blann, *Nucl. Phys.* **A142**, 542 (1972)
[24] H Machner, *Phys. Rep.* **127**, 309 (1985)
[25] C Kalbach, *Phys. Rev.* **C23**, 124 (1984)
C Kalbach, *Phys. Rev.* **24**, 819 (1981)
[26] C Kalbach, PRECO-D2. *Program for calculating pre-equilibrium and direct reaction double-differential cross sections*, LOS Alamos National Laboratory Report LA-10248-MS, 1985

PRAMANA
— journal of
physics

© Printed in India

Vol. 41, No. 4,
October 1993
pp. 339–344

Sub-barrier fission fragment angular distributions for the system $^{19}F + ^{232}Th$

S KAILAS, A NAVIN, A CHATTERJEE, P SINGH, A SAXENA,
D M NADKARNI, D C BISWAS, R K CHOUDHURY and S S KAPOOR
Nuclear Physics Division, Bhabha Atomic Research Centre, Bombay 400085, India

MS received 24 June 1993

Abstract. The measurements of fission fragment angular distributions for the system $^{19}F + ^{232}Th$ have been extended to the sub-barrier energies of 89·3, 91·5 and 93·6 MeV. The measured anisotropies, within errors are nearly the same over this energy region. However, the deviation of the experimental values of anisotropies from that of standard statistical model predictions increases as the bombarding energy is lowered.

Keywords. Fission reactions at sub-barrier energies; $^{19}F + ^{232}Th$ system.

PACS No. **25·85**

1. Introduction

The observation of anomalous fission fragment anisotropies [1, 2] as compared to the predictions of the standard saddle point statistical model (SSPSM) has led to a revival of interest in the study of fission fragment anisotropies in heavy ion-induced fission. The deviation from SSPSM behaviour has been observed over a wide range of energies, from below to above barrier energies and for different target-projectile combinations. In an earlier work at energies mostly above the barrier, for projectiles like ^{16}O and ^{19}F it has been suggested [3, 4] that the deviation from SSPSM can be explained if one assumes that for cases where fission barriers and the temperatures are comparable, in addition to the normal statistical compound nucleus fission process a new process of pre-equilibrium fission (unequilibrated in K-degree of freedom) also contributes to the observed fissions. However, at near- and sub-barrier energies the deviation from SSPSM could also arise at least in part due to increase in $\langle I^2 \rangle$ (as compared to that expected from one-dimensional barrier penetration model) due to coupling to other degrees of freedom [2]. Recent data of fission fragment anisotropies for several systems measured at sub-barrier energies [5, 6] are significantly higher as compared to SSPSM predictions irrespective of the entrance channel asymmetry of the interacting system. The reasons for this observed anomalous behaviour are yet to be understood.

From a measurement of fission fragments using mica track detectors, Zhang *et al* [7, 8] have reported not only abnormally large values of anisotropies but also a peak-like structure in the anisotropy versus energy plot for the system $^{19}F + ^{232}Th$ at a sub-barrier energy of $E(\text{Lab}) = 91{\cdot}4$ MeV. There is also the unpublished preliminary results of fission fragment angular distribution measurements of Fujiwara *et al* [9] for this system at $E(\text{Lab}) = 90$, 92 and 94 MeV employing single window ionization chamber as a fission detector. Their results do not indicate the presence of a peak-like structure. From other detailed investigations [10, 11] it is clear that such a peak-like behaviour in anisotropy versus energy plot cannot arise due to possible small admixture of transfer induced fissions (involving particle transfers). This peak-like structure, if confirmed, would imply the presence of a new reaction mechanism in the sub-barrier region which is not incorporated in the present models. To verify the presence of this peak-like structure in the anisotropy versus energy plot, we have extended our earlier measurements [4] of fission fragment angular distributions for this system to the sub-barrier energies using silicon/gas detectors.

2. Experimental procedure and results

The present experiment was performed using the ^{19}F beam available from the BARC–TIFR 14 UD Pelletron accelerator at Bombay. The fission fragment angular distributions were measured at laboratory, bombarding energies of 89·3, 91·5 and 93·6 MeV, utilizing a natural thorium target of thickness 200 μg/cm^2 (thickness estimated from alpha counting) deposited on a 10 μm thick aluminium backing. The above-mentioned effective bombarding energies have been obtained after correcting for Th target thickness and small carbon build up present in the target [12]. The fission fragments were detected using two thin silicon detectors of 20 μm thickness. The elastic and the inelastic scattering events of ^{19}F from the ^{232}Th target were rejected using ‘veto’ detectors placed behind the thin Si detectors. The fission fragment angular distribution measurements were carried out in the angular range of $\theta = 85°$ to 170°. The fission spectra measured at 90° and 170° (at $E(\text{Lab}) = 93{\cdot}6$ MeV) are shown in figure 1. On the low energy side of the spectrum there is an interference from alpha particles probably emitted in reactions with the backing and having energies too low to reach the veto detector. (The source of contamination has been checked in a separate measurement using gas-Si telescope and identifying the particle groups). This leads to uncertainty of less than 5% in fission yield extraction in the worst case. The overall uncertainty on the measured anisotropy varied from 8 to 10%. At $E(\text{Lab}) = 93{\cdot}6$ MeV, a gas (ΔE)-Si(E) telescope [13] was also used and the anisotropy value obtained agreed with that from using the former set-up. As the data measured with the latter set up were of lower statistics due to smaller solid angle, they are not shown in figure. A monitor detector was placed at 50° to detect the elastically scattered F from Th. Fission cross-sections were obtained by normalizing the fission yield to the monitor yield, assuming the latter to arise from Rutherford scattering. The measured fission fragment angular distributions were transformed to the centre-of-mass system assuming symmetric mass division and Viola systematics [14] for the total fragment kinetic energy. The angular distributions were fitted using the relation $W(\theta) = a + b\cos^2\theta + c\cos^4\theta$ with a, b and c as adjustable parameters. In figure 2 the angular distributions normalized to W (90°) values evaluated from the above fits are shown. The experimental anisotropy values $A = W(180°)/W(90°)$ deduced from the fits to the data are shown in figure 3 along with the results of earlier measurements of Zhang *et al* [7] and Fujiwara *et al* [9]. In the inset of figure 3 the anisotropy values measured in the entire energy range of 80 to 100 MeV by our group [4] and by Zhang *et al* [7] are shown. The main conclusion of the present work (seen from figure 3) is that not only the anisotropy values measured here are significantly smaller than the ones reported by Zhang *et al* [7] but also do not show the appearance of a peak-like structure in the anisotropy versus energy plot.

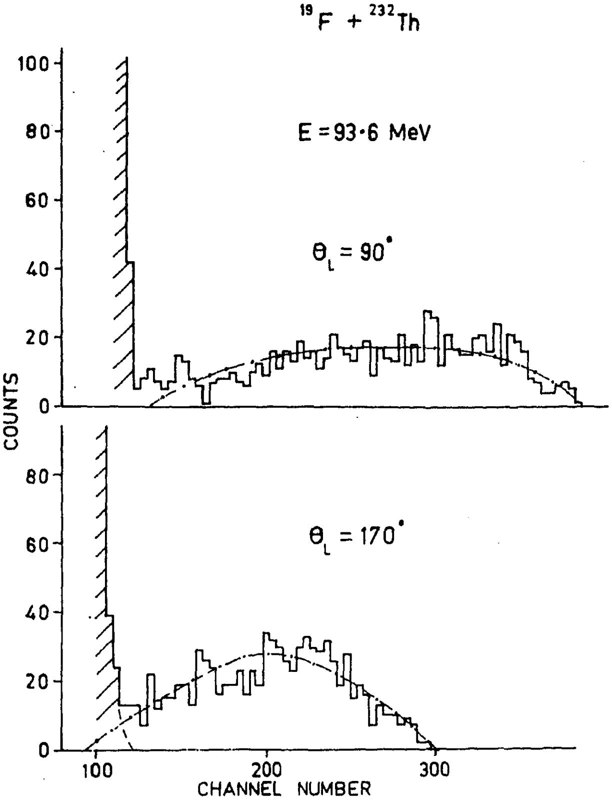

Figure 1. Fission fragment spectra measured using thin Si detector (plus a veto detector) at $\theta = 90°$ and 170° at E(Lab) = 93·6 MeV. The low energy contaminant is shown by a shaded area (see text for details). The dash-dot line is drawn to guide the eye.

Table 1. Summary of the experimental and the theoretical results $^{19}F + ^{232}Th$.

E (MeV) (Lab)	σ_F (mb) (expt)	σ_F (mb) (cal)	$\langle I^2 \rangle$	K_0	A (cal)	A (expt)
89·3	4·5 ± 0·5	4·1	122	16·2	1·12	1·75 ± 0·20
91·5	13·4 ± 1·4	14·4	189	16·5	1·19	1·85 ± 0·20
93·6	28·0 ± 3·0	31·6	258	16·6	1·24	1·95 ± 0·15

Note. cal = calculation. expt = experimental value
K_0^2 is the variance of K distribution (refs [3, 4] for more details).

The angular distributions were integrated to obtain the total fission cross-section (σ_F) and the resultant fission excitation function is displayed in figure 4. The other data sets on fission cross-sections in the literature [4, 7, 9, 15] are also shown in figure.

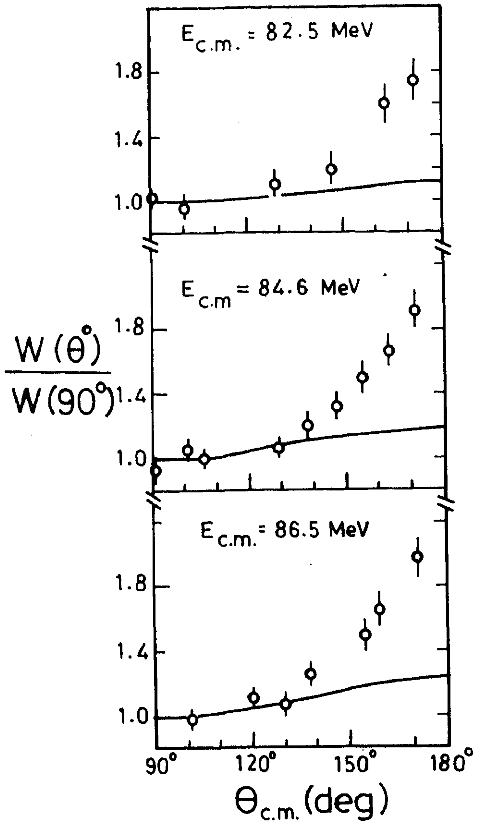

Figure 2. Fission fragment angular distributions for the system $^{19}F + ^{232}Th$ at $E_{cm} = 82{\cdot}5$, $84{\cdot}6$ and $86{\cdot}5$ MeV. The solid lines are the standard saddle point statistical model calculations as discussed in the text.

3. Analysis and discussion

In order to determine the spin distribution values at each energy a Wong model fit to the cross-section data (including the deformation of the target) has been made following the procedure discussed earlier [4] and this is shown as a continuous line in figure 4. While the cross-section values reported by Fujiwara *et al* [9] are consistent with the present measurements, the results of Zhang *et al* [7] are somewhat higher and this may partly be due to their finding larger anisotropies (larger cross-section at backward angles). While the above three groups obtained the total fission cross section by integrating the angular distribution data, Leigh [15] determined the same assuming $W(\theta)\alpha 1/\sin(\theta)$, a procedure which may lead to higher values of σ_F. The somewhat higher values of cross-sections reported by Leigh may be related to this aspect.

The fission fragment angular distributions and the anisotropies have been calculated using the procedure discussed by Ramamurthy *et al* [3] and the $\langle I^2 \rangle$ values determined from Wong model fit to cross-section data. Summary of the results is given in table 1. It may be pointed out that the measurements reported in [7, 9] and the present one

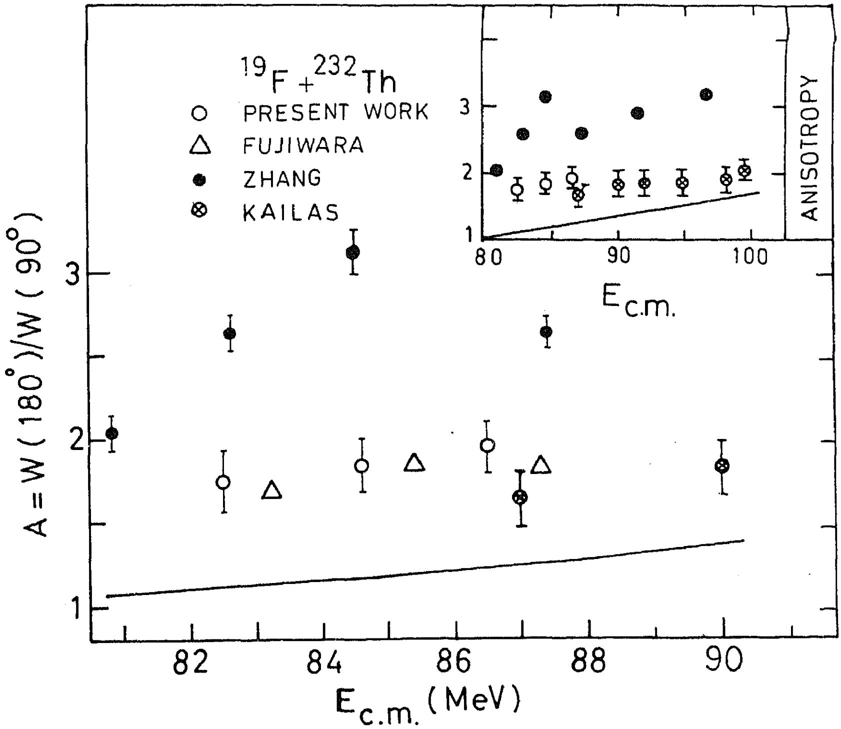

Figure 3. The experimental fission fragment anisotropies for the ^{19}F + ^{232}Th system. The anisotropy values measured by Kailas *et al* [4], Zhang *et al* [7] and Fujiwara *et al* [9] are also shown. The solid line represents the SSPSM calculation. The inset shows our data in the energy region 80 to 100 MeV compared with those of Zhang *et al* and the SSPSM calculation.

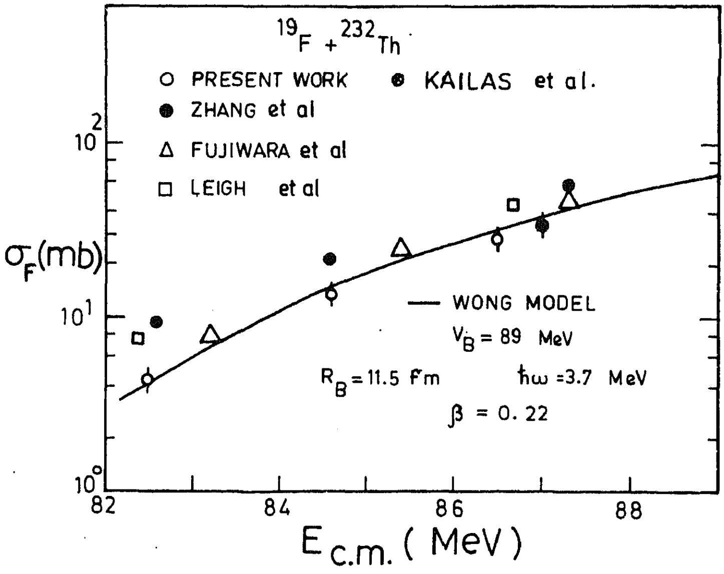

Figure 4. Measured fission excitation function for the system ^{19}F + ^{232}Th compared with the Wong model fit. The cross-section values determined by Kailas *et al* [4], Zhang *et al* [7], Leigh [15] and Fujiwara *et al* [9] are also shown.

are inclusive and they contain mainly fusion-fission and small amounts of transfer-fission events. As transfer fission is not separated in these measurements, the $\langle I^2 \rangle$ values obtained assuming the measured fission cross-section is all due to complete momentum transfer and hence the anisotropy values calculated can be considered to be upper limits. In figures 2 and 3 these calculations are shown as continuous lines. It is observed from the present angular distribution data and the measured anisotropies that though the anisotropy values are significantly smaller than the ones of Zhang *et al* [7] they are still higher and anomalous as compared to the SSPSM predictions.

4. Conclusion

In conclusion, the present measurements of fission fragment angular distributions for the system ^{19}F + ^{232}Th and the data of Fujiwara *et al* [9] are in strong disagreement with the results of Zhang *et al* [7]. The present results, within errors, do not support the observation of a peak-like structure in the anisotropy versus energy plot at these sub-barrier energies covering the energy region of 89·3 to 93·6 MeV.

Acknowledgements

We thank Mr V S Ambekar for his help and Dr R J Singh for making the Th target. Thanks are also due to Prof. R Vandenbosch for useful correspondence on this work. We thank the Pelletron Accelerator crew for the fine operation of the machine.

References

[1] L Vaz and J M Alexander, *Phys. Rep.* **97**, 1 (1983)
[2] R Vandenbosch, T Murakami, C C Sahm, D D Leach, A Ray and M J Murphys, *Phys. Rev. Lett.* **56**, 1234 (1986)
[3] V S Ramamurthy *et al*, *Phys. Rev. Lett.* **65**, 25 (1990)
[4] S Kailas *et al*, *Phys. Rev.* **C43**, 1466 (1991)
[5] H Zhang, Z Liu, J Xu, X Qian, S Chen and L Lu, *Phys. Rev.* **C47**, 1309 (1993)
[6] A Karnik, S Kailas, A Chatterjee, P Singh, A Navin, D C Biswas, D M Nadkarni and S S Kapoor, *Symp. Nucl. Phys.* (*India*) **B35**, 286 (1992)
[7] H Zhang, J Xu, Z Liu, J Lu, K Xu and M Ruan, *Phys. Lett.* **B218**, 133 (1989)
[8] H Zhang, J Xu, Z Liu, J Lu, M Ruan and K Xu, *Phys. Rev.* **C42**, 1086 (1990)
[9] H Fujiwara, S C Jeong, Y H Pu, T Mizota, H Kugoh, Y Futami, Y Nagashima and S M Lee *et al*, Annual report of university of Tsukuba, Japan (unpublished) (1989) p. 52
[10] J P Lestone, R Leigh, J O Newton and J X Wei, *Nucl. Phys.* **A509**, 178 (1990)
[11] B B Back, R R Betts, P Fernandez, B G Glagola, T Happ, D Henderson, H Ikezoe and P Benet, *Sixth winter workshop on nuclear dynamics* (Wyoming, USA 1990)
[12] J V Ramana, Sanjivkumar, V S Raju, S Gangadharan and S Kailas, *Symp. Nucl. Phys.* (*India*) **B34**, 423 (1991)
[13] D C Biswas, M N Rao and R K Choudhury, *Nucl. Instrum. Methods* **B53**, 251 (1991)
[14] V E Viola, K Kwiatkowski and M Walker, *Phys. Rev.* **C31**, 1550 (1985)
[15] J R Leigh, *Cross sections as reported in Zhang et al* (1989)

PRAMANA
— journal of
physics

© Printed in India

Vol. 41, No. 4,
October 1993
pp. 345–362

Ab-initio Hartree–Fock self-consistent-field calculations—An indigenous development of computer programs

SAMBHU N DATTA
Department of Chemistry, Indian Institute of Technology, Powai, Bombay 400076, India

MS received 24 May 1993; revised 19 August 1993

Abstract. A set of indigenously developed computer programs for ab-initio Hartree–Fock calculations on both closed- and open-shell molecules have been described. These programs have been written for calculations using GTO basis sets. Integral formulae have been taken from Taketa *et al* [8]. Structures and functions of the programs have been discussed. These programs have been extensively tested. Molecular integrals over GTO basis sets have been chosen for tests and as numerical examples in this paper. Results of calculations using very accurate minimal bases have been given for methane. Time taken for these computations in a CDC Cyber 180/840 machine has been indicated. Trends in the calculations have also been illustrated by employing 4-gaussian expansions for the STO's and by varying the basis size for LiH and BH^+.

Keywords. Hartree–Fock; ab-initio; program development; open shell.

PACS Nos **31·15; 31·20**

1. Introduction

The quantitative bonding theory developed by theoretical chemists and physicists is mature. A small collection of flexible and powerful techniques, exercised with caution and insight, gives a full and subtle account of structural details and chemical reactivity for a wide range of molecules. Among these techniques, the Hartree–Fock theory [1, 2] and Hartree–Fock–Roothaan self-consistent-field calculations [3] together occupy a central position, a position revered as the mean field or the one-electron approximation. The theory and the technique of calculation are not new. What is new in this article is the algorithm for an indigenously prepared computer program for the ab-initio, nonrelativistic, Hartree–Fock self-consistent-field calculation on closed- and open-shell molecules using gaussian basis sets [4]. A few newly computed results are also given.

The programs developed can be easily extended for nonrelativistic configuration interaction calculations, and with suitable considerations, for relativistic Hartree–Fock and relativistic correlation treatments. These extensions will be described in a series of papers to be published in the near future.

The calculations involved are under two major and one minor approximations. The major approximations are theoretical in nature. These are (i) the Born–Oppenheimer approximation and (ii) the neglect of the polarization of mass [5]. The minor approximation is rather technical in nature. It is assumed that the Hartree–Fock orbitals are given by linear combinations of the basis functions employed. Since only a finite number of basis functions will be in use in one calculation, the description of the Hartree–Fock orbitals as linear expansions in the basis set is by no means complete. That is, the calculated functions will be approximate Hartree–Fock orbitals. The Hartree–Fock equations are essentially second-order differential equations that can be solved by numerical integration techniques to any desired degree of accuracy in total energy. Such numerical calculations were performed for atoms [6]. Results of these numerical calculations are very close to the exact solutions of the atomic Hartree–Fock equations, and the same results are said to be in the Hartree–Fock limit. Results obtained from a calculation with analytical basis functions can be compared with the near Hartree–Fock results, the differences serving as a measure of the accuracy of the "analytical" calculation. This accuracy can be improved by extending the basis set, that is, by using more basis functions. The basis set truncation error can also be reduced by improving the basis function, that is, by optimizing the GTO's and by increasing the number of optimized GTO's in each basis function [7].

This article is arranged as follows. The GTO basis set is described in § 2. Calculation of integrals over basis functions is described in § 3. The discussion involves the nature of integrals, the calculation of these integrals over gaussians as prescribed by Taketa *et al* [8] and the calculation of integrals in the atomic case. Structures of the programs developed are described in detail in § 4. Computed results for a few molecules (CH_4, LiH and BH^+) are discussed in § 5 and A few remarks on the trend of calculations are included.

2. GTO basis set

The gaussian functions to be used as input are of the form

$$g_i^{in} = N_i r^{-l_i} e^{-\alpha_i r^2} \bar{Y}_{l_i} \tag{1}$$

where $\bar{Y}_{l_i}$ is a real spherical harmonics of type

$$\bar{Y}_{l_i} = N_Y \sum_{l=0}^{l_i} \sum_{m=0}^{(l_i-l)} \eta_{l,m,l_i-l-m} r^{-l_i} x^l y^m z^{(l_i-l-m)} \tag{2}$$

and N_i is the normalization constant of the radial function,

$$N_i = \frac{2^{l_i+7/4} \alpha^{l_i/2+3/4}}{\pi^{1/4}[(2l+1)!!]^{1/2}}. \tag{3}$$

For instance, for the d_{z^2} gaussian

$$\bar{Y} = (5/16\pi)^{1/2} \frac{2z^2 - x^2 - y^2}{r^2}, \tag{4}$$

$l_i = 2$ and $N_y = (5/16\pi)^{1/2}$; here the only nonvanishing coefficients are $\eta_{2,0,0} (= -1)$, $\eta_{0,2,0} (= -1)$ and $\eta_{0,0,2} (= 2)$.

Hence the input gaussians can be written as

$$g_i^{in} = \sum_j g_j c_{ji} \tag{5}$$

where g_j is a cartesian gaussian of the form

$$g_j = x^l y^m z^{l_i-l-m} e^{-\alpha_i r^2}, \tag{6}$$

c_{ji} is given by

$$c_{ji} = N_i N_Y \eta_{l,m,l_i-l-m}, \tag{7}$$

and the sum over the index j in (5) covers the sum over all possible combinations of l and m with nonvanishing coefficients (η's).

The basis functions are of the form

$$\phi_\mu = \sum_i g_i^{in} a_{i\mu}. \tag{8}$$

The input involves coordinates of the centre of the gaussians g_i^{in}, angular type representing the l, m and $(l_i - l - m)$ values, exponent α_i and coefficient a_i. The initial program converts the basis function into a linear combination of cartesian gaussians,

$$\phi_\mu = \sum_j g_j d_{j\mu}. \tag{9}$$

One can easily see that the coefficient $d_{j\mu}$ of the cartesian gaussian $\bar{g}_j$ is given by

$$d_{j\mu} = \sum_i c_{ji} a_{i\mu}. \tag{10}$$

These coefficients of the cartesian gaussians are calculated and printed.

3. Calculation of integrals

Types of integrals

The integrals involved in a nonrelativistic Hartree–Fock calculation are as follows:

(i) Overlap integrals, $S_{\mu\nu} = \langle \phi_\mu | \phi_\nu \rangle$

(ii) Kinetic energy integrals, $T_{\mu\nu} = -\frac{1}{2}\langle \phi_\mu | \nabla^2 | \phi_\nu \rangle$

(iii) Nuclear attraction integrals, $V_{\mu\nu} = -Z_m \left\langle \phi_\mu \middle| \frac{1}{|\mathbf{r} - \mathbf{R}_m|} \middle| \phi_\nu \right\rangle$

(iv) Electron repulsion integrals,

$$(\mu\nu|\sigma\delta) = \int \mathrm{d}v_1 \int \mathrm{d}v_2\, \phi_\mu(r_1)\phi_\sigma(r_2) r_{12}^{-1} \phi_\nu(r_1)\phi_\delta(r_2).$$

Calculation

Following (6), the GTO g_j centered at atom A is written as

$$g_j(A) = x_A^{l} y_A^{m_j} z_A^{n_j} \exp(-\alpha_j r_A^2). \tag{11}$$

The coordinates x_A, y_A and z_A are components of the position vector $\mathbf{r}_A$ relative to the centre of the atom A. Then we have

$$S_{\mu\nu} = \sum_{i,j} d_{i\mu} \mathrm{d}_{j\nu} \langle g_i | g_j \rangle, \tag{12}$$

$$T_{\mu\nu} = -1/2 \sum_{i,j} \mathrm{d}_{i\mu} \mathrm{d}_{j\nu} \langle g_i | \nabla^2 | g_j \rangle,$$

$$V_{\mu\nu}^m = -Z_m \sum_{i,j} \mathrm{d}_{i\mu} \mathrm{d}_{j\nu} \left\langle g_i \middle| \frac{1}{|\mathbf{r} - \mathbf{R}_m|} \middle| g_j \right\rangle,$$

$$(\mu\nu|\sigma\delta) = \sum_{ijkl} \mathrm{d}_{i\mu} \mathrm{d}_{j\nu} \mathrm{d}_{k\sigma} \mathrm{d}_{l\delta} (g_i g_j | g_k g_l).$$

Calculation of the integrals $\langle g_i|g_j\rangle$, $\langle g_i|\nabla^2|g_j\rangle$, $\left\langle g_i\left|\frac{1}{|\mathbf{r}-\mathbf{R}_m|}\right|g_j\right\rangle$ and $(g_ig_j|g_kg_l)$ has been discussed by Taketa *et al* [8] and the formulae derived have been used in the preparation of the first two computer programs. The working equations have been assembled in Appendix I. For a full derivation of these equations refer [8].

Integrals (iii) and (iv) involve functions G and H (equations 8 and 11 in Appendix I). Explicit forms for the functions G and H have been calculated by Taketa *et al* up to the combinations $l_1+l_2=4$ and $(l_1=2,\ l_2=2)$ respectively. Our systematics for computing G and H functions for these values of l_1 and l_2 as well as higher values are given in tables 1 and 2.

Atomic calculations

For calculations on atoms or atomic ions, the formulae become much simplified. So it is useful to separate the atomic calculations from the main body of the programs. This requires only one (or two) additional subroutine (s).

The atomic simplification arises from two observations: (i) the factor f_j given by (3) of Appendix I reduces to

$$f_j=\delta_{j,l_1+l_2} \tag{13}$$

for $0\leqslant j\leqslant l_1+l_2$, and (ii) there is only one nucleus that can be conveniently located at the origin so that $R_A=R_B=R_C=R_D=R_P=R_Q=0$. We get the following simplified expressions.

1. Overlap integral

$$\langle g_1|g_2\rangle=0,\ \text{if any of the sums } (l_1+l_2),\ (m_1+m_2) \text{ and } (n_1+n_2) \text{ is odd,}$$

$$=\left(\frac{\pi}{\gamma}\right)^{3/2}\frac{(l_1+l_2-1)!!(m_1+m_2-1)!!(n_1+n_2-1)!!}{(2\gamma)^{(l_1+m_1+n_1+l_2+m_2+n_2)/2}}\ \text{otherwise.} \tag{14}$$

2. Kinetic energy integral

$$(-1/2)\langle g_1|\nabla^2|g_2\rangle$$

$$=0,\ \text{if any of the sums } (l_1+l_2),\ (m_1+m_2) \text{ and } (n_1+n_2) \text{ is odd}$$

$$=\Bigg(\alpha_2[2(l_2+m_2+n_2)+3]-\frac{\alpha_2^2}{\gamma}[l_1+l_2+m_1+m_2+n_1+n_2+3]$$

$$-\gamma\left[\frac{l_2(l_2-1)}{(l_1+l_2-1)}+\frac{m_2(m_2-1)}{(m_1+m_2-1)}+\frac{n_2(n_2-1)}{(n_1+n_2-1)}\right]\Bigg)\langle g_1|g_2\rangle\ \text{otherwise.} \tag{15}$$

3. Nuclear attraction energy integrals

$$\left\langle g_1\left|-\frac{Z}{r}\right|g_2\right\rangle$$

$$=0,\ \text{if any of the sums } (l_1+l_2),\ (m_1+m_2) \text{ and } (n_1+n_2) \text{ is odd}$$

$$=-\frac{2\pi Z}{\gamma}\sum_{I=0}^{l_2+l_2}\sum_{J=0}^{m_1+m_2}\sum_{K=0}^{n_1+n_2}G_{Ix}G_{Jy}G_{Kz}/[2(I+J+K)+1]\ \text{otherwise,} \tag{16}$$

Table 1. Algorithm for preparing G_x functions for various $(l_1 + l_2)$. The parameter p is given by $p = X_P - X_C$. In each expression G_{lx} represents the expression for G_{lx} for the preceding $l_1 + l_2$. The parameter $f_{l_1+l_2}$ is 1 for every $(l_1 + l_2)$.

$(l_1 + l_2)$	l	$G_l(l_1, l_2, x_A - x_P, x_B - x_P, p)$
0	0	f_0
1	0	G_{0x}
	1	$-f_1 p$
2	0	$G_{0x} + f_2/2\gamma$
	1	$G_{1x} - f_2/2\gamma$
	2	$f_2 p^2$
3	0	G_{0x}
	1	$G_{1x} - 3f_3 p/2\gamma$
	2	$G_{2x} + 3f_3 p/2\gamma$
	3	$-f_3 p^3$
4	0	$G_{0x} + 3f_4/4\gamma^2$
	1	$G_{1x} - 3f_4/2\gamma^2$
	2	$G_{2x} + 3f_4 p^2/\gamma + 3f_4/4\gamma^2$
	3	$G_{3x} - 3f_4 p^2/\gamma$
	4	$f_4 p^4$
5	0	G_{0x}
	1	$G_{1x} - 15f_5 p/4\gamma^2$
	2	$G_{2x} + 15f_5 p/2\gamma^2$
	3	$G_{3x} - 15f_5 p/4\gamma^2 - 5f_5 p^3/\gamma$
	4	$G_{4x} + 5f_5 p^3/\gamma$
	5	$-f_5 p^5$
6	0	$G_{0x} + 15f_6/8\gamma^3$
	1	$G_{1x} - 45f_6/8\gamma^3$
	2	$G_{2x} + 45f_6 p^2/4\gamma^2 + 45f_6/8\gamma^3$
	3	$G_{3x} - 45f_6 p^2/2\gamma^2 - 15f_6/8\gamma^3$
	4	$G_{4x} + 15f_6 p^4/2\gamma + 45f_6 p^2/4\gamma^2$
	5	$G_{5x} - 15f_6 p^4/2\gamma$
	6	$f_6 p^6$
7	0	G_{0x}
	1	$G_{1x} - 105f_7 p/8\gamma^3$
	2	$G_{2x} + 315f_7 p/8\gamma^3$
	3	$G_{3x} - 105f_7 p^3/4\gamma^2 - 315f_7 p/8\gamma^3$
	4	$G_{4x} + 105f_7 p^3/2\gamma^2 + 105f_7 p/8\gamma^3$
	5	$G_{5x} - 21f_7 p^5/2\gamma - 105f_7 p^3/4\gamma^2$
	6	$G_{6x} + 21f_7 p^5/2\gamma$
	7	$-f_7 p^7$
8	0	$G_{0x} + 105f_8/16\gamma^4$
	1	$G_{1x} - 105f_8/4\gamma^4$
	2	$G_{2x} + 105f_8 p^2/2\gamma^3 + 315f_8/8\gamma^4$
	3	$G_{3x} - 315f_8 p^2/2\gamma^3 - 105f_8/4\gamma^4$
	4	$G_{4x} + 105f_8 p^4/2\gamma^2 + 315f_8 p^2/2\gamma^3 + 105f_8/16\gamma^4$
	5	$G_{5x} - 105f_8 p^4/\gamma^2 - 105f_8 p^2/2\gamma^3$
	6	$G_{6x} + 14f_8 p^6/\gamma + 105f_8 p^4/2\gamma^2$
	7	$G_{7x} - 14f_8 p^6/\gamma$
	8	$f_8 p^8$

Table 2. Algorithm for preparing H_L functions for various (l_1+l_2). In each expression H_L represents the expression for H_L for the preceding l_1+l_2. The parameter $f_{l_1+l_2}$ is 1 for every (l_1+l_2).

(l_1+l_2)	L	$H_L(l_1, l_2, a, b, \gamma)$
0	0	f_0
1	0	H_0
	1	$f_1/4\gamma$
2	0	$H_0+f_2/2\gamma$
	1	H_1
	2	$f_2/(4\gamma)^2$
3	0	H_0
	1	$H_1+6f_3/(4\gamma)^2$
	2	H_2
	3	$f_3/(4\gamma)^3$
4	0	$H_0+12f_4/(4\gamma)^2$
	1	H_1
	2	$H_2+12f_4/(4\gamma)^3$
	3	H_3
	4	$f_4/(4\gamma)^4$
5	0	H_0
	1	$H_1+60f_5/(4\gamma)^3$
	2	H_2
	3	$H_3+20f_5/(4\gamma)^4$
	4	H_4
	5	$f_5/(4\gamma)^5$
6	0	$H_0+120f_6/(4\gamma)^3$
	1	H_1
	2	$H_2+180f_6/(4\gamma)^4$
	3	H_3
	4	$H_4+30f_6/(4\gamma)^5$
	5	H_5
	6	$f_6/(4\gamma)^6$
7	0	H_0
	1	$H_1+840f_7/(4\gamma)^4$
	2	H_2
	3	$H_3+420f_7/(4\gamma)^5$
	4	H_4
	5	$H_5+42f_7/(4\gamma)^6$
	6	H_6
	7	$f_7/(4\gamma)^7$
8	0	$H_0+1680f_8/(4\gamma)^4$
	1	H_1
	2	$H_2+3360f_8/(4\gamma)^5$
	3	H_3
	4	$H_4+840f_8/(4\gamma)^6$
	5	H_5
	6	$H_6+56f_8/(4\gamma)^7$
	7	H_7
	8	$f_8/(4\gamma)^8$

where

$$G_{Ix}=\frac{(-1)^{I}(l_1+l_2)!}{\left(\frac{l_1+l_2}{2}-I\right)!\,I!\,(4\gamma)^{(l_1+l_2)/2}} \tag{17}$$

etc.

4. Electron repulsion integrals

$$(g_1g_2|g_3g_4)=\frac{2\pi^2}{\gamma_1+\gamma_2}\left(\frac{\pi}{\gamma_1+\gamma_2}\right)^{1/2}\sum_{I,J,K}C_{Ix}C_{Jy}C_{kz}/(2[I+J+K]+1) \tag{18}$$

where

$$C_{Ix}=\sum_{\substack{L\\(L+M=2I)}}^{(l_1+l_2)}\ \sum_{M}^{(l_2+l_3)}H_L(l_1,l_2,0,0,\gamma_1)(-1)^{I-L}H_M(l_3,l_4,0,0,\gamma_2)\times\frac{(2I)!}{I!\,[(\gamma_1+\gamma_2)/4\gamma_1\gamma_2]^{I}} \tag{19}$$

and

$$H_L=\frac{(l_1+l_2)!}{[(l_1+l_2-L)/2]!\,L!\,(4\gamma_1)^{(l_1+l_2+L)/2}}. \tag{20}$$

4. Program structures

Plan: The development of these programs has been completely indigenous. The whole scheme of calculation is covered by three programs to be executed successively, and the option is kept open for the execution of two more programs for the calculation of molecular properties and the configuration interaction treatment. The plan is exhibited in figure 1. The order of execution is indicated by arrows. Output of any

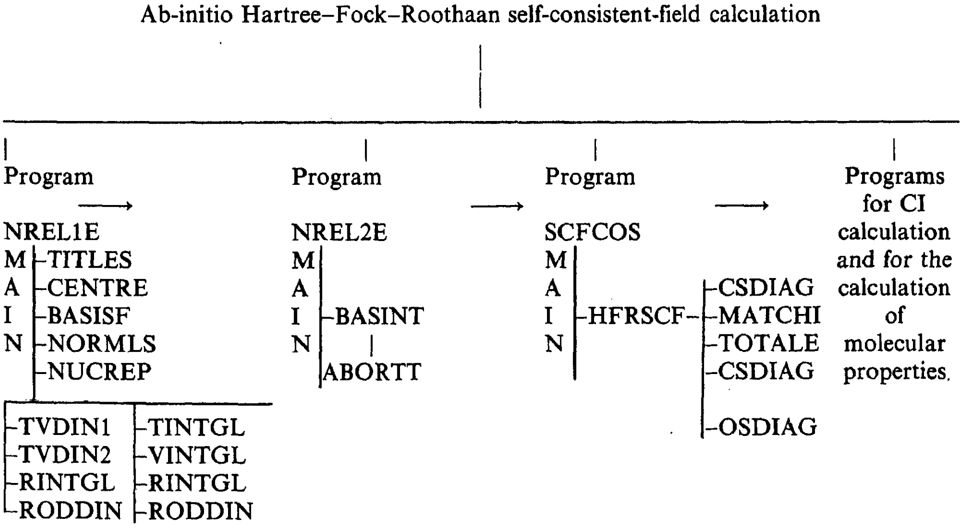

Figure 1. Scheme for carrying out ab-initio Hartree–Fock self-consistent-field calculations on closed- and open-shell molecules by using the GTO basis sets and the calling sequences for subroutiness in the programs used.

program is to be used in all subsequent executions. Thus output of NREL1E is used in executing NREL2E, SCFCOS and FUTURE, etc. Functions of the programs are as follows.

Functions

NREL1E	Calculates the nonrelativistic one-electron integrals, viz., (i) overlap integrals, (ii) kinetic energy integrals (integrals of $-2^{-1}\nabla^2$), (iii) electron-nuclear attractive potential energy integrals (integrals of $-Z_n|\mathbf{r}_i-\mathbf{R}_n|^{-1}$), and optionally (for atoms) (iv) r^n integrals (where $n=-3, -2, -1, 1, 2, 4, 6$) over nonrelativistic basis functions.
NREL2E	Calculates the nonrelativistic two-electron integrals, that is, two-electron repulsion integrals (integrals of r_{12}^{-1}) over nonrelativistic basis functions.
SCFCOS	Carries out the Hartree–Fock–Roothaan Self-Consistent-Field calculations, and optionally (for atoms) calculates the $\langle r^n \rangle$ expectation values for (atomic) orbitals.
FUTURE	The two aspects covered by these programs are (i) the calculation of molecular properties and (ii) configurations interaction treatment. The SDCI program has already been developed [9]. The full CI and molecular properties packages will be reported in the near future.

Subroutines of the first three programs are listed in table 3. Their functions are explained in the following.

Program NREL1E

Nonrelativistic one-electron integrals are calculated with the help of 13 subroutines in addition to the main program.

ABORTT	aborts execution in case of emergencies.
BASISF	reads specifications for the GTO basis.
CENTER	reads specifications for the centres of basis functions.
CONVRT	carries out (optionally) conversions necessary for a valence-electron calculation instead of an all-electron calculation.
MAIN	
NORMLS	normalizes the basis functions.
NUCREP	calculates internuclear repulsion energy.
RINTGL	calculates r^n matrices where n is even (optionally, for atomic cases).

Table 3. List of subroutines.

Program[1]	Subroutine					
NREL1E (1712)	ABORTT, NUCREP, TVDIN2,	BASISF, RINTGL, VINTGL	CENTER, RODDIN,	CONVRT, TINTGL,	MAIN, TITLES,	NORMLS, TVDIN1,
NREL2E (1172)	ABORTT,	BASINT,	MAIN			
SCFCOS (1249)	CSDIAG,	HFRSCF,	MAIN,	MATCHI,	OSDIAG,	TOTALE

[1] Total number of statements is indicated in paranthesis under the name of each program.

RODDIN	calculates r^n matrices where n is odd (optionally, for atomic cases).
TINTGL	calculates kinetic energy matrix.
TITLES	reads the heading of the job.
TVDIN1, TVDIN2	optionally performs atomic calculations, avoiding NORMLS, TINTGL and VINTGL: each of these subroutines can be written to completion while a TV dinner is cooked, hence the nomenclature.
VINTGL	calculates nuclear attraction energy matrix.

Program NREL2E

Nonrelativistic two-electron integrals are calculated.

ABORTT	aborts execution.
BASINT	calculates two-electron integrals over basis functions.
MAIN	

Program SCFCOS

Hartree–Fock–Roothaan SCF treatment is carried out for closed and open shell molecules.

CSDIAG	diagonalizes the closed-shell Fock matrix.
HFRSCF	carries out the SCF calculations.
MAIN	
MATCHI	matches indices for two-electron integrals and selects the stored values for preparing Fock matrices.
OSDIAG	diagonalizes the open-shell Fock matrix.
TOTALE	calculates total energy in every SCF loop.

Test

All the molecular integrals quoted in tables 1–5 in the paper of Taketa *et al* [8] have been computed and verified.

5. Concluding remarks

The difficulties in calculations employing the GTO basis sets are well known [8]. The main difficulty is the need to compute about $(1/8)N^4$ basic summands for two-electron integrals where N is the total number of gaussians. This is coupled with the problem of slow convergence of the calculated results as the number of terms in the expansion of each basis function increases. The advantages of using the GTO basis are that an exact analytical expression is available for each integral and the computation of these expressions is reasonably fast.

For illustration I show in table 4(a) one-electron integrals for π electrons in the benzene molecule with C–C distance 2·6320755 a.u. For the $2p_z$ orbital of carbon atom I have used 8 –, 11 –, and 13-gaussian expansions calculated by Partridge [10]. Pi-electron repulsion integrals are given in table 4(b). The performance of the expansions due to Partridge is gratifying,. The 13-gaussian expansion represents the atomic Hartree–Fock limit and obviously the values calculated with this expansion are the accurate values for integrals over $2p_z$ orbitals of carbon atoms with the chosen molecular geometry. Trends in the calculated values parallel the trends in the radial

Table 4(a). One-electron integrals: $2p\pi - 2p\pi$ for the benzene molecule (a. u.).

Integrals	Partridge basis set 8p	11p	13p
$\langle 2p_{za} \vert 2p_{zb} \rangle$			
12	0·3228027	0·3228235	0·3228243
13	0·0805732	0·0806314	0·0806334
14	0·0466768	0·0467444	0·0467467
$-(1/2)\langle 2p_{za} \vert \nabla^2 \vert 2p_{zb} \rangle$			
11	1·2536583	1·2536686	1·2536697
12	0·1053507	0·1053380	0·1053378
13	0·0048302	0·0048334	0·0048336
14	0·0001659	0·0001652	0·0001628
$\sum_C \left\langle 2p_{za} \middle\vert \frac{1}{r_C} \middle\vert 2p_{zb} \right\rangle$			
11	2·072825	2·072813	2·072813
12	0·6044734	0·6044812	0·6044816
13	0·1458726	0·1459341	0·1459359
14	0·0839891	0·0840590	0·0840600

Table 4(b). Pi-electron repulsion integrals for the benzene molecule (a.u.). Carbon–carbon bond distance used is 2·6320755 a.u.

Integrals	Partridge basis set[a] 8p	11p	13p
11 11	0·5775441	0·5775322	0·5775317
11 12	0·1376486	0·1376476	0·1376476
11 13	0·0260711	0·0266185	0·0266188
11 14	0·0142159	0·0142275	0·0142277
11 22	0·0454505	0·0434194	0·0429192
11 23	0·0092344	0·0092377	0·0092378
11 24	0·0045394	0·0045432	0·0045433
11 25	0·0075520	0·0075555	0·0075556
11 26	0·0342107	0·0342116	0·0342116
11 33	0·0022881	0·0022879	0·0023143
11 34	0·0011852	0·0011866	0·0011867
11 35	0·0018567	0·0018582	0·0018583
11 44	0·0007190	0·0007200	0·0007210
12 12	0·3210676	0·3210609	0·3210606
12 13	0·0822259	0·0822270	0·0822271
12 14	0·0198691	0·0198782	0·0198785
12 15	0·0132073	0·0132180	0·0132183
12 16	0·0295130	0·0295222	0·0295225
12 34	0·0021339	0·0021355	0·0021356
12 35	0·0011913	0·0011927	0·0011927
12 43	0·0043401	0·0043436	0·0043437
12 45	0·0007078	0·0007089	0·0007089

(*Continued*)

Table 4(b). (*Continued*)

Integrals	Partridge basis set[a] 8p	11p	13p
12 53	0·0061509	0·0061539	0·0061540
12 63	0·0234139	0·0234152	0·0234152
13 13	0·2058286	0·2058256	0·2058255
13 14	0·0630221	0·0630237	0·0630237
13 15	0·0176700	0·0176782	0·0176785
13 64	0·0206595	0·0206608	0·0206609
14 14	0·1808739	0·1808717	0·1808716
Time (seconds)[b]	180	578	1028

(a) Ref. [10]
(b) CDC Cyber 180/840 machine (with about 1 MFLOPS available speed for computation) was used.

Table 5. Calculated radial moments of 2p orbitals of carbon atom.

	Partridge basis set [10] 8p	11p	13p
$\langle r^{-2} \rangle$	0·8919758	0·8920567	0·8920611
$\langle r^{-1} \rangle$	0·7835025	0·7835024	0·7835025
$\langle r \rangle$	1·714385	1·714490	1·714494
$\langle r^{2} \rangle$	3·745603	3·746742	3·746793

moments for the 2p orbitals of carbon atom in table 5. Integrals given in tables 4(a) and 4(b) can be directly used in a suitable (all-electron, effective potential or π-electron) calculation. The last entries in table 4(b) refer to the time taken for each computation in a CDC Cyber 180/840 machine installed in IIT Bombay. The machine offers an effective computing speed of about 1 million floating point operations per second.

Preliminary results on the methane molecule are given in table 6(a). The basis sets used have been minimal (carbon: 1s, 2s and 2p functions; hydrogen 1s function) but elaborate, that is, near exact Hartree–Fock solutions for atoms. The first set consists of 13S8P bases for carbon [10] and STO-10G basis for hydrogen [11]. The second set has 18S13P bases for carbon [10] and a STO-12G basis (modified from the STO-10G basis) for hydrogen [4]. The C–H distance has been taken to be 1·093 Å [12]. A tetrahedral geometry has been adopted. A break-up for the time taken in different steps of these calculations is also shown in this table. Table 6(b) shows the radial moments of the atomic orbitals used in the basis sets.

We choose to give some sample results on the LiH and BH$^+$ molecules here. LiH is a closed-shell molecule and BH$^+$ is an open-shell molecular ion. Experimental bond lengths have been chosen in both the cases ($R_{\mathrm{LiH}} = 3{\cdot}015$ bohr; $R_{\mathrm{BH}^+} = 2{\cdot}296$ bohr) such that a comparison can be made between the presently computed values and results available in the literature. The present calculations are based on 4-gaussian expansions of STO's. Exponents of the STO's have been taken from Cade and Huo

Table 6(a). Computed results for the methane molecule (tetrahedral geometry; C–H bond length = 1·093 Å or 2·06547 bohr). All energy values are in hartree.

	Basis I[a]	Basis II[b]
Total energy (E)	−40·0552448	−40·0553007
V/T[c]	−2·0198969	−2·0198935
Orbital energies (ε)		
$1A_1$	−11·386921	−11·386976
$2A_1$	−1·004501	−1·004535
$1T_2$	−0·606479	−0·606517
Time in seconds[d]		
1-electron integrals	146	203
2-electron integrals	576	1485
SCF calculation	40	36

(a) Partridge 13S8P basis for carbon and STO-10G expansion for hydrogen 1*s* orbital: total number of gaussians is 90.
(b) Partridge 18S13P basis for carbon and STO-12G expansion for hydrogen 1*s* orbital: total number of gaussians is 122.
(c) V/T is the ratio of potential and kinetic energies.
(d) Time taken by a CDC Cyber 180/840 machine.

Table 6(b). Radial moments of atomic orbitals.

	Basis I	Basis II
$\langle r^{-2}\rangle$		
C 1*s*	65·227519	65·232129
C 2*s*	3·255063	3·254940
C 2*p*	0·891976	0·892061
H 1*s*	1·999600	1·999860
$\langle r^{-1}\rangle$		
C 1*s*	5·664434	5·664437
C 2*s*	0·896807	0·896798
C 2*p*	0·783502	0·783502
H 1*s*	0·999993	0·999994
$\langle r\rangle$		
C 1*s*	0·268442	0·268443
C 2*s*	1·589225	1·589341
C 2*p*	1·714385	1·714494
H 1*s*	1·500006	1·500005
$\langle r^2\rangle$		
C 1*s*	0·097198	0·097199
C 2*s*	3·051006	3·052031
C 2*p*	3·745603	3·746793
H 1*s*	3·000023	3·000019

[13]. The calculations of Cade and Huo involve very large STO bases and their results are of high quality, near the Hartree–Fock limit for each molecule.

The minimal basis results on LiH were given earlier [4]. These results are surprisingly good, which is obviously an outcome of employing the near Hartree–Fock atomic orbitals due to Partridge [10] as basis functions. These are shown alongside the presently calculated values in table 7. One of the present calculations has been performed with 4-gaussian expansions for $1s$, $1s'$, $2s$, $2s'$, $3s$ and $2p$ STO's of Li and $1s$, $1s'$, $2s$ and $2p$ STO's of H (Basis I). The second calculation has utilized 4-gaussian expansions for $2p'$, $2p''$ and $3p$ STO's of Li in addition to the basis functions used in the first calculation (Basis II). Results from these calculations are compared with those computed by Cade and Huo [13] using a STO basis set ($1s$, $1s'$, $2s$, $2s'$, $3s$, $2p$, $2p'$, $2p''$, $3p$ and also $3d$, $3d'$ and $4f$ STO's for Li; $1s$, $1s'$, $2s$, and $2p$ STO's for H). Differences

Table 7. Computed results for LiH. The bond length employed is 3·015 bohr. All energies are in hartree.

		Present calculations			
	Minimal Basis[a]	Minimal STO-4G[b]	Basis I[b]	Basis II[b]	Cade and Huo[c]
Li Basis	$1s$, $2s$	$1s$, $2s$	$1s$, $1s'$, $2s$, $2s'$, $3s$, $2p$	$1s$, $1s'$, $2s$, $2s'$, $3s$, $2p$, $2p'$, $2p''$, $3p$	$1s$, $1s'$, $2s$, $2s'$, $3s$, $2p$, $2p'$, $2p''$, $3p$, $3d$, $3d'$, $4f$
$\langle r^{-2}\rangle$ $1s$	14·8885	12·3788	14·5807	14·5807	
$2s$	0·4354	1·0797	0·5597	0·5597	
$2p$	—	—	0·1793	0·0983	
$\langle r^{-1}\rangle$ $1s$	2·6850	2·5166	2·6817	2·6817	
$2s$	0·3454	0·5186	0·3999	0·3999	
$2p$	—	—	0·3680	0·2796	
$\langle r\rangle$ $1s$	0·5731	0·5947	0·5748	0·5748	
$2s$	3·8736	2·7823	3·2321	3·2321	
$2p$	—	—	3·3928	4·2002	
$\langle r^{2}\rangle$ $1s$	0·4468	0·4711	0·4503	0·4503	
$2s$	17·7376	8·9909	11·7342	11·7342	
$2p$	—	—	13·8123	20·0973	
H Basis	$1s$	$1s$	$1s$, $1s'$, $2s$, $2p$	$1s$, $1s'$, $2s$, $2p$	$1s$, $1s'$, $2s$, $2p$
$\langle r^{-2}\rangle$ $1s$	1·9999	1·5346	1·9517	1·9517	
$\langle r^{-1}\rangle$ $1s$	1·0000	0·8861	0·9903	0·9903	
$\langle r\rangle$ $1s$	1·5000	1·6893	1·5442	1·5442	
$\langle r^{2}\rangle$ $1s$	3·0000	3·8011	3·2420	3·2420	
Molecular results					
E	−7·96039	−7·9061	−7·9713	−7·9732	−7·98731
V/T[d]	−1·98615	−2·0939	−1·9960	−1·9960	−1·99950
$\varepsilon_{1\sigma}$	−2·46882	−2·4538	−2·4429	−2·4355	−2·44525
$\varepsilon_{2\sigma}$	−0·29481	−0·2844	−0·2974	−0·2968	−0·30172

(a) This minimal basis calculation had used Partridge's 18S basis for Li and a 12-gaussian expansion for H $1s$ orbital [4].
(b) Each STO was expanded into a linear sum of four gaussians.
(c) STO calculation by Cade and Huo [13].
(d) V/T is the ratio of potential and kinetic energies.

from the results of Cade and Huo are mainly attributable to the very approximate nature of the 4-gaussian expansions and to a lesser extent to the absence of the $3d$, $3d'$ and $4f$ basis functions.

For BH$^+$ we have taken similar expansions for $1s$, $1s'$, $2s$, $2s'$, $3s$ and $2p$ STO's of B (Basis I) and additionally $2p'$, $2p''$ and $2p'''$ STO's of B (Basis II). The hydrogen basis remains as before but the exponents differ. The minimal basis calculation has been carried out using the B ^{2}P ($18s$ $13p$) basis set due to Partridge and a 12-gaussian expansion for the $1s$ orbital of hydrogen. The calculated values are shown along with the values from the STO calculation of Cade and Huo in table 8.

The results computed for both the molecules using the first basis sets show encouraging improvements over the minimal STO-4G results. In each case the total

Table 8. Computed results for BH$^+$. The bond length employed is 2·296 bohr. All energies are in hartree.

	Present calculations				
	Minimal Basis^a	Minimal STO-4G^b	Basis I^b	Basis II^b	Cade and Huo^c
B Basis	$1s$, $2s$ $2p$	$1s$, $2s$, $2p$	$1s$, $1s'$, $2s$, $2s'$, $3s$, $2p$	$1s$, $1s'$, $2s$, $2s'$, $3s$, $2p$, $2p'$, $2p''$, $2p'''$	$1s$, $1s'$, $2s$, $2s'$, $3s$, $2p$, $2p'$, $2p''$, $2p'''$, $3d$, $3d'$, $4f$
$\langle r^{-2}\rangle$ $1s$	44·5364	30·1466	43·6587	43·6587	
$2s$	2·0243	0·9289	2·0868	1·6123	
$2p$	0·5299	0·2738	0·2738	1·2361	
$\langle r^{-1}\rangle$ $1s$	4·6743	3·9339	4·6745	4·6601	
$2s$	0·7129	0·5696	0·7351	0·6525	
$2p$	0·6050	0·4548	0·4548	1·1999	
$\langle r\rangle$ $1s$	0·3259	0·3796	0·3261	0·3278	
$2s$	1·9771	2·2402	1·8990	2·0955	
$2p$	2·2048	2·7452	2·7452	2·7468	
$\langle r^2\rangle$ $1s$	0·1434	0·1943	0·1439	0·1457	
$2s$	4·7091	5·7989	4·2748	5·1636	
$2p$	6·1461	9·0423	9·0423	6·1500	
H Basis	$1s$	$1s$	$1s$, $1s'$, $2s$, $2p$	$1s$, $1s'$, $2s$, $2p$	$1s$, $1s'$, $2s$, $2p$
$\langle r^{-2}\rangle$ $1s$	1·9999	2·7239	2·0181	2·0181	
$\langle r^{-1}\rangle$ $1s$	1·0000	1·1805	1·0218	1·0218	
$\langle r\rangle$ $1s$	1·5000	1·2679	1·4425	1·4425	
$\langle r^{-2}\rangle$ $1s$	3·0000	2·1415	2·7116	2·7116	
Molecular results					
E	−24·71738	−23·9268	−24·6898	−24·7829	−24·82064
V/T^d	−2·02667	−2·4027	−2·0051	−2·0004	−2·00122
$\varepsilon_{1\sigma}$	−8·31101	−8·4302	−8·2368	−8·0985	−8·10898
$\varepsilon_{2\sigma}$	−1·01561	−1·0077	−1·0141	−0·9759	−0·97699
$\varepsilon_{3\sigma}$	−0·83275	−0·7768	−0·7439	−0·8201	−0·81953

(a) This minimal basis calculation used Partridge's 18S13P basis for B and a 12-gaussian expansion for H $1s$ orbital.

(b) Each STO was expanded into a linear sum of four gaussians.

(c) STO calculation by Cade and Huo [13].

(d) V/T is the ratio of potential and kinetic energies.

energy computed by using the set of near Hartree–Fock atomic orbitals differs by a large amount from that computed by using the minimal STO-4G basis set, indicating the importance of a large, more accurate expansion for each STO. The gross inadequacy of the minimal STO-4G basis set is also reflected by the large (20%) deviation of the virial ratio in table 8. The poor quality of the basis functions (atomic valence functions) is evident from the radial moments shown in the same table. An interesting observation is that for BH^+ the minimal Partridge basis calculation gives a total energy that is even superior to the value calculated using Basis I. Values computed by using the second basis sets are closed to the STO results of Cade and Huo [13]. The differences can be made smaller by using a larger expansion for each STO and using STO's of symmetries d and f. A few standard GTO expansions have been determined by Ohata *et al* [11]. These can be of invaluable assistance in carrying out ab-initio calculations on molecules of lighter elements.

Note added while revising the manuscript: The author could not directly compare the speed of the present programs with that of GAUSSIAN. The execution for LiH with basis 6–311g** (24 basis functions, 39 gaussian primitives) gave results ($E = -7{\cdot}98577$, $V/T = -2{\cdot}0003$, $\varepsilon_{1\sigma} = -2{\cdot}44759$, $\varepsilon_{2\sigma} = -0{\cdot}30154$) in agreement with the results of GAUSSIAN 90 for LiH with bond length 1·595 Å. The GAUSSIAN 90 results were obtained from Ewig and Trindle. The time taken was as follows: 219 cp seconds using Cyber (with speed about 1 MFLOPS) for the calculation of two-electron integrals; about 2·8 s using IBM RS/6000 550 system (speed 15–20 MFLOPS) and about 11·6 s using Silicon Graphics 4D/35 (speed 5–10 MFLOPS) for the whole execution of GAUSSIAN 90. This indicates that the generation of two-electron integrals by the present program is 3–4 times slower. But the 6–311g** basis is very nicely suited for GAUSSIAN as s and p orbitals of lithium atom have been given common exponents, whereas in the programs reported here no provision has been made for exploiting this situation. So the speed of computing the two-electron integrals over general basis functions is expected to be comparable to the speed of GAUSSIAN. The disc memory required for the execution in Cyber was about 3·5 MB compared to about 6 MB required for the execution of GAUSSIAN.

Appendix A

Integrals over gaussians

(1) The overlap integral between gaussians g_1 on atom A and g_2 on atom B with exponents α_1 and α_2 respectively is given by [8]

$$\begin{aligned}\langle g_1|g_2\rangle = \left(\frac{\pi}{\gamma}\right)^{3/2} & \exp(-\alpha_1\alpha_2 R_{AB}^2/\gamma) \\ & \times \sum_{i=0}^{[(l_1+l_2)/2]} f_{2i}(l_1, l_2, X_A - X_P, X_B - X_P)\frac{(2i-1)!!}{(2\gamma)^i} \\ & \times \sum_{j=0}^{[(m_1+m_2)/2]} f_{2j}(m_1, m_2, Y_A - Y_P, Y_B - Y_P)\frac{(2j-1)!!}{(2\gamma)^j} \\ & \times \sum_{k=0}^{[(n_1+n_2)/2]} f_{2k}(n_1, n_2, Z_A - Z_P, Z_B - Z_P)\frac{(2k-1)!!}{(2\gamma)^k} \qquad \text{(A1)}\end{aligned}$$

where $\mathbf{R}_A$, $\mathbf{R}_B$, etc. denote the position vectors for the centres of atoms A, B, etc.,

R_{AB} is the distance between atom centres A and B,

$$\gamma = \alpha_1 + \alpha_2, \tag{A2}$$

$$\mathbf{R}_p = (\alpha_1 \mathbf{R}_A + \alpha_2 \mathbf{R}_B)/\gamma,$$

$$(2i-1)!! = (2i)!/[2^i i!],$$

and $[N]$ represents the largest integer less than or equal to N. The factor f_j is the coefficient of X_p^j in the product $X_A^{l_1} X_B^{l_2}$,

$$X_A^{l_1} X_B^{l_2} = \sum_{j=0}^{l_1+l_2} f_j(l_1, l_2, X_A - X_P, X_B - X_P) X_P^j \tag{A3}$$

such that

$$f_j(l_1, l_2, X_A - X_P, X_B - X_P) = \sum_{k_1=0}^{l_1} \sum_{\substack{k_2=0 \\ (k_1+k_2=j)}}^{l_2} \binom{l_1}{k_1}\binom{l_2}{k_2} (X_A - X_P)^{l_1-k_1} (X_B - X_P)^{l_2-k_2}. \tag{A4}$$

(2) The kinetic energy integral is calculated to be [8]

$$\begin{aligned}\langle g_1|(-1/2)\nabla^2|g_2\rangle &= \alpha_2[2(l_2+m_2+n_2)+3]s(l_1,m_1,n_1;l_2,m_2,n_2)\\ &\quad - 2\alpha_2^2[s(l_1,m_1,n_1;l_2+2,m_2,n_2) + s(l_1,m_1,n_1;l_2,m_2+2,n_2)\\ &\quad + s(l_1,m_1,n_1;l_2,m_2,n_2+2)]\\ &\quad - 2^{-1}[l_2(l_2-1)s(l_1,m_1,n_1;l_2-2,m_2,n_2)\\ &\quad + m_2(m_2-1)s(l_1,m_1,n_1;l_2,m_2-2,n_2)\\ &\quad + n_2(n_2-1)s(l_1,m_1,n_1;l_2,m_2,n_2-2)]\end{aligned} \tag{A5}$$

where s is the overlap integral over the two gaussians represented by the quantum numbers involved.

(3) The nuclear attraction integral has been calculated as [8]

$$\left\langle g_1 \left| \frac{1}{|\mathbf{r} - \mathbf{R}_C|} \right| g_2 \right\rangle = \frac{2\pi}{\gamma} \exp(-\alpha_1 \alpha_2 R_{AB}^2/\gamma) \sum_{I=0}^{l_1+l_2} \sum_{J=0}^{m_1+m_2} \sum_{K=0}^{n_1+n_2} G_{Ix} G_{Jy} G_{Kz} F_{I+J+K}(\gamma |R_P - R_C|^2) \tag{A6}$$

where

$$F_L(t) = \int_0^1 x^{2L} \exp(-tx^2) \mathrm{d}x \tag{A7}$$

and

$$G_{Ix} = \sum_{i=0}^{(l_1+l_2)} \sum_{\substack{r=0 \\ (i-2r-u=I)}}^{[i/2]} \sum_{u=0}^{[(i-2r)/2]} (-1)^i f_i(l_1, l_2, X_A - X_P, X_B - X_P) \cdot \frac{(-1)^u i! (X_P - X_C)^{i-2r-2u}}{r! u! (i-2r-2u)! (4\gamma)^{r+u}} \tag{A8}$$

etc.

(4) The electron repulsion integral over gaussians g_1 on atom A, g_2 on atom B, g_3 on atom C and g_4 on atom D and with exponents α_1, α_2, α_3 and α_4 respectively is obtained as [8]

$$
\begin{aligned}
(g_1g_2|g_3g_4) &= \frac{2\pi^2}{\gamma_1+\gamma_2}\left(\frac{\pi}{\gamma_1+\gamma_2}\right)^{1/2}\exp\left[-\frac{\alpha_1\alpha_2R_{\mathrm{AB}}^2}{\gamma_1}-\frac{\alpha_3\alpha_4R_{\mathrm{CD}}^2}{\gamma_2}\right]\\
&\quad \sum_{I,J,K} C_{Ix}C_{Jy}C_{Kz}F_{I+J+K}\left(\frac{\gamma_1+\gamma_2}{\gamma_1\gamma_2}R_{\mathrm{PQ}}^2\right) \qquad \text{(A9)}
\end{aligned}
$$

where

$$\gamma_1=\alpha_1+\alpha_2,$$

$$\gamma_2=\alpha_3+\alpha_4$$

and

$$\mathbf{R}_{\mathrm{Q}}=(\alpha_3\mathbf{R}_{\mathrm{C}}+\alpha_4\mathbf{R}_{\mathrm{D}})/\gamma_2.$$

The term C_I is given by

$$
\begin{aligned}
C_I &= \sum_{\substack{L\\(L+M-u=I)}}^{(l_1+l_2)}\ \sum_{M}^{(l_3+l_4)}\ \sum_{u} H_L(l_1,l_2,X_{\mathrm{A}}-X_{\mathrm{P}},X_{\mathrm{B}}-X_{\mathrm{P}},\gamma_1)\\
&\quad (-1)^M H_M(l_3,l_4,X_{\mathrm{C}}-X_{\mathrm{Q}},X_{\mathrm{D}}-X_{\mathrm{Q}},\gamma_2)\\
&\quad \times\frac{(L+M)!(-1)^u(X_{\mathrm{Q}}-X_{\mathrm{P}})^{(L+M-2u)}}{u!(L+M-2u)!((\gamma_1+\gamma_2)/4\gamma_1\gamma_2)^{L+M-u}} \qquad \text{(A10)}
\end{aligned}
$$

where

$$H_L(l_1,l_2,a,b,\gamma)=\sum_{\substack{i=0\\(i-2r=L)}}^{(l_1+l_2)}\ \sum_{r=0}^{[i/2]}\frac{i!f_i(l_1,l_2,a,b,\gamma)}{r!(i-2r)!(4\gamma)^{i-r}}. \qquad \text{(A11)}$$

Integrals for atomic computations (given in § 3) are calculated from these expressions.

Acknowledgements

The author gratefully acknowledges cooperation from all the personnel in Cyber Centre, IIT, Bombay. He is also indebted to Dr H Partridge who has provided the near Hartree–Fock quality GTO basis sets, and to Dr C Ewig and Dr C Trindle for supplying the GAUSSIAN results.

References

[1] D R Hartree, *Proc. Cambridge Philos. Soc.* **24**, 89 (1927)
[2] V Fock, *Z. Phys.* **61**, 126 (1930); **62**, 795 (1930)
[3] C C J Roothaan, *Rev. Mod. Phys.* **23**, 69 (1951)
[4] S N Datta, *Pramana – J. Phys.* (submitted) (1993)
[5] H Bethe and E E Salpeter, *Quantum mechanics of one- and two-electron atoms* (Springer-Verlag, Berlin, 1957)
[6] C F Fischer, *Comput. Phys. Commun.* **4**, 107 (1972); C F Fischer, *The Hartree–Fock method for atoms*, (J Wiley, New York, 1977)

[7] P Carsky and M Urban, Ab-initio calculations, Lecture Notes in Chemistry No. 16, (Springer, Berlin, 1980); C E Dykstra, *Ab-initio calculations of the structures and properties of molecules*, (Elsevier, Amsterdam, 1988)

[8] H Taketa, S Huzinaga and K O-Ohata, *J. Phys. Soc. Jpn.* **21**, 2313 (1966)

[9] S N Datta, *Pramana – J. Phys.* **38**, 51 (1992)

[10] H Partridge, NASA Technical Memorandum 101044 (NASA, Moffet Field, 1989)

[11] K O-Ohata, H Taketa and S Huzinaga, *J. Phys. Soc. Jpn.* **21**, 2306 (1966)

[12] H C Allen and E K Plyler, *J. Chem. Phys.* **26**, 972 (1957)

[13] P E Cade and W Huo, *At. Data Nucl. Data Tables* **12**, 415 (1973)

PRAMANA
— journal of
physics

© Printed in India

Vol. 41, No. 4,
October 1993
pp. 363–370

Ab-initio nonrelativistic and relativistic Hartree-Fock calculations for both closed- and open-shell molecules using GTO basis

SAMBHU N DATTA
Department of Chemistry, Indian Institute of Technology, Powai, Bombay 400076, India

MS received 12 April 1993; revised 5 June 1993

Abstract. Computer programs for *ab-initio* Hartree-Fock and Dirac-Hartree-Fock calculations on closed- and open-shell atoms and molecules have been indigenously developed. Sample results of high quality are given for Li, Be, LiH and Be_2. As a byproduct of these calculations the importance of considering relativistic effects in the investigation of the elusive bound-state structure of Be_2 is clearly indicated.

Keywords. Hartree-Fock; Dirac-Hartree-Fock; ab-initio; program development.

PACS Nos **31·15; 31·30; 03·65; 11·10**

1. Introduction

This communication is to announce the indigenous development of computer programs for *ab-initio* nonrelativistic and relativistic Hartree-Fock calculations on molecules. Two sets of programs have been prepared, one set for nonrelativistic Hartree-Fock (HF) calculations and the other set for Dirac-Hartree-Fock (DHF) calculations. Options have been kept for both closed-shell and open-shell self-consistent-field treatments. These programs have been written for calculations with gaussian type orbitals (GTOs). These have been extensively tested for accuracy. Integrals of the nonrelativistic type have been calculated using the formulae derived by Taketa *et al* [1]. The programs for the DHF calculation were actually developed by us more than a decade back, but these could not be tried here owing to lack of adequate computing facilities. These were tested elsewhere [2]. We have now rewritten and adapted these programs for execution in CDC Cyber 180/840 mainframe computer presently available to us. The detailed description of the method of calculations, the structure of the programs belonging to the two sets and the choice of the relativistic basis spinors will be published as broad follow-up papers later.

2. Hamiltonian

The N-electron Hamiltonians used for the nonrelativistic and relativistic calculations are as follows. The nonrelativistic Hartree-Fock calculations are based on the nonrelativistic Hamiltonian

$$H_{\text{nonrel}} = \sum_{i=1}^{N} h(i) + \sum_{i<j} |r_i - r_j|^{-1} \tag{1}$$

where the one-electron Hamiltonian h is given by

$$h(i) = -2^{-1}\nabla_i^2 - \sum_n^{\text{nuclei}} Z_n|r_i - R_n|^{-1}. \tag{2}$$

The relativistic (Dirac-Hartree-Fock) calculations are based on the Dirac-Coulomb Hamiltonian

$$H_{\mathrm{DC}} = \sum_{i=1}^{N} h_{\mathrm{D}}(i) + \sum_{i<j} |r_i - r_j|^{-1} \tag{3}$$

where the one-electron Dirac Hamiltonian is given by

$$h_{\mathrm{D}}(i) = c\alpha_i \cdot p_i + c^2\beta_i - 1_i \sum_n^{\text{nuclei}} Z_n|r_i - R_n|^{-1} \tag{4}$$

Atomic units have been used throughout. In the above r_i indicates the position vector of the ith electron and R_n the position vector of nucleus n.

The use of these Hamiltonian operators amounts to performing the Hartree-Fock calculations under two conventional approximations. These approximations are as follows. First, we ignore the effect of mass correction as discussed by Bethe and Salpeter [3]. Second, these calculations are done under the Born–Oppenheimer approximation. Therefore, the total energy will be calculated by adding V_{nn} to the computed total energy for electrons, where V_{nn} is the energy of nucleus–nucleus interaction,

$$V_{nn} = \sum_{m<n}^{\text{nuclei}}\sum Z_m Z_n |R_m - R_n|^{-1}. \tag{5}$$

The nonrelativistic Hartree-Fock equations and the Hartree-Fock-Roothaan equations for solving the self-consistent-field problem are common knowledge. The relativistic Hartree-Fock equations for a general molecule have been discussed by several authors including Malli and Oreg [4], Malli [5], Datta and Ewig [2] and Datta and Devaiah [6]. Due to paucity of space these equations are not described in this paper. Instead we give an account of the most important features of nonrelativistic and relativistic Hartree-Fock treatments in the following.

3. Special features

The relativistic calculations are associated with several theoretical and technical difficulties. The theoretical difficulties are referred to as variational collapse [7, 8] and continuum dissolution [9]. Physicists have suggested the use of positive-energy projected Hamiltonians for the Dirac-Hartree-Fock calculations [9, 10]. Mittleman [11] has shown that the Hartree-Fock reduction of H_{DC} results in the same orbital energies as the Hartree-Fock reduction of the appropriately projected Hamiltonian. Nevertheless, by considering a "maximization followed by minimization" procedure, the DHF equations can be derived without the use of projection operators and without any scruple [6]. The step of maximization leads to a trial function belonging to the "positive-energy subspace" (that is, this function corresponds to the N-electron sector of Fock space). In a basis set expansion procedure one may not *explicitly* carry out the first step of maximization. In that case the possibility of variational collapse, or rather the possibility of getting a wrong estimate of the relativistic corrections, gives rise to a difficulty in the choice of a good basis set [7, 12]. This difficulty is a technical one. As stated earlier, the choice of relativistic basis sets will be described elsewhere. Another technical difficulty involves the excessive load on computation as the number of primitive functions required for a relativistic calculation should be four times the number of primitives needed for an equivalent nonrelativistic calculation.

The Breit operator embodies the most important effects of the interaction of the electron with a virtual (transverse) photon. The correction to total energy due to Breit interaction can be calculated with a minor modification of the present programs. The computations, however, will be expensive. This development will be reported elsewhere.

For the nonrelativistic treatment we have employed the usual LCAO-MO scheme. The LCAS-MS (linear combinations of atomic spinors as molecular spinors) scheme [2, 4] has been adopted in the relativistic work with the generalization that the 'atomic' spinors need to be four-component basis spinors with atomic angular momentum symmetries retained in each nonvanishing component of every spinor to expedite the computation. Thus one may even choose basis spinors with vanishing upper components or vanishing lower components. For the calculations reported here, however, we have employed basis spinors which look like relativistic atomic orbitals.

The open-shell calculations, both nonrelativistic and relativistic, are under the constraints that only one open shell for a given symmetry is allowed and that in the direct product of the additional irreducible species of more than one open shells, a given irreducible species does not occur more than once [5]. The speed of light has been taken to be 137·036 a.u. We present here the results of a few sample calculations carried out within the context of the procedure and limitations discussed above.

4. Results and discussion

Table 1 gives a summary of the function of all the programs developed indigenously as part of our laboratory programme on HF and DHF calculations. A detailed description will be published in the near future.

The atomic calculations (open-shell and closed-shell) have all been carried out with extensive basis sets. The results are always near the Hartree-Fock and Dirac-Fock limits. Calculations on LiH and Be_2 molecules (both closed-shell) have been performed with the minimal basis sets. The molecular calculations have been performed with atomic orbitals (spinors) of near Hartree-Fock (near Dirac-Fock) quality as basis functions. Therefore, the results obtained are in reality standards for minimal basis calculations.

For the nonrelativistic treatment we have selected the near Hartree-Fock quality GTO basis sets for lithim and beryllium (Li ^2S 18s and Be ^1S 18s) where each basis function is expanded into a set of eighteen atom-centered gaussian functions [13]. For hydrogen the 10-gaussian expansion of O–Ohata *et al* [14] has been augmented by two more gaussians of exponents 10000·0 and 5000·0. The resulting 12-gaussian expansion gives a difference of $1{\cdot}2 \times 10^{-6}$ a.u. in the 1s orbital energy. Molecular calculations have been performed at the experimental bond length ($R = 3{\cdot}015$ a.u.) for LiH and at two bond lengths, $R = 4.2$ a.u. (2·22 Å) and $R = 4{\cdot}63$ a.u. (2·45 Å), for Be_2.

Table 1. Functions of the programs developed. The figure in parenthesis under the name of each program indicates the number of statements.

Program	Functions
Nonrelativistic Hartree-Fock calculation (program set: LCAOMO)	
NREL1E (1712)	Calculates nonrelativistic one-electron integrals: overlap integrals kinetic energy integrals electron-nuclear potential energy integrals r^n integrals for atoms ($n = -3, -2, -1, 1, 2, 3, 4, 6$)
NREL2E (1172)	Calculates nonrelativistic two-electron repulsion integrals over gaussians and over basis functions.
SCFCOS (1249)	Performs Hartree-Fock-Roothaan self-consistent-field calculation for both closed- shell and open-shell molecules. It also calculates $\langle r^n \rangle$ expectation values for each atomic orbital.
Relativistic Hartree-Fock calculation (program set: LCASMS)	
REL1E (3392)	Calculates relativistic one-electron integrals. Integrals over the nonrelativistic basis functions are calculated first. These involve overlap integrals, integrals of $\partial/\partial x$ etc., nuclear attraction integrals and for atoms, r^n integrals. Integrals over the basis spinors are then calculated.
REL2E (1702)	Calculates two-electron repulsion integrals over nonrelativistic basis functions and then calculates two-electron repulsion integrals over basis spinors.
RELCOS (1736)	Performs the self-consistent-field calculation for both closed-shell and open-shell molecules. It also calculates $\langle r^n \rangle$ expectation values for each atomic orbital.

The bond length 4·2 a.u. was chosen to compare our present result with the result calculated earlier [2]. The bond length 4·63 a.u. is the experimentally found equilibrium bond length of Be_2 in vapour phase [15].

The nonrelativistic total and orbital energies are given in table 2. The atomic results are only for the purpose of comparison. They agree very nicely with the near Hartree-Fock results calculated by Partridge [13]. In table 2 the molecular orbital energies are given to sixth decimal place and total energy to seventh decimal. A convergence factor of 10^{-9} for total energy has been used in these calculations. The total and orbital energies calculated for Be_2 with internuclear separation 4.2 a.u. represent an improvement over the results of our earlier calculation [2] that employed a 10-gaussian expansion for each basis function. The improvement is caused by the 18-gaussian expansion used in the present work, and it occurs at the fourth place after the decimal point in every energy value.

The form of the relativistic $s_{1/2}$ spinors is shown in table 3. The lower component functions have been generated by applying the operator $(2c)^{-1}\sigma.p$ on the upper component functions and then multiplying the results by a suitable factor (close to 1·0) so as to maintain the correct virial ratio (ratio of potential and kinetic energies).

Relativistic total and orbital energies are given in table 4. There is an excellent agreement between the computed total energies for atoms and the total energies calculated numerically by Desclaux [16]. The computed relativistic orbital energies, however, differ slightly (in the fifth significant digit) from the numerically calculated values. The reason for this difference is as follows. Since nonrelativistic basis functions have been used to form the two upper components, the charge density for each orbital

Table 2. Computed nonrelativistic total and orbital energies in atomic units. Total energy is indicated by E and orbital energy is shown against the name of the orbital.

Species		Computed values (this work)	Literature value	Reference
H	E	−0·4999988	−0·500000	
Li	E	−7·4327266	−7·432727	Partridge
	1s	−2·4777400	−2·477741	[13]
	2s	−0·1963226	−0·196323	
Be	E	−14·5730223	−14·573023	Partridge
	1s	−4·7326690	−4·732669	[13]
	2s	−0·3092692	−0·309269	
LiH	E	−7·9603942	−7·794720	Sundholm
($R = 3{\cdot}015$ a.u.)	1σ	−2·468815		[17][a]
	2σ	−0·294808		
Be_2	E	−29·0750463	−29·0743	Datta and Ewig
($R = 4{\cdot}2$ a.u.)	$1\sigma g$	−4·750917	−4·7510	[2][b]
	$1\sigma u$	−4·750820	−4·7509	
	$2\sigma g$	−0·405697	−0·4060	
	$2\sigma u$	−0·251723	−0·2516	
Be_2	E	−29·1003704		
($R = 4{\cdot}63$ a.u.)	$1\sigma g$	−4·739462		
	$1\sigma u$	−4·739438		
	$2\sigma g$	−0·387109		
	$2\sigma u$	−0·258397		

(a) Numerical Hartree-Fock-Slater calculation.
(b) Each STO expanded in a set of ten GTO's.

Table 3. Form of relativistic $s_{1/2}$ basis spinors. The basis functions, s, p_x, p_y and p_z are not individually normalized. The basis spinors are normalized.

$m_j = 1/2$	$m_j = -1/2$
s	0
0	$-s$
$-i3^{-1/2}p_z$	$3^{-1/2}(p_y + ip_x)$
$3^{-1/2}(p_y - ip_x)$	$-i3^{-1/2}p_z$

is slightly less than the actual value near the nucleus. The charge density is again slightly less in the outermost region as the GTO's fall off faster than exponential functions. This is made clear by the expectation values $\langle r^n \rangle$ for atomic orbitals in table 5 where we find a slight decrease for $n = -2, -1$ and (sometimes for) 6 and a slight increase for $n = 1$, 2 and 4 from the numerically calculated values.

Relativistic total and orbital energies for LiH and Be_2 are given in table 6. Although we have carried out only a minimal basis calculation, the total energies calculated for LiH are seen to be consistently better than those obtained from two-dimensional

Table 4. Relativistic total and orbital energies ($E_{\rm rel}$ and ε) for atoms. Energy values are in atomic unit.

	Present work	Numerical calculation Desclaux [16]
Hydrogen	Virial ratio = −1·00000998	
$E_{\rm rel}$	−0·500005465	−0·500006656[a]
$E_{\rm rel} - E_{\rm nonrel}$	−0·000006655	−0·000006656[a]
Lithium	Virial ratio = −1·00000006	
$E_{\rm rel}$	−7·4335330	−7·43353
$E_{\rm rel} - E_{\rm nonrel}$	−0·0008064	−0·00080
$^{\varepsilon}1s_{1/2}$	−2·478126	−2·477979
$^{\varepsilon}2s_{1/2}$	−0·1963400	−0·1963389
Beryllium	Virial ratio = −1·00000032	
$E_{\rm rel}$	−14·5758908	−14·57590
$E_{\rm rel} - E_{\rm nonrel}$	−0·0028684	−0·00288
$^{\varepsilon}1s_{1/2}$	−4·734000	−4·733498
$^{\varepsilon}2s_{1/2}$	−0·3093576	−0·3093221

(a) Exact solutions.

Table 5. Expectation values of r^n for the relativistic atomic orbitals. Numerically calculated values are also shown.

n		−2	−1	1	2	4	6
H	1*s* PW	1·9999	0·99999	1·5000	3·0000	22·501	315·17
	Num	2·0002	1·0000	1·5000	2·9999	22·499	314·98
Li	1*s* PW	14·889	2·6851	0·57311	0·44678	0·53216	1·2501
	Num	14·898	2·6856	0·57305	0·44670	0·53208	1·2472
	2*s* PW	0·43521	0·34537	3·8736	17·738	565·64	28883·00
	Num	0·43572	0·34544	3·8733	17·736	565·71	28949·00
Be	1*s* PW	27·752	3·6820	4·1498	0·23293	0·14201	0·16665
	Num	27·786	3·6833	4·1498	0·23286	0·14196	0·16655
	2*s* PW	1·0549	0·52246	2·6494	8·4263	135·17	3649·0
	Num	1·0571	0·52267	2·6489	8·4236	135·11	3649·6

PW: Present work.
Num: Numerical calculation [16].

fully numerical Hartree-Fock-Slater (HFS) and Dirac-Slater (DS) calculations [17]. The relativistic correction to total energy, defined as the difference between the calculated relativistic and nonrelativistic energies ($E_{\rm rel}$ and $E_{\rm nonrel}$), more or less agrees with the correction calculated by the numerical method. For Be_2($R = 4{\cdot}2$ a.u.) we find a relativistic correction to total energy that is about 20% smaller in absolute magnitude than the correction calculated earlier with a much smaller basis set.

The molecule Be_2 has proved to be very difficult to be described theoretically. The experimental dissociation energy is only 0·0036 a.u. [15]. Several configuration-interaction and other sophisticated nonrelativistic treatments involving static and dynamical correlation effects have been attempted, but it has been found that the shape of the calculated energy surface drastically changes from method to method

Table 6. Relativistic total and orbital energies (E_{rel} and ε) for molecules in atomic unit.

	Present work	Literature value	Reference
LiH($R = 3{\cdot}015$ a.u.)			
E_{rel}	− 7·9612147	− 7·7955230	Sundholm
$E_{\mathrm{rel}} - E_{\mathrm{nonrel}}$	− 0·0008205	− 0·0008030	[17][a]
$^{\varepsilon}1\sigma$	− 2·469200		
$^{\varepsilon}2\sigma$	− 0·294835		
Be_2($R = 4{\cdot}2$ a.u.)			
E_{rel}	− 29·0808065	− 29·0815	Datta and Ewig
$E_{\mathrm{rel}} - E_{\mathrm{nonrel}}$	− 0·0057602	− 0·0072	[2][b]
$^{\varepsilon}1g1/2$	− 4·752247	− 4·7523	
$^{\varepsilon}1u1/2$	− 4·752151	− 4·7522	
$^{\varepsilon}2g1/2$	− 0·405788	− 0·4064	
$^{\varepsilon}2u1/2$	− 0·251821	− 0·2521	
Be_2($R = 4.63$ a.u.)			
E_{rel}	− 29·1061287		
$E_{\mathrm{rel}} - E_{\mathrm{nonrel}}$	− 0·0057583		
$^{\varepsilon}1g1/2$	− 4·740792		
$^{\varepsilon}1u1/2$	− 4·740768		
$^{\varepsilon}2g1/2$	− 0·387195		
$^{\varepsilon}2u1/2$	− 0·258499		

(a) Numerical Hartree-Fock-Slater and Dirac-Slater calculations.

(b) Each basis function was expanded as a linear combination of ten gaussians. The Q-dependent two-electron integrals were not included in the calculation and a slightly different value of speed of light was used.

[18]. Our calculation shows that at the experimental equilibrium bond length ($R = 4{\cdot}63$ a.u.) the relativistic correction to total energy is about − 0·0058 a.u. (minimal basis results). The relativistic correction to binding energy is found to be $+ 2{\cdot}145 \times 10^{-5}$ a.u. only. However, for the internuclear separation of 4·2 a.u. we find that the relativistic correction to the binding energy is $- 2{\cdot}334 \times 10^{-5}$ a.u. Thus in going from $R = 4{\cdot}63$ a.u. to $R = 4{\cdot}2$ a.u. relativistic correction to the binding energy changes by $- 4{\cdot}5 \times 10^{-5}$ a.u. that is about 1·25% of the experimental binding energy (at $R = 4{\cdot}63$ a.u.). This change should be compared with the change in binding energy due to correlation, the latter change being only a few per cent of the experimental binding energy. This indicates that relativistic effects play a rather prominent role in determining the shape of the energy surface for this molecule, and any successful explanation of the electronic structure of Be_2 should be based on a relativistic theory.

Acknowledgement

The author gratefully acknowledges constant help from the personnel of computer center, IIT, Bombay.

References

[1] H Taketa, S Huzinaga and K O–Ohata, *J. Phys. Soc. Jpn.* **21**, 2313 (1966)
[2] S N Datta and C S Ewig, *Chem. Phys. Lett.* **85**, 443 (1982)

[3] H A Bethe and E E Salpeter, *Quantum mechanics of one- and two- electron atoms* (Springer-Verlag, Berlin, 1957) p. 167
[4] G Malli and J Oreg, *J. Chem. Phys.* **68**, 529 (1979)
[5] G Malli, *Chem Phys. Lett.* **73**, 510 (1980)
[6] S N Datta and G Devaiah, *Pramana – J. Phys.* **30**, 387 (1988)
[7] S N Datta, *Chem. Phys. Lett.* **74**, 568 (1980)
[8] W Kutzelnigg, *Int. J. Quantum Chem.* **25**, 107 (1984)
[9] J Sucher, *Phys. Rev.* **A30**, 703 (1980)
[10] G E Brown and D G Ravenhall, *Proc. R. Soc. London* **A208**, 532 (1951)
[11] M H Mittleman, *Phys. Rev.* **A24**, 1167 (1981)
[12] W H E Schwarz and E Wechsel-Trakowski, *Chem. Phys. Lett.* **85**, 94 (1982)
[13] H Partridge, *J. Chem. Phys.* **87**, 6643 (1989); Nasa Technical Memorandum 101044 (NASA, Moffet Field, 1989)
[14] K O–Ohata, H Taketa and S Huzinaga, *J. Phys. Soc. Jpn.* **21**, 2306 (1966)
[15] V E Bondybey, *Chem. Phys. Lett.* **109**, 436 (1984)
[16] J P Desclaux, *At. Data Nucl. Data Tables* **12**, 311 (1973); *Comput. Phys. Commun.* **9**, 31 (1975)
[17] D Sundholm, *Chem. Phys. Lett.* **149**, 251 (1988)
[18] C Sosa, J Noga and R J Bartlett, *J. Chem. Phys.* **88**, 5974 (1988)

PRAMANA
— journal of
physics

© Printed in India

Vol. 41, No. 4,
October 1993
pp. 371–388

Electron impact excitation of Ni XIX using the *R*-matrix method

MAN MOHAN*, M LE DOURNEUF†, A HIBBERT‡ and V M BURKE‡
*Department of Physics and Astrophysics, Delhi University, Delhi 110007, India
†Laboratoire de Théorie des Processus Atomiques et Moléculaires (U.P.R. 261 du C.N.R.S.), Départment "Atomes et Molécules en Astrophysique", Observatoire de Paris, 92195 Meudon, France
‡Department of Applied Mathematics and Theoretical Physics, The Queen's University, Belfast BT7 1NN, UK

MS received 12 July 1993

Abstract. Collision strengths for all the transitions between the 15 lowest states of neon-like Ni XIX have been calculated for electron impact in the 80–140 Ry energy range. Configuration-interaction wavefunctions have been used to represent the target states. The standard *R*-matrix code has been used to calculate the lower scattering partial waves ($L \leqslant 9$), while a no-exchange version of the same code has been used to compute efficiently the higher partial waves ($L \geqslant 10$). Effective collision strengths for 105 excitation transitions between the ground state $2s^2 2p^6\,{}^1S^e$ and the 14 $2s^2 2p^5 3l$ Rydberg states are tabulated for electron temperatures in the range $\log T = 5{\cdot}40$ to $\log T = 7{\cdot}00$, with T expressed in °K.

Keywords. Collision strength; configuration interaction.

PACS No. 34·80

1. Introduction

The interaction of electrons and photons with ionized atoms, particularly with metallic impurities such as Ti, Cr, Fe and Ni, plays an important role in fusion plasmas, as discussed in the recent meeting of the International Atomic Energy Agency [1]. Data on these processes are required both for plasma diagnostics and in plasma modelling. They are also required in laser research, especially in the soft X-ray region where Ne-like ions play a specific role in the electron excitation scheme as illustrated by the recent work of Matthews *et al* [2].

The first line of identifications for Ni XIX were made by Feldman *et al* [3], who reported transitions from the $2p^5 3s$, $2p^5 3d$ and $2s2p^6 3p$ configurations. A complete line classification, usable for the identification of solar features, was then undertaken by Swartz *et al* [4]. By analysing the soft X-ray spectra from 8 to 18 Å for the ions of Cr, Mn, Fe, Co, Ni and Cu, they identified lines originating from the $2p^5 4s$, $2p^5 5d$ and $2p^5 6d$ configurations.

Several theoreticians have reported calculations of atomic data for the Ne-like ions. Bhatia *et al* [5] have used the distorted wave approximation to compute collision strengths for the transitions from the ground level to the $n = 3$ Ry levels of the Ne-like ions with nuclear charge $Z = 14$, 18, 22, 26, 32 and 36. Zhang *et al* have reported collision strengths for excitation from the ground to the $n = 3$ and $n = 4$ levels in 20 neon-like ions with nuclear charge Z in the range $18 \leqslant Z \leqslant 74$, using the Coulomb–Born (1987) and relativistic distorted wave (1989) methods. Hagelstein and Jung [6] have also used a relativistic distorted wave, method to obtain collision strengths for neon-like ions with $Z = 26$, 34, 39, 42 and 47.

In the present work, we have used the R-matrix method [7], which allows the explicit introduction of the effect of resonances converging on to all the excited target terms included in the calculation. We have performed a 15-state calculation in LS coupling. The 15 target states $2s^2 2p^6 (^1S^e)$, $2s^2 2p^5 3s(^{1,3}P^0)$, $2s^2 2p^5 3p(^{1,3}S^e, {}^{1,3}P^e, {}^{1,3}D^e)$, $2s^2 2p^5 3d(^{1,3}P^0, {}^{1,3}D^0, {}^{1,3}F^0)$ are represented by configuration interaction wavefunctions. The effective collision strengths, obtained by averaging the collision strengths over a Maxwellian distribution for the velocity of the incident electron, are tabulated over a wide range of temperatures.

We have used the standard R-matrix code of Berrington *et al* [8, 9] for low partial waves ($L \leqslant 9$) and the no-exchange R-matrix program recently developed by Burke *et al* [10] for partial waves $10 \leqslant L \leqslant 40$. In addition, for optically allowed transitions, a 'top up' procedure based on the sum rule of Burgess *et al* [11] has been used to account approximately for $L > 40$.

2. Target calculation

Using the general configuration interaction (CI) code CIV3 [12], Hibbert *et al* [13] have calculated CI wavefunctions for all the states of the $[1s^2]$ $2s^2 2p^6$, $2s^2 2p^5 3l$, $2s2p^6 3l(l = s, p, d)$ configurations of many ions of the neon isoelectronic sequence, including Ni XIX. In the present scattering calculation, the fifteen lowest ionic states belonging to the ground $2s^2 2p^6$ and the $n = 3$ Rydberg $2s^2 2p^5 3l(l = s, p, d)$ configurations are represented by restricted CI expansions, which include the most important configurations while keeping the scattering calculation tractable.

The wavefunctions are represented by expansions of the form

$$\Phi(LS) = \sum_{i=1}^{M} a_i \phi_i(\alpha_i, LS), \tag{1}$$

where the single configuration functions ϕ_i are constructed from one electron orbitals, whose angular momenta are coupled as specified by α_i to form total L and S common to the M configurations. The radial part of each orbital is written as a linear combination of normalized Slater-type orbitals:

$$P_{nl} = \sum_{i=1}^{k} b_i \left[\frac{(2\zeta_i)^{2p_i+1}}{(2p_i)!} \right]^{1/2} r^{p_i} \exp(-\zeta_i r) \tag{2}$$

The parameters b_i, ζ_i in eq (2) and the mixing coefficients a_i in (1) are determined variationally as described by Hibbert *et al* [13].

In order to represent in a balanced way the ground and all the $n = 3$ Ry states, we used eight orthogonal one-electron orbitals $1s$, $2s$, $2p$, $3s$, $3p$, $4p$, $3d$, $4d$. The $1s$, $2s$ and $2p$ orbitals were initially chosen as the Hartree–Fock orbitals for the ground $^2P^0$ state of the fluorine-like Ni XX ion [14], with the $1s$ and $2s$ functions kept frozen throughout the calculation. The $3s$ function was first optimized on the energy of the lowest $2p^5 3s\,^3P^0$ Rydberg state of Ni XIX. The $2p$ was then reoptimized on the same state. Since the new $2p$ function is not the best one to represent the $2s^2 2p^6\,^1S^e$ ground state, we introduced a $3p$ function to compensate for this, optimising its parameters by minimizing the lowest energy eigenvalue in the $(2s^2 2p^6 + 2s^2 2p^5 3p)\ {}^1S^e$ subspace. This $3p$ function then provided some flexibility to represent the '$2p$' orbitals optimal for the different target states. The $4p$ orbital was optimized on the lowest eigenvalue in the $(2p^5 3p + 2p^5 4p)\ {}^3S^e$ subspace. The $3d$ function was chosen to optimize the lowest energy eigenvalue arising from the configurations $(2s^2 2p^5 3s + 2s 3d 2p^5 3s)\ {}^3P^0$, in order to account for the important $s-d$ angular correlation. Finally, the $4d$ orbital was optimized by minimizing the lowest eigenvalue in the subspace $(2p^5 3d + 2p^5 4d)$ ${}^3D^0$.

In table 1, we present our optimized parameters b_i, p_i and ζ_i for the 3s, 2p, 3p, 4p, 3d and 4d orbitals. Table 2 gives the restricted list of configurations included in the scattering calculation to represent the 15 target states, which are indexed in order of

Table 1. Values of parameters b_i, p_i and ξ_i for bound orbitals of Ni XIX.

Orbital	Clementi coefficient b_i	Power of r p_i	Exponent ζ_i
$3s$	0·23125	1	20·60692
	− 1·12640	2	8·98607
	1·60027	3	6·92923
$2p$	0·33249	2	12·46111
	0·09747	2	19·34179
	0·58600	2	10·93709
$3p$	2·38031	2	9·83896
	− 2·76992	3	10·38145
$4p$	1·78688	2	10·37242
	− 3·15633	3	10·10618
	2·01926	4	7·75928
$3d$	1·00000	3	13·18651
$4d$	0·63329	3	14·11282
	− 1·14731	4	7·81852

Table 2. Configurations used in the CI expansion of Ni XIX target states.

Target states	State Number	Configuration used
${}^1S^e$	1, 9	$[1s^2]2s^2 2p^6, 2s^2 2p^5 3p, 2s^2 2p^5 4p, 2s 2p^6 3s$
${}^3P^0$	2, 10	$[1s^2]2s^2 2p^5 3s, 2s^2 2p^5 3d, 2s^2 2p^5 4d,$ $2s 2p^6 3p, 2s 2p^6 4p$
${}^1P^0$	3, 15	$[1s^2]2s^2 2p^5 3s, 2s^2 2p^5 3d, 2s^2 2p^5 4d,$ $2s 2p^6 3p, 2s 2p^6 4p$
${}^3S^e$	4	$[1s^2]2s^2 2p^5 3p, 2s^2 2p^5 4p, 2s 2p^6 3s$
${}^3D^e$	5	$[1s^2]2s^2 2p^5 3p, 2s^2 2p^5 4p, 2s 2p^6 3d, 2s 2p^6 4d$
${}^1D^e$	6	$[1s^2]2s^2 2p^5 3p, 2s^2 2p^5 4p, 2s 2p^6 3d, 2s 2p^6 4d$
${}^3P^e$	7	$[1s^2]2s^2 2p^5 3p, 2s^2 2p^5 4p$
${}^1P^e$	8	$[1s^2]2s^2 2p^5 3p, 2s^2 2p^5 4p$
${}^3F^0$	11	$[1s^2]2s^2 2p^5 3d, 2s^2 2p^5 4d$
${}^1F^0$	12	$[1s^2]2s^2 2p^5 3d, 2s^2 2p^5 4d$
${}^3D^0$	13	$[1s^2]2s^2 2p^5 3d, 2s^2 2p^5 4d$
${}^1D^0$	14	$[1s^2]2s^2 2p^5 3d, 2s^2 2p^5 4d$

Table 3. Excitation thresholds for Ni XIX (in Ryd.).

Key	Configuration	State	Theory	Experiment
1	$1s^2 2s^2 2p^6$	${}^1S^e$	0·00000	0·00000
2	$1s^2 2s^2 2p^5 3s$	${}^3P^0$	65·14602	64·80838
3	$1s^2 2s^2 2p^5 3s$	${}^1P^0$	65·40276	66·18554
4	$1s^2 2s^2 2p^5 3p$	${}^3S^e$	67·30349	
5	$1s^2 2s^2 2p^5 3p$	${}^3D^e$	67·77201	
6	$1s^2 2s^2 2p^5 3p$	${}^1D^e$	67·98450	
7	$1s^2 2s^2 2p^5 3p$	${}^3P^e$	68·03022	
8	$1s^2 2s^2 2p^5 3p$	${}^1P^e$	68·03022	
9	$1s^2 2s^2 2p^5 3p$	${}^1S^e$	69·74102	
10	$1s^2 2s^2 2p^5 3d$	${}^3P^0$	71·07860	71·19752
11	$1s^2 2s^2 2p^5 3d$	${}^3F^0$	71·30784	
12	$1s^2 2s^2 2p^5 3d$	${}^1F^0$	71·56094	
13	$1s^2 2s^2 2p^5 3d$	${}^3D^0$	71·64446	72·04501
14	$1s^2 2s^2 2p^5 3d$	${}^1D^0$	71·64446	
15	$1s^2 2s^2 2p^5 3d$	${}^1P^0$	72·61951	73·37546

increasing energy. Table 3 shows that the excitation thresholds, calculated with these fairly simple wavefunctions, agree reasonably well with the experimental results of Corliss and Sugar [15].

3. Scattering calculation

In an inner region $r < a$ containing the charge distribution of the N-electron target, the total wavefunction describing the $(N + 1)$-electron system is expanded on a discrete basis of R-matrix states [16, 8]:

$$\Psi_k = \mathscr{A}\sum_{ij} c_{ijk}\Phi_i(x_1\cdots x_N, \hat{\mathbf{r}}_{N+1}, \sigma_{N+1})u_{ij}(r_{N+1}) + \sum_j d_{jk}\phi_j(x_1\cdots x_{N+1}), \qquad (3)$$

where $\mathscr{A}$ is the antisymmetrization operator which accounts for electron exchange, Φ_i are channel functions formed by coupling the target states of coordinates $x_i = \{r_i, \hat{\mathbf{r}}_i, \sigma_i\}$ with the spin angle function of the scattered electron. The $\{u_{ij}\}$ form a discrete R-matrix basis of continuum orbitals for the scattered electron and the $\{\phi_j\}$ are $(N + 1)$ electron bound configurations, which account for the orthogonality of the continuum orbitals u_{ij} to the bound orbitals and for additional short range correlation effects.

The continuum orbitals u_{ij} in (3) are solutions of the zero-order radial differential equation:

$$\left[-\frac{\mathrm{d}^2}{\mathrm{d}r^2} + \frac{l_i(l_i+1)}{r^2} + 2V(r) - k_i^2\right]u_{ij}(r) = \sum_k \lambda_{ijk}P_k(r), \qquad (4)$$

which satisfy the boundary conditions:

$$u_{ij}(0) = 0 \qquad (5a)$$

$$\left.\frac{a}{u_{ij}}\frac{du_{ij}}{dr}\right|_{r=a} = b. \qquad (5b)$$

In (4), l_i is the angular momentum of the scattered electron, $V(r)$ is the static potential of the target in its ground state and λ_{ijk} are Lagrange multipliers which are determined in order to ensure the orthogonality of the continuum orbitals to the bound radial orbitals $P_{kl_i}(r)$ having the same angular momentum l_i. We imposed a zero logarithmic derivative $b = 0$ at the R-matrix boundary radius $a = 3{\cdot}5$ a.u. and we retained 20 continuum orbitals for each angular symmetry, to ensure convergence in the energy range considered here, namely up to 172 Ryd.

The coefficients c_{ijk} and d_{jk} in (3) were determined by diagonalizing the $(N+1)$-electron Hamiltonian matrix in the inner region. In the outer region ($r \geqslant a$), the radial equations were solved, using the asymptotic code of Berrington *et al* [9] which treats multipole couplings by first order perturbation theory [17]. The LS coupled K matrices, obtained by matching the inner and outer solutions at the R-matrix boundary, were used to calculate collision strengths. We have considered all partial waves, up to $L = 9$ for both parities and spin multiplicities (doublet and quartet). This was sufficient to obtain converged results for forbidden transitions from the ground state ${}^1S^e$. However, for dipole allowed transitions, such as $2p^6\,{}^1S^e \rightarrow 3s\,{}^1P^0$, it was necessary to include the contribution of higher partial waves for convergence. Since exchange effects were found to be negligible for $L \geqslant 10$, a no-exchange R-matrix approximation, which amounts to neglecting the antisymmetrization and the bound-type part of expansion (3), is sufficient for higher partial waves. A fast no-exchange R-matrix code, recently developed by Burke *et al* [10], has therefore been used to calculate the contributions from $L = 10$ to 40 and, finally, a 'top up' procedure, based on the sum rule of Burgess *et al* [11], accounts approximately for $L > 40$.

Another important aspect of the calculation is that, above all thresholds, the pseudo-resonances, induced in the low partial waves by some bound-type terms in expansion (3), have been removed by smoothing the T-matrix according to the method of Burke *et al* [16].

4. Results and discussion

The importance of the smoothing procedure on the collision strengths is illustrated in figure 1 and table 4 which compare the raw Ω_{EX} and the smoothed $\bar{\Omega}_{\mathrm{EX}}$ contributions of the $L \leqslant 9$ partial waves, including exchange, for the $2p^5 3p\,{}^3S^e \rightarrow {}^3D^e$ transition from 85 to 160 Rydberg. Table 4 also illustrates the importance of the no-exchange contributions Ω_{NE} obtained by the no-exchange code for $10 \leqslant L \leqslant 40$ and the 'top up' procedure for $L > 40$. Indeed, for the ${}^3S^e \rightarrow {}^3D^e$ transition, the $L \geqslant 10$ partial waves contribute from 6% to 14% of the total collision strength when the energy increases from 85 to 100 Ryd.

The present R-matrix (RM) calculation is the first one to give excitation collision strengths between the $n = 3$ Rydberg states (table 5). Comparison with the previous relativistic distorted wave (RDW) calculation of Zhang *et al* [18] is therefore limited to the collision strengths for excitation from the ground state. Since the RDW results were obtained at impact energies which are multiples of each threshold excitation energy E_I, a spline interpolation of our RM results has been made to facilitate the comparison. In addition, since our calculation is performed in LS coupling, we limit our comparison in table 6 to transitions involving pure ${}^3P_2^0$ and nearly pure ${}^1S_0^e$ states. For the spin-forbidden transition to the first excited level, $2p^6\,{}^1S_0^e \rightarrow 2p^5 3s\,{}^3P_2^0$, we notice that the results of the two calculations decrease monotonically at high

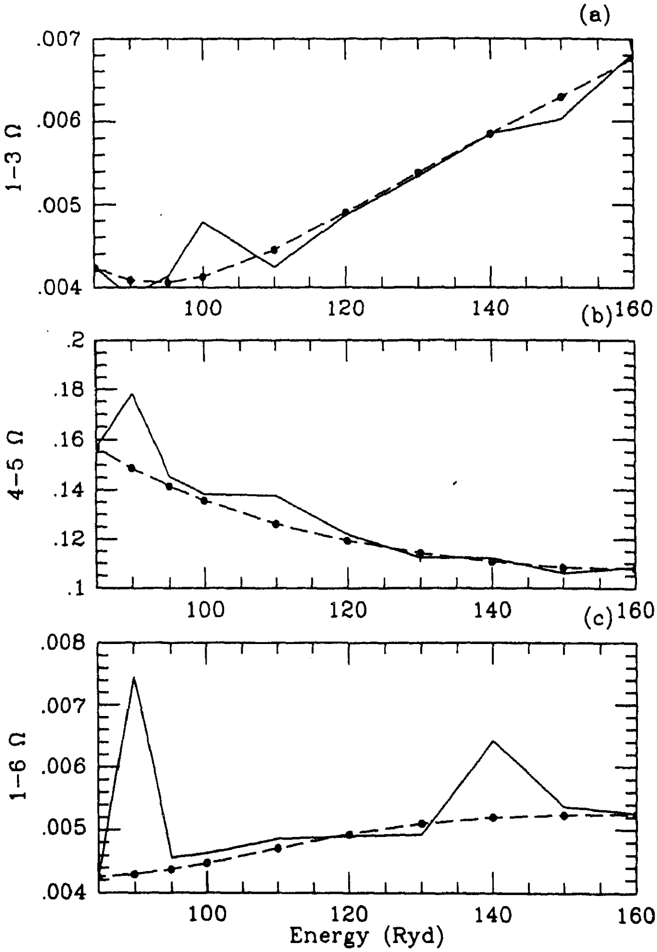

Figure 1. Collision strengths for various transitions as a function of electron energy. Full curves: raw collision strengths, broken curves: collision strengths obtained by averaging over pseudo-resonances.

Table 4. Influence of higher partial waves and of the smoothing of pseudo-resonances on the collision strength for the $2p^5 3p\,^3P^e \to {}^3D^e$ transition.

Energy in Ryd.	Ω_{EX} $L \leqslant 9$	$\bar{\Omega}_{\mathrm{EX}}$ $L \leqslant 9$	Ω_{NE} $10 \leqslant L \leqslant 40$ + 'top up'	Total $\Omega = \bar{\Omega}_{\mathrm{EX}} + \Omega_{\mathrm{NE}}$
85·00	0·1569	0·1569	0·0128	0·1697
90·00	0·1781	0·1485	0·0151	0·1636
93·00	0·1454	0·1415	0·0172	0·1587
100·00	0·1382	0·1356	0·0194	0·1550

energies, the RDW results are globally smaller and their relative difference decreases from more than 40% at $E/E_I = 1{\cdot}5$ to 28% at $E/E_I = 1{\cdot}9$. For the $2p^6\,{}^1S^e_0 \to 2p^5 3d\,{}^3P^0_2$ transition, we observe the same trends, with the relative difference between the two calculations decreasing from 40% at $E/E_I = 1{\cdot}2$ to 27% at $E/E_I = 1{\cdot}9$. In the case of

Table 5. Collision strengths for transitions in Ni XIX in the energy range 80–140 Ryd. ($a \pm b \equiv a \times 10^{\pm b}$).

Transition		Energy (Ryd.)								
i	f	80·00	85·00	90·00	95·00	100·00	110·00	120·00	130·00	140·00
1	2	2·866 − 3	2·903 − 3	2·640 − 3	2·416 − 3	2·225 − 3	1·915 − 3	1·673 − 3	1·473 − 3	1·300 − 3
1	3	3·181 − 3	4·240 − 3	4·101 − 3	4·089 − 3	4·177 − 3	4·564 − 3	5·117 − 3	5·740 − 3	6·371 − 3
1	4	4·346 − 3	4·188 − 3	3·678 − 3	3·263 − 3	2·930 − 3	2·468 − 3	2·224 − 3	2·156 − 3	2·251 − 3
1	5	8·266 − 3	7·852 − 3	6·620 − 3	5·668 − 3	4·943 − 3	4·012 − 3	3·589 − 3	3·585 − 3	4·054 − 3
1	6	4·124 − 3	4·278 − 3	4·338 − 3	4·444 − 3	4·584 − 3	4·925 − 3	5·292 − 3	5·635 − 3	5·932 − 3
1	7	3·204 − 3	3·054 − 3	2·599 − 3	2·235 − 3	1·948 − 3	1·561 − 3	1·370 − 3	1·333 − 3	1·445 − 3
1	8	1·274 − 3	1·218 − 3	1·051 − 3	9·165 − 4	8·071 − 4	6·568 − 4	5·771 − 4	5·539 − 4	5·821 − 4
1	9	3·441 − 2	3·483 − 2	3·202 − 2	3·008 − 2	2·886 − 2	2·824 − 2	2·975 − 2	3·348 − 2	4·001 − 2
1	10	1·564 − 2	1·455 − 2	1·330 − 2	1·223 − 2	1·129 − 2	9·720 − 3	8·453 − 3	7·443 − 3	6·742 − 3
1	11	1·413 − 2	1·306 − 2	1·165 − 2	1·033 − 2	9·332 − 3	7·827 − 3	6·759 − 3	6·042 − 3	5·781 − 3
1	12	3·344 − 3	3·535 − 3	3·532 − 3	3·585 − 3	3·679 − 3	3·942 − 3	4·246 − 3	4·547 − 3	4·845 − 3
1	13	5·641 − 3	5·133 − 3	4·496 − 3	3·981 − 3	3·562 − 3	2·918 − 3	2·445 − 3	2·103 − 3	1·940 − 3
1	14	1·958 − 3	1·745 − 3	1·568 − 3	1·420 − 3	1·297 − 3	1·100 − 3	9·492 − 4	8·351 − 4	7·655 − 4
1	15	5·564 − 2	5·495 − 2	5·429 − 2	5·390 − 2	5·356 − 2	5·342 − 2	5·349 − 2	5·359 − 2	5·347 − 2
2	3	9·945 − 2	1·055 − 1	1·095 − 1	1·140 − 1	1·186 − 1	1·285 − 1	1·387 − 1	1·491 − 1	1·591 − 1
2	4	4·852 − 2	4·495 − 2	4·188 − 2	3·922 − 2	3·478 − 2	3·113 − 2	2·807 − 2	2·562 − 2	2·411 − 2
2	5	1·546 − 0	1·625 − 0	1·690 − 0	1·753 − 0	1·828 − 0	1·915 − 0	1·960 − 0	2·013 − 0	2·067 − 0
2	6	8·664 − 0	9·015 − 0	9·360 − 0	9·629 − 0	1·001 + 1	1·047 + 1	1·073 + 1	1·102 + 1	1·130 + 1
2	7	1·081 − 2	9·386 − 3	8·197 − 3	7·210 − 3	5·712 − 3	4·668 − 3	3·908 − 3	3·308 − 3	2·799 − 3
2	8	5·147 − 0	5·340 − 0	5·590 − 0	5·760 − 0	6·004 − 0	6·276 − 0	6·464 − 0	6·653 − 0	6·831 − 0
2	9	6·534 − 3	5·674 − 3	4·957 − 3	4·362 − 3	3·463 − 3	2·841 − 3	2·392 − 3	2·044 − 3	1·752 − 3
2	10	2·209 − 3	1·922 − 3	1·683 − 3	1·487 − 3	1·189 − 3	9·804 − 4	8·248 − 4	6·974 − 4	5·854 − 4
2	11	2·229 − 1	2·465 − 1	2·838 − 1	3·213 − 1	3·581 − 1	3·254 − 1	2·548 − 1	2·466 − 1	4·656 − 1
2	12	5·110 − 1	5·130 − 1	5·155 − 1	5·187 − 1	5·242 − 1	5·301 − 1	5·319 − 1	5·311 − 1	5·279 − 1
2	13	1·599 − 2	1·378 − 2	1·194 − 2	1·041 − 2	8·086 − 3	6·473 − 3	5·329 − 3	4·507 − 3	3·952 − 3
2	14	3·541 − 1	3·527 − 1	3·549 − 1	3·567 − 1	3·609 − 1	3·651 − 1	3·679 − 1	3·711 − 1	3·784 − 1
2	15	1·135 − 2	9·743 − 3	8·457 − 3	7·416 − 3	5·836 − 3	4·665 − 3	3·778 − 3	3·268 − 3	3·440 − 3

(*Continued*)

Table 5. (*Continued*)

Transition		Energy (Ryd.)								
i	f	80·00	85·00	90·00	95·00	100·00	110·00	120·00	130·00	140·00
3	4	7·547 − 3	6·520 − 3	5·654 − 3	4·927 − 3	3·811 − 3	3·029 − 3	2·471 − 3	2·056 − 3	1·737 − 3
3	5	2·044 − 3	1·774 − 3	1·552 − 3	1·371 − 3	1·102 − 3	9·186 − 4	7·848 − 4	6·773 − 4	5·850 − 4
3	6	1·078 − 2	9·475 − 3	8·375 − 3	7·449 − 3	6·009 − 3	4·960 − 3	4·153 − 3	3·486 − 3	2·896 − 3
3	7	2·950 − 0	3·070 − 0	3·190 − 0	3·284 − 0	3·441 − 0	3·549 − 0	3·662 − 0	3·785 − 0	3·858 − 0
3	8	6·328 − 3	5·492 − 3	4·799 − 3	4·227 − 3	3·366 − 3	2·769 − 3	2·333 − 3	1·988 − 3	1·697 − 3
3	9	1·692 − 0	1·759 − 0	1·842 − 0	1·898 − 0	1·988 − 0	2·061 − 0	2·130 − 0	2·199 − 0	2·249 − 0
3	10	5·253 − 1	5·497 − 1	5·732 − 1	5·933 − 1	6·284 − 1	6·522 − 1	6·817 − 1	7·119 − 1	7·290 − 1
3	11	7·071 − 3	5·944 − 3	5·094 − 3	4·443 − 3	3·505 − 3	2·813 − 3	2·291 − 3	2·106 − 3	2·663 − 3
3	12	1·591 − 2	1·357 − 2	1·169 − 2	1·019 − 2	7·972 − 3	6·436 − 3	5·295 − 3	4·477 − 3	4·120 − 3
3	13	1·603 − 1	1·615 − 1	1·628 − 1	1·644 − 1	1·675 − 1	1·706 − 1	1·733 − 1	1·756 − 1	1·765 − 1
3	14	1·089 − 2	9·516 − 3	8·374 − 3	7·417 − 3	5·907 − 3	4·755 − 3	3·843 − 3	3·167 − 3	2·833 − 3
3	15	1·087 − 1	1·092 − 1	1·105 − 1	1·115 − 1	1·135 − 1	1·155 − 1	1·171 − 1	1·182 − 1	1·186 − 1
4	5	7·271 − 2	7·365 − 2	7·451 − 2	7·554 − 2	7·776 − 2	7·973 − 2	8·159 − 2	8·312 − 2	8·390 − 2
4	6	1·697 − 1	1·637 − 1	1·588 − 1	1·550 − 1	1·497 − 1	1·469 − 1	1·455 − 1	1·456 − 1	1·467 − 1
4	7	6·509 − 3	5·885 − 3	5·386 − 3	4·986 − 3	4·392 − 3	3·976 − 3	3·686 − 3	3·548 − 3	3·664 − 3
4	8	1·753 − 2	1·555 − 2	1·387 − 2	1·247 − 2	1·033 − 2	9·022 − 3	8·275 − 3	8·138 − 3	8·642 − 3
4	9	2·180 − 3	1·929 − 3	1·731 − 3	1·574 − 3	1·349 − 3	1·199 − 3	1·101 − 3	1·059 − 3	1·110 − 3
4	10	3·944 − 3	3·579 − 3	3·274 − 3	3·021 − 3	2·649 − 3	2·416 − 3	2·286 − 3	2·232 − 3	2·238 − 3
4	11	2·187 − 0	2·287 − 0	2·373 − 0	2·446 − 0	2·540 − 0	2·671 − 0	2·749 − 0	2·840 − 0	2·934 − 0
4	12	3·066 − 2	2·961 − 2	2·895 − 2	2·861 − 2	2·856 − 2	2·902 − 2	2·965 − 2	3·025 − 2	3·073 − 2
4	13	6·007 − 3	5·115 − 3	4·385 − 3	3·788 − 3	2·907 − 3	2·316 − 3	1·907 − 3	1·618 − 3	1·434 − 3
4	14	4·420 − 3	3·812 − 3	3·292 − 3	2·850 − 3	2·143 − 3	1·609 − 3	1·200 − 3	8·994 − 4	7·223 − 4
4	15	1·453 − 3	1·110 − 3	8·501 − 4	6·561 − 4	4·136 − 4	2·978 − 4	2·567 − 4	2·711 − 4	3·551 − 4
5	6	5·272 − 3	4·446 − 3	3·789 − 3	3·268 − 3	2·525 − 3	2·041 − 3	1·704 − 3	1·467 − 3	1·345 − 3
5	7	5·880 − 2	5·262 − 2	4·760 − 2	4·354 − 2	3·757 − 2	3·362 − 2	3·101 − 2	2·953 − 2	2·941 − 2
5	8	7·653 − 1	7·482 − 1	7·382 − 1	7·289 − 1	7·163 − 1	7·094 − 1	7·074 − 1	7·075 − 1	7·104 − 1

5	9	4·972 − 2	4·450 − 2	4·009 − 2	3·638 − 2	3·065 − 2	2·670 − 2	2·416 − 2	2·290 − 2	2·304 − 2
5	10	6·474 − 3	5·992 − 3	5·595 − 3	5·264 − 3	4·741 − 3	4·326 − 3	3·955 − 3	3·595 − 3	3·252 − 3
5	11	9·337 − 2	9·238 − 2	9·227 − 2	9·250 − 2	9·347 − 2	9·626 − 2	9·847 − 2	1·010 − 1	1·038 − 1
5	12	9·822 − 0	1·026 + 1	1·071 + 1	1·105 + 1	1·147 + 1	1·206 + 1	1·239 + 1	1·275 + 1	1·310 + 1
5	13	3·292 − 2	2·826 − 2	2·439 − 2	2·120 − 2	1·640 − 2	1·315 − 2	1·090 − 2	9·306 − 3	8·207 − 3
5	14	1·848 − 0	1·914 − 0	2·006 − 0	2·069 − 0	2·152 − 0	2·253 − 0	2·332 − 0	2·405 − 0	2·474 − 0
5	15	1·744 − 2	1·480 − 2	1·263 − 2	1·087 − 2	8·281 − 3	6·577 − 3	5·429 − 3	4·645 − 3	4·171 − 3
6	7	1·155 − 2	9·458 − 3	7·855 − 3	6·636 − 3	5·008 − 3	4·033 − 3	3·401 − 3	3·032 − 3	3·080 − 3
6	8	4·979 − 2	4·419 − 2	3·950 − 2	3·558 − 2	2·965 − 2	2·572 − 2	2·340 − 2	2·255 − 2	2·333 − 2
6	9	2·404 − 1	2·379 − 1	2·371 − 1	2·361 − 1	2·339 − 1	2·321 − 1	2·293 − 1	2·257 − 1	2·222 − 1
6	10	4·267 − 2	4·236 − 2	4·218 − 2	4·211 − 2	4·217 − 2	4·239 − 2	4·267 − 2	4·293 − 2	4·304 − 2
6	11	1·097 − 2	9·411 − 3	8·134 − 3	7·083 − 3	5·490 − 3	4·354 − 3	3·499 − 3	2·853 − 3	2·444 − 3
6	12	3·239 − 2	2·716 − 2	2·296 − 2	1·960 − 2	1·482 − 2	1·179 − 2	9·780 − 3	8·390 − 3	7·513 − 3
6	13	3·263 − 0	3·411 − 0	3·566 − 0	3·680 − 0	3·855 − 0	3·998 − 0	4·140 − 0	4·290 − 0	4·382 − 0
6	14	1·748 − 2	1·486 − 2	1·273 − 2	1·099 − 2	8·430 − 3	6·668 − 3	5·384 − 3	4·425 − 3	3·809 − 3
6	15	6·180 − 1	6·420 − 1	6·754 − 1	6·984 − 1	7·314 − 1	7·599 − 1	7·903 − 1	8·187 − 1	8·392 − 1
7	8	1·701 − 2	1·746 − 2	1·802 − 2	1·859 − 2	1·973 − 2	2·073 − 2	2·158 − 2	2·225 − 2	2·262 − 2
7	9	2·319 − 2	2·127 − 2	1·963 − 2	1·822 − 2	1·596 − 2	1·427 − 2	1·302 − 2	1·217 − 2	1·175 − 2
7	10	2·096 − 3	1·884 − 3	1·708 − 3	1·564 − 3	1·347 − 3	1·203 − 3	1·112 − 3	1·066 − 3	1·070 − 3
7	11	1·781 − 0	1·858 − 0	1·944 − 0	2·006 − 0	2·084 − 0	2·191 − 0	2·256 − 0	2·326 − 0	2·393 − 0
7	12	7·381 − 2	7·056 − 2	6·828 − 2	6·675 − 2	6·526 − 2	6·505 − 2	6·538 − 2	6·603 − 2	6·716 − 2
7	13	1·267 − 2	1·073 − 2	9·148 − 3	7·856 − 3	5·957 − 3	4·701 − 3	3·860 − 3	3·309 − 3	3·032 − 3
7	14	5·414 − 0	5·605 − 0	5·900 − 0	6·082 − 0	6·317 − 0	6·612 − 0	6·828 − 0	7·037 − 0	7·230 − 0
7	15	1·828 − 2	1·543 − 2	1·312 − 2	1·127 − 2	8·593 − 3	6·877 − 3	5·750 − 3	4·997 − 3	4·562 − 3
8	9	6·163 − 3	5·103 − 3	4·271 − 3	3·624 − 3	2·727 − 3	2·168 − 3	1·798 − 3	1·560 − 3	1·493 − 3
8	10	1·592 − 3	1·469 − 3	1·363 − 3	1·270 − 3	1·119 − 3	9·954 − 4	9·063 − 4	8·304 − 4	7·463 − 4
8	11	5·479 − 3	4·699 − 3	4·059 − 3	3·533 − 3	2·731 − 3	2·150 − 3	1·696 − 3	1·328 − 3	1·056 − 3
8	12	1·273 − 2	1·095 − 2	9·469 − 3	8·248 − 3	6·403 − 3	5·127 − 3	4·212 − 3	3·533 − 3	3·047 − 3
8	13	1·558 − 2	1·575 − 2	1·604 − 2	1·641 − 2	1·727 − 2	1·816 − 2	1·989 − 2	1·954 − 2	1·997 − 2
8	14	1·810 − 2	1·550 − 2	1·338 − 2	1·155 − 2	9·058 − 3	7·239 − 3	5·883 − 3	4·848 − 3	4·160 − 3
8	15	1·793 − 0	1·858 − 0	1·959 − 0	2·022 − 0	2·108 − 0	2·195 − 0	2·273 − 0	2·346 − 0	2·404 − 0

(Continued)

Table 5. (*Continued*)

Transition		Energy (Ryd.)								
i	*f*	80·00	85·00	90·00	95·00	100·00	110·00	120·00	130·00	140·00
9	10	5·534 − 1	5·784 − 1	6·091 − 1	6·328 − 1	6·699 − 1	6·991 − 1	7·275 − 1	7·577 − 1	7·765 − 1
9	11	5·207 − 3	4·309 − 3	3·607 − 3	3·063 − 3	2·327 − 3	1·899 − 3	1·657 − 3	1·552 − 3	1·615 − 3
9	12	6·155 − 3	5·045 − 3	4·203 − 3	3·565 − 3	2·714 − 3	2·211 − 3	1·901 − 3	1·762 − 3	1·899 − 3
9	13	6·737 − 3	6·985 − 3	7·259 − 3	7·542 − 3	8·098 − 3	8·581 − 3	8·947 − 3	9·183 − 3	9·301 − 3
9	14	1·575 − 3	1·266 − 3	1·027 − 3	8·438 − 4	5·978 − 4	4·546 − 4	3·701 − 4	3·300 − 4	3·501 − 4
9	15	7·645 − 4	6·493 − 4	5·587 − 4	4·870 − 4	3·822 − 4	3·080 − 4	2·530 − 4	2·206 − 4	2·294 − 4
10	11	7·176 − 1	7·571 − 1	7·882 − 1	8·133 − 1	8·542 − 1	8·819 − 1	9·116 − 1	9·457 − 1	9·628 − 1
10	12	1·439 − 1	1·329 − 1	1·236 − 1	1·154 − 1	1·015 − 1	9·014 − 2	8·024 − 2	7·162 − 2	6·462 − 2
10	13	4·850 − 2	4·286 − 2	3·807 − 2	3·402 − 2	2·771 − 2	2·326 − 2	2·011 − 2	1·791 − 2	1·647 − 2
10	14	2·414 − 1	2·248 − 1	2·115 − 1	2·014 − 1	1·876 − 1	1·794 − 1	1·751 − 1	1·771 − 1	1·896 − 1
10	15	2·114 − 2	1·828 − 2	1·594 − 2	1·402 − 2	1·118 − 2	9·291 − 3	8·088 − 3	7·510 − 3	7·696 − 3
11	12	2·495 − 2	2·206 − 2	1·966 − 2	1·768 − 2	1·471 − 2	1·265 − 2	1·115 − 2	9·944 − 3	8·894 − 3
11	13	1·368 − 1	1·214 − 1	1·082 − 1	9·689 − 2	7·892 − 2	6·565 − 2	5·561 − 2	4·771 − 2	4·125 − 2
11	14	5·753 − 1	5·622 − 1	5·528 − 1	5·445 − 1	5·296 − 1	5·148 − 1	4·994 − 1	4·851 − 1	4·770 − 1
11	15	9·852 − 2	8·729 − 2	7·756 − 2	6·916 − 2	5·575 − 2	4·595 − 2	3·887 − 2	3·386 − 2	3·047 − 2
12	13	4·920 − 2	4·353 − 2	3·869 − 2	3·456 − 2	2·808 − 2	2·343 − 2	2·008 − 2	1·765 − 2	1·590 − 2
12	14	9·902 − 2	8·829 − 2	7·890 − 2	7·068 − 2	5·722 − 2	4·697 − 2	3·913 − 2	3·314 − 2	2·861 − 2
12	15	1·454 − 1	1·436 − 1	1·430 − 1	1·426 − 1	1·428 − 1	1·441 − 1	1·459 − 1	1·479 − 1	1·501 − 1
13	14	9·036 − 3	8·805 − 3	8·724 − 3	8·762 − 3	9·085 − 3	9·590 − 3	1·015 − 2	1·069 − 2	1·118 − 2
13	15	9·797 − 2	8·798 − 2	7·928 − 2	7·168 − 2	5·914 − 2	4·926 − 2	4·126 − 2	3·470 − 2	2·945 − 2
14	15	2·227 − 2	1·949 − 2	1·718 − 2	1·524 − 2	1·229 − 2	1·019 − 2	8·617 − 3	7·360 − 3	6·298 − 3

Table 6. Comparison of our *LS R*-matrix results (a) and the relativistic distorted wave results of Zhang *et al* [18] (b) for transitions between the ground level $2p^6\,{}^1S^e_0$ and the (nearly) pure $2p^5 3l^{2S+1}L^{\pi}_j$ levels for selected energy ratios E/E_I, where E_I is the relevant exciation threshold energy. Our *LSJ* results are deduced from the *LS* results by an algebraic recoupling analogous to relation (9).

Transition		Calc.	Energy ratio E/E_I		
			1·2	1·5	1·9
$2b^6\,{}^1S^e_0$	$2p^5 3s\,{}^3P^0_2$	*a*		1·282 − 3	8·856 − 4
		b		0·904 − 3	6·90 − 4
	$2p^5 3d\,{}^3P^0_2$	*a*	8·044 − 3	5·672 − 3	3·916 − 3
		b	5·73 − 3	4·31 − 3	3·99 − 3
	$2p^5 3p\,{}^1S^e_0$	*a*	3·516 − 2	2·832 − 2	3·483 − 2
		b	3·90 − 2	4·03 − 2	4·16 − 3

the spin-allowed monopole transition $2p^6\,{}^1S^e_0 - 2p^5 3p\,{}^1S^e_0$, the energy variations of the two calculations differ qualitatively, since the RDW results increase monotonically and slowly in this energy range, while the RM results present a minimum around $E/E_I = 1{\cdot}5$ and rise more sharply at high energies. These differences may be related to the fact that the RM calculation accounts non perturbatively and thoroughly for the strong monopole coupling.

Since the excitation collision strengths vary rapidly with energy in the threshold region, it is not practicable to tabulate them here. However, for many plasma applications, excitation rate coefficients rather than collision strengths are needed. They are obtained by integrating the collision strengths over the distribution of incident electron velocities. While Maxwellian distributions' are the usual distributions in astrophysical plasmas in local thermodynamical equilibrium, the effective collision rates for any other distribution could be calculated using our collision strengths listed in table 5. The excitation rate coefficient [19] for a transition from state *i* to state *f* at an electron temperature *T* is given by:

$$C(i\to f) = \frac{8{\cdot}6287\times 10^{-6}}{g_i T^{1/2}}\,\gamma(i\to f)\exp\left[-\frac{\Delta E_{if}}{kT}\right]\mathrm{cm}^3\,\mathrm{s}^{-1}, \tag{7}$$

where $g_i = (2L_i + 1)(2S_i + 1)$ is the statistical weight of the lower state *i*, $\Delta E_{if} = E_f - E_i$ is the excitation energy and $\gamma(i\to f)$ is the effective collision strength defined as:

$$\gamma(i\to f) = \int_0^{\infty} \Omega(i\to f)\exp(-\varepsilon_f/\mathrm{kT})\,d(\varepsilon_f/kT), \tag{8}$$

where $\Omega(i\to f)$ is the dimensionless collision strength for the transition from *i* to *f*, ε_f is the energy of the incident electron with respect to upper level *f*, and *k* is the Boltzmann constant. To perform the infinite integral in (8), the collision strengths were fitted to the correct asymptotic form as described by Berrington *et al* [19].

In table 7, we have given $\gamma(i\to f)$ for all the 105 transitions between the ground state and the $n = 3$ Rydberg states, over a wide range of electron temperatures, from $\log T = 5{\cdot}4$ to $\log T = 7{\cdot}0$, where *T* is given in °K. In general, the values of effective

Table 7. Effective collision strengths for transitions in Ni XIX. ($a \pm b \equiv a \times 10^{\pm b}$).

Transition		Temperature (log K)										
i	*f*	5·40	5·60	5·80	6·00	6·20	6·40	6·50	6·70	6·80	6·90	7·00
1	2	4·966 − 2	4·091 − 2	3·190 − 2	2·386 − 2	1·739 − 2	1·251 − 2	1·059 − 2	7·580 − 3	6·411 − 3	5·420 − 3	4·577 − 3
1	3	4·665 − 2	4·226 − 2	3·495 − 2	2·707 − 2	2·024 − 2	1·508 − 2	1·316 − 2	1·074 − 2	1·040 − 2	1·082 − 2	1·213 − 2
1	4	1·604 − 2	1·411 − 2	1·188 − 2	9·777 − 3	7·980 − 3	6·505 − 3	5·875 − 3	4·791 − 3	4·313 − 3	3·863 − 3	3·433 − 3
1	5	3·405 − 2	3·087 − 2	2·617 − 2	2·134 − 2	1·708 − 2	1·355 − 2	1·206 − 2	9·550 − 3	8·467 − 3	7·465 − 3	6·527 − 3
1	6	1·478 − 2	1·227 − 2	9·992 − 3	8·185 − 3	6·896 − 3	6·082 − 3	5·833 − 3	5·595 − 3	5·576 − 3	5·596 − 3	5·635 − 3
1	7	1·186 − 2	1·012 − 2	8·374 − 3	6·837 − 3	5·563 − 3	4·517 − 3	4·066 − 3	3·277 − 3	2·923 − 3	2·588 − 3	2·269 − 3
1	8	1·762 − 2	1·428 − 2	1·096 − 2	8·120 − 3	5·896 − 3	4·247 − 3	3·604 − 3	2·605 − 3	2·218 − 3	1·887 − 3	1·602 − 3
1	9	4·603 − 2	4·335 − 2	4·085 − 2	3·867 − 2	3·676 − 2	3·522 − 2	3·465 − 2	3·346 − 2	3·243 − 2	3·090 − 2	2·883 − 2
1	10	2·081 − 2	1·966 − 2	1·856 − 2	1·745 − 2	1·625 − 2	1·487 − 2	1·408 − 2	1·229 − 2	1·127 − 2	1·018 − 2	9·058 − 3
1	11	1·867 − 2	1·761 − 2	1·661 − 2	1·560 − 2	1·445 − 2	1·310 − 2	1·235 − 2	1·069 − 2	9·768 − 3	8·803 − 3	7·815 − 3
1	12	4·354 − 3	3·997 − 3	3·761 − 3	3·629 − 3	3·587 − 3	3·638 − 3	3·705 − 3	3·924 − 3	4·066 − 3	4·212 − 3	4·345 − 3
1	13	8·085 − 3	7·471 − 3	6·925 − 3	6·400 − 3	5·843 − 3	5·221 − 3	4·885 − 3	4·160 − 3	3·774 − 3	3·378 − 3	2·981 − 3
1	14	5·020 − 3	4·041 − 3	3·340 − 3	2·824 − 3	2·418 − 3	2·074 − 3	1·919 − 3	1·653 − 3	1·557 − 3	1·501 − 3	1·492 − 3
1	15	9·196 − 2	9·312 − 2	9·494 − 2	9·762 − 2	1·016 − 1	1·074 − 1	1·112 − 1	1·199 − 1	1·238 − 1	1·264 − 1	1·270 − 1
2	3	3·558 − 1	3·071 − 1	2·486 − 1	1·939 − 1	1·489 − 1	1·142 − 1	1·002 − 1	7·750 − 2	6·817 − 2	5·984 − 2	5·231 − 2
2	4	1·015 − 0	1·019 − 0	1·064 − 0	1·146 − 0	1·253 − 0	1·375 − 0	1·441 − 0	1·582 − 0	1·658 − 0	1·738 − 0	1·820 − 0
2	5	5·550 − 0	5·670 − 0	5·994 − 0	6·490 − 0	7·088 − 0	7·742 − 0	8·085 − 0	8·805 − 0	9·185 − 0	9·575 − 0	9·964 − 0
2	6	6·762 − 2	5·616 − 2	4·510 − 2	3·551 − 2	2·768 − 2	2·144 − 2	1·881 − 2	1·435 − 2	1·246 − 2	1·077 − 2	9·253 − 3
2	7	3·681 − 0	3·722 − 0	3·867 − 0	4·101 − 0	4·398 − 0	4·746 − 0	4·951 − 0	5·577 − 0	6·133 − 0	6·971 − 0	8·151 − 0
2	8	3·967 − 2	3·527 − 2	2·947 − 2	2·361 − 2	1·845 − 2	1·422 − 2	1·242 − 2	9·386 − 3	8·111 − 3	6·974 − 3	5·965 − 3
2	9	1·010 − 2	8·351 − 3	6·782 − 3	5·466 − 3	4·391 − 3	3·510 − 3	3·127 − 3	2·455 − 3	2·160 − 3	1·891 − 3	1·647 − 3
2	10	2·286 − 1	2·248 − 1	2·233 − 1	2·256 − 1	2·341 − 1	2·496 − 1	2·591 − 1	2·745 − 1	2·759 − 1	2·705 − 1	2·581 − 1
2	11	4·867 − 1	4·893 − 1	4·931 − 1	4·973 − 1	5·019 − 1	5·066 − 1	5·086 − 1	5·068 − 1	4·993 − 1	4·845 − 1	4·613 − 1
2	12	2·363 − 2	2·283 − 2	2·180 − 2	2·043 − 2	1·866 − 2	1·649 − 2	1·529 − 2	1·272 − 2	1·140 − 2	1·008 − 2	8·799 − 3
2	13	3·373 − 1	3·398 − 1	3·425 − 1	3·452 − 1	3·479 − 1	3·509 − 1	3·523 − 1	3·529 − 1	3·502 − 1	3·441 − 1	3·338 − 1
2	14	1·677 − 2	1·621 − 2	1·547 − 2	1·449 − 2	1·323 − 2	1·171 − 2	1·091 − 2	9·588 − 3	9·386 − 3	9·776 − 3	1·094 − 2
2	15	1·052 − 2	1·023 − 2	9·818 − 3	9·237 − 3	8·462 − 3	7·497 − 3	6·955 − 3	5·792 − 3	5·191 − 3	4·593 − 3	4·010 − 3

3	4	2·688 − 2	2·154 − 2	1·652 − 2	1·231 − 2	9·024 − 3	6·567 − 3	5·593 − 3	4·041 − 3	3·425 − 3	2·895 − 3	2·438 − 3
3	5	8·201 − 2	6·879 − 2	5·513 − 2	4·290 − 2	3·288 − 2	2·500 − 2	2·174 − 2	1·630 − 2	1·402 − 2	1·200 − 2	1·019 − 2
3	6	1·876 − 0	1·905 − 0	2·016 − 0	2·191 − 0	2·401 − 0	2·630 − 0	2·749 − 0	2·994 − 0	3·116 − 0	3·235 − 0	3·343 − 0
3	7	3·809 − 2	3·343 − 2	2·774 − 2	2·216 − 2	1·733 − 2	1·338 − 2	1·171 − 2	8·876 − 3	7·683 − 3	6·617 − 3	5·668 − 3
3	8	1·197 − 0	1·203 − 0	1·249 − 0	1·329 − 0	1·431 − 0	1·549 − 0	1·613 − 0	1·755 − 0	1·835 − 0	1·923 − 0	2·019 − 0
3	9	4·572 − 1	4·540 − 1	4·587 − 1	4·706 − 1	4·896 − 1	5·163 − 1	5·328 − 1	5·743 − 1	6·006 − 1	6·318 − 1	6·679 − 1
3	10	1·429 − 2	1·271 − 2	1·138 − 2	1·018 − 2	8·993 − 3	7·772 − 3	7·155 − 3	5·923 − 3	5·313 − 3	4·710 − 3	4·125 − 3
3	11	2·875 − 2	2·631 − 2	2·411 − 2	2·194 − 2	1·962 − 2	1·709 − 2	1·576 − 2	1·299 − 2	1·160 − 2	1·022 − 2	8·891 − 3
3	12	1·455 − 1	1·477 − 1	1·500 − 1	1·524 − 1	1·550 − 1	1·579 − 1	1·595 − 1	1·631 − 1	1·651 − 1	1·672 − 1	1·694 − 1
3	13	1·603 − 2	1·549 − 2	1·480 − 2	1·388 − 2	1·271 − 2	1·129 − 2	1·049 − 2	8·783 − 3	7·889 − 3	6·993 − 3	6·115 − 3
3	14	1·063 − 1	1·060 − 1	1·060 − 1	1·063 − 1	1·071 − 1	1·084 − 1	1·091 − 1	1·102 − 1	1·100 − 1	1·091 − 1	1·070 − 1
3	15	6·783 − 2	6·822 − 2	6·886 − 2	6·975 − 2	7·090 − 2	7·236 − 2	7·313 − 2	7·385 − 2	7·313 − 2	7·121 − 2	6·795 − 2
4	5	2·826 − 1	2·606 − 1	2·391 − 1	2·200 − 1	2·038 − 1	1·906 − 1	1·863 − 1	1·904 − 1	2·042 − 1	2·290 − 1	2·649 − 1
4	6	4·033 − 2	3·311 − 2	2·618 − 2	2·036 − 2	1·582 − 2	1·238 − 2	1·099 − 2	8·685 − 3	7·704 − 3	6·800 − 3	5·956 − 3
4	7	2·639 − 1	2·153 − 1	1·650 − 1	1·216 − 1	8·794 − 2	6·385 − 2	5·649 − 2	6·403 − 2	8·949 − 2	1·375 − 1	2·115 − 1
4	8	2·172 − 2	1·735 − 2	1·322 − 2	9·837 − 3	7·277 − 3	5·407 − 3	4·675 − 3	3·509 − 3	3·036 − 3	2·618 − 3	2·245 − 3
4	9	7·945 − 3	7·066 − 3	6·308 − 3	5·650 − 3	5·056 − 3	4·519 − 3	4·326 − 3	4·649 − 3	5·625 − 3	7·503 − 3	1·044 − 2
4	10	1·620 − 0	1·703 − 0	1·792 − 0	1·890 − 0	1·999 − 0	2·122 − 0	2·192 − 0	2·346 − 0	2·431 − 0	2·519 − 0	2·609 − 0
4	11	3·384 − 2	3·344 − 2	3·296 − 2	3·239 − 2	3·173 − 2	3·108 − 2	3·078 − 2	3·009 − 2	2·951 − 2	2·861 − 2	2·731 − 2
4	12	9·163 − 3	8·856 − 3	8·434 − 3	7·867 − 3	7·140 − 3	6·266 − 3	5·788 − 3	4·785 − 3	4·276 − 3	3·775 − 3	3·290 − 3
4	13	7·582 − 3	7·250 − 3	6·820 − 3	6·276 − 3	5·621 − 3	4·869 − 3	4·470 − 3	3·679 − 3	3·314 − 3	2·984 − 3	2·696 − 3
4	14	2·746 − 3	2·583 − 3	2·387 − 3	2·153 − 3	1·878 − 3	1·574 − 3	1·424 − 3	1·200 − 3	1·177 − 3	1·261 − 3	1·480 − 3
4	15	7·709 − 3	7·468 − 3	7·127 − 3	6·655 − 3	6·042 − 3	5·304 − 3	4·901 − 3	4·060 − 3	3·632 − 3	3·210 − 3	2·801 − 3
5	6	2·265 − 1	1·940 − 1	1·618 − 1	1·332 − 1	1·094 − 1	8·991 − 2	8·172 − 2	6·902 − 2	6·496 − 2	6·268 − 2	6·213 − 2
5	7	1·633 − 0	1·505 − 0	1·347 − 0	1·192 − 0	1·061 − 0	9·604 − 1	9·270 − 1	9·428 − 1	1·031 − 0	1·202 − 0	1·469 − 0
5	8	1·614 − 1	1·454 − 1	1·256 − 1	1·059 − 1	8·843 − 2	7·340 − 2	6·682 − 2	5·577 − 2	5·145 − 2	4·794 − 2	4·518 − 2
5	9	2·127 − 2	1·776 − 2	1·473 − 2	1·227 − 2	1·032 − 2	8·745 − 3	8·051 − 3	6·747 − 3	6·105 − 3	5·461 − 3	4·822 − 3
5	10	1·343 − 1	1·214 − 1	1·122 − 1	1·058 − 1	1·014 − 1	9·884 − 2	9·835 − 2	9·974 − 2	1·020 − 1	1·054 − 1	1·097 − 1
5	11	6·830 − 0	7·357 − 0	7·886 − 0	8·412 − 0	8·954 − 0	9·528 − 0	9·804 − 0	1·012 + 01	1·004 + 01	9·733 − 0	9·205 − 0
5	12	5·152 − 2	4·954 − 2	4·701 − 2	4·374 − 2	3·964 − 2	3·478 − 2	3·214 − 2	2·657 − 2	2·374 − 2	2·094 − 2	1·823 − 2
5	13	1·507 − 0	1·556 − 0	1·609 − 0	1·670 − 0	1·742 − 0	1·832 − 0	1·885 − 0	2·006 − 0	2·074 − 0	2·146 − 0	2·218 − 0
5	14	2·754 − 2	2·647 − 2	2·507 − 2	2·327 − 2	2·101 − 2	1·835 − 2	1·692 − 2	1·394 − 2	1·245 − 2	1·098 − 2	9·577 − 3
5	15	1·699 − 2	1·645 − 2	1·568 − 2	1·460 − 2	1·319 − 2	1·149 − 2	1·058 − 2	8·704 − 3	7·766 − 3	6·846 − 3	5·961 − 3

(*Continued*)

Table 7. (*Continued*)

Transition		Temperature (log K)										
i	*f*	5·40	5·60	5·80	6·00	6·20	6·40	6·50	6·70	6·80	6·90	7·00
6	7	1·704 − 1	1·514 − 1	1·296 − 1	1·086 − 1	9·011 − 2	7·438 − 2	6·760 − 2	5·707 − 2	5·403 − 2	5·301 − 2	5·420 − 2
6	8	5·065 − 1	4·595 − 1	4·081 − 1	3·614 − 1	3·236 − 1	2·951 − 1	2·837 − 1	2·639 − 1	2·534 − 1	2·410 − 1	2·258 − 1
6	9	5·190 − 2	4·932 − 2	4·730 − 2	4·579 − 2	4·469 − 2	4·387 − 2	4·344 − 2	4·182 − 2	4·025 − 2	3·804 − 2	3·520 − 2
6	10	3·176 − 2	2·631 − 2	2·212 − 2	1·879 − 2	1·595 − 2	1·337 − 2	1·214 − 2	9·778 − 3	8·654 − 3	7·579 − 3	6·564 − 3
6	11	6·930 − 2	6·094 − 2	5·420 − 2	4·815 − 2	4·220 − 2	3·608 − 2	3·297 − 2	2·677 − 2	2·373 − 2	2·080 − 2	1·801 − 2
6	12	2·328 − 0	2·492 − 0	2·655 − 0	2·819 − 0	2·994 − 0	3·187 − 0	3·294 − 0	3·527 − 0	3·652 − 0	3·778 − 0	3·898 − 0
6	13	2·699 − 2	2·608 − 2	2·482 − 2	2·312 − 2	2·094 − 2	1·833 − 2	1·691 − 2	1·394 − 2	1·244 − 2	1·097 − 2	9·559 − 3
6	14	4·883 − 1	5·064 − 1	5·265 − 1	5·493 − 1	5·767 − 1	6·100 − 1	6·289 − 1	6·688 − 1	6·871 − 1	7·014 − 1	7·094 − 1
6	15	1·567 − 2	1·577 − 2	1·595 − 2	1·622 − 2	1·664 − 2	1·727 − 2	1·767 − 2	1·872 − 2	1·940 − 2	2·022 − 2	2·117 − 2
7	8	2·674 − 1	2·280 − 1	1·818 − 1	1·384 − 1	1·027 − 1	7·552 − 2	6·490 − 2	4·920 − 2	4·419 − 2	4·119 − 2	4·017 − 2
7	9	4·893 − 3	4·228 − 3	3·655 − 3	3·181 − 3	2·783 − 3	2·431 − 3	2·263 − 3	1·928 − 3	1·754 − 3	1·577 − 3	1·397 − 3
7	10	1·288 − 0	1·361 − 0	1·442 − 0	1·528 − 0	1·622 − 0	1·728 − 0	1·787 − 0	1·918 − 0	1·989 − 0	2·061 − 0	2·130 − 0
7	11	1·224 − 1	1·090 − 1	9·891 − 2	9·115 − 2	8·491 − 2	7·990 − 2	7·807 − 2	7·714 − 2	7·885 − 2	8·238 − 2	8·765 − 2
7	12	2·106 − 2	1·989 − 2	1·865 − 2	1·719 − 2	1·545 − 2	1·346 − 2	1·238 − 2	1·017 − 2	9·066 − 3	7·981 − 3	6·939 − 3
7	13	4·115 − 0	4·326 − 0	4·546 − 0	4·777 − 0	5·031 − 0	5·322 − 0	5·485 − 0	5·837 − 0	6·014 − 0	6·181 − 0	6·322 − 0
7	14	2·782 − 2	2·690 − 2	2·562 − 2	2·390 − 2	2·166 − 2	1·898 − 2	1·752 − 2	1·447 − 2	1·294 − 2	1·144 − 2	9·984 − 3
7	15	9·355 − 3	9·042 − 3	8·596 − 3	7·982 − 3	7·190 − 3	6·251 − 3	5·746 − 3	4·708 − 3	4·189 − 3	3·682 − 3	3·196 − 3
8	9	3·014 − 1	2·080 − 1	1·402 − 1	9·287 − 2	6·085 − 2	3·962 − 2	3·193 − 2	2·073 − 2	1·669 − 2	1·343 − 2	1·080 − 2
8	10	1·450 − 2	1·243 − 2	1·070 − 2	9·232 − 3	7·905 − 3	6·652 − 3	6·043 − 3	4·861 − 3	4·295 − 3	3·754 − 3	3·245 − 3
8	11	3·341 − 2	2·861 − 2	2·461 − 2	2·120 − 2	1·816 − 2	1·531 − 2	1·392 − 2	1·124 − 2	9·947 − 3	8·702 − 3	7·524 − 3
8	12	1·659 − 2	1·595 − 2	1·559 − 2	1·546 − 2	1·554 − 2	1·583 − 2	1·606 − 2	1·665 − 2	1·697 − 2	1·725 − 2	1·747 − 2
8	13	2·926 − 2	2·785 − 2	2·620 − 2	2·423 − 2	2·187 − 2	1·915 − 2	1·767 − 2	1·459 − 2	1·302 − 2	1·147 − 2	9·983 − 3
8	14	1·357 − 0	1·425 − 0	1·498 − 0	1·575 − 0	1·662 − 0	1·763 − 0	1·823 − 0	2·005 − 0	2·157 − 0	2·375 − 0	2·670 − 0
8	15	4·920 − 1	4·979 − 1	5·067 − 1	5·197 − 1	5·388 − 1	5·654 − 1	5·814 − 1	6·137 − 1	6·248 − 1	6·278 − 1	6·194 − 1

9	10	1·026 − 2	9·413 − 3	8·564 − 3	7·696 − 3	6·777 − 3	5·808 − 3	5·315 − 3	4·337 − 3	3·859 − 3	3·394 − 3	2·950 − 3
9	11	1·594 − 2	1·391 − 2	1·204 − 2	1·036 − 2	8·813 − 3	7·359 − 3	6·667 − 3	5·355 − 3	4·736 − 3	4·146 − 3	3·590 − 3
9	12	6·437 − 3	6·329 − 3	6·298 − 3	6·361 − 3	6·531 − 3	6·821 − 3	7·011 − 3	7·473 − 3	7·738 − 3	8·015 − 3	8·293 − 3
9	13	3·709 − 3	3·311 − 3	2·931 − 3	2·565 − 3	2·199 − 3	1·833 − 3	1·654 − 3	1·310 − 3	1·149 − 3	9·978 − 4	8·569 − 4
9	14	5·758 − 3	4·516 − 3	3·445 − 3	2·604 − 3	1·966 − 3	1·487 − 3	1·294 − 3	9·990 − 4	9·073 − 4	8·654 − 4	8·814 − 4
9	15	6·058 − 1	6·154 − 1	6·311 − 1	6·534 − 1	6·829 − 1	7·200 − 1	7·427 − 1	8·080 − 1	8·610 − 1	9·367 − 1	1·040 − 0
10	11	2·145 − 1	2·046 − 1	1·942 − 1	1·825 − 1	1·694 − 1	1·637 − 1	1·855 − 1	4·650 − 1	8·727 − 1	1·580 − 0	2·648 − 0
10	12	7·116 − 2	6·893 − 2	6·591 − 2	6·192 − 2	5·685 − 2	5·081 − 2	4·755 − 2	4·109 − 2	3·816 − 2	3·557 − 2	3·336 − 2
10	13	2·897 − 1	2·862 − 1	2·803 − 1	2·714 − 1	2·594 − 1	2·455 − 1	2·388 − 1	2·298 − 1	2·288 − 1	2·303 − 1	2·339 − 1
10	14	3·335 − 2	3·212 − 2	3·046 − 2	2·832 − 2	2·567 − 2	2·264 − 2	2·105 − 2	1·787 − 2	1·631 − 2	1·474 − 2	1·317 − 2
10	15	3·613 − 2	3·500 − 2	3·343 − 2	3·136 − 2	2·877 − 2	2·576 − 2	2·418 − 2	2·130 − 2	2·025 − 2	1·961 − 2	1·943 − 2
11	12	2·043 − 1	1·978 − 1	1·889 − 1	1·771 − 1	1·624 − 1	1·448 − 1	1·353 − 1	1·168 − 1	1·087 − 1	1·019 − 1	9·673 − 2
11	13	6·518 − 1	6·457 − 1	6·365 − 1	6·237 − 1	6·081 − 1	5·906 − 1	5·824 − 1	5·743 − 1	5·783 − 1	5·894 − 1	6·073 − 1
11	14	1·437 − 1	1·393 − 1	1·333 − 1	1·253 − 1	1·151 − 1	1·027 − 1	9·592 − 2	8·179 − 2	7·485 − 2	6·829 − 2	6·227 − 2
11	15	6·939 − 2	6·743 − 2	6·465 − 2	6·085 − 2	5·596 − 2	5·005 − 2	4·679 − 2	3·989 − 2	3·634 − 2	3·279 − 2	2·927 − 2
12	13	1·430 − 1	1·390 − 1	1·334 − 1	1·256 − 1	1·156 − 1	1·034 − 1	9·660 − 2	8·219 − 2	7·491 − 2	6·781 − 2	6·103 − 2
12	14	1·477 − 1	1·481 − 1	1·481 − 1	1·477 − 1	1·469 − 1	1·462 − 1	1·459 − 1	1·452 − 1	1·442 − 1	1·423 − 1	1·390 − 1
12	15	1·011 − 2	9·976 − 3	9·811 − 3	9·624 − 3	9·450 − 3	9·371 − 3	9·406 − 3	9·745 − 3	1·010 − 2	1·060 − 2	1·122 − 2
13	14	1·417 − 1	1·377 − 1	1·320 − 1	1·243 − 1	1·146 − 1	1·028 − 1	9·624 − 2	8·193 − 2	7·433 − 2	6·658 − 2	5·883 − 2
13	15	3·357 − 2	3·244 − 2	3·087 − 2	2·879 − 2	2·621 − 2	2·318 − 2	2·155 − 2	1·817 − 2	1·648 − 2	1·483 − 2	1·323 − 2
14	15	5·855 − 2	5·823 − 2	5·784 − 2	5·732 − 2	5·668 − 2	5·600 − 2	5·567 − 2	5·507 − 2	5·482 − 2	5·461 − 2	5·439 − 2

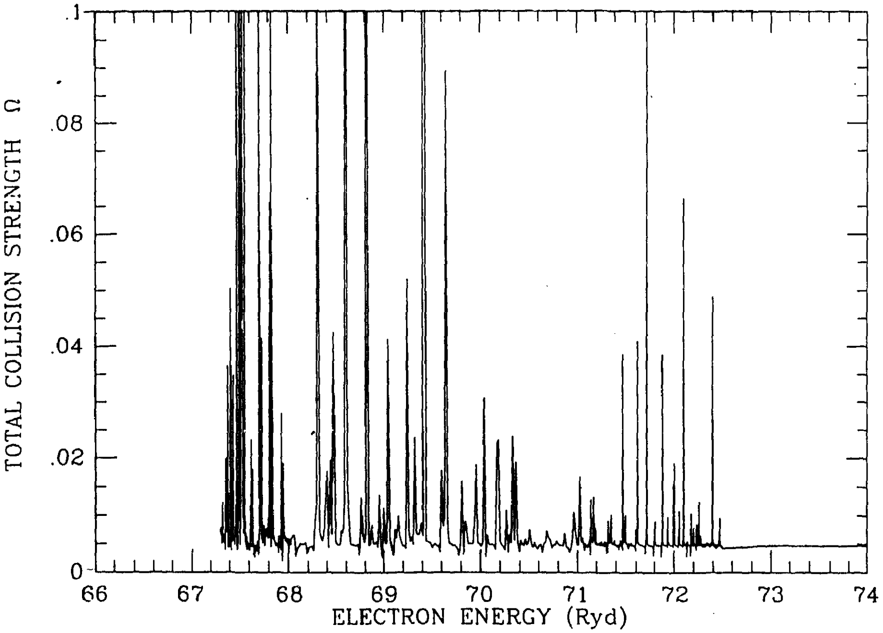

Figure 2. Total collision strength for the transition $1s^2 2s^2 2p^6\,{}^1S^e \rightarrow 1s^2 2s^2 2p^5 3s\,{}^1P^0$ in Ni XIX as a function of electron energy in Rydberg.

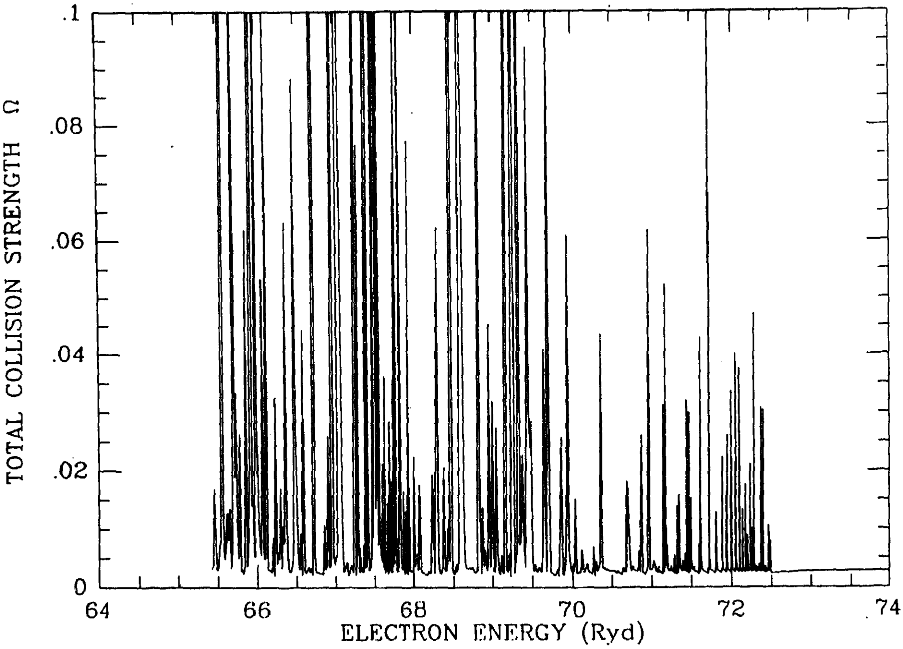

Figure 3. Total collision strength for the transition $1s^2 2s^2 2p^6\,{}^1S^e \rightarrow 1s^2 2s^2 2p^5 3p\,{}^3S^e$ in Ni XIX as a function of electron energy in Rydberg.

collision strengths γ are larger for allowed transitions than for spin-forbidden transitions. Among the $2p^6\,{}^1S^e \rightarrow 2p^5 3p$ transitions, the value of γ is largest for the monopole-allowed $2p^6\,{}^1S^e$–$2p^5 3p\,{}^1S^e$ transition, as already found by Zhang *et al* [18, 20]. In contrast, for the $2p^6\,{}^1S^e - 2p^5 3d$ transitions, the largest γ corresponds to the dipole-allowed $2p^6\,{}^1S^e - 2p^5 3d\,{}^1P^0$ transition, which involves the promotion of a $2p$ electron to a $3d$ orbital. Similarly, for the transitions from $2p^5 3s\,{}^3P^0$, the largest γ corresponds to the dipole-allowed $2p^5 3s\,{}^3P^0 - 2p^5 3d\,{}^2D^e$ transition. Among all the 105 transitions, the value of γ is the largest for the $2p^5 3p\,{}^3D^e \rightarrow 2p^5 3d\,{}^3F^0$ transition, which is again dipole-allowed and involves the promotion of a $3p$ electron to a $3d$ orbital. The next largest γ corresponds to the $2p^5 3p\,{}^3P^e \rightarrow 2p^5 3d\,{}^3D^0$ transition.

Since the ground state $2p^6\,{}^1S^e$ and the singlet excited states $2p^5 3s\,{}^1P^0$, $2p^5 3p\,{}^1D^e$, ${}^1P^e$, ${}^1S^e$ and $2p^5 3d\,{}^1F^0$, ${}^1D^0$, ${}^1P^0$ states have no fine structure, if one assumes the term mixing to be negligible, one can easily deduce the effective collision strengths for the transitions between their fine structure sublevels, from our results in the *LS* coupling scheme using the following relation:

$$\frac{1}{2J+1}\gamma({}^1L_L^{\pi} - {}^3L_J'^{\pi'}) = \frac{1}{3(2L'+1)}\gamma({}^1L^{\pi} - {}^3L'^{\pi'}). \tag{9}$$

5. Conclusion

The conclude, we would like to mention that, to date, our results are the only collision strengths and rate coefficients available for all the 105 transitions between the ground and the $n = 3$ Rydberg states of Ni XIX, where the influence of resonance effects is included. We have accounted for exchange, channel coupling, short range correlation effects and the contribution of higher partial waves. On the other hand, we have made no allowance for relativistic effects, either in the target wave-functions or in the scattering calculations.

Acknowledgements

We would like to thank the Indo-French Centre for the Promotion of Advanced Research/Centre Franco-Indien pour la Promotion de la Recherche Avancée and the EC contract SCI-0168C for financial support. One of us (MM) is thankful to DST (India), UGC (India) and SERC (UK) for financial support. (MM an IUCAA associate) is also thankful to Inter University Centre for Astronomy and Astrophysics (IUCAA) for facilities and financial support. The computing in this work was carried out on the CRAY-XMP/48 at the Rutherford Appleton Laboratory, UK, via a workstation at the Queen's University of Belfast. The allocation of computer time under a SERC Rolling Grant is gratefully acknowledged.

References

[1] R K Janev, *Phys. Scr.* **T37**, 5–7 (1991)
[2] D L Matthews, *et al*, *Phys. Rev. Lett.* **54**, 110–113 (1985)
[3] U Feldman, L Cohen and M Swartz, *Astrophys. J.* **148**, 585 (1967)
[4] M Swartz, S Kastner, E Rothe and W Neupert *J. Phys.* **4**, 1747 (1971)
[5] A K Bhatia, U Feldman and J F Seely, *At. Data Nucl. Data Tables* **32**, 435–467 (1985)
[6] P L Hagelstein and R K Jung, *At. Data Nucl. Data Tables* **37**, 64–121 (1987)
[7] P G Burke and W D Robb, *Adv. At. Mol. Phys.* **11**, 143–214 (1975)

[8] K A Berrington, P G Burke, M Le Dourneuf, W D Robb, K T Taylor and L Vo Ky, *Comput. Phys. Commun.* **14**, 367 (1978)

[9] K A Berrington, P G Burke, K Butler, M J Seaton, P J Storey, K T Taylor and Y Yu, *J. Phys.* **B20**, 6379 (1987)

[10] V M Burke, P G Burke and N S Scott, *Comput. Phys. Commun.*, in press (1991)

[11] A Burgess, D G Hummer and J A Tully, *Proc. Trans. R. Soc.* **A266**, 225 (1970)

[12] A Hibbert, *Comput. Phys. Commun.* **9**, 141–172 (1975)

[13] A Hibbert, M Le Dourneuf and M Mohan (to be published) (1991)

[14] E Clementi and C Roetti, *At. Data Nucl. Data Tables* **14**, 177–478 (1974)

[15] C Corliss and J Sugar, *J. Phys. Chem. Ref. Data* **10**, 278 (1981)

[16] P G Burke, K A Berrington and C V Sukumar, *J. Phys.* **B14**, 287 (1981)

[17] M J Seaton, *J. Phys.* **B18**, 2111–31 (1985)

[18] H Zhang and D H Sampson, *At. Data Nucl. Data Tables* **43**, 1–69 (1989)

[19] W Eissner and M J Seaton, *J. Phys.* **B7**, 2533–2548 (1974)

[20] H Zhang, D H Sampson, R E M Clark and J B Mann, *At. Data Nucl. Data Tables* **37**, 17–40 (1987)

PRAMANA
— journal of
physics

© Printed in India

Vol. 41, No. 4,
October 1993
pp. 389–399

Dynamics of immiscible radial viscous fingering: A numerical study

SUBIR K SARKAR and DAVID JASNOW*
School of Physical Sciences, Jawaharlal Nehru University, New Delhi 110 067, India
*Department of Physics and Astronomy, University of Pittsburgh, Pittsburgh, PA 15260, USA

MS received 17 May 1993; revised 12 August 1993

Abstract. In this paper we undertake a numerical investigation of the dynamics of the interface in the problem of immiscible radial viscous fingering in a Hele–Shaw cell when the areal flow rate is maintained constant. Comparison is made with experimental results to check if there is a need to introduce velocity-dependent boundary conditions and to incorporate the effect of thickness of the film left behind by the moving interface. Some new scaling results are suggested by the numerical data. These data, along with those available from laboratory experiments, provide support for a mean field theory for radial immiscible viscous fingering published recently [*Phys. Rev. Lett.* **65**, 2680 (1990)].

Keywords. Viscous fingering; Fractals; Hele–Shaw flow.

PACS Nos 47·10; 68·10; 47·20; 81·30

1. Introduction

Viscous fingering in Hele–Shaw cells has served as a prototype of nonlocal interfacial pattern formation in systems far from equilibrium [1–6]. An important reason for this is that the equations of motion and the boundary conditions governing the dynamics of the interface as well as the conditions under which they are valid are known without any substantial ambiguity [3, 6]. The material parameters of the problem can be determined very accurately. Not all of these statements are applicable to the other two problems that have been studied rather extensively, namely free dendritic growth and directional solidification [7–9]. For this reason viscous fingering affords us an ideal system for quantitative tests of the various theoretical ideas that have been proposed. In particular, in the context of steady state pattern selection, it has provided a rather convenient testing ground for an accurate verification of the scenario of 'microscopic solvability' as the underlying mechanism [10, 11]. In contrast to the case of the rectangular geometry, much less progress has been made for fingering phenomena in the radial geometry [4, 5]. Here the steady state phenomena are replaced, in the simplest case, by a tip splitting cascade—leading to the generation of fractals; the problem is to understand the relationship between the structure and the dynamics [12, 13]. This problem has a lot of formal similarity with the diffusion-limited-aggregation (DLA) model proposed by Witten and Sander [14–16]. However, this relationship breaks down if the two fluids involved in the displacement process are immiscible. This is precisely the regime that we are interested in. Carefully controlled experiments on immiscible radial viscous fingering phenomena have been performed [5] and the present work is an effort to complement and analyze the experimental data.

The goals of the present work are: (i) To study the dynamics on a computer and in the process satisfy ourselves that the dynamical equations employed do indeed provide a complete description of the observed data. In particular we have in mind whether velocity-dependent boundary conditions and allowing for finite film thickness are crucial [6, 10, 11]. This is important since any analytical work will be based upon these equations, and it is essential to establish their adequacy. (ii) To collect data that are not available from the experiments and (iii) to discover possible new aspects of the problem with special reference to scaling properties. Part (i) is qualitative to some extent since one can only detect qualitative deviations from those laboratory data which are not characterized in a precise quantitative manner. The organization of this paper is as follows: In § 2 we review the equations of motion of the interface. The field equations as well as the boundary integral version are given. Section 3 describes the numerical results in detail and § 4 contains the conclusions of this work. Here we should note that extensions have been made on the code used here to generate data on the domain of growth substantially beyond what is reported here. It seems that there is a crossover in some scaling properties as one goes beyond the 'intermediate' domain that we deal with here [17]. In this paper we limit ourselves to the task of presenting the numerical data in this intermediate time domain. This and ref. [5] provide the basis for a mean field theory of scaling in immiscible radial viscous fingering—a summary of which has already been published [13].

2. Equations of motion

In a radial Hele–Shaw viscous fingering experiment a fluid of lower viscosity drives out a liquid of higher viscosity—the first fluid being injected at the center of the cell. The cell is made up of a pair of thick and transparent circular plates, one placed on top of the other with a small gap. The plates are very smooth and the placement must be such that the spacing between the plates is constant to a very high degree (1% or better). For reasons to be explained below, we shall deal with a situation in which the displacing fluid is a gas. Also we choose the displaced liquid to be one that wets the cell. The experiment can be most simply performed under two kinds of operating conditions: (1) The displacing fluid is injected at a constant pressure and (2) the areal rate of the displacement of the liquid is constant. As in ref. [5] we choose the second condition since it offers some very definite advantages which will be noted below. Figure 1 is a schematic representation of the experimental arrangement to which the following equations refer.

The relationship between the fluid velocity **u**, averaged over the direction transverse to the plates, and the pressure field (which does not vary in the transverse direction) is given by:

$$\mathbf{u} = -(b^2/12\mu)\nabla p \tag{1}$$

Here p is the pressure in the fluid and is a function of the x and y coordinates, the axes being in the plane of the plates; μ is the viscosity of the fluid and b is the spacing between the plates. Since we choose the displacing fluid to be a gas, μ is very small and it follows from (1) that the pressure is uniform within the gas, although it could be a function of time. Next, since the displaced liquid is incompressible, $\nabla\cdot\mathbf{u} = 0$,

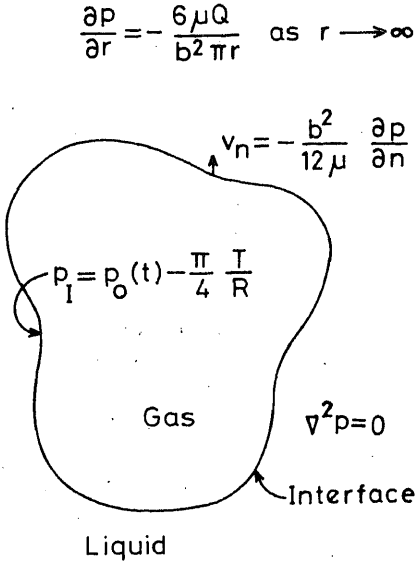
$\frac{\partial p}{\partial r} = -\frac{6\mu Q}{b^2 \pi r}$ as $r \longrightarrow \infty$
$v_n = -\frac{b^2}{12\mu}\frac{\partial p}{\partial n}$
$p_I = p_o(t) - \frac{\pi}{4}\frac{T}{R}$
Gas
$\nabla^2 p = 0$
Interface
Liquid

Figure 1. Schematic diagram of the experimental arrangement and the equations of motion.

which leads to the field equation for the pressure:

$$\nabla^2 p = 0. \tag{2}$$

During the motion of the interface, the liquid is not completely displaced by the gas even if the liquid wets the cell. For values of the normal velocity of the interface not too large, the thickness (t) of the liquid layer left behind on each of the plates is given by

$$t = 0{\cdot}67b(\mu v_n/T)^{2/3}. \tag{3}$$

v_n,the normal velocity of the interface, is related to the normal velocity (u_n) of the liquid immediately ahead by

$$u_n = v_n(1 - 2t/b). \tag{4}$$

Equation (1) gives the instantaneous normal velocity of the interface once the pressure field is determined. But for this one needs to know the boundary conditions in addition to the field equation (2). The far field boundary condition is determined from the fact that the velocity field is radially outward and is independent of the angular position. Combining this with the fact that the flux is constant, one can determine the pressure gradient from (1). Hence at large distances

$$\mathrm{d}p/\mathrm{d}r = -(6\mu Q/b^2 \pi r), \tag{5}$$

where Q is the areal displacement rate. On the liquid side of the interface, the pressure (p_l) is given by the Park–Homsy equation [6]:

$$p_l = p_0(t) - [(\pi T/4R) + 7{\cdot}6(T/b)(\mu v_n/T)^{2/3}]. \tag{6}$$

This equation is valid when ($\mu v_n/T$) is much less than unity and the liquid wets the cell. Here $p_0\,(t)$ is the uniform pressure within the gas, R is the radius of curvature of the interface in the plane of the plates and T is the surface tension between the two fluids. Unfortunately, in (3), (4) and (6) one has to deal with nonlinear terms which would make numerical computation of the dynamics even more extensive. For this reason, we assume that the velocity-dependent terms in the boundary condition and the finiteness of the film left behind can be ignored; in this work we have set $t=0$ and $u_n = v_n$. In the constant-flux operating mode the maximum interfacial velocity decreases as the structure grows so that the velocity-dependent correction decreases in absolute terms. But given the fact that the deviation from the constant pressure condition on the interface is small anyway compared to the viscous pressure drop and that small terms are known to affect long-term dynamics in these problems, one cannot be sure, a priori, about the validity of this approximation. In fact, by way of comparison with experimental data, we want to check that ignoring the velocity-dependent correction does not at least introduce qualitative changes. One more advantage of having constant flux and ignoring velocity-dependent terms as well as film thickness is that the dynamics can be made entirely dimensionless by choosing appropriate units for pressure, length and time [18]. So the description becomes completely independent of material parameters and is thus applicable to any liquid-gas pair.

Since we are interested in the dynamics of the interface and not in the pressure field everywhere, a convenient way to do the numerical calculation is provided by an equation which involves only the interfacial degrees of freedom. In the dimensionless units mentioned above, this equation is [19]:

$$-(1/2R(s)) = \int_{\text{Interface}} [G(s,s')v_n(s') - (1/R(s'))\nabla' G\cdot \mathbf{n}(s')]\,\mathrm{d}s' + C_0(t). \tag{7}$$

The dynamics are described in terms of a function $\Theta(s)$ which is the tangent angle as a function of the arclength parameter (s). G is the Green's function given by $G(s, s') = -(1/2\pi)\ln|\mathbf{r}(s)-\mathbf{r}(s')|$, $\mathbf{r}(s)$ being the two-dimensional position vector for the interfacial point with the arclength coordinate s. $C_0(t)$ depends on time only and is found as a part of the solution. $\mathbf{n}(s')$ is the unit normal vector directed into the displaced fluid at the point s'. The flux conservation equation is given by

$$\int_{\text{Interface}} v_n(s)\,\mathrm{d}s = 2\pi \tag{8}$$

The constant $C_0(t)$ has its origin in the boundary condition on the pressure field at infinity and its instantaneous value can be determined by combining (7) and (8). Once the normal velocities are found from (7) and (8), the change in the interface follows from geometrical considerations. The time evolution of $\Theta(s)$ is calculated from the equation

$$\mathrm{d}\Theta(\alpha)/\mathrm{d}t = -(1/S_T)(\partial v_n/\partial\alpha) - (S_T/R(\alpha))[g(\alpha) - \alpha g(1)], \tag{9}$$

where $\alpha = s/S_T$, S_T being the instantaneous total length of the interface. Thus $0 \leqq s \leqq S_T$. $g(\alpha)$ is defined by

$$g(\alpha) = \int_0^\alpha [v_n(\alpha')/R(\alpha')]\,\mathrm{d}\alpha'. \tag{10}$$

The time dependence of S_T is given by

$$dS_T/dt = S_T g(1). \tag{11}$$

A numerical scheme for solving this type of integro-differential equations has been described elsewhere [19].

3. Results

Before comparing the numerical results directly with the experimental data, it is important to remember certain aspects of the code we use. For a sinusoidal perturbation of m-fold symmetry, the initially circular interface becomes unstable when the radius of the circle exceeds some critical value r_m. In an experiment the initial deformation is typically of five bulges, but they are certainly not fully symmetric. The source of this perturbation presumably is the nonuniformity of the spacing between the plates (which is always present and cannot be controlled beyond a certain limit). In the numerical scheme there is no such noise except for what is inherent to any such code and in the initial deformation of the interface with four-fold symmetry. Ideally one would like to start with a radius near r_4. Unfortunately we have to take an initial radius several times this value. The reason being that the interface is discretized into N_G points equally spaced in arclength. In order to maintain a proper level of resolution N_G is dynamically increased as the structure grows. However, for a given choice of the dimensionless growth step ε (defined as the maximum value of the ratio of the local normal interface displacement to the local radius of curvature in one step of integration) and for a given value of S_T, N_G cannot be increased beyond a limit without introducing numerical instabilities. At the same time, if the value of N_G is lower than about 100 (even for a near circular interface) the resolution is unacceptable. The only way to satisfy all these constraints is to start with a radius which is substantially higher than r_4. We always start with a total arclength of 1900 and a small four-fold symmetric perturbation so that $\Theta(\alpha)$ is of the form

$$\Theta(\alpha) = 2\pi\alpha + \beta \sin(8\pi\alpha), \tag{12}$$

with $\beta = 0{\cdot}05$. But, as we have mentioned already, the radius is much higher than r_4 so that we are starting with a small perturbation in a domain where the interface is well into the region of instability. Clearly, this fails to mimic the 'real life' growth at early times. However, at later times this may become immaterial. In particular, we hope that it does not influence the scaling aspects of the dynamics. Our final remark is concerned with the numerical detection of the existence of scaling itself. A basic criterion for this is that the data should span a sufficiently wide range of scales. In our simulations the range of the data available before numerical errors become unacceptable is essentially the same as in with the data the laboratory setup of ref. [5]. For some pairs of variables this range provides convincing evidence of scaling. But for some others it is not so satisfactory and our search for scaling has been guided partially by the mean field theory that has been developed [13].

3.1 *Fractal geometry and fractal dimension*

Sander *et al* [20] have also performed numerical integration on the same problem, but with the difference that in their work the pressure was maintained constant inside the driving fluid. In contrast we maintain a constant flux condition. Except for the

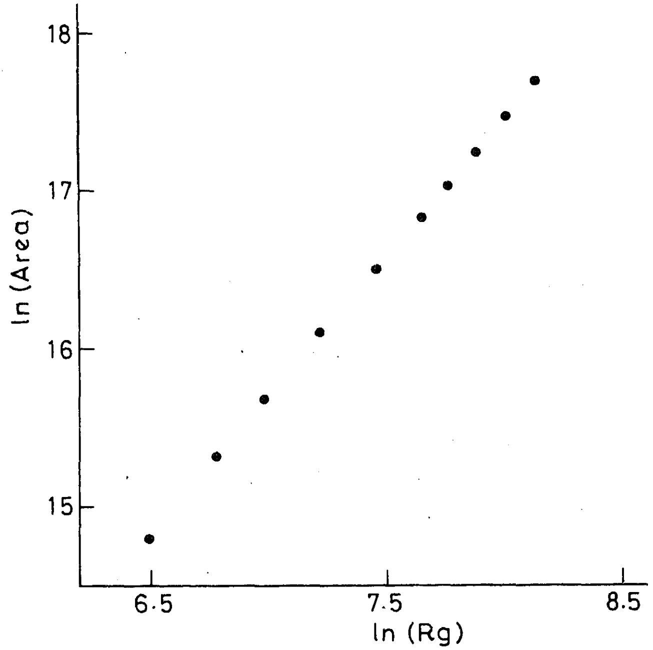

Figure 2. Area vs radius of gyration in one run. The slope is d_f.

artificial four-fold symmetry we impose, there is no qualitative distinction between the time evolution of the interface in the laboratory and in the numerical experiments. The fractal nature of the structure is reflected in figure 2 from which the fractal dimension d_f is measured to be 1·77. The experimental value for d_f obtained by May and Maher [5] is $1{\cdot}79 \pm 0{\cdot}04$.

3.2 *Radius of gyration R_g vs radius of structure R*

In the context of radial viscous fingering in porous media, it is known [21] that the radius of gyration is proportional to the radius of the structure (the distance between the center of the structure defined as the point where the growth started and the point of the structure farthest from the centre)–with the constant of proportionality $h = R/R_g$ equal to $1{\cdot}98 \pm 0{\cdot}03$. Data on this aspect have not been reported in ref.[5]. Our numerical data (figure 3) demonstrate that for the present problem also, the proportionality is satisfied very well but with a rather different value of h. Here $h = 1{\cdot}53$. This lower value of h is due to the fact that in the present case the tips have the shape of pies that increase in width in the radially outward direction, and thus the parts of the structure which are further away from the centre receive a higher weighting in the radius of gyration as compared with the case of fingering in porous media. There the structure is very stringy and the width of the branches are only very weakly dependent on the distance from the centre. Thus for a given value of the radius of the structure, the radius of gyration would be expected to be larger in the case of immiscible radial viscous fingering than in the case of fingering in porous media. By the same argument, the value of h for the standard DLA model of Witten and Sander [14] should also be higher than the value for our present problem. One of the physical quantities defined by Rauseo *et al* [5] is the area of mixing (A_{mix}) which is equal to $\pi(r_{\max}^2 - r_{\min}^2)$ where $r_{\max}$ and $r_{\min}$ are the maximum and minimum

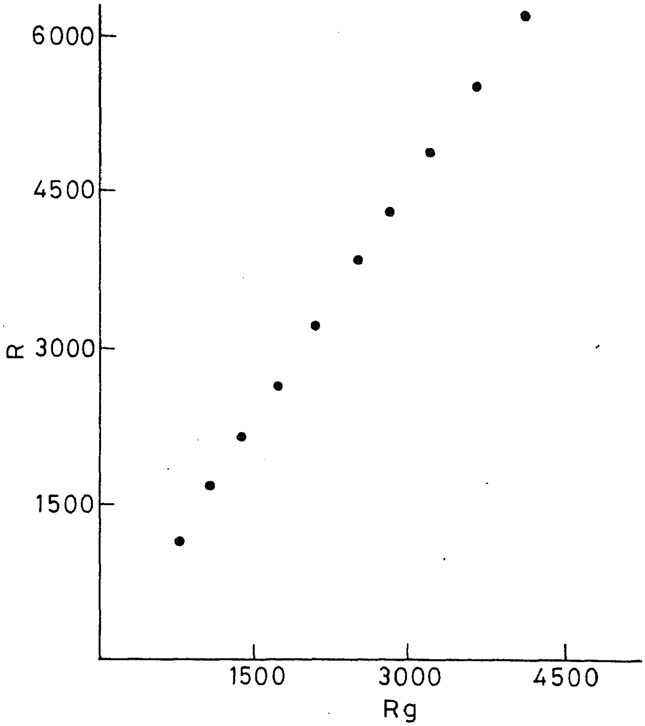

Figure 3. Radius of the structure vs. radius of gyration.

values of the radial coordinate over all the points of the interface. Thus $r_{\max}$ is nothing but the radius of the structure. $r_{\min}$ corresponds to some point deep in the interior, and since the growth is essentially absent in such shielded regions, $r_{\min}$ changes little during the growth and very soon $r^2_{\max}$ dominates. Thus A_{mix} is essentially equal to πR^2 and is equivalent to the radius of the structure (R) from the point of view of scaling properties. For this reason we do not separately analyze A_{mix} in this paper.

3.3 *Total arclength* (S_T) *of the interface*

In the classical 2-*d* DLA problem on a square lattice, one can define the arclength as the number of interfacial points. Here the interfacial points are those points of the aggregate which have at least one empty neighboring point. But since the probablity of having all the four neighbouring lattice points occupied is rather small, the length of the interface as defined above is essentially the same as the mass of the aggregate. One encounters a similar problem of definition for radial miscible viscous fingering [16] or for fingering in porous media [21]. In the present problem these difficulties are absent, and the total arclength is an interesting and independent parameter to study. Reference [5] also defines a reduced quantity called the stretching parameter $\varphi = [(S_T/2\pi\sqrt{2}R_g) - 1]$. Obviously its scaling properties are not independent of those of S_T which is what we will limit our attention to here. However, to obtain a qualitative comparison with the data of ref.[5], we present our numerical results on the stretching parameter along with the laboratory data in figure 4. To uncover possible new scaling relations, $\ln(S_T)$ is plotted as a function of ln(area) in figure 5a. The experimental data displayed in figure 5b combines data from several

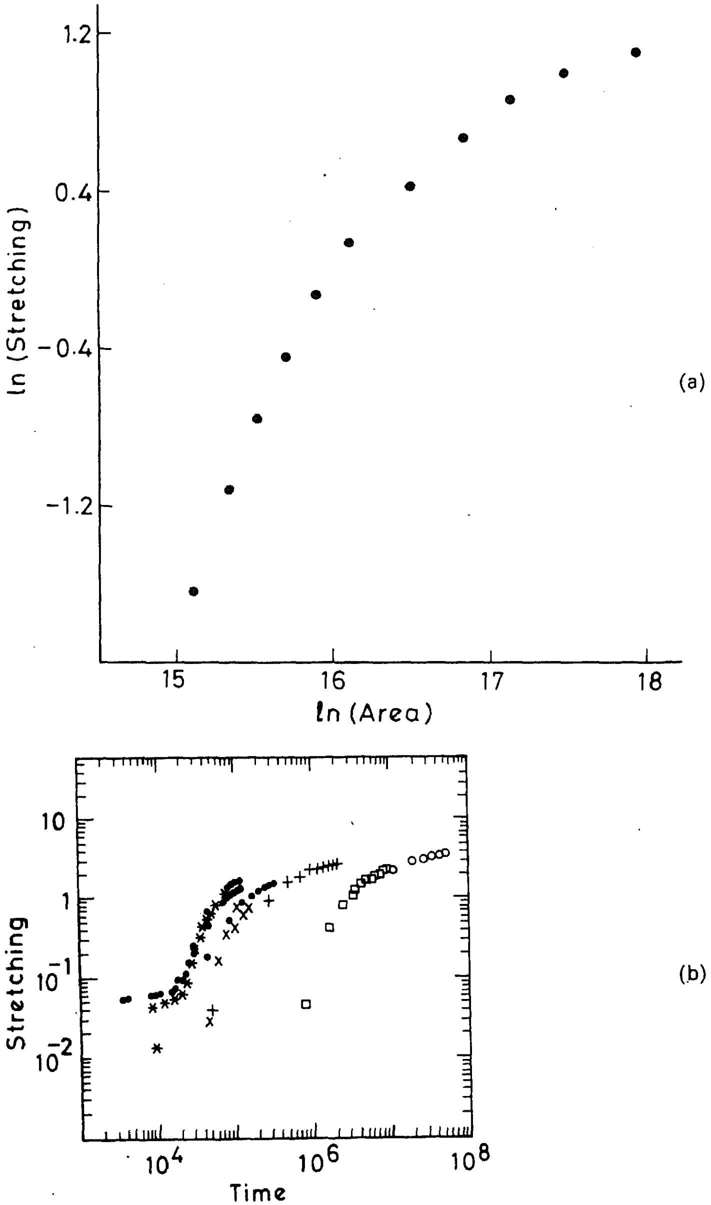

Figure 4. (**a**) Stretching vs area for a typical run in the numerical experiment. (**b**) Log–log plot of stretching vs area from laboratory experiment (ref. 5). Different symbols are used for data for different runs which have different areal flow rates and/or plate spacings. Since the areal flow rate in dimensionless units is always equal to 2π, time is equivalent to area.

runs with different values of flow rates and/or gap width of the Hele-Shaw cell. If we use the data from our numerical calculation or from a single run in figure 5b (to which the numerical data corresponds), the value of the scaling index thus obtained would be too uncertain. For this reason we have used the data of figure 5b which spans a much wider range and helps us obtain a much less uncertain value of the

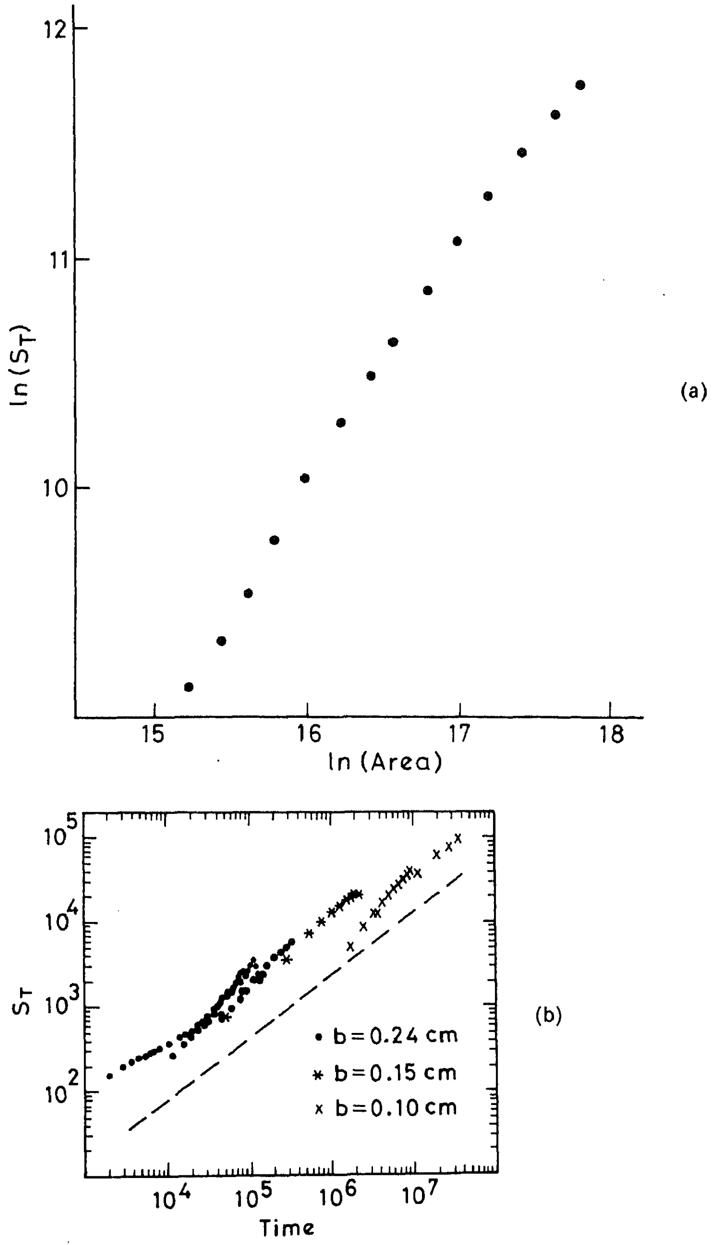

Figure 5. (**a**) Total arclength vs area. (**b**) Total arclength vs area from laboratory data (ref. 5). Different symbols are for different runs. Time is equivalent to area.

scaling index d_{SA}—defined here as the slope of $\ln(S_T)$ vs ln(area). The estimate for d_{SA} is 0·74 (calculated on the basis of the dashed straight line in figure 5b). The assumption made here implicitly is that the total arclength is proportional to $(\text{area})^z$ where $z = d_{SA}$ and the constant of proportionality depends on the area at the most in a rather weak manner. If this constant of proportionality is different for different runs, then this determination of d_{SA} by combining data from different runs is no more reliable than what would be the case if we tried to evaluate it from a single run. The assumption that we have made is trivially true for a growing circle and is also consistent with the data in figure 5b.

We note here that a recent work [22] also provides data on this although the boundary conditions are rather different. Translated to our problem, this work presents numerical data on a flow in which the pressure is maintained constant at a higher value inside the gas and at a lower value on a circle of large radius. A log-log plot of $(S_T/\sqrt{\text{area}})$ as a function of S_T is presented. The linearity of the curve is convincing and we read off the slope to be approximately 0·35. The value of 0·74 for d_{SA}, as obtained from figure 5b, would imply a value of 0·324 for this slope. However, one has to carefully analyze the implications of the difference of boundary conditions to see whether they should influence the scaling properties. If one can demonstrate that the scaling, at least for this pair of variables, should be identical for these two different kinds of boundary conditions then this work supports the present one.

4. Conclusions

We have not seen any qualitative difference between the experimental data and our numerical results using a model that excludes the velocity-dependent part of the boundary condition and the effect of finite film thickness. Of course this, by itself, does not ensure that these factors can be ignored for all purposes. But our conclusion is further supported by the excellent agreement between the laboratory and the numerical data for the value of the fractal dimension. The numerics also provide a very precise value for the ratio between the radius of the structure and the radius of gyration. Unfortunately this ratio is not available for the laboratory experiments.

To summarize, these results lead us to believe that a model with just the surface tension in the boundary condition should be adequate for a theoretical description of the radial immiscible viscous fingering experiments of ref. [5]. It is significant that there was no need to incorporate noise explicitly to trigger tip-splitting. The results for the scaling of the total length of the interface as a function of the radius of gyration are new and have found theoretical support [13]. The mean field analysis of ref. [13] also predicts that scaling in this problem is subject to a periodic modulation. Thus if x and y are the scaling variables of interest, then if $\ln(x)$ is plotted as a function of $\ln(y)$, one should obtain a periodically modulated straight line. The amplitude of modulation depends on the particular pair of variables concerned. In such a curve, a segment spanning only about one period will indeed look like the data for a single run from both the numerical and the laboratory experiments as has been reported in this paper. Also the amplitude of modulation will determine the degree of uncertainty of the estimated value of the slope of the underlying straight line if one has such limited data. Finally, it should be noted that we have avoided quoting estimates of error bars on the various scaling amplitudes or exponents. As should be obvious from the context, none of the standard techniques of estimation of error bars work in the present case. The way to do is to generate the data on the interface dynamics for many different initial conditions, estimate exponents or amplitudes the way it has been done here and then to perform statistical analysis in order to estimate the error bars. Obviously, this error bar would be a measure of the sensitivity of the scaling aspects with respect to the initial conditions.

Acknowledgements

The authors wish to thank the Pittsburgh Supercomputer Centre for providing the computing facilities needed for this work. Part of the financial support was provided by the National Science Foundation. The authors also thank James V. Maher and Mark DiFrancisco for many useful discussions on the various aspects of the experiment.

References

[1] J S Langer, *Rev. Mod. Phys.* **52**, 1 (1980)
[2] P Pelcé: *Dynamics of curved fronts* (Perspectives in Physics series), edited by H Araki, A Libchaber and G Parisi (Academic Press, New York, 1988)
[3] D Bensimon, L P Kadanoff, S Liang, B I Shraiman, and C Tang, *Rev. Mod. Phys.* **58**, 977 (1986)
D A Kessler, J Koplik and H Levine, *Adv. Phys.* **37**, 255 (1988)
[4] J Bataille, *Rev. Inst. Pétrole* **23**, 1349 (1968)
L Paterson, *J. Fluid Mech.* **113**, 513 (1981)
[5] S N Rauseo, P D Barnes, and J V Maher, *Phys. Rev.* **A35**, 1245 (1987)
S E May and J V Maher, *Phys. Rev.* **A40**, 1723 (1989)
[6] C W Park and G M Homsy, *J. Fluid Mech.* **139**, 291 (1984)
[7] S C Huang and M E Glicksman, *Acta Metall.* **29**, 701, 717 (1981)
[8] K Somboonsuk, J T Mason and R Trivedi, *Metall. Trans.* **A15**, 967 (1984)
R Trivedi, *Metall. Trans.* **A15**, 977 (1984)
[9] S de Cheveigné, C Guthmann, and M M Lebrun, *J. Phys.* (*Paris*) **47**, 2095 (1986)
[10] P G Saffman and G I Taylor, *Proc. R. Soc. London, Ser.* **A245**, 312 (1958)
P Tabeling and A Libchaber, *Phys. Rev.* **A33**, 794 (1986)
P Tabeling, G Zocchi, and A Libchaber, *J. Fluid Mech.* **177**, 67 (1987)
[11] S K Sarkar and D Jasnow, *Phys. Rev.* **A35**, 4900 (1987) and references therein.
[12] H Thomé, M Rabaud, V Hakim and Y Couder, *Phys. Fluids* **A1**, 224 (1989)
M Ben-Amar, *Phys. Rev.* **A43**, 5724 (1991)
[13] S K Sarkar *Phys. Rev. Lett.* **65**, 2680 (1990)
[14] T A Witten and L M Sander, *Phys. Rev. Lett.* **47**, 1400 (1981)
[15] L Paterson, *Phys. Fluids* **28**, 26 (1985)
[16] G Daccord, J Nittmann and H E Stanley, *Phys. Rev. Lett.* **56**, 336 (1986)
[17] D Jasnow and C Yeung, *Phys. Rev.* **E47** 1087 (1993)
[18] S K Sarkar, *Superlattices and microstructures* **3**, 589 (1987)
[19] S K Sarkar and D Jasnow, *Phys. Rev.* **A39**, 5299 (1989)
[20] L M Sander, P Ramanlal and E Ben-Jacob, *Phys. Rev.* **A32**, 3160 (1985)
[21] K J Måløy, F Boger, J Feder and T Jøssang, *in Time dependent effects in disordered materials,* edited by R Pynn and T Riste (Plenum, New York, 1987)
[22] T H Tong and J A O'Brien, *Phys. Rev.* **A41**, 4430 (1990)

PRAMANA
— journal of
physics

© Printed in India

Vol. 41, No. 5,
November 1993
pp. 401–419

A model for the analysis of the heat release from a supercooled liquid at the glass transition

M RAJESWARI[†] and A K RAYCHAUDHURI
Department of Physics, Indian Institute of Science, Bangalore 560012, India
[†] Present address: Center for Superconductivity Research, Department of Physics, University of Maryland, College Park, MD 20742, USA

MS received 19 April 1993; revised 17 September 1993

Abstract. In this paper we present a phenomenological model to analyze the heat release at the glass transition as observed in the continuous cooling calorimetry when a supercooled liquid freezes into the glassy state. We developed this model for the quantitative analysis of the experimental data to obtain the specific heat and the parameters which govern the structural relaxation. A description of the model and the detailed analysis are presented and the relaxation parameters are compared with the corresponding values obtained from the specific heat spectroscopy. Our analysis reveals several interesting aspects which include the effects of delayed enthalpy relaxation and the nonequilibrium structural relaxation time on the observed specific heat, the temperature dependence of the equilibrium configurational specific heat and the validity of the Vogel-Fulcher equation for the relaxation time.

Keywords. Time-dependent specific heat; glass transition; structural relaxation.

PACS Nos **64·70; 65·4**

1. Introduction

The experimentally observed specific heat undergoes a step-like fall in the temperature range where the supercooled liquid freezes into the glassy state. This fall in the specific heat near the glass transition temperature (T_g) is largely associated with the increase in the structural relaxation time τ_s with decreasing temperature. In the glass transition temperature range where τ_s becomes comparable to the experimental time scale τ_{exp}, the configurational degrees of freedom do not contribute to the observed changes in enthalpy. This accounts for the fall in the specific heat. The observed specific heat at the glass transition is a nonequilibrium time dependent quantity which contains information about the nature of the structural relaxation. Recently we have reported our studies of the specific heat at the glass transition which employ a novel technique known as the continuous cooling calorimetry [1,2]. In this paper we describe a phenomenological model which we have developed to enable us to obtain the parameters governing the structural relaxation from the observed heat release at the glass transition. Since the specific heat at the glass transition is a nonequilibrium quantity, the measured specific heat is sensitive to the kinetics of the calorimetric technique employed.

At the outset we would like to point out that the continuous cooling calorimetry at the glass transition is distinct from most of the earlier studies of the glass transition which employ differential scanning calorimetry (DSC) [3] or adiabatic calorimetry [4, 5] where the specific heat measured as a quenched glass is reheated through the glass transition range. The specific heat observed during this reheating is strongly influenced by the relaxation of the enthalpy frozen-in during quenching. The specific heat peaks observed at the glass transition in the heating experiments (as in DSC and adiabatic calorimetry) have their origin in the delayed enthalpy relaxation. The analysis and modeling of these experiments [3] are thus complicated by the thermal history built into the system during quenching. In contrast, in the continuous cooling method, the specific heat is measured as the supercooled liquid freezes into the glassy state from an initial equilibrium state at $T \gg T_g$. In this case there is no thermal history built into the system prior to the cooling process. The specific heat during cooling does not show the enthalpy relaxation peaks seen in the data during reheating after quenching. As a result, the modeling and the analysis are simpler and more direct here. The continuous cooling calorimetry may be thought of as a large amplitude time domain analog of the specific heat spectroscopy experiment [6] which studies the specific heat in the linear response regime in the supercooled liquid. It should be mentioned here that when the glass is thermally cycled through T_g the specific heat shows a dip below T_g which is sensitive to the thermal history [1]. However in the present report we do not discuss the thermal cycling experiments.

In the remainder of this paper we describe the development of the model and show its application to the quantitative analysis of the data in one glass former (glycerol). The model is general and may be applied to any glass former. It may also be extended for the analysis of similar data (other than specific heat) where one deals with kinetic freezing.

In § 2 we briefly describe the experiment and present some typical data. In § 3 we discuss our treatment of the time dependent specific heat and the structural relaxation time. In § 4 we present the model followed by its application to glycerol in § 5. In § 6 we discuss the structural relaxation parameters obtained for glycerol which is followed by the concluding summary in § 7.

2. The experimental technique

The continuous cooling method of specific heat measurement which is based on the principles of relaxation calorimetry [7] has been described in detail earlier [2]. The sample kept in a vacuum environment is linked to a heat bath maintained at liquid nitrogen temperature by a thermal link whose heat loss rate $\dot{Q}(T)$ is experimentally determined. The sample is annealed at a temperature $T_A > T_g$ by holding it at T_A for several hours. The heat input is then turned off and the sample cools below T_g by losing heat through the link. The specific heat is determined from the cooling rate dT/dt as the sample cools from T_A. The cooling process is shown schematically in figure 1. For glycerol the values of T_A, T_g and the average cooling rate are also indicated in the figure.

In the absence of any heat input, the heat capacity of the cooling thermal mass is related to the cooling rate dT/dt by

$$C(T) = \dot{Q}(T)/(dT/dt). \tag{1}$$

Thus the heat capacity may be obtained if the cooling rate dT/dt and the heat loss rate through the link $\dot{Q}(T)$ are known. In this experiment we measure $T(t)$ as the

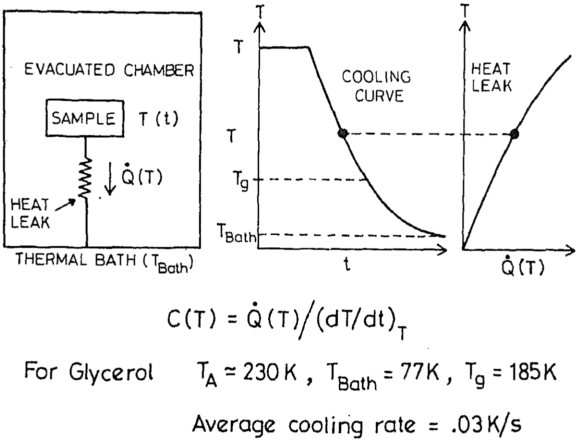
EVACUATED CHAMBER
SAMPLE
T (t)
$\dot{Q}(T)$
HEAT LEAK
THERMAL BATH (T_{Bath})
T
T
T
T_g
T_{Bath}
t
COOLING CURVE
T
HEAT LEAK
$\dot{Q}(T)$
$C(T) = \dot{Q}(T)/(dT/dt)_T$
For Glycerol $T_A \simeq 230$ K, $T_{Bath} = 77$K, $T_g = 185$K
Average cooling rate = .03 K/s

Figure 1. Schematics of the experimental set-up along with the measured cooling curve ($T-t$) and the heat leak curve ($Q(T)-T$). The slope $(\mathrm{d}T/\mathrm{d}t)_T$ is obtained from the cooling curve. $Q(T)$ is determined in a separate run as described in the text.

sample cools through the link from which the cooling rate $\mathrm{d}T/\mathrm{d}t$ is determined. The rate of heat loss through the link $\dot{Q}(T)$ is determined separately by measuring the power input needed to stabilize the sample at several closely spaced temperature values and subsequently obtaining a polynomial fit. $\dot{Q}(T)$ is then a measure of the heat release from the sample which arises from the enthalpy relaxation in a time scale faster than the experimental time scale τ_{exp} corresponding to the cooling rate employed. Equation (1) strictly holds in the temperature regime where the structural relaxation time τ_s satisfies the condition $\tau_s \ll \tau_{\mathrm{exp}}$. In the glass transition region where $\tau_s \sim \tau_{\mathrm{exp}}$ and in the sub-T_g region where $\tau_s \gg \tau_{\mathrm{exp}}$, $C(T)$ will not be the complete equilibrium heat capacity as the configurational states do not equilibrate in the time scale τ_{exp}. We can however treat (1) as an operational definition of the heat capacity. In the analysis that follows, we show how we relate the observed heat capacity to the equilibrium heat capacity in the framework of a kinetic model of enthalpy relaxation.

In figure 2 we present the specific heat data of glycerol and compare it with the data from earlier adiabatic calorimetric experiments [8]. The data and analysis for other glass formers we have studied may be found elsewhere [9]. (Here we focus on glycerol as a representative case of our analysis). As seen in figure 2, in the supercooled liquid region and the sub-T_g region there is reasonable agreement (to within $\sim 5\%$) between the two sets of data. The glass transition region however shows significant variation which is to be expected since the data in this range are sensitive to the experimental kinetics. In table 1 we compare the different parameters associated with the glass transition namely the glass transition temperature T_g, the width of the transition ΔT_g and the change in the specific heat across the transition ΔC_p. In earlier studies these quantities have been defined by employing various arbitrary criteria. We define these quantities from the derivatives of the $C(T)$ curves which allows a less arbitrary definition. Since we obtain $C(T)$ in a continuous temperature sweep, the data are sufficiently closely-spaced in temperature to determine the derivatives $\mathrm{d}C/\mathrm{d}T$ and $\mathrm{d}^2C/\mathrm{d}T^2$ with sufficient accuracy. The change in the specific heat across

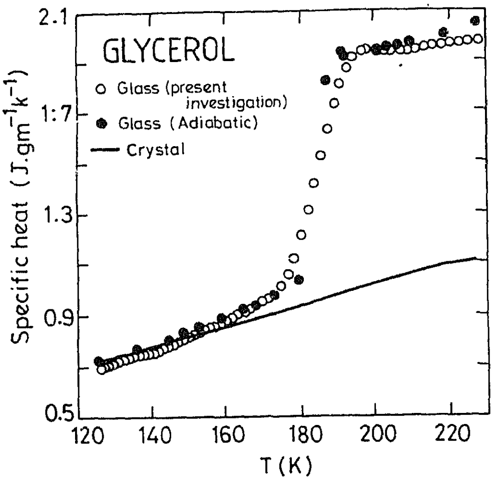

Figure 2. The specific heat of glycerol obtained from continuous cooling calorimetry compared to the values reported in literature [9].

Table 1. The glass transition temperature (T_g), transition width ΔT_g and the specific heat change across the transition (ΔC_p) of glycerol from the continuous cooling calorimetry compared with the same quantities from adiabatic calorimetry.

	Continuous cooling calorimetry (present study)	Adiabatic calorimetry [8]
T_g(K)	185	180–190
ΔT_g(K)	29	19
ΔC_p ($\mathrm{Jg^{-1}K^{-1}}$)	0·97	0·91
$\Delta C_p/C_p$ (liquid)	0·50	0·47

the glass transition interval is defined as

$$\Delta C_p = C_p(T_u) - C_p(T_l)$$

where T_u and T_l correspond to the upper and lower limits of the transition interval as indicated in figure 3. The width of the transition interval is defined as $\Delta T_g = T_u - T_l$. As shown in table 1 the quantities T_g and ΔT_g as obtained from the continuous cooling calorimetry experiment differ from the adiabatic calorimetry data, the difference being due to the variation in τ_{exp}.

Our task in the following sections is to obtain quantitative information about the structural relaxation from the $C(T)$ data in figure 3.

3. The time-dependent specific heat and structural relaxation time near the glass transition

A glass being a system frozen far from equilibrium, the specific heat is time dependent at all $T < T_g$. However there are only two temperature regions where the time

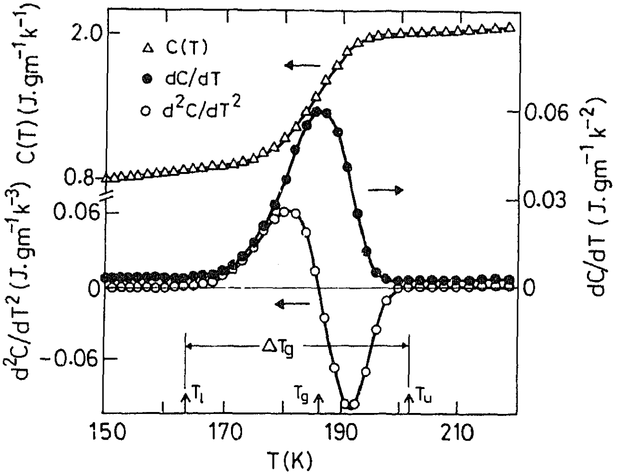

Figure 3. The specific heat $C(T)$ ($Jg^{-1}K^{-1}$) and its temperature derivatives dC/dT ($Jg^{-1}K^{-2}$) and d^2C/dT^2($Jg^{-1}K^{-3}$) of glycerol indicating the glass transition interval (T_g and ΔT_g).

dependence is experimentally observable. Fiirst is the region at $T \sim T_g$ where the enthalpy change associated with the structural relaxation is observable in experimental time scales. The second is another temperature range at very low temperatures ($T < 1$ K) where the time dependent specific heat associated with the tunneling states is observable.

The heat capacity of the system in the supercooled state and the glass transition region may be considered to be made up of two components – the lattice component C_L and the configurational component C_F. The lattice component includes contribution to the heat capacity from the vibrational degrees of freedom in the sample which equilibrate in time scales $\sim 10^{-12}$ s which is much shorter than the time scale of observation. C_L could also include contributions from configurational degrees (such as localized motion about defect sites) with short relaxation time ($\tau_s \ll \tau_{exp}$). The second component of the heat capacity denoted as C_F is associated with the configurational degrees of freedom which relax on time scales resolvable by experiment (i.e. $\tau_s \sim \tau_{exp}$) in the glass transition range. (It should be mentioned here that considering the glass heat capacity to be the sum of two components is only an operational approximation and is not rigorously valid). The relaxational nature of C_F is then manifested in the experimental observation as a time dependent specific heat. In the framework of the relaxational models of the glass transition the time dependence of C_F may be expressed as

$$C_F(T,t) = C_{FO}[1 - \phi(T,t)]. \tag{2}$$

Here C_{FO} is the complete equilibrium heat capacity which is observable only in the temperature range where $\tau_s \ll \tau_{exp}$ and $\phi(T,t)$ is the relaxation function describing the time dependence of the configurational enthalpy change. The relaxation function at a temperature T may be defined from the enthalpy change corresponding to an instantaneous change in temperature ΔT as

$$\phi(T,t) = \frac{H(T,t) - H_{eq}(T)}{H(T,t=0^+) - H_{eq}(T)}. \tag{2a}$$

At $t \sim 0$ $\phi(T,t) = 1$ and at $t \to \infty$ $H(T,t) = H_{\mathrm{eq}}(T)$ and $\phi(T,t) = 0$. The significant change of $\phi(T,t)$ occurs in the time scale $\sim \tau_s$.

The relaxation function associated with the supercooled liquid and glassy relaxations have been found to be nonlinear and non-debye in nature. The non-debye nature is observed in response to even infinitesimal perturbations from equilibrium while nonlinearity arises in the regime of large amplitude perturbations. An empirical expression which has been found to describe a variety of non-debye relaxation processes [10] is of the form

$$\phi(T,t) = \exp[-(t/\tau_s(T,t))^{\beta}] \tag{3}$$

here τ_s is the structural relaxation time and β is a parameter $(0 < \beta < 1)$ related to the width of the spectrum of relaxation times. The limit $\beta = 1$ corresponds to the Debye relaxation with a single relaxation time. We have used the form of $\phi(T,t)$ in (3) in our model of the enthalpy relaxation.

The temperature dependence of the structural relaxation time τ_s and its nonequilibrium nature primarily govern the relaxation at the glass transition. In addition to the strong temperature dependence, τ_s is also time dependent near the glass transition because the structure itself relaxes. Thus the effective value of τ_s is different from its value $\tau_{\mathrm{eq}}(T)$ associated with the equilibrium structure at a temperature T. We will discuss the time dependence of τ_s shortly. The temperature dependence of τ_{eq} has been found to obey the empirical relation

$$\tau_{\mathrm{eq}} = \tau_0 \exp[A/(T - T_0)] \tag{4}$$

which is referred to as the Vogel–Tamman–Fulcher (VTF) expression. The VTF expression (as distinct from the Arrhenius form with $T_0 = 0$) implies that the apparent activation energy increases with decreasing temperature and τ_{eq} diverges at a finite temperature T_0. We have used the VTF form for the temperature dependence of τ_{eq} in our model. The parameter T_0 is usually taken to be temperature independent and a thermodynamic significance is associated with it as representing an ideal phase transition underlying the kinetic glass transition [11]. We find that we need to incorporate a temperature dependent T_0 in our model to adequately describe the experimental observations. We discuss this aspect in a later section.

As already mentioned, the relaxation function $\phi(T,t)$ near the glass transition exhibits nonlinear behavior in response to large amplitude perturbations. The nonlinear behavior is associated with the nonequilibrium nature of the relaxation time τ_s which, as already discussed, has a time dependence in addition to the temperature dependence. The time dependent τ_s attains its equilibrium value $\tau_{\mathrm{eq}}(T)$ only when the system is retained isothermally at T for a time longer than τ_{eq} itself. Thus in (4) we need to incorporate the time dependence of the relaxation time. The time dependence arises due to the dependence of the relaxation time on the structural state which itself is changing during the course of the relaxation process. The dependence of the nonequilibrium relaxation time on structure implies that if the system is not in its equilibrium state, τ_s would depend on thermal history and hence is not a unique function of temperature. The nonequilibrium nature of τ_s becomes significant for large amplitude perturbations from equilibrium as in the present experiment.

The time dependent relaxation time has been described by a phenomenological model [12] which uses the fictive temperature concept [13] to quantify the structural state of the system. The relaxation time τ_s is considered to depend on the temperature T as well as on the fictive temperature T_F.

Another equivalent approach has been developed by Kovacs [14] to take into account the time dependence of τ_s. Kovacs's method considers the nonequilibrium relaxation time as a function of the temperature as well as of the excess enthalpy or the excess free volume in the system. The excess enthalpy or the excess free volume is a measure of the deviation of the system from equilibrium. The nonequilibrium nature of τ_s is thus taken into account by its dependence on the structural state through a quantity which tracks the deviation of the system from the equilibrium configuration. We have used Kovacs' model to incorporate the time dependence of τ_s in our model. Our choice of this model is based on the computational ease. Kovacs' approach should be essentially equivalent to Narayanaswamy's model since both are one parameter models which take into account the time dependence of the relaxation time. We will show the equivalence of the two approaches later on. In a separate section, we describe in detail Kovacs' approach to calculate the time dependent τ_s.

4. Description of the model

We now present the model which describes the heat release and the specific heat observed in the continuous cooling experiment as the supercooled liquid is cooled through the glass transition interval starting from a temperature $T > T_g$. The essential feature of this model is that it keeps track of: (i) the heat released from the system during a cooling step, (ii) the heat trapped due to the incomplete relaxation and (iii) the delayed heat release in subsequent steps. Figure 4 is a schematic representation of the model. The heat capacity of the thermal mass connected to the heat bath (via. the thermal link) is made up of two components—the lattice component C_L and the configurational component C_F. C_L is associated with an instantaneous response in the time scale of the experiment while C_F has an observable time dependence given by (2) and (3). As shown in figure 4, there is an effective heat source Q^h present in the system which arises due to the delayed heat release from the configurational modes as the system continuously moves towards thermal equilibrium. The delayed heat release is associated with the unrelaxed enthalpy in the system which we call the trapped heat the nature of which we discuss shortly.

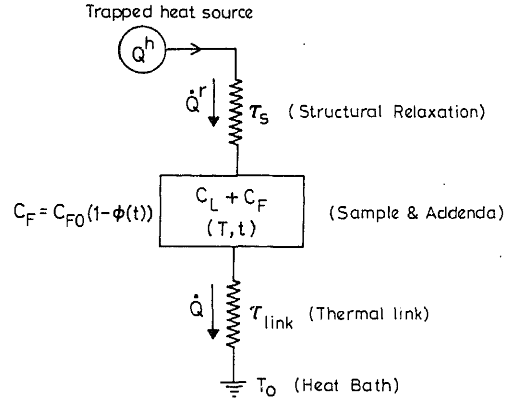

Figure 4. Schematic representation of the model.

We consider the system comprising of $C_L + C_F$ cooling through the link from a temperature $T > T_g$. The continuous cooling process in the experiment is approximated by a step cooling program in the model. The cooling occurs in temperature steps of ΔT followed by isothermal holds of duration Δt with

$$\Delta t = \Delta T/q \tag{5}$$

where q is a cooling rate appropriate to the experiment. It may be mentioned here that the relaxational behavior observed in our model is not sensitive to the particular value of Δt chosen as long as $\Delta T/\Delta t$ corresponds to the cooling rate q and the temperature step ΔT is not too large. We have taken a value of $\Delta t = 60\,\text{s}$, the corresponding ΔT at T_g being $\sim 1\,\text{K}$. This choice was mainly decided by considerations of the computation time.

One of the observed quantities in our experiment is the cooling rate ($\mathrm{d}T/\mathrm{d}t$) from which the specific heat is calculated using (1). Analogously, in the model we compute the cooling rate of the system (consisting of the sample plus the addenda) the heat capacity of which is given by $C_L + C_F$. We denote the effective time dependent heat capacity of the system as $C_{\text{eff}}(T, t)$ given by

$$C_{\text{eff}}(T,t) = C_L(T) + C_{FO}(T)[1 - \phi(T,t)] \tag{6}$$

[Note that the second term in this equation is the time-dependent specific heat in (2)].

In the above equation and the subsequent discussions, the time interval t is the isothermal hold time Δt. At $t \ll \tau_s$ (i.e. $t = 0^+$) it can be seen from equation 2(a) that $\phi(T,t) \sim 1$ and $C_{\text{eff}}(T,t) \sim C_L$. At longer times $t \gg \tau_s$, $\phi(T,t) \sim 0$ and $C_{\text{eff}}(T,t) \sim C_L(T) + C_{FO}(T)$. Since τ_s is a rapidly varying function of temperature, cooling the liquid through T_g is equivalent to going from the limit $t \gg \tau_s$ (at $T > T_g$) to $t \ll \tau_s$ (at $T < T_g$) and $C_{\text{eff}}(T,t)$ in effect gives the relaxation function $\phi(T,t)$. If the thermal link transports heat at a rate $\dot{Q}(T)$ as a result of which the temperature of the system changes by ΔT in a time interval Δt we have the following heat balance equation

$$\Delta T = (\dot{Q}(T)\Delta t - Q^r{}_n)/C_{\text{eff}}(T,t). \tag{7}$$

In the above equation the signs of the terms are so chosen that the cooling process represents a positive ΔT. The term Q^r_n in the numerator arises from the effective heat source Q^h shown in figure 4 which is due to the delayed heat release associated with the unrelaxed excess enthalpy. The excess enthalpy which cannot relax in a given time step relaxes progressively during subsequent steps giving rise to the delayed heat release from the system. We call this the trapped heat release Q^r. We calculate the trapped heat release cumulatively at each step. For the nth step in the cooling program the trapped heat (i.e. the unrelaxed excess enthalpy) at the beginning of the step is given by

$$Q_n{}^h = (C_F \Delta T_{n-1} + Q_{n-1}{}^h)\phi(t, T_{n-1}). \tag{8}$$

The trapped heat consists of two parts. The first term in (8) is the unrelaxed excess enthalpy from the previous $n-1$th step. The second term is the cumulative unrelaxed excess enthalpy due to all the previous $(n-2)$ steps which remain unrelaxed at the beginning of the nth step. [It may be noted that for a property P which follows the relaxation function $\phi(T,t)$ the relaxed part after time t is $P\,[1 - \phi(T,t)]$ and the corresponding unrelaxed part is $P[\phi(T,t)]$. The amount of trapped heat released at the *n*th step is given by

$$Q_n{}^r = Q_{n-1}{}^h[1 - \phi(t, T_n)]. \tag{9}$$

We would like to mention here that incorporating the effect of the delayed heat release is an important aspect of our model. The trapped heat release has a significant effect on the shape of the observed specific heat at the glass transition. The experimentally obtained specific heat cannot be reproduced without including this term. In other words, it is not only the relaxation of the enthalpy at a given temperature step but also the cumulative effect of the unrelaxed enthalpy (which relaxes progressively in subsequent steps) that describes the effective specific heat near the glass transition. The effect of this unrelaxed enthalpy and the associated delayed heat release are incorporated through the terms Q^h and Q^r in our model.

The temperature dependence of the trapped heat release also shows interesting behavior associated with the glass transition which we discuss in a later section.

From (7) we obtain the cooling rate for the *n*th step as

$$(\mathrm{d}T/\mathrm{d}t)_T = (\dot{Q}(T_n) - \dot{Q}^r{}_n)/C_{\mathrm{eff}} \tag{10}$$

where $\dot{Q}(T_n)$ is the rate of heat leak through the link at the temperature T_n as determined from the experiment. The heat capacity from the model which is obtained from this cooling rate (as in the actual experiment) can then be calculated from (1). From the total heat capacity, the addenda heat capacity is subtracted to obtain the sample heat capacity.

The parameters which are treated as adjustable in the model are the equilibrium configurational heat capacity C_{FO} and the parameters associated with the time dependent relaxation time τ_s. These parameters are adjusted to get the best agreement between the specific heat calculated from the model and that obtained from the experiment. The parameters thus obtained are taken to be those representative of the structural relaxation in the system.

5. Application of the model to the analysis of the heat release in glycerol

The model described above is now applied to the analysis of the specific heat of glycerol shown in figure 2. To do so we need to calculate the time dependent τ_s and the trapped heat release from the cooling program. In this section we discuss our method of obtaining τ_s as well as the behavior of the trapped heat release Q^r and the fictive temperature T_F obtained from the trapped heat Q^h.

5.1 *The time-dependent relaxation time τ_s*

As mentioned earlier we have adopted Kovacs' method where the nonequilibrium τ_s is obtained by allowing τ_s to depend on a quantity like excess enthalpy or excess volume which tracks the deviation of the system from equilibrium. This dependence is introduced by incorporating into the temperature dependence of τ_s, a term which retards the increase of τ_s as temperature is lowered. This term accounts for the effect of high temperature configurations that are frozen-in during cooling. Due to the presence of such non-equilibrium configurations, at any given temperature the system has shorter relaxation times than those associated with equilibrium configurations.

The expression for τ_s is given by

$$\tau_s = \tau_0 \exp[1/(f + \delta)]. \tag{11}$$

The term δ in (11) has a time dependence given by

$$\mathrm{d}\delta/\mathrm{d}t = -Dq - (\delta/\tau_s). \tag{12}$$

In equilibrium $\delta = 0$ and (11) should represent the VTF expression in (4). It therefore follows that f has the form

$$f = (T - T_0)/A \tag{13}$$

where A and T_0 correspond to the activation energy and T_0 as in the VTF expression for τ_s.

In (12) which governs the time dependence of δ, q is the cooling rate and the parameter D corresponds to the change (across the glass transition) in the derivative of the thermodynamic quantity whose relaxation is being considered. We have treated D as an adjustable parameter in the model. In our experiment we start cooling the liquid from a temperature $T_A > T_g$ after the liquid has been held at T_A long enough to ensure that it attains equilibrium at this temperature. Correspondingly in the model the cooling starts at a temperature where $\delta = 0$. The value of δ at each subsequent temperature step ΔT is obtained by analytically integrating (12) which gives

$$\delta(T + \Delta T) = Dq\tau_s(T)[\exp(-\Delta t/\tau_s(T)) - 1] + \delta(T)[\exp(-\Delta t/\tau_s(T)] \tag{14}$$

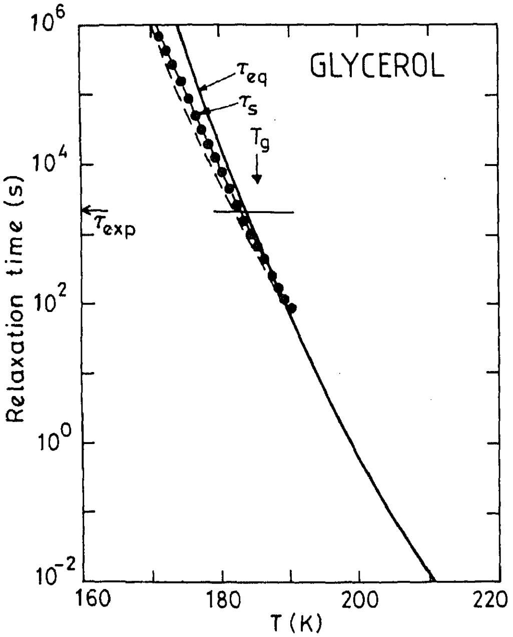

Figure 5. The nonequilibrium relaxation time (τ_s) as compared to the equilibrium relaxation time (τ_{eq}) and the experimental time scale (τ_{exp}).

During cooling for each temperature step ΔT, δ at the end of the step is calculated from (14) using the value of τ_s at the beginning of the step. Using this value of δ, τ_s at the end of the step is calculated from (1)). This procedure is continued to generate τ_s at each temperature. The τ_s thus obtained is used in (1), (8), and (10) to calculate the specific heat from the model. In figure 5 we show the behavior of the time dependent τ_s for glycerol generated by the above method which is also compared to the experimental time scale τ_{exp} and the equilibrium relaxation time τ_{eq} calculated from the VTF expression in (4). The values of τ_s depart from τ_{eq} in the glass transition range where $\tau_s \sim \tau_{\mathrm{exp}}$. When $T > T_g$ and $\Delta t \gg \tau_s$ we have $\delta \sim 0$ as a result of which $\tau_s \sim \tau_{\mathrm{eq}}$. When $T \sim T_g$, δ becomes large enough to introduce an appreciable difference between τ_s and τ_{eq}.

The various parameters in the calculation of τ_s are discussed in a later section.

5.2 *Temperature dependence of the rate of trapped heat release Q^r*

Before coming to the results of the analysis we discuss briefly the behavior of the trapped heat release rate Q^r in our model. In figure 6(a) we show the temperature dependence of Q^r from the model. As seen in the figure. Q^r passes through a maximum at $T > T_g$ and falls abruptly at $T \sim T_g$. For glycerol the peak occurs at $\sim 1{\cdot}03\,T_g$. This behavior of Q^r may be explained as follows. When $T > T_g$, $\tau_s \ll \tau_{\mathrm{exp}}$ and the configurational modes equilibrate almost completely in the time scale τ_{exp}. As a result there is very little trapped heat Q^h (excess enthalpy) in the system. As the cooling proceeds, τ_s increases and the amount of trapped heat Q^h as well as the rate of release of the trapped heat Q^r increases. As the system is cooled down to T_g and below, though the trapped heat continues to accumulate, the rate of trapped heat release decreases as the condition $\tau_s \gg \tau_{\mathrm{exp}}$ is approached. In other words, the approach to equilibrium has slowed down to such an extent that the trapped heat release is not observable in the experimental time scale τ_{exp}. This explains the peak at T_g. The amount of trapped heat in the system (Q^h) however increases monotonically as the system cools below T_g.

5.3 *Fictive temperature from the trapped heat*

Earlier we had briefly discussed the fictive temperature concept which has been used to calculate the nonequilibrium relaxation times. In this section we discuss how the fictive temperature may be obtained from Q^h which we have earlier referred to as the trapped heat in the system (see equation 11). Fictive temperature T_F for enthalpy relaxation is defined by (10)

$$H(T) = H_e(T_F) + C_{pg}\mathrm{d}T \tag{15}$$

where $H_e(T_F)$ is the equilibrium enthalpy of the liquid at temperature T_F and C_{pg} is the specific heat of the glass. Equation (15) implies that the configurational enthalpy $H_{\mathrm{conf}}(T)$ corresponds to the equilibrium configurational enthalpy at $T = T_F$.

It follows that the excess enthalpy at T relative to the enthalpy of the equilibrium liquid is given as

$$H_{\mathrm{ex}}(T) = H_e(T_F) - H_e(T) \simeq C_{\mathrm{FO}}(T_F - T) \tag{16}$$

(The approximation involved in the last part of this equality is due to a small correction due to the temperature dependence of C_{FO}).

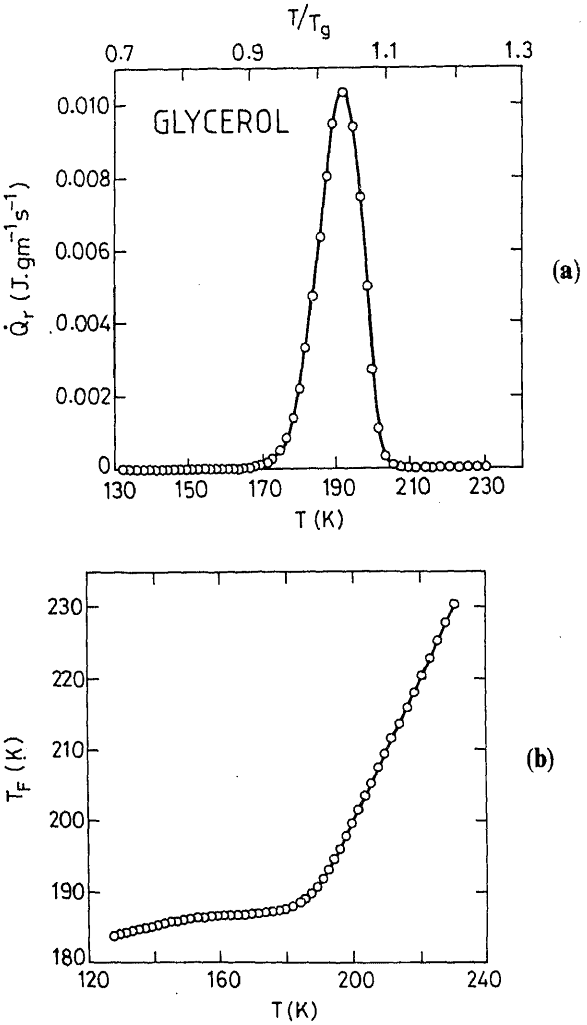

Figure 6. (**a**) The rate of trapped heat release as a function of temperature. (**b**) The fictive temperature T_F calculated from the trapped heat, as a function of temperature.

It can be seen that the excess enthalpy H_{ex} in (16) is the same as the trapped heat $Q^h(T)$ computed in our model according to (8). We thus have

$$Q^h(T) = C_{FO}(T_F - T). \tag{17}$$

We can use (17) to calculate $T_F(T)$ since both Q^h and C_{FO} are obtained from our analysis. The fictive temperature curve thus obtained is shown in figure 6(b). It can be seen that for $T > T_g$ when $\tau_s \ll \tau_{exp}$ (in the supercooled liquid region), Q^h is small and $T_F \sim T$. When $T \sim T_g$, trapped heat is accumulated in the system and Q^h builds up to give $T_F > T$. The above discussion of the fictive temperature shows clearly the physical significance of the quantity which we call the trapped heat in our model.

6. Results of the analysis for glycerol

The procedure discussed in the preceding paragraphs has been applied to the analysis of the specific heat data of glycerol shown in figure 2. The range of the parameters which gives a reasonable agreement between the model and the experiment are identified and these are compared with the corresponding parameters from other experiments. More operational details on the analysis of glycerol as well as the other materials has been reported elsewhere [9, 16].

In figure 7 we show the comparison of the specific heat of glycerol calculated from the model with the experimental data. In the inset we show the deviation of the calculated value from the experiment. The model agrees with the experiment within 3% over a temperature range of ~ 100 K spanning the supercooled liquid and glassy regimes. The limit of 3% is also our experimental precision and accuracy. The crucial point in the quantitative analysis is to find the proper region in the parameter space which gives us the best fit. In addition it is necessary that the parameters are physically justifiable and are in agreement with those obtained from ac specific heat spectroscopy dielectric and mechanical spectroscopy etc. We now discuss the values of the parameters in the model which lead to the best agreement.

6.1 *Lattice heat capacity C_L*

C_L is taken to be the sum of the heat capacity of crystalline glycerol and that of the addenda. This involves the assumption that the vibrational contribution to the specific heat in the supercooled liquid and glass is the same as that in the crystal which seems to hold within our experimental accuracy of 3%. Both the above quantities are determined from the experiment.

6.2 *Equilibrium configurational heat capacity C_{FO}*

This quantity is treated as an adjustable parameter in our model. Our analysis indicates that it is necessary to incorporate a temperature dependence of C_{FO} to

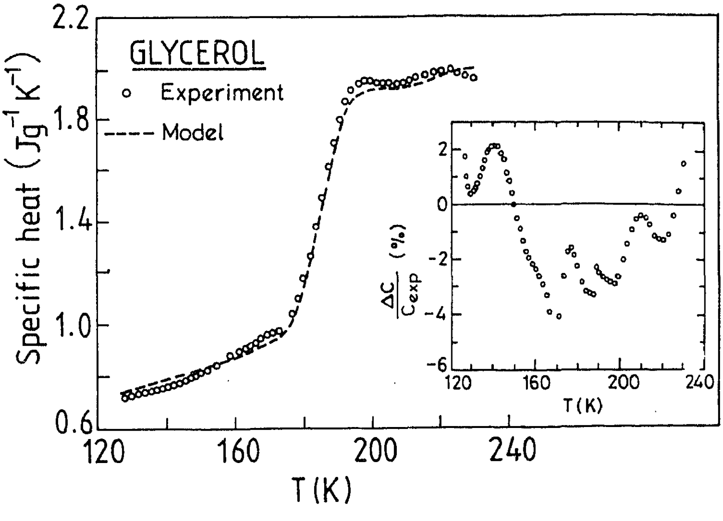

Figure 7. The specific heat of glycerol obtained from the model as compared to the experimental data. The inset shows the % variation.

obtain the experimentally observed specific heat near the glass transition. C_{FO} which gives the best agreement between the model and the experiment is of the form

$$C_{FO}(T) = C_0 + b/T \tag{22}$$

where C_0 is taken to be the value of $C_{liq} - C_{crystal}$ at $T \sim T_m$ and b is treated as a fit parameter. The increase in the equilibrium configurational specific heat C_{FO} according to (22) as seen in our points to the important fact that the drop in the specific heat observed at the glass transition could be attributed entirely to kinetic effects. *In other words there is no decrease in the equilibrium configurational specific heat at the glass transition.* This is contrary to some of the prevalent ideas which associate the behavior of the specific heat at the glass transition with a phase transition. In figure 8 we compare the behavior of the equilibrium configurational specific heat C_{FO} with the relaxational (i.e. observable) part of the configurational specific heat given by C_{FO} $(1 - \phi(T, t))$. The relaxational contribution to the observed specific heat becomes comparable to the experimental accuracy at $T < 160$ K for glycerol. Hence we can say that the $C_{FO}(T)$ as seen in our model continues to increase with temperature down to 160 K i.e. $(T/T_g \sim 0{\cdot}85)$. If the rise in C_{FO} is the signature of the onset of a phase transition it must be occurring below $T/T_g \sim 0{\cdot}85$. The rise in C_{FO} at lower temperatures may also be the tail of a Schottky specific heat associated with the two level systems which must show a peak at a lower temperature. The significant point here is that the temperature dependence of C_{FO} at least down to $T/T_g \sim 0{\cdot}85$ where the relaxational part falls below our experimental accuracy clearly indicates that the observed drop in the specific heat at T_g is purely due to relaxational effects. We consider the indication of a temperature independent C_{FO} as a significant result of our analysis.

6.3 *Parameters associated with the relaxation time*

These parameters include the activation energy A, the pre-exponential factor τ_0 in the VTF expression and the parameter D in the calculation of δ in [12]. The values

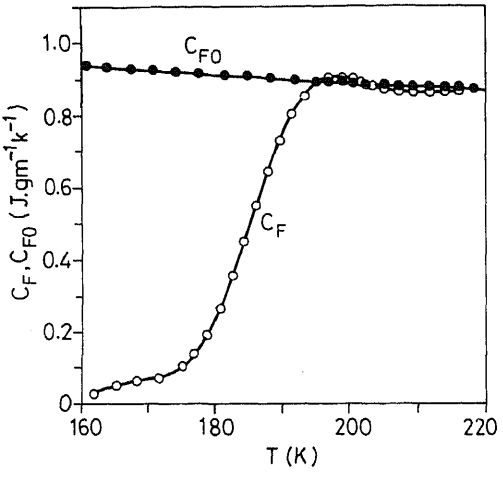

Figure 8. The relaxational part of C_{FO}(—○—) compared to the equilibrium configurational specific heat from the model.

Table 2. The structural relaxation parameters obtained from the analysis of the continuous cooling calorimetry for glycerol. The numbers in parantheses are those obtained from specific heat spectroscopy.

	Glycerol	
Activation energy A(K)	2500 ± 100	(2500 ± 100)*
Pre-exponential factor τ_0(s)	$2 \times 10^{-15} - 3 \times 10^{-16}$	$(2 \times 10^{-14} - 3 \times 10^{-16})$*
Divergence temperature T_0(K)	120–128	(128 ± 5)*
Non-debye parameter (β)	$0{\cdot}55 \pm 0{\cdot}02$	$(0{\cdot}65 \pm 0{\cdot}03)$
Parameter $D(\mathrm{K}^{-1})$ (equation (16))	$6 \pm 0{\cdot}5 \times 10{\cdot}5$	
Parameter $b(\mathrm{Jg}^{-1})$ (equation (19))	38–42	
Parameter $C_0(\mathrm{Jg}^{-1}\,\mathrm{K}^{-1})$ (equation (19))	0·68–0·70	

of these parameters for glycerol are listed in table 2. Here we briefly comment on these parameters. The value of A obtained from our model is 2500 ± 100 K, which corresponds to an activation energy of ~ 10 kJ/mol. The pre-exponential factor τ_0 is in the range of 10^{-15} to 10^{-16} s. Both these parameters are in reasonable agreement with those obtained from specific heat spectroscopy [15]. The parameter T_0 however shows a different behavior in our analysis. With a constant T_0 we could not obtain a reasonable agreement between the model and the experiment. The specific heat calculated from the model shown in figure 7 was obtained by smoothly varying T_0 between 128 K and 120 K in the temperature range $190\,\mathrm{K} > T > 160\,\mathrm{K}$. A decrease of T_0 with temperature typically ~ 7 to 10% has also been found for other materials in our study [9, 16]. The most pronounced decrease of T_0 ($\sim 24\%$) has been seen for the case of propylene carbonate which is also the most fragile (17) system among those we investigated. It has been previously observed that in fragile systems τ_{eq} obtained from viscosity measurements reverts back to Arrhenius behavior ($T_0 \approx 0$) as $T \sim T_g$. The decrease of T_0 observed in our analysis points to a similar behavior. However in systems like glycerol which lie in intermediate range between the strong and fragile glass formers the VTF relation has been found to hold throughout [17]. The tendency of T_0 for glycerol to decrease as observed in our model is at variance with this earlier idea and questions the universality of the VTF expression for the relaxation time. It should be mentioned that even for propylene carbonate despite the decrease in T_0 we do not observe a cross-over to complete Arrhenius behavior ($T_0 = 0$) down to the lowest temperature limit ($T/T_g \sim 0{\cdot}85$) of our analysis. Similar conclusions have been reached on the basis of ac calorimetry experiments [18] on o-terphenyl mixtures which also represent a fragile system. This in conjunction with our results which seems to suggest that the fragile behavior seen in mechanical relaxation may not be extendible to enthalpy relaxation.

We now come to the parameter D in (16) for the calculation of the quantity δ which incorporates the time dependence of τ_s. In Kovacs' model as applied to volume relaxation [19] D was taken to be the change of the thermal expansion coefficient ($\Delta\alpha$) at the glass transition. The analogous quantity for enthalpy relaxation should be represented by ΔC_p scaled by some appropriate enthalpy. In our model we have treated D as a fit parameter. The values of D which give the best agreement lie in the range $D \sim 6{\cdot}5 \times 10^{-5}\,\mathrm{K}^{-1}$. This value of D corresponds to $D \sim \Delta C_p / H_0$ where H_0 has a magnitude comparable to the zero point enthalpy given by $H_0 \sim N_A \hbar\omega_0$ with $\omega_0 \sim 2\pi\tau_0$ and N_A is the Avogadro number. For glycerol with $\Delta C_p \sim 100\,\mathrm{J\,mol^{-1}\,K^{-1}}$ we have $D \sim 4 \times 10^{-5}\,\mathrm{K}^{-1}$ which is of the order of D obtained from our analysis.

In figure 9 we show the effect of varying D on the nonequilibrium τ_s. With increasing values of D (which corresponds to the increasing deviation of the system from equilibrium) τ_s increasingly departs from the VTF behavior saturating below T_g. It is interesting to note the sensitivity of τ_s to D. Below T_g, τ_s is essentially determined by δ and hence by the parameter D. As T approaches T_0, the dependence on D prevents the divergence of τ_s (equations 15 and 17). This also implies that in a real experiment with a finite cooling rate (however small) one cannot see the true divergence of τ_s because even a small value of δ will tend to saturate τ_s as T approaches T_0.

6.4 *The parameter β in the relaxation function*

As mentioned earlier, the parameter $\beta (0 < \beta < 1)$ in (3) takes into account the non-debye nature of the relaxation function which is related to a spectrum of relaxation times. A value of $\beta = 1$ represents Debye relaxation with a single relaxation time, smaller values of β corresponding to a broader relaxation time spectrum. For glycerol, our analysis shows that $\beta = 0{\cdot}55 \pm 0{\cdot}05$ gives a satisfactory agreement between the model and the experiment. We compare this value with that obtained from ac specific heat spectroscopy in the next section.

6.5 *Comparison with ac specific heat spectroscopy*

In table 2 we have given a comparison of the parameters obtained from the analysis of our experiment with those obtained from the specific heat spectroscopy (15). As seen in the table, the activation energy A and the pre-exponential factor τ_0 from the

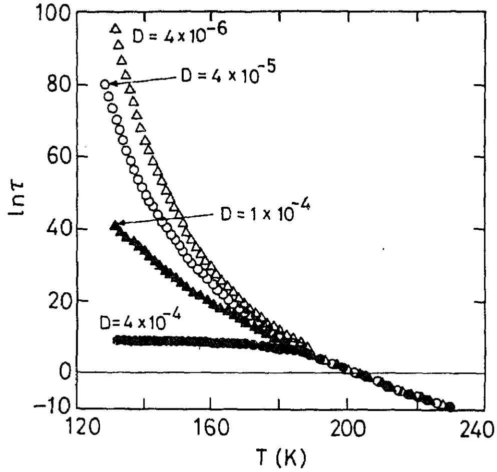

Figure 9. The nonequilibrium τ_s generated from the different values of D. D: 4×10^{-4}(●); 1×10^{-4}(▲); 4×10^{-5}(○); 4×10^{-6}(△).

two experiments are in good agreement. A significant difference is the temperature dependence of the parameter T_0 in our analysis while T_0 is temperature independent as obtained from the specific heat spectroscopy experiment. Another important difference is the wider spectrum of relaxation times as indicated by the smaller value of β in our experiment. These differences may be understood in view of the following facts. The time scale of the specific heat spectroscopy experiment is much smaller as compared to the present experiment as a result of which the relaxational effects are observable at higher temperatures. In other words, specific heat spectroscopy is probing the equilibrium response at higher temperatures. In contrast, our experiment is most sensitive to these parameters in the glass transition range where the system falls out of equilibrium.

6.6 *The effect of variation of the parameters on the calculated specific heat*

The parameters discussed above almost independently determine the various attributes of the behavior of the calculated specific heat. We observe the following from our analysis:

(1) The equilibrium configurational specific heat C_{FO} governs the slope of the specific heat in the supercooled liquid state ($T > T_g$) close to the glass transition.
(2) The parameters τ_0, A and T_0 govern the temperature of onset of the glass transition.
(3) The parameter β and the temperature dependence of T_0 affects the slope of the specific heat in the transition range and hence the width of the transition.

The calculated specific heat is most sensitive to these parameters in the transition range as expected since the relaxational contribution is maximum here. A detailed analysis of the effect of each of the parameters on the specific heat in the three regimes—the supercooled liquid region, the glass transition region and the glassy regime—may be found elsewhere [19]. We have been able to deduce these parameters unambiguously within a narrow range of the parameter space by minimizing the difference between the specific heat observed in the experiment and that calculated in the model. An average percentage error ΔC is defined in the three relaxational regimes mentioned above as

$$\Delta C = 1/n \Sigma |C_{\text{expt}} - C_{\text{model}}| \tag{23}$$

where n is the number of points in each temperature interval over which ΔC is averaged. We find deep or moderately deep minima in this difference around the best fit values of the parameters. As examples we show in figure 10(a–d) the effect of varying the parameters A, τ_0, D and b respectively showing the minimum in ΔC in a narrow range of the values of these parameters. A, D and τ_0 control the relaxation time τ_s and b governs the temperature dependence of the equilibrium specific heat C_{FO}.

As pointed out earlier, the specific heat in the glass transition interval is most sensitive to τ_s because in this temperature region the time dependence of the relaxation function $\phi(T,t)$ contributes to the calculated specific heat. At $T \gg T_g$, $\phi(T,t) \sim 0$ and the system is in thermal equilibrium. At $T \ll T_g, \phi(T,t) \sim 1$ and as a result the variation of τ_s does not affect the calculated specific heat. If the variation of any of the parameters increase τ_s then freezing occurs at a higher temperature and for all temperatures $C_{\text{model}} < C_{\text{expt}}$. Similarly, if τ_s decreases, the glass transition is shifted to lower temperatures and we have $C_{\text{model}} > C_{\text{expt}}$. Of particular interest is the variation in the

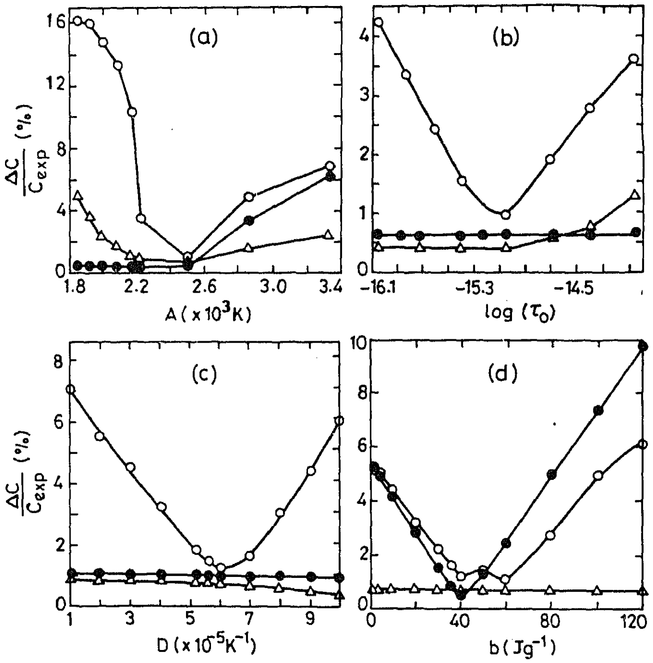

Figure 10a–d. The effect of the parameters A, D, τ_0 and b on ΔC in the three relaxational regimes: supercooled liquid (●); glass transition range (○); sub-T_g region (△). Note that minima are obtained in ΔC when the parameters have the best fit values.

activation energy A, which for a given change around the best fit value ($A \sim 2500\,\mathrm{K}$) gives the maximum change in ΔC (see figure 10). In the transition range ΔC is changed almost symmetrically for increasing or decreasing A. The situation is somewhat different for the regions in the range $T > T_g$ and $T < T_g$. For the supercooled liquid region ($T > T_g$) since the system is close to thermal equilibrium a decrease in A (i.e. a decrease in τ_s) does not lead to any change but an increase in A (i.e. an increase in τ_s leads to the system moving farther out of equilibrium as a result of which $C_{\mathrm{model}} < C_{\mathrm{expt}}$ and ΔC increases. Similar arguments apply for the sub-T_g region. This method of analysis thus not only helps us to identify the best fit value of the parameter A but also physically reveals the dependence of C_{model} on the variation of τ_s achieved through the variation of A.

The arguments given for A also apply for D and τ_0 and one can identify the extent of the change in C_{model} when these parameters are varied. Since the parameter b controls the slope of $C_{\mathrm{FO}}(T)$ and not τ_s, the variation of b has the largest effect in the supercooled liquid region ($T > T_g$) where C_{FO} contributes most to the specific heat. As expected the parameter b has no sgnificant effect on the specific heat below the glass transition region where the configuratianal component freezes out.

7. Concluding summary

We have presented a model to analyze the specific heat at the glass transition as observed in the continuous cooling calorimetry experiment. In the framework of this model we have been able to obtain several parameters associated with the enthalpy relaxation at the glass transition from the experimentally observed specific heat data. We consider the following as the most significant results of our analysis.

(1) The incorporation of the effects of delayed enthalpy relaxation through the quantity called trapped heat release is an important feature in our model. Our analysis brings out the interesting behavior of this quantity at the glass transition.
(2) The temperature dependence of the equilibrium configurational specific heat points to the fact that the observed fall in the specific heat at the glass transition is entirely relaxational in origin.
(3) The temperature dependence of the parameter T_0 indicates the tendency of the system to move towards Arrhenius behavior close to the glass transition.
(4) The behavior of the nonequilibrium structural relaxation time and its effect on the observed specific heat is clearly brought out in the model.
(5) The identification of the excess (unrelaxed) enthalpy as the cumulative trapped heat in the model allows us to determine the fictive temperature. The fictive temperature thus obtained shows the expected behavior at the glass transition.

Finally we would like to mention that the model described here has also been applied to the analysis of the specific heat in partially crystallized glasses [19, 20] to understand the effects of partial crystallization on the structural relaxation. Further the model is sufficiently general to be applicable to the analysis of any time-domain experiment which probes the structural relaxation at the glass transition. With small modifications, the model may also be extended to include the effects of built-in thermal history where the experiment involves thermal cycling across the glass transition interval.

References

[1] A K Raychaudhuri and M Rajeswari, *Rev. Solid State Sci.* **3**, (1989)
M Rajeswari and A K Raychaudhuri, *Euro. Phys. Lett.* **10**, 699 (1989)
[2] M Rajeswari, S K Ramasesha and A K Raychaudhuri, *J. Phys.* **E21**, 101 (1988)
[3] C T Moynihan, A J Easteal, M A deBolt and J Tucker, *J. Am. Ceram. Soc.* **59**, 312 (1976)
[4] G S Parks and H M Huffman, *J. Phys. Chem.* **31**, 1842 (1927)
[5] S S Chang and A B Bestul, *J. Chem. Phys.* **56**, 503 (1974)
[6] N O Birge and S R Nagel, *Phys. Rev. Lett.* **54**, 2674 (1985)
[7] R Bachmann, F J Jr DiSalvo, T H Geballe, R L Greene, R E Howard, C N King, H C Kirsch, K N Lee, R E Schwall, H U Thomas and R B Zubeck, *Rev. Sci. Instrum.* **43**, 205 (1972)
[8] G E Gibson and W F Giaque, *J. Am. Chem. Soc.* **42**, 1547 (1920)
[9] M Rajeswari, '*An experimental study of the specific heat at the glass transition during cooling*' Ph D Thesis, Indian Institute of Science, Bangalore (1990)
[10] S A Brawer, *J. Chem. Phys.* **81**, 954 (1984)
[11] C A Angell and W Sichina, *Ann. N. Y. Acad. Sci.* **279**, 53 (1976)
[12] O S Narayanaswami, *J. Am. Ceram. Soc.* **54**, 491 (1971)
[13] A Q Tool, *J. Am. Ceram. Soc.* **54**, 491 (1946)
[14] A J Kovacs, *Ann. N. Y. Acad. Sci.* **371**, 21 (1981)
[15] N O Birge, *Phys. Rev.* **B34**, 1631 (1986)
[16] M Rajeswari and A K Raychaudhuri, *Phys. Rev.* **B47**, 3036 (1992)
[17] C A Angell, *J. Phys. Chem. Sol.* **49**, 863 (1988)
[18] P Dixon and S R Nagel, *Phys. Rev. Lett.* **61**, 341 (1988)
[19] A Alegria and J Barandiaran, *Phys. Status Solidi* **B120**, 349 (1983)
[20] M Rajeswari and A K Raychaudhuri (unpublished)

PRAMANA
— journal of
physics

© Printed in India

Vol. 41, No. 5,
November 1993
pp. 421–428

Thermal expansion of orthorhombic and tetragonal phases of the high T_c superconductors $RE_1Ba_2Cu_3O_y$ (RE = Y, Gd, Dy)

OM PRAKASH, ASHOK RAO, O PRAKASH* and P N DHEER
Department of Physics and Astrophysics, University of Delhi, Delhi 110 007, India
*Materials Science Division, Indian Institute of Technology, Bombay 400 076, India

MS received 29 March 1993; revised 2 July 1993

Abstract. Measurements of the coefficient of linear thermal expansion α have been carried out for the orthorhombic and tetragonal phases of $RE_1Ba_2Cu_3O_y$ (RE = Y, Gd, Dy) compounds using a high resolution capacitance dilatometer in the temperature range 77–300 K. All the superconducting samples exhibit a jump $\Delta\alpha$ at their respective transition temperatures, T_c. Evidences of, sample-to-sample variation in α values and dependence of $\Delta\alpha$ on the sample preparation conditions, have been obtained. The non-superconducting samples, in general, exhibit lower values of α possibly because of lowering of oxygen content.

Keywords. Thermal expansion; high temperature superconductors; discontinuity in α; growth conditions; iodometric titration.

PACS No. 65·70

1. Introduction

Thermal expansion of solids provides a useful experimental tool for the study of phase transitions and dynamics of lattice vibrations. A second order phase transition like the transition from normal to superconducting state is, for example, characterized by a discontinuity in the coefficient of thermal expansion α, at the transition temperature T_c. Early experiments on high-T_c superconductors failed to show any discontinuity in α [1–5] possibly because of the inadequate sensitivity of measuring technique. Later, more accurate measurements revealed a clear discontinuity $\Delta\alpha$ [6–12]. However, the reported values of $\Delta\alpha$ vary over a wide range. For example Meingast *et al* [10] found $\Delta\alpha = 4{\cdot}5 \times 10^{-8}(\mathrm{K})^{-1}$ whereas Schnelle *et al* [8] have reported $\Delta\alpha = 8 \times 10^{-8}(\mathrm{K})^{-1}$. Occasionally additional anomalies, such as a first order transition at a temperature above T_c [12, 13] and time dependent changes in the specimen dimensions [14] have also been reported. These anomalies are probably characteristic of the samples used and do not represent intrinsic property of the material. Sometimes anomalies have also been observed [3] which are probably due to the expansion of the sample mounting system. Om Prakash *et al* [15] have recently developed a dilatometer based on the three terminal capacitance technique in which there are no significant changes in the dimensions of the sample mounting system on heating the sample and thus, in principle, yields absolute measurements of α. In practice, however, a small correction term arises because of the expansion of the condenser plate mounted on the sample. This correction term can however, be accurately determined experimentally. It was therefore interesting to carry out measurements on high T_c superconductors using this dilatometer. This paper reports results obtained on $RE_1Ba_2Cu_3O_y$ (where RE = Y, Gd, Dy) compounds. All the superconducting samples exhibit a jump $\Delta\alpha$ at their respective transition temperatures, T_c. However, none of the specimens has shown additional anomalies of the type mentioned above. Evidence has also been obtained that the values of $\Delta\alpha$ depend upon the conditions of specimen preparation. Measurements have also been carried out on non-superconducting (tetragonal phase) samples of each rare earth compound.

2. Experimental details

Specimens of each compound were prepared using the standard solid state reaction technique [16]. Appropriate amounts of RE_2O_3 (RE = Y, Gd, Dy), $BaCO_3$ and CuO (all > 99·9% pure) were thoroughly mixed and fired at 930°C in flowing oxygen for 24 h. The mixing and firing was repeated three times to ensure homogeneity. The powder was pressed into cylindrical rods using isostatic press. The rods were then sintered at 950°C in flowing oxygen for 48 h followed by slow cooling to 450°C. They were kept at 450°C for 72 h and then gradually cooled to room temperature. The specimens were examined by X-ray diffraction at room temperature using PW-1820 X-ray diffractometer. The X-ray diffraction analysis of all the samples confirm their being single phased. The X-ray diffraction patterns for typical superconducting specimens are shown in figure 1. Non-superconducting samples were obtained by rapid cooling from 950°C to liquid nitrogen temperature. The X-ray diffraction pattern confirmed the tetragonal structure of the non-superconducting samples.

The transition temperature T_c, width ΔT_c of the resistive transition, the susceptibility χ at 77 K and the oxygen content y have been measured for each specimen. T_c and ΔT_c were determined by measuring the temperature dependence of the electrical resistance in the range 77–300 K using the standard four-probe technique. χ was determined using the mutual inductance technique. The oxygen content of each sample was determined using the iodometric titration procedure suggested by Nazzal *et al* [17]. The procedure has the advantage that systematic errors including those associated with the calibration are eliminated. Reproducibility was checked by performing the titration twice for each sample. High purity argon gas was used to create an inert atmosphere. The accuracy in the determination of oxygen content was about $\pm 0{\cdot}03$.

Measurements of linear thermal expansion α were carried out in the temperature range 77–300 K using the three terminal capacitance dilatometer as developed by Om Prakash *et al* [15]. The apparatus has a sensitivity $\Delta l/l_0 \sim 10^{-8}$. The dilatometer was evacuated and filled with helium gas at low pressure. This was followed by cooling the specimen to liquid nitrogen temperature. After the specimen attained the bath temperature, the dilatometer was evacuated to a pressure of about 10^{-6} Torr. The specimen was heated to successively higher temperatures T. At each temperature it was made sure that the specimen was in thermal equilibrium and the changes $(l_T - l_{77})$ in the length of the specimen was measured by the usual three terminal capacitance technique. In the present set up we could control temperature within ± 5 mK. The performance of this dilatometer was first tested by the measurement of the linear thermal expansion of a copper rod and the results are reported elsewhere [15]. It may be mentioned that the results on copper are in good agreement with literature values. A copper-constantan thermocouple was used to measure the

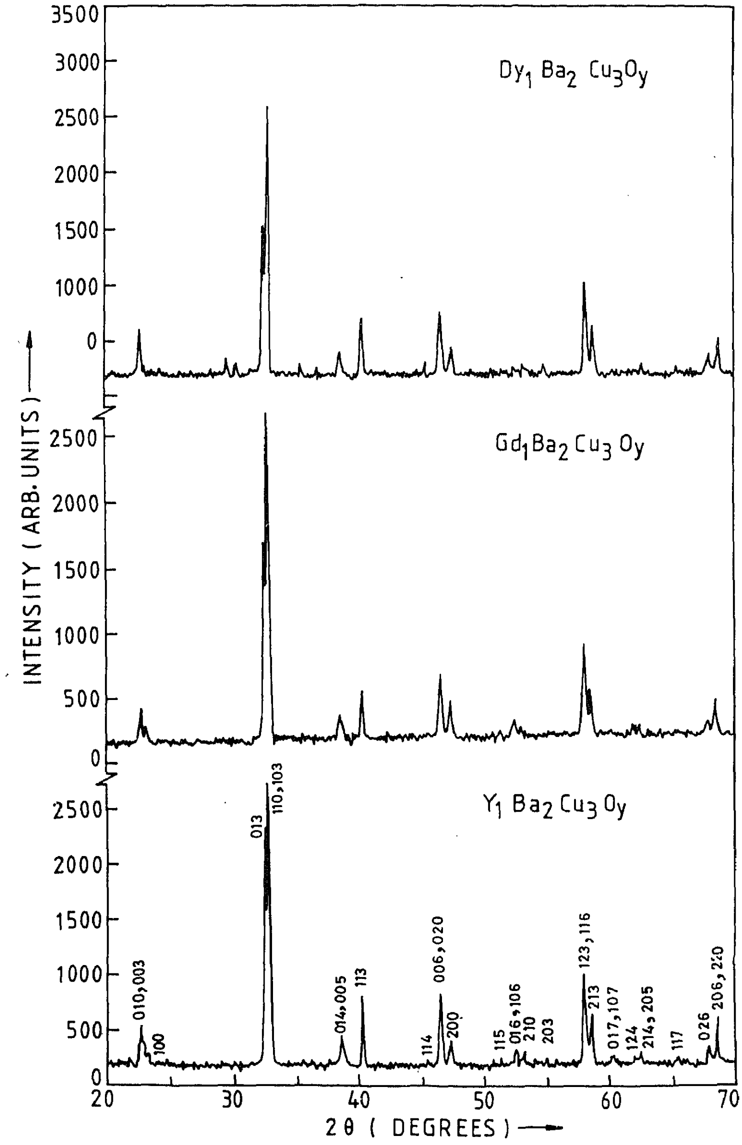

Figure 1. X-ray powder diffraction patterns for typical compounds at room temperature.

temperatures. A differential thermocouple was used to check if there were any temperature gradients along the sample. In the present investigation the temperature difference between the two ends of the specimen was always less than 5 mK.

3. Results and discussion

The observed temperature dependence of the thermal strain $(\Delta l/l_0) = (l_T - l_{77})/l_{77}$ for a typical specimen is shown in figure 2. The only anomaly seen is the change in the slope at the onset of the transition (around 91·8 K)—shown on an enlarged scale in

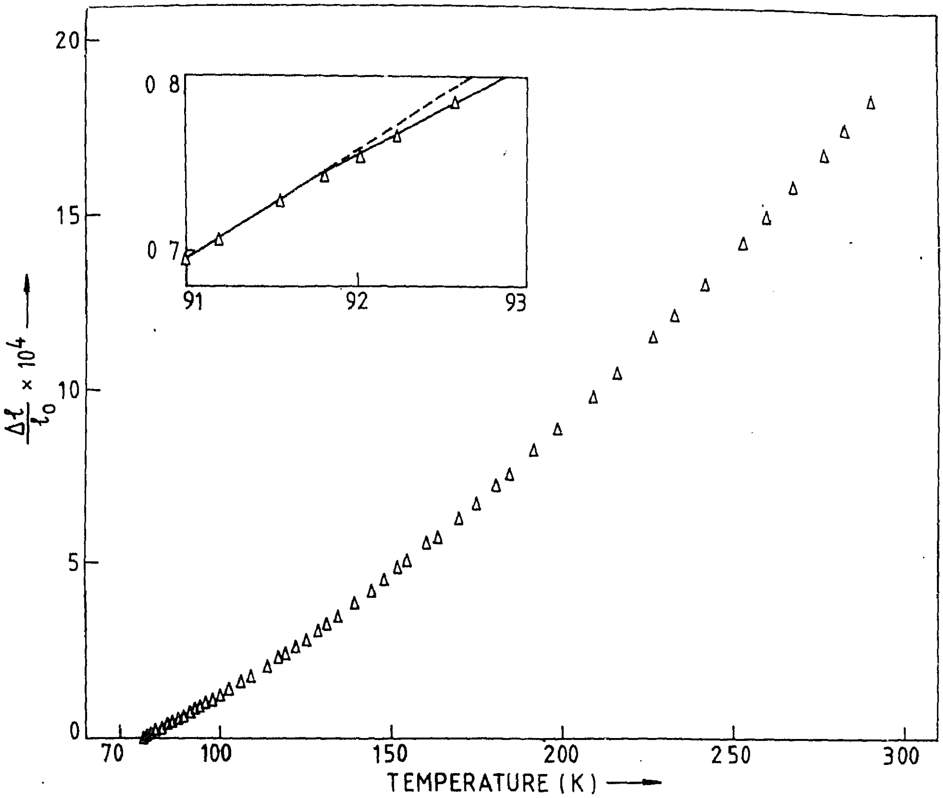

Figure 2. Thermal strain, $\Delta l/l_0$ for the sample Y_2, as a function of temperature.

the inset. The coefficient of linear thermal expansion α was determined by the following procedure. The $(\Delta l/l_0)$ data were fitted using two fifth order polynomials in temperature T—one below T_c and the other above T_c. At any temperature the thermal expansion coefficient α was obtained by differentiating the polynomial. The error in determination of α is estimated to be about $\pm 1{\cdot}5 \times 10^{-8}(\mathrm{K})^{-1}$. Figure 3 shows the behaviour of coefficient of linear thermal expansion $\alpha = (l_{T_1} - l_{T_2})/(T_1 - T_2)l_{77}$ in the temperature range $77 < T < 300$ K. Figure 4 shows the behaviour of α in the transition region for a typical sample. In conventional superconductors like Sn, the superconducting transition is very sharp—transition widths are usually of about 0·001 K in carefully prepared specimens. As a result a sharp discontinuity is observed in the thermal expansion coefficient at the transition temperature. In contrast, the superconducting transition in high T_c superconductors is quite broad (~ 1 K even in carefully prepared samples). Consequently the discontinuity in α is smeared and the experimental results instead of showing a sharp discontinuity in α at T_c, show a gradual change in α as the samples undergo transition from superconducting to normal state. These results, therefore, can at best be used to estimate the jump $\Delta\alpha$ in the coefficient of linear expansion α at the transition temperature T_c by extrapolating the portions of α vs T curves, below and above the transition temperature, to T_c as shown by solid lines in figure 4. The error in determination of $\Delta\alpha$ is estimated to be about $\pm 1{\cdot}5 \times 10^{-8}(\mathrm{K})^{-1}$. In order to ascertain that the values of $\Delta\alpha$ thus obtained

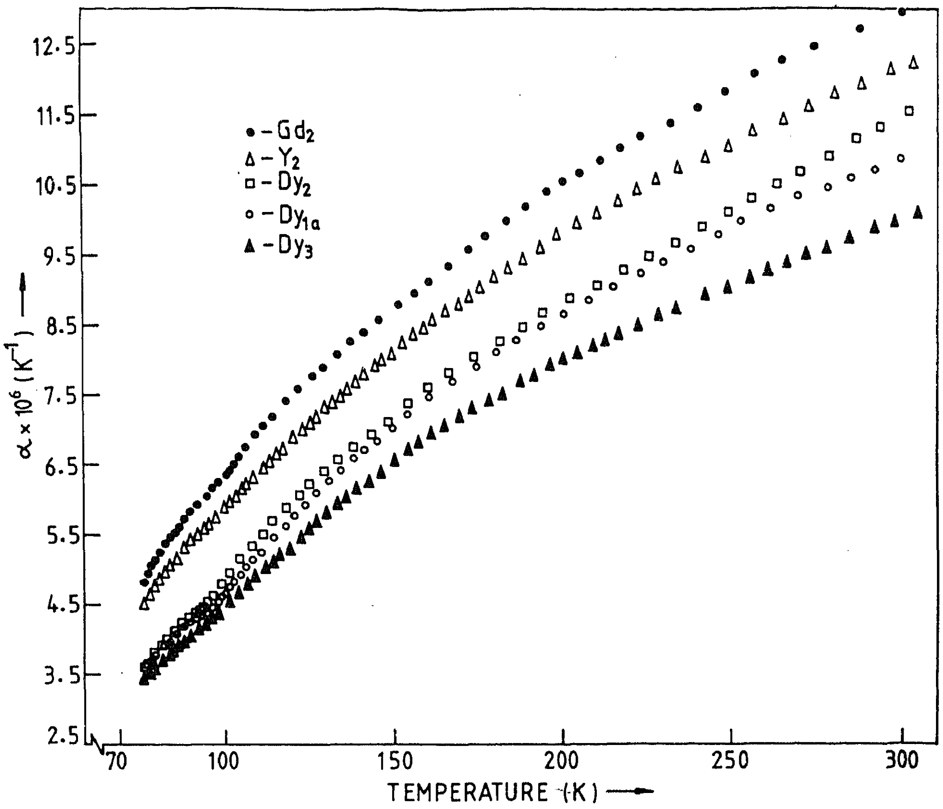

Figure 3. Temperature dependence of the linear thermal expansion coefficient α.

are indeed associated with the superconducting transition (and not due to any anomalies introduced by the extrapolation procedure), the same procedure was applied to the non-superconducting samples. It was found that in such samples the difference $\delta\alpha$ (at $T \approx 92\,\mathrm{K}$) in the two extrapolated values of α was always less than $1 \times 10^{-8}(\mathrm{K})^{-1}$ which is well within the experimental error. Some of the important parameters for all the specimens viz. the transition temperature T_c, oxygen content y, density ρ and the discontinuity $\Delta\alpha$ at T_c are depicted in table 1. Table 2 shows the α values for all the samples at three different temperatures.

It can be seen from figure 3 and table 2 that for all the superconducting compounds the behaviour of α is slightly specimen dependent. The reasons for this are not quite clear; it might probably be due to slight and unavoidable differences in the conditions of sample growth. Similar results have been reported earlier (see e.g. White *et al* [3]). For a given compound, α for superconducting phase has always been found to be greater than that for the non-superconducting phase. This could be due to the lower oxygen content of the non-superconducting sample. Olekhnovich *et al* [18] have indeed observed that in $Y_1Ba_2Cu_3O_y$ compounds, α decreases with decrease in the oxygen content y. It might also be mentioned that our values of α for Y and Dy compounds are in good agreement with those of White *et al* [3] and Schnelle *et al* [8]. Similarly α for Gd compounds agrees well with the results obtained by Kadowaki *et al* [6]. The present results, on the relative values of α for Y, Gd and Dy compounds, however, do not seem to agree with the results obtained by del Moral *et al* [4]. The

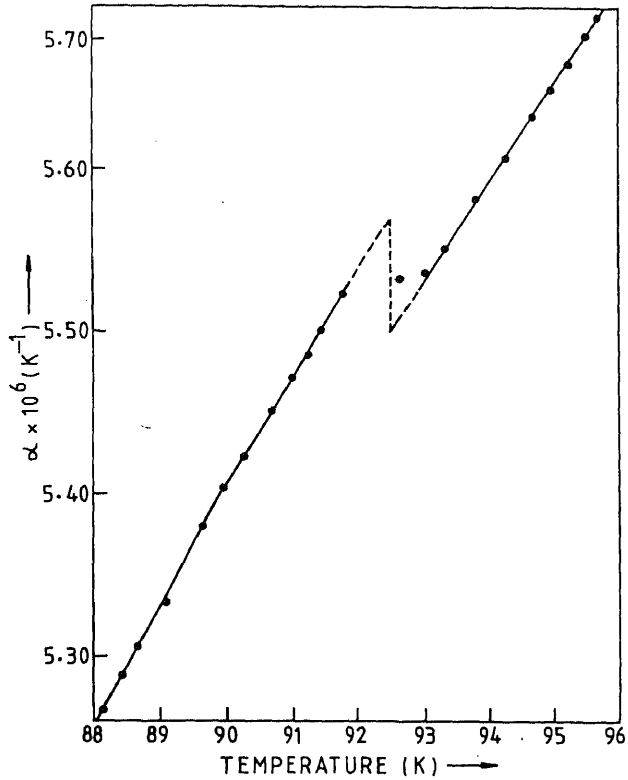

Figure 4. Behaviour of α in the vicinity of the transition temperature for the sample Y_2.

Table 1. The characteristic parameters of samples.

Sample	ρ gm/cm^3	y	T_c (K)	ΔT_c (K)	χ (at 77 K) (S.I. units)	$\Delta\alpha$ ($\times 10^{-8}$) (K)$^{-1}$
Y_1	5·23	6·93	92·0	1·4	−0·81	6·3
Y_2	5·54	6·92	92·4	1·0	−0·84	6·7
Y_3	5·54	6·43	not superconducting			
Gd_{11}	5·11	6·85	89·3	3·8	−0·78	3·1
Gd_1	5·11	6·93	90·6	1·2	−0·83	8·2
Gd_2	5·06	6·91	92·0	0·9	−0·85	8·7
Gd_3	5·06	6·39	not superconducting			
Dy_{11}	5·49	6·83	90·5	4·1	−0·73	7·2
Dy_1	5·49	6·92	92·0	1·1	−0·81	10·5
Dy_2	5·13	6·93	91·5	1·0	−0·84	11·4
Dy_3	5·13	6·45	not superconducting			

Table 2. The thermal expansion coefficient α of samples at various temperatures.

Sample	$\alpha(\times 10^{-6})$ (K)$^{-1}$ 80 K	100 K	250 K
Y_1	4·78	5·92	11·2
Y_2	4·76	5·88	10·60
Y_3	4·66	5·75	10·32
Gd_{11}	4·96	6·13	11·47
Gd_1	5·00	6·20	11·68
Gd_2	5·13	6·38	11·92
Gd_3	4·90	6·12	10·88
Dy_{11}	3·72	4·62	9·60
Dy_1	3·76	4·68	9·91
Dy_2	3·82	4·87	10·15
Dy_3	3·60	4·50	9·05

present study shows α values to be highest for Gd compounds and lowest for Dy compounds. On the other hand del Moral *et al* [4] have observed highest values for Dy and lowest values for Y compounds.

It is clear from table 1 that the values of $\Delta\alpha$ obtained in the present investigation for various superconducting compounds are in reasonable agreement with those reported in the literature. The absence of quantitative agreement between the results of different investigations might be due to the slight differences in the specimen growth conditions especially the final heat treatment. Experimental evidences for such a dependence on the condition of heat treatment has been obtained both for Gd and Dy samples (Gd_{11} and Dy_{11}). Sample Gd_{11} kept during the initial preparation at 450 °C in flowing oxygen for 36 h showed a jump $\Delta\alpha = (3{\cdot}1 \pm 1{\cdot}5) \times 10^{-8}(\text{K})^{-1}$. When the same sample was further annealed at 450 °C for another 36 h, the jump increased to $(8{\cdot}2 \pm 1{\cdot}5) \times 10^{-8}(\text{K})^{-1}$. The absolute values of α obtained before and after additional annealing were however, nearly same. The oxygen content also increased only slightly viz. from $y = 6{\cdot}85$ to 6·93. ΔT_c however, showed a marked change; decreasing from 3·8 to 1·2 K. Similar results were obtained for Dy samples and are shown in table 1.

Acknowledgements

The authors are indebted to Prof. A Mansingh for providing the GR 1620 capacitance bridge assembly and for many useful discussions. The authors will also like to thank Shri S N Das for helping with the iodometric titrations and Shri Somdutt Mehta for computational help. Financial assistance received from UGC, India, by one of the authors (AR) in the form of Senior Research Fellowship is gratefully acknowledged.

References

[1] V Bayot, C Dewitte, J P Erauw, X Gonze, M Lambricht and J P Michenand, *Solid State Commun.* **64**, 327 (1987)

[2] E du Tremolet de Lacheisserie, B Barbara and J H Henry, *J. Magn. Magn. Mater* **71**, L125 (1988)

[3] G K White, S J Collocott, R Driver, R B Roberts and A M Stewart, *J. Phys.* **C21**, L631 (1988)
[4] A del Moral, M R Ibarra, P A Algarabel and J I Arnaudas, *Physica* **C161**, 48 (1989)
[5] E Salomons, H Hemmes, J L Scholtz, N Koeman, R Brouwer, A Driessen, D G De Groot and R Griessen, *Physica* **B145**, 253 (1987)
[6] K Kadowaki, F E Kayzel and J J M Franse, *Physica* **C153–155**, 1028 (1988)
[7] Y Horie and S Mase, *Solid State Commun.* **69**, 535 (1989)
[8] W Schnelle, E Braun, H Broicher, R Domel, S Rupple, W Braunisch, J Harnischmacher and D Wohlleben, *Physica* **C168**, 465 (1990)
[9] E Braun, W Schnelle, H Broicher, J Harnischmacher, D Wohlleben, C Allgeier, W Reith, J S Schilling, J Bock, E Preisler and G J Vogt, *Z. Phys.* **B84**, 331 (1991)
[10] C Meingast, R Ahrens, B Blank, H Burkle, B Rudoff and H Wuhl, *Physica* **C173**, 309 (1991) (1991)
[11] S K Misra, M Kahrizi, J Kotlinski and M O Steinitz, *Solid State Commun.* **81**, 503 (1992)
[12] Y Z Ruan, L P Li, X L Hu, D K Peng, I B Hu and Y H Zhang, *Mod. Phys. Lett.* **B3**, 325 (1989)
[13] O I Kisil, A B Kruglov, A V Kuznetsov, E A Proasov and V P Sobolev, *Sov. J. Low Temp. Phys.* **15**, 543 (1989)
[14] M Lang, R Kursch, F Steglich, M Tachika and T Wolf, *Physica* **C185–189**, 939 (1991)
[15] Om Prakash, Ashok Rao and P N Dheer, *Pramana – J. Phys.* **39**, 665 (1992)
[16] S N Das, R Kapoor, S S Dubey and P N Dheer, *Physica* **B163**, 245 (1990)
[17] A I Nazzal, V Y Lee, E M Engler, R D Jacowitz, Y Tokura and J B Torrance, *Physica* **C153–155**, 1367 (1988)
[18] N M Olekhnovich, T E Zhabko, N S Orlova, V D Janovich, O I Pashkovskii and T L Zykova, *Cryst. Res. Technol.* **26**, 747 (1991)

PRAMANA
— journal of
physics

© Printed in India

Vol. 41, No. 5,
November 1993
pp. 429–442

Magnetic properties of ultra-fine particles of $Mn_{0\cdot5}Fe_{0\cdot5}Fe_2O_4$ spinel system

R V UPADHYAY and R V MEHTA
Department of Physics, Bhavnagar University, Bhavnagar 364 002, India

MS received 12 July 1993

Abstract. A systematic study of the magnetic properties of ultra-fine particles of $Mn_{0\cdot5}Fe_{0\cdot5}Fe_2O_4$ spinel system has been undertaken. The effect of temperature on the magnetic properties of particles and the ferrofluid has been studied. Analysis of the data yields information on the anisotropy constant, particle size distribution and superparamagnetic behaviour. The results are explained on the basis of existing theories.

Keywords. Magnetic properties; ferrofluid; particles

PACS Nos **75·50; 75·60**

1. Introduction

Study of transition metal oxides having a spinel structure is of much interest because of their remarkable electrical and magnetic properties [1–3]. These properties depend upon the type of magnetic ions residing on the tetrahedral (A) site and octahedral (B) site of the spinel lattice and the relative strength of the inter- and intra-sublattice interactions. This so-called cation distribution depends upon the preparation conditions [4–8]. It is well-known that the magnetic properties of ferrites depend upon the crystallite size of particles, because the properties of fine particles are drastically different from the bulk. This opens up an area of research that is very challenging scientifically as well as technologically. Fine particles are widely used for magnetic recording media, magnetic fluids (ferrofluids), catalysts, medical diagnostics, drug delivery systems and pigments in paints and ceramics [9–12]. Ultra-fine particles are single domain with diameter typically of the order of 100 A–150 A. For such particles, if the thermal energy (kT, where k is a Boltzmann constant and T the absolute temperature) is comparable to the magnetic anisotropy energy (KV, $K =$ anisotropy constant, $V =$ volume of the particle), the magnetic moment of the particle can relax during the measuring time which in turn, gives rise to a net zero magnetization in the absence of an applied magnetic field. Thus, an assembly of such particles exhibits superparamagnetic behaviour, i.e., zero remanence and coercivity [13]. In a real system of fine particles there exists a distribution of particle sizes. Therefore, in the magnetic properties of fine particles, the size distribution affects much, because of the relatively large surface to volume ratio.

In this paper we report a study of the ultra-fine ferrite particles of $Mn_{0\cdot5}Fe_{0\cdot5}Fe_2O_4$ (MF5) spinel system. The choice of this system is because of: (i) high value of domain magnetization (M_d) of $MnFe_2O_4$ (560 emu/cc) compared to Fe_3O_4 (510 emu/cc) at 0 K [1], (ii) the magnetocrystalline anisotropy (K_1) of $MnFe_2O_4$ ($0\cdot4 * 10^5$ erg/cc) is much lower than Fe_3O_4 ($1{\cdot}1*10^6$ erg/cc) at room temperature [14], (iii) low Curie temperature of $MnFe_2O_4$ (573 K compared to 858 K of Fe_3O_4) [1]. These properties are useful for preparation of ferro-fluid or magnetic fluid and their related applications.

A magnetic fluid consists of ultra-fine ferro-ferri-magnetic particles colloidally dispersed in a carrier liquid. Under the influence of an external magnetic field, such a fluid exhibits certain novel phenomena and several of its physical properties are modified [15–17]. The most commonly used magnetic material in ferrofluid at present is iron oxide, like magnetite, maghemite, etc. Many new engineering devices like rotating shaft seals, ferrofluid dampers, sensors, etc. are developed using ferrofluids [18–22]. But all these devices have different requirements for the properties of fluids. For example, in ink-jet printer for a character recognition, a ferrofluid involving particles of high remanence is required, while in rotating shaft seals, one prefers particles with low magnetocrystalline anisotropies. For some applications where movement of the fluid around a close loop is required, one needs fluid which has a large change in magnetization with a small change in temperature, i.e., low Curie temperature with large M_s. This property is the basis of an energy conversion system [23]. Therefore it is very important to know, before carrying out any fine particle preparation for magnetic fluid, for what exact application one needs this particles. Here our aim is to prepare a fluid with high saturation magnetization and low viscosity, which may be suitable for rotary shaft seals. Recently we have synthesized a stable magnetic fluid using 10% Mn substitution in Fe_3O_4 and studied its rheological properties [24]. This paper reports a detailed study of 50% Mn substituted Fe_3O_4 system.

2. Experimental details

2.1 *Preparation of fine particles and fluid*

Generally, a large number of techniques were used to prepare magnetic fine particles, like chemical reduction, sputtering, aersol synthesis, etc. [25–30], but here we have used a standard co-precipitation technique to produce fine particles of $Mn_{0{\cdot}5}Fe_{0{\cdot}5}Fe_2O_4$ system. The GPR grades, $FeCl_3 6H_2O$, $MnSO_4 4H_2O$ and $FeSO_4 7H_2O$ were used to obtain Fe^{3+}, Mn^{2+} and Fe^{2+} ions in an aqueous solution. These salts were mixed in required molar ratio in distilled water and added to 8M NaOH solution with constant stirring at room temperature. The precipitate was heated to 80°C with constant stirring and pH was maintained at 10·5. Aliquots of the reaction mixture was collected and washed with distilled water many times. Finally, the precipitate was washed with acetone and dried in air. The composition was checked by atomic absorption spectrometer. The result is given in table 1. The particles were coated with oleic acid and heated to 95°C for 5 min. In order to coagulate the oleic acid coated particles an acidic solution was added. After decantation, the product was washed with distilled water and acetone. This acetone wet slurry was dispersed in ISOPAR-M carrier and acetone was removed by warming the solution. The resulting fluid was found to be stable. The dispersion was liquid at room temperature and solid below 200 K.

2.2 *Structural characterization*

X-ray powder diffraction pattern was recorded on a Philips PW1130/90 X-ray diffractometer using CuKα radiation ($\lambda = 1{\cdot}5414$ A). The average particle size ($D_x A$)

Table 1. Characteristics properties of $Mn_{0·5}Fe_{0·5}Fe_2O_4$ system. D_e, D_x and D_m are electron microscopy, X-ray and magnetic particle size, respectively.

	: Fe/Mn	Ratio		
Chemical Analysis	: (Cal)	5	(Obs)	4·99
Structural Analysis				
a(Å)	: 8·445			
D_x(Å)	: 70			
D_e(Å)	: 69			
D_m(Å)	: 69			
σ_e	: 0·32			
σ_m	: 0·46			
Magnetic properties	: n_B(Bohr magneton)			
300 K	: 2·6			
4·2 K	: 3·3			

was calculated using Scherrer's formula, using the full width at half maximum intensity of the plane (311) of the pattern. The specimen was also examined using an AEI Cornith Transmission Electron Microscope (TEM).

2.3 *Magnetization measurements*

Room temperature magnetization measurements were carried out using a vibrating sample magnetometer (VSM). Low temperature measurements were performed using Oxford Instruments CF1200 cryostat. The magnetometer was calibrated using a nickel standard. DC-susceptibility measurement for fluid was carried out after the sample was cooled in zero field (i.e. randomly oriented anisotropy axes) and then warmed in presence of a small magnetic field ($H = 15$ Oe). The temperature decay of remanence (of fluid) was performed after the sample was cooled to 4·2 K in zero field. A saturating field of 10 kOe was applied, after setting the field to zero the remanence magnetization (M_r) was measured after 100 s. This procedure was repeated for each temperature.

2.4 *AC-susceptibility measurements*

The temperature dependence of the ac-susceptibility was measured between 80 K and 300 K using the technique described in [31]. The induced voltage was measured with both decreasing and increasing temperature for which no detectable hysteresis was measured (because the ac-susceptibility technique does not detect the irreversible component of magnetization).

2.5 *Mössbauer measurements*

Mössbauer measurements were carried out using a constant acceleration Mössbauer spectrometer with ^{57}Co source. Magnetic field was applied perpendicular to the direction of gamma ray propogation.

3. Results and discussion

3.1 *Microstructure analysis*

Figure 1 shows the X-ray diffraction pattern of MF5 with Miller indices (*hkl*). The structure of the powder prepared was definitely confirmed as isostructural with spinel i.e. cubic with space group F*d*3*m*. It is known [32] that if a sufficient amount of Mn^{3+} ion is present in the B-site, a tetragonally deformed ferrite coexists with the cubic spinel structure. In the present case no such peaks were observed, indicating the complete transformation of hydroxide into the spinel ferrite which is further confirmed by the atomic absorption technique, (table 1). In table 1 structure parameter, $a(A)$, and particle size, $D_x(A)$ are given. In comparison with magnetite, the value of $a(A)$ is greater. This observed increase can be explained by considering the ionic size effect. Because larger Mn^{2+} ion (0·81 A) replaces the smaller Fe^{3+} ion (0·63 A) from A-site, resulting in increase in $a(A)$. Considering the site preference energies of the constitutent ions [33] the cation distribution can be written as,

$$(\mathrm{Mn}^{2+}_{0\cdot5}\mathrm{Fe}^{3+}_{0\cdot5})^{\mathrm{A}}[\mathrm{Fe}^{2+}_{0\cdot5}+\mathrm{Fe}^{3+}_{1\cdot5}]^{\mathrm{B}}\mathrm{O}^{2-}_{4}. \tag{1}$$

Figure 2 shows the electron micrograph for the MF5. The particle size and distribution parameters were obtained using Carl-Zeiss particle size analyser and method of O'Grady *et al* [34]. The line through the data points in figure 3 corresponds to the log-normal distribution best fit to the data given by,

$$F(D)dD=(1/\sigma D\sqrt{2\pi})*\exp[-\{\ln(D/D_0)\}^2/(2\sigma^2)]dD \tag{2}$$

where, $F(D)$ is the frequency function, D is the diameter of the particle, D_0 is the median physical diameter of the particle, σ is the standard deviation of $\ln(D/D_0)$. The parameters obtained are given in table 1. The result is in good agreement with the particle size determined from X-ray diffraction.

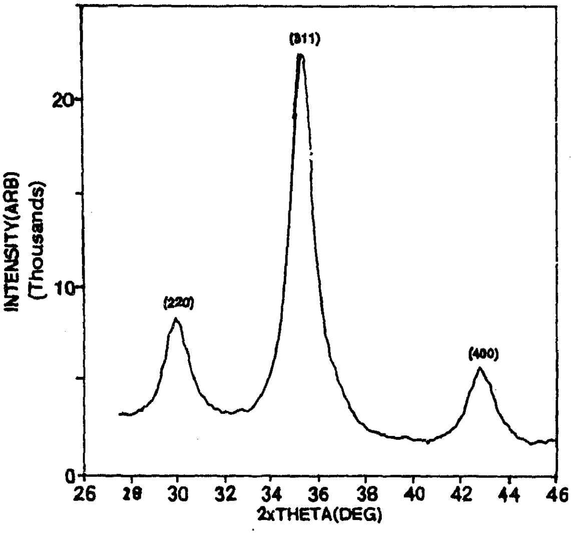

Figure 1. X-ray diffractogram pattern of MF5 fine particles.

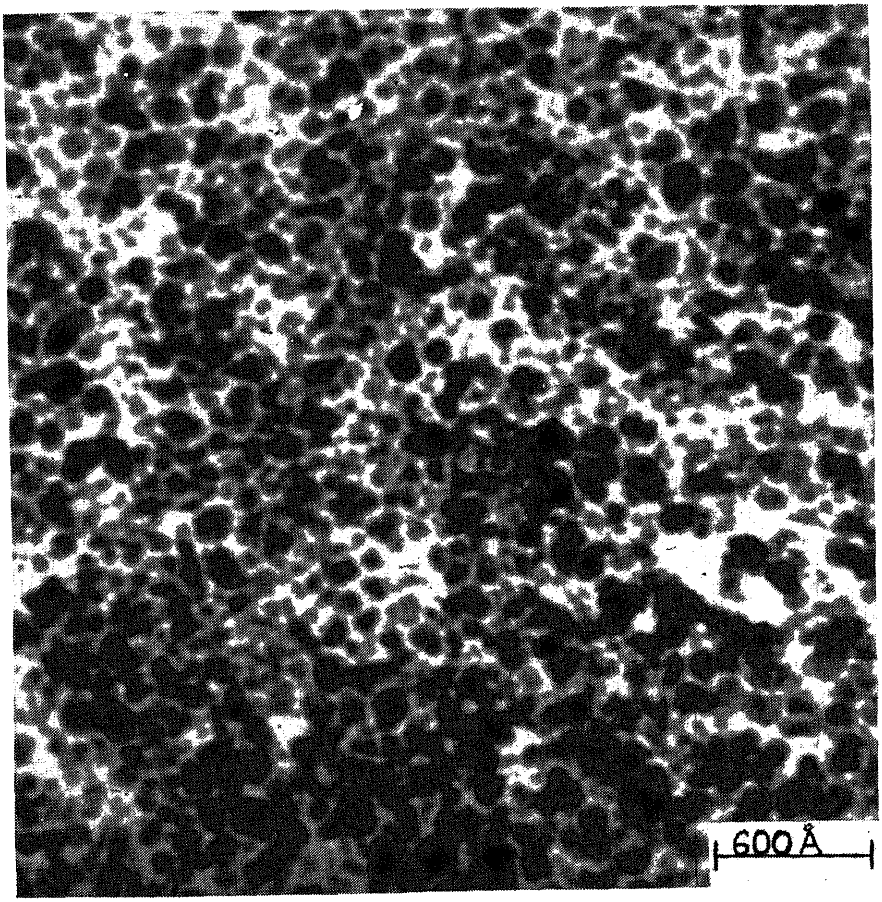

Figure 2. Electron micrograph of MF5 system.

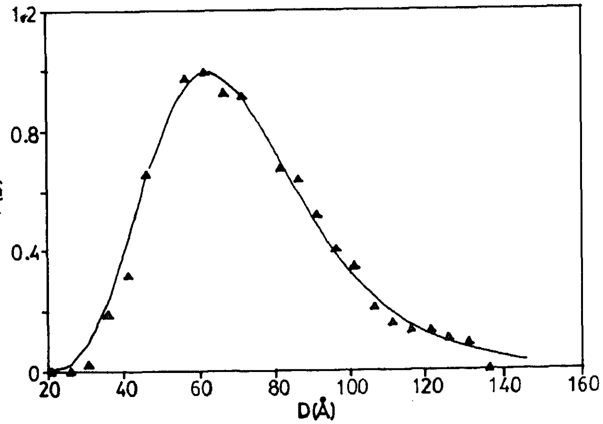

Figure 3. Particle size distribution determined from figure 2. The line corresponds to best fit of equation (2).

3.2 *Magnetic properties of particles*

Using the value of saturation magnetization, M_s, obtained from the M versus $1/H$ curve, the magnetic moment per formula unit, n_B, in Bohr magneton was calculated (table 1). Figure 4 shows the variation of saturation magnetization with temperature. The M_s value at 0 K was obtained by extrapolating the curve of M versus T at 0 K, and n_B was calculated. This n_B value is much lower than that calculated using (1). Therefore, the observed low value of magnetic moment cannot simply be explained by considering the cation distribution. It is evident from the X-ray and electron microscopy results that the particle size of ~ 70 A. Therefore one possibility of low M_s or n_B may be due to decrease in particle size. As the particle size decreases, the percentage of the atoms on the surface of the particle increases, as a result of this there are large number of spins which are uncoupled on the surface, i.e., spin pinning effect. Hence n_B decreases. The observed low value of Curie temperature also supports the concept of weakened spin coupling in the disordered surface layer. Inset in figure 4 shows the reduced magnetization variation with reduced temperature. The line through the data points is a line derived from Weiss–Langevin theory of ferromagnetism for the classical case, i.e. $J = \infty$. The low field data show that the particles have zero remanence and coercivity, indicating that the system is superparamagnetic at the time scale of measurement (100 s). In order to get further insight into this Mössbauer study was carried out.

Figure 5a shows the room temperature Mössbauer spectrum of the particles. The observed relaxation behaviour is explained as follows. It is known that [35] when particle size reduces below 200 A the magnetic anisotropy energy (KV) may become comparable to the thermal energy (kT) as a result the phenomena of fluctuation of direction of the magnetization commences. If we consider a particle with uniaxial anisotropy and with the magnetic energy given by the expression:

$$E(\theta) = KV \sin^2(\theta) \tag{3}$$

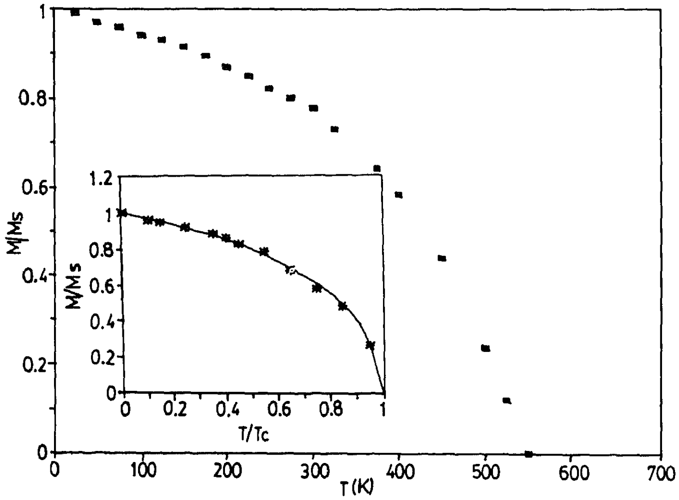

Figure 4. Temperature variation of magnetization for uncoated particles. Inset: Reduced magnetization versus reduced temperature, line is the classical case i.e. $J = \infty$ (see text).

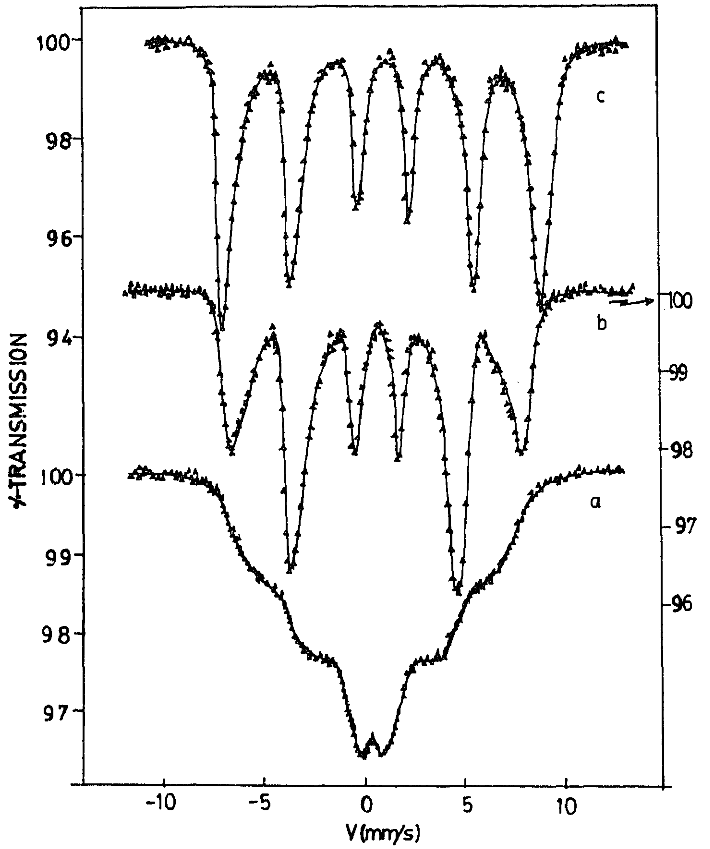

Figure 5. Mössbauer spectra of uncoated particles. (a) $T = 298\,\mathrm{K}$, $H = 0\,\mathrm{kOe}$. (b) $T = 298\,\mathrm{K}$, $H = 6\,\mathrm{kOe}$, (c) $T = 80\,\mathrm{K}$, $H = 0\,\mathrm{kOe}$.

where θ is the angle between the magnetization direction and an easy direction of magnetization, there are two potential modes, (i) collective magnetic excitation and (ii) superparamagnetic relaxation (SP). In (i) the magnetization vector performs small fluctuation around an easy direction. If these fluctuations are fast compared to the Mössbauer time scale, there will be a reduction in average magnetic hyperfine field given by [35]):

$$B_{\mathrm{obs}} = B_0[1 - 1/2(kT/KV)] \tag{4}$$

for $KV \gg kT$. Where, B_0 is the hyperfine field of a larger particle, i.e. in the absence of fluctuation. In (ii) the magnetization vector fluctuates between the two energy minima, $\theta = 0$ and π (equation 3). For this case the superparamagnetic relaxation time is given by [36, 37]

$$\tau = \tau_0 \exp[KV/kT] \tag{5}$$

where τ_0 is a proportionality constant (10^{-10}–10^{-12} s). The temperature at which the magnetic hyperfine splitting collapses due to fast SP relaxation is called SP blocking temperature, T_B. Therefore, the observed behaviour at 300 K may be because of these two effects. But as the SP relaxation can be suppressed effectively by applying an external magnetic field, a field of 6 kOe was applied at room temperature. Figure 5b shows the effect of this field on the Mössbauer spectra. This confirms the SP behaviour in the system. Figure 5c shows the 80 K spectrum of MF5, which clearly indicates that for this system the T_B is > 80 K (in Mössbauer time scale i.e. $5 * 10^{-9}$ for ^{57}Fe).

3.3 *Magnetic properties of ferrofluid*

The above fine particles were used to prepare the magnetic fluid. Long range stability was achieved by coating particles with long chain surfactant. At room temperature M-H curve shows zero remanence and coercivity (figure 6). To describe magnetization of the magnetic fluid several theoretical models are being used [38]. The simplest is the Langevin's model, where each magnetic particle is considered to be independent, and the system resembles a paramagnetic gas. The magnetization M as a function of applied field H is given by,

$$M = M_s\, L(\alpha),\ L(\alpha) = \coth(\alpha) - 1/\alpha,\ \alpha = \mathrm{m}H/kT. \tag{6}$$

Applying the above function for a log-normal distribution of particles, Chantrell *et al* [39] deduced a relation to determine the mean grain diameter D_m and the standard deviation σ which is given by

$$D_m = [(18kT/\pi M_d)\{\chi_i/3\Phi M_d H_0\}^{1/2}]^{1/3} \tag{7}$$

$$\sigma = [\ln(3\chi_i H_0/\Phi M_d)^{1/2}]/3 \tag{8}$$

where, χ_i = initial susceptibility, Φ = volume fraction of particles in fluid, $1/H_0$ = point where the extrapolation of linear part of $M - 1/H$ curve crosses the $M = 0$ axis (large H). Using (7, 8) mean diameter and σ were calculated and same are given in table 1. Equations (7) and (8) are useful when there is no particle-particle interaction, because this makes a rather small correction to particle diameter, whereas there is a large correction to the standard deviation (30 to 40%) [40]. Recent studies by Hilo *et al*

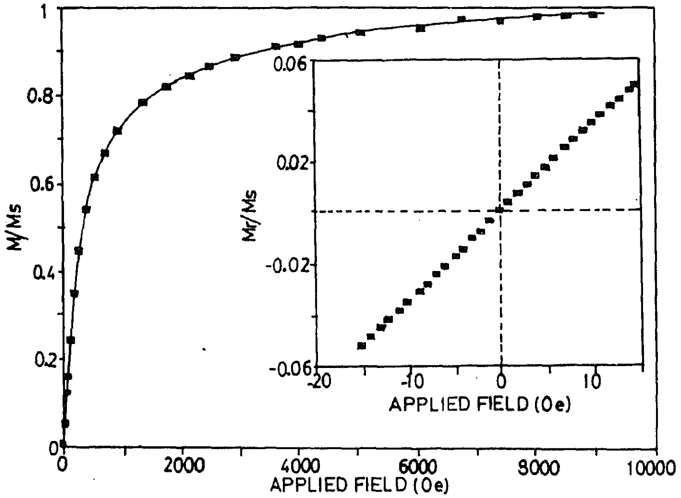

Figure 6. Isothermal magnetization as a function of applied field for MF5 fluid at 298 K. Line through the data points is calculated using equation (11). Inset: The low field data.

[41] indicate that even in most dilute system there exists a possibility of particle-particle interaction. Therefore, in our earlier study [42] we have used the method given by Shah and Mehta [43]. According to this method at low field larger particles are completely oriented while the finer particles are oriented at high field. Therefore one can find a uniform distribution extending from a minimum volume (V_{min}) to a maximum volume (V_{max}). Using the asymptotic behaviour of (6) one obtains for low field region, i.e. $mH/kT \ll 1$,

$$\bar{M} = M/M_s = x^a/3 \tag{9}$$

and for high field region, i.e. $mH/kT \gg 1$,

$$\bar{M} = M/M_s = 1 - 1/x^b \tag{10}$$

where, $x^a = M_d\, V_{\mathrm{max}} H/kT$, and $x^b = M_d\, V_{\mathrm{min}} H/kT$. These values of V_{max} and V_{min} can be obtained from the reduced initial susceptibility, $\chi_i = \mathrm{d}\bar{M}/\mathrm{d}H$ for $H < 30\,\mathrm{Oe}$, and plot of M versus $1/H$ in high field region, respectively. Using these values one can obtain the magnetization curve using the relation,

$$\begin{aligned}\bar{M} &= \int_{V_{\mathrm{min}}}^{V_{\mathrm{max}}} L(M_d\, VH/kT)\mathrm{d}V/(V_{\mathrm{max}} - V_{\mathrm{min}}) \\ &= kT/[M_d H(V_{\mathrm{max}} - V_{\mathrm{min}})] \ln\{(V_{\mathrm{min}}/V_{\mathrm{max}})\sinh(x^b)/\sinh(x^a)\}.\end{aligned} \tag{11}$$

Figure 6 shows the M/M_s versus H curve for this fluid. Using the values of V_{min} and V_{max} from this result and using (11) M was calculated for each value of H and same is shown as solid line in figure 6. In the present case the values of diameters correspond to these volumes are 30 A and 107 A, respectively. The average value of these is 69 A which is in good agreement with X-ray and electron microscopy results (table 1).

Figure 7 shows the variation of dc-susceptibility with temperature. The observed behaviour can be explained by considering Néel's model [37]. For a dc-measurement the experimental time is taken to be 100 s. This gives a critical volume, V_p, defined

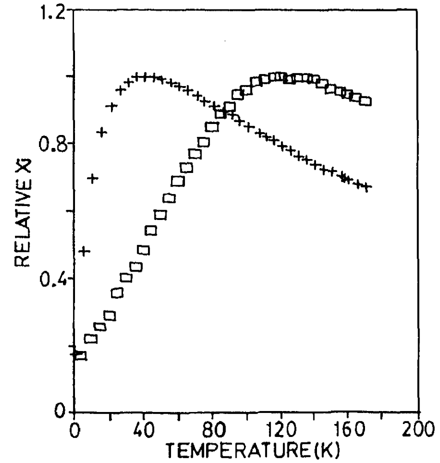

Figure 7. DC-susceptibility variation with temperature. (+) calculated using equation (15) and (□) experimental.

by [13],

$$K V_p = \ln(t_m f_0) k T_{\rm B} \tag{12}$$

where, t_m is measuring time. According to Wohlfarth [44] the susceptibility for a particle with volume V is given by

$$\begin{aligned} \chi_i &= M_d^2/3K, \qquad T < T_B, \text{ (Block)} \\ \chi_i &= M_d^2\, V/3kT, \quad T > T_B, \text{ (SP)} \end{aligned} \tag{13}$$

But as we have discussed earlier, in real system there will be a distribution of particle size, i.e. distribution of T_B, therefore the mean blocking temperature, $\langle T_B \rangle$, corresponding to mean volume, V_m, within a system can be defined as [13]

$$\langle T_B \rangle = [K V_m / k \ln(t_m f_0)]. \tag{14}$$

For a non-interacting fine particle system with randomly oriented easy axes the reduced initial susceptibility, $\bar{\chi}_i (= \chi_i/M_s)$ is given by [41],

$$\bar{\chi}_i(T) = (M_d V_m/3kT) \int_0^{y_p(H,T)} y f(y) \mathrm{d}y + (M_d/3K) \int_{y_p(H,T)}^{\infty} f(y) \mathrm{d}y \tag{15}$$

where, $y = V/V_m$ and $y_p(H, T) = V_p(H, T)/V_m$. For dc-measurement, when $H \to 0$, the critical limit for SP behaviour will be $V_p(H, T) = V_p(0, T)$. If K remains invariant, the reduced critical limit for SP is $y_p(0, T) = T/T_B$. In (15), the first integral represents the contribution of SP particles, which is the main contribution to susceptibility, and second represents the contribution of blocked particles. Therefore the variation of χ_i with T will give a peak at $T = T_g$. But recently El-Hilo *et al* [41] have studied the influence of dipolar interaction between the particles on the value of T_g by considering the effects of particle interaction on the blocking temperature. They found that in the case of weakly interacting system the effective mean blocking temperature, $\langle T_{B_{\rm eff}} \rangle$, is given by

$$\langle T_{B_{\rm eff}} \rangle = 1/2[\langle T_B \rangle + \langle T_B \rangle \{1 + (4\xi_1 M_d^4 \ln(t_m f_0)/3K^2)\}^{1/2}] \tag{16}$$

where ξ_1 is an interaction parameter. When $\xi_1 \to 0$, $\langle T_{B_{\rm eff}} \rangle \to \langle T_B \rangle$. Since the temperature of the peak in dc-susceptibility is directly related to $\langle T_{B_{\rm eff}} \rangle$, i.e. mean energy barrier, T_g will occur at higher temperature, due to the dipolar interaction. This is shown in figure 7. The position of the peak was found to shift to lower temperature with dilution, but even for dilute system position of the peak does not superimpose on the curve obtained using (15) indicating that even in this case there exist a finite clustering in the system. In order to find the energy barrier distribution, i.e. blocking temperature distribution, the temperature decay of remanence measurement was carried out.

Figure 8 shows the temperature dependence of remanent magnetization. These data show the classical behaviour similar to that previously reported [41, 45]. As it is known that the remanence at any temperature gives the measure of the particle fraction which are blocked, the energy distribution can be obtained by fitting the decay curve using the expression of Tari *et al* [46]

$$M_r(T) = M_r(0) \left[\int_{T/\langle T_B \rangle}^{\infty} f(T_R) \mathrm{d}y \right] \tag{17}$$

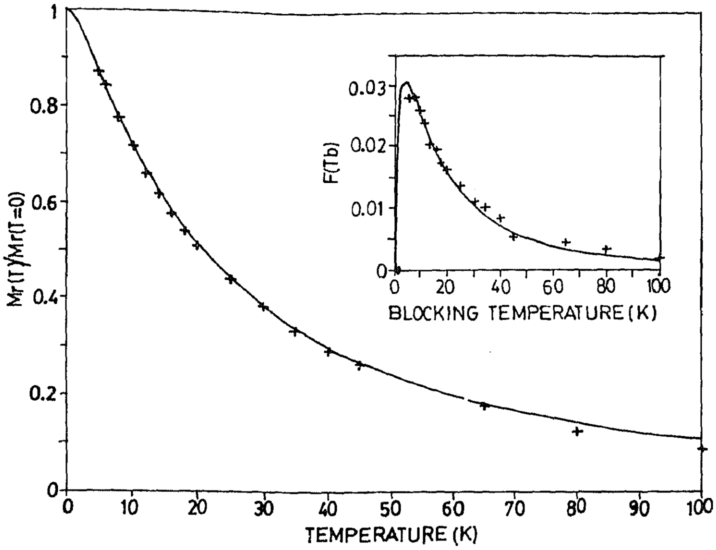

Figure 8. Temperature decay of remanence for magnetic fluid. Inset: Distribution of blocking temperature. Solid line is the theoretical fit to the data (see text).

where, $T_R = T_B/\langle T_B \rangle$ = reduced blocking temperature and $f(T_R)$ is the distribution of reduced blocking temperature. The curve in figure 8 was fitted to the solid line which was computed from equation (17) using a log-normal distribution of T_R, i.e.,

$$f(T_R) = (1/(\sigma_y T_R \sqrt{2\pi}))[\exp(-(\ln T_R)^2/2\sigma_y^2)] \tag{18}$$

The fit was achieved using only two variable parameters, $\langle T_B \rangle$ and σ_y. Here $\langle T_B \rangle$ is the temperature at which half of the total magnetic volume will exhibit blocked behaviour. The distribution parameter used were $\langle T_B \rangle = 18\,\mathrm{K}$ and $\sigma_y = 1{\cdot}2$ of log-normal distribution. Since $T_B \propto KV$, and $\mathrm{d}M_r/\mathrm{d}T$ is proportional to $f(T_B)$. The inset in figure 8 represents the differential of remanence data. The solid line through the data points is calculated using the above values of blocking temperature and σ_y. This value of $\langle T_B \rangle$ was used to estimate the value of anisotropy constant, K, using the relation [47],

$$KV_m = 32k\langle T_B \rangle. \tag{19}$$

Here we have used the value of $f_0 = 10^{12}\,\mathrm{s}^{-1}$. This calculation gives the value of $K = 2{\cdot}9 \times 10^5\,\mathrm{erg/cm^3}$. According to Hilo *et al* [41] the remanence measurements are not sensitive to interaction effect, therefore the value of blocking temperature is a true value, not effective T_B. In the present system it was observed that at 4·2 K the value of $M_r/M_s = 0{\cdot}39$ and which on extrapolation to 0 K gives 0·42. This indicates that 16% (because for randomly oriented axes the value reaches 0·5 [48]) of the particle does not contribute to remanence. Similar effects were also observed by other workers [41, 45]. It is seen from figure 8 that remanence is nearly zero for $T > 115\,\mathrm{K}$, indicating that for a time scale of 100 s the system becomes SP above this temperature. For such a system equation (11) can be applied and when M/M_s versus H/T is plotted one observes the superposition of curves for different temperatures. Figure 9 shows the H/T superposition for two different temperature. The solid line through the data

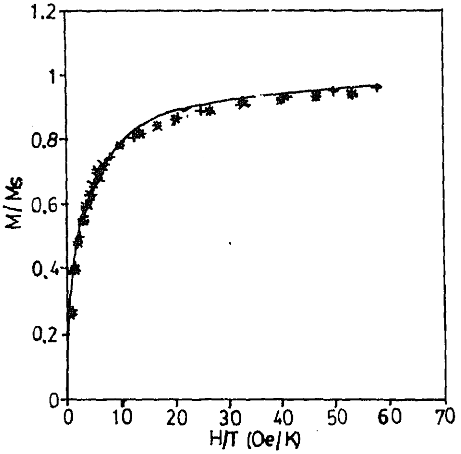

Figure 9. H/T superposition for MF5 fluid. + 121 K, $*$ 145 K.

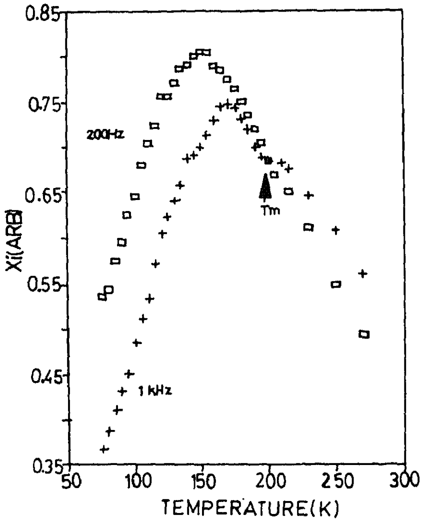

Figure 10. Variation of ac-susceptibility with temperature.

point is calculated using (11). The observed agreement and superposition of curves clearly suggests that the system is SP for $T > 120$ K, which is in accordance with the observed zero remanence and coercivity and SP behaviour in Mössbauer for the particles and the fluid.

Figure 10 shows the ac-susceptibility measurements for two different frequencies. The ac-susceptibility measures only a reversible part of magnetization curve. Based on our earlier discussion it is certain that the observed peak is connected with the thermally activated reversal process of the magnetic moments of SP particles, i.e. blocking temperature. At T_B the relaxation time of thermal activation of grain volume becomes equal to the reciprocal of measuring frequency. Therefore higher the frequency the T_B will be higher, this is observed in the present case (figure 10). The change in the behaviour around 200 K is due to the change in the state, i.e. solid to liquid. Therefore the system exhibits two relaxation times in magnetization dynamics;

(i) t_N, for Néel process and (ii) t_B, Brownian motion. Below the melting temperature t_B becomes infinity therefore the main contribution to the relaxation mechanism will be Neel, while above the melting point it depends upon the magnitude of the individual. Both these relaxation times are given by,

$$t_N = t_0 \exp(KV/kT),$$
$$t_B = 3V'\eta/kT. \tag{20}$$

where, V' = hydrodynamic volume, η = viscosity of fluid. From (20) it can be seen that the relaxation domain for t_N is very large compared to t_B, i.e. t_N varies with particle size from 10^{-12} to 10^{12}s while t_B changes only by one order, 10^{-5} to 10^{-6}s. Because of these one can use the frequency dependence of ac-susceptibility technique (above melting point) for the characterization of magnetic fluid, i.e. agglomeration or clustering.

Conclusion

The present study reveals that
(1) With 50% substitution of Mn it is possible to synthesize ultra-fine particles having average diameter of 70 A. (2) The value of saturation magnetization of uncoated particles are affected by surface pinning effect. (3) Sterically stabilized colloidal dispersion of these particles gives a stable magnetic fluid of 350 G. (4) This system was found to obey log-normal particle size distribution. (5) Temperature decay of remanence gives the anisotropy value of $2{\cdot}9 \times 10^5$ erg/cc. (6) System behaves as superparamagnet above 80 K.

Acknowledgements

The authors are thankful to Drs S W Charles and Steen Mørup for providing experimental facilities and valuable discussion.

References

[1] J Smit and H P J Wijn, "*Ferrites*" (Eindhoven, Philips, 1959)
[2] J B Goodenough, *Prog. Solid State Chem.*, **5**, 145 (1971)
[3] C P Poole and H A Farach, *Z. Phys.*, **B47**, 55 (1982)
[4] J Schuele and V D Deetscreek, *J. Appl. Phys.*, **32**, 235S (1961)
[5] T Sato, C Kuroda, M Saito and M Sugihara, *Proc. Int. Conf. on ferrite.*, Tyoto, 1970 (University Park Press, Tokyo, 1972) 72
[6] R E Vadenberghe, R Vanleerberghe and Robbrecht, *J. Magn. Magn. Mater.*, **15–18**, 1117 (1980)
[7] T Sato, *IEEE Trans. Magn.*, **MAG-6**, 795 (1970)
[8] M Kiyama, *Bull. Chem. Soc. Jpn.*, **951**, 134 (1978)
[9] E Matijevic, *MRS bulletin*, **XIV**, 19 (1989)
[10] M Ozaki, *MRS bulletin*, **XIV**, 35 (1989)
[11] M P Scharrock and R E Bodnar, *J. Appl. Phys.*, **57**, 3919 (1989)
[12] R E Rosensweig, *U.S. Patent* **3**, 917 538 (1975)
[13] C P Bean and J D Livingston, *J. Appl. Phys.*, **305**, 120S (1959)
[14] R F Penoyer and M W Shafer, *J. Appl. Phys.*, **30**, 315S (1959)
[15] R E Rosensweig, *Adv. Electron. Electron. Phys.*, **48**, 103 (1979)
[16] R V Mehta, *J. Sci. Ind. Res.*, **44**, 500 (1985)

[17] S W Charles and J Popplewell, *Endeavour*, **6**, 153 (1982)
[18] M Zahn and K E Shanton, *IEEE Trans. Magn.*, **MAG-16**, 387 (1980)
[19] S W Charles and R E Rosensweig, *J. Magn. Magn. Mater.*, **39**, 190 (1983)
[20] S Kamiyama and R E Rosensweig, *J. Magn. Magn. Mater.*, **65**, 401 (1987)
[21] E Blums, R Ozols and R E Rosensweig, *J. Magn. Magn. Mater.*, **85**, 303 (1990)
[22] R K Bhatt, P M Trivedi, G M Sutariya, R V Upadhyay and R V Mehta, *Indian J. Pure Appl. Phys.*, **33**, 113 (1993)
[23] E L Resler and R E Rosensweig, *AIAA J.*, **2**, 1418 (1964)
[24] G M Sutariya, R V Upadhyay and R V Mehta, *J. Colloid. Interface Sci.*, **155**, 152 (1993)
[25] T Miyahara and K Wawakauri, *IEEE Trans. Magn.*, **MAG-23**, 2877 (1987)
[26] S Komarneni, E Fregau, E Breval and R Roy, *J. Am. Ceram. Soc.*, **71**, C-26 (1988)
[27] G Xiao and C L Chien, *J. Appl. Phys.*, **61**, 3308 (1987)
[28] C F Kernizan, K H Klabunde, C M Sorensen and G C Hadjipanayis, *J. Appl. Phys.*, **67**, 5897 (1990)
[29] C Hayashi, *J. Vac. Sci. Technol.*, **A5**, 1375 (1987)
[30] V Pillai, P Kumar and D O Shah, *J. Magn. Magn. Mater.*, **116**, L299 (1992)
[31] F Soffge and Schmidbauer, *J. Magn. Magn. Mater.*, **24**, 54 (1981)
[32] J B Goodenough, *Magnetism and Chemical Bond* (Wiley, New York, 1963)
[33] M Robbins, *J. Phys. Chem. Solid*, **26**, 831 (1965)
[34] K O'Grady and A Bradbury, *J. Magn. Magn. Mater.*, **39**, 91 (1984)
[35] S Mørup, J A Dumesic and H Topsøe, "*Application of Mössbauer Spectroscopy*" Edited by R L Cohen (New York, Academic Press, 1980) 1
[36] S Mørup, H Topsøe and B S Clausen, *Phys. Scr.*, **25**, 713 (1982)
[37] L Neél, *Ann. Geophys.*, **5**, 99 (1949)
[38] M I Shliomis, A F Pshenichnikov, K I Morozov and I Yu Shurubor, *J. Magn. Magn. Mater.*, **85**, 40 (1990)
[39] R W Chantrell, J Popplewell and S W Charles, *IEEE Trans. Magn.*, **MAG-14**, 975 (1978)
[40] A Bradbury, S Menear, K O'Grady and R W Chantrell, *IEEE Trans. Magn.* **MAG-20**, 1846 (1984)
[41] M El-Hilo, K O'Grady and R W Chantrell, *J. Magn. Magn. Mater.*, **114**, 295, 307 (1992)
[42] R V Upadhyay, G M Sutariya and R V Mehta, *J. Magn. Magn. Mater.*, **123**, 262 (1993)
[43] H S Shah and R V Mehta, *Indian J. Pure Appl. Phys.*, **11**, 537 (1973)
[44] E P Wohlfarth, *Phys. Lett.*, **A70**, 489 (1989)
[45] R W Chantrell, M El-Hilo and K O'Grady, *IEEE Trans. Magn.*, **MAG-27**, 3570 (1991)
[46] A Tari, R W Chantrell, S W Charles and J Popplewell, *Physica* **B97**, 599 (1984)
[47] D P E Dickson, N M K Reid, C A Hunt, H D Williams, M El-Hilo and K O'Grady, (In Press) (1993)
[48] E C Stoner and E P Wahlfarth, *Philos. Trans. R. Soc., London*, ser **A240**, 599 (1948)

PRAMANA
— journal of
physics

© Printed in India

Vol. 41, No. 5,
November 1993
pp. 443–451

Electric field gradient in transition metal – scandium

B B PANIGRAHI and N C MOHAPATRA*
Department of Physics, Khallikote College, Berhampur 760001, India
*Department of Physics, Berhampur University, Berhampur 760007, India

MS received 9 March 1993; revised 29 July 1993

Abstract. Electric field gradient in *hcp* transition metal scandium has been calculated as the sum of contributions from lattice ions and conduction electrons. For the lattice contribution q_{latt}, a point-charge model has been assumed. The contribution from conduction electrons q_{el}, on the other hand, has been evaluated by carrying out an energy-band calculation using non-local transition-metal model potential. The results obtained are: $q_{\text{el}} = -106{\cdot}11 \times 10^{13}\,\text{esu/cm}^3$ and $q_{\text{latt}} = 122{\cdot}17 \times 10^{13}\,\text{esu/cm}^3$. The net field gradient $(q_{\text{el}} + q_{\text{latt}})$ of $16{\cdot}06 \times 10^{13}\,\text{esu/cm}^3$ agrees quite well with the experimental result, $|q_{\text{expt}}| = 13 \times 10^{13}\,\text{esu/cm}^3$. Directions of further improvement in the theory are discussed.

Keywords. Electric field gradient; scandium metal; model potential

PACS No. 76·60

1. Introduction

It is now well-known [1, 2] that if conduction electron wave-functions are determined in the conventional crystal potential (i.e. its $l = 0$ component only), electric field gradient (EFG) due to these electrons would consist of two contributions: one from the anisotropic distribution of electrons in Fermi volume and the other from the perturbation of the Fermi surface electrons by the $l = 2$ component of the crystal potential. The latter, referred to [1] as the Watson–Gossard–Yafet (WGY) mechanism [2], is particularly important for transition metals which have high density of electron states at Fermi-energy. The contribution to EFG from WGY mechanism is opposite in sign to the lattice contribution and may be as large as two or three orders of magnitude of the latter.

On the other hand, if model potentials are used in determining the band wave functions, the resulting EFG due to conduction electrons will be given exclusively by the electrons in the Fermi volume. This is because model potential parameters are determined by fitting with experimental data and the latter is expected to include the effect of the full crystal potential. As to the reliability of model potential calculations, it is well-known that using model potential, electronic properties of metals like phonon spectra, liquid metal resistivity, energy-bands, EFG's and a host of other properties have been predicted with reasonably good accuracy.

In the present calculation of EFG in *hcp* transition metal scandium, a non-local model potential has been used to determine the band wave functions. The motivation behind using a non-local model potential instead of a local potential is the following: EFG in a solid is sensitive to its potential distribution and the latter is non-local in character due to electronic exchange and correlation effects. A non-local model potential is therefore expected to simulate the potential distribution in a metal better than a local model potential. The net EFG is expressed as a sum of lattice contribution q_{latt} and the conduction electron contribution q_{el}. The former is evaluated using the point-ion approximation [3, 4] for all the lattice ions except the one at whose nuclear site EFG is required. This is a good approximation in view of the fact that the overlap of the spherical cores of the distant ions with that of the ion in question is negligible. The effect arising from the deformation of the core of the ion in question by the distant ions and the nuclear quadrupole moment has been included through the Sternheimer antishielding factor [5]. But the contribution to EFG due to the deformed cores of the distant ions, which is expected to be small has been neglected. Unlike lattice contribution, the shielding/antishielding of electronic contribution is however very small [2] and in the absence of radially dependent antishielding factor $\gamma(r)$ [6] for Sc, it is estimated fairly accurately.

The results from the present calculation are compared with experiment as well as with other calculations [7–9]. The paper is organised as follows. In § 2, the theory of electric quadrupole interaction in Sc is briefly described. Results and discussions are presented in § 3 and § 4 summarises the conclusions.

2. Theory

In Sc, the electrons in 1*s* through 3*p* orbitals are treated as core electrons and those in 3*d* and 4*s* are treated as conduction electrons. The model Hamiltonian expressed in atomic units (au) is given by

$$H = -\nabla^2 + V_m, \tag{1}$$

where V_m is the model potential. It consists of a local and a non-local part and has the form

$$V_m(E) = V_L - \sum_l A_l(E) P_l. \tag{2}$$

The parameters A_l as well as the model potential V_m are in general energy dependent. V_L is the local energy – independent part of the model potential and P_l is the standard angular momentum projection operator. The parameters A_l that are listed in literature [10] are however evaluated at Fermi energy E_f. But for the study of electronic properties of Fermi volume electrons, it is essential to use the energy dependent model potential. Therefore, to express $V_m(E)$ in terms of $V_m(E_f)$, we expand the former in a Taylor series about E_f. Retaining terms to first power in $(E - E_f)$ in the said expansion, we obtain

$$V_m(E) = V_m(E_f) + (E - E_f)(\partial V_m / \partial E)_{E_f}, \tag{3}$$

which in view of (2) reduces to

$$V_m(E) = V_L - \sum_i A_l(E_f) P_l - (E - E_f) \sum_l \left(\frac{\partial A_l}{\partial E} \right)_{E_f} P_l. \tag{4}$$

For narrow band metals the third term in (4) is expected to be negligible for two reasons. (1) The energy interval $E - E_f$ would be small and (2) the parameters A_l known to be slowly varying function of E [11] would remain almost constant in the narrow energy range of occupied bands. Thus, for narrow band metals, one could approximate $V_m(E)$ as

$$V_m(E) \simeq V_L - \sum_l A_l(E_f)P_l. \tag{5}$$

i.e. one may use the same model parameters as evaluated at E_f for all the occupied energies in narrow band metals.

The model potential used in the present work is that of Animalu [10]. The corresponding screened form factor is expressed as the sum of a local V_L and non-local V_{NL} contribution. That is,

$$\frac{V(\mathbf{k}+\mathbf{K},\mathbf{k}+\mathbf{K}')}{\varepsilon(|\mathbf{K}'-\mathbf{K}|)} = \frac{V_L(|\mathbf{K}'-\mathbf{K}|) + V_{NL}(\mathbf{k}+\mathbf{K},\mathbf{k}+\mathbf{K}')}{\varepsilon(|\mathbf{K}'-\mathbf{K}|)}, \tag{6}$$

where

$$\begin{aligned} V_L(|\mathbf{K}'-\mathbf{K}|) = {} & \frac{-4\pi d}{\Omega|\mathbf{K}'-\mathbf{K}|^3}\{\sin(|\mathbf{K}'-\mathbf{K}|R_m) - |\mathbf{K}'-\mathbf{K}|R_m\cos(|\mathbf{K}'-\mathbf{K}|R_m)\} \\ & \frac{-8\pi Z}{\Omega|\mathbf{K}'-\mathbf{K}|^2}\cos(|\mathbf{K}'-\mathbf{K}|R_m) \\ & + \left\{\frac{4\pi}{\Omega}\frac{|Ec|}{|\mathbf{K}'-\mathbf{K}|^3} - \frac{24\pi Z\alpha_{\text{eff}}}{|\mathbf{K}'-\mathbf{K}|^5 R_c^3\Omega}\right\}\{\sin(|\mathbf{K}'-\mathbf{K}|R_c) \\ & - |\mathbf{K}'-\mathbf{K}|R_c\cos(|\mathbf{K}'-\mathbf{K}|R_c)\}, \end{aligned} \tag{7}$$

and

$$\begin{aligned} V_{NL}(\mathbf{k}+\mathbf{K},\mathbf{k}+\mathbf{K}') = {} & \frac{-4\pi R_m^3}{\Omega(x^2-y^2)}\sum_{l=0}^{2}(A_l-d)(2l+1)P_l(\cos\theta_{\mathbf{k}+\mathbf{K},\,\mathbf{k}+\mathbf{K}'}) \\ & \times\{yj_l(x)j_{l-1}(y) - xj_l(y)j_{l-1}(x)\}, \end{aligned} \tag{8}$$

In (7) the last line is the contribution to local potential arising from correlation and orthogonalization correction [10]. x and y occurring in (8) stand for $|\mathbf{k}+\mathbf{K}|R_m$ and $|\mathbf{k}+\mathbf{K}'|R_m$ respectively. $j_l(x)$ is the spherical Bessel function of order l. The parameter $d = (2Z/R_m)$ and Z is the valency of the ion. The values of all the other parameters are given in [10]. The dielectric function ε used in the present work for screening the bare ion form factor is given [10] by

$$\begin{aligned} \varepsilon(q) = 1 + {} & \frac{6\pi Z(1+\alpha_{\text{eff}})}{\Omega E_f q^2}\left\{1 - \frac{q^2}{2(q^2+k_f^2+2k_f/\pi)}\right\} \\ & \times\left[1 + \frac{1}{2}\frac{1-(q/2k_f)^2}{(q/2k_f)}\log\left|\frac{1+q/2k_f}{1-q/2k_f}\right|\right], \end{aligned} \tag{9}$$

where k_f is the Fermi wave vector. It may be remarked here that the screening of the bare ion model potential by dielectric constant of the valence electron gas builds into the procedure the self-consistency of electron potential to a large extent.

The model wave function χ_n is expanded in a basis of plane waves,

$$|\chi_n(\mathbf{k})\rangle = \sum_{\mathbf{K}} C_n(\mathbf{k}+\mathbf{K})|\text{PW}(\mathbf{k}+\mathbf{K})\rangle. \tag{10}$$

The band energies $E_n(\mathbf{k})$ and the coefficients $C_n(\mathbf{k}+\mathbf{K})$, where n is the band index, are determined as solutions of the secular equation,

$$|H_{\mathbf{k}+\mathbf{K},\mathbf{k}+\mathbf{K}'} - E_n(\mathbf{k})\delta_{\mathbf{K}\,\mathbf{K}'}| = 0. \tag{11}$$

The true wave function $\Psi_n(\mathbf{k},\mathbf{r})$ is constructed from the corresponding model wave function $\chi_n(\mathbf{k},\mathbf{r})$ by orthogonalising the latter to the core states.
That is,

$$|\Psi_n(\mathbf{k})\rangle = \sum_{\mathbf{K}} C_n(\mathbf{k}+\mathbf{K})[|\mathrm{PW}(\mathbf{k}+\mathbf{K})\rangle - \sum_t \langle\phi_t(\mathbf{k})|\mathrm{PW}(\mathbf{k}+\mathbf{K})\rangle\phi_t(\mathbf{k})\rangle], \tag{12}$$

where $\phi_t(\mathbf{k},\mathbf{r})$ is the tight-binding (TB) function representing the tth core state in metal and $\langle\phi_t(\mathbf{k})|\mathrm{PW}(\mathbf{k}+\mathbf{K})\rangle$ is the orthogonalisation coefficient.

The contribution to EFG from the conduction electrons is calculated using the relation [4],

$$q_{\mathrm{el}} = -\sum_{n\mathbf{k}} \int \Psi_n^*(\mathbf{k},\mathbf{r}) \frac{3\cos^2\theta - 1}{r^3}[1 - \gamma(r)]\Psi_n(\mathbf{k},\mathbf{r})\mathrm{d}^3 r, \tag{13}$$

where the negative sign is a consequence of the negative charge on electron. r and θ refer to the nucleus in question as the origin and the c-axis as the z direction. The sum in (13) is taken over the occupied bands at the reduced wave vector $\mathbf{k}$ in the Brillouin Zone (BZ).

The lattice contribution, on the other hand, is evaluated using the standard expression [3, 4],

$$q_{\mathrm{latt}} = Z(1 - \gamma_\infty)[0{\cdot}0065 - 4{\cdot}4584(c/a - 1{\cdot}633)]/a^3, \tag{14}$$

which results from summing over the ionic EFG due to all the distant point-ions located at the lattice sites. Z and γ_∞ in (14) denote the valency and Sternheimer antishielding factor respectively and c and a are lattice parameters of the *hcp* crystal.

The factor $1 - \gamma(r)$ in (13) shields the electronic contribution. This would have negligible effect on the contribution arising from the part involving TB function of $\Psi_n(\mathbf{k},\mathbf{r})$. This is because in the region where the amplitude of core functions is large, $\gamma(r)$ is negligible and in the region where $\gamma(r)$ is large, the amplitude of core function is negligible. On the other hand, the effect of shielding on plane wave contribution is likely to be significant because of the long range nature of plane wave states and the saturation value of $\gamma(r)$ at large distance.

3. Results and discussion

The lattice parameters $a = 6{\cdot}2391$ au and $c = 9{\cdot}9316$ au are taken from the work of Das [12]. The model potential parameters used are those of Animalu [10]. Energies and band wave functions are calculated at 3456 representative $\mathbf{k}$ points chosen throughout the full BZ. For this purpose, in each of the 1/24th irreducible part of BZ, 144 $\mathbf{k}$ points distributed suitably over nine equidistant planes sliced perpendicular to c-axis are chosen. To each of these $\mathbf{k}$ points a weight factor in proportion to the volume it represents is assigned. Accuracy of EFG with respect to variation in the number of $\mathbf{k}$ points has been tested and found good to within 1% for the number of $\mathbf{k}$ points chosen in the present work. At each $\mathbf{k}$ point the model wave function $\chi_n(\mathbf{k},\mathbf{r})$

is expanded in 23 plane waves corresponding to the shortest 23 wave vectors $|\mathbf{k}+\mathbf{K}|$ for that $\mathbf{k}$ point. Thus the size of the matrix diagonalised at each $\mathbf{k}$ point is 23 × 23. With this choice the convergence of energy and eigen function is found good. For this purpose energies of occupied bands were calculated by varying the size of the matrix successively and the corresponding rate of changes in energy were noted. With 23 × 23 matrix the bands have converged to within 0·001 Ry.

The difference between E_f and the energy of the lowest occupied band at most of the representative $\mathbf{k}$ points chosen in the present work is found to be less than 0·5 Ry. This justifies the narrow band approximation in Sc.

The shape of energy bands calculated at symmetry points in the present work is compared with the one obtained by Das [12]. Except for the absolute value of energy, the shape of the band structure agrees fairly well with that of Das [12]. The difference in the absolute values of energy at any given symmetry point is attributed to the different choices of the zero of energy scale in both the calculations. The density of states at Fermi energy in the present work is about 9 states Ry^{-1} atom^{-1}. This is somewhat lower than the value obtained by Das [12]. This may suggest that the contributions to specific heat from lattice phonons and electron paramagnon interaction in Sc are more important than the electronic contribution at the temperature (11°K) considered.

Since $\gamma(r)$ for Sc is not available, the unshielded value of q_{el} (i.e. by putting $\gamma(r)=0$) has been calculated from (13). As pointed out in § 3, this would not however affect the contribution involving tight-binding part of $\Psi_n(\mathbf{k},\mathbf{r})$. It would only affect the pure plane wave (PW–PW) contribution. An estimation for the shielded PW–PW contribution will be discussed later.

The total electronic contribution is divided into the components of the type PW–PW, $s-d$, $p-p$, $p-f$ and distant. While the term PW–PW arises from the pure plane wave part of $\Psi_n(\mathbf{k},\mathbf{r})$, $s-d$, $p-p$ and $p-f$ arise from the non-plane wave (i.e. TB–TB, PW–TB and TB–PW) part. The latter contributions result from the allowed angular momentum components [4] and are denoted in spectroscopic notations. The ‘distant’ type contribution, on the other hand, represents the contribution from the $l=0$ component of the electronic charge distribution centred on ions other than the one in question. Details about this contribution can be found in [13].

The various components of q_{el} (unshielded) obtained by taking the weighted sum of the contributions from all the occupied bands at each of the representative $\mathbf{k}$ points in the full BZ are displayed in table 1. The lattice contribution q_{latt} as well as experimental result [7, 14] and the theoretical result from Blaha *et al* [7] are also listed in this table. In obtaining the lattice contribution the value of $\gamma_\infty(=-23{\cdot}104)$ for Sc is taken from the work of Schmidt *et al* [15]. The latter result obtained by using Watson sphere model approximation [15] for the crystal potential would be more appropriate for solid state calculations than the free-ion γ_∞. Besides, it also includes the contribution from electron self-consistency effect, a contribution which is often neglected in other works. In view of these facts γ_∞ used in the present work is expected to be quite accurate. The core functions used in the present work are those of Clementi [16].

Column 3 in table 1 gives the shielded PW–PW contribution, whose estimation is discussed later. Columns 10 and 11 list the net unshielded and shielded EFG respectively. From this table, one notes that among the unshielded contributions, the dominant is the $p-p$ term. This is understandable because the most asymmetric state with the lowest l is the p state. Next bigger contribution is the $s-d$ term. This

Table 1. Various components of EFG in *hcp* scandium metal. All the EFG's are expressed in units of 10^{13} esu/cm^3.

	Present work											
	q_{el}											
q_{latt}	PW–PW unshi-elded	PW–PW shiel-ded	$s-d$	$p-p$	$p-f$	dist.	Total (unshi-elded)	Total (shiel-ded)	Net q Colm. 1 + Colm. 8	Net q Colm. 1 + Colm. 9	Other work* q	Expt. $\|q\|$
122·17	−0·63	−7·91	−4·72	−91·98	−1·31	−0·19	−98·83	−106·11	23·34	16·06	32·0	13·0

*Blaha *et al* [7]

arises from the *s* part of TB function and the *d* part of plane wave states. The net q_{el} is of opposite sign to q_{latt} and thus screens the latter. The net field gradient (unshielded) comes to $23{\cdot}34 \times 10^{13}$ esu/cm^3.

We now wish to present the estimation for the shielded PW–PW contribution. For this purpose we refer to the Mahapatra *et al* [4] on the EFG in Cd and Zn. In their work, it was shown that the maximum shielding (antishielding) of PW–PW contribution will be by a factor $(1-(\gamma_\infty/2))$. This is supported by a recent calculation [17] in which free-ion $\gamma(r)$ has been used to evaluate the shielded PW–PW contribution in Fe and Cu metals. The exact shielding factor obtained [17] for Fe and Cu are respectively 3·59 and 7·88, which are smaller than 6·6 and 9·3, the respective values of $1-(\gamma_\infty/2)$ for Fe and Cu. As $\gamma(r)$ for Sc is not available, we have assumed the shielding factor to be $1-(\gamma_\infty/2)$. Using the latter, the shielded PW–PW contribution comes to $-7{\cdot}91 \times 10^{13}$ esu/cm^3 and the total electronic contribution comes to $-106{\cdot}11 \times 10^{13}$ esu/cm^3. Adding q_{latt} to the latter would give the net EFG equal to $16{\cdot}06 \times 10^{13}$ esu/cm^3 (colm. 11), which agrees quite well with experiment [7]. It is true that some inaccuracy has crept in by using the approximate shielding factor $1-(\gamma_\infty/2)$. But surely, the exact factor cannot exceed $1-\gamma_\infty$, the limiting value of antishielding by a distant ion. With a view to finding how much the net EFG would become if $1-\gamma_\infty$ is used in place of $1-(\gamma_\infty/2)$, we have recalculated the shielded PW–PW contribution using $1-\gamma_\infty$. This leads to a net EFG of $8{\cdot}78 \times 10^{13}$ esu/cm^3. Therefore, considering the uncertainty in the shielding factor the present result may be stated to lie anywhere between $8{\cdot}78 \times 10^{13}$ esu/cm^3 (corresponding to shielding by $1-\gamma_\infty$) and $23{\cdot}34 \times 10^{13}$ esu/cm^3 (corresponding to no shielding). That is, the present result may be quoted as, $q = (16{\cdot}06 \pm 7{\cdot}28) \times 10^{13}$ esu/cm^3. It may be noted that the experimental value [7] of q falls in this range.

Now we compare the present results with those calculated by Blaha *et al* [7]. They had used the full potential linearized augmented-plane-wave procedure to calculate EFG in a number of *hcp* metals including Sc. The net EFG in their work [7] for Sc is $+32 \times 10^{13}$ esu/cm^3 which differs considerably from experiment and also from the present result. The dominant term in their work is $p-p$ as it is in the present work but with the following difference. The magnitude of $p-p$ contribution in their work is about one-half of the present result and the sign is opposite. This may have something to do with their partitioning of core electrons into semi-core and true-core states and treating the semicore electrons (namely, 3*s* and 3*p* states in Sc) as completely band states. The convergence of the band wave functions corresponding to the 3*s* and 3*p* is normally not very good unless one uses a relatively large number of basis functions. This aspect needs some re-examination. Further it seems that a factor of 2 is missing on the right hand side of (2) in their work [7]. If it is not due to typographical omission, their results would change by this factor making agreement with experiment worse.

The authors [7] of LAPW procedure claim that they have considered all charges including nuclear charges for determining the potential. It is however not clear as to whether the non-spherical nature of nuclear charge distribution has been duly taken note of in their work. If not, the quadrupole moment of nuclear charge would perturb both the true-core and semi-core states in their work to give additional contribution to EFG through Sternheimer antishielding mechanism. These contributions, particularly the ones from 2*p* and 3*p* states are likely to be significant. The present work does include these contributions.

Another difference one notices between the present result and those of Blaha *et al*

[7] is in regard to the magnitude of lattice contribution to EFG. While the latter contribution is significant in the present work, it is negligible in their work. This difference may be attributed to the different ways of partitioning the electrons in two procedures. Whereas in the present work, $1s$ through $3p$ states, treated as core states, contribute to lattice EFG, in LAPW procedure, $1s$ through $2p$ states, treated as true-core contribute to lattice and $3s-3p$, treated as semi-core states, contribute to valence EFG. If the latter contributions $(3s-3p)$ in LAPW procedure are calculated in the presence of nuclear quadrupole moment (which is perhaps not done) and added to lattice EFG instead of valence, the resulting lattice contribution may not be negligible. The reason for treating $3s$ and $3p$ as core states in the present work is their small and negligible overlap on nearest neighbour atoms in Sc metal. The calculated overlap of atomic $3p$ orbital on nearest neighbour atom in Sc is found to be less than 0·02%. We consider this to be negligible enough to regard $3p$ and also $3s$ as non-overlapping core states.

The sign of q from experiment [14, 7] is not available. We wish to remark here that irrespective of the sign of experimental q, the present result would be more close to experiment than those of Blaha *et al* [7]. Before we conclude this section we wish to suggest the following refinements in the present theory.

1] The band wave functions be redetermined in an energy dependent model potential of the form given in (3). This would not only give more accurate q_{el} than obtained at present but also throw light on the validity of approximation leading to (5) in narrow band metals.
2] Radially dependent antishielding factor $\gamma(r)$ appropriate for solid state be calculated so that using the latter the shielded (PW–PW) contribution to EFG be evaluated more accurately than estimated here.

In addition, fresh attempts be made in the experimental side to determine the sign of EFG so that it would serve as a more positive yardstick to assess the accuracy of theoretical calculations.

4. Conclusions

We conclude that by using a non-local transition metal model potential for the energy band calculations in Sc, the net EFG calculated as the sum of lattice and conduction electron contributions agrees quite well with experiment. This not only reaffirms confidence in the use of model potential for the study of such electronic properties in metals but also provides indirect support to the accuracy of point-ion approximation for the lattice contribution. Further, we hope that the present results would improve in the right direction if $\gamma(r)$ is used for obtaining the shielded (PW–PW) contribution.

References

[1] P Jena, S D Mahanti and T P Das, *Phys. Rev.* **B7**, 975 (1973)
[2] R E Watson, A C Gossard and Y Yafet, *Phys. Rev.* **140**, A375 (1965)
[3] M Pomerantz and T P Das, *Phys. Rev.* **123**, 2070 (1961)
[4] N C Mohapatra, P C Pattnaik, M D Thompson and T P Das, *Phys. Rev.* **B16**, 3001 (1977)
[5] R M Sternheimer, *Phys. Rev.* **130**, 1423 (1963)
[6] K K P Rao and N C Mohapatra, *Phys. Rev.* **A24**, 10 (1981)
[7] P Blaha, K Schwartz and P H Dederichs, *Phys. Rev.* **B37**, 2792 (1988)
[8] B Drittler, M Weinert, R Zeller and P H Dederichs, *Phys. Rev.* **B42**, 9336 (1990)

[9] R Coehoorn and K H J Buschow, *Phys. Rev.* **B42**, 4645 (1990)
[10] A O E Animalu, *Phys. Rev.* **B8**, 3542 (1973)
[11] I V Abarenkov and V Heine, *Philos. Mag.* **12**, 529 (1965)
[12] S G Das, *Phys. Rev.* **B13**, 3978 (1976)
[13] N C Mohapatra, C M Singal, T P Das and P Jena, *Phys. Rev. Lett.* **29**, 456 (
[14] E N Kaufmann and R J Vianden, *Rev. Mod. Phys.* **51**, 161 (1979)
[15] P C Schmidt, K D Sen, T P Das and A Weiss, *Phys. Rev.* **B22**, 4167 (1980)
[16] E Clementi, *Tables of atomic functions* (New York: IBM, 1965)
[17] P Tripathi and N C Mohapatra, *Pramana – J. Phys.* **37**, 513 (1991)

PRAMANA
— journal of
physics

© Printed in India

Vol. 41, No. 5,
November 1993
pp.453–465

Heating mechanism in relation to the laser machining process

BEKIR S YILBAS and AHMET Z SAHIN
Mechanical Engineering Department, King Fahd University of Petroleum and Minerals, Dhahran 31261, Saudi Arabia

MS received 26 March 1993; revised 12 July 1993

Abstract. Laser workpiece interaction mechanism is an important phenomenon which will assist in the development of laser machining systems. The interaction mechanism is generally complicated and depends on the laser and workpiece properties. In the present study a mathematical analysis for the laser material removal by evaporation and radial ejection of liquid is carried out. In the analysis the time unsteady problem is solved and nucleation explosions are predicted.

Keywords. Laser interaction; heat transfer model.

PACS No. 44·90

1. Introduction

When the output from a pulsed laser is focused, intensities sufficient to allow the welding and drilling of engineering materials can be produced [1]. The interaction mechanism between a laser beam and such materials, notably metals, depends upon the power density produced by the beam at the workpiece.

The interaction is generally complicated by the change in the proportion of power absorbed as the pulse proceeds, the dependence of material properties on temperature and the temporal variation of power within the pulse. The last would require a complex mathematical model, so for simplicity, the beam power is usually assumed to be uniform. Also, the workpiece is assumed to be isotropic and homogeneous so that its macroscopic properties can be used in this case.

In the present study, absorption, conduction, evaporation and nucleation within the liquid phase are investigated during the laser heating process. To extend the analysis for the evaporation process the recoil pressure and radial flow of liquid from the irradiated cavity are included. Consequently, the rate of material removal by evaporation and radial ejection of liquid are predicted.

A numerical approach based on finite difference formulation is employed to solve the equation of state, equation of continuity, momentum and energy equations with the relevant boundary conditions. In the analysis, time unsteady two dimensional model is developed for laser-metal interaction process.

2. Absorption

Absorption of light in metals leads initially to an increase in the temperature of the free electron gas which then transfers energy to the lattice by collision. The latter process is by far the slower, the relaxation time for the conditions important for laser machining being in the order of 10^{-11}s [2]. However, since the spike time is in the order of 10^{-6}s, equilibrium conditions will be reached. The absorption process can therefore be described by

$$I(z) = I_0 \exp(-\delta z), \tag{1}$$

where I_0 is the power density absorbed at the surface. Relating this to the power density incident at the surface, one can write:

$$I(z) = I_0(I - R')\exp(-\delta z) \tag{2}$$

where the reflectivity, R', is dependent upon the power density.

Yilbas *et al* [3] have shown theoretically that the absorption coefficient of metals increases with temperature, in many cases linearly.

3. Conduction

Energy arriving at the surface of the workpiece is transferred into the bulk of the material by conduction. To completely describe the temperature distribution, the Fourier heat conduction equation must include the absorption term, giving:

$$K\nabla^2 T + (1 - R')\delta I_0(r)\exp(-\delta z) = \rho C_p \frac{\partial T}{\partial t} \tag{3}$$

$I_0(r)$ gives the radial variation of the power intensity arriving at the surface, the temporal variation from the spikes being omitted.

Equation (3) has been solved by Yilbas *et al* [4] for the heating of sheet metals for welding applications, assuming a Gaussian distribution of the power intensity. This work has been extended to two-layer plates allowing for both ideal and non-ideal contact [5]. In all three cases, the absorption term was omitted from the conduction equation, and introduced instead as a boundary condition.

Ehlotzky [6] has solved (3) for one-dimensional case assuming a uniform power intensity across the spot. He concludes that even for the long, microsecond spikes of a free running laser the surface temperature closely follows the spike profile. However he bases this on his calculations for Q switched (i.e. nanosecond range) pulses, where the temperatures return to initial conditions after approximately 1 μs for a 40 ns pulse.

Yilbas and Apalak [7] have examined theoretically the effect of spiking on the temperature profile of metal sheets and concludes that above a certain spike frequency, the laser source appears continuous. For a semi-infinite target, this frequency is low enough for a free-running laser pulse to be considered continuous.

4. Evaporation

The analysis above is sufficient to describe temperature profiles up to the time where the material surface reaches its vaporization temperature. Beyond this point, allowance must be made for the loss of material by evaporation. Yilbas *et al* [8] derived an expression for the steady state velocity of the vaporization front in terms of the absorbed power density, assuming that the surface is at its vaporization temperature.

$$V_s = \frac{I_0}{\rho(L + C_P T_v)}. \tag{4}$$

The previous experimental results [9] are in reasonable agreement with this theory, although in general the observed hole depth is less than the calculated depth. Yilbas [10] extended this work to introduce the surface velocity as:

$$V_s = \frac{I_0}{\rho(L + C_P T_s)}. \tag{5}$$

In (4) and (5), the situation is assumed to have reached a steady state. So, to determine the vaporization front velocity, V_s, one can use the equilibrium condition giving, after some rearrangement

$$V_s = a_v \exp - (\Delta h_v / kT_s). \tag{6}$$

Anisimov [11] postulates that a high power intensities, the material may become superheated, and Yilbas and Apalak [7] have analyzed this problem more closely. They use a moving coordinate system and solve the equation:

$$K \frac{\partial^2 T}{\partial z^2} + \rho C_p V_s \frac{\partial T}{\partial z} + I_0 \delta \exp(-\delta z) = 0 \tag{7}$$

with V_s and T_s being found from the simultaneous eq. (5) and:

$$V_s = \frac{kT_s}{\sqrt{2\pi m}} \exp - \left(\frac{\Delta h_v(T_s)}{kT_s} \right) \tag{8}$$

In (8) for V_s Yilbas *et al* [8] have corrected Anisimov's [11] derivation, (6), based on the Debye frequency and assuming constant latent heat of vaporization. As a result, Yilbas *et al* [8] concluded that the temperature will rise more slowly than Anisimov's [11] predictions.

The boundary condition:

$$\frac{\partial T}{\partial z} = \rho V_s \frac{L}{K} \text{ at } z = 0 \tag{9}$$

is used to correct the assumption that the temperature gradient is zero at the surface. Yilbas and Apalak [7] predict that superheating will commence at power intensities in excess of 1 MW/cm^2.

The production of surface plasma in the vapor phase was studied previously [12]. At high power intensities ($I_0 > 10^{14}$ W/m^2) laser deposited energy heats a thin surface layer to a high temperature and pressure, generating a compression shock which propagates into the target (upstream) and a hot low density plasma which expands towards the laser (downstream). The plasma expanding downstream is optically tenuous whereas the shocked material is opaque so that the laser beam energy transmitted through the hot plasma is absorbed in a small depth of shocked material referred to as deflagration zone [12]. Where the laser machining is concerned high power laser beam interaction becomes inapplicable. Therefore, in the present study plasma formation and shock propagation are not included.

5. Recoil pressure

The recoil pressure exerted by vapor leaving the surface has been studied previously [13], i.e.:

$$p = \alpha I_0 \frac{V_{\text{vap}}}{(L + 1/2 V_{\text{vap}}^2)}. \tag{10}$$

The factor α is the proportion of the absorbed power which is used for evaporation. Here again, the situation is assumed to be in equilibrium since the situation is analyzed for steady-state evaporation.

Nevertheless, the recoil pressure determines the behaviour of the liquid phase and controls the extent of liquid ejection as a material removal mechanism. If the recoil pressure is less than the saturated vapor pressure, the liquid is superheated, in which case, nucleation will occur giving vapor bubbles within the bulk of the liquid. Explosion of these vapor regions will result in the ejection of liquid from the crater [14].

6. Nucleation within the liquid phase

The nucleation phenomenon has been analyzed by Yilbas and Apalak [7] assuming a homogeneous steady-state process. The expression obtained for the nucleation rate is:

$$J = qn\sqrt{2V/m}\exp(-16\pi\sigma^3/3P_b^{*2}kT). \tag{11}$$

For copper, nucleation only becomes significant at 7000°C [7]. This corresponds to a 30 J, 1 μs pulse absorbed in an area 0·5 mm in diameter giving a front velocity of 86 m/s. The latter is a factor 2·5 times greater than that found experimentally. However, there is much evidence that liquid expulsion does occur. Yilbas [15] has observed resolidified liquid globules on the microscope slide used to protect the focussing lens, and has taken high speed cine-film clearly showing ejected globules. The streak photograph reveals the presence of liquid ejecta. Yilbas *et al* have measured the ratio of liquid to vapor expelled and found that for free running pulses liquid ejection is the predominant removal mechanism [14].

Thome [13] points out that the homogeneous steady-state theory is also insufficient to explain nucleation for water, probably due to the presence of foreign bodies which can reduce the critical free energy difference for the phase change, ΔF^*, and allow heterogeneous nucleation. By reducing the value of ΔF^*, by a factor of $2{\cdot}65 \times 10^{-6}$ (i.e. the same as that required to explain the observed rate of water), he shows that nucleation in copper becomes significant above 5500°C. The fact that this temperature still exceeds Yilbas and Apalak's [7] computed maximum for nucleation in copper shows that the mechanism is still not fully understood.

7. Radial flow of liquid

If the output power intensity from the laser is considered to be Gaussian, itself an oversimplification, the power intensity at the workpiece would also be Gaussian, giving:

$$I_0(r) = \hat{I}_0 \exp - (r/R)^2 \tag{12}$$

The surface temperature, and hence the recoil pressure, would fall as the radius increases, so that the liquid metal would move down the pressure gradient and be expelled from the sides of the hole. Yilbas's [16] streak photographs of the drilling process show this radial ejection and give a clearer indication of the time of commencement and direction of expulsion of liquid ejecta.

Yilbas [17] showed that liquid ejection begins to dominate evaporation as the pulse proceeds in drilling process.

In formulating the problem, radial symmetry is assumed, together with an incompressible and inviscid liquid phase, for simplicity. The energy dissipated within the target, and the momentum and continuity equations for the flow of liquid, are then described as follows:

Energy:

$$\rho C_p \frac{\partial T}{\partial t} = \frac{\partial}{\partial z}\left(K\frac{\partial T}{\partial z}\right) + \frac{\partial}{\partial r}\left(K\frac{\partial T}{\partial r}\right) + \frac{K}{r}\left(\frac{\partial T}{\partial r}\right)$$

$$+ I_0(r)\delta \exp[-\delta(z - z_0)] - \rho C_p V_r \frac{\partial T}{\partial r} - \frac{\partial}{\partial z}(\rho C_P V_z T) \tag{13}$$

Continuity:

$$\frac{\partial V_z}{\partial z} + \frac{1}{r}\frac{\partial}{\partial r}(rV_r) = 0 \tag{14}$$

Momentum:

$$\rho\left(V_r\frac{\partial V_z}{\partial r} + V_z\frac{\partial V_z}{\partial z} + \frac{\partial V_z}{\partial t}\right) = -\frac{\partial p}{\partial z}, \tag{15}$$

$$\rho\left(V_r\frac{\partial V_r}{\partial r} + V_z\frac{\partial V_r}{\partial z} + \frac{\partial V_r}{\partial t}\right) = -\frac{\partial p}{\partial r}. \tag{16}$$

The last two terms in the energy equation (13) allow for convection by the liquid radially and axially. This equation is subject to the boundary conditions:

$$\begin{array}{ll} \text{(i)} & \partial T/\partial r = 0 \quad \text{at} \quad r = 0 \\ \text{(ii)} & T = T_i \quad \text{at} \quad r = \infty \\ \text{(iii)} & \left.\dfrac{\partial T}{\partial s}\right|_{s=0}^{\text{liq}} = \rho V_{\text{liq}} L/K_{\text{liq}} \\ \text{(iv)} & T = T_i \quad \text{at} \quad z = \infty \\ \text{(v)} & T = T_i \quad \text{at} \quad t = 0. \end{array} \tag{17}$$

At the liquid surface, the vapor velocity and the recession velocity of the surface are determined from kinetic theory:

$$V_{\text{vap}} = (kT_s/m)^{1/2} \tag{18}$$

$$V_{\text{liq}}|_{s=0} = (kT_s/2m)^{1/2} \exp -\left(\frac{\Delta h_v}{kT_s}\right) \tag{19}$$

while the recoil pressure is defined by the rate of evaporation. Momentum considerations yield:

$$P_s = \rho V_{\text{liq}} V_{\text{vap}} \tag{20}$$

for $V_{\text{vap}} \gg V_{\text{liq}}$, V_{vap} and V_{liq} being found from (18) and (19) respectively. The remaining boundary conditions for the continuity and momentum equations are:

$$\begin{aligned} V_r &= 0 && \text{at } r = 0 \\ V_r &= 0 && \text{at } t = 0 \\ \frac{\partial V_z}{\partial r} &= 0 && \text{at } r = 0 \\ V_z &= 0 && \text{at } t = 0 \\ \frac{P_z}{\rho^{\gamma}} + \frac{V_z^2}{2} &= \frac{P_s}{\rho^{\gamma}} + \frac{V_s^2}{2} && \text{at } r = 0. \end{aligned}$$

An attempt to introduce a stream function into (14) to (16) to produce second order equations leads to a pair of very difficult non-linear equations. This method was therefore abandoned. A system of moving coordinates (based on the liquid surface) is not useful in this instance since firstly, the liquid surface will in general be curved, secondly, the curvature will change with time so that the coordinates would have to be reset periodically, and thirdly, a great deal of interpolation would be required to transfer the information obtained to a set of cylindrical coordinates for examination of the propagation process. The approach was therefore to retain the cylindrical coordinate system and to measure axial distances from the original surface of the workpiece as shown in figure 1.

The energy equation was considered separately from the continuity and momentum equations, information on velocities from the latter being fed back into the convection terms, while the liquid surface temperatures determined from the energy equation defined the velocity boundary condition (19).

Equations (14) to (16) can be rearranged as follows:

$$\frac{\partial V_z}{\partial t} = -\ V_r \frac{\partial V_z}{\partial r} - \ V_z \frac{\partial V_z}{\partial z} - \frac{1}{\rho}\frac{\partial p}{\partial z} = f(V_z, V_r, p, r, z) \tag{22}$$

$$\frac{\partial V_r}{\partial r} = \frac{\partial V_z}{\partial z} - \frac{V_r}{r} = g(V_z, V_r, r, z) \tag{23}$$

$$\frac{\partial p}{\partial r} = -\rho\left(V_r \frac{\partial V_r}{\partial r} + \ V_z \frac{\partial V_r}{\partial z} + \frac{\partial V_r}{\partial t}\right) = h(V_z, V_r, r, z, t). \tag{24}$$

Although equations (22) to (24) are simultaneous, they cannot be solved by standard techniques, since (22) must be integrated with respect to "t", whereas (23) to (24) must be integrated with respect to "r". The solution envisaged applies a Runge–Kutta method (22) to determine the axial velocities at all grid points (figure 1) after a time increment Δt: (23) is then solved similarly to determine all the radial velocities, using the new axial velocity data, and the pressures may be found similarly from (24) using the new axial and radial velocity values. Thus, the values of V_r, V_z and P are stepped forward in time.

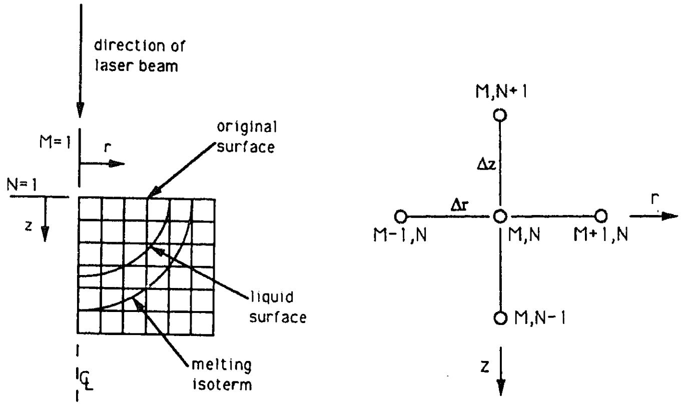

Figure 1. Arrangements of the points in the spatial plane.

The solution is terminated at a radius less than the hole radius in order to obviate the necessity of analyzing the liquid ejection from the edge of the hole. All the liquid flowing through these artificial boundaries is assumed to be ejected.

8. Computer program and results

A computer program has been developed to solve equations (13) and (22) to (24) incorporating the boundary condition equations (18) to (21).

The procedure is first to solve the energy equation (13) throughout the material, with all convection terms set to zero. The temperature distribution obtained determines the liquid region for which the axial velocity equation may be solved, with a surface velocity determined from the surface temperature just found. Radial velocities are then determined from the axial velocity data, and finally the pressures are found from both radial and axial velocity information. Thus all results are now available at a time Δt after the start ($t=0$): the process is repeated to determine values at $t = 2\Delta t$, etc., with convection terms now included in the energy equation.

The energy equation may be solved by the method of Ozisik [18]. Putting (13) into finite difference form and rearranging gives, for the general case:

$$\begin{aligned}
T_{M,N}^{t+1} = T_{M,N}^{t} \Bigg\{ & 1 - \frac{\Delta t}{\rho_{M,N}^{t} C_{pM,N}^{t}} K_{M,N}^{t} \left(\frac{2}{(\Delta r)^2} + \frac{2}{(\Delta z)^2} \right) \\
& + \rho_{M,N}^{t} C_{pM,N}^{t} \left(\frac{V_{rM+1,N}^{t} + V_{rM-1,N}^{t}}{2\Delta r} + \frac{V_{rM,N}^{t}}{(M-1)\Delta r} + \frac{V_{zM,N+1}^{t} - V_{zM,N-1}^{t}}{2\Delta z} \right) \\
& + \rho_{M,N}^{t} (C_{pM,N+1}^{t} - C_{pM,N-1}^{t}) \frac{V_{rM,N}^{t} + V_{zM,N}^{t}}{2\Delta z} \\
& + C_{pM,N}^{t} V_{rM,N}^{t} \frac{\rho_{M+1,N}^{t} - \rho_{M-1,N}^{t}}{2\Delta r} + C_{pM,N}^{t} V_{zM,N}^{t} \frac{\rho_{M,N+1}^{t} - \rho_{M,N-1}^{t}}{2\Delta z} \Bigg\} \\
& + \frac{\Delta t T_{M,N+1}^{t}}{\rho_{M,N}^{t} C_{pM,N}^{t}} \left(\frac{K_{M,N}^{t}}{(\Delta z)^2} + \frac{K_{M,N+1}^{t} - K_{M,N-1}^{t}}{4(\Delta z)^2} - \frac{\rho_{M,N}^{t} C_{pM,N}^{t} V_{zM,N}^{t}}{2\Delta z} \right)
\end{aligned}$$

$$
\begin{aligned}
&+\frac{\Delta t T^t_{M,N-1}}{\rho^t_{M,N} C^t_{pM,N}}\left(\frac{K^t_{M,N}}{(\Delta z)^2}-\frac{K^t_{M,N+1}-K^t_{M,N-1}}{4(\Delta z)^2}+\frac{\rho^t_{M,N} C^t_{pM,N} V^t_{zM,N}}{2\Delta z}\right)\\
&+\frac{\Delta t T^t_{M+1,N}}{\rho^t_{M,N} C^t_{pM,N}}\left\{\frac{K^t_{M,N}}{(\Delta r)^2}\left[1+\frac{1}{2(M-1)}\right]\right.\\
&\left.+\frac{K^t_{M+1,N}-K^t_{M-1,N}}{4(\Delta r)^2}-\frac{\rho^t_{M,N} C^t_{pM,N} V^t_{rM,N}}{2\Delta r}\right\}\\
&+\frac{\Delta t T^t_{M-1,N}}{\rho^t_{M,N} C^t_{pM,N}}\left\{\frac{K^t_{M,N}}{(\Delta r)^2}\left[1+\frac{1}{2(M-1)}\right]\right.\\
&\left.-\frac{K^t_{M+1,N}-K^t_{M-1,N}}{4(\Delta r)^2}+\frac{\rho^t_{M,N} C^t_{pM,N} V^t_{rM,N}}{2\Delta r}\right\}\\
&+\frac{I_{0M}\delta \exp[-\delta(Z_n-Z_0)]\Delta t}{\rho^t_{M,N} C^t_{pM,N}}. \qquad (25)
\end{aligned}
$$

Again this equation is modified at the boundaries by insertion of conditions specified in (17). The above equation is subject to stability criterion, in the general case:

$$
\begin{aligned}
\Delta t \geqslant \rho^t_{M,N} C^t_{pM,N}&\left\{K_{M,N}\left[\frac{2}{(\Delta r)^2}+\frac{2}{(\Delta z)^2}\right]+\right.\\
&\rho^t_{M,N} C^t_{pM,N}\left[\frac{V^t_{rM+1,N}-V^t_{rM-1,N}}{2\Delta r}+\frac{V^t_{rM,N}}{(M-1)\Delta r}+\frac{V^t_{zM,N+1}-V^t_{zM,N-1}}{2\Delta z}\right]\\
&+\rho^t_{M,N}[C^t_{pM,N+1}-C^t_{pM,N-1}]\frac{V^t_{M,N}+V^t_{zM,N}}{2\Delta z}\\
&+C^t_{pM,N} V^t_{rM,N}\frac{\rho^t_{M+1,N}-\rho^t_{M-1,N}}{2\Delta r}\\
&\left.+C^t_{pM,N} V^t_{zM,N}\frac{\rho^t_{M,N+1}-\rho^t_{M,N-1}}{2\Delta z}\right\}^{-1}. \qquad (26)
\end{aligned}
$$

This stability criterion is altered both for $r=0$ and at the surface, and is in fact more constricting than (26) suggests. The surface boundary condition (17 (iii)) is a complex function of the temperature, which means that the stability criterion cannot be formulated in the usual manner. It was finally selected by trial and error for a specific case, after ensuring that stability was satisfied along $r=0$.

Laser power intensities introduced in the numerical solution are in the form of a square pulse of zero rise time and 1·5 ms pulse length. The intensity is varied by varying the amplitude of this pulse.

Results are presented for the case of pure evaporation with a radially dependant power intensity distribution on the surface of the material. The assumed gaussian distribution has its $1/e$ points 240 μm out from the centerline. No temporal variation is assumed in the power intensity, and its rise time is taken to be zero. The development of temperature profiles and surface velocities with time are presented in figures 2 to 8.

It is important here to point out one particular difficulty encountered in the solution of equations (13) and (17) to (19). Metals have values of δ in the region of $10^8\,\mathrm{m}^{-1}$

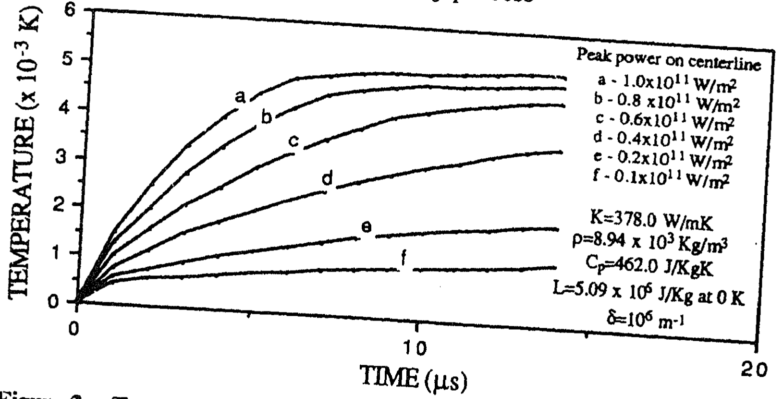

Figure 2. Temperature at the center line of the heated surface given with time.

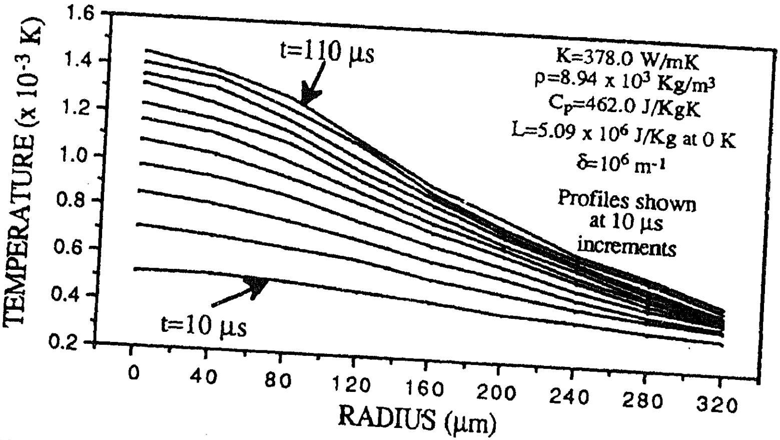

Figure 3. Temperature profiles across the surface given at peak power intensity of $10^{10}\,W/m^2$.

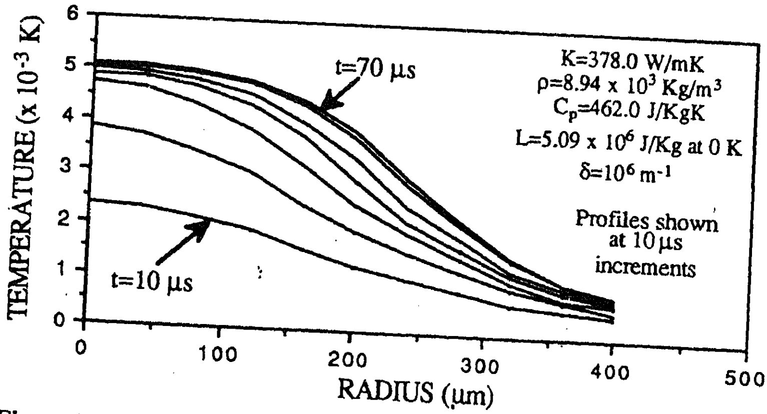

Figure 4. Temperature profiles across the surface given at peak power intensity of $10^{11}\,W/m^2$.

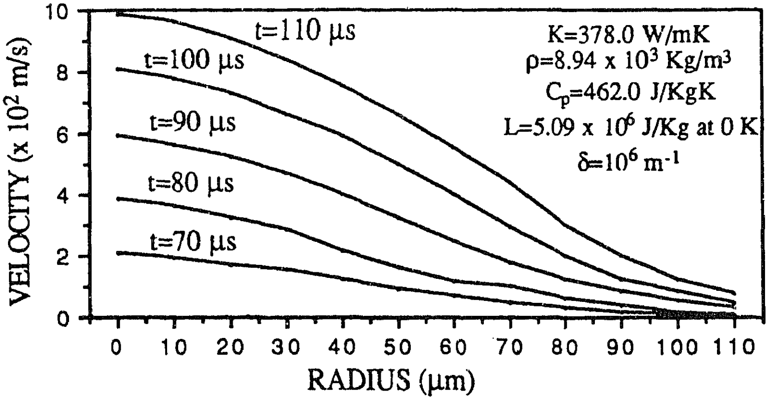

Figure 5. Temperature profiles across the surface given at peak power intensity of $0{\cdot}4 \times 10^{11}\,\mathrm{W/m^2}$.

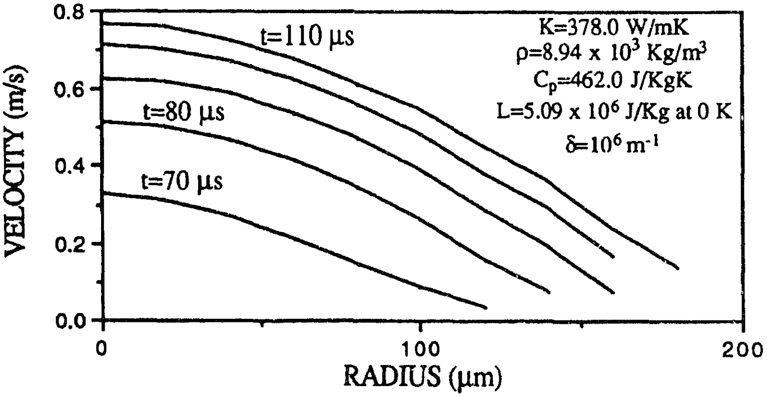

Figure 6. Velocity of evaporating surface across the heated spot given at peak power intensity of $10^{11}\,\mathrm{W/m^2}$.

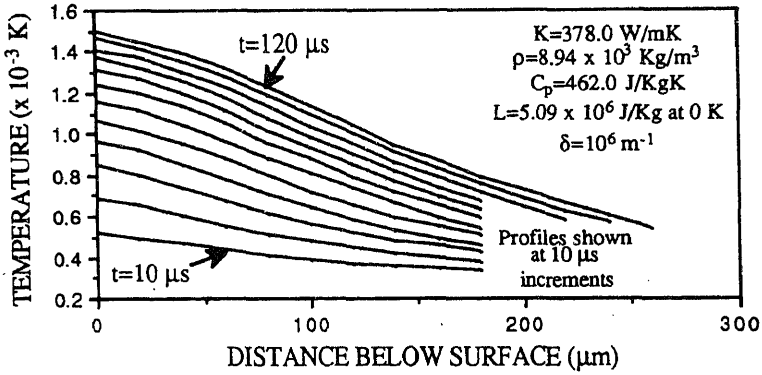

Figure 7. Temperature on the center line inside the material given at peak power intensity of $10^{10}\,\mathrm{W/m^2}$.

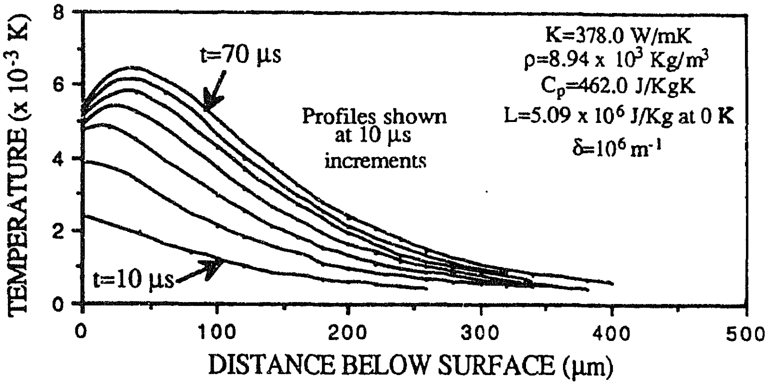

Figure 8. Temperature on the center line inside the material is given at peak power intensity of $10^{11}\,W/m^2$.

so that $1/\delta$ is in the region of 100 Å. It is therefore necessary to have values of Δz in the program far less than 100 Å, in order to fully describe the absorption process. This results in a vast number of grid points in the axial direction and also reduces the value of Δt for stability to approximately 10^{-14}. The spatial increments used are $\Delta r = 40\,\mu m$ and $\Delta z = 20\,\mu m$, resulting in a value of Δt of 1 μs to ensure stability. The approach for determining the variation of latent heat of evaporation with temperature is adopted [7], so that:

$$L(T) = L_0\left(1 - \left(\frac{T_s}{T_c}\right)^2\right)^{1/2}. \tag{27}$$

Little error is incurred in taking L_0 as the latent heat at normal temperatures. Equation (27) is used in conjuction with (17) to determine the temperature boundary condition at the surface. The critical temperature for copper is taken as 8500 K and melting point as 1356 K. Figure 2 shows the temporal variation of surface temperature on the centerline of the power intensity distribution for intensities between $0{\cdot}1 \times 10^{11}$–$1 \times 10^{11}\,W/m^2$. As expected, the higher intensities produce higher surface temperatures and a shorter time to reach steady state. The radial variation of surface temperatures for the same conditions, as time increases, are shown in figures 3 and 4. Steady state temperatures in excess of the melting point are reached at the radius corresponding to the $1/e$ point of the power intensity distribution only at intensities in excess of about $0{\cdot}3/10^{11}\,W/m^2$ shown in figures 5 and 6. The situation for intensities of 0·1 and $0{\cdot}2 \times 10^{11}\,W/m^2$ are not examined, as the surface temperatures at these levels are not sufficiently high to produce velocities in excess of about 10^{-3} m/s. For all cases, it is evident that the major portion of the evaporation occurs within a region bounded by the $1/e$ points of the intensity distribution.

The growth of the temperature profile with time along the centerline for different intensities is presented in figures 7 and 8. Equation (17) contains a condition which permits only zero or positive gradients at the surface. The apparent negative gradients seen in some cases are due to the fact that a zero gradient extends for too short a distance to be noticeable on the scale shown. Figure 7 shows that positive gradients are not achieved at intensities up to $0{\cdot}2 \times 10^{11}\,W/m^2$: the surface velocity is too small to change the gradient appreciably from zero. However, at higher intensities, for example $10^{11}\,W/m^2$ in figure 8, a positive gradient is observed once the surface temperature exceeds about 4000 K (corresponding to a velocity of 0·057 m/s). As time increases from here, the position of the point of maximum temperature progresses into the material, reaching a steady state at approximately 40 μm below the surface. This is 0·4 of the absorption length $(1/\delta)$, which agrees with the situation analyzed by Yilbas and Apalak [7] (for steady state only) for δ in the region of 10^8, where the maximum occurs at 10^{-9} m below the surface.

This increased temperature below the surface suggests two possibilities for material removal, both involving some sort of explosion. Firstly, the nucleation rate, as expressed by (11), will be higher, so that material may be exploded from the hole, provided that the saturated vapor pressure in the nucleating region exceeds the surface pressure, provided that the material is superheated. Examination of figure 8, for the case of a surface temperature of $5{\cdot}1 \times 10^3$ K and a maximum temperature of $6{\cdot}4 \times 10^3$ K, and using Yilbas and Apalak's [7] data for surface (recoil) pressure and saturated vapor pressure for copper, we get the recoil pressure of 46 atmosphere and the saturated vapor pressure at the point of maximum temperature of 210 atmosphere. This indicates that a violent explosion is feasible. Yilbas and Apalak's [7] approach would take the saturated vapor pressure at the surface of 53 atmosphere and conclude that an explosion is only just possible.

The second possibility for material removal occurs when the power intensity is high enough for the maximum temperature in the material to reach the critical point and become vapor. Then, an explosion can occur if the saturated vapor pressure at the critical temperature exceeds the recoil pressure. Yilbas and Apalak's [7] data show that this mechanism is feasible in copper, provided that the surface temperature does not exceed 7100 K. By considering only surface temperatures, in which case superheating ceases above 5000 K. This process cannot be the dominant removal mechanism in cases where it does occur, is correct only when the intensity at the surface is too low to allow sub-surface temperatures to reach critical.

9. Conclusion

Previous theoretical approaches to laser/material interaction problem have been presented and discussed. Results have been given for the case of pure evaporation with radially dependant power intensity on the workpiece surface. This approach is basically two dimensional. The time unsteady problem has been solved. Nucleation explosions and critical point explosions are predicted.

A theoretical approach has been presented to the problem of liquid ejection by radial flow due to a radially dependant pressure gradient on the surface. A computer program has been developed to solve the problem.

It is found that the major portion of the evaproation occurs within a region bounded by the $1/e$ points of the intensity distribution. As the heating time increases, the positive gradient is observed once the surface temperature exceeds the melting temperature. As heating time increases further, maximum temperatures progress into the material. This high temperature below the surface suggests: i) high nucleation rate, ii) sudden vaporization due to high temperature for material removal. In both cases, removal mechanism involves in some kind of explosions.

Acknowledgement

The authors wish to acknowledge the support provided by King Fahd University of Petroleum and Minerals, Dhahran, Saudi Arabia for this work.

References

[1] B S Yilbas and G Cinar, *Symposium on high power lasers*, SPIE Proceedings, (The Hange, Netherlands, 1987) p. 125
[2] B S Yilbas, *Int. J. Eng. Sci.* **24**, 1325 (1986)
[3] B S Yilbas, K Danisman and Z Yilbas, *Meas. Sci. Tech.* **2**, 668 (1991)
[4] B S Yilbas, R Davies and Z Yilbas, *J. Mater. Processing Technol.* **15**, 139 (1991)
[5] B S Yilbas, A Koc and N Akcakoyun, *Mech. Inc. Engrs.*, IMechIE **27** (1991)
[6] F Ehlotzky, *Proceedings of a seminar held at Oberginge*, Austria (Springer Verlag Press, Berlin, 1985)
[7] B S Yilbas and K Apalak, *Egypt. J. Phys.* **18**, 133 (1987)
[8] B S Yilbas, R Davies and Z Yilbas, *Proc. Inst. Mech. Eng.* **204**, 105 (1990)
[9] B S Yilbas, *Trans. of ASME, J. Eng. Mater. Technol.* **109**, 282 (1987)
[10] B S Yilbas, *J. Opt.* **15**, 108 (1986)
[11] S I Anisimov *et al*, *Sov. Phys. Tech. Phys.* **11**, 945 (1967)
[12] B S Yilbas, R Davies, Z Yilbas, A Gorur and I Acar, *Pramana – J. Phys.* **38**, 195 (1992)
[13] J K Thome, *Hemisphere* (Publ. Corp., New York, 1990)
[14] B S Yilbas, Doga Tr., *J. Eng. Environ. Sci.* **10**, 89 (1986)
[15] B S Yilbas, *Opt. Laser Eng.* **7**, 1 (1987)
[16] B S Yilbas, *Jpn. J. Appl. Phys.* **24**, 1417 (1985)
[17] B S Yilbas, *Proc. Int. Laser-Congress*, West Germany (1988) **33**
[18] M N Ozisik, *Heat conduction* (John Wiley and Sons, New York, 1980)
[19] B S Yilbas and Z Yilbas, *Res. Mechanica* **24**, 237 (1988)

PRAMANA
— journal of
physics

© Printed in India

Vol. 41, No. 5,
November 1993
pp. 467–472

SERS studies on 1–4 dihydroxyanthraquinone at Ag electrode

V G SRIKANTH, S EDWIN JAYARAJ and V RAMAKRISHNAN*
Department of Microprocessor and Computer, School of Physics, Madurai Kamaraj University
Madurai 625021, India
*Author to whom correspondence should be made

MS received 4 January 1993; 12 July 1993

Abstract. Raman scattering studies on 1–4 dihydroxyanthraquinone (DHAQ) at Ag electrode have been carried out to investigate the enhancement in the spectral line intensity after adsorption. Charge transfer between the adsorbate and the substrate is more pronounced for certain normal modes of vibration. It is found that the DHAQ molecules are lying with their molecular plane on the top of the metal surface. Laser induced fluorescence spectra of DHAQ have also been analysed with a view to assign the relative orientation of absorption and emission dipoles.

Keywords. Adsorption; charge transfer; flat on configuration.

PACS No. 33·20

1. Introduction

Surface enhanced Raman scattering (SERS) is a promising tool for the study of electrode/electrolyte region [1] and it is found to be a very sensitive technique for elucidating the structure and properties of the molecules adsorbed on roughened electrodes [2]. Despite intense investigation, a complete qualitative understanding of SERS has not been achieved so far. However, it is agreed that the causes of enhancement may be due to electromagnetic and chemical mechanisms [3]. In the case of electromagnetic mechanism, the enhancement arises, because of the greatly increased surface electromagnetic fields on the roughened surface that are used as SERS substrate and these fields are due to the excitation of electromagnetic resonances of conduction electrons. In the case of chemical mechanism, the enhancement depends strongly on the adsorbed species. This shows that the enhancement may be due to some short-range interaction between the adsorbed molecule and the surface [4].

It has been known that dye molecules adsorbed on some substrate surfaces can produce obvious SERS effects. Once each enhanced spectral band is assigned, a lot of structural data would be obtained which will be helpful for understanding the interaction between dye molecule and metal surface and also in understanding light catalysts and the photographic process [5].

Recently our group investigated SERS studies of certain α-amino anthraquinones in silver sol [6, 7]. It is found that the carbonyl oxygen which is charged partially negative (9th position) and lone pair electrons of nitrogen atom form good binding sites for the surface adsorption. Here, we have investigated to know the nature and dynamics of DHAQ at silver electrode.

In the present study, we have also analysed laser-induced fluorescence spectra of

DHAQ, with a view to assign the relative orientation of absorption and emission dipoles.

2. Experimental

Based on various SERS studies, Ag is found to be an effective substrate and Ag electrode system was used in our analysis. Oxidation and reduction cycles have been performed between − 1 and + 1 V for the Ag electrode system. DHAQ solution was etched on the Ag electrode.

The experimental set up used for Raman studies has been given earlier [6]. The power of the laser source is approximately 60 mW. The intensity of the scattered light remains constant as the solution has sufficient stability throughout the experiment.

The excitation source employed for fluorescence measurements is a Spectra Physics 2020–04S 4 W all line argon ion laser. A glass tube of 10 mm diameter, and 25 mm length is used as a liquid cell. The home-built sample compartment has a special feature, so that measurements at all possible scattering angle (15° to 345° in steps of 15°) can be made. The typical laser power ($\lambda_{ex} = 501{\cdot}7$ nm) at the sample is ≈ 40 mW. Fluorescence measurements are made at various time intervals to ensure that photo decomposition does not take place as evidenced by the absence of distortion in the fluorescent spectrum. The angular variation of fluorescence is also investigated.

3. Results and discussion

3.1 *Raman spectrum*

Figure 1 gives the structure of DHAQ used in our study. DHAQ belongs to C_s point group. By assuming that all the atoms of DHAQ are lying on the same plane, it has 72 normal modes. Figure 2 shows the schematic diagram of SERS spectrum of the dye molecule (DHAQ) adsorbed at Ag metal surface. For comparison, the normal Raman spectrum and the Raman spectrum after adsorption on Au/Ag sol are also given. The normal Raman spectrum of DHAQ gives only 8 lines, but the Raman spectrum due to adsorption on Au/Ag sol gives 16 lines. The Raman spectrum due to adsorption at Ag electrode system gives 18 lines. Due to adsorption the intensity of the spectral lines are enhanced and the enhancement factor is about 35 orders of magnitude.

In the Ag electrode system a weak band at 420 cm^{-1} has appeared due to ring deformation. However, two spectral bands at 617, and 651 cm^{-1} are observed in the SERS spectrum (Au/Ag sol).

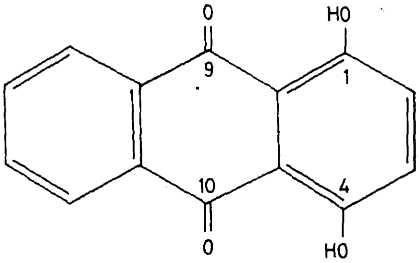

Figure 1. Structure of DHAQ.

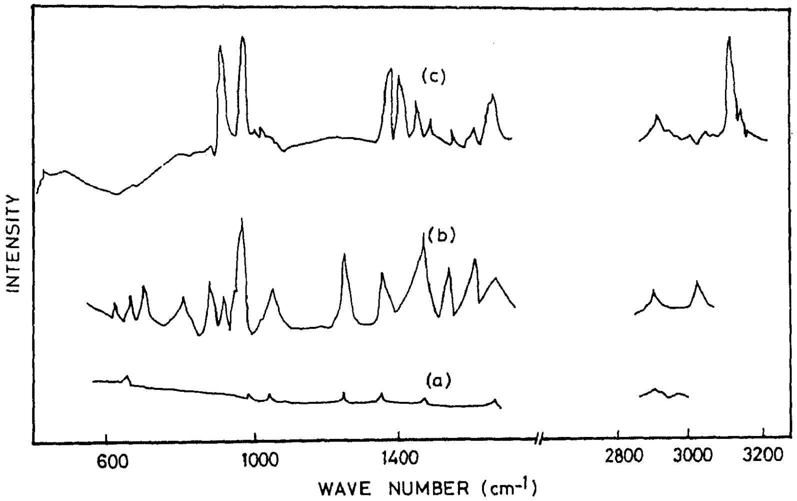

Figure 2. (**a**) Normal solution Raman spectrum of DHAQ; (**b**) Raman spectrum of $0{\cdot}1 \times 10^{-3}$ DHAQ in Au/Ag sol; (**c**) Raman spectrum of $0{\cdot}1 \times 10^{-3}$ DHAQ on Ag electrode.

The electrode system shows bands at 873, 889 and 993 cm^{-1} due to out-of-plane bending (γ) of C-H group. At 889 cm^{-1} the band intensity is well pronounced. The ring breathing mode appeared at 961 cm^{-1} in both normal and SERS spectra (Au/Ag sol) but for the Ag electrode an intense band at 955 cm^{-1} has been observed.

SERS spectrum (Ag electrode) shows a weak band at 1014 cm^{-1} which is due to in-plane bending (β) vibration of C–H group. A band is observed at 1042 cm^{-1} in the normal Raman spectrum which is shifted to 1059 cm^{-1} in SERS spectrum [Au/Ag sol], and these are due to in-plane bending (β) of C–H group. An intense band at 1248 cm^{-1} is observed in the normal Raman spectrum as well as in SERS spectrum (Au/Ag sol) and this band is assigned to O–H(β) in-plane bending mode.

The C–O(H) stretching mode is observed at 1373 cm^{-1} in the case of SERS spectrum (Ag electrode). Two medium intense bands appeared at 1392 and 1440 cm^{-1} in the SERS spectrum (Ag electrode) due to CH_3 and CH_2 deformation.

A weak band at 1469 cm^{-1} which appeared due to ring stretching mode in normal Raman spectrum shifted to 1480 cm^{-1} in the SERS spectrum (Ag electrode).

A band with medium intensity at 1594 cm^{-1} is observed both on Au/Ag sol and in Ag electrode. At 1557 cm^{-1} a band has appeared in SERS spectrum (Ag electrode), and it is shifted down to 1537 cm^{-1} in the case of SERS spectrum (Au/Ag sol). Also a band is observed at 1674 cm^{-1} in both normal Raman spectrum and SERS spectrum (Au/Ag sol) and is shifted down to 1648 cm^{-1} in SERS spectrum (Ag electrode).

At 2900 cm^{-1} a weak band is observed in all the three cases. In the SERS spectrum (Ag electrode) bands at 2987, 3035, 3100, 3127 and 3150 cm^{-1} are assigned to CH stretching vibrations. The proposed assignments are given in table 1.

In SERS spectrum (Ag electrode), the bands at 889, 955, 1373, 1392, 1648 and 3100 cm^{-1} are well pronounced. The bands on Au/Ag sol and also at Ag electrode system have frequency shifts due to the adsorption and subsequently, due to the interaction between substrate-adsorbate. This deviations (or) shifts are due to the chemical environmental effect on molecular vibrations.

Generally aromatic compounds which are not possessing the binding sites are

Table 1. Spectral data and assignments.

Normal Raman spectrum DHAQ + Methanol (cm^{-1})	SERS spectrum DHAQ + Methanol (cm^{-1})		Assignment
	In Au/Ag sol	At Ag electrode	
		420	
	617		Ring deform
651	651		
	692		
	799		γ-CH
	866	873	
	912	889	
961	961	955	Ring breathing
		993	γ-CH
1042	1059	1014	β-CH
1248	1248		β-CH
1354	1354	1373	C–O(H)
		1392	CH_3 deformation
		1440	CH_2 deformation
1469	1469	1480	
	1537	1557	Ring stretch
	1594	1594	
1674	1674	1648	C=O stretch
2900	2900	2900	O–H stretch
	3011	2987	
		3035	
		3100	CH stretch
		3127	
		3150	

β – in plane bending mode; γ – out of plane bending mode.

adsorbed through their pi-orbital system. Even though DHAQ molecule has coordinating site (C = O), the hydrogen bond formation between C=O and O–H groups does not allow the molecule to get adsorbed through this site. These molecules are adsorbed flat on the top of the metal surface. Because of the planar structure, the interaction between the metal and the adsorbed molecule is strengthened during vibration. So the link of the molecule with surface cannot be destroyed. The charge transfer between the adsorbate and the substrate is more pronounced. So the enhancement may be due to the change in molecular polarizability.

3·2 *Fluorescence*

The fluorescence maxima for DHAQ in CCl_4, chloroform and acetone is around 566 nm. However the shift observed due to solvent effect (solvent polarity) is negligible. This shows that there is no solvent-solute interaction. It can be assumed that the polar groups of DHAQ [C=O] do not have any interaction with the solvent, making the absence of dipole-dipole interactions. This helps us to understand that only the π orbital system is available for the surface adsorption.

Since light is emitted in 3 dimensions, the true composition of the fluorescent light is a mixture of I(parallel) and I(perpendicular) components of the beam, parallel and perpendicular to the incident electric vector direction respectively. The intensity of these components depends on the polarization behaviour of the molecule. Polarization measurements have been carried out in order to understand the relative orientation of the absorption and emission dipoles. It is known that the intrinsic polarization (P_0) will have values $1/2 \leqslant P_0 \leqslant -1/3$ when the molecules is excited by polarized light. Figure 3 shows that P_0 value is negative for DHAQ in all the solvents. In the case of various aminoanthraquinones, it is found that $S_1(\pi\pi^*) - T_2(n\pi^*)$ energy gap is small. As the density of electronic states in the vicinity of S_1 and T_2 is much higher the intersystem crossing between these states is more efficient [8]. This is indicative of the fact that the molecule is excited to a particular energy state and the emission is from a different energy state. This can be ascertained from the fact that the absorption and emission oscillators have different transition moment directions. It is observed that $|P_0|$ value changes with the polarity of the solvent. The variation of K_{ISC} with the solvent polarity is also responsible for the change in P_0 value and fluorescence yield.

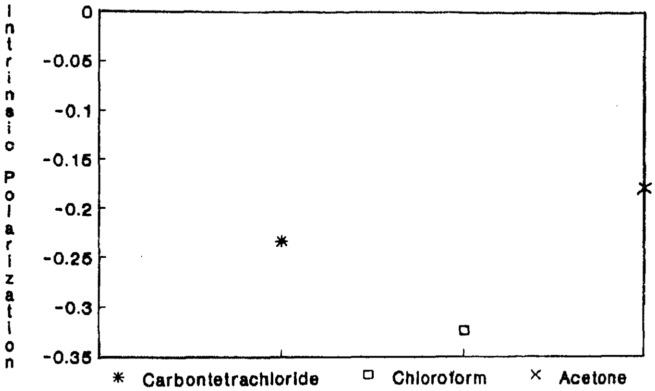

Figure 3. Intrinsic polarization of DHAQ. (*) carbontetrachloride (□) chloroform (×) acetone.

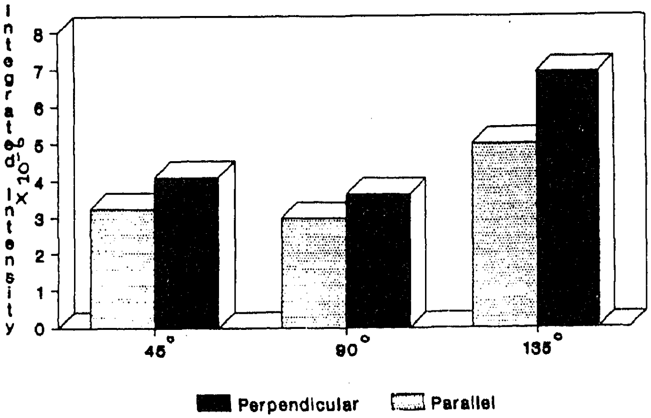

Figure 4. Integrated intensity of DHAQ with carbontetrachloride (■) perpendicular (□) parallel.

One of the factors to be considered in the fluorescence study is the geometry of the sample chamber and its influence on the fluorescent intensity. As the fluorescence is radially dispersed, only a very small portion of the emitted light is observed by the detector. The integrated intensity evaluated for various scattering angles measurements are given in figure 4. It is found that the integrated intensity is higher for I (perpendicular) measurements. This is being reflected from the negative values observed for P_0. The comparison of the intensity at various angles shows that at 135° (225°), the intensity is the highest. This may be due to the fact that the detector receives a good amount of emitted light (from the region of the sample) at this particular angle.

4. Conclusion

The DHAQ molecules are lying with their molecular planes on the top of the metal surface. The molecules are chemisorbed rather than physisorbed. The enhancement factor is found to be about 35 orders of magnitude.

SERS studies at Ag electrode system is shown to be a powerful technique for studying vibrational spectrum of DHAQ dye molecule on a metal surface.

Acknowledgements

The authors are grateful to the Department of Science and Technology, Government of India for financial assistance in the form of a project to one of the authors (VRK). The authors also thank Mr. M Gurunathan (USIC, Madurai Kamaraj University) for his technical assistance in laser Raman measurements and Dr. R Ramaraj (School of Chemistry) for the use of cycli voltamogram. One of the authors (SEJ) is grateful to Madurai Kamaraj University for the award of USRF. The authors are very much thankful to Dr T P Srinivasan for the help in design and fabrication of sample compartment.

References

[1] D E Irish, L Stolberg and D M Shoesmith, *Surf. Sci.* **158**, 238 (1985)
[2] D P Dilella, R R Smardzewski, S Guha and P A Lund, *Surf. Sci.* **158**, 295 (1985)
[3] Alan Campion and David R Mullins, *Surf. Sci.* **158**, 263 (1985)
[4] W Schutze, K P Charle and U Kloss, *Surf. Sci.* **156**, 822 (1985)
[5] Li Xia Li, Chunanpu Lia, Yuezhu Gu, Young You Guo and Yongjia Yin, *Chem. Phys. Lett.* **144**, 378 (1985)
[6] V Ramakrishnan, M Krishnamurthy, M Gurunathan and V J P Srivatsavoy, *Spectrochim. Acta* **A46**, 1615 (1990)
[7] V Ramakrishnan, M Krishnamurthy, A Dickson Benjamin and V J P Srivatsavoy, *Surf. Sci.* (communicated) (1992)
[8] S R Flom and P F Barbara, *J. Phys. Chem.* **89**, 4489 (1985)

PRAMANA
— journal of
physics

© Printed in India

Vol. 41, No. 5,
November 1993
pp. 473–477

A design of an inexpensive demountable *X*-ray tube

V S PAI, N V MOGHE and V B SAPRE
Department of Physics, Nagpur University, Nagpur 440010, India

MS received 21 June 1993; revised 15 September 1993

Abstract. An inexpensive and simple demountable X-ray source, having facilities to excite X-rays either by bombardment of a target by electrons or by fluorescence, has been developed using a stainless steel chamber having six ports. A cathode assembly from a burnt out sealed off Machlett X-ray tube was carefully removed and reused in the present set-up after replacing the filament. A conventional vacuum system consisting of a rotary and diffusion pumps has been utilized for evacuating the chamber. The set-up can be conveniently utilized to carry out X-ray emission spectroscopic work.

Keywords. Demountable; X-ray emission; fluorescence.

PACS No. 78·70

1. Introduction

It is well-known that the X-ray emission spectrum, which corresponds to transitions from filled orbitals to momentary vacancies created in inner shells, gives energy distribution of occupied orbitals. On the other hand, X-ray absorption spectrum corresponds to the transitions of the ejected photoelectrons to unoccupied orbitals of higher energy and hence displays the distribution of the normally empty energy levels. The processes are thus complementary.

A considerable amount of work on X-ray absorption spectroscopy has been carried out in our laboratory. To extend this to X-ray emission spectroscopy, especially to study the chemical shifts and shapes of X-ray emission lines, we have designed and fabricated a simple inexpensive demountable X-ray tube. It is mounted on a standard vacuum system, consisting of a rotary and a diffusion pump (figure 1). A control panel can also be seen on the right hand side.

2. Design and fabrication

The design of an X-ray emission tube is shown in figure 2 with necessary details. It consists of a stainless steel chamber with six ports, one of which is directly connected to the vacuum system. Through the other two, mutually perpendicular ports, the target and the cathode assembly are inserted. The window port is exactly opposite to the target.

The target is a circular disc of copper inclined at an angle of 45° with the direction of the flow of electrons and is brazed to a stainless steel pipe of length 11·5 cm and diameter 1·3 cm. It is further fixed on a flange which when mounted puts the target at the centre of the cross. The target can be cooled by a continuous flow of water.

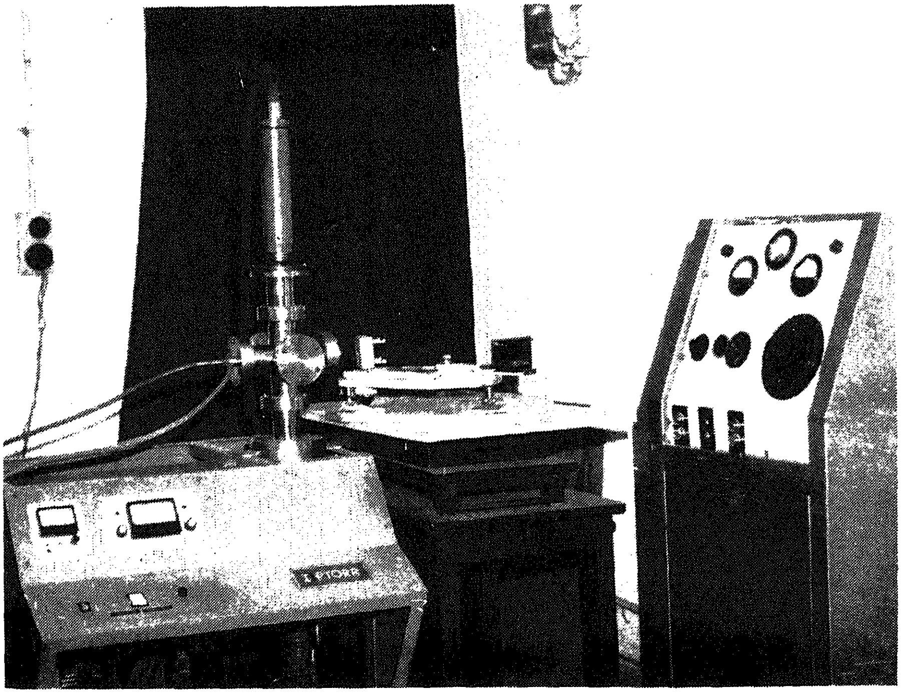

Figure 1. Demountable X-ray tube—a complete set up.

Twenty blind holes with diameter and depth of about 1·5 mm have been drilled on the surface of the target. A finely powdered sample can be pressed into these pits without using an adhesive. Another target assembly [1], wherein the target can be cleaned in vacuum, has also been designed and fabricated.

The cathode assembly from a burnt out sealed off Machlett X-ray tube, which was available in our laboratory was carefully removed and reused [2] in the present work. This helped us in reducing the cost of the demountable X-ray tube since we did not have to buy the expensive high voltage feed-throughs. It also allowed us to use the connectors and cable, coupling the tube with the generator, for operation of X-ray tube.

A stainless steel cup of 2·5 cm diameter is connected to the leads of the cathode assembly with proper insulation. A filament of 1 cm is made by winding a tungsten wire of diameter 0·02 cm on a pin of diameter 0·05 cm and is positioned at the centre of the stainless steel cup, which acts as an electron beam collimator.

The window is a circular opening of about 1 cm diameter in the centre of a stainless steel flange which is covered with three layers of cellophane tape. A hollow pipe of length 10 cm and diameter 1·6 cm is kept between the window and the target which acts as a collimator for the X-ray beam.

The distance between the target and the filament is about 0·8 cm and that between the target and the collimator is about 1 cm.

The tube is evacuated to the order of 10^{-6} torr using conventional vacuum system made by IBP Co., Bombay consisting of a rotary and a diffusion pump.

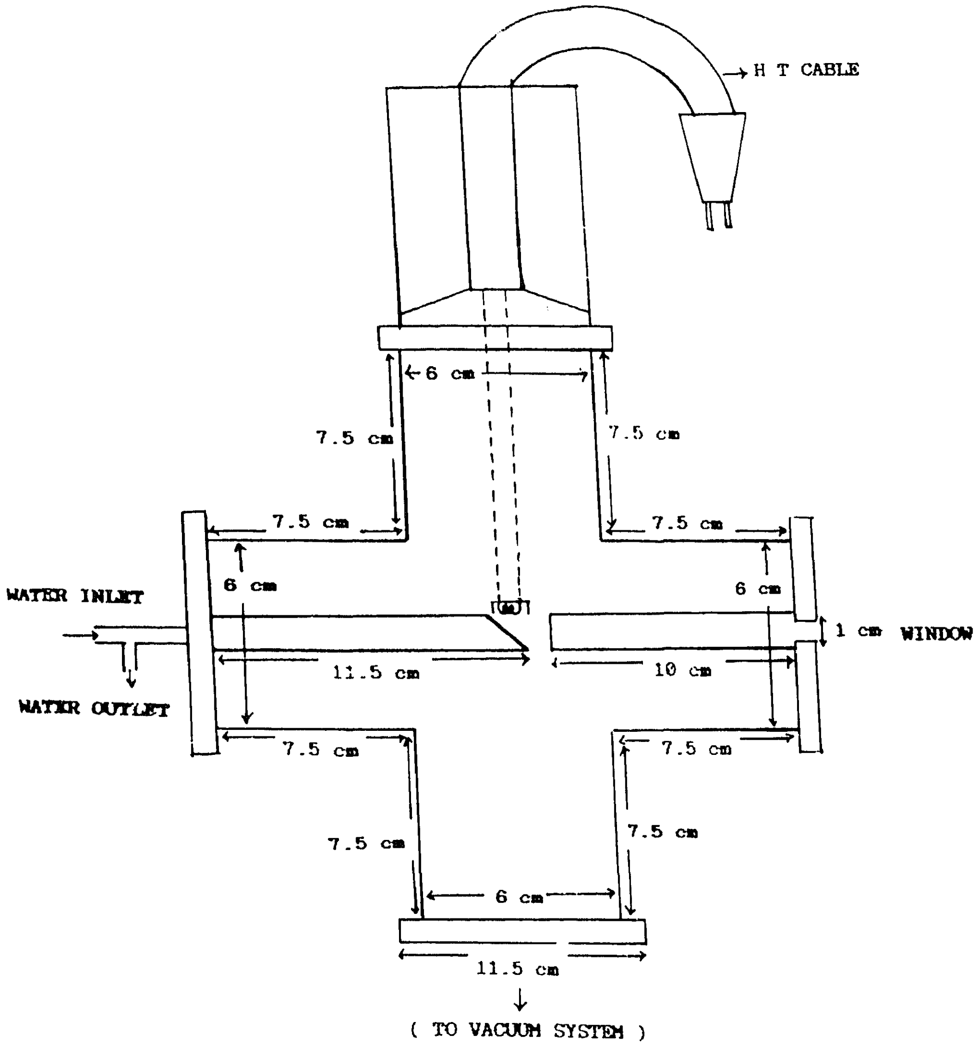

Figure 2. Demountable X-ray tube.

3. Working

The high D C Voltage, for operating the X-ray tube, is obtained from a high voltage transformer giving maximum 50 kV after rectification by means of silicon rectifires. The negative terminal is connected to the cathode, while the anti-cathode and the body of the X-ray tube are earthed.

The emission spectrum of the target, shown in figure 3, has been recorded by employing a 40 cm Cauchois type bent crystal X-ray spectrograph using (220) planes of a silicon crystal [3] to disperse various wavelengths. The spectrum can be recorded in 30 s by operating the tube at 20 kV and 10 mA. However, for obtaining a good contrast, the spectrum shown in figure 3 has been obtained by giving an exposure of 10 min.

The analysis of an X-ray spectrum, recorded photographically, has been performed by using automated and computerised Carl-Zeiss (MD, 100) Microdensitometer [4].

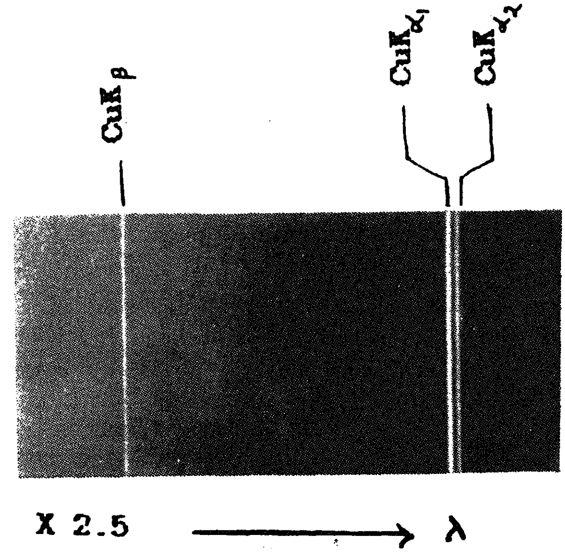

Figure 3. Cu K emission spectrum.

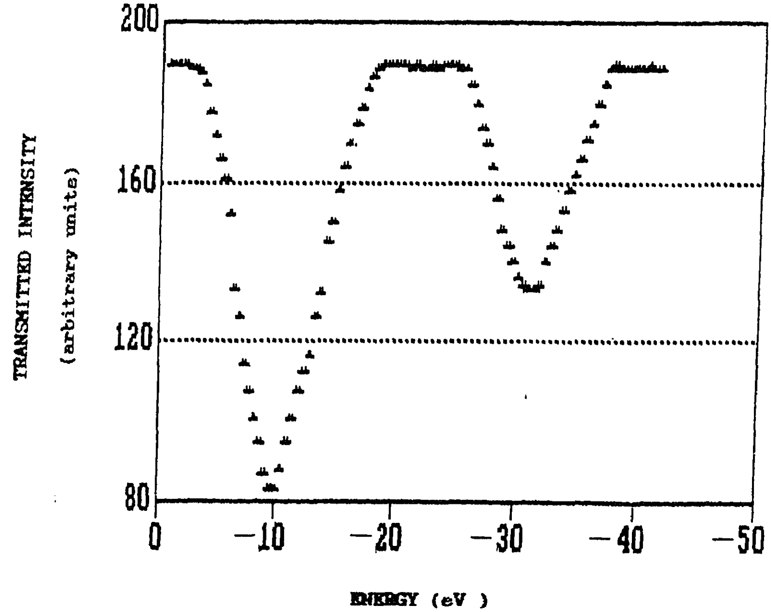

Figure 4. Microphotometer record of CuK emission spectrum.

A typical microdensitometer record of CuK$_\alpha$ emission spectrum recorded in 45 s is shown in figure 4. It is very clearly seen that the intensity of CuKα_1 line is about twice that of CuKα_2, indicating that the photodensity S of the film is proportional to the incident X-ray intensity, I. A comparison of the intensities of same spectral lines recorded using readymade generators, manufactured by M/s Carl-Zeiss, Germany and M/s Radon House, India, that are available in our laboratory, indicates that the intensity of the source designed by us is satisfactory. The full width at half maximum (FWHM) of the line is calculated using computerised curve. Our measurements on the FWHM of CuKα_1 and CuKα_2 are found to be in agreement with those of the earlier workers [5, 6].

4. Advantages

The target can be easily removed and the pits on the target can be filled with the sample under investigation. The sample which is likely to decompose due to the bombardment of high energy electrons, can also be studied by properly mounting it inside the chamber and exciting it by fluorescence. The spectrum recorded in either case would contain the lines from the sample as well as from the base material which can be used as reference lines for the measurement of chemical shifts.

Acknowledgement

We are thankful to the University Grants Commision, New Delhi, for the financial support.

References

[1] V B Sapre and R J Liefeld, *Bull. Ind. Vac. Soc.* **20**, 49–52
[2] V B Sapre, *Research and Industry*, **25**, 204 (1980)
[3] S D Deshpande, N V Moghe, V B Sapre and C Mande, *Meas. Sci. Technol.* **1**, 1250 (1990)
[4] Nitin Moghe, Narendra Mathurkar, G M Bhongale and V B Sapre, *Meas. Sci. Technol.* **3**, 557 (1992)
[5] S K Allison, *Phys. Rev.* **44**, 63 (1933)
[6] L G Parratt, *Phys. Rev.* **50**, 1 (1936)

PRAMANA
— journal of
physics

© Printed in India

Vol. 41, No. 5,
November 1993
pp. L479–L481

Geometric phase as a simple closed-form integral

APOORVA G WAGH and VEER CHAND RAKHECHA
Solid State Physics Division, Bhabha Atomic Research Centre, Bombay 400085, India

MS received 1 September 1993

Abstract. For a general evolution of a quantal system, the geometric phase measured with reference to a given initial state is derived as an integral of a function of the pure state density operator by invoking the Pancharatnam connection continuously.

Keywords. Geometric phase; density operator; Pancharatnam connection.

PACS Nos 03·65; 42·25

1. Introduction

It was a decade ago that a general nonintegrable, Hamiltonian-independent part of the phase, viz. geometric phase, was delineated [1] in the context of adiabatic quantal evolutions. The prevalence of geometric phase in completely general evolutions and in a wide range of physical phenomena has since been recognised. The origin of geometric phase has been traced to the anholonomy in the ray space [2] of a parallel transported [3, 4] quantum state. The geometric phase is thus a property of the ray space alone.

In this communication, we bring out in a simple manner the exclusive dependence of the geometric phase on the geometry of the curve C traced in the ray space, without any reference to the Hilbert space. We present the general geometric phase as an explicit closed-form integral in the ray space.

When a quantal system evolves from an initial state $|\psi_0\rangle$ to a state $|\psi\rangle$, it acquires a phase Φ prescribed by the Pancharatnam connection [3, 4] as

$$\exp(i\Phi) = \langle\psi_0|\psi\rangle/|\langle\psi_0|\psi\rangle| = \langle\psi_0|\psi\rangle/(\langle\psi_0|\psi\rangle\langle\psi|\psi_0\rangle)^{1/2}. \tag{1}$$

Hence

$$i\mathrm{d}\Phi = \langle\psi_0|\mathrm{d}\psi\rangle/\langle\psi_0|\psi\rangle - \tfrac{1}{2}\langle\psi_0|\mathrm{d}(|\psi\rangle\langle\psi|)|\psi_0\rangle/(\langle\psi_0|\psi\rangle\langle\psi|\psi_0\rangle).$$

i.e.

$$\Phi = \tfrac{1}{2}i\int_{|\psi_0\rangle}^{|\psi\rangle}\{\langle\psi_0|(|\psi\rangle\langle\mathrm{d}\psi| - |\mathrm{d}\psi\rangle\langle\psi|)|\psi_0\rangle/(\langle\psi_0|\psi\rangle\langle\psi|\psi_0\rangle)\}. \tag{1a}$$

The integrable, Hamiltonian-dependent part of this phase Φ, viz. the dynamical phase Φ_D, can be expressed as [2, 5]

$$\Phi_D = \mathrm{Im}\int_{|\psi_0\rangle}^{|\psi\rangle}\{\langle\psi|\mathrm{d}\psi\rangle/\langle\psi|\psi\rangle\}$$

$$= -\tfrac{1}{2}i\int_{|\psi_0\rangle}^{|\psi\rangle}\{(\langle\psi|\mathrm{d}\psi\rangle - \langle\mathrm{d}\psi|\psi\rangle)/\langle\psi|\psi\rangle\}$$

$$= -\tfrac{1}{2} i \int_{|\psi_0\rangle}^{|\psi\rangle} \{\langle\psi_0|(\rho|\mathrm{d}\psi\rangle\langle\psi| - |\psi\rangle\langle\mathrm{d}\psi|\rho)|\psi_0\rangle/(\langle\psi_0|\psi\rangle\langle\psi|\psi_0\rangle)\}. \tag{2}$$

Here $\rho = |\psi\rangle\langle\psi|/\langle\psi|\psi\rangle$, represents the pure state density operator with the familiar properties: $\rho^\dagger = \rho, \rho^2 = \rho$ and $\mathrm{tr}(\rho) = 1$. The operator ρ remains unaltered if $|\psi\rangle$ is multiplied by a complex number. Thus the information about the variations in the phase and the norm of $|\psi\rangle$ is switched off in the ρ representation. Therefore ρ yields an image of $|\psi\rangle$ in the ray space.

The remaining part of Φ, viz. the geometric phase, therefore equals

$$\begin{aligned}\Phi_G = \Phi - \Phi_D &= \tfrac{1}{2} i \int_{\rho_0}^{\rho} \left\{\langle\psi_0|[\rho, \mathrm{d}\rho]|\psi_0\rangle/\langle\psi_0|\rho|\psi_0\rangle\right\} \\ &= \tfrac{1}{2} i \int_{\rho_0}^{\rho} \{\mathrm{tr}\, \rho_0[\rho, \mathrm{d}\rho]/\mathrm{tr}\, \rho_0\rho\}. \end{aligned} \tag{3}$$

Geometric phase thus originates directly from the noncommutability between the density operator and its differential and from the consequent geometric anholonomy in the ray space.

If the final ray is orthogonal to the initial ray, i.e. $\langle\psi_0|\psi\rangle = 0$ and $\rho_0\rho = \mathbf{0}$, the total phase Φ and therefore the geometric phase Φ_G, becomes indeterminate (eqs (1) and (3)). However for a nonorthogonal final ray, (3) is valid even if the curve C passes through an orthogonal ray during its evolution. At the orthogonal ray, both the numerator and denominator of the integrand in (3) vanish, yet the integrand is determinate, given by its limit at the orthogonal ray along C.

Since ρ and $\mathrm{d}\rho$ are both Hermitian operators, (3) can be rewritten as

$$\begin{aligned}\Phi_G &= -\mathrm{Im} \int_{\rho_0}^{\rho} \{\mathrm{tr}\, \rho_0\rho\mathrm{d}\rho/\mathrm{tr}\, \rho_0\rho\} \\ &= i \underset{\mathrm{C}}{\int_{\rho_0}^{\rho}} \{\mathrm{tr}\, \rho_0(\rho - \tfrac{1}{2}\mathbf{1})\mathrm{d}\rho/\mathrm{tr}\, \rho_0\rho\}. \end{aligned} \tag{4}$$

as the Hermitian part of $\rho\mathrm{d}\rho$ equals $[\rho\mathrm{d}\rho + (\mathrm{d}\rho)\rho]/2 = \mathrm{d}(\rho^2)/2 = \mathrm{d}\rho/2$. The symbol **1** denotes the unity operator. Equation (4) expresses the geometric phase as a simple closed-form integral purely over the parameters in the ray space, thus bringing out the sole dependence of Φ_G on the the geometry of the curve C traced out in the ray space. This relation holds for a general evolution; it does not require the evolution to be adiabatic, cyclic or even unitary. The relation (4) is identical to the equation

$$\Phi_G = i \int_C \langle\tilde{\psi}|\mathrm{d}\tilde{\psi}\rangle, \tag{5}$$

with $|\tilde{\psi}\rangle = |\psi\rangle \exp(-i\Phi)/\langle\psi|\psi\rangle^{1/2}$ symbolising the normalized form of $|\psi\rangle \exp(-i\Phi)$, Φ being specified by the Pancharatnam connection (1). In the special case of a unitary cyclic evolution, the curve C gets closed and (5) for Φ_G reduces to the nonadiabatic geometric phase [2] derived previously.

We illustrate the result (4) by applying it to the case of a 2-state system as a spin 1/2 particle. Here

$$\rho = (\mathbf{1} + \mathbf{s}\cdot\boldsymbol{\sigma})/2, \tag{6}$$

where $\mathbf{s} = \langle\psi|\boldsymbol{\sigma}|\psi\rangle$ denotes a unit vector in the direction of the 'spin', $\boldsymbol{\sigma}$ signifying the vector of the Pauli spin operators. Then

$$\begin{aligned}(\rho - \tfrac{1}{2}\mathbf{1})\mathrm{d}\rho &= \tfrac{1}{4}(\mathbf{s}\cdot\boldsymbol{\sigma})(\mathrm{d}\mathbf{s}\cdot\boldsymbol{\sigma}) = \tfrac{1}{4}i(\mathbf{s}\times \mathrm{d}\mathbf{s})\cdot\boldsymbol{\sigma})\\ &= \tfrac{1}{4}i(-\sin\theta\mathrm{d}\phi\,\hat{\theta} + \mathrm{d}\theta\,\hat{\phi})\cdot\boldsymbol{\sigma}.\end{aligned} \tag{7}$$

Here (θ, ϕ) stand for the polar coordinates of $\mathbf{s}$ on the unit sphere of spin directions. The mutually orthogonal unit vectors

$$\begin{aligned}&\mathbf{s} = (\sin\theta\cos\phi,\ \sin\theta\sin\phi,\ \cos\theta)\\ &\hat{\theta} = (\cos\theta\cos\phi,\ \cos\theta\sin\phi,\ -\sin\theta) \text{ and}\\ &\hat{\phi} = (-\sin\phi,\ \cos\phi,\ 0)\end{aligned} \tag{7a}$$

directed respectively along the local surface normal, longitude and latitude on the spin sphere form a right-handed triad [6]. The geometric phase (4) then becomes

$$\Phi_G = -\tfrac{1}{2}\int_{\mathrm{C}} (\mathbf{s}_0\cdot\mathbf{s}\times \mathrm{d}\mathbf{s})/(1 + \mathbf{s}\cdot\mathbf{s}_0), \tag{8}$$

$\mathbf{s}_0 = \langle\psi_0|\boldsymbol{\sigma}|\psi_0\rangle$ representing the initial spin direction. A substitution from (7) and (7a) in (8) leads to the result [6]

$$\begin{aligned}\Phi_G &= \tfrac{1}{2}\underset{\mathrm{C}}{\int_{(\theta_0,\phi_0)}^{(\theta,\phi)}} \cos\theta\,\mathrm{d}\phi - \arctan\{\cos\tfrac{1}{2}(\theta_0+\theta)\tan\tfrac{1}{2}(\phi-\phi_0)/\cos\tfrac{1}{2}(\theta_0-\theta)\}\Bigr\}\\ &= -\tfrac{1}{2}\Omega(\mathrm{C}),\ \mathrm{mod}\ 2\pi,\end{aligned} \tag{9}$$

derived previously. Here Ω (C) denotes the solid angle subtended at the centre of the spin sphere by the closed circuit obtained by joining [3, 4] the ends (θ, ϕ) and (θ_0, ϕ_0) of C with the shorter arc of the great circle passing through them.

We acknowledge a discussion on the relation (5) with A K Pati of Theoretical Physics Division. We wish to thank the referee for helpful suggestions.

References

[1] M V Berry, *Proc. R. Soc. London* **A392**, 45 (1984)
[2] Y Aharonov and J Anandan, *Phys. Rev. Lett.* **58**, 1593 (1987)
[3] S Pancharatnam, *Proc. Indian Acad. Sci.* **A44**, 247 (1956)
[4] J Samuel and R Bhandari, *Phys. Rev. Lett.* **60**, 2339 (1988)
[5] A G Wagh and V C Rakhecha, *Phys. Lett.* **A170**, 71 (1992)
[6] A G Wagh and V C Rakhecha, (to be published)

PRAMANA
— journal of
physics

© Printed in India

Vol. 41, No. 6,
December 1993
pp. 483–491

Uniqueness of the solutions of multichannel scattering equation in three particle system

SUPROKASH MUKHERJEE
Theoretical Physics Group, Saha Institute of Nuclear Physics, Bidhannagar, Calcutta 700064, India

MS received 19 January 1993; revised 23 August 1993

Abstract. A new approach is made to investigate the old problem of non-uniqueness of the solution of Lippmann–Schwinger equation of three particle system and it is found that even the necessary condition for the existence of the problem is not satisfied.

Keywords. Lippman–Schwinger equation; multichannel scattering.

PACS Nos 03·65; 25·10

1. Introduction

The solutions of the inhomogeneous Lippmann–Schwinger (LS) equations for three particle system are considered to be non-unique [1]. The scattering states $|\psi_\alpha^\pm(E_\alpha)\rangle$ in α-channel at energy E_α, satisfy one inhomogeneous LS-equation and several homogeneous LS-equations, so that the solution $|\psi_\alpha^\pm(E_\alpha)\rangle$ of the inhomogeneous LS-equation have arbitrary admixture of the similar other states $|\psi_\beta^+(E_\alpha)\rangle$ with $\beta \neq \alpha$. That is, $|\psi_\alpha^\pm(E_\alpha)\rangle$ as well as $|\Phi_\beta^\pm(E_\alpha)\rangle = |\psi_\alpha^\pm(E_\alpha)\rangle + \sum_{\beta\neq\alpha} C_\beta |\psi_\beta^\pm(E_\alpha)\rangle$ with arbitrary coefficient C_β, are solutions of same inhomogeneous LS-integral equation, as straightforward algebra would seem to indicate. Such analysis, of course, tacitly assumes without proof that the homogeneous LS-equation have non-trivial solutions and that these are considered to be same functions as those obtained by solving appropriate inhomogeneous LS-equations, as Lippmann's identity seem to indicate. However, in the Fredholm theory of simultaneous integral equations one obtains (Colton and Kress [2]) an extra condition of consistency, called solvability condition for simultaneous existence of inhomogeneous and homogeneous integral equations for the same Kernel. In the light of such analysis in Fredholm theory, we reexamine the question about the condition of coexistence of homogeneous and inhomogeneous LS-equations and do find that this requires that the transition matrix of the rearrangement scattering be identically zero, at any arbitrary energy. This striking new result, therefore, rules out the coexistence of the homogeneous and inhomogeneous LS-equations vis-a-vis the said problem of the non-uniqueness of the solutions of LS-equations. These are discussed in § 2 along with its consequences. It is argued that this result is an indirect proof that either Lippmann's identity is wrong, as it is responsible for the appearance of the homogeneous LS-equations, or that the homogeneous LS-equation if exist, can admit only trivial (null) solutions, so that the said non-uniqueness problem does not arise in any case. This conclusion is similar to that obtained earlier [3] which showed that the Lippmann's identity is wrong if LS-equations are regarded as valid in the distribution theoretic sense.

2. Theory

In the Fredholm theory of integral equations it can be proved [2, 4] that the solution of the inhomogeneous integral equation, when it exists, is non-unique if the corresponding homogeneous integral equation has non-trivial solutions provided some conditions of consistency are satisfied. Corresponding to the Fredholm Kernel $K(x, y)$, let the homogeneous equation has non-trivial solutions

$$\phi_m(x) = \int K(x, y)\phi_m(y)\mathrm{d}y \tag{1}$$

for $m = 1, 2, \ldots, n$ then the claim is that the inhomogeneous integral equation for the same Kernel

$$\phi(x) = f(x) + \int K(x, y)\phi(y)\mathrm{d}y \tag{2}$$

for a square integrable inhomogeneous term $f(x)$, has either no solution, or when solvable, the L_2-solution of it is non-unique, being of the form

$$\phi(x) = \tilde{\phi}(x) + \sum_{m=1}^{n} C_m\phi_m(x) \tag{3}$$

where $\tilde{\phi}(x)$ is a particular solution of (2), C_m's are arbitrary constants, $\phi_1(x)$, $\phi_2(x), \ldots, \phi_m(x)$ are linearly independent solutions homogeneous equation of (1) (see corollary 1.19 [2]. In addition to this, in order that (1) is compatible with (2), a consistency condition, called solvability condition (see Th. 1.29 of [2]) is required to be satisfied, which demands that the inhomogeneous term $f(x)$ of (2) be orthogonal to all the solutions of the adjoint homogeneous equation, which is

$$\langle\psi_m|f\rangle = \int \psi_m(x)f(x)\mathrm{d}x = 0 \tag{4}$$

where $\psi_m(x)$ satisfies

$$\psi_m(x) = \int \mathrm{d}y\psi_m(y)K(y, x) \tag{5}$$

for $m = 1, 2, \ldots, n$. It can further be shown that in Fredholm theory, the condition (4) is a necessary and sufficient one that the inhomogeneous equation (2) has nontrivial solutions wherever the homogeneous equation (1), coexists with it, (2), nontrivially. In a multichannel scattering theory, the scattering state at a given energy satisfies the homogeneous and inhomogeneous Lippmann–Schwinger equation simultaneously and one concludes Glöckle [1] that the solution of the LS-equation is non-unique, perhaps in analogy with what is contained in (3) above. However, in the literature of multichannel scattering there is no mention of any solvability conditions corresponding to (4), which happens to be a necessary and sufficient condition for the coexistence of homogeneous and inhomogeneous equations (1) and (2). Although this result of L_2-theory of Fredholm integral equation cannot be applied to the LS-equation for $|\psi^+_\alpha(E_\alpha)\rangle$ (as $|\phi_\alpha(E_\alpha)\rangle$ and $V^\alpha|\psi^\pm_\alpha(E_\alpha)\rangle$ are not L_2-objects), one can still find a necessary condition for coexistence homogeneous and inhomogeneous equations of scattering.

The scattering states $|\psi^\pm_\alpha(E_\alpha)\rangle$ for α-channel, at a given energy E_α, are given by the following Lippmann–Schwinger equations: (we use the notation of Glöckle [1], mostly, with minor changes)

$$|\psi^\pm_\alpha(E_\alpha)\rangle = |\phi_\alpha(E_\alpha)\rangle + G^\pm_\alpha(E_\alpha)\, V^\alpha|\psi^\pm_\alpha(E_\alpha)\rangle \tag{6}$$

The superscripts + (or −) refer to solutions with outgoing (or incoming) wave boundary condition. This equation is normally derived by using the following equations:

$$|\psi_\alpha(E_\alpha + i\eta)\rangle = i\eta G_\alpha(E_\alpha + i\eta)|\phi_\alpha(E_\alpha)\rangle \tag{7}$$

$$|\psi^\pm_\alpha(E_\alpha)\rangle = \lim_{\eta\to 0^+} |\psi_\alpha(E_\alpha \pm i\eta)\rangle \tag{8}$$

$$G_\alpha(Z) = (Z - H_\alpha)^{-1},\quad G^\pm_\alpha(E_\alpha) = \lim_{\eta\to 0^+} G_\alpha(E_\alpha \pm i\eta - H_\alpha)^{-1} \tag{9}$$

$$G(Z) = (Z - H)^{-1} = G_\alpha(Z) + G_\alpha(Z)\, V^\alpha G(Z) \tag{10}$$

The total Hamiltonian is $H = H_0 + V = H_\alpha + V^\alpha$; H_0 and $V = V_\alpha + V^\alpha$ being, respectively, the total kinetic and potential energy operators; the α-channel Hamiltonian $H_\alpha = H_0 + V_\alpha$ has its eigenfunctions $|\phi_\alpha(E_\alpha)\rangle$ with energy E_α. If one uses the Lippmann's identity given by:

$$\lim_{\eta\to 0^+} i\eta G_\beta(E_\alpha + i\eta)|\phi_\alpha(E_\alpha)\rangle = \delta_{\alpha\beta}|\phi_\alpha(E_\alpha)\rangle \tag{11}$$

then, from (7) expressing $G(Z)$ in terms of $G_\beta(Z)$ through (10), we have the homogeneous equation of scattering, from (7), (8), (10) and (11):

$$|\psi_\alpha(E_\alpha + i\varepsilon)\rangle = i\eta G_\beta(E_\alpha + i\eta)|\phi_\alpha(E_\alpha)\rangle + G_\beta(E_\alpha + i\eta)\, V^\beta|\psi_\alpha(E_\alpha + i\eta)\rangle \tag{12}$$

$$|\psi^\pm_\alpha(E_\alpha)\rangle = G^\pm_\beta(E_\alpha)\, V^\beta|\psi^\pm_\alpha(E_\alpha)\rangle \tag{13}$$

where $\beta \neq \alpha$. Equation (13) gives the homogeneous equations of the scattering state $|\psi^\pm_\alpha(E_\alpha)\rangle$ (see eqn (3.51) of Glockle [1]), which yields a number of homogeneous equations, for all β other than $\beta = \alpha$. Again, for channel β we, similarly, obtain

$$|\psi^\pm_\beta(E_\alpha)\rangle = |\phi_\beta(E_\alpha)\rangle + G^\pm_\beta(E_\alpha)\, V^\beta|\psi^+_\beta(E_\alpha)\rangle \tag{14}$$

$$|\psi^\pm_\beta(E_\alpha)\rangle = G^\pm_\alpha(E_\alpha)\, V^\alpha|\psi^\pm_\beta(E_\alpha)\rangle \tag{15}$$

where $\phi_\beta(E_\alpha)$ is an eigenfunction of $H_\beta = H_0 + V_\beta$. Equations (6) and (15) are simultaneous inhomogeneous and homogeneous integral equations corresponding to same kernel $G^\pm_\alpha V^\alpha$. Equations (13) and (14) are in similar situations for the channel β. From the nature of the above derivations, using (7) to (15), it is to be noted that $|\psi^+_\alpha(E_\alpha)\rangle$, the solution of the inhomogeneous equation (6), defines the same function as that of the homogeneous equations (13) for all $\beta \neq \alpha$, and that happens as a consequence of Lippmann's identity (11). In the following discussion, we rewrite the homogeneous equations (13) and (15) as

$$|\psi^{\pm}_{\alpha' h\beta}(E_\alpha)\rangle = G^{\pm}_{\beta}(E_\alpha)\, V^{\beta}|\psi^{\pm}_{\alpha' h\beta}(E_\alpha)\rangle \tag{16}$$

$$|\psi^{\pm}_{\beta' h\alpha}(E_\alpha)\rangle = G^{\pm}_{\alpha}(E_\alpha)\, V^{\alpha}|\psi^{\pm}_{\beta' h\alpha}(E_\alpha)\rangle \tag{17}$$

to emphasize that, $|\psi^{\pm}_{\alpha' h\beta}(E_\alpha)\rangle$ is a solution of a homogeneous integral equation, eq (16), but we may note, in addition, that the solution of (16) is assumed to give the same function as the solution of (13) and also of (6):

$$|\psi^{\pm}_{\alpha' h\beta}(E_\alpha)\rangle = |\psi^{\pm}_{\alpha}(E_\alpha)\rangle. \tag{18}$$

It is further seen that, if $|\psi^{\pm}_{\alpha}(E_\alpha)\rangle$ is a particular solution of (6), so is $|\Phi^{\pm}_{\alpha}(E_\alpha)\rangle$ where

$$|\Phi^{\pm}_{\alpha}(E_\alpha)\rangle = |\psi^{\pm}_{\alpha}(E_\alpha)\rangle + \sum_{\beta\neq\alpha} C_\beta|\psi^{\pm}_{\beta, h\alpha}(E_\alpha)\rangle \tag{19}$$

the summation over β in (19) being for all channels other than α. Equation (19) is analogous to (3) and is the customary statement of the problem of non-uniqueness of the solutions Lippmann–Schwinger equation (6). It is important to remember that the results Fredholm theory of integral equation is not straightaway applicable to the integral equation of scattering (6) and (15), for their kernels $G^{\pm}_{\alpha}(E_\alpha)\, V^{\alpha}$ are not Fredholm type. Thus, although (19) is a consequence of (6) and (17), the result of compatibility condition corresponding to (4) of Fredholm theory, cannot be written down right away. We can, however, proceed to obtain a necessary condition for the coexistence of homogeneous and inhomogeneous integral equations. This is a pertinent question to ask for, in the present situation, $|\psi^{+}_{\alpha}(E_\alpha)\rangle$ in a three-particle system, obeys one inhomogeneous integral equation of the type (6) for kernel $G^{+}_{\alpha}(E_\alpha)\, V^{\alpha}$ and two different homogeneous integral equations of the type (13), with a different kernel $G^{+}_{\beta}(E_\alpha)\, V^{\beta}$ for $\beta\neq\alpha$, so the question of its being overdetermined vis-a-vis compatibility of equations concerned is to be looked into.

From (17), one would by complex conjugation write, for $\beta\neq\alpha$:

$$\langle\psi^{\pm}_{\beta' h\alpha}(E_\alpha)| = \langle\psi^{\pm}_{\beta' h\alpha}(E_\alpha)|\, V^{\alpha} G^{\mp}_{\alpha}(E_\alpha) \tag{20}$$

so that

$$\langle\psi^{-}_{\beta' h\alpha}(E_\alpha)|\, V^{\alpha}\psi^{+}_{\alpha}(E_\alpha)\rangle = \langle\psi^{-}_{\beta' h\alpha}(E_\alpha)|\, V^{\alpha} G^{+}_{\alpha}(E_\alpha)|\, V^{\alpha}\psi^{+}_{\alpha}(E_\alpha)\rangle \tag{21}$$

Further, using (6), we may write

$$\begin{aligned}\langle\psi^{-}_{\beta' h\alpha}(E_\alpha)|\, V^{\alpha}\psi^{+}_{\alpha}(E_\alpha)\rangle &= \langle\psi^{-}_{\beta' h\alpha}(E_\alpha)|\, V^{\alpha}\phi_{\alpha}(E_\alpha)\rangle\\ &\quad + \langle\psi^{-}_{\beta' h\alpha}(E_\alpha)|\, V^{\alpha} G^{+}_{\alpha}(E_\alpha)\, V^{\alpha}|\psi^{+}_{\alpha}(E_\alpha)\rangle\end{aligned} \tag{22}$$

from (21) and (22) we have

$$\langle\psi^{-}_{\beta' h\alpha}(E_\alpha)|\, V^{\alpha}\phi_{\alpha}(E_\alpha)\rangle = 0 \tag{23}$$

and using (18), we rewrite (23) to obtain ($\beta\neq\alpha$) for all E_α

$$T^{-}_{\beta\alpha}(E_\alpha) = \langle\psi^{-}_{\beta}(E_\alpha)|\, V^{\alpha}|\phi_{\alpha}(E_\alpha)\rangle = 0. \tag{24}$$

A word of caution is perhaps necessary when operation of complex conjugation is performed on terms which are capable of contributing finitely from surface integrals at infinity, as shown by the following: Using Schrodinger equation for

$$|\psi^+_\alpha(E_\alpha)\rangle : (E_\alpha - \mathbf{H}_\alpha)|\psi^+_\alpha(E_\alpha)\rangle = V^\alpha|\psi^+_\alpha(E_\alpha)\rangle \tag{25}$$

we may write:

$$\langle\xi|\, V^\alpha\psi^+_\alpha(E_\alpha)\rangle = \langle\xi|(E_\alpha - \mathbf{H}_\alpha)|\psi^+_\alpha(E_\alpha)\rangle \tag{26}$$

$$= \langle(E_\alpha - \mathbf{H}_\alpha)\xi|\psi^+_\alpha(E_\alpha)\rangle - \mathscr{I}(\langle\xi|, |\psi^+_\alpha(E_\alpha)\rangle \tag{27}$$

where the surface integral $\mathscr{I}(\langle\psi_1|, |\psi_2)$ is defined as

$$\mathscr{I}(\langle\psi_1|, |\psi_2\rangle) = \langle\psi_1|\mathbf{H}_0\psi_2\rangle - \langle\mathbf{H}_0\psi_1|\psi_2\rangle. \tag{28}$$

Here $(\mathbf{H}_0\psi_1)$ means H_0 operating ϕ_1 etc. (Gerjuoy [5]) where H_0 is the kinetic energy operator and hence the integral on the RHS of (28) can be converted into surface integral at infinity by Green's theorem. Using (27) we can write

$$\langle\psi^-_{\beta' h\alpha}(E_\alpha)|\, V^\alpha\psi^+_\alpha(E_\alpha)\rangle = \langle\, V^\alpha\psi^-_{\beta' h\alpha}(E_\alpha)|\psi^+_\alpha(E_\alpha)\rangle$$
$$- \mathscr{I}(\langle\psi^-_{\beta, h\alpha}(E_\alpha)|, |\psi^+_a(E_\alpha)\rangle. \tag{29}$$

Substituting for $\psi^+_\alpha(E_\alpha)$ on LHS in (29), using (6), and $\psi^-_{\beta' h\alpha}(E_\alpha)$ on RHS, using (15), we have

$$\langle\psi^-_{\beta' h\alpha}(E_\alpha)|\, V^\alpha\phi_\alpha(E_\alpha)\rangle + \langle\psi^-_{\beta' h\alpha}(E_\alpha)|\, V^\alpha G^+_\alpha(E_\alpha)\, V^\alpha\psi^+_\alpha(E_\alpha)\rangle$$
$$= \langle\, V^\alpha G^-_\alpha(E_\alpha)\, V^\alpha\psi^-_{\beta' h\alpha}|\psi^+_\alpha(E_\alpha)\rangle - \mathscr{I}(\langle\psi^-_{\beta' h\alpha}(E_\alpha)|, |\psi^+_\alpha(E_\alpha)\rangle. \tag{30}$$

Since $(G^-_\alpha)^+ = G^+_\alpha$ and V^α is hermitian, $(V^\alpha G^-_\alpha(E_\alpha)\, V^\alpha)^+ = (V^\alpha G^+_\alpha(E_\alpha)\, V^\alpha)$ Glöckle [1] we have, instead of (23):

$$\langle\psi^-_{\beta' h\alpha}(E_\alpha)|\, V^\alpha\phi_\alpha(E_\alpha)\rangle = -\mathscr{I}(\langle\psi^-_{\beta' h\alpha}(E_\alpha)|, |\psi^+_\alpha(E_\alpha)\rangle) \tag{31}$$

From (31), using (18), we get the following expression for the scattering matrix for all $\beta \neq \alpha$,

$$T^-_{\beta\alpha}(E_\alpha) = \langle\psi^-_\beta(E_\alpha)|\, V^\alpha\phi_\alpha(E_\alpha)\rangle = -\mathscr{I}(\langle\psi^-_\beta(E_\alpha)|, |\psi^+_\alpha(E_\alpha)\rangle) \tag{32}$$

The appearance of the extra surface integrals in (29) to (32) may be noted in comparison with the corresponding equations in (21) to (24). Now, for rearrangement scattering $\beta \neq \alpha$, each particle in the system is bound either to the target or to the projectile both initially as well as finally, so that the surface integral (32) at infinity is zero for all $\beta \neq \alpha$ Gerjuoy [5, 6]. Hence we have again,

$$T^-_{\beta\alpha}(E_\alpha) = \langle\psi^-_\beta(E_\alpha)|\, V^\alpha\phi_\alpha(E_\alpha)\rangle = 0 \tag{33}$$

for all $\beta \neq \alpha$. Equation (33), therefore, follows as a "necessary condition" whenever the inhomogeneous eqn. (6) co-exist with the homogeneous eqn. (15) for the case of rearrangement scattering $\beta \neq \alpha$.

Since

$$T^{(-)}_{\beta\alpha} = T^+_{\beta\alpha},\ T^+_{\beta\alpha}(E_\alpha) = \langle\phi_\beta|\, V^\beta|\psi^+_\alpha(E_\alpha)\rangle = 0 \tag{34}$$

on the energy shell, we conclude that the vanishing of the on-shell transition matrix $T^{+}_{\beta\alpha}(E_\alpha)$ for rearrangement scattering at arbitrary energy E_α is a "necessary condition" for the coexistence of the homogeneous and inhomogeneous equation of LS-type corresponding to same Kernel. Since the rearrangement scattering matrix $T^{+}_{\beta\alpha}(E_\alpha)$ cannot vanish identically for arbitrary energy E_α, we conclude that the homogeneous and inhomogeneous LS-equations, (6) and (15) (or (13) and (14)) cannot hold simultaneously. And since the inhomogeneous LS-equation (6) has some physical basis, the homogeneous LS-equation (15) either does not exist or admits only trivial solutions. This in turn cast doubts as to the validity of Lippmann's identity. It may be noted that the existence of a homogeneous integral equation does not necessarily mean that it has a non-trivial solution, in first place. Frėdholm theory states that the homogeneous Fredholm integral equation (1) has only a finite number of solution Kolton and Kress [2]. But the corresponding exercise has not been done for (13) or (15). The way the homogeneous LS-equation are derived, by use of Lippmann's identity (11), the homogeneous integral equations (13) or (15) appear to have infinite number of solutions corresponding to every arbitrary E_α. For, similar algebraic operation lead to inhomogeneous and homogeneous equations, and same function $|\psi^{\pm}_{\alpha}(E_\alpha)\rangle$ (or $|\psi^{\pm}_{\beta}(E_\alpha)\rangle$) appear in (13) (or (14)) as well as in (6) (or (15)), assuming Lippmann's identity to be valid, and one would be tempted to assume that the non-trivial solutions of homogeneous LS-equation (15) give the same function given by solution of the inhomogeneous LS-equation (6).

In summary, we might say that the Lippmann's identity is infructuous as the homogeneous LS-equation it yields can only be permitted to have trivial solution and that the non-uniqueness problem of the solutions of LS-equations do not exist.

It may be noted that the above analysis carried out for three particle systems can be extended easily for many-particle systems without much changes in the text (see Ch. 3 of [1]).

In some of my earlier publications [3, 7–11] I had shown the defects in the treatment of the non-uniqueness problem by Gerjuoy [5] and others [1].

A brief discussion highlighting the defects in the arguments of [5] and [6] is presented below. The principal equations that we consider for the purpose are as follows:

$$(E_\alpha - \mathbf{H})|\psi^{+}_{\alpha}(E_\alpha)\rangle = 0 \tag{35}$$

$$(E_\alpha - \mathbf{H}_\alpha)|\phi_\alpha(E_\alpha)\rangle = 0 \tag{36}$$

$$|\psi^{+}_{\alpha}(E_\alpha)\rangle = |\phi_\alpha(E_\alpha)\rangle + |\chi^{+}_{\alpha}(E_\alpha)\rangle \tag{37}$$

$$(E_\alpha - \mathbf{H}_\alpha)|\psi^{+}_{\alpha}(E_\alpha)\rangle = (E_\alpha - \mathbf{H}_\alpha)|\chi^{+}_{\alpha}(E_\alpha)\rangle = \bar{V}_\alpha|\psi^{+}_{\alpha}(E_\alpha)\rangle \tag{38}$$

$$G^{+}_{\alpha}(E_\alpha)(E_\alpha - \mathbf{H}_\alpha) = (E_\alpha - \mathbf{H}_\alpha)G^{+}_{\alpha}(E_\alpha) = I \tag{39}$$

where I is the unity operator, $|\chi^{+}_{\alpha}(E_\alpha)\rangle$ is the scattered part of $|\psi^{+}_{\alpha}(E_\alpha)\rangle$. Multiplying (39) on the right by $|\chi^{+}_{\alpha}(E_\alpha)\rangle$ and (38) on the left by $G^{+}_{\alpha}(E_\alpha)$ and subtracting, Gerjuoy gets [5]:

$$\begin{aligned} G^{+}_{\alpha}(E_\alpha)\,\bar{V}_\alpha|\psi^{+}_{\alpha}(E_\alpha)\rangle - |\chi^{+}_{\alpha}(E_\alpha)\rangle &= G^{+}_{\alpha}(E_\alpha)\cdot(E_\alpha - \mathbf{H}_\alpha)|\chi^{+}_{\alpha}(E_\alpha)\rangle \\ &- G^{+}_{\alpha}(E_\alpha)(E_\alpha - \mathbf{H}_\alpha)|\chi^{+}_{\alpha}(E_\alpha)\rangle = -\mathscr{I}(G^{+}_{\alpha}(E_\alpha), |\chi^{+}_{\alpha}(E_\alpha)\rangle) \end{aligned} \tag{40}$$

Similar manipulations, with $|\psi_\alpha^+(E_\alpha)\rangle$, yields [6]:

$$G_\alpha^+(E_\alpha)\cdot \bar{V}_\alpha|\psi_\alpha^+(E_\alpha)\rangle - |\psi_\alpha^+(E_\alpha)\rangle = -\mathscr{I}(G_\alpha^+(E), |\psi_\alpha^+(E_\alpha)\rangle). \tag{41}$$

Similarly, with (36) and (39), Gerjuoy *et al* [6] deduce:

$$\mathscr{I}(G_\alpha^+(E_\alpha), |\phi_\alpha(E_\alpha)\rangle) = G_\alpha^+(E_\alpha)(E_\alpha - \mathbf{H}_\alpha)|\phi_\alpha(E_\alpha)\rangle - G_\alpha^+(E_\alpha)\cdot(E_\alpha - \mathbf{H}_\alpha)\cdot|\phi_\alpha(E_\alpha)\rangle \tag{42}$$

$$= |\phi_\alpha(E_\alpha)\rangle. \tag{43}$$

Now, using the definition of Green's function (9) and (10) we get

$$(Z - \mathbf{H}_\alpha)G_\alpha(Z) = G_\alpha(Z)(Z - \mathbf{H}_\alpha) = I \tag{43}$$

$$(Z - \mathbf{H})G(Z) = G(Z)(Z - \mathbf{H}) = I. \tag{44}$$

From the definition of surface integrals in (28) we have

$$F_\alpha(Z) = \mathscr{I}(G_\alpha(Z), |\phi_\alpha(E_\alpha)\rangle) \tag{45}$$

$$= G_\alpha(Z)(Z - \mathbf{H}_\alpha)|\phi_\alpha(E_\alpha)\rangle - G_\alpha(Z)(Z - \mathbf{H}_\alpha)|\phi_\alpha(E_\alpha)\rangle$$

$$= |\phi_\alpha(E_\alpha)\rangle - (Z - E_\alpha)\cdot G_\alpha(Z)|\phi_\alpha(E_\alpha)\rangle$$

$$= |\phi_\alpha(E_\alpha)\rangle - (Z - E_\alpha)\cdot \frac{1}{Z - E_\alpha}|\phi_\alpha(E_\alpha)\rangle \tag{46}$$

$$= 0 \text{ for } Z \neq E_\alpha. \tag{47}$$

clearly $F_\alpha(Z)$ as a well defined analytic function of the complex variable Z, vanishing identically everywhere in the complex Z-plane, excepting at points E_α on the real energy axis corresponding eigenvalues of H_α (the spectrum), where $F_\alpha(Z)$ is undefined, being of the indeterminate (see (46)) form 0/0. But $F_\alpha(Z)$ has a unique value zero as real axis is approached, from above or below:

$$\mathscr{I}(G_\alpha^+(E_\alpha), |\phi_\alpha(E_\alpha)\rangle) = \lim_{n\to 0} F_\alpha(E_\alpha + i\eta) = 0. \tag{48}$$

It is known that for suitable class of potentials, the coordinate representatives of Green's function $G_\alpha(Z)$ is an analytic function of Z in the entire Z-plane, excepting at the spectrum (the eigenvalues E_α) of $H_{\alpha'}$ so that the singularities of $G_\alpha(Z)$ are poles in the negative real axis, corresponding to boundstates of $H_{\alpha'}$ and a cut along the positive real axis, across which $G_\alpha(Z)$ is discontinuous, and that $G_\alpha(Z)$ becomes unbounded, when real axis is approached from above or below, being bounded as

$$\|G_\alpha(Z)\| \leqslant \frac{C}{|\mathscr{I}_m(Z)|} \tag{49}$$

(C is a constant). Hence $F_\alpha(Z)$ remains bounded as real axis is approached from above or below. Further, from (43), we have for $Z = E_\alpha + i\eta$:

$$(E_\alpha - \mathbf{H}_\alpha)G_\alpha(E_\alpha + i\eta) = G_\alpha(E_\alpha + i\eta)(E_\alpha - \mathbf{H}_\alpha) = I - i\eta\, G_\alpha(E_\alpha + i\eta) \tag{50}$$

so that, instead of (39), we have

$$(E_\alpha - \mathbf{H}_\alpha)G_\alpha^+(E_\alpha) = G_\alpha^+(E_\alpha)(E_\alpha - \mathbf{H}_\alpha) = I - \lim_{n\to 0} i\eta\, G_\alpha(E_\alpha + i\eta). \tag{51}$$

Since for all $\eta \neq 0$ we have $i\eta\, G_\alpha(E_\alpha + i\eta)|\phi_\alpha(E_\alpha)\rangle = |\phi_\alpha(E_\alpha)\rangle$ identically, we may take

$$P_\alpha(E_\alpha)\cdot|\phi_\alpha(E_\alpha)\rangle = \lim_{n\to 0} i\eta\, G_\alpha(E_\alpha + i\eta)|\phi_\alpha(E_\alpha)\rangle = |\phi_\alpha(E_\alpha)\rangle \tag{52}$$

Thus, curiously enough, we get from (51), (52) [8–11]:

$$(E_\alpha - \mathbf{H}_\alpha)G_\alpha^+(E_\alpha)|\phi_\alpha(E_\alpha)\rangle = G_\alpha^+(E_\alpha)(E - \mathbf{H}_\alpha)|\phi_\alpha(E_\alpha)\rangle = 0. \tag{53}$$

This result already shows that the general equation (43) for Green's function in the complex plane, defined as an inverse of the operator $(Z - H_\alpha)$, does not automatically lead to (39) as a defining for Green's function for real energies. Clearly, for arbitrary vector $|f\rangle$, which does not contain a constant multiple of $|\varphi_\alpha(E)\rangle$, we have

$$P_\alpha(E_\alpha)|f\rangle = 0 \tag{54}$$

so that (51) behaves the same way as (39) does. Then it is wrong to use (39) as universally valid. Stated otherwise, it is important to know the domain of an operator before using it, as mathematicians would insist. Gerjuoy fell into the trap by treating (39) as universally valid, even though he started from (43) and (44) (see (1.4) in [5]). As a result Gerjuoy *et al* ends up getting $|\phi_\alpha(E_\alpha)\rangle$ for the RHS of (43), instead of zero for it, obtained as in (48). Ironically, this erroneous result (43) emerged as a strong point in the criticism of Gerjuoy *et al* in either criticism against my work. They did not realize that in going from (42) to (44) they have actually used algebraic operations which are not permissible. For example, they have taken $E_\alpha G_\alpha^+(E_\alpha)|\phi_\alpha(E_\alpha)\rangle - E_\alpha G_\alpha^+ (E_\alpha)|\phi_\alpha, (E_\alpha)\rangle = 0$, which looks innocent but it actually involves division by zero, for $G_\alpha^+(E_\alpha)|\phi_\alpha(E_\alpha)\rangle = (1/0)|\phi_\alpha(E_\alpha)$ and hence the above cancellation is not a permissible step in mathematics ($\beta - \beta = 0$ provided β is an element of algebra which excludes β obtained through division by zero). This then makes the most important result (43) (eqn. (12) of [6]) meaningless and invalid, alongwith it their strong criticism (see last three para of [6]) of my work. They, instead, claimed to have trivially derived. $F_\alpha(E_\alpha) = |\phi_\alpha(E_0) > (= \mathscr{J}(E)$ in [6]) without realising that $F_\alpha(E_\alpha)$ cannot be "calculated" for E_α is a singular point of $F_\alpha(Z)$ and $G_\alpha(Z)$, and it is onlv meaningful to talk about $F_\alpha(E_\alpha + i\eta)$ for $\eta \to 0$ which remains well defined. Further $F_\alpha(E_\alpha + i\eta)$ is zero identically and not because of the exponentially decreasing boundary condition which they thought to be the case. In fact $G_\alpha(Z)$ of (43) is definable in abstract manner as the inverse of the operator $(Z - H_\alpha)$ without assumption about the behaviour of $G_\alpha(Z)$ at large distances.

Another questionable feature in Gerjuoy's analysis is the prescription [6] that

$$\mathscr{J}(G^+(E_\alpha), |\chi_\alpha^+(E_\alpha)\rangle) = 0 \tag{55}$$

$$\mathscr{J}(G_\alpha^+(E_\alpha), |\chi_\alpha(E_\alpha)\rangle) = 0 \tag{56}$$

In fact the mathematical content of these prescriptions were never presented in their paper and the arguments had only been handwaving in nature. It was originally [5] presented more as an appeal to the common sense – as something intuitively expected, that the scattered wave $|\chi_\alpha^+(E_\alpha)\rangle$ is everywhere outgoing and hence (55) was thought to the consequence which cannot but include (56). Thus they got rid of this terms from (40) to get the standard result for scattered wave. They have then essentially assumed (55) and (56) to be true initially [5], and later [6] taken (55) to be the definition of the term everywhere outgoing and though "reasonable to assume" that (56) to be true (see discussion following (15) in [6]).

It should however be noted in passing that (55) or (56) is not just one condition on scattered wave, but is actually an infinite number of conditions, as can be seen be converting the volume integral to surface integral by Green's theorem, integral should vanish in every direction on the surface. But then the important question that stands out is about the status/meaning of the solution of a second order differential equation (35) constrained to satisfy these infinite number of conditions. In fact the conditions such as (55) or (56) can only be satisfied if they are zero identically. Gerjuoy [5] or [6] is unperturbed about or perhaps do not appear to have realised the real implication of (55) or (56). It may be mentioned here that, for completely different reasons (55) and (56) are actually true, as proved [see eqs. (19) and (20) in [8]).

In view of the above, I consider the criticism of Gerjuoy *et al* [6] of my work as totally invalid and conclude that the non-uniqueness problem of the solutions of LS-equations for three or many particle systems does not exist.

References

[1] W Glockle, *The quantum mechanical few-body problem*, (Springer-Verlag, 1983)
[2] D Colton and R Kress, *in Integral equation methods in scattering theory*, (John Wiley, New York, 1983)
[3] S Mukherjee, *Pramana – J. Phys.* **34**, 173 (1990)
[4] R Courant and D Hilbert, *Methods of mathematical physics* (Academic, New York, 1963)
[5] E Gerjuoy, *Phys. Rev.* **109**, 1806 (1958)
[6] E Gerjuoy and S K Adhikari *Phys. Lett.* **A115** 1 (1986)
[7] S Mukherjee, *Phys. Lett.* **A81**, 207 (1981)
[8] S Mukherjee, *Phys. Lett.* **A83**, 1 (1981)
[9] S Mukherjee, *Pramana – J. Phys.* **16**, 81 (1981)
[10] S Mukherjee, *Pramana – J. Phys.* **18**, 495 (1982)
[11] S Mukherjee, *Pramana – J. Phys.* **27**, 623 (1986)
[12] M Reed and B Simon, *Methods of modern mathematical physics* (New York, Academic, 1979) Vol. I, III

PRAMANA
— journal of
physics

© Printed in India

Vol. 41, No. 6,
December 1993
pp. 493–502

Energy levels of a two-dimensional anharmonic oscillator: Hill determinant approach

M R M WITWIT
Department of Applied Mathematics, University of Hull, Hull, HU6 7RX, UK

MS received 28 June 1993; revised 8 September 1993

Abstract. The energy levels of the Schrödinger equation for the potential $x^2 + y^2 + \lambda[a_{xx}x^4 + 2a_{xy}x^2y^2 + a_{yy}y^4]$ are calculated using Hill determinant approach for several eigenstates and over a wide range of values of perturbation parameters. The obtained numerical results agree with those previously reported by other methods.

Keywords. Schrödinger equations; Hill determinant; numerical results.

PACS No. 03·65

1. Introduction

Harmonic oscillator models have played an important role in the evolution of a number of areas of physics ranging from vibrations of crystal lattices to black body radiation to elasticity to acoustic, to molecular dynamics, etc.

This paper aims to calculate the energy levels of the two-dimensional oscillator which is expressed by the potential

$$V(x,y) = x^2 + y^2 + \lambda[a_{xx}x^4 + 2a_{xy}x^2y^2 + a_{yy}y^4]. \tag{1}$$

The two-dimensional anharmonic oscillator $V(x,y)$ has received a lot of attention recently as it is related to several interesting physical problems. Many techniques have been used to obtain the energy eigenvalues [1–8].

In this paper, some extended numerical calculations are, presented, using the Hill determinant approach (iterative technique) to calculate the energy levels of the Schrödinger equation for the potential (1) over a wide range of values of the perturbation parameters and for various eigenstates. The convergence of the energy depends upon the choice of an adjustable parameter β. However the convergence rate is relatively good, with better choice of β as will see later.

In rectangular coordinates the Schrödinger equation for the potential $V(x,y)$ can be written as:

$$\left[-\frac{\partial^2}{\partial x^2} - \frac{\partial^2}{\partial y^2} + V(x,y)\right]\Psi_{nx,ny}(x,y) = E\Psi_{nx,ny}(x,y). \tag{2}$$

The energy $E_{nx,ny}$ and wavefunction $\Psi_{nx,ny}(x,y)$ corresponding to the Schrödinger equation (2) when the perturbation parameter $\lambda = 0$ can be expressed as:

$$E_{nx,ny} = (2nx+1) + (2ny+1) \equiv 2n+2 \quad n_x, n_y = 0,1,2\ldots \tag{3}$$

$$\Psi_{nx,ny}(x,y) = \phi_{nx}(x)\phi_{ny}(y), \tag{4}$$

$$\phi_{nx}(x) = \left[\frac{1}{2^{nx}nx!}(\alpha/\pi)^{\frac{1}{2}}\right]^{\frac{1}{2}} \quad H_{nx}(\sqrt{\alpha}x)\exp-(\alpha/2)x^2. \tag{5}$$

As indicated earlier [7], eq (2) has a circular symmetry when the relationship $a_{xx} = a_{yy} = a_{xy} = 1$ holds for the potential (2). The energy levels are then most appropriately characterized by the quantum numbers (n_r, M) rather than (n_x, n_y). The radial part of the eigenvalue equation (2) can be expressed as:

$$\left[-\frac{\mathrm{d}^2}{\mathrm{d}r^2} + \left[M^2 - \frac{1}{4}\right]r^{-2} + r^2 + \lambda r^4\right]\Psi(r) = E\Psi(r). \tag{6}$$

The unperturbative energy in polar coordinates can be expressed as:

$$E_{nr,M} = 4n_r + 2|M| + 2 \equiv E_{nx,ny} \tag{7}$$

where $n_r = 0, 1, 2, 3, \ldots.$ and $M = 0, \mp 1, \mp 2, \ldots.$ are the orbital quantum number and the magnetic quantum number.

In each state the energy levels depend on the pair quantum numbers (n_x, n_y). The degeneracy degree of nth level is equal to the number of ways in which n can be divided into the sum of two positive integral (or zero) numbers; which is $n + 1$.

In (2) we have supposed that, to each eigenvalue $E_{nx,ny}$ there corresponds just one eigenfunction $\Psi_{nx,ny}(x,y)$. In the degenerate case several eigenfunctions correspond to the same eigenvalue. We notice that, as a result of the perturbation, an originally degenerate energy level ceases in general to be degenerate, because the perturbation removes the degeneracy. For example the states (1, 1; even-0, 2; even-2, 0; odd) start off to degenerate at $\lambda = 0$, but split up into three separate levels respectively as λ increases.

2. Hill determinant approach and its implementation to the two-dimensional oscillator and its recurrence relations

The Hill determinant approach is a non-perturbative technique and can handle numerical calculations of the eigenvalue problem in one-dimensional case for various types of potentials [10, 11, 12].

The polynomial potential given by (1) is non-separable in cartesian coordinates, but shows a high symmetry. Due to this symmetry it is possible to cut down the amount of computation needed in the program. The more general anisotropic case can also be treated by our technique.

We stress that the Hill determinant approach has been found comparable to the inner product method when applied to the same perturbation in multidimensional systems.

To find the recurrence relations which allow us to calculate the eigenvalues, we introduce the following wavefunction:

$$\Psi_{nx,ny}(x,y) = \exp\left[-\frac{\beta}{2}(x^2 + y^2)\right]\sum_{L,I} F(L,I)(x^L y^I). \tag{8}$$

By substituting $\Psi_{nx,ny}(x,y)$ in (2) and after some algebra, we get the following recurrence relation,

$$F(L,I) = W(L,I)[2\beta(L+I+1)-E]^{-1}, \tag{9}$$

where

$$W(L,I) = (L+2)(L+1)F(L+2,I)+(I+2)(I+1)F(L,I+2)+(\beta^2-1)[F(L-2,I)+F(L,I-2)] - \lambda[a_{xx}F(L-4,I)+a_{yy}F(L,I-4)+2a_{xy}F(L-2,I-2)]. \tag{10}$$

For calculations, we set the initial coefficient $F(L_0,I_0)=1$. All the $S(L,I)$ with $(L,I)\neq(L_0,I_0)$ are treated according to (9) for some trial values of β and E. From experience it is seen that the best initial energy to start the calculation should be a little higher than the required eigenvalue [13]. The value of β increases as the perturbation parameter λ increases. At this stage, naturally, the question that arises is whether β can give the best convergence eigenvalue. In the present calculations, the value of β which gave the best converged eigenvalue was taken. Table 1 shows the rate of convergence by this technique for some eigenstates for $\lambda = 0{\cdot}1$, 10, 100, 10^5 in the special case, wherein the potential has circular symmetry. It is known from experience, that the rate of the convergence decreases as values of the perturbation parameter λ and eigenstate number (n_x, n_y) increase.

The standard technique for evaluation of the energy is based on (9), that for the special case $L=L_0$, $I=I_0$, the coefficient on the left-hand side becomes $F(L_0,I_0)=1$, and this initial condition is imposed on the algorithm. After this adjustment a revised E estimate is calculated using the assignment statements

$$E_e = 2\beta(L_0+I_0+1) - W(L_0,I_0). \tag{11}$$

$$E = RE_e + (1-R)E. \tag{12}$$

The value of the relaxation parameter R can be decreased or increased to help in improving and stabilizing a convergence of the eigenvalue to a reasonable accuracy. The parity index P_{xy} (for interchange coordinates $x\leftrightarrow y$) is used for the potential $V(x,y)$, in the case of symmetry interaction which means $a_{IJ}=a_{JI}$. The relation between the coefficients hold (for interchange $x\leftrightarrow y$).

$$F(L,I) = P_{xy}F(I,L). \tag{13}$$

For even eigenstates $P_{xy}=1$ and for odd eigenstates $P_{xy}=-1$ and β is varied to give the best possible convergence of the estimated energy.

3. Results and discussion

The Hill determinant approach has been applied in this paper to the Schrödinger equation with a perturbed potential in a two-dimensional system. It is found very effective to treat symmetry perturbation i.e. $a_{IJ}=a_{JI}$ and unsymmetry perturbation i.e. $a_{IJ}\neq a_{JI}$ for several eigenstates and various values of perturbation parameters.

The adjustable parameter β plays an important role in the convergence aspects of the present calculations. The β values for the dimensional oscillator $V(x,y)$ calculation are in the range $1{\cdot}3 \leqslant \beta \leqslant 350$. The general consideration that governs our choice is that, as λ increases, β also increases, for example $\beta = 1{\cdot}3$ at $\lambda = 0{\cdot}01$ and $\beta = 350$ at $\lambda = 10^6$.

Table 1. Convergence for some eigenvalues for $(n_x, n_y; \pi)$ of the two dimensional oscillator for the case $a_{xx} = a_{yy} = a_{zz} = 1$, for $\lambda = 0{\cdot}1, 10, 100, 10^5$ with various values of the adjustable parameter β. The empty spaces mean the corresponding eigenvalues cannot be obtained with these values of β.

λ	$(0, 0; +)$	β	$(1, 0; \mp)$	β	$(1, 1; +) = (2, 0; -)$	β
0·1		0·5		1		1
	2·16	1	4·4776003	1·5	6·9083321	1·6
	2·1685972	1·4	4·47760036076	1·7	6·908332111231871	2·0
	2·1685972112693	1·8	4·47760036076821	2·0	6·908332111231871	2·2
	2·168597211269291	2·5	4·47760036076821	2·5	6·908332111231871	2·5
10		3		4		5
	5·3493	6	12·138224	7	19·936	7
	5·349352819406	8	12·1382247388	8	19·936900374	8
	5·34935281940641	9	12·13822473889884	9	19·9369003740113	9
	5·34935281940641	10	12·13822473889884	10	19·9369003740113	10
100		8		8		10
	11·023	12	25·27998	14	41·76874	15
	11·0235979	15	25·2799851433	17	41·76874434397	18
	11·0235979287809	20	25·27998514334519	20	41·7687443439749	20
	11·0235979287809	24	25·27998514334519	24	41·7687443439749	24
10^5		80		90		100
	108·85135	140	250·402	140	414·4377	150
	108·8513595772	180	250·4021140684	180	414·4377597604	180
	108·851359577201	200	250·402114068453	200	414·437759760461	200
	108·851359577201	220	250·402114068453	220	414·437759760461	220

Table 2. Eenrgy values of $(n_x, n_y; \pi)$, for the potential $V(x, y)$ for several sets of perturbation parameters. The parity label $\pi = +, -$; even, odd for the $x \leftrightarrow y$ interchange symmetry.

	$a_{xx} = a_{yy} = 0, a_{xy} = \frac{1}{2}$			
λ	$(0, 0; +)$	$(1, 0; \pm)$	$(1, 1; +)$	$(2, 0; -)$
0·1	2·02413832141573	4·0708639128944	6·2082907985657	6·0716400174184
0·2	2·04679571883258	4·1350822342067	6·3912911417583	6·1377408133565
0·3	2·068242130731	4·1942935736199	6·5564773059808	6·1995318631918
0·4	2·088667659069	4·2495313630102	6·7081422885770	6·2578183515335
0·5	2·108213779698	4·301504505315	6·8490530489122	6·313168654731
0·6	2·126989929539	4·35072736225	6·9811280772305	6·36600479493
0·7	2·1450832429	4·3975886228	7·1057672375444	6·4166518870
0·8	2·1625646859	4·4423912545	7·2240314806597	6·465367562
0·9	2·1794931153	4·485377268	7·3367489236663	6·512360604
1·0	2·195918086	4·526743874	7·444581361569	6·557803326
2·0	2·3395662	4·87770957	8·3394493229	6·9506339
3·0	2·4583769	5·1579605	9·034854244	7·271682
4·0	2·5616266	5·396806	9·6175878	7·549157
5·0	2·6539097	5·60757	10·1256931	7·79644
6·0	2·7379188	5·79769	10·5798578	8·0212
7·0	2·8153967	5·97184	10·0992791	8·2283
8·0	2·8875504	6·13341	11·372950	8·4214
9·0	2·955257	6·28596	11·726290	8·6019
10·0	3·019178	6·42591	12·057188	8·773
15·0	3·29685	7·03842	13·469681	9·515
20·0	3·52692	7·54125	14·616918	10·131
50·0	4·47652	9·60194	19·21721	12·685
100	5·46097	12·2666	23·86291	15·349
1000	11·23243	24·2562	50·39571	31·13
5000	19·03854	41·2135	85·85665	52·61
10000	23·94599	51·6251	108·0969	66·13
10^5	51·4718	110·5191	232·6638	142·2

	$a_{xx}=a_{yy}=1,\ a_{xy}=-1$		$a_{xx}=\frac{1}{2},\ a_{yy}=\frac{1}{4},\ a_{xy}=\frac{1}{8}$	
λ	$(0,0;+)$	$(1,0;\pm)$	$(1,0;-)$	$(1,1;+)$
0·01	2·00985521060372	4·0292889726409	4·02220907755723	6·033322273821
0·1	2·08866765907315	4·2495313630310	4·2014184255855	6·302730175585
0·5	2·339566211	4·87770957	4·776661317376	7·170817128601
1	2·56162658	5·3968039	5·28444637458	7·9385946295
10	4·21175722	9·02688	8·99050466	13·54179268
100	8·36832652	17·984	18·139463	27·355525
1000	17·68691	37·96	38·4951	58·0717
2000	22·2399	47·74	48·4255	73·0545
10000	37·945	81·48	82·6619	124·7086

	$a_{xx}=1,\ a_{yy}=\frac{1}{2},\ a_{xy}=\frac{1}{4}$		$a_{xx}=\frac{1}{3},\ a_{yy}=\frac{1}{4},\ a_{xy}=\frac{1}{2}$	
λ	$(0,0;+)$	$(1,0;-)$	$(0,0;+)$	$(1,0;-)$
0·01	2·01231228718489	4·0438677204024	2·0068218851034	4·021621108365
1	2·6863516426	6·02495513951	2·4550321766714	5·281706465822
5	3·8255941189	8·9905464633	3·32198865267	7·47632663472
10	4·619200437	10·991656058	3·95089995457	9·01371371691
50	7·50300538	18·13946345	6·28890732395	14·6138003405
100	9·3555061	22·69326466	7·80745103125	18·2150199295
500	15·809344	38·4950971	13·12621353	30·767112789
1000	19·87269	48·425489	16·48332214	38·671655693
10000	42·6818	104·112662	35·35459	83·04905
10^5	91·8949	224·20318	76·09585	178·7999

	$a_{xx}=\frac{1}{3},\ a_{yy}=\frac{1}{6},\ a_{xy}=\frac{1}{5}$		$a_{xx}=0,\ a_{yy}=1,\ a_{xy}=\frac{1}{2}$	
λ	$(0,1;+)$	$(1,0;-)$	$(0,0;+)$	$(1,1;+)$
0·01	4·0116729015606	4·016594932356	2·00982882574815	6·058318025551
0·1	4·1106369197386	4·154229422204	2·08694982082748	6·485730943303
0·5	4·466738393841	4·622448523457	2·32310658866	7·65887777919
1	4·81001774999	5·053036645166	2·52658354	8·6065492
10	7·59082621315	8·335444773	4·00772	15·05018
100	14·8799478	16·63230785	7·7615	30·53609
1000	31·3501683	35·2005676	16·26	64·8681
5000	53·387759	59·9954	27·67	110·636
10000	67·2109	75·5418	34·83	139·323
100000	144·648	162·612	74·9	299·96

	$a_{xx}=\frac{1}{3},\ a_{yy}=\frac{1}{4},\ a_{xy}=\frac{1}{2}$	$a_{xx}=\frac{1}{4},\ a_{yy}=\frac{1}{5},\ a_{xy}=\frac{1}{6}$	$a_{xx}=a_{yy}=\frac{1}{3},\ a_{xy}=\frac{1}{4}$	
λ	$(1,1;+)$	$(1,1;+)$	$(0,2;+)$	$(2,0;-)$
0·01	6·0436934891649	6·0241668378937	6·043135666616	6·038232473314
1	8·3665961639843	7·5602656974176	8·38684555658	8·164167323602
5	12·1540605363882	10·4238563537005	12·2283227870	11·733936775982
10	14·75829350949	12·471386219668	14·8663230227	14·207348368038
50	24·149078364	20·0155548073	24·3660855	23·1626619844
100	30·158605748	24·893689976	30·4406285	28·9045928065
500	51·0558236	41·9417026	51·555132	48·8897072
1000	64·201194	52·690847	64·834505	61·4667308
10000	137·95683	113·0797	139·3334	132·05022
100000	297·0515	243·418	300·0232	284·3189

	$a_{xx} = a_{yy} = a_{xy} = 1$			$a_{xx} = a_{yy} = 1,\ a_{xy} = 0$
λ	$(0, 0; +)$	$(0, 1; \mp)$	$(1, 1; +) = (2, 0; -)$	$(1, 1; +)$
0·01	2·0195708085219	4·0581733885884	6·115306125265	6·073056060903
1	2·952050091966	6·46290599986	10·390627295503	9·297625408424
5	4·3810888395	9·87059482807	16·146296004255	14·026958371634
10	5·3493528194	12·13822473884	19·936900374011	17·198006909616
50	8·814283232	20·1770296484	33·304412267221	28·48341399182
100	11·023597928	25·2798514335	41·768744343975	35·66038543191
500	18·69290316	42·9558103393	71·054463932988	60·5430105116
1000	23·51338918	54·0548557958	89·943343403375	76·173669187
10000	50·54804495	116·267380968	192·420561201906	163·806633902
100000	108·85135957	250·402114065	414·437759760460	352·769246001
10^6	234·48942203	539·433981018	892·823487959	759·952638

	$a_{xx} = a_{yy} = 1,\ a_{xy} = 0$		$a_{xx} = 1\ \ a_{yy} = \frac{1}{2},\ a_{xy} = 1$	
λ	$(0, 0; +)$	$(0, 1; \mp)$	$(0, 1; +)$	$(1, 0; -)$
0·01	2·0147473441627	4·0438989765947	4·040310310588	4·054616746577
1	2·7847032830606	6·0411643457423	5·929093989647	6·361312813522
5	4·0366812987306	9·0318198351823	8·8068361776	9·66976839748
10	4·898348144236	11·0481775269262	10·7552685288	11·87757748425
50	8·007985536555	18·245699764189	17·7255829568	19·7159195444
100	9·998835090275	22·829610261090	22·1694645877	24·6950247031
500	16·923285258162	38·733147884922	35·5949254503	41·9482797882
1000	21·279577422656	48·72662217071	47·2902582298	52·7836179925
10000	45·723217740545	104·76492582355	101·6637536694	113·5233045707
100000	98·450895516845	225·61007058467	218·9257185534	244·4877262122
10^6	212·07965847	486·01614822	471·611371845	526·69067889

The results are in good agreement with available literature. For accurate results, the best values of β, have been chosen, which were obtained by testing many parameter values until the best convergence was obtained.

Some important consequences of our investigation are as follows:

1. The Hill determinant approach can be used to calculate several eigenstates with excellent accuracy for the two-dimensional oscillator for several perturbation parameters. Table 2 covers a wide range of λ values ($10^{-2} \leqslant \lambda \leqslant 10^6$) and various cases wherein the potential has interchange symmetry. The λ value obtained by us is twice the λ value obtained by Nasit and Demiralp [1] and Hioe *et al* [3] and their Hamiltonian differs by a factor 1/2.

Several external checks were devised to verify the correctness of the energy values. For example using the inner product technique, we obtained agreement between some of the present results and those obtained by inner product [7]. For the two special cases $a_{xx} = a_{yy} = a_{xy} = 1$ and $a_{xx} = a_{yy} = 1$, $a_{xy} = 0$, the potential (1) has circular symmetry, and reduces to the two independent oscillators respectively. We have checked the energies obtained by the present technique against results obtained by the hypervirial method [7].

2. For symmetric perturbation i.e. $a_{IJ} = a_{JI}$, it is seen from our calculations that the energy levels characterized by eigenstates $(n_x, n_y,)$ with n_x and n_y having different parity, i.e. (odd, even) or (even, odd) remain doubly degenerated and unsplit as λ is varied from zero value. This means that the perturbation does not break the degeneracy of the perturbed system. The energy levels which show such behaviour in our calculations are (E_{10}, E_{01}). Unsymmetry perturbation i.e. $a_{IJ} \neq a_{JI}$ shows interesting splitting effects as a_{IJ} and a_{JI} vary. In this case the degeneracy is broken by the perturbation and this behaviour is clear from our calculations in table 2.

Also there is a crossing between the energy levels for the two eigenstates E_{11}^{+} and E_{20}^{-} at $a_{xx} = a_{yy} = a_{xy} = 1$; (circular symmetry), but when this symmetry is removed, the doubly degenerate levels split into different levels, and this confirmed by our results in table 2.

3. The phenomenon of bogus convergence is avoided by computing the energy eigenvalues for different values of the adjustable parameter β. To select the correct converge energy we require stability of the results with respect to the small variation of β at a given value of the perturbation parameter λ.

We have also used Aitken's transformation [14] to improve the convergence of the calculations and it has helped in improving our results.

Acknowledgement

The author is grateful to the referee for valuable comments and suggestions.

References

[1] Ari Nasit and Metin Demiralp, *J. Math. Phys.* **26**, 1179 (1985)
[2] R Blankenbecler, T DE Grand and R L Sugar, *Phys. Rev.* **D21**, 1055 (1980)
[3] F T Hioe, Don MacMkllen and E W Montroll, *Phys. Rep.* **43** 305 (1978)
[4] F M Fernandez, A M Meson and E A Castro, *Phys. Lett.* **A112**, 107 (1985)
[5] J P Killingbeck and M N Jones, *J. Phys.* **A19**, 705 (1986)
[6] J P Killingbeck, *Microcomputer algorithms* (Bristol, Adam Hillger, 1991)
[7] M R M Witwit, *J. Phys.* **A24**, 4035 (1991)

[8] F Arias de Saavedra and E Buendia, *J. Phys.* **A24** L1209 (1991)
[9] M R M Witwit, *J. Phys.* **A24**, 3053 (1991)
[10] S N Biswas, K Datta, R P Saxena, P K Srivastava and V S Varma, *Phys. Rev.* **D4**, 3617 (1971)
[11] S N Biswas, K Datta, R P Saxena, P K Srivastava and V S Varma, *J. Math. Phys.* **14**, 1190 (1973)
[12] K Banerjee, *Proc. R. Soc. London* **A364**, 265 (1978)
[13] M R M Witwit, *J. Math. Phys.* **33**, 4196 (1992)
[14] A C Aitken, *Proc. Edinburgh Math. Soc.* **3** 56 (1932)

PRAMANA
— journal of
physics

© Printed in India

Vol. 41, No. 6,
December 1993
pp. 503–507

Integration method for the Dirac equation

V G BAGROV and V V OBUKHOV
Institute of High Current Electronics, Russian Academy of Sciences, Siberian Division, Akademichesky ave. 4, Tomsk 634 055, Russia

MS received 6 April 1992; revised 25 May 1993

Abstract. An integration method for the Dirac equation is proposed. The method, based on diagonalization, reduces the problem to one of integration of independent second-order differential equations.

Keywords. Dirac equation; diagonalization.

PACS Nos **03·50; 04·40**

We start from the Dirac equation presented in the form (Chandrasekhar [1])

$$\mathscr{H}_1 = \sigma^i_{AB'} i\partial_i V^A - m\bar{W}_{B'} = 0,$$
$$\mathscr{H}_2 = \sigma^i_{AB'} i\partial_i W^A - m\bar{V}_{B'} = 0$$

and we carry out the next transformations:

$$\text{a)}\ \mathscr{H}_1 = 0 \Rightarrow \sigma_{2DB'}(\varepsilon^{B'C'}\sigma^i_{AC'} i\partial_i V^A - m\bar{W}^{B'}) = 0,$$
$$\text{b)}\ \mathscr{H}_2 = 0 \Rightarrow (\varepsilon^{BC}\bar{\sigma}^i_{A'C} i\partial_i \bar{W}^{A'} + mV^B) = 0 \Rightarrow$$
$$\Rightarrow \sigma_{2D'B}(\varepsilon^{BC}\bar{\sigma}^i_{A'C} i\partial_i \bar{W}^{A'} + mV^B) = 0,$$
$$\text{c)}\ i\partial_i \Rightarrow i\partial_i + A_i$$

(A_i is electromagnetic potential).

Then Dirac equation can be presented in a spinor form:

$$\hat{\mathscr{H}}\hat{\Psi} = \left[\begin{pmatrix} \hat{0} & \hat{\Box}_1 \\ \sigma_2 \hat{\Box}_2 \sigma_2 & \hat{0} \end{pmatrix} + im\begin{pmatrix} \sigma_2 & \hat{0} \\ \hat{0} & -\hat{\sigma}_2 \end{pmatrix}\right]\begin{pmatrix} V^A \\ \bar{W}^A \end{pmatrix} = 0, \tag{1}$$

$$\hat{\Box}_1 = \sqrt{2}(\hat{1}P_1 + \hat{4}P_0 - \hat{2}P_3 - \hat{3}P_2), \quad \Box_2 = \sqrt{2}(\hat{1}P_0 + \hat{4}P_1 + \hat{2}P_3 + \hat{3}P_2),$$

$$P_i = i\partial_i + A_i, \quad \partial_i = \partial/\partial u^i, \quad \sqrt{2}u^0 = (x^0 + x^1), \quad \sqrt{2}u^1 = (x^0 - x^1),$$

$$\sqrt{2}u^2 = (x^2 + ix^3), \quad u^3 = \overline{u^2}, \quad \hat{0} = \begin{pmatrix} 0 & 0 \\ 0 & 0 \end{pmatrix}, \quad \hat{1} = \begin{pmatrix} 1 & 0 \\ 0 & 0 \end{pmatrix},$$

$$\hat{2} = \begin{pmatrix} 0 & 1 \\ 0 & 0 \end{pmatrix}, \quad \hat{3} = \begin{pmatrix} 0 & 0 \\ 1 & 0 \end{pmatrix}, \quad \hat{4} = \begin{pmatrix} 0 & 0 \\ 0 & 1 \end{pmatrix}, \quad \hat{E} = \begin{pmatrix} 1 & 0 \\ 0 & 1 \end{pmatrix},$$

$\sigma_i = (\hat{2} + \hat{3})$, $\sigma_2 = i(\hat{2} - \hat{3})$, $\sigma_3 = (\hat{1} - \hat{4})$, x^i are Descartes coordinates, V^A, W^A are spinor fields. Propose the first order linear differential operator $\hat{A}$, the matrix $\hat{\Omega}$ and the linear diagonal second order differential operator $\hat{\mathscr{L}}$ satisfying the condition

$$\mathscr{H}\hat{A} = \hat{\Omega}\hat{\mathscr{L}} \tag{2}$$

exist. (The problem for the Dirac–Fock–Ivanenko squared equation was studied by Bagrov and Obukhov [2]. Then the integration problem for the Dirac equation may be reduced to one of integration of independent second-order differential equations:

$$\hat{\mathscr{L}}\hat{\Phi} = 0 \Rightarrow \hat{\Psi} = \hat{A}\hat{\Phi}. \tag{3}$$

One can show that operator $\hat{A}$ has a form

$$\hat{A} = \hat{H}\hat{\Omega} + \hat{\Gamma},$$
$$\hat{H} = \begin{pmatrix} \hat{0} & \sigma_2\hat{\Box}_1\sigma_2 \\ \hat{\Box}_2 & \hat{0} \end{pmatrix} + im\begin{pmatrix} \sigma_2 & 0 \\ 0 & -\sigma_2 \end{pmatrix}. \tag{4}$$

Note that in this case the condition det $\hat{\Omega} \neq 0$ is not considered. Let us denote

$$\hat{\Omega} = \begin{pmatrix} \hat{B} & \hat{B}^* \\ \hat{\hat{Y}} & \hat{\hat{Y}}^* \end{pmatrix}, \quad \hat{\Gamma} = \begin{pmatrix} \hat{\bar{\tau}} & \hat{\bar{\tau}}^* \\ \hat{\gamma} & \hat{\gamma}^* \end{pmatrix}, \quad \hat{\Phi} = \begin{pmatrix} -\Phi_1, & -\Phi_2 \\ \Phi_0, & \Phi_1 \end{pmatrix},$$
$$\hat{\mathscr{L}} = \Box + 2i\left[\begin{pmatrix} \hat{R} & \hat{0} \\ \hat{0} & \hat{R}^* \end{pmatrix} P_0 + \begin{pmatrix} \hat{T} & \hat{0} \\ \hat{0} & \hat{T}^* \end{pmatrix} P_1 - \begin{pmatrix} \hat{K} & \hat{0} \\ \hat{0} & \hat{K}^* \end{pmatrix} P_2 - \right.$$
$$\left. - \begin{pmatrix} \hat{N} & \hat{0} \\ \hat{0} & \hat{N}^* \end{pmatrix} P_3 - \begin{pmatrix} \hat{P} & \hat{0} \\ \hat{0} & \hat{P}^* \end{pmatrix}\right],$$
$$\Phi_0 = F_{02}, \quad \Phi_2 = (F_{01} + F_{32})/2, \quad \Phi_3 = F_{31},$$

$\Box$ is the Klein–Gordon–Fock operator. Then (2) takes the form

$$\begin{aligned} &\hat{B}_{,0} + \hat{1}\hat{\gamma} = \hat{B}\hat{T}, \qquad && \hat{Y}_{,0} + \hat{1}\hat{t} = \hat{Y}\hat{\hat{T}}, \\ &\hat{B}_{,1} + \hat{4}\hat{\gamma} = \hat{B}\hat{R}, && \hat{Y}_{,1} + \hat{4}\hat{t} = \hat{Y}\hat{\hat{R}}, \\ &\hat{B}_{,2} + \hat{2}\hat{\gamma} = \hat{B}\hat{N}, && \hat{Y}_{,2} + \hat{3}\hat{t} = \hat{Y}\hat{\hat{N}}, \\ &\hat{B}_{,3} + \hat{3}\hat{\gamma} = \hat{B}\hat{K}, && \hat{Y}_{,3} + \hat{2}\hat{t} = \hat{Y}\hat{\hat{K}}, \end{aligned} \tag{5}$$

$$\hat{B}_{,01} - \hat{B}_{,23} + \mu\sigma_2\hat{t} - i\hat{\Phi}\hat{B} + \hat{1}\hat{\gamma}_{,1} - \hat{2}\hat{\gamma}_{,3} - \hat{3}\hat{\gamma}_{,2} + \hat{4}\hat{\gamma}_{,0} = i\hat{B}\hat{P}, \tag{6}$$

$$\hat{Y}_{,01} - \hat{Y}_{,23} + \mu\sigma_2\hat{\bar{\gamma}} - i\hat{\Phi}\hat{Y} + \hat{1}\hat{t}_{,1} - \hat{2}\hat{t}_{,3} - \hat{3}\hat{t}_{,2} + \hat{4}\hat{t}_{,0} = -i\hat{Y}\hat{\hat{P}}, \tag{7}$$

$$\mu = m/\sqrt{2}.$$

The quantities with the asterisks have the same form, hence they have not been considered here. We present all solutions of (5)

$$\begin{aligned} &\text{I. } \hat{B} = \hat{u}\hat{a} + \hat{k}, \quad \hat{Y} = \hat{u}\hat{b} + \hat{n}, \quad \hat{T} = \hat{R} = \hat{K} = \hat{N} = 0, \\ &\quad \hat{\gamma} = -\hat{a}, \quad \hat{t} = -\hat{b}, \quad \hat{u} = u^0\hat{1} + u^2\hat{2} + u^3\hat{3} + u^1\hat{4}. \end{aligned} \tag{8}$$

$$\begin{aligned} &\text{II. } \hat{B} = \hat{2} + \hat{4}\exp Q + \hat{u}(a_1\hat{1} + a_3\hat{3} + \hat{4}), \quad \hat{Y} = \hat{u}(b_1\hat{1} + b_3\hat{3}) + n_1\hat{1} + n_3\hat{3}. \\ &\quad \hat{\gamma} = -a_1\hat{1} + Q_{,0}\hat{2} - a_3\hat{3} - Q_{,1}\hat{4}, \quad \hat{t} = -(b_1\hat{1} + b_3\hat{3}). \end{aligned} \tag{9}$$

The function Q satisfies the set of equations

$$Q_{,0} + (\exp Q)_{,3} = 0,$$
$$Q_{,2} + (\exp Q)_{,1} = 0.$$

$$\text{III. } \hat{B} = \hat{1} + Q\hat{3}, \quad \hat{Y} = \hat{2} + J\hat{4}, \quad \hat{\gamma} = \hat{1}Q_{,0}/Q - \hat{3}Q_{,1}, \quad \hat{\tau} = \hat{2}J_{,0}/J - \hat{4}J_{,1}. \tag{10}$$

The functions Q, J satisfy the sets of equations

$$Q_{,3} + Q_{,0}/Q = 0 \quad J_{,1} + J_{,3}/Q = 0$$
$$Q_{,1} + Q_{,2}/Q = 0' \quad J_{,2} + J_{,0}/Q = 0 .$$

The matrices

$$\hat{a} = a_1\hat{1} + a_2\hat{2} + a_3\hat{3} + a_4\hat{4}, \quad \hat{b} = b_1\hat{1} + b_2\hat{2} + b_3\hat{3} + b_4\hat{4},$$
$$\hat{k} = k_1\hat{1} + k_2\hat{2} + k_3\hat{3} + k_4\hat{4}, \quad \hat{n} = n_1\hat{1} + n_2\hat{2} + n_3\hat{3} + n_4\hat{4} \tag{11}$$

are constants.

Let us show that due to the sets (6) and (7), solutions II, III reduce to solution I. Indeed using solution II one can present the set (7) to the form:

$$\mu\sigma_2(-a_1\hat{1} + Q_{,0}\hat{2} - a_3\hat{3} - Q_{,1}\hat{4}) + i(-\Phi_1\hat{1} - \Phi_2\hat{2} + \Phi_0\hat{3} + \Phi_1\hat{4})$$
$$(Y_1\hat{1} + Y_3\hat{3}) + i(Y_1\hat{1} + Y_3\hat{3})(\bar{\mathscr{P}}_1\hat{1} + \mathscr{P}_2\hat{2}) = 0. \tag{12}$$

Hence $Q_{,0} = Q_{,1} = 0$ and from set (9) it follows that $Q = \text{constant}$. The same approach for solution III gives the result: Q, $J = \text{constant}$.

That is why we believe that $\hat{B}$, $\hat{Y}$, $\hat{T}$, $\hat{R}$, $\hat{K}$, $\hat{N}$, $\hat{\gamma}$, $\hat{\tau}$ are given by correlations (8). The sets (6), (7) now have the form

$$\hat{\Phi}\hat{B} + i\mu\sigma_2\hat{\hat{b}} = \hat{\Phi}\hat{P}, \tag{13}$$

$$\hat{\Phi}\hat{Y} + i\mu\sigma_2\hat{\hat{a}} = \hat{Y}\hat{\hat{P}}. \tag{14}$$

Obviously the transformations rule for the matrices is valid:

$$\begin{cases} \hat{k}' = \hat{\Lambda}\hat{k}, \quad \hat{n}' = \hat{\Lambda}\hat{n}, \quad \hat{a}' = \hat{\hat{l}}\hat{a}, \quad \hat{b}' = \hat{\hat{l}}\hat{b}, & (15) \\ \det\hat{\Lambda} = \det\hat{l} = 1, \quad \hat{\Lambda}\hat{l} = \hat{I}. & (16) \end{cases}$$

Moreover, the matrices $\hat{B}$, $\hat{Y}$ can be acted by transformation

$$\hat{B}' = \hat{J}^{-1}\hat{B}\hat{J}.$$

Provided that operator $\hat{L}'$

$$\hat{L}' = \hat{J}^{-1}\hat{L}\hat{J}$$

remains diagonal.

All these transformations form a group. Using the group let us classify matrices $\hat{a}$, $\hat{b}$, $\hat{n}$ $\hat{k}$ in the following manner

A) $\hat{a} = \hat{I}$.
  1) $\hat{k} = i(\alpha\hat{1} + \beta\hat{4}) + \gamma(\hat{2} - \hat{3})$;
  2) $\hat{k} = i(\alpha\hat{1} + \beta\hat{4})$

a) $\hat{b}=0, \quad \hat{n}=n_1\hat{1}+n(\hat{2}+\varepsilon\hat{3})+n_4\hat{4} \quad (\varepsilon=\pm 1)$
b) $\hat{b}=b_1(\exp i\gamma)\hat{1}+\text{æ} b_2\hat{2}+\hat{3}b_3/\text{æ}+\hat{4}b_4\exp(-i\gamma)$.

B) $\hat{a}=\hat{1}, \quad \hat{k}=i\alpha\hat{1}+k_2\hat{2}+k_4\hat{4}$.
1) $\hat{b}=\alpha\hat{1}+\xi\hat{2}$, 2) $\hat{b}=\xi_1\hat{3}(\exp i\beta)+\xi\hat{4}$,
3) $\hat{b}=\hat{0} \quad (\xi_1,\xi=0,1)$.

C) $\hat{a}=\hat{1}+\hat{2}, \quad \hat{k}=i\alpha\hat{1}+k_2\hat{2}+k_4\hat{4}$.
1) $\hat{b}=\alpha\hat{1}+b\hat{2}, \quad \alpha b\neq 0$, 2) $\hat{b}=\hat{3}(\exp i\alpha)+b\hat{4}$,

D) $\hat{a}=\hat{b}=\hat{0}$.

The last version (D) was considered by Meshkov [3]. Solving the sets (13), (14), one has to consider next variants: I. det $\hat{B}\hat{Y}\neq 0$; II. det $\hat{B}\neq 0$, det $\hat{Y}=0$; III. det $\hat{B}=$ det $\hat{Y}=0$. For example, let det $\hat{B}\hat{Y}\neq 0$, then the set (13), (14) can be presented in the form:

$$2(B_3B_4T_1-Y_3Y_4T_2)=\mu[(\bar{b}_1B_4-\bar{b}_2B_3)/B+(\bar{a}_1Y_4-\bar{a}_2Y_3)/Y], \tag{17}$$

$$2(B_1B_2T_1-Y_1Y_2T_2)=\mu[(\bar{b}_4B_1-\bar{b}_3B_2)/B+(\bar{a}_4Y_1-\bar{a}_3Y_2)/Y], \tag{18}$$

$$\begin{aligned} &Y[(\bar{b}_1B_1+\bar{b}_3B_3)(B_2Y_3-B_4Y_1)(Y_4B_2-Y_2B_4)-\\ &\quad-(\bar{b}_2B_2+\bar{b}_4B_4)(B_1Y_3-B_3Y_1)(Y_4B_2-Y_2B_4)]+\\ &\quad+B[(\bar{a}_4Y_4+\bar{a}_2Y_2)(Y_3B_2-Y_1B_4)(Y_3B_1-Y_1B_3)-\\ &\quad-(\bar{a}_1Y_1+\bar{a}_3Y_3)(Y_4B_1-Y_2B_3)(B_2Y_4-B_4Y_2)]=0; \end{aligned} \tag{19}$$

$$B(a_1\bar{Y}_2-a_2\bar{Y}_1+a_3\bar{Y}_4-a_4\bar{Y}_3)=Y(-\bar{b}_1B_2+\bar{b}_2B_1-\bar{b}_3B_4+\bar{b}_4B_3); \tag{20}$$

$$\begin{aligned} &\Phi_0=[2B_3B_4\mathscr{J}_1-\mu(\bar{b}_1B_4-\bar{b}_2B_3)]/B,\\ &\Phi_1=[-2(B_1B_4+B_2B_3)\mathscr{J}_1+\mu(\bar{b}_1B_2-\bar{b}_2B_1-\bar{b}_3B_4+\bar{b}_4B_3)]/2B,\\ &\Phi_2=[2B_1B_2\mathscr{J}_1+\mu(\bar{b}_3B_2-\bar{b}_4B_1)]/B,\\ &\mathscr{J}_2=-\mu(\bar{b}_1B_2-\bar{b}_2B_1+\bar{b}_3B_4-\bar{b}_4B_3)/2B. \end{aligned}$$

Here $B=$ det $\hat{B}$, $Y=$ det $\hat{Y}$, $\mathscr{P}_1=\mathscr{J}_1+\mathscr{J}_2$, $\mathscr{P}_2=\mathscr{J}_2-\mathscr{J}_1$, $T_1=\mathscr{J}_1/B$, $T_2=\bar{\mathscr{J}}_1/Y$, $\hat{B}=B_1\hat{1}+B_2\hat{2}+B_3\hat{3}+B_4\hat{4}$, $\hat{Y}=Y_1\hat{1}+Y_2\hat{2}+Y_3\hat{3}+Y_4\hat{4}$. The matrices $\hat{B}$, $\hat{Y}$ contain the arbitrary constants. To determine the constants one has to consider (17) and (20). The problem of finding these constants is not difficult but appropriate calculations are rather cumbersome. That is why we do not present them here. We give all nonequivalent matrices $\hat{B}$, $\hat{Y}$ and all electromagnetic fields Φ_0, Φ_1, Φ_2 for all variants in Appendix.

Appendix

I. det $\hat{B}$ det $\hat{Y}\neq 0, \quad W=u^0u^1-u^2u^3$.

1) $\Phi_0=2iu^1u^3\theta(u)+\mu u^3\xi/W$,
$\Phi_1=-i(u^0u^1+u^2u^3)\theta(u)+\mu\xi(u^0-u^1)/2W$,
$\Phi_2=2iu^0u^2\theta(u)+\mu u^2\xi/W$,
$\hat{a}=\hat{I}, \quad \hat{b}=i\xi\hat{\sigma}_2, \quad \hat{k}=\hat{n}=0, \quad \xi=\pm 1$,
$\hat{L}=\square+2W\theta(u)\sigma_3+i\mu\xi(u^0+u^1)/W$.

2) $\Phi_0 = \mu(\alpha u^3 - \gamma u^1)/W, \quad \Phi_1 = \mu[\gamma(u^2 - u^3) - \alpha u^0 - \beta u^1]/2W,$
$\Phi_2 = \mu(\gamma u^0 + \beta u^2)/W,$
$\gamma^2 + \alpha\beta = -1, \quad \hat{a} = \hat{E}, \quad \hat{b} = \gamma\sigma_3 + \alpha\hat{2} + \beta\hat{3}, \quad \hat{k} = \hat{n} = 0,$
$\hat{L} = \Box + 2i\mu[\gamma(u^2 + u^3) - \alpha u^0 + \beta u^i]/W.$

3) $\Phi_0 = \mu[i\alpha c\gamma^2 - (\gamma^2 + c\bar{c})(\bar{c}(u^3)^2 + u^3(c\bar{c} - i\alpha))]/\gamma\alpha c\bar{c}(u^0 + i\beta),$
$\Phi_1 = \mu(\gamma^2 + c\bar{c})(\bar{c}u^3 + (c\bar{c} - i\alpha)/2)/\alpha\gamma c\bar{c},$
$\Phi_2 = -\mu(\gamma^2 + c\bar{c})(u^0 + i\beta)/\alpha\gamma c,$
$\hat{a} = \hat{1} + \hat{2}, \quad \hat{b} = i\gamma(\hat{1} + \hat{2})/c,$
$\hat{k} = i\beta(\hat{1} + \hat{2}) + (c - i\alpha/\bar{c})\hat{4}, \quad \hat{n} = -\alpha\gamma/c^2(\hat{4} - \hat{3}),$
$\hat{L} = \Box + i\mu(i\alpha - c\bar{c})(\gamma^2 + c\bar{c})\sigma_3/2\alpha\gamma c\bar{c}.$

II. $\det \hat{B} \det \hat{Y} = 0.$

4) $\Phi_0 = -[\mu(1 + c\bar{c})u^3 + \mu\bar{c}\alpha - 2i(cu^3 + \alpha)u^3\theta(u)]/\alpha(u^0 + i\beta),$
$2\alpha\Phi_1 = \mu(1 + c\bar{c}) - 2i(2cu^3 + \alpha)\theta(u),$
$\Phi_2 = 2ic(u^0 + i\beta)\theta(u)/\alpha,$
$\hat{a} = \hat{1}, \quad \hat{b} = c\hat{1}, \quad \hat{k} = i\beta\hat{1}, \quad \hat{n} = ic\beta\hat{1} + \alpha\hat{3},$
$\hat{L} = \Box + 2\theta + i\mu(1 + c\bar{c})/\alpha.$

III. $\hat{a} = \hat{b} = 0.$

5) $\Phi_0 = 0, \quad \hat{k} = \hat{1}, \quad \hat{n} = n\hat{2}, \quad \hat{L} = \Box + 2i(\Phi_1\hat{1} + \Phi_1\hat{4}).$

In these formulas the real constants are denoted by small Greek letters, the complex ones by small Latin letters. We do not consider here the case $R_{ijkl} \neq 0$. Note that some of the presented fields depend on m. Apparently these variants can be used to study the integration problem of the Dirac–Maxwell equation.

Acknowledgement

This work is supported by Russia Fundamental Research Foundation.

References

[1] Chandrasekhar S, *The mathematical theory of black holes*, (Oxford University Press, N.Y., 1983) pp. 543–546
[2] Bagrov V G and Obukhov V V, *J. Math. Phys.*, **33**, 2279 (1992)
[3] Meshkov A G, *Izv. vuzov SSSR*. **12**, 41 (1980)

PRAMANA
— journal of
physics

© Printed in India

Vol. 41, No. 6,
December 1993
pp. 509–513

Quantum instability for a wave packet kicked periodically by a quadratic potential

A K SIKRI and M L NARCHAL
Department of Physics, Punjabi University, Patiala 147 002, India

MS received 23 April 1993; revised 16 August 1993

Abstract. The quantal behaviour of wave packet periodically kicked by a quadratic potential has been investigated using Floquet theory. The wave function of the particle after N kicks has been determined. This wave function has been utilized to obtain the packet width, energy and loss of memory as a function of the number of kicks. It has also been shown that the free particle wave packet quasienergy spectrum makes a transition from discrete to absolutely continuous at $\varepsilon T = 2$. The behaviour for $\varepsilon T > 2$ is quantum mechanically irregular.

Keywords. Quantum recurrence; quantum instability; chaos.

PACS No. 05·45

1. Introduction

There has been tremendous interest in recent years in the study of quantum systems with time dependent Hamiltonians which show instability or chaos in the classical limit. A lot of literature [1–10] has thus appeared, pioneering among them are those of Casati *et al* [1], Berry [2], Fishman *et al* [3] and Bellissard [6]. The principal motivation behind these studies is to determine as to how far the quantum systems mimic their classical counterparts. For example if the classical behaviour goes from regular to irregular as a certain system parameter crosses a critical value, does the quantum behaviour do so? The system which has been most studied is the quantum kicked rotator because of its link with the Anderson localization in disordered solids [3, 4]. It has been shown [11, 12] that the system is capable of showing both quantum mechanically recurrent as well as nonrecurrent behaviour depending upon whether the quasienergy states are localized or extended. A situation in which the quasienergy states are extended and the energy is unbounded is a quantally unstable situation without chaos whereas if the energy growth is diffusive the situation may be termed as quantum mechanically chaotic. Evidence for short time diffusive growth of energy exists in a quantum kicked rotator whereas the long time growth is not diffusive [11]. Thus as far as the present understanding goes, one has only obtained short time quantum chaos which gets scuttled by quantum effects with the passage of time.

Besides the quantum kicked rotator, several other problems have been studied in which the system shows nonrecurrent behaviour [8, 13]. Casati *et al* [11] have evolved a criterion to test whether the nonrecurrent behaviour is irregular or chaotic. In terms of this criterion if the quasienergy spectrum is absolutely continuous then the system behaviour is irregular whereas if it is singularly continuous the behaviour is chaotic.

The simplest time dependent system which shows classical instability is that of a free particle kicked periodically by a potential quadratic or higher in space. Classical studies of this problem have been reported by various workers [8, 14, 15]. There is no exact quantum mechanical solution of this problem which gives a unified view of regular as well as irregular behaviour. This paper presents an exact analytical solution to this problem. In § 2 we obtain the wave function of the particle after N kicks and utilize this wave function in § 3 to obtain the packet width, energy and loss of memory as a function of the number of kicks. The results are summarized in § 4.

2. Wave function of a system after N kicks

Consider a free particle of mass m described by the time dependent Hamiltonian

$$H = H_0 + \frac{1}{2} m\varepsilon^2 x^2 \sum_n \delta(t - nT) \tag{1}$$

where $H_0 = p^2/2m$ is the free particle Hamiltonian ε, determines the strength of the kick and T is time of kick. The evolution of the system is governed by one step Floquet operator

$$U = \exp(-(i/\hbar)H_0 T)\exp(-im\varepsilon^2 x^2 T/2\hbar). \tag{2}$$

Following Blumel *et al* [13] this operator may be written as

$$U = \exp(-iGT/\hbar) \tag{3}$$

where

$$G = \lambda\left[\frac{p^2}{2m} + \frac{1}{2} m\varepsilon^2 x^2 + \frac{\varepsilon^2 T}{4}(xp + px)\right] \tag{4}$$

$$\lambda = \sin^{-1}(r\varepsilon T)/r\varepsilon T, \tag{5}$$

$$r^2 = 1 - \varepsilon^2 T^2/4. \tag{6}$$

Equation (6) shows that r is real if $\varepsilon T < 2$ whereas it becomes imaginary for $\varepsilon T > 2$. Thus the spectrum of operator G will be determined by the value of εT.

Let $|\psi_0\rangle$ be the wave function of the free particle at time $t = 0$. Then its wave function after N kicks is

$$|\psi_N\rangle = U^N \quad |\psi_0\rangle. \tag{7}$$

Using (3) it takes the form

$$|\psi_N\rangle = \exp(-iNGT/\hbar) \quad |\psi_0\rangle. \tag{8}$$

In the position representation it may be written as

$$\psi_N(x) = \int_{-\infty}^{\infty} \langle x|\exp(-iNGT/\hbar)|x'\rangle \quad \psi_0(x')\mathrm{d}x'. \tag{9}$$

We represent the free particle by the wave packet of width σ at $t = 0$ by

$$\psi_0(x') = \frac{1}{(2\pi\sigma^2)^{1/4}}\exp((-x'^2/4\sigma^2) + ikx'). \tag{10}$$

Thus the expression for $\psi_N(x)$ becomes

$$\psi_N(x) = \frac{1}{(2\pi\sigma^2)^{1/4}} \int_{-\infty}^{\infty} \langle x|\exp(-iNGT/\hbar)|x'\rangle \exp(-x'^2/4\sigma^2) + ikx' \, \mathrm{d}x'. \tag{11}$$

This integral can be evaluated by proceeding on the lines adopted by Blumel *et al* [13]. Thus the wave function after N kicks takes the form

$$\psi_N(x) = \left(-\frac{v}{2\pi\sigma^2}\right)^{1/4} \exp\{(-1/4\sigma^2)(vx^2 + (kv\sin(\eta)x/br) + (k^2 v\sin^2\eta/4b^2r^2))$$
$$\times \exp(-i(bdx^2 - (kav\sin(\eta)x/r) + \tfrac{1}{2}\tan^{-1}(4ab\sigma^2) - (k^2 av\sin^2\eta/4br^2))). \tag{12}$$

where

$$b = m\varepsilon/2\hbar, \tag{13}$$

$$v = r^2\left[\frac{\sin^2\eta}{16b^2\sigma^4} + \left(r\cos\eta + \frac{\varepsilon T}{2}\sin\eta\right)^2\right]^{-1}, \tag{14}$$

$$\eta = N\sin^{-1}(\varepsilon rT), \tag{15}$$

$$d = a(1-v) - \varepsilon T, \tag{16}$$

$$a = r\cot\eta + \frac{\varepsilon T}{2}. \tag{17}$$

3. Packet width, energy and loss of memory

The width of wave packet after N kicks is given by

$$\delta_N = [\langle x^2\rangle_N - \langle x\rangle_N^2]^{1/2}, \tag{18}$$

where $\langle\ \rangle_N$ represents the expectation value with respect to wave function ψ_N. Using (12) it takes the form

$$\delta_N = \frac{\sigma}{r}\left[\frac{\sin^2\eta}{16b^2\sigma^4} + \left(r\cos\eta + \frac{\varepsilon T}{2}\sin\eta\right)^2\right]^{1/2}. \tag{19}$$

This equation shows that for $\varepsilon T < 2$ the width oscillates in time with frequency $|\sin^{-1}(\varepsilon rT)|/T$. This is the manifestation of quantum recurrence. For $\varepsilon T > 2$, η becomes imaginary and $\sin\eta$ and $\cos\eta$ become $i\sinh\eta$ and $\cosh\eta$ respectively. So the width grows exponentially with time scale $T/|\sin^{-1}(\varepsilon rT)|$. This may be compared with the natural spreading of the wave packet which takes place even in the absence of kicks. The natural width of the wave packet at any time t can be obtained be letting $\varepsilon \to 0$ in (19). This gives

$$\delta_0 = \sigma\left(1 + \frac{\hbar^2 t^2}{4m^2\sigma^4}\right)^{1/2}, \tag{20}$$

where $t = NT$. We observe that the increase of width is much faster in the presence of kicks as compared to natural spreading. This increase is determined by the product of kicking strength and time of kick.

The energy of free particle after N kicks is given by

$$E_N = \langle \psi_N | H_0 | \psi_N \rangle. \tag{21}$$

Using (12) we obtain

$$E_N = \frac{\hbar^2}{2m}\left[\frac{\nu}{4\sigma^2} + \frac{2b^2 d^2 \sigma^2}{\nu} + \frac{k^2 \sin^2 \eta}{r^2}(a\nu + d)^2\right]. \tag{22}$$

For $\varepsilon T < 2$, the energy oscillates showing quantum recurrence whereas for $\varepsilon T > 2$, the energy shows an exponential growth with a time scale proportional to the kicking strength.

The loss of memory after N kicks is determined by the absolute value of overlap integral $\langle \psi_N | \psi_0 \rangle$. That is

$$C_N = |\langle \psi_N | \psi_0 \rangle|. \tag{23}$$

Using (10) and (12) we obtain

$$C_N = \left(\frac{4\nu}{(\nu+1)^2 + 8b^2\sigma^2 d^2}\right)^{1/4} e^{\beta}, \tag{24}$$

where

$$\beta = \frac{k^2}{8D\sigma^2}\left[\frac{\nu^2 \sin^2 \eta}{r^2}\left\{(\nu+1)\left(\frac{1 - 8a^2 b^2 \sigma^2}{8b^2\sigma^2}\right) - 2ad - \frac{D}{b^2 \nu}\right\} + \frac{2\nu \sin \eta}{r}(2a - \varepsilon T) - (\nu + 1)\right]. \tag{25}$$

$$D = \left(\frac{\nu+1}{4\sigma^2}\right)^2 + b^2 d^2. \tag{26}$$

We find that C_N is a periodic function of N for $\varepsilon T < 2$ which shows that any loss of memory which may take place initially is subsequently recovered. This is again a manifestation of recurrence. For $\varepsilon T > 2$ we find that

$$\operatorname*{Lt}_{N \to \infty} C_N = 0. \tag{27}$$

The system completely forgets about its intial state with the passage of time.

The probability that the free particle makes a transition from initial state $|p'\rangle$ of H_0 to final state $|p\rangle$ after N kicks is proportional to the square of the probability amplitude. That is

$$P_{p' \to p} \propto |\langle p | U^N | p' \rangle|^2. \tag{28}$$

For $\varepsilon T > 2$ the spectrum of U is continuous. In order that U possesses absolutely continuous spectrum [12] it is necessary that

$$\operatorname*{Lt}_{N \to \infty} P_{p' \to p} = 0 \quad \text{for all } p \text{ and } p'. \tag{29}$$

Using (3) the expression for probability becomes

$$P_{p' \to p} \propto |\langle p | \exp(-iNGT/\hbar) | p' \rangle|^2. \tag{30}$$

Following Blumel *et al* [13] it can be shown that

$$\operatorname*{Lt}_{N\to\infty} P_{p'\to p} = 0. \tag{31}$$

Thus we conclude that the spectrum of Floquet operator for free particle in region $\varepsilon T > 2$ is absolutely continuous. This is an indication of a quantum mechanically irregular behaviour.

4. Conclusions

The exact analytical solution of a free particle wave packet subject to a sequence of δ function quadratic kicks has been obtained. There is only one parameter εT which decides the behaviour of the system. The quasienergy spectrum makes a transition from discrete to absolutely continuous at $\varepsilon T = 2$. Since the spectrum is absolutely continuous for $\varepsilon T > 2$, the system may be described as quantum mechanically irregular in this region.

An explicit expression for the energy after an arbitrary number of kicks has been obtained. The system shows markedly different behaviour on the two sides of transition point. The energy of the system for $\varepsilon T < 2$ is bounded and this agrees with the corresponding classical predictions. For $\varepsilon T > 2$ there is exponential growth of energy with the increase in the number of kicks. This is a manifestation of irregular behaviour of the system. Thus we observe that the system faithfully imitates the classical behaviour.

Besides energy, the width of the wave packet and overlap integral behave differently across the transition point. For $\varepsilon T > 2$ the packet width grows exponentially with time but it oscillates in time for $\varepsilon T < 2$. The overlap integral, which is a measure of the loss of memory of initial state, is a periodic function of time for $\varepsilon T < 2$ whereas it decays to zero with the passage of time for $\varepsilon T > 2$. This means that for regular behaviour there is a temporary loss of memory which is subsequently recovered whereas for irregular behaviour there is a permanent loss of memory.

References

[1] G Casati, B V Chirikov, F M Izrailev and J Ford, in *Stochastic behaviour in classical and quantum Hamiltonian systems*, edited by G Casati and J Ford, Lecture Notes in Physics (Springer-Berlin, 1979) vol. 93

[2] M V Berry, *Proc. of Les-Houches Summer School*, edited by G Iooss, R H G Helleman and R Stora (North Holland, Amsterdam, 1983)

[3] S Fishman, D R Grempel and R E Prange, *Phys. Rev. Lett.* **49**, 509 (1982)

[4] D R Grempel, R E Prange and S Fishman, *Phys. Rev.* **A29**, 1639 (1984)

[5] T Hogg and B A Huberman, *Phys. Rev.* **A28**, 22 (1983)

[6] J Bellissard, in *Trends and developments in the eighties*, edited by S Albeverio and Ph. Blanchard (World Scientific, Singapore, 1985)

[7] J V Jose, *Phys. Rev. Lett.* **56**, 290 (1986)

[8] A Cohen and S Fishman, *Int. J. Mod. Phys.* **2**, 103 (1988)

[9] Petr. Seba, *Phys. Rev.* **A41**, 2306 (1990)

[10] M Combescure, *J. Stat. Phys.* **59**, 679 (1990)

[11] G Casati, J Ford, I Guarneri and F Vivaldi, *Phys. Rev.* **A34**, 1413 (1986)

[12] B Milek and P Seba, *Phys. Rev.* **A42**, 3213 (1990)

[13] R Blumel, R Meir and U Smilansky, *Phys. Lett.* **A103**, 353 (1984)

[14] M V Berry, N L Balazs, M Tabor and A Voros, *Ann. Phys.* (NY) **122**, 26 (1979)

[15] H J Korsch and M V Berry, *Physica* **D3**, 627 (1981)

PRAMANA
— journal of
physics

© Printed in India

Vol. 41, No. 6,
December 1993
pp. 515–524

A semi-empirical formula for the energy spacings in Λ-hypernuclear excitation spectra

M Z RAHMAN KHAN and NASRA NEELOFER
Department of Physics, Aligarh Muslim University, Aligarh 202 002, India

MS received 1 September 1993

Abstract. A semi-empirical formula is presented which gives a semi-quantitative account of the excitation energies in Λ-hypernuclear excitation spectra. Many elaborate studies made were numerical, but our studies yield an analytical expression. Different three-dimensional harmonic oscillators for the Λ- and the neutron-hole reproduce the observed energy spacings fairly well. However, it would be misleading that the oscillators give the wave functions of the corresponding states also. In the light of harmonic excitations, we briefly discuss some phenomenological and microscopic Λ-hypernuclear calculations.

Keywords. Semi-empirical; Λ-hypernuclear excitation energy; hyperon-nucleon interactions.

PACS Nos 21·80; 13·75

1. Introduction

Λ-hypernuclei has been studied extensively over the last three decades. In the last decade, the strangeness exchange reaction (K^-, π^-) on nuclei has played a central role in hypernuclear spectroscopy. These reactions are characterized by small momentum transfer and are effective in producing substitutional states in which Λ has the same orbital as the neutron it replaces. They populate preferentially states of low angular momentum. In (K^-, π^-) spectra of medium and heavy nuclei, the states corresponding to deep-lying hyperon orbitals are generally not observed.

Recently, the associated production reaction (π^+, K^+) has been found to be effective in populating the deeply bound Λ-single particle levels in heavy hypernuclei. For nuclei over a large mass number range, Λ-single particle states have been obtained by this method [1–3].

Some of the earlier Λ-hypernuclear spectra were analysed by Bouyssy [4] who gave an apparently satisfactory account of the then available data by assuming pure particle-hole states in a single particle Λ-nucleus Woods-Saxon (WS) potential with an empirical term giving the nucleon, rather the neutron-hole spin-orbit splittings. A residual interaction was assumed which enabled removal of degeneracy of the different J-values resulting from the configurations. This made it possible to assign the J to the given state. At about this time, an alternative approach was adopted [5–7] to describe the states observed in the reactions as a coherent sum of particle-hole states designated as analog and supersymmetric. At that time, it was felt that the angular distributions would decide between the pure particle-hole states of Bouyssy [4] and the mixed states considered by Dalitz and Gal [5] and others.

With the analysis of the angular distribution, the matter seems to have been decided definitely in favour of the mixed states [6, 7], but that is not our concern here.

Without the slightest prejudice to the accepted nature of these states, we find that the Λ-hypernuclear excitation energy over the whole range of mass numbers can be described fairly well as the combined excitation of a three-dimensional harmonic oscillator describing the Λ and another, the neutron-hole (N_h) along with a suitable spin-orbit potential for the N_h. We do not suggest even obliquely that the oscillators give the corresponding wave functions, but the fact remains that they certainly give a semi-quantitative account of the energy spacings. The frequency of the Λ-oscillator is described by two adjustable parameters and that of the N_h by a single parameter only. Another adjustable parameter is for the spin-orbit splitting. The oscillator has been broadly mentioned in the context of the spectra, but no one seems to have performed such calculations earlier. However, besides Bouyssy [4], Dalitz and Gal [5], many numerical calculations have been carried out which gave a good account of the binding energies, cross-sections, angular distributions etc. Λ-single-particle energies have also been successfully analysed in the Skyrme Hartree-Fock approach in terms of Λ-nucleus potentials [8] and taking three-body ΛNN force [9] into account. A comprehensive review of Λ-single-particle states produced in (K^-, π^-) and (π^+, K^+) experiments has been given by Bando *et al* [10]. Many elaborate calculations discussed are numerical, whereas the present study is analytical, although more approximate.

As most of the data used here is obtained from the diagrams given in the literature and also as experimental errors in all the binding energies considered here are not available, we have assigned a plausible value to experimental errors to construct what we call the simulated chi-square (χ^2). This has been done simply to provide a criterion for adjusting the parameters and judging the quality of the fit.

Wave function notwithstanding, Bouyssy [4] was able to give a satisfactory account of the energy spacings by performing numerical calculations with his potential. Our work is broadly in the spirit of Bouyssy and the other workers, except that we confine ourselves to predicting the energy spacings. Use of the oscillators gives us an analytical expression, though certainly somewhat crude, for the energy spacings. It is clear that the fair amount of success achieved here should not be taken as any indication of the correctness of Bouyssy's philosophy of pure particle-hole states. Our objective is very limited, i.e., to give a semi-empirical formula for the energy spacings of the observed spectra. The analytical expressions, though approximate, enables one to see some dependences.

The quantum numbers of the outermost neutron orbit, required for the calculation of the energy spacings, as given by (13) in § 3, are taken to be those given by the standard shell model sequence of the single-particle states. The successive excited states are obtained by varying the quantum numbers of the two oscillators and these are listed in table 1 to enable a quick check to be made on the calculations.

2. General hypernuclear excitations

The picture required for our limited purpose has already been mentioned in the introduction. This is the basis of the calculations leading to the semi-empirical formula for the energy spacings. We do not take this picture literally. It is useful to us in so far as it gives a fairly good account of the observed spectral energy spacings.

In general, we assume that the hypernuclear spectra arise from Λ- and N_h-excitations in their respective harmonic oscillator potentials. Thus, the excitation energy of the hypernucleus can be considered to be the sum of Λ- and the N_h- excitations. The

Λ-excitation is measured from the ground state of Λ-particle, while the N_h-excitation from the topmost occupied neutron level where a hole corresponds to an unexcited core. The sum of these two quantities is the total excitation energy of the system.

The Λ-excitation energy E^*_Λ is given as

$$E^*_\Lambda = E_{nl} - E_{10}, \tag{1}$$

where E_{nl} is the energy eigenvalue of the Λ-3-dimensional isotropic harmonic oscillator corresponding to (nl)-state. It is given as

$$E_{nl} = (2n_\Lambda + l_\Lambda - \tfrac{1}{2})\hbar\omega_\Lambda, \tag{2}$$

where $n_\Lambda = 1, 2, 3\ldots$ and $l_\Lambda = 0, 1, 2\ldots$; E_{10} is the oscillator ground state energy corresponding to $n_\Lambda = 1$ and $l_\Lambda = 0$. The Λ-oscillator frequency [11] is taken to be of the form

$$\hbar\omega_\Lambda = C_{\Lambda 1} A_c^{-1/3} - C_{\Lambda 2} A_c^{-2/3}, \tag{3}$$

where $C_{\Lambda 1}$ and $C_{\Lambda 2}$ are parameters to be fixed from analysis of the data.

As the spin-orbit splitting for Λ is known to be extremely small [4] it is not taken into consideration. Consequently, the Λ-energy is labelled by (nl) only. However, spin-orbit splitting has to be taken into account for N_h, the energy of which is, therefore, labelled by (nlj).

Employing a 3-dimensional isotropic harmonic oscillator for the N_h as well, its excitation energy can be written as

$$E^*_{N_h} = E_{n_1 l_1 j_1} - E_{n_2 l_2 j_2}, \tag{4}$$

where $(n_1 l_1 j_1)$ represents the topmost oscillator orbital occupied by neutrons and $(n_2 l_2 j_2)$ is the oscillator orbital which is actually occupied by the N_h. We have

$$E_{nlj} = (2n + l - \tfrac{1}{2})\hbar\omega_{N_h} + \tfrac{1}{2}[j(j+1) - l(l+1) - \tfrac{3}{4}] \times \int \psi^*_{nl}(r)\, V^{ls}_{N_h}(r)\psi_{nl}(r)\,\mathrm{d}\tau, \tag{5}$$

where $\psi_{nl}(r)$ is the harmonic oscillator wave function and the N_h spin-orbit potential is chosen, for convenience, to be of the form

$$V^{ls}_{N_h}(r) = \bar{v}^{ls}_{N_h} g(r), \tag{6}$$

where the radial dependence of the N_h spin-orbit potential is taken to be of the form

$$g(r) = \frac{r \cdot r_0^3}{\sqrt{2}R^4} \exp[-(r^2/2R^2)], \tag{7}$$

where $R = r_0 A_c^{1/3}$, r_0 being a parameter fixed at a fairly reasonable value of 1·0 fm. Small changes in r_0 necessitate changes in $\bar{v}^{ls}_{N_h}$ without spoiling the fit. The surface peaking of $g(r)$ is in accord with well established ideas about the spin-orbit potential. For harmonic oscillator wave function and $V^{ls}_{N_h}(r)$ given above, eq. (5) reduces to (for

Table 1. Predicted and observed energy spacings of the excited states. The observed energies are given in the parenthesis below the predicted value. Also given are the quantum numbers of Λ and N_h represented as (nl, nlj) for a given state, where nl are the quantum numbers of Λ and nlj those of N_h. Values marked by a star are those which do not involve any N_h-transition in our picture of the oscillators. In ${}^{40}_{\Lambda}$Ca, there are 5 more predicted excited states out of which the 15th predicted excited state has energy 30·84 MeV, whereas the observed value is 31·50 MeV. Only one energy level has been observed in ${}^{209}_{\Lambda}$Bi which according to our calculations seems to be the 38th excited state.

Hyper-nuclei	Energy spacings of the excited states (MeV) numbered as 1, 2, 3, ...									
	1	2	3	4	5	6	7	8	9	10
${}^{6}_{\Lambda}$Li	10·85* (10·00) $(11, 11\frac{3}{2})$	19·18 (19·00) $(10, 10\frac{1}{2})$	21·71* (–) $(12, 11\frac{3}{2})$	30·04 (28·50) $(11, 10\frac{1}{2})$						
${}^{7}_{\Lambda}$Li	10·87 (10·50) $(11, 11\frac{3}{2})$	19·59 (21·50) $(10, 10\frac{1}{2})$	21·73* (–) $(12, 11\frac{3}{2})$	30·46 (30·50) $(11, 10\frac{1}{2})$						
${}^{9}_{\Lambda}$Be	10·74* (13·00) $(11, 11\frac{3}{2})$									
${}^{12}_{\Lambda}$C	10·44* (11·50) $(11, 11\frac{3}{2})$	19·37 (19·00) $(10, 10\frac{1}{2})$								
${}^{13}_{\Lambda}$C	10·33* (10·80) $(11, 11\frac{5}{2})$									
${}^{16}_{\Lambda}$O	6·51 (6·50) $(10, 11\frac{5}{2})$	10·03* (11·00) $(11, 11\frac{1}{2})$	18·54 (17·00) $(11, 11\frac{5}{2})$							
${}^{27}_{\Lambda}$Al	8·14* (8·00) $(11, 12\frac{5}{2})$	15·82 (–) $(10, 11\frac{5}{2})$	18·27* (17·00) $(12, 12\frac{5}{2})$							
	9·07*	15·72	18·14*							

$^{28}_{\Lambda}$Si	(8·80) (11, 12$\frac{5}{2}$)	(–) (10, 11$\frac{3}{2}$)	(18·00) (12, 12$\frac{5}{2}$)							
$^{32}_{\Lambda}$S	8·83* (–) (11, 20$\frac{1}{2}$)	11·17 (11·00) (11, 12$\frac{5}{2}$)	17·65* (–) (12, 20$\frac{1}{2}$)	18·21 (–) (10, 11$\frac{3}{2}$)	20·54 (20·00) (12, 12$\frac{5}{2}$)	24·00 (–) (11, 11$\frac{1}{2}$)	26·48* (–) (13, 20$\frac{1}{2}$)	27·04 (–) (11, 11$\frac{3}{2}$)	29·37 (30·50) (13, 12$\frac{5}{2}$)	
$^{40}_{\Lambda}$Ca	3·41 (–) (10, 20$\frac{1}{2}$)	5·69 (–) (10, 12$\frac{5}{2}$)	8·41* (9·00) (11, 12$\frac{3}{2}$)	11·83 (–) (11, 20$\frac{1}{2}$)	14·11 (–) (11, 12$\frac{5}{2}$)	16·83* (17·00) (12, 12$\frac{3}{2}$)	17·94 (–) (10, 11$\frac{1}{2}$)	20·24 (–) (12, 20$\frac{1}{2}$)	20·32 (–) (10, 11$\frac{3}{2}$)	22·52 (23·00) (12, 12$\frac{5}{2}$)
$^{51}_{\Lambda}$V	7·97* (9·00) (11, 13$\frac{7}{2}$)	8·93 (–) (10, 12$\frac{3}{2}$)	11·57 (–) (10, 20$\frac{1}{2}$)	13·33 (–) (10, 12$\frac{5}{2}$)	15·93* (15·50) (12, 13$\frac{7}{2}$)	16·90 (–) (11, 12$\frac{3}{2}$)	19·53 (–) (11, 20$\frac{1}{2}$)	21·29 (–) (11, 12$\frac{5}{2}$)	23·89 (23·00) (13, 13$\frac{7}{2}$)	
$^{89}_{\Lambda}$Y	6·96* (7·00) (11, 14$\frac{9}{2}$)	11·41 (–) (10, 13$\frac{7}{2}$)	11·34 (–) (10, 21$\frac{3}{2}$)	12·78 (–) (11, 21$\frac{1}{2}$)	13·92* (14·00) (12, 14$\frac{9}{2}$)	18·29 (–) (11, 21$\frac{3}{2}$)	18·42 (–) (11, 13$\frac{7}{2}$)	19·74 (–) (12, 12$\frac{1}{2}$)	20·68 (–) (10, 12$\frac{3}{2}$)	20·87* (21·00) (13, 14$\frac{9}{2}$)

$n = 1$)

$$E_{nlj} = [2n + l - \tfrac{1}{2}]\hbar\omega_{N_h} + [j(j+1) - l(l+1) - \tfrac{3}{4}]\bar{v}^{ls}_{N_h} \times \left[\frac{\pi(n-1)!(l+2)!r_0^3}{\sqrt{2}R^4 R_b^{(l+3)} b_{N_h}^{(2l+3)}\Gamma(n+l+\frac{1}{2})}\right]\left\{\binom{n+l-\frac{1}{2}}{n-1}^2\right\}, \tag{8}$$

where $R_b = \dfrac{2R^2 + b_{N_h}^2}{2R^2 b_{N_h}^2}$, $b_{N_h} = \left[\dfrac{\hbar}{m_N\omega_N}\right]^{1/2}$ and $\bar{v}^{ls}_{N_h}$ is the N_h spin-orbit strength which will be treated as an adjustable parameter. For $n = 2$, rest is same as given by (8) but the expression within the curly bracket in (8) is

$$\left\{\binom{n+l-\frac{1}{2}}{n-1}^2 - \frac{(l+2)}{R_b b_{N_h}}\binom{n+l-\frac{1}{2}}{n-1}\binom{n+l-\frac{1}{2}}{n-2} + \frac{(l+3)(l+4)}{R_b^2 b_{N_h}^2}\binom{n+l-\frac{1}{2}}{n-2}^2\right\}. \tag{9}$$

The oscillator frequency of the N_h is taken to be of the same form as given in the literature for the neutron oscillator frequency [12]

$$\hbar\omega_{N_h} = C_{N_h 1}A_c^{-1/3} - C_{N_h 2}A_c^{-1}, \tag{10}$$

with $C_{N_h 1} = C_{N1} - d_{N_h}$ and $C_{N_h 2} = C_{N2} - d_{N_h}$, where C_{N1} and C_{N2} are parameters for the neutron given in the standard literature [12]. These have been obtained by fitting the r.m.s. radius of the nuclei. Since there is no apriori reason to assume that the values of the parameters for N_h and the neutron are same, we take d_{N_h} as an adjustable parameter.

Thus, excitation energy of the Λ-hypernucleus (measured from the ground level) can be written as (for $n_1 = n_2 = 1$)

$$\begin{aligned} E^* &= E^*_\Lambda + E^*_{N_h} \\ &= [2n_\Lambda + l_\Lambda - 2]\hbar\omega_\Lambda + [(2n_1 + l_1) - (2n_2 + l_2)]\hbar\omega_{N_h} + \bar{v}^{ls}_{N_h}\frac{\pi r_0^3}{\sqrt{2}R^4} \\ &\quad\times\left[\frac{(n_1-1)!(l_1+2)![j_1(j_1+1) - l_1(l_1+1) - \frac{3}{4}]}{R_b^{(l_1+3)} b_{N_h}^{(2l_1+3)}\Gamma(n_1+l_1+\frac{1}{2})}\left\{\binom{n_1+l_1-\frac{1}{2}}{n_1-1}^2\right\}\right. \\ &\quad\left. - \frac{(n_2-1)!(l_2+2)![j_2(j_2+1) - l_2(l_2+1) - \frac{3}{4}]}{R_b^{(l_2+3)} b_{N_h}^{(2l_2+3)}\Gamma(n_2+l_2+\frac{1}{2})}\left\{\binom{n_2+l_2-\frac{1}{2}}{n_2-1}^2\right\}\right]. \end{aligned} \tag{11}$$

For either n_1 or $n_2 = 2$, their respective expression within the curly bracket, in the above equation, should be replaced by (9). At the expense of some additional small error, we could have used, for the N_h spin-orbit splitting, the simpler formula for the nucleon spin-orbit splitting given in the literature [13]

$$\Delta E^{ls} = 1{\cdot}4\, V_N^{ls}(l + \tfrac{1}{2})A_c^{-2/3}. \tag{12}$$

Thus, the excitation energy E^* (using (12)) may be written as:

$$E^* = [2n_\Lambda + l_\Lambda - 2]\hbar\omega_\Lambda + [(2n_1 + l_1) - (2n_2 + l_2)]\hbar\omega_{N_h} + 0{\cdot}7\, V^{ls}_{N_h}A_c^{-2/3}$$

$$\times [[l_1\delta_{j_1(l_1-\frac{1}{2})} - (l_1+1)\delta_{j_1(l_1+\frac{1}{2})}] \times (1-\delta_{l_1 0}) - [l_2\delta_{j_2(l_2-\frac{1}{2})} - (l_2+1)\delta_{j_2(l_2+\frac{1}{2})}] \times (1-\delta_{l_2 0})]. \qquad (11')$$

3. Results and discussion

Using (11), we carry out χ^2-fitting of all the available excitation data over a large range of mass numbers assuming a certain fixed percentage error for all the nuclei considered. The χ^2 is defined to be the quantity

$$\sum_i \left[\frac{Q^{\mathrm{exp}}(i) - Q^{\mathrm{th}}(i)}{\Delta Q^{\mathrm{exp}}(i)}\right]^2,$$

where the experimentally quoted value is taken to be $Q_i^{\mathrm{exp}} \pm \Delta Q_i^{\mathrm{exp}}$, the summation extending to all the data points. $\Delta Q_i^{\mathrm{exp}}$ is chosen to be an average percentage error of 5% for all the nuclei. This seems quite realistic. Here the value of χ^2 is not to be taken as justifying the above picture which is over-simplistic, as already indicated. The value of the simulated χ^2 should be taken only to convince that ours is a semi-quantitative formula for the spectral energy spacings. Our input data consist of the spectra of the hypernuclei, ${}^{6}_{\Lambda}\mathrm{Li}$, ${}^{7}_{\Lambda}\mathrm{Li}$, ${}^{9}_{\Lambda}\mathrm{Be}$, ${}^{12}_{\Lambda}\mathrm{C}$, ${}^{13}_{\Lambda}\mathrm{C}$, ${}^{16}_{\Lambda}\mathrm{O}$, ${}^{27}_{\Lambda}\mathrm{Al}$, ${}^{28}_{\Lambda}\mathrm{Si}$, ${}^{32}_{\Lambda}\mathrm{S}$, ${}^{40}_{\Lambda}\mathrm{Ca}$, ${}^{51}_{\Lambda}\mathrm{V}$, ${}^{89}_{\Lambda}\mathrm{Y}$ and ${}^{209}_{\Lambda}\mathrm{Bi}$.

Keeping C_{N1} and C_{N2} fixed at their respective values given in the standard literature [12], χ^2-fitting of all the available hypernuclear data treating $C_{\Lambda 1}$, $C_{\Lambda 2}$, d_{N_h} and $\bar{v}^{ls}_{N_h}$ as adjustable has been carried out. The results are given in table 1. The best fit parameters, for $\Delta Q_i^{\mathrm{exp}}$ taken as 5%, are $C_{\Lambda 1} = 38{\cdot}684\,\mathrm{MeV}$, $C_{\Lambda 2} = 34{\cdot}411\,\mathrm{MeV}$, $d_{N_h} = -19{\cdot}479\,\mathrm{MeV}$ and $\bar{v}^{ls}_{N_h} = -4{\cdot}467\,\mathrm{MeV}$, giving total $\chi^2 = 49{\cdot}78$ for thirty two data points. With our limitation it is justified to regard this as a semi-quantitative fit. If we use (11′) we get more or less similar results, with $\chi^2 = 59{\cdot}86$. So, we may use the simpler formula, at the expense of a small increase in the total χ^2. The best fit parameters in this case are $C_{\Lambda 1} = 38{\cdot}356\,\mathrm{MeV}$, $C_{\Lambda 2} = 33{\cdot}877\,\mathrm{MeV}$, $d_{N_h} = 25{\cdot}418\,\mathrm{MeV}$ and $V^{ls}_{N_h}$ 18·037 MeV. Our spin-orbit splitting for N_h is comparable to that for ordinary nucleons in conventional nuclear physics obtained from nucleon–nucleus scattering, etc.

We employ Bouyssy's notation for the ground state only for the purpose of getting the level-spacing with respect to the ground state energy and then the successive excited states are obtained by varying the quantum numbers. The task is easier if the somewhat more approximate formula (11′) is employed.

The results are given in table 1. For the hypernuclei studied in this work, all the excitation energies up to the highest value observed for that nucleus are calculated. Transitions marked by an asterisk do not involve any N_h transition in our picture of the oscillators. It is seen that many levels have not been observed in the experimental spectra. Such a situation is well-known. We may point out that relatively a smaller number of the starred states is not observed. Possibly some of the unobserved states have merged out to produce the neighbouring state observed in the experiment. We note that in most cases, the first excited state arises from pure Λ-excitations, but in two of our cases (i.e. ${}^{16}_{\Lambda}\mathrm{O}$ and ${}^{40}_{\Lambda}\mathrm{Ca}$), the first excited state arises from neutron-hole excitation. In ${}^{16}_{\Lambda}\mathrm{O}$ the hole transition is $1p_{1/2} \rightarrow 1p_{3/2}$ and in ${}^{40}_{\Lambda}\mathrm{Ca}$ it is $1d_{3/2} \rightarrow 2s_{1/2}$. In passing, we may mention that the simulated χ^2 would be reduced by about 4 if the observed excitation of 21·5 MeV for ${}^{7}_{\Lambda}$Li is identified with the third rather than the second excited state.

In ${}^{40}_{\Lambda}$Ca, 15 excited states have been calculated (only 10 are shown in the table). The energies of the 15th predicted and the observed excited states are 30·94 MeV and 31·50 MeV, respectively. In ${}^{209}_{\Lambda}$Bi, only one state has been observed and on the basis of our calculations it is the 38th excited state. Remembering that the energy resolution is about 3 MeV, it seems that almost all of these states have been averaged out because of their close spacing. Therefore, such levels as arise from spin-flip etc. or where the single-particle states are too close are all washed out giving an average distribution in accordance with observations. Further, since the deep hole states are highly excited, these have a large width. Consequently, these are almost completely washed out giving a smooth cross-section. Thus, whereas in (K^-, π^-) reaction giving ${}^{40}_{\Lambda}$Ca some structure corresponding to rather deep holes is observed, the cross-section is completely smoothed out where the same nucleus is produced in (π^+, K^+) reaction.

Since in the region of heavy nuclei, for most states, the spacing is very small, and since our formula gives the energy spacings with an error of a little over 1 MeV, it follows that the formula would be useful for nuclei ranging from light to medium-heavy but generally not as useful for very heavy nuclei like Bi. In the region where the neutron sub-shells are bunched rather closely or those hypernuclei of the 1p-shell in which the outer-most neutrons are in the 1p-shell, one should expect that the neutron-hole excitation would occur at a lower energy than the Λ-excitation. So, one expects that for these hypernuclei, the first excited state arises from neutron-hole excitation only. However, for reasons given above, this only makes sense if the hypernucleus is not too heavy. The situation in ${}^{16}_{\Lambda}$O and ${}^{40}_{\Lambda}$Ca is according to the above expectations.

4. Prediction of pure Λ-excitations from some hypernuclear ground state calculations

For states of pure Λ-excitations, i.e. those in which the N_h is in the topmost occupied orbital, the Λ-binding energy in an oscillator orbit (nl), denoted as $(B_\Lambda)_{nl}$, may be written as

$$(B_\Lambda)_{nl} = (B_\Lambda)_g + [2 - (2n + l)]\hbar\omega_\Lambda, \tag{13}$$

where $(B_\Lambda)_g$ denotes the ground state Λ-binding energy and $\hbar\omega_\Lambda$ is the Λ-oscillator frequency.

It can be easily seen that the condition for having only one bound state in the Λ-nucleus potential is

$$(B_\Lambda)_g < \hbar\omega_\Lambda. \tag{14}$$

In microscopic calculations, the wave function may be regarded as a superposition of several oscillator states. However, if crudely, the Λ is assigned a pure oscillator state of a certain frequency ω_Λ, the latter may be obtained by equating the expectation value of the kinetic energy to $\frac{3}{4}\hbar\omega_\Lambda$. Variational Monte Carlo calculations [14, 15] of B_Λ, from which ω_Λ can be extracted in the above manner, are available to us for ${}^{3}_{\Lambda}$H, ${}^{4}_{\Lambda}$H, ${}^{4}_{\Lambda}$He, ${}^{5}_{\Lambda}$He and ${}^{9}_{\Lambda}$Be. It can be easily seen from the value of our parameters that the distance between the neighbouring N_h-shells is always larger than that between the Λ-shells. Therefore, it is predicted that the first excited state in all 1s-shell nuclei shall be a pure Λ-excitation. In $1s_{1/2}$-shell, N_h-transition seems to have no meaning. We can easily see that for the $1p$-shell nuclei having nucleons up to $1p_{3/2}$-shell only but not in the $1p_{1/2}$-shell the only N_h-transition can be from $1p_{3/2} \rightarrow 1s_{1/2}$. From the simpler formula (11′) it can be easily seen that for all these nuclei the N_h-transition energy is certainly larger than the pure Λ-excitation energy. Further, for $1p$-shell nuclei having nucleons in the $1p_{1/2}$-shell as well, the lowest N_h-transition is $1p_{1/2} \rightarrow 1p_{3/2}$ and this energy is also larger than that of lowest pure Λ-excitation. Therefore, the lowest excitation for all the nuclei is the Λ-excitation i.e. the excitation energy is $\hbar\omega_\Lambda$.

However, the excitation data are available only in respect of ${}^{9}_{\Lambda}$Be which is a $1p$-shell hypernucleus. Thus, the first excited state arise from pure Λ-excitation. The value of $\hbar\omega_\Lambda$ extracted from microscopic calculations satisfies inequality (14) above in accordance with the observation in that this nucleus has only one bound excited state.

Results of $1p$-shell phenomenological calculations of Shoeb and Rahman Khan [16], using oscillator wave functions, and employing, in addition to the two-body ΛN force also a three-body ΛNN force, are consistent with the above predictions in all the cases for which the data are available and for which the calculations were carried out. Two of the four gaussian ΛN potentials, along with the three-body ΛNN force, employed by Ansari *et al* [17] are also consistent with the predictions. A comparison with the work of Mujib *et al* [18] brings out the significance of three-body ΛNN force in this context.

The predicted values of $\hbar\omega_\Lambda$ from empirical relations, $\hbar\omega_\Lambda = 60\,A_c^{-2/3}$, given by Auerbach and Gal [19]; $\hbar\omega_\Lambda = 27\,A_c^{-1/3}$; given by Bouyssy [4] and $\hbar\omega_\Lambda = C_{\Lambda 1} A_c^{-1/3} - C_{\Lambda 2} A_c^{-2/3}$ used by us are not very different for medium and heavy nuclei, but are markedly different for light nuclei. It, therefore, follows that spectral studies of light nuclei would help in discriminating between the various formulae for $\hbar\omega_\Lambda$.

5. Conclusion

A semi-quantitative formula, giving the energy spacings of the Λ-hypernuclear excitation data over a large mass number range, is presented. However, the simple picture of the oscillators employed for the purpose of giving the semi-empirical formula is not close to reality, although it might well turn out that by inclusion of a residual interaction and some alteration in the value of the parameters, it might get us quite close to the more realistic situation. We entertain this hope because the agreement achieved cannot be entirely fortuitous, but such conjectures are not crucial for the justification of the work reported here. The picture is used only to obtain a semi-empirical formula to account for the observed spectral energy spacings. Our formula seems to be satisfactory for light and medium nuclei and perhaps not useful for heavier ones.

The idea of harmonic excitation allows us to make reasonable predictions about the excited states from microscopic or phenomenological calculations of hypernuclear ground states.

It is pointed out that study of light nuclei is likely to be more useful for discriminating between the various empirical formulae for $\hbar\omega_\Lambda$. The same should apply to formulae for $\hbar\omega_{N_h}$. Our formulae show that the level spacings due to pure Λ-excitations as well as due to N_h-transition get smaller and smaller with increasing mass number. This is, indeed, what one expects on general grounds and this is responsible for the smearing out of the spectra rendering formulae like ours almost useless.

Acknowledgements

We are grateful to Dr. Mohammad Shoeb for some valuable discussions. We are also thankful to the staff of Computer Centre of the University, for their help and cooperation in using VAX 11/780 computer.

References

[1] R Chrien, Proceedings of XIth International Conference on Particles and Nuclei, Kyoto, 1987 *Nucl. Phys.* **A478**, 705c (1988)]

[2] P H Pile, *Nuovo Cimento.* **102**, 413 (1989)

[3] P H Pile *et al*, *Phys. Rev. Lett.* **66**, 2585 (1991)

[4] A Bouyssy, *Nukleonika* **25**, 413 (1980)

[5] R H Dalitz and A Gal, *Phys. Rev. Letts.* **36**, 362 (1976)

[6] M May *et al*, *Phys. Rev. Lett.* **47**, 1106 (1981)

[7] E H Auerbach, A J Baltz, C B Dover, A Gal, S H Kahana, L Ludeking and D J Millener, *Phys. Rev. Letts.* **47**, 1110 (1981)

[8] D J Millener, C B Dover and A Gal, *Phys. Rev.* **C38**, 2700 (1988)

[9] Y Yamamoto, H Bandō and J Žofka, *Prog. Theor. Phys.* 80, 757 (1988)

[10] H Bandō, T Motoba and J Žofka, *Perspective of meson science* (Elsevier Science Publishers, North Holland, 1992) pp. 571

[11] C A Lalazissis, M E Grypeos and S E Massen, *Phys. Rev.* **C37**, 2098 (1988)

[12] C B Daskaloyannis, M E Grypeos, C G Koutroulos, S E Massen and D S Saloupis, *Phys. Lett.* **B121**, 91 (1983)

[13] A Bohr and R Mottelson Ben, *Nuclear structure*, (W A Bengamin, Inc., New York, Amsterdam, 1969) vol. 1 218

[14] M Shoeb, Q N Usmani and A R Bodmer, *Nucl. Phys. A* (Submitted 1993)

[15] Nasra Neelofer and Mohammad Shoeb, *Proc. of DAE Symp. on Nucl. Phys.*, Dec. 26–30, **B34**, 313 (1991)

[16] M Shoeb and M Z Rahman Khan, *J. Phys.* **G10**, 1047 (1984)

[17] H H Ansari, M Shoeb, Q N Usmani and M Z Rahman Khan, *J. Phys.* **G12**, 1369 (1986)

[18] F Mujib, M Shoeb, Q N Usmani and M Z Rahman Khan, *J. Phys.* **G5** 541 (1979)

[19] N Auerbach and A Gal, *Phys. Lett.* **B48**, 22 (1974)

PRAMA
— journ
ph

L-de

S V S
Nuclea

MS rec

Abstrac
of ^{16}O
kinetic
channel
functio
potenti
these q

Keywor
model.

PACS

1. Intr

The sa
fusion
aroun
sub-ba
one-di
fusion
deforn
potent
can be
Howe
which
coupli
in a si
has be
a full
E and
couple
barrie
kineti
energ
poten
depen
optica

PRAMANA
— journal of
physics

© Printed in India

Vol. 41, No. 6,
December 1993
pp. 525–534

L-dependent heavy ion fusion potentials

S V S SASTRY, A K MOHANTY and S K KATARIA
Nuclear Physics Division, Bhabha Atomic Research Centre, Bombay 400 085, India

MS received 10 May 1993; revised 6 August 1993

Abstract. The energy E and angular momentum l dependence of optical potential for fusion of $^{16}O + ^{208}Pb$ system, observed by Christley *et al* [5], is expressed as a function of radial kinetic energy (ε) instead of explicit E and l dependence. It is shown that the effects of different channel couplings, which result in different effective potentials, can also be parametrized as a function of ε. A correlation is obtained between the energy dependent part of this effective potential and the maximum of the spin enhancement around the Coulomb barrier and both these quantities depend on the details of the channel couplings.

Keywords. l-dependent potential; fusion cross-section; spin distribution; barrier penetration model.

PACS Nos 25·70; 24·10

1. Introduction

The salient features found in the fusion of heavy ions are the enhanced sub-barrier fusion cross-section and the broadening of the compound nucleus spin distribution around the Coulomb barrier which seem to be closely related. The observed sub-barrier fusion cross-sections are not compatible with the predictions of the one-dimensional barrier penetration model (BPM). Earlier studies of sub-barrier fusion enhancement in BPM invoked the influence of orientation of statically deformed reaction partners and of zero point shape fluctuations on the height of potential barrier. In a more general microscopic description, sub-barrier enhancement can be explained by including the coupling to the inelastic and transfer channels. However, one can use a macroscopic model with inclusion of neck degree of freedom which provides an alternate path for fusion process. These dynamical effects of channel coupling or neck opening can be incorporated in an optical model analysis or even in a simple BPM by constructing an effective energy-dependent potential [1, 2]. It has been shown that only energy-dependent effective potential is not consistent with a full dynamical coupled channel calculations [3], unless it depends on both energy E and angular momentum l [4, 5]. It has been shown that [4], the results of a model coupled channel calculation can be reproduced by a simple BPM when the effective barrier height is expressed as function of effective kinetic energy ε, which is the radial kinetic energy at the interaction barrier given by $\varepsilon = E - E_R$ where the rotational energy $E_R = l(l+1)\hbar^2/(2\mu R_b^2)$. Therefore, this simple dependence of the effective potential on ε makes the barrier height (hence the nuclear potential) both E and l dependent. Further evidence for E and l dependent nuclear potential comes from the optical model analysis [5] of fusion for $^{16}O + ^{208}Pb$ system, where the diffuseness

Acknowledgements

We are grateful to Dr. Mohammad Shoeb for some valuable discussions. We are also thankful to the staff of Computer Centre of the University, for their help and cooperation in using VAX 11/780 computer.

References

[1] R Chrien, Proceedings of XI$^{\text{th}}$ International Conference on Particles and Nuclei, Kyoto, 1987 *Nucl. Phys.* **A478**, 705c (1988)]

[2] P H Pile, *Nuovo Cimento.* **102**, 413 (1989)

[3] P H Pile *et al*, *Phys. Rev. Lett.* **66**, 2585 (1991)

[4] A Bouyssy, *Nukleonika* **25**, 413 (1980)

[5] R H Dalitz and A Gal, *Phys. Rev. Letts.* **36**, 362 (1976)

[6] M May *et al*, *Phys. Rev. Lett.* **47**, 1106 (1981)

[7] E H Auerbach, A J Baltz, C B Dover, A Gal, S H Kahana, L Ludeking and D J Millener, *Phys. Rev. Letts.* **47**, 1110 (1981)

[8] D J Millener, C B Dover and A Gal, *Phys. Rev.* **C38**, 2700 (1988)

[9] Y Yamamoto, H Bandō and J Žofka, *Prog. Theor. Phys.* 80, 757 (1988)

[10] H Bandō, T Motoba and J Žofka, *Perspective of meson science* (Elsevier Science Publishers, North Holland, 1992) pp. 571

[11] C A Lalazissis, M E Grypeos and S E Massen, *Phys. Rev.* **C37**, 2098 (1988)

[12] C B Daskaloyannis, M E Grypeos, C G Koutroulos, S E Massen and D S Saloupis, *Phys. Lett.* **B121**, 91 (1983)

[13] A Bohr and R Mottelson Ben, *Nuclear structure*, (W A Bengamin, Inc., New York, Amsterdam, 1969) vol. 1 218

[14] M Shoeb, Q N Usmani and A R Bodmer, *Nucl. Phys. A* (Submitted 1993)

[15] Nasra Neelofer and Mohammad Shoeb, *Proc. of DAE Symp. on Nucl. Phys.*, Dec. 26–30, **B34**, 313 (1991)

[16] M Shoeb and M Z Rahman Khan, *J. Phys.* **G10**, 1047 (1984)

[17] H H Ansari, M Shoeb, Q N Usmani and M Z Rahman Khan, *J. Phys.* **G12**, 1369 (1986)

[18] F Mujib, M Shoeb, Q N Usmani and M Z Rahman Khan, *J. Phys.* **G5** 541 (1979)

[19] N Auerbach and A Gal, *Phys. Lett.* **B48**, 22 (1974)

PRAMANA
— journal of
physics

© Printed in India

Vol. 41, No. 6,
December 1993
pp. 525–534

L-dependent heavy ion fusion potentials

S V S SASTRY, A K MOHANTY and S K KATARIA
Nuclear Physics Division, Bhabha Atomic Research Centre, Bombay 400085, India

MS received 10 May 1993; revised 6 August 1993

Abstract. The energy E and angular momentum l dependence of optical potential for fusion of $^{16}O + ^{208}Pb$ system, observed by Christley *et al* [5], is expressed as a function of radial kinetic energy (ε) instead of explicit E and l dependence. It is shown that the effects of different channel couplings, which result in different effective potentials, can also be parametrized as a function of ε. A correlation is obtained between the energy dependent part of this effective potential and the maximum of the spin enhancement around the Coulomb barrier and both these quantities depend on the details of the channel couplings.

Keywords. l-dependent potential; fusion cross-section; spin distribution; barrier penetration model.

PACS Nos 25·70; 24·10

1. Introduction

The salient features found in the fusion of heavy ions are the enhanced sub-barrier fusion cross-section and the broadening of the compound nucleus spin distribution around the Coulomb barrier which seem to be closely related. The observed sub-barrier fusion cross-sections are not compatible with the predictions of the one-dimensional barrier penetration model (BPM). Earlier studies of sub-barrier fusion enhancement in BPM invoked the influence of orientation of statically deformed reaction partners and of zero point shape fluctuations on the height of potential barrier. In a more general microscopic description, sub-barrier enhancement can be explained by including the coupling to the inelastic and transfer channels. However, one can use a macroscopic model with inclusion of neck degree of freedom which provides an alternate path for fusion process. These dynamical effects of channel coupling or neck opening can be incorporated in an optical model analysis or even in a simple BPM by constructing an effective energy-dependent potential [1, 2]. It has been shown that only energy-dependent effective potential is not consistent with a full dynamical coupled channel calculations [3], unless it depends on both energy E and angular momentum l [4, 5]. It has been shown that [4], the results of a model coupled channel calculation can be reproduced by a simple BPM when the effective barrier height is expressed as function of effective kinetic energy ε, which is the radial kinetic energy at the interaction barrier given by $\varepsilon = E - E_R$ where the rotational energy $E_R = l(l+1)\hbar^2/(2\mu R_b^2)$. Therefore, this simple dependence of the effective potential on ε makes the barrier height (hence the nuclear potential) both E and l dependent. Further evidence for E and l dependent nuclear potential comes from the optical model analysis [5] of fusion for $^{16}O + ^{208}Pb$ system, where the diffuseness parameter 'a' of the imaginary potential has been varied as a function of both E and l in order to reproduce coupled reaction channel (CRC) results. In § 3 of the present work, it is shown that, diffuseness parameter $a(E, l)$ can also be expressed as a function of ε, instead of an explicit E and l dependence used in [5]. Further, it is shown in § 4 that the effect of different channel couplings (i.e. coupling to inelastic and transfer channels) results in different one channel effective real barrier height which can be parametrized as a suitable function of ε. In other words, a simple parametric form of $V_{\mathrm{eff}}(\varepsilon)$ in BPM can be used to explain the enhancement of fusion cross-section and broadening of compound nucleus spin distribution.

The effective potential can be written as a sum of an energy independent part and an energy dependent part: $V_{\mathrm{eff}} = V_b + \Delta V_p(\varepsilon)$ where ΔV_p can be identified as the polarization potential. In the elastic scattering analysis also one needs a similar energy dependent potential where the strength of the real and imaginary optical potentials show a rapid variation around the Coulomb barrier, known as threshold anomaly [6]. Further evidence shows the strength of the real potential versus energy is a bell-shaped maxima in the vicinity of the Coulomb barrier. In the present case also $\Delta V_p(\varepsilon)$ has a similar behaviour, however instead of energy E it depends on the effective energy ε. The peak of this polarization potential does not necessarily occur at Coulomb barrier, rather it depends on Q value of the non-elastic and transfer channels. In § 5, it is shown that this polarization potential which arises due to various channel couplings, shows a maximum at an energy lower than the Coulomb barrier. However, the effects of these channel couplings on the moments of the spin distribution is maximum at around the Coulomb barrier. It is shown here that the strength of the polarization potential and the spin enhancement around the Coulomb barrier are strongly correlated.

2. The model

The fusion cross-section for a given energy E and partial wave l is written as

$$\sigma_l = (\pi/k^2)(2l+1)\, T_l(E), \tag{1}$$

where $T_l(E)$ is the penetration probability of lth partial wave at energy E. Using barrier penetration model, it can be written as

$$T_l(E) = 1/[1 + \exp\{(2\pi/\hbar\omega)(V_b + E_R - E)\}], \tag{2}$$

where E_R is the rotational energy, R_b is the position and $\hbar\omega$ is the width of the s-wave barrier. The total fusion cross-section and the average spin value are given by

$$\sigma_f = \sum_l \sigma_l, \tag{3}$$

and

$$\langle l \rangle = \frac{\Sigma l \sigma_l}{\Sigma \sigma_l}. \tag{4}$$

3. *L*-dependent potential

In an earlier study [4], it was shown that the effects of channel couplings can be introduced by making the barrier height V_b to be energy and l dependent. This was accomplished by parametrizing V_b as a function of ε. Similarly, to reproduce the

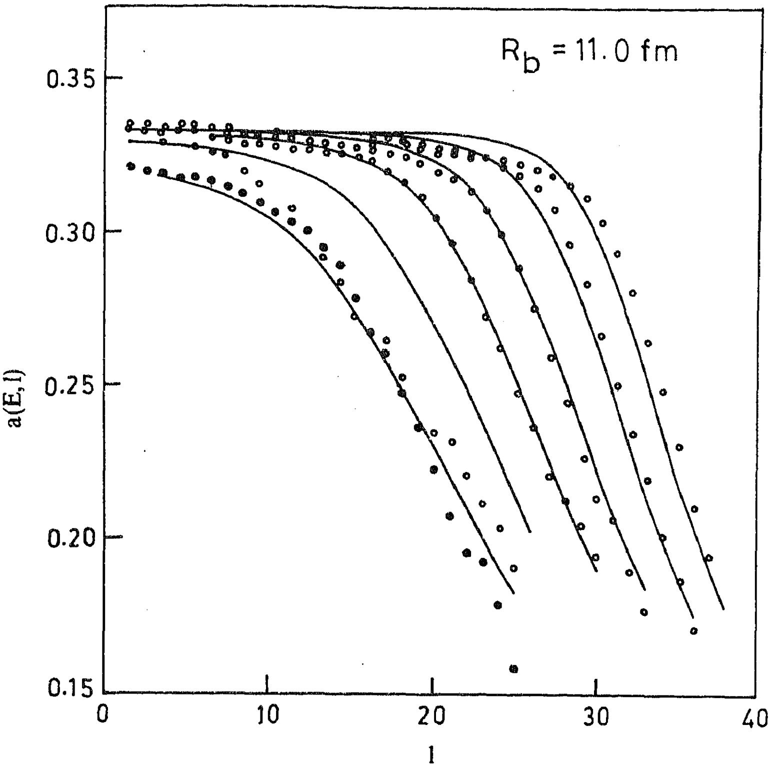

Figure 1. The diffuseness parameter $a(E, l)$ versus l at different laboratory energies from 90, 88, 86, 84, 80 MeV (○) and 82 MeV (●) taken from ref. [5]. The smooth curve is obtained using (9) with parametrization $R_s = 12$ fm, $R_0 = 10{\cdot}38$ fm, $E_e = 72{\cdot}2$ MeV and $a_e = 1{\cdot}4$ MeV.

fusion mean square spin values of $^{16}O + ^{208}Pb$ system is an optical model study, the imaginary potential was expressed as a function of ε [8]. The need to have both E and l dependence has also been studied by Christley *et al* [5], where the diffuseness parameter of the imaginary potential was varied as a function of l. Figure 1 shows the diffuseness parameters as a function of l for different energies E taken from [5]. However, we show here that the observed $a(E, l)$ dependence can also be obtained as a consequence of ε-dependence of the strength of the imaginary potential [8]. In these calculations, the imaginary potential is written as a product of two functions i.e. the radial part $f(r)$ and the ε dependent part $g(\varepsilon)$. Therefore, the imaginary potential is written as

$$W_f(r) = W_0 f(r) g(\varepsilon), \tag{5}$$

and

$$f(r) = 1/\{1 + \exp[(r - R_0)/a_0]\}, \tag{6}$$

and

$$g(\varepsilon) = 1/\{1 + \exp[(E_e - \varepsilon)/a_e]\}. \tag{7}$$

As seen from (7), $g(\varepsilon)$ has an implicit E and l dependence through the variable ε. The value of E_e is very close to the Coulomb barrier. Alternatively, energy and l dependence of $W_f(r)$ can be introduced through the radial diffuseness parameter

$a(E,l)$ as in [5]. In this parametrization W_f can be written as

$$W_f(r) = W_0/\{1+\exp[(r-R_0)/a_b(E,l)]\}. \tag{8}$$

Comparing the strength of (5) and (8) at strong absorption radius $r = R_s$, we can write

$$a_b(E,l) = (R_s - R_0)/\log[\{f(R_s)g(\varepsilon)\}^{-1} - 1]. \tag{9}$$

The diffuseness values obtained by Christley *et al* [5] (see figure 1) can be reproduced using (9) (solid curve in figure 1) except at 82 MeV with $R_0 = 10{\cdot}38$, $a_0 = 0{\cdot}33$, $E_e = 72{\cdot}2$ MeV and $a_e = 1{\cdot}4$ MeV and $R_s = 12$ fm. The value of Coulomb barrier for this system is 74·6 MeV which is quite close to E_e. These $a(E,l)$ values are also shown in figure 2 as a function of ε for different bombarding energies. For calculation of ε, the value of R_b is taken as 11 fm which is close to the position of the Coulomb barrier. In spite of different E and l dependence of $a(E,l)$ as in figure 1, they all merge into a single curve in ε-scale except for 82 MeV. This data set at 82 MeV does not follow the general systematics with energy and needs to be studied more carefully.

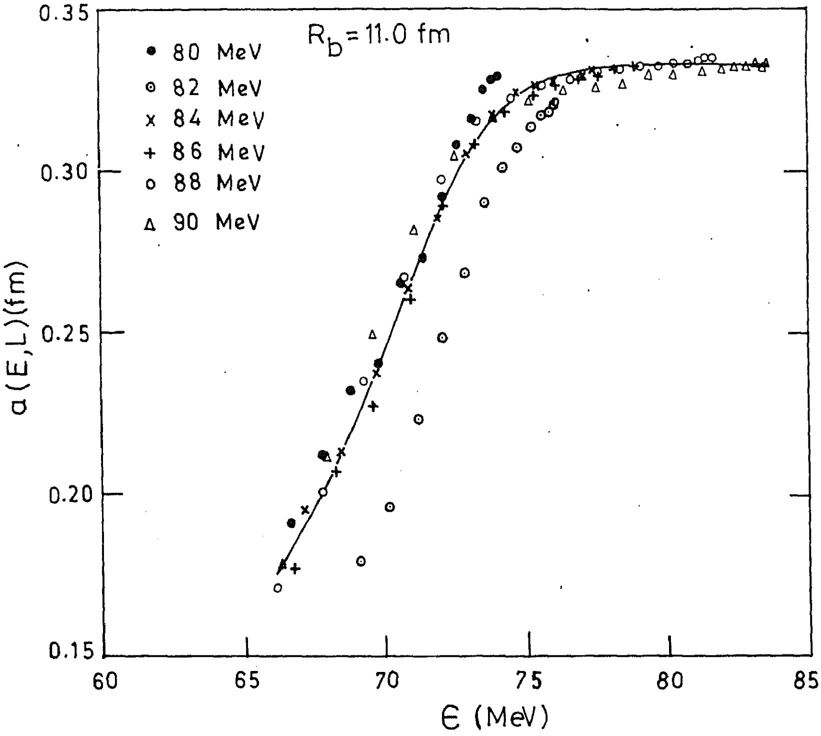

Figure 2. Diffuseness $a(\varepsilon)$ versus ε. The smooth line is the result of parametrization given by (9) as in figure 1. The discrete values with different symbols show the value of $a(\varepsilon)$ for different energies taken for ref. [5].

4. Effective fusion barrier

The effective barrier $V_{\text{eff}}(\varepsilon)$ can be parametrized as [4]

$$\begin{aligned}
&\text{if} \quad \varepsilon > E_2 \text{ then } V_{\text{eff}} = V_2 \\
&\text{if} \quad E_1 < \varepsilon < E_2, \text{ then } V_{\text{eff}} = \beta\varepsilon + C \\
&\text{if} \quad \varepsilon < E_1 \text{ then } V_{\text{eff}} = V_1.
\end{aligned} \tag{10}$$

In this schematic model, we have two limiting barrier heights V_2 and V_1, known as sudden and adiabatic barriers. The difference $\Delta B = V_2 - V_1$ is shown to be a monotonically increasing function of $Z_T Z_P$ [9]. The magnitude of ΔB reflects the coupling effects in an average way. It has been realized that the direct coupling of various inelastic and transfer processes highly influence the fusion cross-section and the spin distribution. In addition to these single step processes, the multistep coupling processes also contribute significantly to fusion. Therefore, one needs to solve the coupled equations where all these effects are taken into account. On the other hand, when expressed in terms of an effective potential, the various coupling processes affect the adiabatic barrier V_1 significantly. In other words, the effect of adding more channels results in the effective barrier which can be parametrized as some suitable function of ε. In [4], we had considered the couplings to only inelastic states. However, in the present case we consider the effect of positive Q value transfer channels on effective fusion barrier in addition to the inelastic states.

The coupled channel calculations are carried out for $^{58}\text{Ni} + ^{64}\text{Ni}$ systems using CCFUS code [10]. The dashed curve in figure 3 shows the coupled channel results for fusion cross-sections as a function of energy E_{cm} when coupling to only a few inelastic states are included (2^+, 3^- and 4^+ states of ^{58}Ni and ^{64}Ni). The strength of various inelastic modes are taken from [11]. To find the effective barrier height in BPM which will reproduce the coupled channel results, V_{eff} is calculated by inversion procedure from (1) and (2) as

$$V_{\text{eff}} = \varepsilon + (\hbar\omega/2\pi)\log[(\pi/k^2)(2l+1)/\sigma_1 - 1]. \tag{11}$$

Therefore, knowing l and σ_l from CC calculations, $V_{\text{eff}}(\varepsilon)$ at different bombarding energies is estimated. Figure 4 shows $V_{\text{eff}}(\varepsilon)$ versus ε at two energies; 110 MeV and 100 MeV. It can be seen that irrespective of different bombarding energies, $V_{\text{eff}}(\varepsilon)$ (for different energy E) merge into a single curve. The values chosen are $V_2 = 102$ MeV, $E_2 = 102{\cdot}4$ MeV, $V_1 = 96{\cdot}5$ MeV and $E_1 = 95{\cdot}7$ MeV. The BPM calculation with these parameters results in fusion cross-section shown in figure 3.

As seen in figure 3, coupling to only inelastic channels is not adequate to reproduce the experimental fusion cross-sections. It was pointed out in [11] that it is most likely due to the fact that $^{58}\text{Ni} + ^{64}\text{Ni}$ combination allows for two neutron transfer reactions due to positive Q value. Accordingly, when coupling strength of 1 MeV is added at $Q = +5$ MeV, it results in the dashed-dot line. The corresponding V_{eff} values are shown in figure 4. Therefore, it can be seen that any additional effects of channel coupling results in lowering of the effective barrier height V_{eff}. In other words, channel coupling lowers the adiabatic barrier V_1 (also E_1), whereas the sudden limit values V_2 and E_2 do not change significantly. Further, the CC results (with inclusion of positive Q value transfer channel) enhance the fusion cross-section. It is not sufficient to reproduce the experimental results as the number of channels included are not

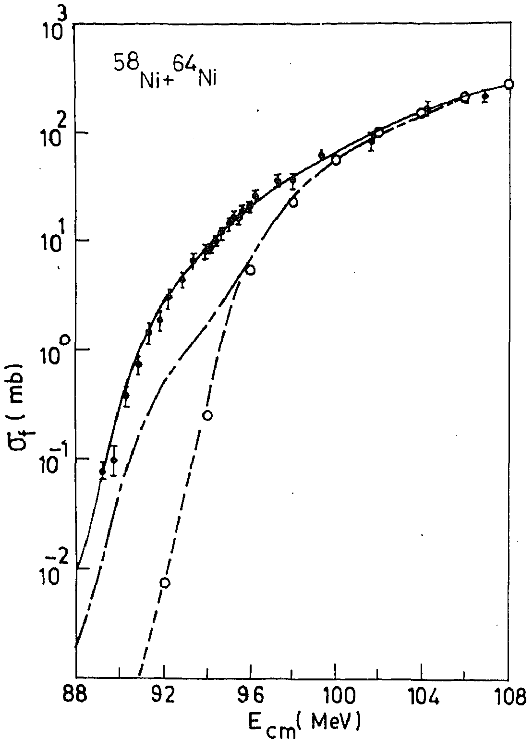

Figure 3. Fusion cross-sections versus E_{cm} for ^{58}Ni + ^{64}Ni systems. (– – –) result of coupled channel calculations with inelastic couplings alone. (–·–·): CC results with transfer channel included. (○) and (———) are the results of ε dependent BPM with the schematic barrier parameters given in figure 4 (smooth line and broken line). The data points are taken from ref. [12].

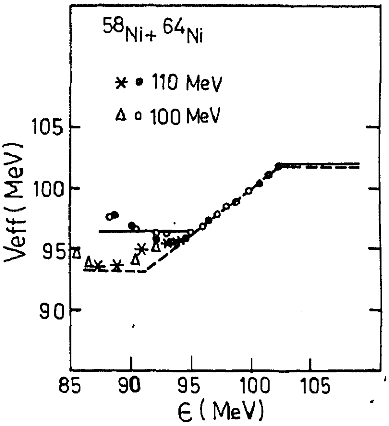

Figure 4. V_{eff} versus ε. The filled and open circles are obtained by inversion from the CC results (with inelastic channels included) using (10) at $E_{\mathrm{cm}} = 110$ and 100 MeV. The stars and triangles are the corresponding values with transfer channel included. The smooth and broken lines are two sets of schematic parameters.

adequate and also using CCFUS, couplings to inelastic and transfer channels are considered in an approximate way [11]. However, the new set of parameters i.e. $V_2 = 101{\cdot}6\,\mathrm{MeV}$, $E_2 = 102{\cdot}2\,\mathrm{MeV}$, $V_1 = 93{\cdot}2\,\mathrm{MeV}$ and $E_1 = 91{\cdot}2\,\mathrm{MeV}$ results in the smooth curve in figure 3, which fits the experimental fusion cross-section rather well. Comparing the parameters of these two sets, it can be seen that the sudden values of V_2 and E_2 remain more or less same but the adiabatic values V_1 and E_1 are different. The difference between two adiabatic barrier heights is about 3·3 MeV which is quite close to the Q value of two neutron-transfer. It is now clear that the effective barrier resulting from inclusion of more and more channels can be parametrized as a function of ε, which is a necessary and relevant parameter for fusion.

Therefore, the schematic model of (10), where the effective barrier height depends on ε, takes into account all the dynamical effects of channel coupling. In the following, we use this model to study the polarization potentials and its effect on the average spin of the compound nucleus, in the vicinity of the Coulomb barrier.

5. Polarization potential and enhancement in spin distribution

Figure 5(a) shows the plot of $\Delta V_p = (V_{\mathrm{eff}} - V_b)$ as a function of ε for $^{58}\mathrm{Ni} + {}^{64}\mathrm{Ni}$ system. V_{eff} is calculated using (11) where σ_l is taken from CCFUS. V_b is the barrier height when channel coupling is not present. The energy dependent part of the effective potential i.e. ΔV_p can be identified as the polarization potential at R_b, which arises due to channel coupling. While calculating V_{eff}, we have used l-dependent $\hbar\omega$ given by $\hbar\omega_1 = \hbar\omega_0 + 0{\cdot}0004\,l^2$ as suggested in [4]. In the first case only 2^+, in the second case 2^+ and 3^- and in the third case 2^+, 3^- and 4^+ states of both target and projectile are included and the results are given in figure 5(a). As seen in the figure, the position of the maximum occurs much below the barrier V_b which is around 99·4 MeV and with more number of channels included, the peak value of the polarization potential increases, while the position of the peak moves slightly to the left.

In the earlier studies [9], the $\langle l \rangle_m$ values derived from this schematic model which fits fusion cross-sections are compared with the $\langle l \rangle_{0d}$ values obtained from energy independent BPM with a constant barrier height V_b adjusted to explain fusion cross-sections at high energies. A general feature of this study is that the ratio of $\langle l \rangle_m / \langle l \rangle_{0d}$ shows a peak at around Coulomb barrier and falls to unity on either side. This enhancement is an indication that effects of channel couplings are maximum near the Coulomb barrier. This is in a way similar to the threshold anomaly seen in the optical potential which explains elastic scattering. This effect is not seen in the fusion cross-section data. However, these features are significant in the moments of the compound nucleus spin distributions.

Figure 5(b) shows the value of $\langle l \rangle_m / \langle l \rangle_{0d}$ as a function of energy with different polarization potentials as shown in figure 5(a). Eventhough, the maximum in the polarization potential is to the left of V_b, the ratio of the moments peak at around V_b. However, the height and the width of the ratio depend very much on the strength of the polarization potential ΔV_p. Figure 5(c) shows the plot of the height and width of the enhancement factor as a function of ΔV_p. In this figure, two additional data points are obtained considering the 2^+, 3^- and 4^+ states of either the target or the projectile. The observed correlation suggests that the height of this enhancement can be treated as a measure of the coupling strength and the width as a measure of the region over which the enhancement takes place. It is also evident from figure 5 that the polarization potential peaks left to the one-dimensional barrier height V_b, depend

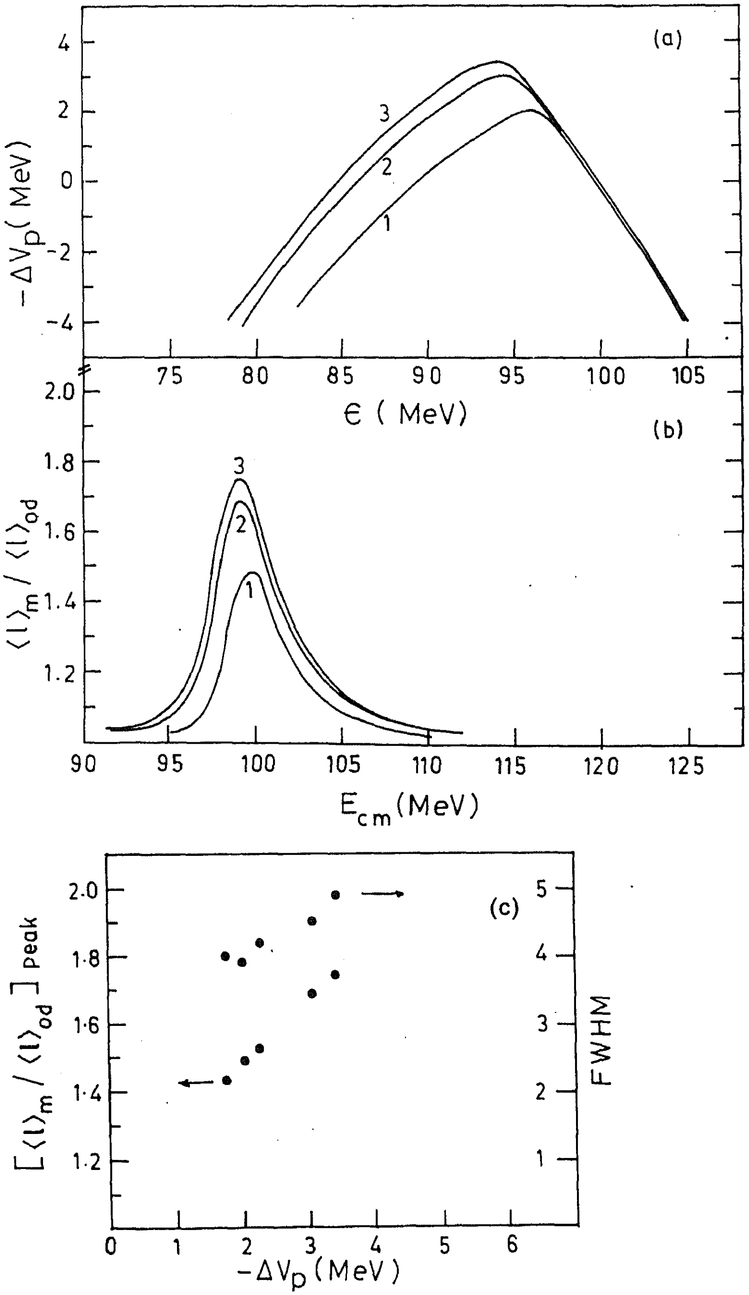

Figure 5(a). $(V_{\text{eff}} - V_b)$ versus ε for ^{58}Ni + ^{64}Ni system derived from CCFUS with different coupling schemes as described in the text **(b)** $\langle l \rangle_m / \langle l \rangle_{0d}$ versus E_{cm} for ^{58}Ni + ^{64}Ni system with same coupling scheme as figure 5(a). **(c)** The peak and the width of the ratio $\langle l \rangle_m / \langle l \rangle_{0d}$ as a function of ΔV_p for ^{58}Ni + ^{64}Ni system.

on the Q value of the channel couplings, while $\langle l \rangle_m / \langle l \rangle_{0d}$ peaks around V_b and this peak position does not depend significantly on the details of the channel couplings. However, the height and the width of the ratio depend strongly on the details of the channel coupling and are model-dependent. Figure 6(a) shows $\langle l\rangle_w/\langle l\rangle_{0d}$ ratio for $^{16}O + {}^{154}Sm$ system using Wong's model with three values of β_2 parameter. It can be inferred that the qualitative behaviour of enhancement for these two models (figures 5(b) and 6(a)) are same. In addition to $\langle l\rangle$, another physical quantity associated with fusion spin distribution is its width i.e. the second central moment of the distribution as given by $\Delta l^2 = \langle l\rangle^2 - \langle l\rangle^2$. The channel couplings broaden the fusion spin distribution and this effect can be seen in Δl as compared to its corresponding one-dimensional BPM result. It contains the information as to how many partial waves are effectively influenced by channel couplings. Figure 6b shows the plot of $\Delta l_w/\Delta l_{0d}$ as a function of E for the same values of V_b and β_2 parameter used in figure 6a. It is seen that, as the coupling effects are maximum around V_b, this ratio peaks around V_b. Thus, the channel coupling effects are best illustrated by the moments of the spin distribution. Figure 7 shows the plot of $\langle l\rangle_m/\langle l\rangle_{0d}$ as function of E with different value of V_b. As seen in this figure, the position of the peak also depends

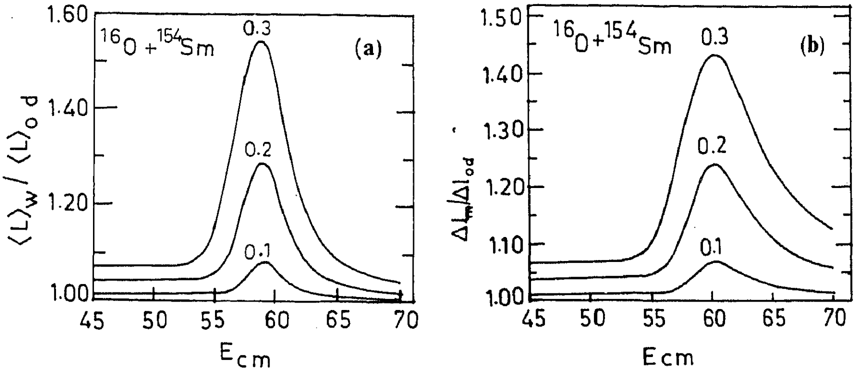

Figure 6(a). $\langle l\rangle_w/\langle l\rangle_{0d}$ versus E_{cm} for $^{16}O + {}^{154}Sm$ system where $\langle l\rangle_w$ has been obtained from Wong's model with three deformation parameter (β_2) as shown in figure, (**b**) $\Delta l_w/\Delta l_{0d}$ versus E_{cm} for $^{16}O + {}^{154}Sm$ system with three β_2 values.

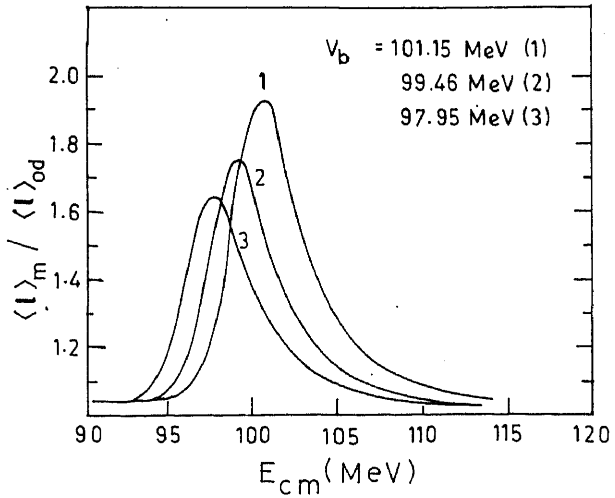

Figure 7. $\langle l\rangle_m/\langle l\rangle_{0d}$ versus E_{cm} for $^{58}Ni + {}^{64}Ni$ system with different one-dimensional barrier V_b as shown in figure.

strongly on V_b. However, in reality V_b is taken as one-dimensional barrier height which fits the high energy fusion cross-sections.

5. Summary

In conclusion, the dynamical effects of channel couplings can be incorporated in the optical model or in BPM through the one-channel effective potential which is both E and l dependent. This explicit E and l dependence of the effective potential has been expressed as a function of ε in both the cases. The observed E and l dependence of radial diffuseness parameter $a(E,l)$ in a recent optical model study is a natural consequence of the dependence of imaginary potential on ε parameter. It is also shown that in a BPM, the ε dependent barrier height can reproduce all the effects of channel couplings. The ratio of $\langle l\rangle_m$, obtained from the coupled channel, to $\langle l\rangle_{0d}$ shows a peak around the coulomb barrier and its correlation with the polarization potential has been studied in detail.

Acknowledgements

The authors are thankful to Dr S S Kapoor and Dr V S Ramamurthy for fruitful discussions.

References

[1] C Mahaux, H Ngo and G R Satchler, *Nucl. Phys.* **A449**, 354 (1986); **A456**, 134 (1986)
[2] V S Ramamurthy, A K Mohanty, S K Kataria and G Rangarajan, *Phys. Rev.* **C41**, 2702 (1990)
[3] C H Dasso, S Landowne and G Pollarolo, *Phys. Lett.* **B217**, 25 (1989)
[4] A K Mohanty, S V S Sastry, S K Kataria and V S Ramamurthy, *Phys. Rev. Lett.* **65**, 1096 (1990)
[5] J A Christley, M A Nagarajan and I J Thompson, *J. Phys.* **G17**, L-163 (1991)
[6] Lilley J S *et al*, *Phys. Lett.* **B151**, 181 (1985)
Fulton B R *et al*, *Phys. Lett.* **B162**, 55 (1985)
Baeza A *et al*, *Nucl. Phys.* **A419**, 412 (1984)
[7] J S Lilley, M A Nagarajan, D W Banes, B R Fulton and I T Thompson, *Nucl. Phys.* **A463**, 710 (1987)
[8] A K Mohanty *et al*, *Phys. Lett.* **B247**, 215 (1990)
[9] A K Mohanty, S V S Sastry, S K Kataria and V S Ramamurthy, *Phys. Rev.* **C46**, 2012 (1992)
[10] C H Dasso and S Landowne, *Comput. Phys. Commun.* **46**, 187 (1987)
[11] R A Broglia, C H Dasso, S L Landowne and G Pollarolo, *Phys. Lett.* **B133**, 34 (1985)
[12] M Beckerman *et al*, *Phys. Rev.* **C23**, 1581 (1981)

PRAMANA
— journal of
physics

© Printed in India

Vol. 41, No. 6,
December 1993
pp. 535–550

Collective bounce-off phenomenon in ^{139}La + Ag(Br) reaction at 1·1 A GeV energy

B SINGH, H S PALSANIA, V KUMAR, K B BHALLA and S LOKANATHAN
Department of Physics, University of Rajasthan, Jaipur 302 004, India

MS received 10 August 1992; revised 12 July 1993

Abstract. Out of a total statistics of 896 ^{139}La + Ag(Br) interactions, 128 interactions having multiplicity of target fragments $(Z \geqslant 1) \geqslant 8$ and projectile fragments $(Z \geqslant 2) \geqslant 4$ have been selected. They correspond to quasi-peripheral interactions. Azimuthal angle correlation between sources of target fragments (TFs) and projectile fragments (PFs) shows the existence of bounce-off effect. Using data of La + Ag(Br) and ^{84}Kr + Ag(Br) reactions it is shown that individual helium [$Z = 2$, PFs] and heavier fragment [$Z \geqslant 3$, PFs] show different emission characteristics. Further, a two prong correlation function $T(\Phi_{ij})$ plotted for heavier fragments and helium fragments separately, indicates the possibility of existence of different physical conditions. This observation is supported by the different momentum widths of helium fragments and heavier fragments. From the momentum width data of Kr + Ag(Br) reactions normalized density comes out to be $\approx 4{\cdot}7$. Using quasi-elastic kinematics for the bounce-off nuclei, the excitation energy has been computed from the experimental data of flow angles. The strength of bounce-off seems to decrease with the increase of excitation energy or temperature.

Keywords. Collective effects; Bounce-off; momentum-width; quasi elastic scattering kinematics; sqeeze-out; impact parameter; fragmentation; participant region; thermalised source.

PACS No. 25·70

1. Introduction

One of the main objectives of relativistic heavy ion physics is to investigate the equation of state of nuclear matter at abnormally high densities. No model independent method exists to know such densities. Manifestation of high density state in the form of collective flow may provide a way out because it can be detected experimentally.

In the process of compression, impact parameter and the energy of colliding nuclei play a crucial role in changing the density of the overlap region. This in turn affects the strength of the collective effects. About a decade ago the collective effects such as bounce-off at middle range impact parameters were taken up for detailed study. From a large number of preliminary experiments using both symmetric and non-symmetric systems of colliding nuclei such as (i) Ca + Ca at 400 A MeV (ii) Nb + Nb at 400 and 650 A MeV (iii) Au + Au at 150 to 800 A MeV due to Gustaffsson *et al* [1] and Ritter *et al* [2] (iv) U + U at 900 A MeV due to Beavis *et al* [3] (v) Ar + Pb at 400 and 800 A MeV due to Beavis *et al* [3] and Renfordt *et al* [4] (vi) Ar + KCl at 1800 A MeV due to Sandoval *et al* [5] (vii) C + Ag and Ne + U at 393 A MeV energy due to Baumgardt *et al* [6] (viii) U + Ag(Br) at 850 A MeV due to Heckmann *et al* [7] (ix) Kr + Ag(Br) at 1400 A MeV due to Arora *et al* [8] it was concluded that the flow angle depends on both energy and mass of the colliding systems but nothing in specific could be inferred about density of the compressed matter.

On the theoretical side, models such as hydro-dynamical due to Scheid *et al* [9], Baumgardt *et al* [6] and Amsden *et al* [10] and modified cascade model due to Cugnon *et al* [11], Braun and Fraenkel [11] and participant-spectator spallation model due to Gosset *et al* [12] have greatly helped in understanding the general behaviour of the relativistic collisions and the mechanism of the flow effects. Predictions of quantum statistical model due to Stocker *et al* [13] reach closer to the main objective of knowing the equation of state. One of such predictions is that the low temperature and high density conditions are the most favourable conditions for a fragment to grow massive. Although it remains to be tested in a large statistics experiment it seems to be useful for knowing the conditions of the source of fragments.

The phenomenon of bounce-off of nuclei contradicts with the 'on the spot spallation' of colliding nuclei into spectators and participants therefore the spectator-participant model cannot be invoked at the moment of collision. In a relativistic collision, high amount of direct compression takes place in the overlap region and as a result squeeze out of the nuclear matter starts through the non-overlap region. This builds up pressure in this region. As a result of pressure difference in the overlap and non-overlap regions the two regions are separated after a while. The two chunks of nuclear matter are fragmented with distinction in the physical conditions of the two regions. In our earlier short publication due to Palsania *et al* [14] we have identified two physically distinct regions of the projectile nucleus one predominantly decaying into small fragments like helium and the other into big fragments (clubbed into $Z \geqslant 3$ bin) using the La + Ag(Br) reaction data.

In this paper a detailed comparison of Kr + Ag(Br) and La + Ag(Br) reactions has been presented which helps in drawing inferences on emission characteristics. Also, an attempt has been made for the experimental estimation of the density of the most compressed zone using the data of nearly symmetric colliding system i.e. Kr + Ag(Br) reactions.

2. Details of exposure and method of measurements

A stack of G-5 emulsions was exposed to ^{139}La-beam of energy $\approx 1{\cdot}1$ GeV/nucleon at Berkeley Bevatron in April 1983 and in all 896 interactions of La with emulsion nuclei were collected by line scan method. For the present study we have selected 128 interactions having $N_{\mathrm{TF}} \geqslant 8$ and $N_{\mathrm{PF}} \geqslant 4$, where N_{TF} and N_{PF} are the number of target fragments ($Z \geqslant 1$) and projectile fragments ($Z \geqslant 2$) respectively. These interactions lie within 3 cm but at different lengths from the entry-edge. Therefore, the projectile energy at the point of interaction will be different for all the interactions. The average energy of interacting beam particles for the selected interactions is $\approx 0{\cdot}8$ A GeV. The selected interactions lie within middle layers of emulsion. To avoid effect of emulsion distortions on measurements interactions within 20 μm layer of emulsion from air and glass surface are avoided. It may also be mentioned here that this category of interactions corresponds to neither central nor peripheral interactions as the surviving average number of projectile fragments (PFs) is $6{\cdot}80 \pm 0{\cdot}18$ and target fragments (TFs) is $21{\cdot}10 \pm 0{\cdot}70$. Angle measurements of all PFs and TFs associated with an interaction are done by following the particle track up to a sufficiently long distance and measuring coordinates (X, Y, Z) at more than two positions. Using dip and projected angles of each track, components of unit vector of each track ($\hat{r}_X, \hat{r}_Y, \hat{r}_Z$) are evaluated to give the principal unit vector of emission for PFs ($\hat{r}_{\mathrm{PF}}$) and TFs ($\hat{r}_{\mathrm{TF}}$) separately. Either from the number of PFs or TFs the unit principal vector can be written as

$$\hat{r} = \frac{\left\{\sum^{n} r_X\right\}\hat{i} + \left\{\sum^{n} r_Y\right\}\hat{j} + \left\{\sum^{n} r_Z\right\}\hat{k}}{\left[\left\{\sum^{n} r_X\right\}^2 + \left\{\sum^{n} r_Y\right\}^2 + \left\{\sum^{n} r_Z\right\}^2\right]^{1/2}} \tag{1}$$

$$= R_X\hat{i} + R_Y\hat{j} + R_Z\hat{k} \tag{2}$$

where $n = N_{\mathrm{PF}}$ when unit principal vector $\hat{r}_{PF}$ is computed and $n = N_{\mathrm{TF}}$ when $\hat{r}_{\mathrm{TF}}$ is computed. Thus, for an event two principal vectors are determined. These principal vectors provide direction of flow of nuclear matter related to projectile and target respectively to a reasonable accuracy because of the following reasons i) all fragments are likely to have identical to beam momentum as on fragmentation they acquire a small $P_{\mathrm{T}} \approx 70$–80 MeV c/n only. Similarly amongst the TFs most of them are evaporated fragments and ii) a large number of fragments are used to determine the principal vectors. The average number of them is indicated earlier.

3. Experimental results and discussion

3.1 *Bounce-off effect*

Distributions of the flow angle of the PFs and TFs deduced from their respective principal vectors on event-by-event basis for La + Ag(Br) reaction have been presented in our earlier paper [14] the average values of the flow angles of PFs ($= \bar{\theta}_{\mathrm{PF}}$) and TFs($= \bar{\theta}_{\mathrm{TF}}$) in La + Ag(Br) reaction at 0·8 A GeV, Kr + Ag(Br) at 1·27 A GeV, ^{238}U + Ag(Br) at 0·85 A GeV and ^{56}Fe + Ag(Br) at 1·88 A GeV [15] have been given in table 1 for comparison. Collective flow of nuclear matter of relativistic projectile at such a large angle ($\approx 3°$) shows the existence of a strong nuclear collective effect. Contribution of coulomb scattering to the flow angle has been shown [7, 8] to be negligibly small. From the data of $\bar{\theta}_{\mathrm{PF}}$ given in table 1 it is clear that the flow angle decreases with increasing projectile energy. It can be pointed out that $\bar{\theta}_{\mathrm{TF}}$ has been evaluated from an average of 21 charged target fragments and existence of flow angle as large as $\approx 31°$ cannot have large spurious error due to limited number of particles. Thus, both $\bar{\theta}_{\mathrm{PF}}$ and $\bar{\theta}_{\mathrm{TF}}$ can be treated as the clear indications of collective flow.

To investigate the correlated scattering of colliding nuclei, the difference of azimuthal angles $\Delta\Phi = |\Phi_{\mathrm{TF}} - \Phi_{\mathrm{PF}}|$ of the principal vectors of TFs and PFs for La + Ag(Br) interactions has been analysed. In figure 1 results of the Monte-Carlo, corresponding to no correlation situation obtained by random generation of the azimuthal angle of each fragment, have also been displayed along with experimental results of $\Delta\Phi$. The numerical values of $\overline{\Delta\Phi}$ obtained from the present data have been compared with those of Kr + Ag(Br), U + Ag(Br) and Fe + Ag(Br) in table 1. It may be mentioned that due to the increase of number of events of Kr + Ag(Br) reactions some of the results presented here have changed slightly as compared to that given in [8]. The strength of back-to-back correlation may be defined by the ratio, R i.e. the ratio of number of events with $\Delta\Phi \geqslant 90°$ to $\Delta\Phi < 90°$. In table 1 R has been given for different colliding systems and it may be noted that R is very high (≈ 24) in U + Ag(Br) reaction as compared to $\approx 2{\cdot}2$ for La + Ag(Br) reaction. It may be inferred from the

Table 1. Comparison of the averages of the flow angle of PFs ($\bar{\theta}_{PF}$) and TFs ($\bar{\theta}_{TF}$); $\overline{\Delta\Phi}$; R; F/B-ratio of TFs; excitation energy E^*.

Property	La + Ag(Br)[14] at 0·8 A GeV	Kr + Ag(Br)[8] at 1·27 A GeV	U + Ag(Br)[7] at 0·85 A GeV	Fe + Ag(Br)[15] at 1·88 A GeV
$\bar{\theta}_{PF}(Z \geqslant 2)$	$2{\cdot}87 \pm 0{\cdot}24^\circ$	$2{\cdot}03 \pm 0{\cdot}14^\circ$	$2{\cdot}35 \pm 0{\cdot}20^\circ$	—
$\bar{\theta}_{TF}(Z \geqslant 1)$	$30{\cdot}39 \pm 1{\cdot}66^\circ$ $(N_{TF} \geqslant 8, N_{PF} \geqslant 4)$	$32{\cdot}86 \pm 1{\cdot}29^\circ$ $(N_{TF} \geqslant 8, N_{PF} \geqslant 4)$	$47{\cdot}10 \pm 2{\cdot}10^\circ$ $(N_{TF} \geqslant 10, N_{PF} \geqslant 8)$	$43{\cdot}20 \pm 1{\cdot}80^\circ$ $(N_{TF} \geqslant 9)$
$\overline{\Delta\Phi} = \langle \lvert \Phi_{TF} - \Phi_{PF} \rvert \rangle$	$114{\cdot}84 \pm 4{\cdot}51^\circ$	$107{\cdot}24 \pm 4{\cdot}32^\circ$	$146{\cdot}00 \pm 4{\cdot}00^\circ$	$101{\cdot}00 \pm 1{\cdot}80^\circ$
R	$2{\cdot}20 \pm 0{\cdot}34$	$1{\cdot}74 \pm 0{\cdot}24$	$23{\cdot}5 \pm 3{\cdot}63$	—
F/B-ratio Obs.	$5{\cdot}42 \pm 0{\cdot}22$	$4{\cdot}74 \pm 0{\cdot}18$	$5{\cdot}94 \pm 0{\cdot}51$	—
Corr.	$4{\cdot}88 \pm 0{\cdot}20$	$4{\cdot}84 \pm 0{\cdot}04$	$5{\cdot}28 \pm 0{\cdot}46$	—
E^*	7·13 GeV	4·90 GeV	5·80 GeV	—

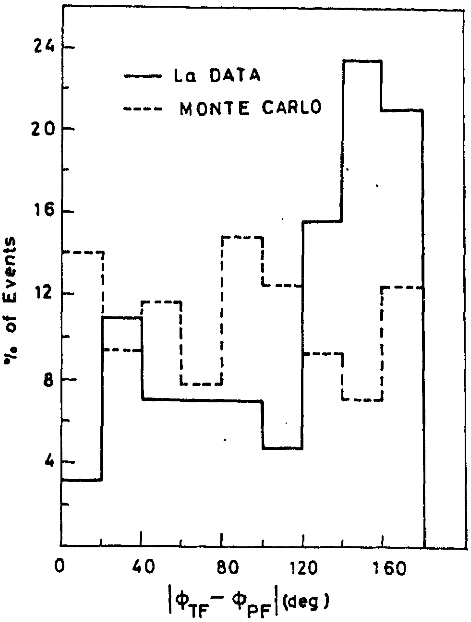

Figure 1. A plot of the difference of azimuthal angles of principal vector of TFs and PFs on event-by-event basis. The dashed line shows no correlation Monte-Carlo (MC) of La + Ag(Br) collision. The MC corresponds to $\overline{\Delta\Phi}(\mathrm{MC}) = 87{\cdot}81 \pm 4{\cdot}67°$ and dispersion $D = 52{\cdot}28 \pm 3{\cdot}27°$.

data that the strength of back-to-back correlation in the azimuthal plane shows dependence on the mass of the colliding system.

3.2 *Emission characteristics*

To study the emission characteristics of bounce-off nuclei, projections of angle θ' (taken separately for helium and heavier fragments) onto the plane containing the principal vector of the PFs have been considered. Here θ' is the angle of a fragment vector with respect to its principal vector. The width of the $dN/d\theta'$ (proj.) distribution corresponds to the momentum width of nucleons in the fragmenting source. Frequency plots of θ'_{He}(proj.) for helium fragments ($Z = 2$) and θ'_{F}(proj.) for $Z \geqslant 3$ projectile-fragments for La + Ag(Br) reactions have been presented in [14]. Similar plots have been made for Kr + Ag(Br) data. Characteristics of these distributions such as dispersion and peakness have been given in table 2 for both the reactions for comparison. It may be noted that there exists difference in the values of dispersion and peakness for helium fragments and heavier fragments in both the reactions. Both helium and heavier fragments show peakness much higher than 3, that is the peakness of a standard gaussian distribution, in both cases of reactions. It may therefore, be inferred that majority of helium as well as heavier fragments are emitted from two different zones or sources of different physical conditions. The values of momentum-width given in table 2 have been computed using the initial beam momentum and the dispersion of θ'(proj.) distribution as given in the first row of table 2. Data of peripheral interactions of Kr + Ag(Br) reactions ($N_h = 0, 1$ events) are given in the last column of table for comparison with the bounce-off events. In general, it can be inferred that

Table 2. Dispersion and peakness of θ'_{He}(proj.) and θ'_F(proj.) distributions for La + Ag(Br) and Kr + Ag(Br) reactions. The momentum width has been calculated using the beam momentum and dispersion data.

Property	La + Ag(Br) at 0·8 A GeV (All b.o. events)		Kr + Ag(Br) at 1·27 A GeV (All b.o. events)		Kr + Ag(Br) at 1·27 A GeV (Peripheral events)	
	Helium fragments	Heavier fragments	Helium fragments	Heavier fragments	Helium fragments	Heavier fragments
Dispersion	2·99 ± 0·09°	2·52 ± 0·11°	2·31 ± 0·07°	2·27 ± 0·1°	1·39 ± 0·1°	1·66 ± 0·2°
Peakness	4·32	7·76	5·36	6·01	3·26	8·53
Momentum width (MeV/c/n)	76·13 ± 2·29	64·18 ± 2·44	79·24 ± 2·44	77·87 ± 3·48	46·67 ± 3·48	56·93 ± 7·31

heavier fragments ($Z \geqslant 3$) have much higher values of peakness compared to that of helium fragments showing the lack of degree of randomness. It may also be said that after collision a big chunk of the nuclear matter even on fragmentation has high coherence. In bounce-off events, widths of helium fragments are in general higher than that of heavy fragments. This is probably because of high modification of original Fermi momentum of a highly compressed part of the projectile nucleus during the collision. Thus, we can make use of the ratio of momentum-widths (σ's) of He-fragments in bounce-off events to that in peripheral events to find out the ratio of densities (ρ) (see Appendix)

$$\frac{\rho_{\text{b.o.}}}{\rho_{\text{Peri}}} = \frac{(\sigma_{\text{b.o.}})^3}{(\sigma_{\text{Peri}})^3}. \tag{3}$$

Here, we assume that in peripheral collision ($N_h = 0, 1$ events) compression of the projectile is insignificant compared to the bounce-off mode. For nearly symmetric collision i.e. Kr + Ag(Br) reactions $\rho_{\text{b.o.}}/\rho_{\text{Peri}} = (79/47)^3 = 4{\cdot}7$. This agrees well with the ratio $\approx 4{\cdot}5$ for the krypton reaction obtained from the relation by Stocker *et al* [16, 17].

Assuming that the target after the bounce-off, gets only a small negligible momentum it is easy to study the forward to backward ratio of the target fragments from the $\cos\theta'_{\text{TF}}$ plots. Here θ'_{TF} is the space-angle of a target fragment with respect to the principal vector of TFs. In figure 2 plots between the logarithm of frequence and $\cos\theta'_{\text{TF}}$ have been given for La + Ag(Br) and Kr + Ag(Br) reactions. The slope of the straight line ($= b$) fitted to the data gives the F/B-ratio [$F/B = \exp(b)$] following the non-relativistic Maxwell–Boltzmann distribution of momentum of nucleons in the target nucleus [7]. In table 1 values of F/B-ratio have been given for La + Ag(Br), Kr + Ag(Br) and U + Ag(Br) reactions. In all the cases F/B-ratio comes out to be much greater than unity confirming the existence of flow of target matter. The corrected value of the F/B-ratio for the two reactions is also given in table. As pointed out by Heckmann *et al* [7] the correction factor $f = [(F/B)_{\text{obs.}}/(F/B)_{\text{MC}}]$ has been estimated by finding out $(F/B)_{\text{Corr.}}$ by Monte-carlo (MC) simulation of 128 events assuming

$$\frac{\mathrm{d}N}{\mathrm{d}(\cos\theta')} \propto \exp(b\cos\theta')$$

distribution with $\theta' = (R_X \times r_x) + (R_Y \times r_y) + (R_Z \times r_z)$. Here R_X, R_Y and R_Z are the three components of empirically determined unit principal vector $\hat{r}_{\text{TF}}$. The fragment vectors r_x, r_y and r_z have been generated randomly and to encompass the range of $(F/B)_{\text{obs}}$ the value of b has also been chosen randomly so that F/B falls in between 4·25 and 7·0. The combined result of 20 times Monte-carlo of each event gives $(F/B)_{\text{MC}} = 4{\cdot}88 \pm 0{\cdot}06$. Thus the corrected value of F/B-ratio can be given by

$$(F/B)_{\text{Corr}} = \left(\frac{1}{f}\right)(F/B)_{\text{Obs}} = 4{\cdot}88 \pm 0{\cdot}20.$$

In figure 2 the lines corresponding to $(F/B)_{\text{Corr}}$ have also been shown for both the reactions. In particular for La + Ag(Br) reaction the slope of the line (MC), $b = 1{\cdot}585$.

In has been shown [7, 8, 14] that the bounce-off nuclei follow the quasi-elastic scattering (QES) kinematics wherein it is assumed that both projectile and target nuclei share equal amount of excitation energy (E^*). In figure 3a $\bar{\theta}_{PF}$ versus $\bar{\theta}_{TF}$ plots for La + Ag(Br) and Kr + Ag(Br) reactions have been given. The curves correspond to the QES at a particular value of E^* fitted to the experimental data of $\bar{\theta}_{PF}$ and $\bar{\theta}_{TF}$ of the reaction. Values of E^* so obtained for La + Ag(Br), Kr + Ag(Br) and U + Ag(Br) reactions are given in table 1. It may be inferred that excitation energies, although different in different reactions, are very high in all the three cases. The difference in E^* values may arise because of different ranges of impact parameters in the three reactions as selection of events at required impact parameter is difficult in emulsion experiments.

In the event of bounce-off of colliding nuclei, at different impact parameters the size of overlap region (so called participant region) will increase with the decrease of impact parameter. In the relatively more compressed overlap region the emission characteristics are likely to change with the conditions of compression. We know that mostly the grey particles ($\bar{N}_g$) are the recoiled target protons with velocity $\beta = 0{\cdot}3$

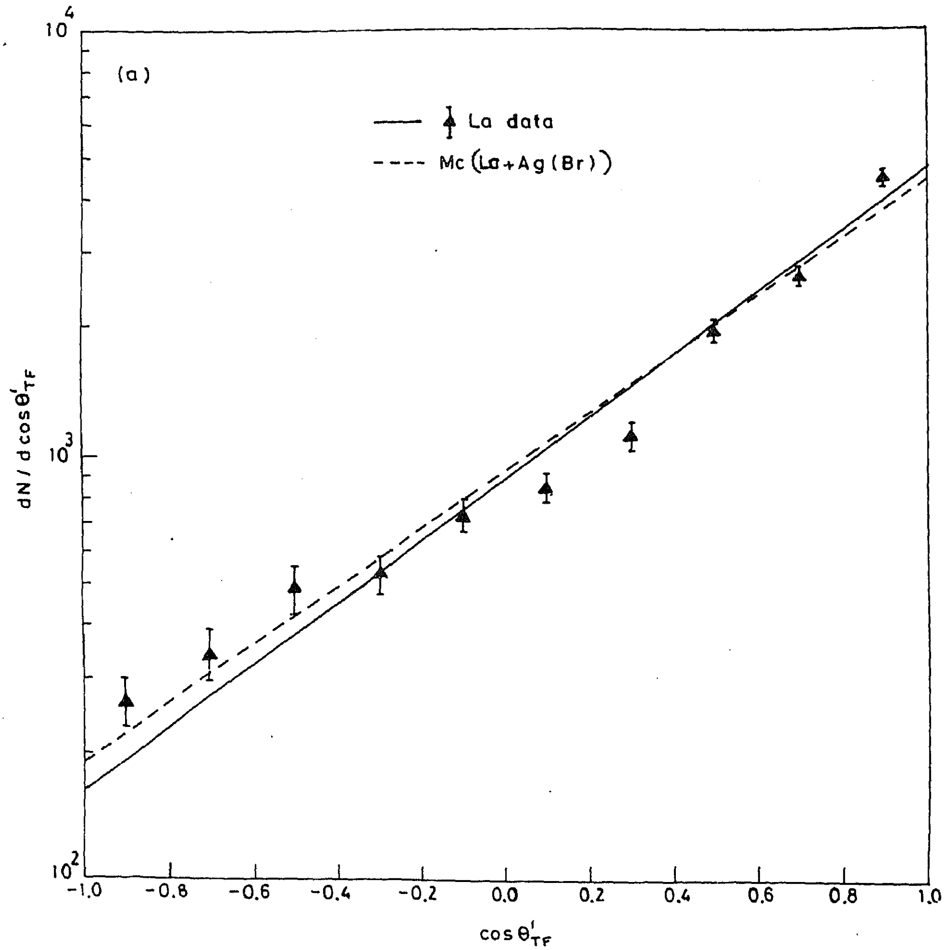

Figure 2a. $\ln(\mathrm{d}N/\mathrm{d}\cos\theta'_{TF})$ versus $\cos\theta'_{TF}$ plot of the target fragments for La + Ag(Br) (▲) reaction. The slope of line through data is to $b = \ln(F/B)_{\mathrm{Obs}} = 1{\cdot}69 \pm 0{\cdot}04$. Dashed line corresponds to Monte-Carlo calculations with $b = 1{\cdot}585$ which reproduces the experimental data.

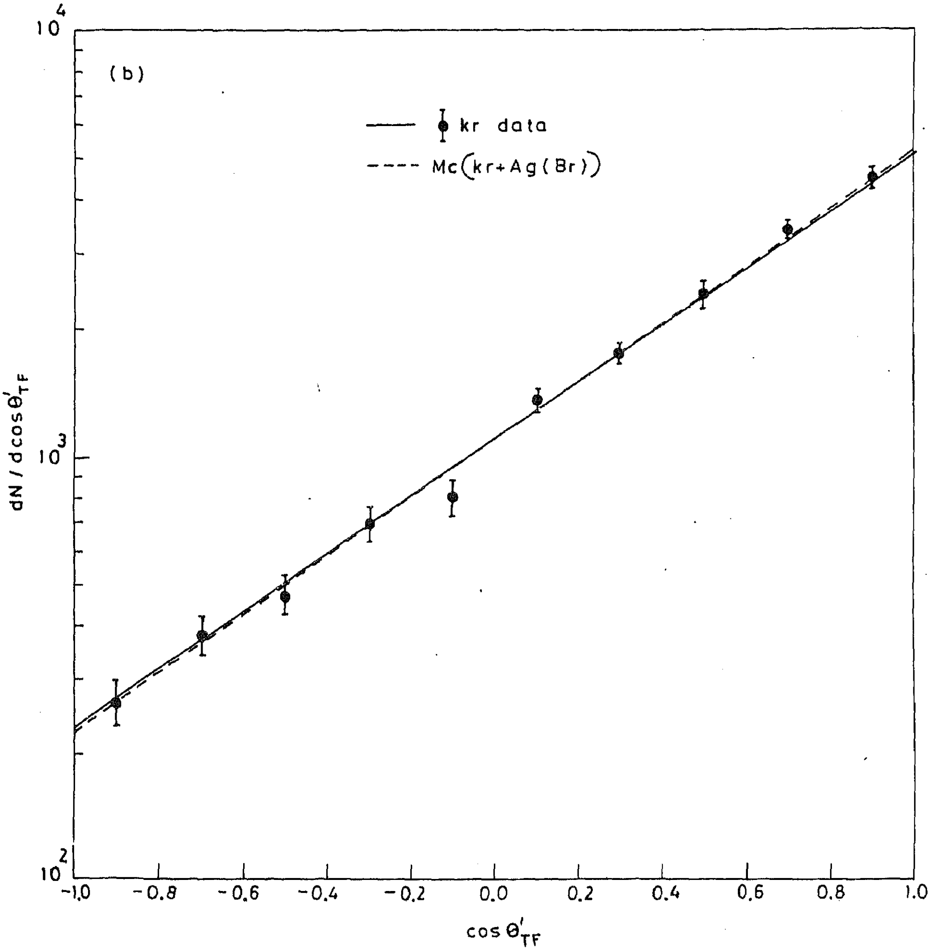

Figure 2b. $\ln(dN/d\cos\theta'_{TF})$ versus $\cos\theta'_{TF}$ plot of the target fragments for Kr + Ag(Br) (●) reaction. The slope of the line through data is to $b = 1{\cdot}55 \pm 0{\cdot}04$ and the dashed line (MC) corresponds to $b = 1{\cdot}578$.

to 0·7 and their number increases with the decrease of impact parameter. In a way, qualitatively speaking, their number represents the size of the participant region. In an attempt to study the effect of density and temperature on collective bounce-off effect, we divide the data of 68 La + Ag(Br) interactions (measurements of these interactions are doubly checked) into the following three categories in order of decreasing size of participant or increasing size of spectator chunk,

(i) $1 \leqslant N_{He} \leqslant 3[\bar{N}_g = 13{\cdot}55 \pm 1{\cdot}80$ or smaller projectile spectator]
(ii) $4 \leqslant N_{He} \leqslant 6[\bar{N}_g = 10{\cdot}94 \pm 0{\cdot}80$ or bigger projectile spectator]
(iii) $N_{He} \geqslant 7[\bar{N}_g = 8{\cdot}86 \pm 1{\cdot}10$ or biggest projectile spectator]

Various characteristics of events such as their number N, average multiplicities of helium and heavier fragments, greys, total target fragments, average space angle of helium fragments, PFs and TFs, azimuthal difference $\overline{\Delta\Phi}$, strength of back-to-back correlation, F/B-ratio of TFs and the excitation energy related to the above three

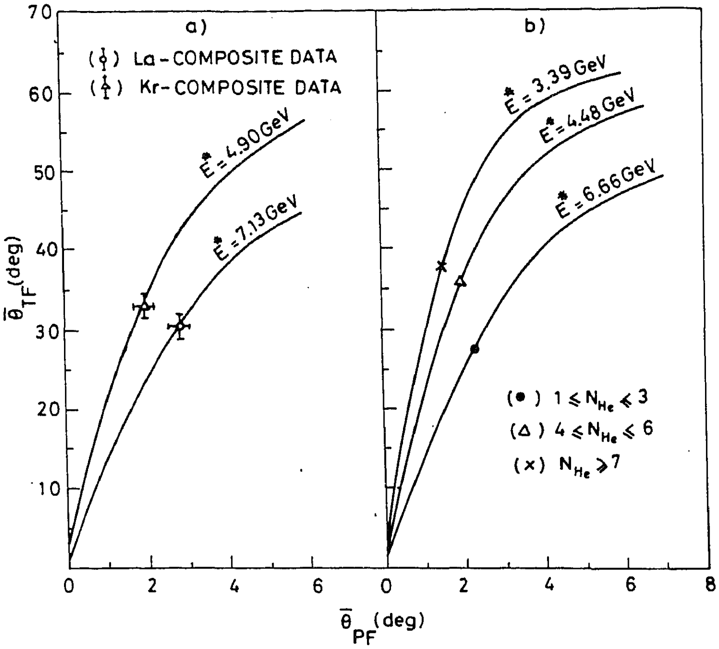

Figure 3. Plots between angles $\bar{\theta}_{PF}$ and $\bar{\theta}_{TF}$ for the (**a**) composite data of La + Ag(Br) and Kr + Ag(Br) reactions separately and for (**b**) three categories $1 \leqslant N_{He} \leqslant 3$, $4 \leqslant N_{He} \leqslant 6$ and $N_{He} \geqslant 7$ of the La + Ag(Br) data. The curves in the figure a) and b) correspond to the quasi elastic scattering (QES) kinematics.

Table 3. Data of various characteristics of events belonging to three categories in the case of La + Ag(Br) collision. The $\bar{\theta}_{He}$ is the space angle of helium fragments with respect to beam direction. F/B-ratio means Forward to Backward ratio of TFs ($Z \geqslant 1$) with respect to direction of their principal vector.

Property	$1 \leqslant N_{He} \leqslant 3$	$4 \leqslant N_{He} \leqslant 6$	$N_{He} \geqslant 7$
N^* (Events)	17	36	14
$\bar{N}_{He}$	2.71 ± 0.66	4.92 ± 0.82	8.00 ± 2.14
$\bar{N}_F$	2.06 ± 0.50	1.97 ± 0.33	1.36 ± 0.36
$\bar{N}_F/\bar{N}_{He}$	0.76	0.40	0.17
$\bar{N}_g$	13.55 ± 1.80	10.94 ± 0.80	8.86 ± 1.10
$\bar{N}_{TF}$	23.47 ± 5.70	22.97 ± 3.83	20.29 ± 5.42
$\bar{\theta}_{He}$	$4.31 \pm 0.64°$	$4.04 \pm 0.30°$	$3.41 \pm 0.32°$
$\bar{\theta}_{PF}$	$2.24 \pm 0.54°$	$1.97 \pm 0.33°$	$1.50 \pm 0.40°$
$\bar{\theta}_{TF}$	$27.35 \pm 6.63°$	$36.11 \pm 6.02°$	$38.27 \pm 10.23°$
$\overline{\Delta\Phi} = \langle \lvert \Phi_{TF} - \Phi_{PF} \rvert \rangle$	$119.80 \pm 11.80°$	$125.90 \pm 8.01°$	$133.70 \pm 13.06°$
R	3.25 ± 0.85	3.00 ± 0.65	6.00 ± 1.58
F/B-ratio	5.76 ± 0.63	5.37 ± 0.41	4.69 ± 0.58
E^*	6.66 GeV	4.48 GeV	3.39 GeV

*Out of 68 events, one is with $N_{He} = 0$.

categories are given in tables 3 and 4. The following observations can be made from the data,

(a) that the events of category (i) show an enhanced average number of fragments ($Z \geqslant 3$), $\bar{N}_F$ than the events in categories (ii) and (iii). It may be mentioned that in this experiment projectile fragments with $Z = 1$ have not been identified hence not included in the study. The number of such fragments would be much larger in category (i) compared to the other two categories.

(b) The average values of $\bar{\theta}_{PF}$ and $\bar{\theta}_{TF}$ corresponding to principal vector of events show significant difference in the three categories. For example, $\bar{\theta}_{PF}$ being larger in category (i) implies larger transverse momentum of the PFs. In a scattering, transverse momentum of projectile source is balanced by the corresponding recoil of target at $\bar{\theta}_{TF}$ angle. This means that the three momentum of the target should be higher in events of category (i) than in categories (ii) and (iii). Using the experimental value of $\bar{\theta}_{TF}$ given in table 3, P_{recoil} comes out to be 22·11, 17·24 and 16·4 GeV/c in categories (i), (ii) and (iii) respectively. In addition, it also indicates that the size of overlap region is biggest in category (i) and smallest in category (iii) as assumed earlier. Calculating the excitation energy E^* from the data of $\bar{\theta}_{PF}$ and $\bar{\theta}_{TF}$, one sees a remarkable difference i.e. $E^* \approx 6{\cdot}66$ GeV for category (i), 4·48 GeV for category (ii) and 3·39 GeV for category (iii). For comparison, figure 3b gives the plots between $\bar{\theta}_{PF}$ and $\bar{\theta}_{TF}$ for the three categories of events, deduced from QES kinematics alongwith the experimental data. On the other hand back-to-back correlation of colliding nuclei has also been studied for the events of three categories and the values of $\overline{\Delta\Phi}$ and R have been calculated from the experimental data. The values of $\overline{\Delta\Phi}$ and R come out to be 119·8° and 3·25 for category (i), 125·9° and 3·0 for category (ii) and 133·7° and 6·0 for category (iii) respectively. Events corresponding to category (iii) exhibit the strongest bounce-off behavior and on reduction in the impact parameter in categories (ii) and (iii) there is significant reduction in the effect. Difference in the values of E^* for the three categories arises because of varying potential energy due to more compression and rescattering at different impact parameters than at large impact parameters.

(c) From the data of momentum width given in table 4 it is evident that the width in helium PFs is in general higher than that of $Z \geqslant 3$ PFs and there is a gradual enhancement in the width when we go from large impact parameter collision (i.e. category (iii)) to smaller impact parameter collision i.e. category (i). Intuitively, this supports the relationship between σ^2 and $\langle P^2 \rangle$ and hence between density and width deduced in Appendix.

3.3 *Azimuthal correlation between alphas and fragments*

Two particles close in space, time and momentum are expected to be correlated. The correlation between heavier ($Z \geqslant 3$) and helium fragments can be studied to some extent following the method given by Koonin [18]. The following simplified two prong azimuthal angle correlation function given by Jakobsson [19] is generally used for this purpose,

$$C(\Phi_{ij}) = 2T(\Phi_{ij}) - \langle n \rangle^2/2\pi \tag{4}$$

where $T(\Phi_{ij}) = (\pi/N)\mathrm{d}N/\mathrm{d}\Phi_{ij}; \Phi_{ij} = |\Phi_i - \Phi_j|$ and $\langle n \rangle$ is the mean multiplicity of prongs used for the purpose of correlation. Φ_i and Φ_j are the azimuthal angles of particle i and j respectively. N is the total number of pairs of two prongs. The relation

Table 4. Data of various characteristics such as dispersion, peakness and momentum width of θ'_{He}(proj) and θ'_{F}(proj) distributions of events belonging to three categories of La + Ag(Br) reaction. The momentum width has been calculated using the beam momentum and dispersion data.

	$1 \leqslant N_{\mathrm{He}} \leqslant 3$		$4 \leqslant N_{\mathrm{He}} \leqslant 6$		$N_{\mathrm{He}} \geqslant 7$	
Property	Helium	Frag.'s	Helium	Frag.'s	Helium	Frag.'s
Dispersion	$2{\cdot}96 \pm 0{\cdot}31°$	$2{\cdot}31 \pm 0{\cdot}27°$	$2{\cdot}77 \pm 0{\cdot}18°$	$2{\cdot}01 \pm 0{\cdot}17°$	$2{\cdot}39 \pm 0{\cdot}16°$	$1{\cdot}09 \pm 0{\cdot}18°$
Peakness	3·37	6·39	3·61	6·44	3·11	3·67
Momentum width (MeV/c/n)	$75{\cdot}37 \pm 7{\cdot}9$	$58{\cdot}83 \pm 6{\cdot}9$	$70{\cdot}53 \pm 4{\cdot}6$	$51{\cdot}19 \pm 4{\cdot}3$	$60{\cdot}87 \pm 4{\cdot}1$	$27{\cdot}76 \pm 4{\cdot}6$

*Out of 68 events one is with $N_{\mathrm{He}} = 0$.

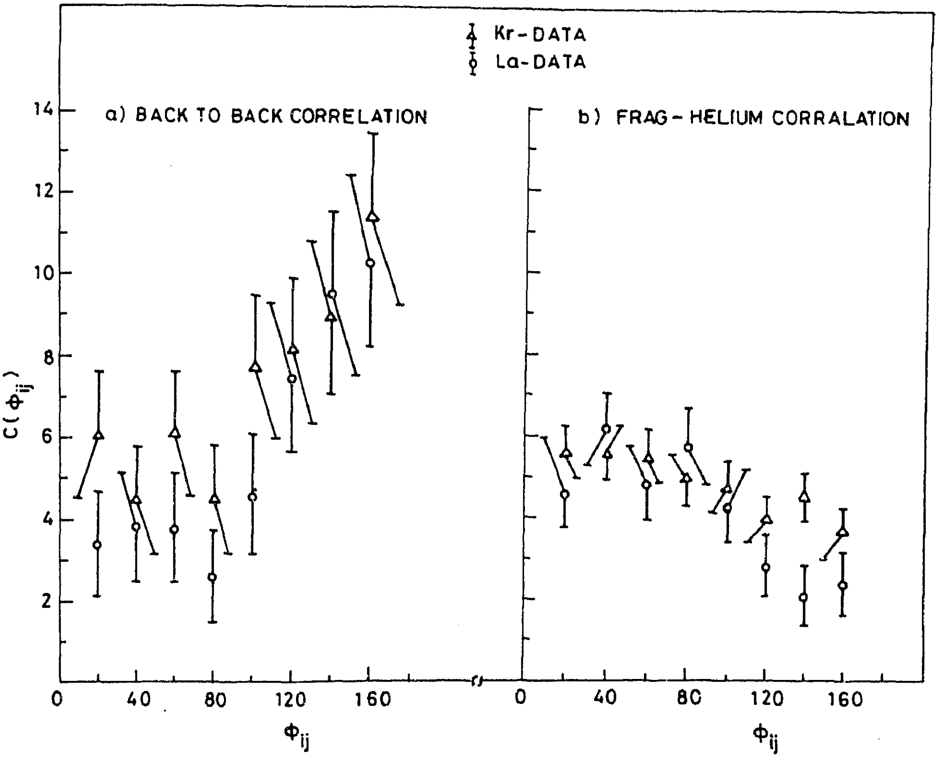

Figure 4. (**a**) Azimuthal angle correlation function $C(\Phi_{ij})$ plotted for bounce-off projectile and target nuclei using data of their principal vectors and (**b**) same two prong correlation function in between helium and heavier fragments ($Z \geqslant 3$) emitted from the bounce-off projectile.

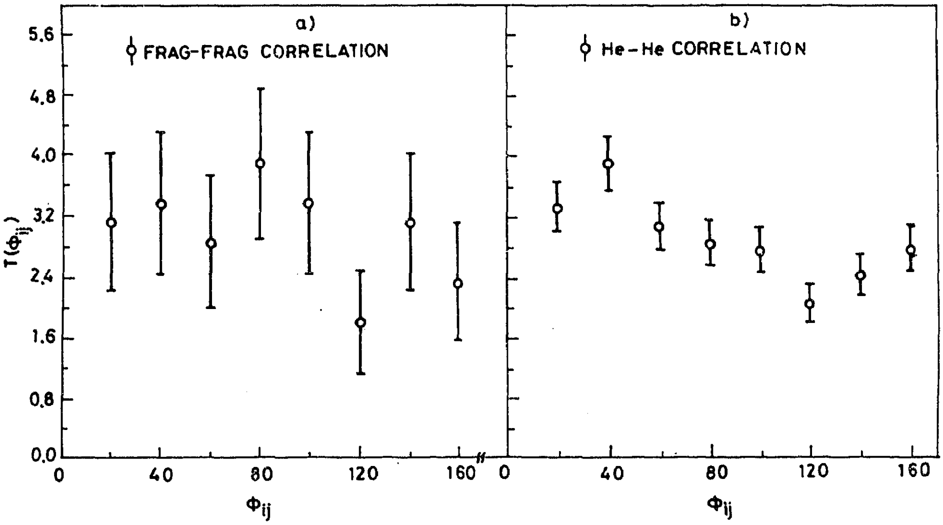

Figure 5. Azimuthal angle correlation function $T(\Phi_{ij})$ versus Φ_{ij} plot for (**a**) fragment–fragment and (**b**) helium-helium in the case of bounce-off events of La + Ag(Br) reaction.

was originally used for the study of proton-proton correlation. Before making its use for helium, heavier fragment correlation we have tested it for back-to-back correlation of La and Kr projectiles on Ag(Br) target. The results are given in figure 4a for both the reactions. The strong back-to-back correlation between projectile and target nuclei as seen earlier in figure 1 is evident from the correlation function $C(\Phi_{ij})$ also. Further, in figure 4b function $C(\Phi_{ij})$ has been plotted for fragment $(Z \geqslant 3)$—helium correlation for the two reactions. The data show a depression beyond $\Phi_{ij} > 80°$. It may be inferred that the heavier and helium fragments are correlated at small Φ_{ij} values. When both were emitted from one thermalised source then they were uncorrelated like the evaporated protons from a fire-ball.

In figures 5a and b, $T(\Phi_{ij})$ versus Φ_{ij} plots have been made for fragment-fragment and helium-helium pairs respectively. It may be seen from the figure that frag-frag correlation is almost absent except at $\Phi_{ij} \approx 90°$ and the source of fragments seems to behave like a fire ball. The abnormal peak at $\Phi_{ij} = 90°$ may be due to the squeeze out. There is a clear existence of helium-helium correlation at small Φ_{ij}.

4. Conclusions

(i) From the data of projected angle distribution given in table 2 for helium and heavier fragments $(Z \geqslant 3)$ separately for the two reactions it is clear that there are significant differences in two categories of fragments. The difference is more in La + Ag(Br) than Kr + Ag(Br) reaction. Data corresponding to helium fragments are closer to the Gaussian distribution as compared to the data of heavier fragments. This result indicates that at some stage of fragmentation, statistically speaking, there might be two chunks of nucleus with different physical conditions. One gives rise predominantly to light fragments like helium and other to heavier fragments. From the study of fragment-fragment and helium-helium correlation function plotted in figures 5a and b respectively the difference becomes more clear. From the data of $\bar{N}_{\mathrm{He}}$ given in table 3 and the momentum widths given in table 4, it can be pointed out that momentum width increases with decrease of helium multiplicity-an effect seen in case of 200 A GeV O^{16} + Em collision by Adamovich *et al* [20]. This may be because of the emission of helium fragments from a relatively more compressed part of nucleus on reduction of the impact parameter. Based on this we have been able to show that average density of the compressed part is $\approx 4{\cdot}7$ times that of the uncompressed nucleus.

(ii) From the result given in § 3·2, regarding the three categories of events it is noted that bounce-off effect is prevalent even at smaller impact parameter [category (i)] though with reduced intensity. The big participant nuclear chunk experiences compression and as a result of fast randomization of longitudinal energy the excitation energy and the temperature are increased. The momentum distribution is also highly modified compared to large impact parameter collision. The high value of $\bar{\theta}_{\mathrm{PF}}$ in category (i) compared to categories (ii) and (iii) may be conjectured as due to the rescattering. According to Stocker *et al* [21] the heating effects may mask the collective motion and our data of $\overline{\Delta\Phi}$ also supports this e.g. events of category (i) correspond to high temperature $\tau \approx 31$ MeV $[\tau = (2/3) \times (E^*/A)]$ and smaller values of $\overline{\Delta\Phi}$ and R compared to events of category (iii) with temperature $\tau \approx 17$ MeV and values of $\overline{\Delta\Phi}$ and R being higher.

Acknowledgements

The author (BS) is grateful to the UGC and another author (HSP) to CSIR (New Delhi) for research fellowships. Thanks are also due to TWAS (ICTP, Italy) research grants. Authors are thankful to Prof. I. Otterlund (Sweden) for the emulsion stack.

Appendix

Fermi momentum, P_F and nucleon density, ρ of normal nuclear matter are related as,

$$P_F = [(3/2) \times (\hbar^3 \pi^2 \rho)]^{1/3}$$

or

$$P_F \propto \rho^{1/3}. \tag{A1}$$

According to Feshbach and Huang [22] momentum square average to the first approximation can be written in terms of Fermi-momentum square,

$$\langle P^2 \rangle = \frac{3}{5} P_F^2 \tag{A2}$$

and for a fragment of given mass, square of the width of the momentum distribution, σ^2 is shown [22, 23] to be proportional to $\langle P^2 \rangle$ i.e.

$$\sigma^2 \propto \langle P^2 \rangle. \tag{A3}$$

In this way σ^2 can be shown to vary with the nuclear density as follows,

$$\sigma^2 \propto \rho^{2/3}$$

or

$$\sigma \propto \rho^{1/3} \tag{A4}$$

It is well-known from the shock wave model of nuclear collisions [17] that at projectile energies 1 to 2 GeV/nucleon resonances affect the density of nuclear matter by an amount which is much smaller than the order of magnitude. Considering that at these energies during the compression nuclear matter does not lose its identity one can therefore make use of the relation (8) for estimating the nuclear density in terms of the width, σ of the projected momentum distribution as explained in the § 3·2.

References

[1] H A Gustafsson, H H Gutbrod, B Kolb, H Lohner, B Ludewigt, A M Poskanzer, T Renner, H Riedesel, H G Ritter, A Warwick, F Weik and H Wieman, *Phys. Rev. Lett.* **52**, 1590 (1984)

[2] H G Ritter, K G R Doss, H A Gustafsson, H H Gutbrod, K H Kampert, B Kolb, H Lohner, B Ludewigt, A M Poskanzer, A Warwick and H Wieman, *Nucl. Phys.* **A447**, 3C (1985)

[3] D Beavis, S Y Chu, S Y Fung, W Gorn, A Huie, D Keane, J J Lu, R T Poe, B C Shen and G Vandalen, *Phys. Rev.* **C27**, 2443 (1983)

[4] R E Renfordt, D Schall, R Bock, R Brockmann, J W Harris, A Sandoval, R Stock, H Strobele, D Bangert, W Rauch, G Odyniec, H G Pugh and L S Schroeder, *Phys. Rev. Lett.* **53**, 763 (1984)

[5] A Sandoval, R Stock, H E Stelzer, R E Renfordt, J W Harris, J P Brannigan, J V Geaga, L J Rosenberg, L S Schroeder and K J Wolf, *Phys. Rev. Lett.* **45**, 874 (1980)

[6] H G Baumgardt, J U Schoot, Y Sakamoto, E Schopper, H Stocker, J Hofmann, W Scheid and W Greiner, *Z. Phys.* **A273**, 359 (1975)

[7] H H Heckmann, Y J Karant and E M Friedlander, *Phys. Rev.* **C34**, 1333 (1986)

[8] R Arora and V Kumar *et al Z. Phys.* **A333**, 373 (1989)

[9] W Scheid, H Muller, M Greiner, *Phys. Lett.* **32**, 741 (1974)

[10] A A Amsden, G F Bertsch, F H Harlow and J R Nix, *Phys. Rev. Lett.* **35**, 905 (1975)

[11] J Cugnon and D L'Hote, *Nucl. Phys.* **A447**, 27C (1985)
J Cugnon *et al Phys. Rev.* **C35**, 861 (1987)
E Braun and Z Fraenkel, *Phys. Rev.* **C34**, 120 (1986)

[12] J Gosset, H H Gutbrod, W G Meyer, A M Poskanzer, A Sandoval, R Stocker and G D Westfall, *Phys. Rev.* **C16**, 629 (1977)

[13] H Stocker, G Buchwald, G Graebner, P Subramanian, J A Maruhn, W Greiner, B V Jacak and G D Westfall, *Nucl. Phys.* **A400**, 63C (1983)

[14] H S Palsania, B Singh, A Gill, V Kumar, K B Bhalla and S Lokanathan, *Mod. Phys. Lett.* **A6**, 2757 (1991)

[15] H Kallies *et al*, Private communication, Marburg University, Oct. (1989)

[16] H Stocker, M Gyulassy and J Boguta, *Phys. Lett.* **B103**, 269 (1981)

[17] H Stocker, J Hofmann, J A Maruhn and W Greiner, *First Workshop on ultra-relativistic nuclear collisions*, **LBL-8957**, 355 (1979)

[18] S E Koonin, *Phys. Rev. Lett.* **39**, 680 (1977)

[19] B Jakobsson, *Phys. Scr.* **17**, 491 (1978)

[20] Adamovich *et al*, *Phys. Rev.* **C40**, 66 (1989)

[21] H Stocker, M Gyulassy and J Boguta, *Phys. Lett.* **B103** 269 (1981)

[22] H Feshbach and K Huang, *Phys. Lett.* **B47**, 300 (1973)

[23] A S Goldhaber, *Phys. Lett.* **B53**, 306 (1974)

Pramana – journal of physics

Volume 41
1993

Published by The Indian Academy of Sciences
Bangalore 560 080

Pramana – journal of physics

Editor

R Nityananda

Raman Research Institute, Bangalore

Associate Editor

H R Krishnamurthy

Indian Institute of Science, Bangalore

Editorial Board

G S Agarwal, *University of Hyderabad, Hyderabad*
V Balakrishnan, *Indian Institute of Technology, Madras*
M Barma, *Tata Institute of Fundamental Research, Bombay*
P Chaddah, *Centre for Advanced Technology, Indore*
B M Deb, *Panjab University, Chandigarh*
P K Kaw, *Institute for Plasma Research, Gandhinagar*
H S Mani, *Indian Institute of Technology, Kanpur*
N Mukunda, *Indian Institute of Science, Bangalore*
T Padmanabhan, *Inter-University Centre for Astronomy and Astrophycs, Pune*
J C Parikh, *Physical Research Laboratory, Ahmedabad*
G Rajasekaran, *Institute of Mathematical Sciences, Madras*
V S Ramamurthy, *Institute of Physics, Bhubaneswar*
R Ramaswamy, *Jawaharlal Nehru University, New Delhi*
K R Rao, *Bhabha Atomic Research Centre, Bombay*
Probir Roy, *Tata Institute of Fundamental Research, Bombay*
A K Sood, *Indian Institute of Science, Bangalore*

Editor of Publications of the Academy

G Srinivasan
Raman Research Institute, Bangalore

Subscription Rates
(Effective from 1989)

All countries except India	1 year	3 years	5 years
(Price includes AIR MAIL charges)	US$ 175	$ 470	$ 700
India	1 year Rs. 100	10 years (1989–1998 only) Rs. 500	

All correspondence regarding subscription should be addressed to the **Circulation Department** of the Academy

Editorial Office

Indian Academy of Sciences, C V Raman Avenue,
P.B. No. 8005, Bangalore 560080, India

Telephone: 334 2546
Telex: 845-2178 ACAD IN
Telefax: 91-80-334 6094

© 1993 by the Indian Academy of Sciences. All rights reserved.

"Information for contributions" is printed in the last issue of every volume.

SUBJECT INDEX

General and Mathematical Physics

Underwater optical generation of sound: Oblique incidence
M S Sodha, V Rai, M P Verma, S Konar and K P Maheshwari 1–7

q-Deformation of algebraic structures of quantum and classical mechanics
Debendranath Sahoo and M C Valsakumar 123–137

Controlling of chaos by weak periodic perturbations in Duffing-van der Pol oscillator *S Rajasekar* 295–309

Quantum instability for a wave packet kicked periodically by a quadratic potential *A K Sikri and M L Narchal* 509–513

Uniqueness of the solutions of multichannel scattering equation
Suprokash Mukherjee 483–491

Energy levels of a two-dimensional anharmonic oscillator: Hill determinant approach *M R M Witwit* 493–502

Integration method for the Dirac equation
V. G Bagrov and V V Obukhov 503–507

Relativity and Gravitation

Inflation driven by energy and curvature dependent bulk viscosity
C Wolf 139–144

Statistical Physics

Dynamics of immiscible radial viscous fingering: A numerical study
Subir K Sarkar and David Jasnow 389–399

Particle Physics

Resolved photon processes *Manuel Drees and Rohini M Godbole* 83–123

Nuclear Physics

$^{6}_{\Lambda\Lambda}$He hypernucleus in $\alpha + 2\Lambda$ cluster model *Mahmood Mian* 145–149

Deutron-induced reactions studies of the nuclear structure of ^{178}Hf *Raymond K Sheline, Michael M Minor, Prakash C Sood and Dennis G Burke* 151–162

Neutron flow or collective degrees of freedom for near barrier heavy-ion fusion *S Kailas and A Navin* 163–169

Mathematical analysis of isobaric decay chain in alpha particle induced reactions *S Mukherjee, N L Singh and J Rama Rao* 311–327

Measurement and analysis of the excitation functions for alpha particle induced reactions on niobium *S Mukherjee, M H Rashid and S N Chintalapudi* 329–338

Sub-barrier fission fragment angular distributions for the system ^{19}F + ^{232}Th *S Kailas, A Navin, A Chatterjee, P Singh, A Saxena, D M Nadkarni, D C Biswas, R K Choudhury and S S Kapoor* 339–344

A semi-empirical formula for the energy spacings in Λ-hypernuclear excitation spectra *M Z Rahman Khan and Nasra Neelofer* 515–524

L-dependent heavy ion fusion potentials *S V S Sastry, A K Mohanty and S K Kataria* 525–534

Collective bounce-off phenomenon in ^{139}La + Ag(Br) reaction at 1.1 A GeV energy *B Singh, H S Palsania, V Kumar, K B Bhalla and S Lokanathan* 535–550

Atomic and Molecular Physics

Momentum space distribution of electrons in an atom using hydrogenic wave functions *Nazakat Ullah* 171–174

L shell/subshell ionization of Au, Pb and Bi by low energy proton impact *K N Pandey, D N Tripathi, R N Chakraborty and D K Rai* 175–184

Ab-initio Hartree-Fock self-consistent-field calculations—An indigenous development of computer programs *Sambhu N Datta* 345–362

Ab-initio nonrelativistic and relativistic Hartree-Fock calculations for both closed- and open-shell molecules using GTO basis *Sambhu N Datta* 363–370

Electron impact excitation of Ni XIX using the *R*-matrix method *Man Mohan, M Le Dourneuf, A Hibbert and V M Burke* 371–388

Lasers, Optics and Spectroscopy

Laser produced plasma: A pumping source for cadmium photoionization laser *Rekha Tambay and Raj K Thareja* 257–269

Heating mechanism in relation to the laser machining process
Bekir S Yilbas and Ahmet Z Sahin 453–465

SERS studies on 1–4 dihydroxyanthraquinone at Ag electrode
V G Srikanth, S Edwin Jayaraj and V Ramakrishnan 467–472

Plasma Physics

Kinetic properties of an acoustic-like mode in a two-ion quasi-neutral plasma *C B Dwivedi* 185–191

Condensed Matter Physics

Dielectric studies of some binary liquid mixtures using microwave cavity techniques *V Subramanian, B S Bellubbi and J Sobhanadri* 9–20

Effect of strain on vibrational modes in strained layer superlattices
Sujata Rath and Sankar P Sanyal 21–29

Second order elastic anomalies in barium titanate from cubic to tetragonal phase transition *B Subramanyam and K S Viswanathan* 31–39

The effect of second neighbour repulsion on fcc binary alloy phase diagrams: A Monte Carlo study *Rita Khanna and T R Welberry* 41–49

Field-cooled measurements of harmonic generation in magnetization of high T_c superconductors *S B Roy, Shailendra Kumar, A K Pradhan, P Chaddah, Ram Prasad, N C Soni and Kalyan Adhikary* 51–60

Critical current density of a sample of melt grown $Y_{1\cdot2}Ba_{1\cdot8}Cu_{2\cdot4}O_x$
V Ganesan, R Srinivasan, R Gopalan and T Rajasekaran 61–66

Electronic structure of a superconducting Bi2212 crystal by angle resolved ultra violet photoemission *N L Saini, J Kanski, P Srivastava, L Ilver, K B Garg and S Durock* 67–73

Anomalies in second order elastic constants and gyrotropic constants of triglycine sulphate near phase transition
B Subramanyam and K S Viswanathan 203–208

Surface acoustic wave distribution and acousto-optic interaction in proton exchanges $LiNbO_3$ waveguides
P Annachelvi, A Selvarajan and G V Anand 209–217

Switching of partially switched $KNbO_3$ single crystals containing cooperatively ordered impurity dipoles *S G Ingle and R N Kakde* 219–232

Investigations on thermoelectric power of lanthanum oxide doped ferroelectric sodium vanadate *D V Pawar, T S Magdum, S P Rasal and S H Chavan* 233–237

Electronic structure of hydrogen and muonium in Al, Mg and Cu *Pawan Singh and S Prakash* 239–255

A model for the analysis of the heat release from a supercooled liquid at the glass transition *M Rajeswari and A K Raychaudhuri* 401–419

Thermal expansion of orthorhombic and tetragonal phases of the high T_c superconductors $Re_1Ba_2Cu_3O_y$ (RE = Y, Gd, Dy) *Om Prakash, Ashok Rao, O Prakash and P N Dheer* 421–428

Magnetic properties of ultra-fine particles of $Mn_{0.5}Fe_{0.5}Fe_2O_4$ spinel system *R V Upadhyay and R V Mehta* 429–442

Electric field gradient in transition metal—scandium *B B Panigrahi and N C Mohapatra* 443–451

Experimental Techniques and Instrumentation

A translational energy spectrometer to probe interatomic potentials: Dissociation dynamics of CO_2^+ ions *M Krishnamurthy, U T Raheja and D Mathur* 271–283

A design of an inexpensive demountable X-ray tube *V S Pai, N V Moghe and V B Sapre* 473–477

Rapid Communications

Symmetry breaking in quantum chaotic systems *Akhilesh Pandey, Ramakrishna Ramaswamy and Pragya Shukla* L75–L81

Conservation laws in stochastic deposition-evaporation models in one dimension *Deepak Dhar and Mustansir Barma* L193–L198

Influence of various gases on single bubble sonoluminescence *Vijay H Arakeri* L291–L294

Geometric phase as a simple closed-form integral *Apoorva G Wagh and Veer Chand Rakhecha* L479–L481

Comments

Comment on: Modified perturbation series for the anharmonic oscillator using linearization technique *Biswanath Rath and K Pattnayak* C199–C200

Reply to the comment on 'Modified perturbation series for the anharmonic oscillator using linearization technique' *Nazakat Ullah* C201–C202

Brief Report

Further studies on Ag/BPSCCO tapes using low purity materials
S R Shukla, Y S Reddy, N Kumar, S K Sharma and R G Sharma 285–289

AUTHOR INDEX

Adhikary Kalyan
  see Roy S B 51
Anand G V
  see Annachelvi P 209
Annachelvi P
  Surface acoustic wave distribution and acousto-optic interaction in proton exchanges $LiNbO_3$ waveguides 209
Arakeri Vijay H
  Influence of various gases on single bubble sonoluminescence L291

Bagrov V G
  Integration method for the Dirac equation 503
Barma Mustansir
  see Dhar Deepak L193
Bellubbi B S
  see Subramanian V 9
Bhalla K B
  see Singh B 535
Biswas D C
  see Kailas S 339
Burke Dennis G
  see Sheline Raymond K 151
Burke V M
  see Man Mohan 371

Chaddah P
  see Roy S B 51
Chakraborty R N
  see Pandey K N 175
Chatterjee A
  see Kailas S 339
Chavan S H
  see Pawar D V 233
Chintalapudi S N
  see Mukherjee S 329
Choudhury R K
  see Kailas S 339

Datta Sambhu N
  Ab-initio Hartree-Fock self-consistent-field calculations—An indigenous development of computer programs 345
  Ab-initio nonrelativistic and relativistic Hartree-Fock calculations for both closed- and open-shell molecules using GTO basis 363
Dhar Deepak
  Conservation laws in stochastic deposition-evaporation models in one dimension L193
Dheer P N
  see Prakash Om 421
Dourneuf M Le
  see Man Mohan 371
Drees Manuel
  Resolved photon processes 83
Durock S
  see Saini N L 67
Dwivedi C B
  Kinetic properties of an acoustic-like mode in a two-ion quasi-neutral plasma 185

Ganesan V
  Critical current density of a sample of melt grown $Y_{1\cdot 2}Ba_{1\cdot 8}Cu_{2\cdot 4}O_6$ 61
Garg K B
  see Saini N L 67
Godbole Rohini M
  see Drees Manuel 83
Gopalan R
  see Ganesan V 61

Hibbert A
  see Man Mohan 371

Ilver L
  see Saini N L 67
Ingle S G
  Switching of partially switched $KNbO_3$ single crystals containing cooperatively ordered impurity dipoles 219

Jasnow David
  see Sarkar Subir K 389
Jayaraj S Edwin
  see Srikanth V G 467
Kailas S
  Neutron flow or collective degrees of freedom for near barrier heavy-ion fusion 163
  Sub-barrier fission fragment angular distributions for the system $^{19}F + ^{232}Th$ 339

Kakde R N
see Ingle S G 219
Kanski J
see Saini N L 67
Kapoor S S
see Kailas S 339
Kataria S K
see Sastry S V S 525
Khanna Rita
The effect of second neighbour repulsion on fcc binary alloy phase diagrams: A Monte Carlo study 41
Konar S
see Sodha M S 1
Krishnamurthy M
A translational energy spectrometer to probe interatomic potentials: Dissociation dynamics of CO_2 ions 271
Kumar N
see Shukla S R 285
Kumar Shailendra
see Roy S B 51
Kumar V
see Singh B 535

Lokanathan S
see Singh B 535

Magdum T S
see Pawar D V 233
Maheshwari K P
see Sodha M S 1
Man Mohan
Electron impact excitation of Ni XIX using the *R*-matrix method 371
Mathur D
see Krishnamurthy M 271
Mehta R V
see Upadhyay R V 429
Mian Mahmood
${}^{6}_{\Lambda\Lambda}$He hypernucleus in $\alpha + 2\Lambda$ cluster model 145
Minor Michael M
see Sheline Raymond K 151
Moghe N V
see Pai V S 473
Mohanty A K
see Sastry S V S 525
Mohapatra N C
see Panigrahi B B 443
Mukherjee S
Mathematical analysis of isobaric decay chain in alpha particle induced reactions 311
Mukherjee S
Measurement and analysis of the excitation functions for alpha particle induced reactions on niobium 329
Mukherjee Suprokash
Uniqueness of the solutions of multichannel scattering equation 483

Nadkarni D M
see Kailas S 339
Narchal M L
see Sikri A K 509
Navin A
see Kailas S 163, 339
Neelofer Nasra
see Khan Rahman M Z 515

Obukhov V V
see Bagrov V G 503

Pai V S
A design of an inexpensive demountable X-ray tube 473
Palsania H S
see Singh B 535
Pandey Akhilesh
Symmetry breaking in quantum chaotic systems L75
Pandey K N
L shell/subshell ionization of Au, Pb and Bi by low energy proton impact 175
Panigrahi B B
Electric field gradient in transition metal—scandium 443
Pattnayak K
see Rath Biswanath C199
Pawar D V
Investigations on thermoelectric power of lanthanum oxide doped ferroelectric sodium vanadate 233
Pradhan A K
see Roy S B 51
Prakash O
see Prakash Om 421
Prakash Om
Thermal expansion of orthorhombic and tetragonal phases of the high T_c superconductors $Re_1Ba_2Cu_3O_y$ (RE = Y, Gd, Dy) 421
Prakash S
see Singh Pawan 239
Prasad Ram
see Roy S B 51

Raheja U T
see Krishnamurthy M 271
Rahman Khan M Z
A semi-empirical formula for the energy spacings in Λ-hyper-nuclear excitation spectra 515

Rai D K
see Pandey K N 175
Rai V
see Sodha M S 1
Rajasekar S
Controlling of chaos by weak periodic perturbations in Duffing-van der Pol oscillator 295
Rajasekaran T
see Ganesan V 61
Rajeswari M
A model for the analysis of the heat release from a supercooled liquid at the glass transition 401
Rakhecha Veer Chand
see Wagh Apoorva G 479
Ramakrishnan V
see Srikanth V G 467
Ramaswamy Ramakrishna
see Pandey Akhilesh L75
Rao Ashok
see Prakash Om 421
Rao J Rama
see Mukherjee S 311
Rasal S P
see Pawar D V 233
Rashid M H
see Mukherjee S 329
Rath Biswanath
Comment on: Modified perturbation series for the anharmonic oscillator using linearization technique C199
Rath Sujata
Effect of strain on vibrational modes in strained layer superlattices 21
Raychaudhuri A K
see Rajeswari M 401
Reddy Y S
see Shukla S R 285
Roy S B
Field-cooled measurements of harmonic generation in magnetization of high T_c superconductors 51

Sahin Ahmed Z
see Yilbas Bekir S 453
Sahoo Debendranath
q-Deformation of algebraic structures of quantum and classical mechanics 125
Saini N L
Electronic structure of a superconducting Bi2212 crystal by angle resolved ultra violet photoemission 67
Sanyal Sankar P
see Rath Sujata 21
Sapre V B
see Pai V S 473
Sarkar Subir K
Dynamics of immiscible radial viscous fingering: A numerical study 389
Sastry S V S
L-dependent heavy ion fusion potentials 525
Saxena A
see Kailas S 339
Selvarajan A
see Annachelvi P 209
Sharma R G
see Shukla S R 285
Sharma S K
see Shukla S R 285
Sheline Raymond K
Deutron-induced reactions studies of the nuclear structure of ^{178}Hf 151
Shukla Pragya
see Pandey Akhilesh L75
Shukla S R
Further studies on Ag/BPSCCO tapes using low purity materials 285
Sikri A K
Quantum instability for a wave packet kicked periodically by a quadratic potential 509
Singh B
Collective bounce-off phenomenon in ^{139}La + Ag(Br) reaction at 1.1 A GeV energy 535
Singh N L
see Mukherjee S 311
Singh P
see Kailas S 339
Singh Pawan
Electronic structure of hydrogen and muonium in Al, Mg and Cu 239
Sobhanadri J
see Subramanian V 9
Sodha M S
Underwater optical generation of sound: Oblique incidence 1
Soni N C
see Roy S B 51
Sood Prakash C
see Sheline Raymond K 151
Srikanth V G
SERS studies on 1–4 dihydroxyanthraquinone at Ag electrode 467
Srinivasan R
see Ganesan V 61
Srivastava P
see Saini N L 67
Subramanian V
Dielectric studies of some binary liquid mixtures using microwave cavity techniques 9

Subramanyam B
  Second order elastic anomalies in barium titanate from cubic to tetragonal phase transition 31
  Anomalies in second order elastic constants and gyrotropic constants of triglycine sulphate near phase transition 203

Tambay Rekha
  Laser produced plasma: A pumping source for cadmium photo-ionization laser 257
Thareja Raj K
  see Tambay Rekha 257
Tripathi D N
  see Pandey K N 175

Ullah Nazakat
  Momentum space distribution of electrons in an atom using hydrogenic wave functions 171
  Reply to the comment on ‘Modified perturbation series for the anharmonic oscillator using linearization technique’ C201
Upadhyay R V
  Magnetic properties of ultra-fine particles of $Mn_{0\cdot5}Fe_{0\cdot5}Fe_2O_4$ spinel system 429

Valsakumar M C
  see Sahoo Debendranath 125
Verma M P
  see Sodha M S 1
Viswanathan K S
  see Subramanyam B 31
  see Subramanyam B 203

Wagh Apoorva G
  Geometric phase as a simple closed-form integral 479
Welberry T R
  see Khanna Rita 41
Witwit M R M
  Energy levels of a two-dimensional anharmonic oscillator: Hill determinant approach 493
Wolf C
  Inflation driven by energy and curvature dependent bulk viscosity 139

Yilbas Bekir S
  Heating mechanism in relation to the laser machining process 453